PSL UNIVERSITÉ PARIS

THÈSE DE DOCTORAT
DE L'UNIVERSITÉ PSL

Préparée à Mines Paris - PSL

Triplet tribologique de la lubrification limite : influence des nanoparticules de TiO_2, des revêtements cold spray composites et d'un courant électrique sur les performances des additifs limites.

Tribological Triplet of Boundary Lubrication: Influence of TiO_2 Nanoparticles, Composite Cold-Spray Coatings, and Electric Current on the Performance of Boundary Additives.

Soutenue par
Adam NASSIF
Le 15 janvier 2026

Dirigée par
Pierre MONTMITONNET

Co-dirigée par
Imène LAHOUIJ
Frédéric GEORGI

École doctorale n° 364
Sciences Fondamentales et Appliquées

Spécialité
Mécanique Numérique et Matériaux

Composition du jury :

Pierre-Henri CORNUAULT Professeur des Universités, HDR Femto-ST Besançon	*Président*
Fabrice DASSENOY Professeur des Universités, HDR Ecole Centrale de Lyon	*Rapporteur*
Cécile LANGLADE Professeure des Universités, HDR Université de Technologie de Belfort-Montbéliard	*Rapporteure*
Karl DELBE Maître de conférences, HDR Ecole Nationale d'Ingénieurs de Tarbes	*Examinateur*
Imène LAHOUIJ Chargée de recherche Mines Paris CEMEF	*Examinatrice*
Pierre MONTMITONNET Directeur de Recherches émérite CNRS, HDR Mines Paris CEMEF	*Directeur de thèse*

MINES PARIS | PSL

TABLE OF CONTENTS

TABLE OF CONTENTS **2**
Remerciements **6**
Introduction **10**
Chapter 1: Literature Review **14**
1.1 Tribology 15
1.2 Lubricating Oils 17
1.2.1 Generalities on Oil-based Lubricants Composition 17
1.2.2 Lubrication Regimes 19
1.2.3 Transmission Oils 20
1.3 Boundary Lubrication Additives 21
1.3.1 Anti-Wear (AW) Additive: Zinc Dialkydithiophosphate (ZDDP) 22
1.3.2 Friction Modifier (FM) Additive: Molybdene Dithiocarbamate (MoDTC) 26
1.3.3 Nanoparticles as Tribological Additives 29
1.3.4 Tribological Interaction between "Traditional Additives" and Nanoparticles 34
1.4 Coatings for Tribological Applications 37
1.4.1 Designing Coatings for Tribological Applications 37
1.4.2 Cold Spray Coatings Background and Principle 40
1.4.3 Cold Spray Coatings in Lubricated Applications 43
1.5 New Challenges Brought by Electrification of Vehicles 47
1.5.1 Increased Stress in the Drivetrain System 47
1.5.2 Wear and Friction under Electrified Conditions 51
1.5.3 Effect of Electrification on Tribological Additives Performance 55
Conclusion 58
Current State of the Art and Research Gaps 60
Bibliography 61
Chapter 2: Materials and Methods **68**
2.1 Base oil, Tribological Additives and Nanoparticles 69
2.1.1 Traditional Boundary Additives 69
2.1.2 TiO_2 Nanoparticles and Stabilizing Methods 70
2.1.3 Blends preparation 72
2.1.4 Blends stability 73
2.2 Tribological testing setup 74

2.2.1 Linear Ball-on-Disc Tribometer 74
2.2.2 Electrified Tribometer Setup 76
2.2.3 Ball and Disc Samples Preparation 82
2.3 Characterization techniques 83
2.3.1 Tribofilm and wear characterization 83
2.4 Cold spray coating 85
2.4.1 Substrate Surface Preparation 86
2.4.2 Cold Spray Coatings Deposition 88
2.4.3 Cold Spray Coatings Characterization 98
Conclusion 102
Bibliography 103
Chapter 3: Synergy between Traditional Additives and TiO_2 nanoparticles 106
3.1 Lubricating Properties of TiO_2 Nanoparticles 108
3.1.1 Effect of the Dispersion Method on Tribological Performance: The Case of Oleic Acid 109
3.1.2 Influence of Functionalizing Agent Chemical Nature: Oleic Acid vs Silane 121
3.2 Interactions Between Nanoparticles and Conventional Lubricant Additives 142
3.2.1 Synergetic Interactions Between MoDTC and TiO_2 142
3.2.1.1 Synergistic Interaction Between MoDTC and unmodified TiO_2 Nanoparticles 142
3.2.1.2 Influence of Functionalizing Agent Chemical Nature on the Synergistic Effects Between MoDTC and TiO_2 Nanoparticles 152
3.2.2 Interactions Between ZDDP and TiO_2 159
3.2.2.1 Influence of the Dispersion Method on the Interactions Between ZDDP and TiO_2 Nanoparticles 159
3.2.2.2 Influence of Functionalizing Agent Chemical Nature on the Interactions Between ZDDP and TiO_2 Nanoparticles 177
3.2.2.2.1 Comparison between oleic- and silane-functionalized TiO_2 nanoparticles blended with ZDDP for enhanced tribological performance. 177
3.2.2.2.2 Tribofilm growth rate study through intermediate cycle testing for silane functionalized TiO_2 nanoparticles and ZDDP blend. 184
Conclusion and Perspectives 201
Bibliography 203
Chapter 4: Cold Sprayed Ti/TiO_x Composite Coatings: from Elaboration to Tribological Properties 205
4.1 Elaboration of the Titanium Matrix Coating 207
4.1.1 Enhancing Interfacial Adhesion with the Substrate 207
4.1.2 Influence of Deposition Parameters on Coating Properties 222

4.2 Optimization of a Ti/TiO_x Composite Cold Spray Coating 234
4.2.1 Influence of Matrix Powder Type on Composite Coatings Characteristics 234
4.2.2 Optimized Cold Spray Composite Coating 241
4.2.2.1 Mechanical and Morphological Characterization of the Coatings 241
4.2.2.2 Coatings Tribological Properties 243
4.2.2.2.1 Composite Cold spray coating performance with a fully formulated gear oil 243
4.2.2.2.2 Tribological properties of composite Cold spray coating lubricated with ZDDP additive 248
4.2.2.2.3 Tribological properties of composite Cold spray coating lubricated with MoDTC additive 257
Conclusion and Perspectives 262
Bibliography 264
Chapter 5: Effects of Electric Current on the Tribological Performance of Boundary Additives 265
5.1 Effect of Electrical Current on Tribofilm Formation 268
5.1.1 Effect of Current on ZDDP Tribofilm Formation 268
5.1.2 Effect of Current on Silane-functionalized TiO_2 Nanoparticles Tribofilm Formation 280
5.1.3 Effect of Current on the lubricating properties of ZDDP / Silane-functionalized TiO_2 Nanoparticles Blend 291
5.2 Durability of Tribofilms under Electrified Tribological Conditions 301
5.2.1 Effect of Current on the Durability of ZDDP Tribofilm 301
5.2.2 Effect of Current on the Durability of a Tribofilm Formed by a blend of ZDDP and Silane-functionalized TiO_2 Nanoparticles 311
Conclusion and Perspectives 330
Bibliography 331
General Conclusion 332
Perspectives 338

Remerciements

Je me souviens encore avoir annoncé à maintes reprises que je ne ferais pas de thèse après avoir fini mon parcours en école d'ingénieur. Et pour cause : je souhaitais rencontrer des problèmes concrets, les étudier et les résoudre. Je me faisais donc une fausse idée de ce que pouvait être une thèse, puisqu'après trois ans je peux dire que cette description est plutôt en accord avec le travail que j'ai réalisé. Je ne regrette donc aucunement de m'être lancé, et surtout d'avoir été accompagné par mes encadrants, qui ont su m'orienter, me corriger et me féliciter le moment venu.

Merci à Imène de m'avoir accompagné au cours de ces trois ans, d'avoir su maintenir le cap de cette aventure et d'avoir mis tous les moyens en œuvre pour qu'elle se déroule au mieux. Je garde un excellent souvenir de tous nos échanges car, étant tous deux têtus, cela nous a souvent amenés à confronter nos idées, ce qui nous a poussés à consolider nos hypothèses et à les faire grandir. Ton leadership a été exemplaire, tantôt à l'écoute de mes idées et de mes besoins, tantôt ferme pour maintenir le niveau scientifique élevé qui se reflète au travers de ce manuscrit et de nos publications passées et à venir.

Merci à Frédéric de m'avoir formé à l'utilisation des techniques d'analyses avancées, que ce soit le profilomètre, le MEB, l'EDX, l'XPS et bien d'autres encore. Merci pour tes enseignements rigoureux, que ce soit dans la préparation des échantillons et des mesures ou dans le traitement des données. Merci également d'avoir été un soutien inconditionnel au cours de ces trois ans, pour ton oreille attentive et ta bonne humeur.

Merci à Pierre pour ton immense savoir, qui t'a permis de nous donner des conseils toujours pertinents sur les différentes problématiques que nous avons pu rencontrer. Merci pour ton savant mélange de curiosité, de rigueur scientifique et de réalisme pratique, qui nous a permis de nous poser les bonnes questions sans nous éloigner des objectifs de cette thèse.

Encore une fois, merci à vous trois. Vous formez une équipe formidable, chacun apportant son expertise, ce qui est primordial dans un domaine aussi pluridisciplinaire que la tribologie. Cela a été un réel plaisir de travailler avec vous et j'espère que d'autres occasions se représenteront. Finalement, au-delà de votre excellence scientifique, le maître mot qui vous rassemble selon moi, et que j'ai pu ressentir durant cette thèse est la bienveillance. Merci pour tout.

Je souhaite également remercier tous ceux qui m'ont permis d'avancer aussi loin : Cyrille, pour parfaire ma maîtrise du MEB et du polissage des échantillons ; Erick et Marc, que je n'ai pas arrêté d'embêter pour fabriquer mes pièces mais qui m'ont aussi beaucoup appris sur l'usinage ; Guillaume, qui a eu la bonne idée de m'introduire au gouffre temporel que représentent les projets Arduino ; Gilbert, avec qui je me suis davantage enfoncé dans ce gouffre, mais qui a surtout toujours été là pour m'aider sur mes montages, mes pannes ou tout simplement pour discuter ; Christophe, qui a toujours un café à la main, une bonne blague à raconter et un rire contagieux, mais qui possède surtout des connaissances et une expérience pratique qui lui donnent une agilité scientifique impressionnante. Enfin, merci à Serge, en quelque sorte mon mentor en conception mécanique, qui m'a donné les bases pour entreprendre et réaliser des assemblages dignes de ce nom : toujours à l'écoute, toujours de bonnes idées et toujours très pédagogue.

Merci à Cynthia pour ta gentillesse et ta bonne humeur, ça a toujours été un plaisir de discuter avec toi et je ne m'inquiète pas concernant la réussite de ta thèse. De même, merci à toi Zhengyuan, pour ta gentillesse, ta fiabilité et ta résilience qui, par résonance, m'ont permis de donner le meilleur de moi-même pour cette thèse.

Évidemment, je souhaite remercier ma famille : ma mère, qui m'a toujours soutenu dans tous les projets que j'ai pu entreprendre et qui continue de le faire ; mon père, qui m'a donné le goût de la minutie dans les tâches manuelles, ce qui m'a permis d'allier connaissances théoriques et pratiques. Merci à mes frères d'avoir toujours été là pour moi et de continuer à le faire. Et enfin, merci à ma compagne, qui a su me soutenir et m'épauler dans cette aventure, et qui a même garanti le succès de ma soutenance en réalisant le superbe design des slides de présentation.

Introduction

In the global effort toward sustainability, energy efficiency, and technological reliability, **tribology - the study of friction, wear, and lubrication** - plays a decisive yet often underestimated role. According to the analyses conducted by Holmberg *et al.* (2017) [1], nearly **23% of the world's total energy consumption** is lost through tribological contacts in engines, transmissions, and industrial machinery. Improvements in friction control and wear mitigation could therefore yield substantial environmental and economic benefits by reducing fuel consumption, extending component lifetime, and enabling the transition toward more efficient technologies.

Over the past decades, tribology has traditionally been approached through the **interaction between two primary elements**: the **surfaces in contact** and the **lubricant** that separates them. These two components have been the focus of most scientific and industrial efforts to control friction and wear. Within this framework, various lubrication regimes have been identified, ranging from full-film hydrodynamic lubrication to the most demanding **boundary lubrication**, where the fluid film is extremely thin and the load is largely borne by surface asperities. In such conditions, the protection of the surfaces relies predominantly on **boundary additives**, such as **anti-wear agents** (e.g., zinc dialkyldithiophosphate, ZDDP) and **friction modifiers** (e.g., molybdenum dithiocarbamate, MoDTC). These additives promote the formation of tribofilm that limit direct contact between asperities and thereby control friction and wear [2].

However, as operating conditions become increasingly severe and environmental regulations more stringent, traditional additive formulations are reaching their performance and sustainability limits. The growing demand for higher efficiency and reduced emissions has prompted the exploration of new lubrication strategies capable of extending the performance of conventional boundary additives. Among the proposed approaches, **nanoparticles**, and in particular **metal oxide nanoparticles such as TiO_2**, have emerged as promising candidates [3–5]. These nano-additives can enhance tribological performance through mechanisms such as rolling, mending, or catalytic effects that promote tribofilm formation. Nevertheless, their **stability** in liquid medium remains a critical challenge, as it strongly limits their tribological performance. Recent studies, however, suggest that **synergistic effects** may arise between nanoparticles and conventional boundary additives [6] [7], opening new perspectives for **hybrid lubrication systems** with enhanced surface protection under boundary conditions. The **efficiency of this synergy** appears to be closely related to the **stabilization state of the nanoparticles**, which influences their availability, reactivity, and interaction with additive-derived tribofilms. This aspect will therefore be specifically considered in the present study, which **aims to elucidate the mechanisms governing the interactions between nanoparticles and traditional boundary additives.**

On the **surface side**, tribological optimization is often achieved through the application of **coatings** that tailor the chemical and mechanical properties of contact interfaces. This strategy enables the use of lightweight or easily machinable bulk materials while maintaining high surface durability. Recent advances in deposition technologies, such as **Cold spray process**, have made it possible to design **composite coatings** that combine the toughness of metals with the hardness of ceramics. The Cold spray technique was selected for its ability to deposit materials in the solid state, **without melting**, thereby preserving their intrinsic properties while ensuring strong adhesion to the substrate [8,9]. In such systems, the **ductile metallic matrix** - in our case titanium - ensures coating cohesion, while the **hard ceramic reinforcement phase** - titanium oxide (TiO_x) - provides enhanced wear resistance and improved tribological performance under boundary lubrication conditions.

However, an important question arises regarding the **chemical compatibility of such coatings with conventional boundary additives**, which are generally formulated to react preferentially with **ferrous surfaces**. Understanding how these additives interact with non-ferrous and composite surfaces is therefore essential to assess their effectiveness and to guide the development of coating-lubricant combinations optimized for boundary lubrication.

In parallel with these advances, the rapid **rise of electric vehicles (EVs)** is profoundly transforming the landscape of mechanical and lubrication engineering. Electric drivetrains operate under conditions that differ significantly from those of conventional internal combustion engines: they deliver **high torque at very low rotational speeds** while being capable of reaching up to **20 000 rpm**. To ensure high efficiency across this wide operating range and to minimize energy losses, manufacturers increasingly rely on **ultra-low-viscosity lubricants**. Although this approach contributes to improved energy efficiency, it also **increases the severity of tribological contacts**, thereby raising the risk of **premature surface degradation** under boundary lubrication conditions. These considerations further emphasize the need for more efficient lubrication solutions capable of ensuring reliable surface protection. [10]

Beyond these mechanical and lubrication constraints, **electrified systems introduce new physicochemical phenomena** associated with the presence of **stray electrical currents** at tribological interfaces. Such currents can induce **localized electrochemical reactions**, alter the **decomposition and reactivity of lubricant additives**, and modify the **kinetics and composition of protective tribofilms**. Consequently, the **influence of electric current on friction, wear, and surface chemistry** has emerged as a major research focus for ensuring the reliability and durability of **next-generation electrified systems**.

These considerations highlight that tribological systems can no longer be described solely by the traditional pair of surfaces and lubricant. Instead, they must now be understood as **multiphysical and multicomponent systems**, where electrical, mechanical, and chemical phenomena coexist and interact. To address this complexity, the present work investigates the concept of the **Tribological Triplet of Boundary Lubrication,** which encompasses three interrelated components:

1. The **lubricant**.
2. The **surface**.
3. The **electrified environment.**

The central objective of this thesis is to **investigate the interactions within this tribological triplet** and to elucidate how the combined effects of these three elements influence friction, wear, and tribofilm formation under boundary lubrication conditions. Through this integrative approach, the work aims to contribute to a deeper understanding of **electrified boundary lubrication systems** and to provide insights relevant for the design of durable and efficient tribological interfaces in emerging industrial applications.

The manuscript is organized into five chapters, each addressing a specific aspect of the research and contributing to the overall understanding of tribological performance improvement under boundary and electrified conditions:

Chapter 1 – Literature Review: This chapter provides a review of the scientific background related to tribology, lubricant formulation, and tribological coatings. It highlights the current understanding of additive mechanisms, the potential of nanoparticles as tribological agents, and the emerging challenges brought by vehicle electrification. Furthermore, it presents the different types of coatings designed for tribological applications, with particular emphasis on those developed using the Cold spray technique.

Chapter 2 – Materials and Methods: This section details the experimental procedures used throughout the thesis, including the preparation and stabilization of lubricant blends, tribological testing protocols under conventional and electrified conditions, and the elaboration and characterization of cold sprayed coatings.

Chapter 3 – Synergy between Traditional Additives and TiO_2 Nanoparticles: This chapter investigates the tribological behavior of TiO_2 nanoparticles alone and in combination with conventional additives such as MoDTC and ZDDP. The results reveal the mechanisms of synergy and competition governing their interactions and their impact on friction and wear performance.

Chapter 4 – Cold Sprayed Ti/TiO_x Composite Coatings: from Elaboration to Tribological Properties: This chapter primarily focuses on the elaboration and optimization of titanium-based composite coatings produced by the Cold Spray technique. It investigates the influence of processing parameters on the physical and mechanical properties of the resulting coatings, as well as their adhesion to the substrate. The last section discusses the tribological performance of the coatings under lubricated contact.

Chapter 5 – Effects of Electric Current on the Tribological Performance of Boundary Additives: The final chapter analyzes how electrical currents influence the formation, composition, and durability of tribofilms generated by traditional additives and nanoparticles. It provides key insights into tribological mechanisms under electrified boundary conditions relevant to modern electric drivetrains.

A **general conclusion** then summarizes the major findings and outlines **perspectives** for future research and industrial applications.

Bibliography

[1] Holmberg K, Erdemir A. Influence of tribology on global energy consumption, costs and emissions. Friction 2017;5:263–84. https://doi.org/10.1007/s40544-017-0183-5.

[2] Spikes H. The History and Mechanisms of ZDDP. Tribology Letters 2004;17:469–89. https://doi.org/10.1023/B:TRIL.0000044495.26882.b5.

[3] Dassenoy F, Jenei IZ, Pavan S, Galipaud J, Thersleff T, Wieber S, Hagemann M, Ness D. Performance and Lubrication Mechanism of New TiO_2 Nanoparticle-Based High-Performance Lubricant Additives. Tribology Transactions 2021;64:325–40. https://doi.org/10.1080/10402004.2020.1838678.

[4] Zhang L, Chen L, Wan H, Chen J, Zhou H. Synthesis and Tribological Properties of Stearic Acid-Modified Anatase (TiO_2) Nanoparticles. Tribol Lett 2011;41:409–16. https://doi.org/10.1007/s11249-010-9724-z.

[5] Bogunovic L, Zuenkeler S, Toensing K, Anselmetti D. An Oil-Based Lubrication System Based on Nanoparticular TiO_2 with Superior Friction and Wear Properties. Tribol Lett 2015;59:29. https://doi.org/10.1007/s11249-015-0557-7.

[6] Sharma V, Timmons RB, Erdemir A, Aswath PB. Synergistic and antagonistic interaction between ZDDP and TiO_2 nanoparticles under boundary lubrication. Tribology International 2025;202:110299. https://doi.org/10.1016/j.triboint.2024.110299.

[7] Deshpande P, Dassenoy F, Minfray C, Jenei IZ, Le Mogne Th, Thiebaut B. Effect of Adding TiO2 Nanoparticles to a Lubricant Containing MoDTC on the Tribological Behavior of Steel/Steel Contacts Under Boundary Lubrication Conditions. Tribol Lett 2020;68:39. https://doi.org/10.1007/s11249-020-1278-0.

[8] Hussain T. Cold Spraying of Titanium: A Review of Bonding Mechanisms, Microstructure and Properties. KEM 2012;533:53–90. https://doi.org/10.4028/www.scientific.net/KEM.533.53.

[9] Assadi H, Kreye H, Gärtner F, Klassen T. Cold spraying – A materials perspective. Acta Materialia 2016;116:382–407. https://doi.org/10.1016/j.actamat.2016.06.034.

[10] Van Rensselar J. Lubrication and tribology trends and challenges in electric vehicles. Society of Tribologists and Lubrication Engineers - STLE 2020. https://www.stle.org/files/TLTArchives/2020/07_July/Webinars.aspx (accessed July 1, 2025).

Chapter 1: Literature Review

Résumé en français :

Ce premier chapitre expose les fondements nécessaires à la compréhension des phénomènes tribologiques en contact lubrifié. Il présente d'abord la composition générale des huiles de lubrification, les différents régimes de lubrification, ainsi que le rôle d'additifs tribologiquement actifs tels que le MoDTC et le ZDDP. La recherche de solutions toujours plus performantes conduit ensuite à envisager l'utilisation de nanoparticules comme alternative potentielle aux additifs conventionnels. Bien que ces dernières présentent de bonnes performances en termes de réduction du frottement et de l'usure, leur utilisation se heurte à des limitations liées à la stabilité des suspensions. La littérature récente met toutefois en évidence des synergies prometteuses entre additifs traditionnels et nanoparticules : utilisés conjointement, ils peuvent offrir de meilleures performances tribologiques ainsi qu'une stabilité colloïdale accrue. Ces aspects constituent la base de connaissance nécessaire à l'interprétation des résultats présentés dans le Chapitre 3 concernant l'étude des nanoparticules de TiO_2, utilisées seules ou en mélange avec le MoDTC ou le ZDDP.

Une autre piste d'amélioration est présentée au travers de l'utilisation de revêtements dans le but de modifier les interactions entre les surfaces en contact. Un accent est mis sur le procédé Cold spray qui permet d'obtenir des revêtements composites avec peu ou pas de modification microstructurale de par la relativement faible température de projection. Cette partie sert de référence aux résultats présentés dans le Chapitre 4 dans lequel des revêtements formés de titane seul ou d'un mélange titane/TiOx (métal/céramique) déposé par Cold spray sont étudiés.

Enfin, l'enjeu de l'électrification des véhicules est abordé à travers plusieurs articles mettant en évidence son impact négatif sur les performances tribologiques. Cet impact peut être d'origine mécanique - notamment en raison de couples moteurs plus élevés à basse vitesse - mais également électrique, la présence de courants parasites pouvant provoquer des phénomènes d'arcing, un échauffement par effet Joule ou encore des réactions d'oxydation. Ces observations établissent un lien direct avec le Chapitre 5, qui étudie l'influence de l'application d'un courant électrique sur les performances tribologiques d'additifs pris individuellement ou en mélange.

1.1 Tribology

Tribology encompasses the entire field of friction, wear, and lubrication science and is generally defined as *"the study of interacting surfaces in relative motion"*. It integrates mechanical, chemical, and materials science perspectives to understand and optimize surface contact phenomena. [1]

Improving current tribological solutions represents a major challenge with significant implications for energy efficiency, economic performance, and environmental sustainability. The seminal work of Kenneth Holmberg and Ali Erdemir has quantified the global impact of friction and wear-related losses, highlighting substantial opportunities for optimization. According to their analyses, approximately **23% of the world's total energy consumption** is related to tribological contacts. Of this, 20% is used to overcome friction, while 3% (16 EJ) is attributed to the production of spare parts due to wear. [2]

The authors estimated that the implementation of advanced surface engineering, improved materials, and more effective lubrication could reduce these losses by **18% in the short term** (8 years) and up to **40% in the long term** (15 years), resulting in energy savings equivalent to 8.7% of total global consumption and a potential 1.4% increase in global GDP. Environmentally, these measures could cut annual CO_2 emissions by up to 3140 million tonnes. The most impacted sectors include transportation and energy production, with potential short-term energy savings of 25% and 20%, respectively. In the long term, these could reach 55% for transportation and 40% for power generation.

From an environmental perspective, the adoption of advanced tribological technologies could reduce **global CO_2 emissions by 1460 million tonnes in the short term** and up to **3140 million tonnes in the long term**. These reductions are associated with cost savings estimated at €450 billion and €970 billion, respectively.

In summary, enhancing tribological performance across mechanical systems worldwide offers a powerful pathway to reducing energy consumption, cutting costs, and mitigating environmental impact.

To respond to these challenges, tribology can thus be studied at different scales, as illustrated in Fig. 1.

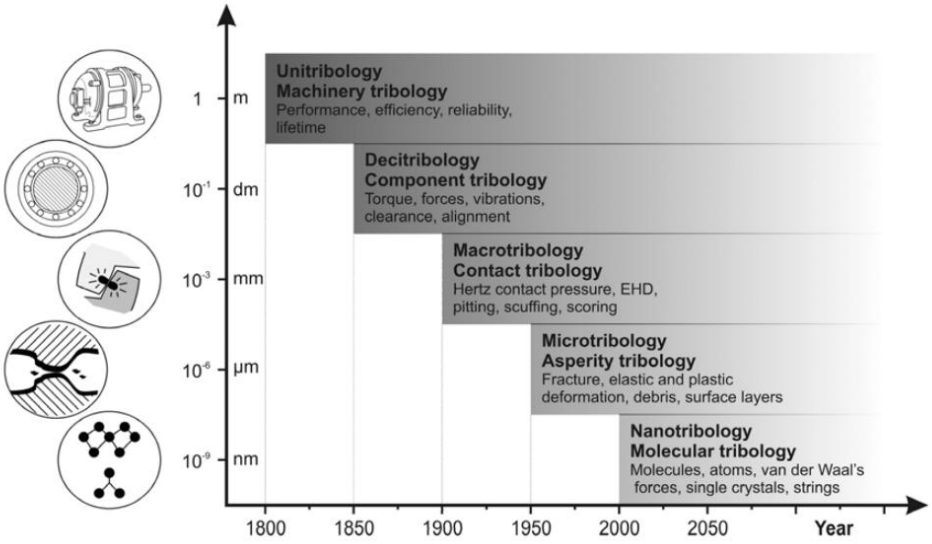

Fig. 1: Presentation of the different scales at which tribology can be studied, ranging from machine reliability, to the analysis of forces and torques, to the investigation of contact between components (such as gears), surface roughness, and finally molecular-scale interactions. [3]

These scales can be viewed as a means to understand the mechanisms leading to frictional losses or, more broadly, wear. Ultimately, this understanding enables the development of strategies to minimize such losses. For instance, at the macro and micro-tribological scales, it becomes evident that the apparent contact area differs from the actual contact area. Due to the roughness of the interacting bodies, only a limited number of asperities come into contact (Fig. 2).

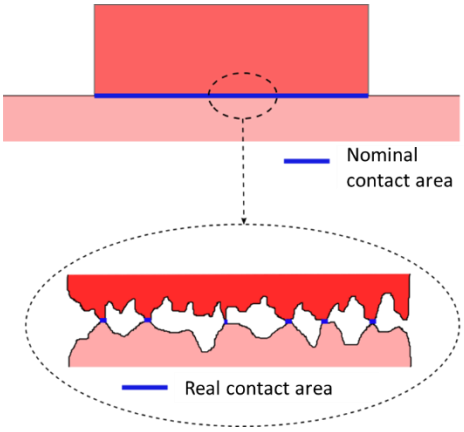

Fig. 2: Diagram illustrating the difference between apparent contact area and real contact area. [4]

Given that the contact pressure is defined as $P = F/S$, where F is the applied force and S the contact area, it follows that the stress is locally very high at asperity peaks and low in the valleys. Stress measurements, which are typically carried out at the macroscopic scale, therefore represent an average between highly loaded regions and unloaded ones.

A direct consequence is the local elastic or plastic deformation (depending on the pressure, roughness and material) of the surfaces, which increases the real contact area and, consequently, friction. In the case of purely elastic deformation, this phenomenon is described by Hertzian theory, which defines the stress distribution and contact area between elastic bodies under load (Fig. 3). Using a harder substrate, or applying a harder coating, increases the load required to induce deformation and can thus help mitigate this phenomenon.

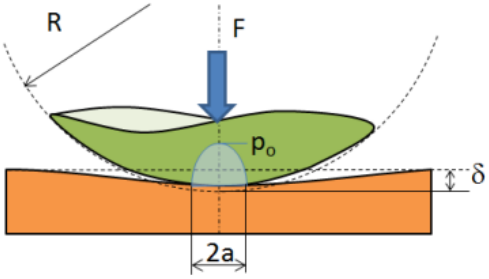

Fig. 3: Hertzian sphere-on-flat contact resulting from the deformation of both solids, which simultaneously leads to an increase in the contact area, with a representing the radius of the contact circle. [1]

Another approach is to tailor surface interactions to reduce friction. This involves modifying interfacial behavior rather than the bulk material properties. In this context, attention is given to viscous liquid lubricants - particularly oil-based ones - which reduce asperity contact and frictional losses.

1.2 Lubricating Oils

1.2.1 Generalities on Oil-based Lubricants Composition

A lubricating oil is formulated by blending a base oil with various functional additives to achieve optimal viscosity, oxidation stability, thermal resistance, detergency, and - most relevant to this work - tribological performance. Main types of additives are presented in Fig. 4.

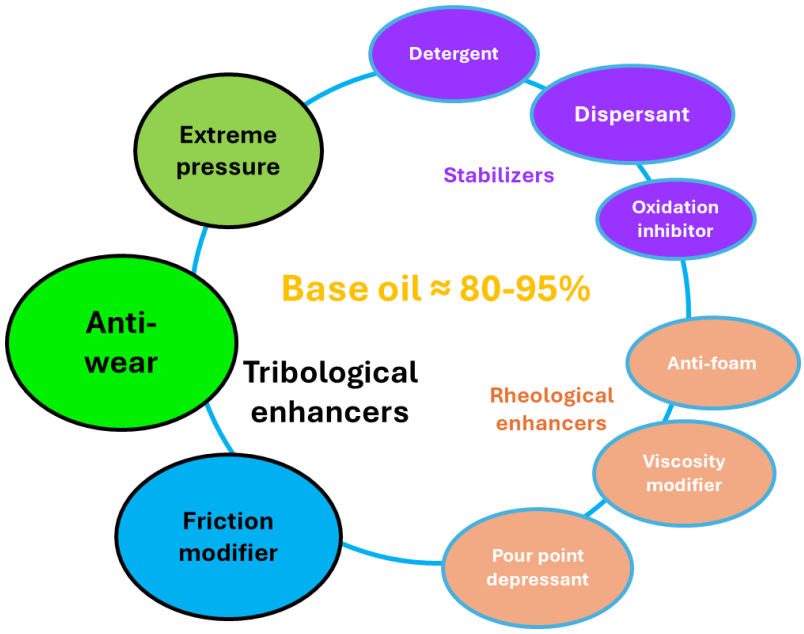

Fig. 4: Main additives types used in a lubricating oil.

These additives are used to enhance the intrinsic properties of a base oil, or a blend of base oils. The American Petroleum Institute (API) classifies base oils into five groups depending on their refining process and composition, as shown in Fig. 5.

	Group	Saturates	Sulphur Weight %	Viscosity Index	Process
Mineral	I	< 90%	> 0.03	80 - 120	Solvent refined
	II	> 90%	< 0.03	80 - 120	Hydro-processed
	II+	> 90%	< 0.03	100 - 120	Hydro-cracked•
	III	> 90%	< 0.03	> 120	(Severe) Hydro-cracked
Synthetic	IV	Polyalphaolefins (PAO's)			Chemical reaction
	V	All other synthetics			

Fig. 5: API base oil categories [5]

In the case of our study, we will focus on Polyalphaolefin (PAO) oils.

PAO oils are synthetic hydrocarbons produced via a two-step process [6]:

- Oligomerization of α-olefins (commonly 1-decene or 1-dodecene), generating oligomers such as dimers, trimers, and tetramers.

- Hydrogenation to saturate double bonds, followed by fractional distillation to isolate desired viscosity grades.

PAOs are classified as API Group IV base oils and are designated according to their kinematic viscosity at 100 °C, for example PAO6, where the number 6 corresponds to the approximate viscosity grade in centistokes, in this case, 6 cSt at 100°C.

An example of PAO chemical structure is presented in Fig. 6.

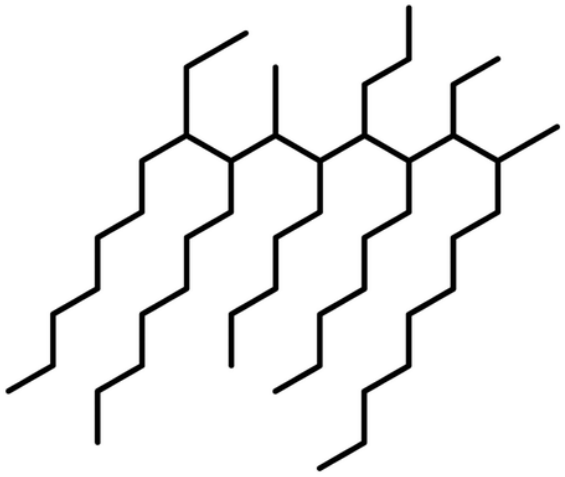

Fig. 6: Chemical structure of a C50 PAO oligomer [7]

These fluids exhibit a high viscosity index, typically in the range of 130-140, which means they maintain relatively stable viscosity across wide temperature variations. They possess excellent low-temperature behavior with pour points as low as -50°C, combined with good thermal and oxidative stability that allows reliable performance under high operating temperatures. Other key attributes include low volatility, a high flash point, and compatibility with mineral oils and most lubricant additives, although their non-polar nature can limit solubility of certain additives. [8]

Their main drawbacks are their higher production cost compared to mineral oils, lower intrinsic lubricity, limited biodegradability, and poor fire resistance, which are compensated in practice through formulation strategies with additives and co-base stocks (synthetic esters, mineral oils, etc…).

1.2.2 Lubrication Regimes

Depending on the operating conditions (load, sliding speed, viscosity), lubrication can occur in three main regimes described by the Stribeck curve, as illustrated in Fig. 7.

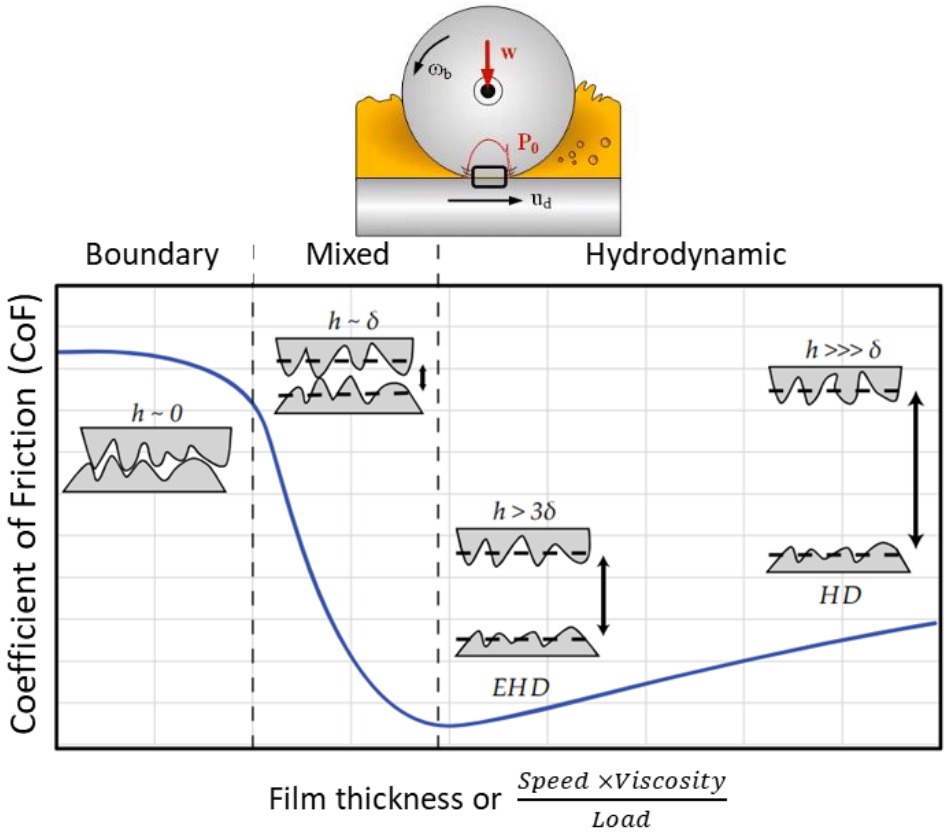

Fig. 7: Stribeck curve illustrating the different lubrication regimes. Two surfaces with a certain roughness are shown at varying distances from each other. [9]

The Stribeck curve characterizes the relationship between the coefficient of friction and the lubrication conditions in a contact, typically represented as a function of a dimensionless parameter [10]:

$$\frac{v \,.\, \eta}{P \,.\, \sigma}$$

where:

η is the dynamic viscosity of the lubricant (Pa.s or (N/m^2).s).

v is the relative sliding velocity (m/s).

P is the applied pressure or load (Pa or N/m^2).

σ corresponds to the combined root mean square of the surface roughness of the contacting surfaces (m): $\sigma = \sqrt{Rq_1^2 + Rq_2^2}$

This curve reveals three primary lubrication regimes:

1. Hydrodynamic Lubrication (HL) / Full-Film Lubrication

In this regime, a continuous fluid film completely separates the two surfaces. There is no direct solid contact, and friction is much lower than in previous regimes as it arises solely from the shearing of the lubricant film. This occurs at higher speeds, higher viscosity, or lower loads. Wear is minimal.

2. Elastohydrodynamic Lubrication (EHL)

In certain situations where contact zones are highly pressurized (e.g., rolling contacts), the lubricant behaves in a non-Newtonian manner, and the surfaces undergo elastic deformation. EHL forms a very thin but continuous film, allowing full separation of the surfaces under high load.

The distinction between hydrodynamic and elastohydrodynamic lubrication can be expressed through the ratio of surface roughness to lubricant film thickness (commonly referred to as the λ-ratio, defined as $\lambda = h / \sigma$, where h is the minimum film thickness and σ the composite surface roughness). In the hydrodynamic regime, λ is much greater than 3, indicating smooth full-film separation, whereas in the EHL regime, λ typically ranges between 2 and 3, corresponding to thinner films that approach the scale of surface asperities.

3. Mixed Lubrication (ML)

Here, the load is partially supported by the lubricant film and partially by asperity contact. Both hydrodynamic and boundary effects coexist. Friction begins to decrease as more of the contact is taken over by the lubricant. This regime represents a transition zone.

4. Boundary Lubrication (BL)

In this regime, the two surfaces are in close contact, and the lubricant film is too thin to fully separate them. Friction and wear are dominated by solid - solid interactions between surface asperities. The lubricant may form adsorbed molecular layers or contain additives (e.g., anti-wear agents) to reduce direct contact. This regime occurs at low speeds, low viscosity, or high loads.

1.2.3 Transmission Oils

Now that the different lubrication regimes have been presented, we will focus our study on transmission lubricants, which differ significantly from engine oils, not only in their formulation but also in their functional priorities. While engine oils are designed to address a complex mixture of thermal, oxidative, and contaminant-related stresses due to combustion by-products, transmission fluids are engineered for precise mechanical efficiency under continuous mechanical contact. Their primary role is to ensure optimal lubrication in gearboxes, differentials, and driveline components, where both sliding and rolling contacts occur in complex kinematic configurations, such as hypoid gears, planetary gear sets, and synchronizers. [11]

These systems are characterized by highly variable load and speed conditions. For instance, electric vehicle (EV) drivetrains can impose immediate and sustained torque at low speeds, resulting in severe boundary lubrication conditions. Conversely, during highway cruising, high-speed operation necessitates hydrodynamic lubrication. Therefore, transmission lubricants must perform reliably across all regimes: boundary (low speed, high load), mixed (moderate speed and load), and hydrodynamic (high speed, low load) [12]. The transition between these regimes can occur rapidly, especially under start-stop or regenerative braking conditions, requiring a fluid with rapid adaptability in its rheological and tribological behavior.

To address these diverse demands, modern transmission oils incorporate highly specialized additive packages, which emphasize anti-wear (AW) and extreme-pressure (EP) protection more than detergency or soot dispersion, which are typical of engine oil formulations. AW additives like ZDDP form protective tribofilms to prevent scuffing, while EP additives such as sulfurized olefins form sacrificial layers under high stress. These are especially crucial in hypoid gears, where sliding and rolling are combined at high contact pressures.

In addition to tribological performance, transmission lubricants must exhibit excellent thermal and oxidative stability to avoid viscosity loss and additive degradation during extended high-load operation. Shear stability is also critical, as shear thinning under load can compromise film thickness and lead to premature wear. Furthermore, modern transmission fluids must be compatible with non-metallic components such as elastomeric seals and polymer synchronizer rings, especially in dual-clutch or automated manual transmissions where precise engagement is essential. [11]

Another challenge is the increasing demand for low-viscosity transmission fluids to reduce churning losses and improve energy efficiency [2]. However, reducing viscosity inherently reduces the minimum film thickness that can be generated, making the fluid more dependent on additive-derived tribofilms for protection. This trend places even greater emphasis on additive performance under boundary and mixed regimes, particularly in EV drivetrains where operational temperatures may be lower, but mechanical and electrical stresses are higher.

In this study, we will focus on the boundary and mixed lubrication regimes, where the use of additives plays a critical role in reducing friction and wear.

1.3 Boundary Lubrication Additives

Lubricant additives are essential for ensuring robust tribological performance, particularly under boundary and mixed lubrication regimes where the fluid film is insufficient to fully separate surfaces. These additives serve various functions, each targeting specific wear or degradation mechanisms:

- **Anti-wear (AW)**: Zinc dialkyldithiophosphate (ZDDP) is the most commonly used AW additive, known for forming a protective tribofilm composed of zinc and iron polyphosphates on steel surfaces. These films are formed via stress-assisted decomposition mechanisms that begin with molecular adsorption and are sustained through sliding-induced mechanochemistry. ZDDP is particularly valued for its dual function as an anti-wear and antioxidant agent [13,14].
- **Friction Modifiers (FM)**: Molybdenum dithiocarbamate (MoDTC) belongs to a class of friction-reducing compounds that form lamellar molybdenum disulfide (MoS_2) tribofilms in situ. These films possess low interlayer shear strength, drastically reducing friction in boundary conditions. However, their effectiveness can diminish over time due to oxidative degradation and additive depletion [15].
- **Extreme Pressure (EP)**: EP additives, such as sulfurized olefins and phosphorus esters, react under high-load, high-temperature conditions to form protective surface layers. These compounds are particularly effective in preventing seizure and scuffing in heavily loaded contacts, such as gear teeth under shock loading. [11,16]

In practice, these additives are not used in isolation but as part of complex additive packages. The formulation of these packages must consider not only the individual efficacy of each component but also their chemical compatibility. For instance, interactions between ZDDP and MoDTC can lead to synergistic or antagonistic effects depending on concentration, temperature, and the presence of other surfactants or dispersants [17]. Consequently, understanding these interactions at both the molecular and macroscopic levels is critical for optimizing lubricant design.

In the following section, we focus more specifically on tribological additives, namely ZDDP, MoDTC, and finally an emerging category: nanoparticles.

1.3.1 Anti-Wear (AW) Additive: Zinc Dialkydithiophosphate (ZDDP)

Zinc dialkyldithiophosphate (ZDDP) has been the most widely used anti-wear (AW) additive in lubricant formulations since its commercial introduction in the 1940s. Originally developed for its antioxidant capabilities, ZDDP quickly became valued for its dual functionality: preventing oxidative degradation of base oils and forming protective surface films under severe mechanical contact. Its versatility has ensured its use across applications ranging from internal combustion engines to heavy-duty gearboxes, hydraulic systems, and industrial machinery. Even today, despite stringent environmental regulations limiting phosphorus and sulfur content, ZDDP remains the benchmark AW additive because no direct drop-in replacement matches its combined performance, stability, and cost-effectiveness. [18,19]

Its general chemical structure is presented in Fig. 8.

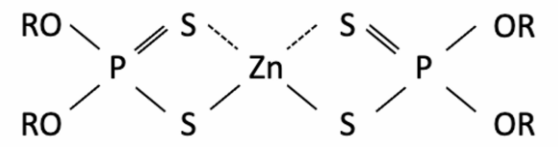

Fig. 8: Chemical structure of ZDDP additives.

ZDDP is a complex additive whose anti-wear effectiveness stems from its ability to form a protective tribofilm on metal surfaces under mechanical and thermal stress. This tribofilm acts as a sacrificial layer, preventing direct contact between moving metal parts and thereby significantly reducing wear, scuffing, and surface fatigue. According to H. Spikes (2025) [13], the tribofilm formation process unfolds through several mechanochemical stages, beginning with the adsorption of ZDDP molecules onto ferrous surfaces. At concentrations as low as 500 ppm of phosphorus, these molecules form an initial monolayer, anchoring via their sulfur atoms. Upon heating, typically beyond 60 °C, partial dissociation occurs, and zinc is lost from the adsorbed layer, suggesting early chemical transformations of the dialkyldithiophosphate group.

Very quickly after adsorption, a thin iron sulphide or sulphate layer forms between the additive and the metal surface. This interfacial film is thought to arise from a direct surface reaction involving sulfur transfer from the ZDDP molecule. While this step is consistently observed, its precise mechanism remains under-investigated. The rapid appearance of this layer indicates it serves as a precursor that facilitates subsequent tribofilm growth. [13]

The core stage of tribofilm formation involves the mechanochemically driven polymerization of phosphate chains to form polyphosphate glass. When sufficient shear stress and temperature are present, ZDDP undergoes decomposition, producing reactive intermediates that polymerize into amorphous polyphosphate glass. This process follows a stress-augmented thermally activated model, where the rate of film growth increases exponentially with applied shear stress. As a result, the polyphosphate film grows preferentially on asperities that experience the highest localized stress, resulting in a characteristic "pad-like" or patchy tribofilm morphology. [14,20]

Over time, the polyphosphate film undergoes structural evolution. Initially composed of long-chain amorphous phosphates, they depolymerize and densify into zinc and iron polyphosphates, often incorporating crystalline phases. This transition is facilitated by the incorporation of metal ions (Zn^{2+} from ZDDP decomposition and Fe^{3+} from the substrate), contributing to film rigidity and wear resistance. The matured film typically exhibits a layered structure, with a phosphate-rich outer layer and a sulphide-rich underlayer, which together provide strong adhesion and load-bearing capacity. [13]

Tribofilm growth is inherently self-limiting. Once a critical thickness, typically between 50 and 150 nanometers, is reached, further growth is significantly hindered. This plateau is primarily attributed to the fact that a sufficiently thick and compliant tribofilm redistributes mechanical stress across the contact interface, thereby reducing the localized shear and pressure that drive the mechanochemical reactions responsible for film formation. The tribofilm also serves as a sacrificial layer, shielding the underlying steel substrate from direct contact and wear. Therefore, an equilibrium is often established when the rates of film formation and removal become balanced, further constraining tribofilm growth. Furthermore, experimental observations have shown that sliding motion is essential for tribofilm development; under pure rolling conditions, where shear is minimal, no film is formed. This highlights the critical role of mechanical activation, in conjunction with temperature, in initiating and sustaining tribochemical film growth. [14]

The ZDDP tribofilm structure can be visualized in Fig. 9.

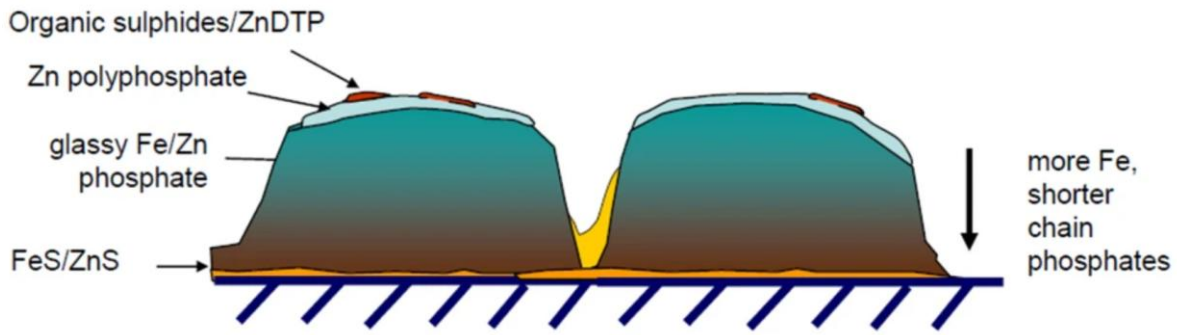

Fig. 9: Schematic of cross section of ZDDP tribofilm. [18]

Atomic Force Microscopy (AFM) studies have contributed to understanding the tribofilm growth kinetics as shown in Fig. 10. The sequence of 2 µm × 2 µm AFM height maps illustrates progressive tribofilm formation on an iron oxide surface lubricated with ZDDP-containing oil during cyclic sliding at 4.2 ± 0.5 GPa. Quantitative analysis of tribofilm volume reveals two distinct regimes: an initial slow, approximately linear growth phase followed by a faster power-law growth phase. The preferential growth on highly stressed asperities leads to a patchy, pad-like morphology that becomes more pronounced with increasing sliding cycles.

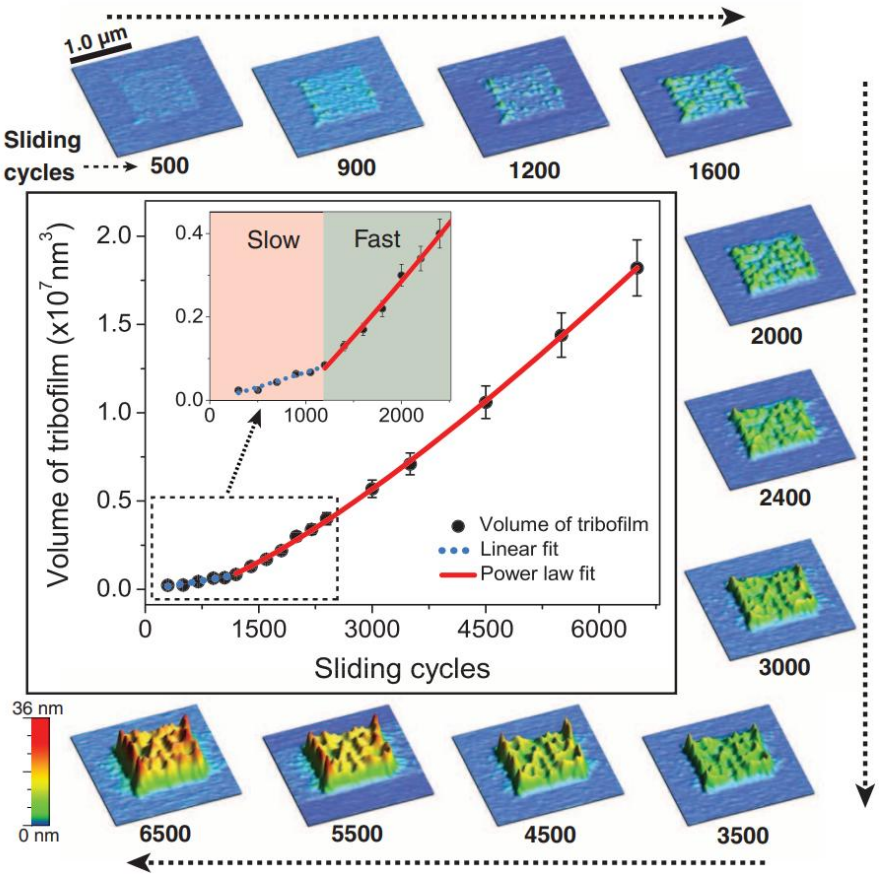

Fig. 10: Tribofilm morphology and growth kinetics: AFM images (2 µm×2 µm) showing progressive film formation on iron oxide in ZDDP-containing oil under cyclic sliding (4.2 ± 0.5 GPa). [21]

This growth is also influenced by tribological conditions such as temperature and contact pressure. In both cases, increasing either temperature or contact pressure leads to an exponential increase in the tribofilm growth rate, consistent with a stress-augmented, thermally activated mechanism. In the case of contact pressure, a plateau is reached at high pressures, beyond which excessive stress promotes tribofilm removal and wear, as shown in Fig. 11.

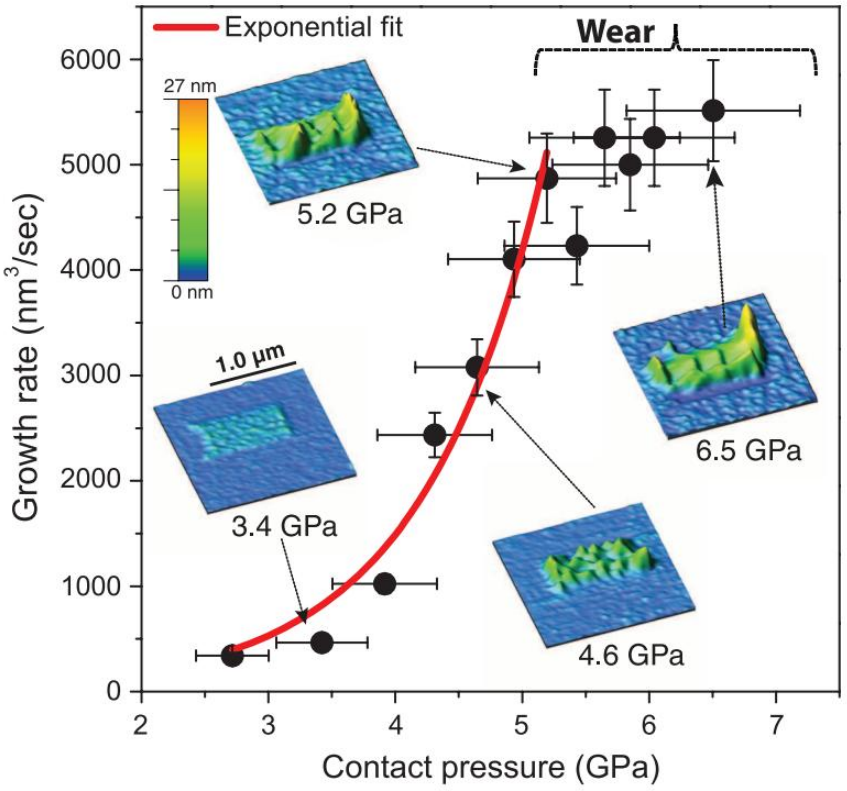

Fig. 11: Contact pressure dependence of ZDDP tribofilm growth rate and morphology at 100°C. [21]

ZDDP tribofilm formation kinetics also depend on the nature of the carbon-chain as described in Fig. 12. For example, secondary ZDDPs tend to form tribofilm faster than primary ones but on the other hand present lower thermal stability. A blend of both primary and secondary ZDDPs is usually used in fully formulated lubrication oils [13].

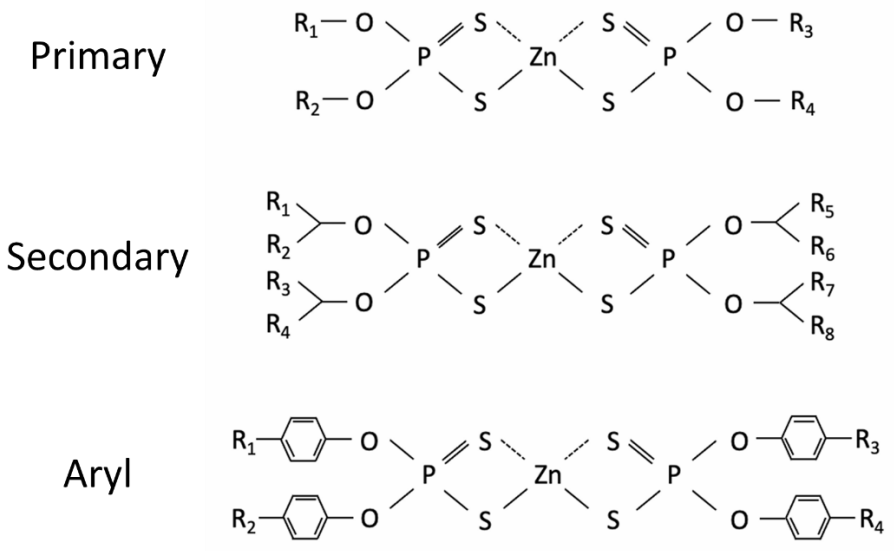

Fig. 12: ZDDP chemical structures. [22]

Beyond its anti-wear capabilities, ZDDP also serves as an effective antioxidant. It inhibits the oxidation of base oils by decomposing hydroperoxides and neutralizing acidic byproducts, which helps prolong oil life and maintain viscosity stability. However, its use is not without drawbacks. The phosphorus and sulfur content in ZDDP can poison catalytic converters of ICE (Internal Combustion Engine) vehicles and contribute to harmful emissions. For this reason, modern lubricant formulations, especially those for passenger car engines, often limit ZDDP concentrations in compliance with environmental regulations.

Despite increasing regulatory constraints, ZDDP remains indispensable in specific contexts, particularly in high-performance engines and heavy-duty machinery, where robust boundary lubrication is critical. The presence of zinc seems essential to maintain good AW properties. Indeed, the use of another metal (nickel, iron, silver, lead, tin, antimony, and bismuth) leads to increase in wear. Only cadmium offers better AW properties but cannot be used because of its high toxicity [23]. This underscores the urgent need to develop alternative tribological solutions that match or exceed ZDDP's performance, while minimizing its environmental and catalytic drawbacks.

1.3.2 Friction Modifier (FM) Additive: Molybdene Dithiocarbamate (MoDTC)

Molybdenum dithiocarbamate (MoDTC) is one of the most effective friction modifiers used in modern lubricants, particularly in engine oils designed to improve fuel economy. Introduced in the late 1980s as an alternative to solid lubricant dispersions, MoDTC provided a soluble, oil-compatible source of molybdenum capable of forming low-shear molybdenum disulfide (MoS_2) tribofilms directly *in situ* during operation. These tribofilms can reduce the coefficient of friction by up to 50% compared to ZDDP-only formulations, making MoDTC a key component in low-viscosity, fuel-efficient oils. [15,24]

Its chemical structure is presented in Fig. 13. This compound exists in an equilibrium between two linkage isomeric forms: one where molybdenum is doubly bonded to an oxygen atom (a), and another where it is doubly bonded to a sulfur atom (b). [25]

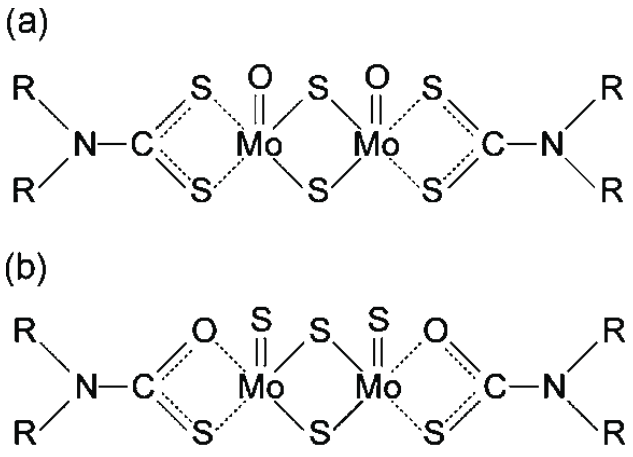

Fig. 13: MoDTC chemical structures. [25]

Its primary mechanism of action is the *in situ* formation of a tribofilm composed of molybdenum disulfide (MoS_2), a layered solid lubricant known for its exceptionally low shear strength between basal planes. Under boundary lubrication conditions and high temperatures, MoDTC decomposes mechanochemically at the surface of steel substrates to generate ultrathin MoS_2 platelets that can be seen with TEM observations as shown in Fig. 14.

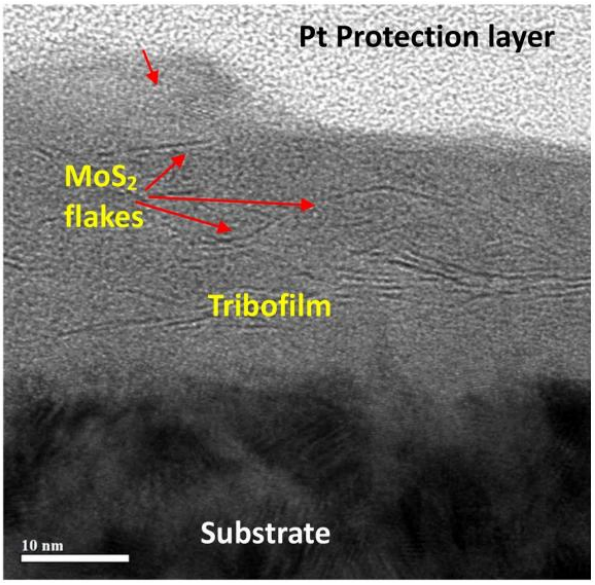

Fig. 14: TEM micrograph of a tribofilm formed on a steel surface, showing the presence of MoS_2 platelets. [26]

Due to their higher electronegativity, sulfur atoms at the surface of MoS_2 platelets carry a partial negative charge, leading to interlayer electrostatic repulsion (Fig. 15). This repulsion weakens the interfacial Van der Waals forces between adjacent platelets, resulting in exceptionally low shear strength and, consequently, the low friction characteristics that make MoS_2 an effective tribological material.

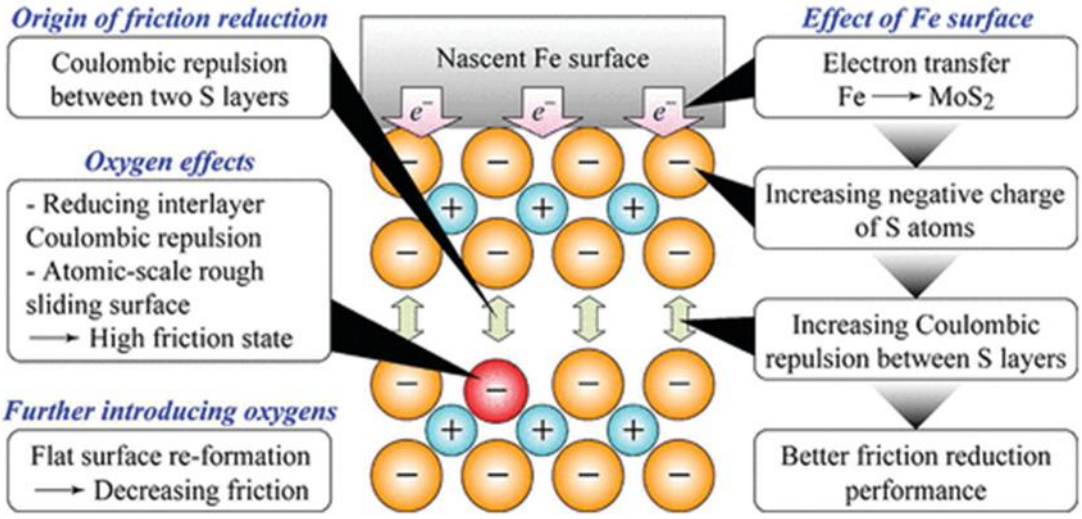

Fig. 15: MoS_2 platelets structure. [25]

The decomposition of MoDTC into MoS_2 nanosheets remains an active area of research, with current understanding based on hypotheses supported by both experimental evidence and numerical simulation studies reported in literature.

A notable molecular-scale insight into this process is provided by Onodera et al. (2010) [25], who combined density functional theory (DFT) with classical molecular dynamics to study the initial reaction dynamics of MoDTC on a nascent Fe (110) surface. Their simulations revealed that:

- Under the influence of temperature, MoDTC is converted to its linkage isomer LI-MoDTC (Fig. 13b) which is adsorbed on the Fe substrate.
- The Mo-O bonds in MoDTC are the most labile and are weakened by electron donation from the Fe surface without breaking.
- It is only when friction is applied that the Mo-O bond is dissociated which leads to the formation of an Mo_2S_4 intermediate as well as the two dithiocarbamate former ligands (Fig. 16).
- Mo_2S_4 is then believed to act as a precursor for MoS_2 sheets formation.
- The decomposition pathway is facilitated by localized surface reactivity: fresh metallic iron surfaces are far more reactive than oxidized ones, suggesting that oxide removal during asperity contact may be a key step in real tribological conditions.

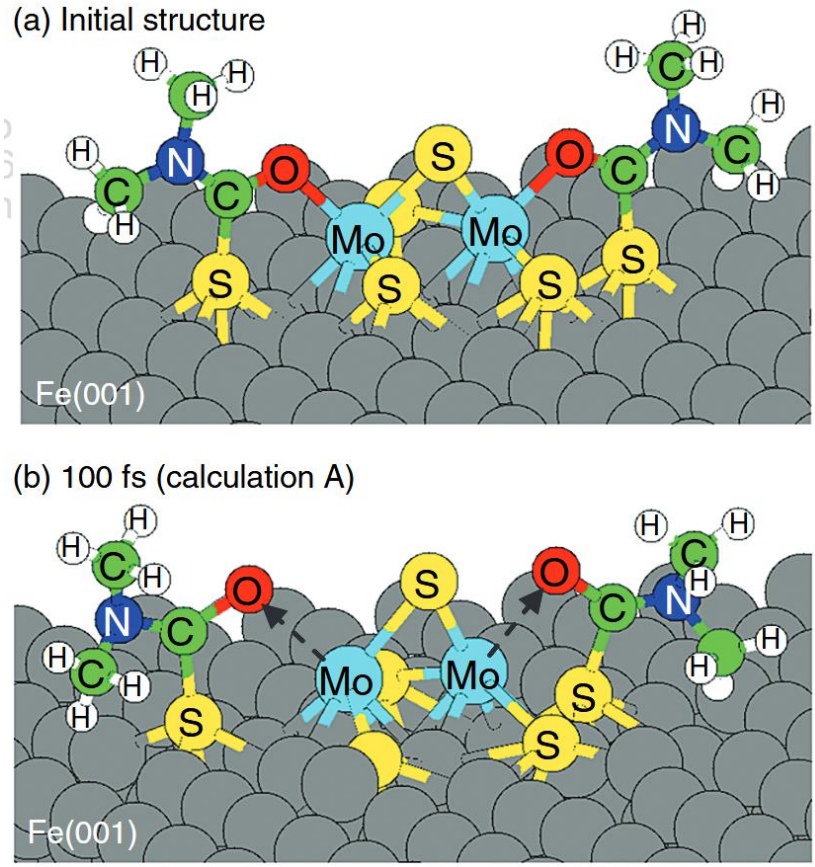

Fig. 16: Snapshots of LI-MoDTC molecule on nascent Fe surface. (a) Initial structure, and structure at 100 fs obtained from the calculations (b). [25]

Although these simulations do not explicitly model mechanical shear, they provide a molecular-level mechanism of the first steps of MoS_2 formation.

More recently, Peeters et al. (2021) [27] demonstrated experimentally, through tribotesting combined with numerical simulation, that this mechanistic pathway is strongly influenced by the substrate's surface chemistry. On oxide-free Fe surfaces, MoS_2 forms rapidly, whereas on oxidized or passivated surfaces the nucleation rate is significantly reduced due to the barrier imposed by the oxide layer, as shown in Fig. 17.

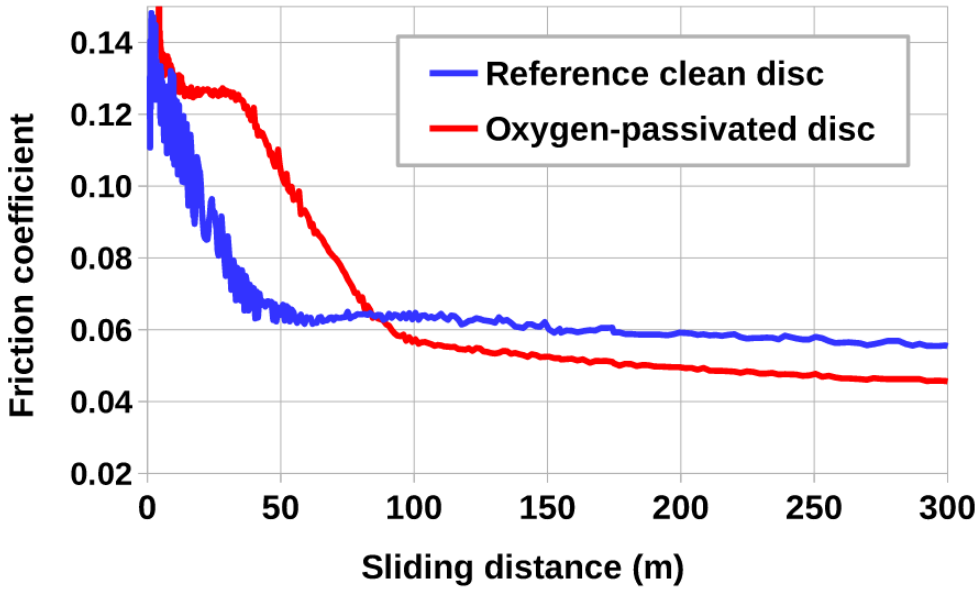

Fig. 17: Tribological tests of the oxidized and the clean mirror 52100 AISI discs under lubrication with a mixture of MoDTC complexes (500ppm of Molybdenum) at 700MPa and 110°C. [27]

Together, these studies establish a coherent mechanism in which MoDTC decomposition proceeds via ligand cleavage, sulfur transfer to the substrate, and subsequent growth of MoS_2 lamellae, with the surface state acting as a key kinetic modulator.

MoDTC's efficiency is time-limited. Once the additive is consumed, MoS_2 formation ceases and friction levels rise. The thermal stability of MoDTC itself is a limiting factor: at temperatures above ~150 °C, the molecule begins to thermally degrade in the bulk oil phase, forming inactive or insoluble molybdenum oxides and other byproducts. This degradation reduces the long-term effectiveness of MoDTC-containing formulations in high-load or high-temperature applications. [15]

Additionally, its friction-reducing performance can be highly sensitive to the chemical environment, particularly the nature of the substrate surface (e.g., oxide layer thickness, roughness, and cleanliness), which influences adsorption and initial decomposition behavior.

1.3.3 Nanoparticles as Tribological Additives

Nanoparticles have emerged as innovative materials owing to their nanoscale dimensions, high surface-area-to-volume ratio, and unique tribo-chemical reactivity. These particles are often classified by their dimensionality, which influences their interaction with contact surfaces:

- 0D (zero-dimensional): Spherical nanoparticles such as some metal oxides (TiO_2, ZrO_2, ZnO, CeO_2, etc…)
- 1D (one-dimensional): Rods or nanotubes like carbon nanotubes (CNTs). [28]
- 2D (two-dimensional): Nanosheets such as MoS_2, graphene, and hexagonal boron nitride (h-BN). [28,29]
- 3D (three-dimensional): Fullerene-like structures including IF-MoS_2 and IF-WS_2. [30]

The use of nanoparticles for wear and friction reduction has gained significant attention over the past two decades. Their appeal lies in their ability to interact with tribological interfaces at the nanoscale, where they can either act as rolling elements, fill surface asperities, or form protective tribofilms under boundary and mixed lubrication regimes. These mechanisms contribute to both friction reduction and enhanced wear resistance. [30–33]

Extensive studies have demonstrated their potential with metal oxide nanoparticles, such as TiO_2 [34–36], ZrO_2 [37,38], CeO_2 , and ZnO [39], due to their ability to form protective tribofilms at the sliding interface. The effectiveness of these tribofilms in mitigating wear depends strongly on the nanoparticle composition, size and operational conditions. Moreover, a significant challenge lies in their tendency to agglomerate and sediment over time, reducing their tribological effectiveness. Addressing this issue requires advanced dispersion strategies. As outlined by Y. Chen *et al.* (2019) [40], two primary methods have been explored:

- Physical Dispersion: this method involves the addition of dispersants to stabilize nanoparticles through physisorption, enhancing suspension stability while allowing particles to more readily enter the contact area. However, this method sacrifices long-term stability.
- Chemical Functionalization: this method relies on surface modification to bond stabilizing compounds to the nanoparticle surface, creating a more permanent and stable suspension. Although more stable, this method can sometimes limit nanoparticle access to the tribological contact point due to steric hindrance or too stable suspension as outlined by P. Rabaso *et al.* (2014) [41].

The balance between achieving stable dispersions and preserving nanoparticle effectiveness in reducing wear remains a critical area of investigation. For example, Inorganic Fullerene (IF) such as IF-MoS_2 nanoparticles present very good friction reduction properties but are subject to sedimentation which affect negatively their performance as shown in Fig. 18. In this particular case, functionalization is difficult to achieve because of the onion-like structure of those nanoparticles.

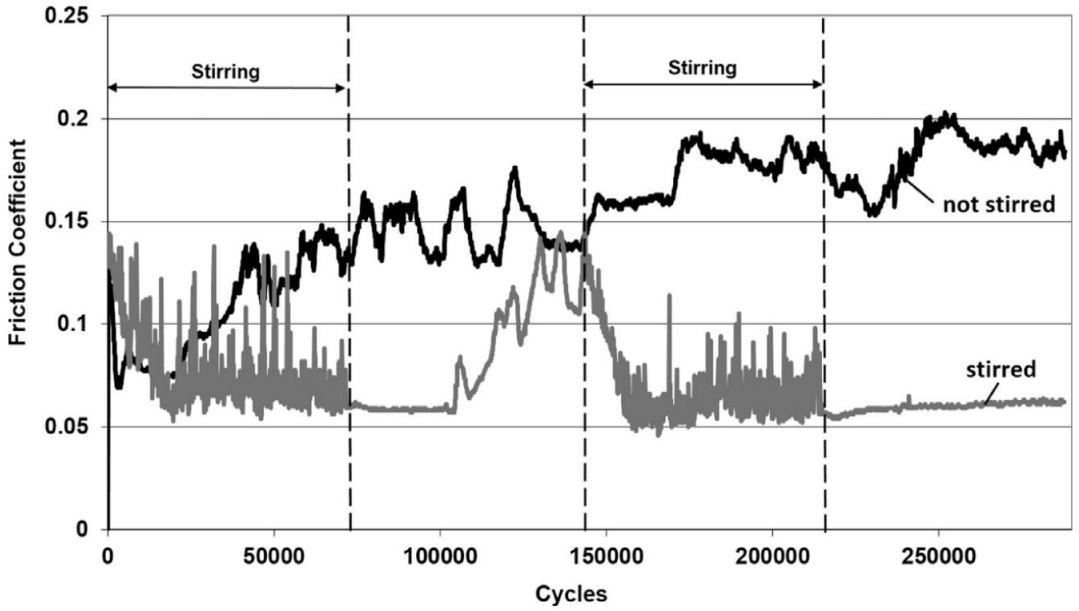

Fig. 18: Influence of oil stirring on the performance of Large Crystalline-type IF-MoS_2 (1 wt%, 1.4 GPa, 80 °C). [42]

Building on these strategies, studies have investigated the tribological performance of metal oxide nanoparticles. The following discussion highlights their potential in forming tribofilms and improving anti-wear properties.

A. Hernandez Battez *et al.* (2006) [39] investigated the use of 20 nm ZnO nanoparticles in polyalphaolefin (PAO6) base oil with OL100 and OL300 (ester dispersants). Results reveal that while non-functionalized ZnO nanoparticles show good behavior under extreme pressure conditions, they may become abrasive in anti-wear tests if not fully stabilized by the dispersant, even though ZnO is softer than the 52100 AISI balls used (32 and 65 HRC, respectively). This justification, however, relies on hardness data of bulk materials, ZnO nanoparticles could have very different properties. An optimal combination of 0.3% ZnO and 3% OL300 demonstrates the best performance, significantly reducing Wear Scar Diameter (WSD). It must be noted that the same WSD reduction was observed with 3% OL300 alone but the addition of ZnO nanoparticles allows for the possible formation of a tribofilm as Zn was found on the wear track with EDX analysis.

Recent studies have explored the lubricating performance of capped 5 nm ZrO_2 nanocrystals (NCs) at both the nanoscale and macroscale. Using an *in situ* AFM tribometer, Khare et al. [37,43] demonstrated that ZrO_2 NCs dispersed in PAO base oil promote the growth of protective tribofilms through a stress-activated tribo-sintering mechanism. The formation of this tribofilm is governed by an initial induction phase that promotes ZrO_2 nucleation, followed by a growth stage until a saturation plateau is reached (Fig. 19).

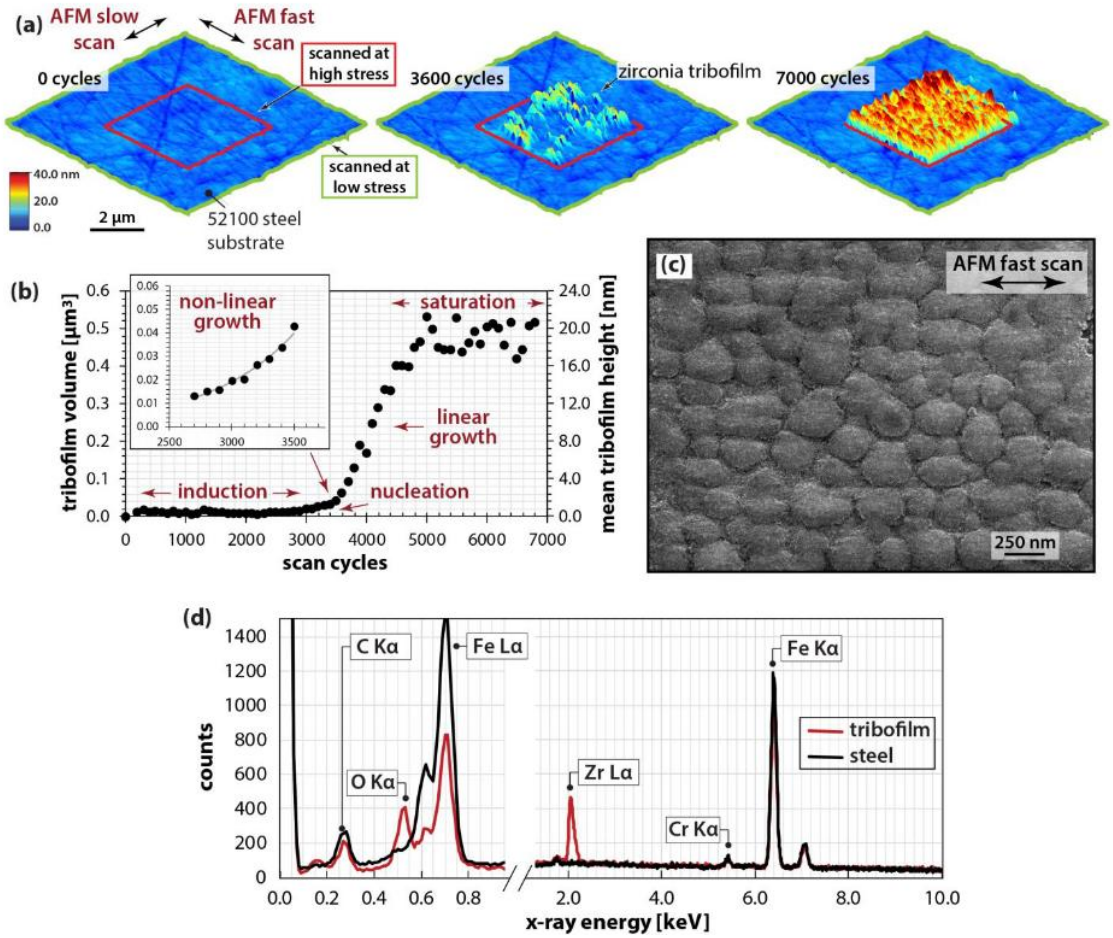

Fig. 19: ZrO_2 Tribofilm in PAO4 (10 wt.%, 25 °C, 183 MPa): (a) AFM Images over sliding cycles; (b) Volumetric/Height growth curve; (c) SEM morphology; (d) EDS spectrum. [37]

This process involves the emergence of a tribofilm at specific sites from nanoparticles present on the surface (referred to as “nucleation” by the authors), sintering, and the removal of dispersing ligands under shear stress conditions. The resulting tribofilms exhibit Young’s modulus and hardness values comparable to those of bulk crystalline materials. Notably, the anti-wear potential of ZrO_2 NCs was confirmed by their ability to form robust tribofilms across a wide range of contact conditions, including variable slide-to-roll ratios (SRR) in mini traction tribometer tests and harsh conditions in micro-pitting rig (MPR) tests [38]. The resulting tribofilm presents a thickness of 100 nm with a crystalline structure as shown in Fig. 20.

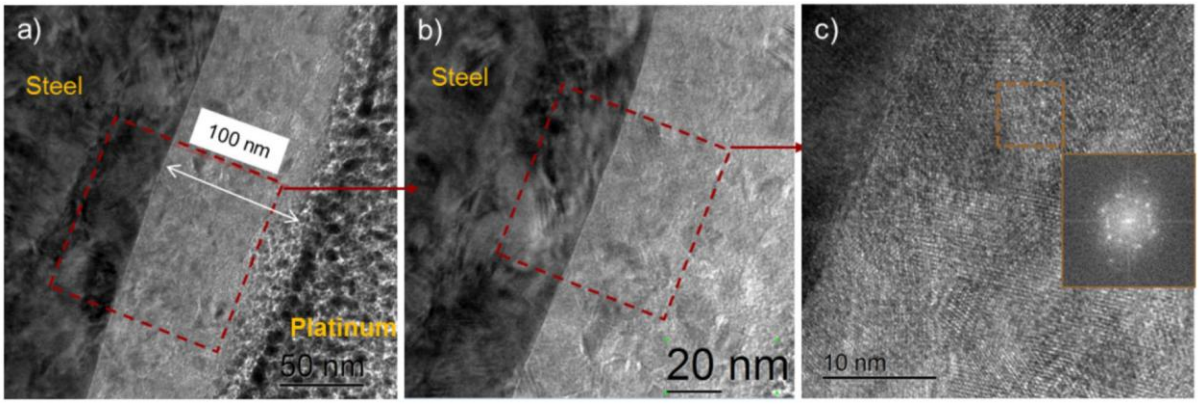

Fig. 20: Cross sectional TEM micrographs of a roller surface lubricated with PAO4 + 1% ZrO_2 at 30% SRR after 4 h of testing. (a) Overview showing a continuous and thick tribofilm (100 nm). (b) Close up of the red box on (a) showing a polished and sharp interface between steel and tribofilm. (c) High resolution TEM image and Two-dimensional Fast Fourier Transform (FFT) analysis showing the dense and crystalline structure of ZrO_2 tribofilm. [38]

Tests with a MTM tribometer were also carried out in a PAO4 base oil and a fully formulated gear oil (75W-80) [44]. They show that the ZrO_2 tribofilm can form across a wide SRR range and even in pure rolling condition (0% SRR). Even though tribofilm formation is observed for both oils, thicker ones are formed with the gear oil as well as better reduction in underlying surface wear (Fig. 21), indicating good compatibility with the additives package. This effect is attributed to a cooperation mechanism: EP additives provide initial protection against wear which gives enough time for ZrO_2 tribofilm to form. It must be noted that the resulting tribofilm also contains P and S elements from EP and AW additives of the gear oil in addition to ZrO_2 according to Raman spectroscopy [44] and TOF-SIMS analysis [45].

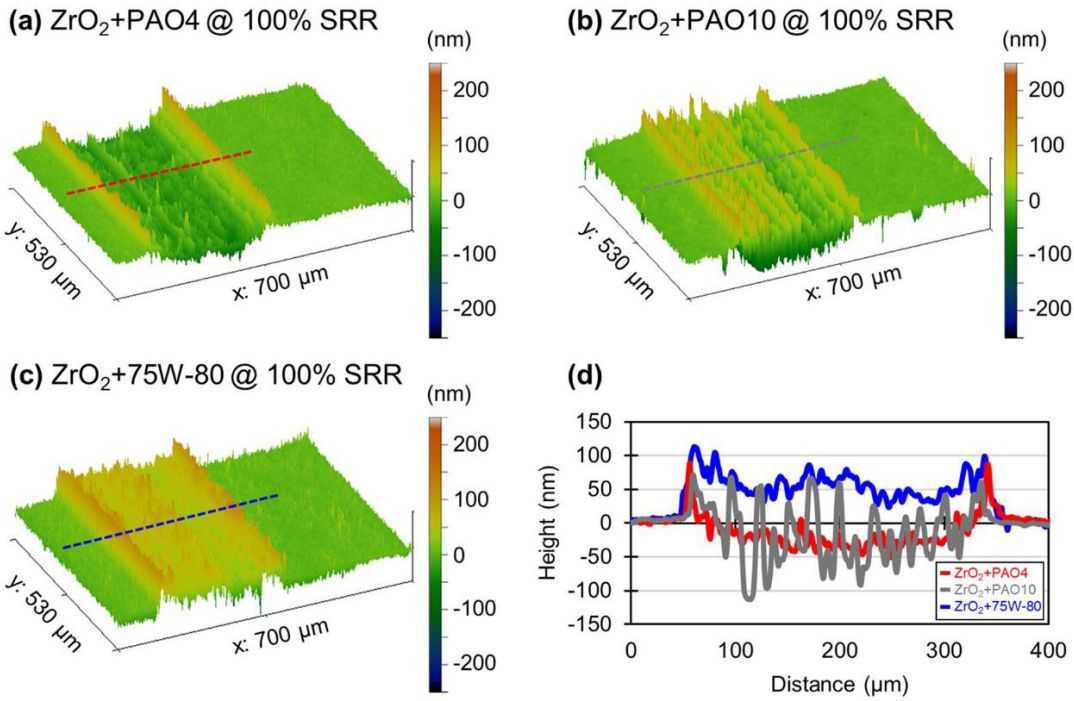

Fig. 21: WLI (White Light interferometry) 3D images (corrected for spherical curvature) for tribofilms formed at 100% SRR: (a) ZrO_2+PAO4, (b) ZrO_2+PAO10, and (c) ZrO_2+75W-80. Corresponding cross-sections are presented in (d). [44]

These results demonstrate that nanoparticles can effectively provide wear protection by promoting the formation of a robust tribofilm, even under sliding-rolling conditions, making them suitable for transmission lubrication applications. TiO_2 nanoparticles also proved to be beneficial for wear reduction as shown by F. Dassenoy *et al.* (2021) [34] with 15-20 nm silane-functionalized anatase TiO_2 nanoparticles. Those nanoparticles were tribologically tested with a 0.1 wt.% solution at 20°C and 100°C and compared with a 1 wt.% ZDDP solution. The functionalized nanoparticles performed better than ZDDP in wear reduction at ambient temperature, even forming a tribofilm, but were less effective at high temperature (Fig. 22). A 1 wt.% nanoparticles solution was also tested but proved to be less effective than the 0.1 wt.% one. XPS and TEM analysis were conducted and confirmed the presence of Ti and O elements, along with Si and a high carbon content, attributed to the silane polymer used as a capping agent, that may participate in tribofilm formation contrary to previously mentioned capped ZrO_2 [37,38].

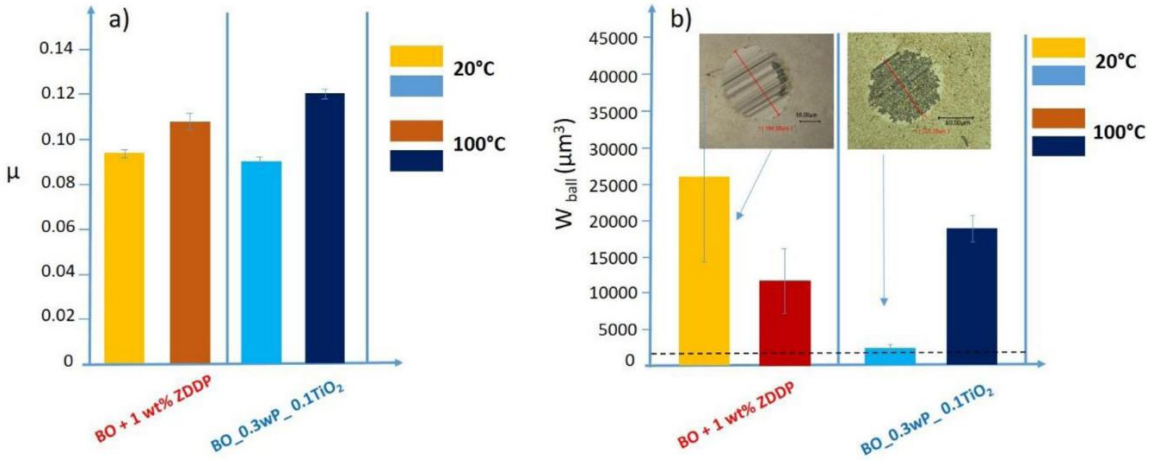

Fig. 22: Comparison of mean friction coefficients (a) and wear volumes (b) for 1 wt% ZDDP and 0.1 wt% TiO_2 (polymer-stabilized) in Group III base oil, tested at 3 mm/s, 1.13 GPa, and 20 or 100 °C. [34]

L. Zhang *et al.* (2011) [35] also studied 10 nm anatase TiO_2 nanoparticles functionalized with stearic acid (SA) and showed enhanced tribological properties in liquid paraffin. The optimal concentration of 0.125 wt% SA-TiO_2 provided the best performance, reducing friction and wear while improving load-carrying capacity. This was due to the effective dispersion of TiO_2 nanoparticles, facilitated by the stearic acid modification, as unmodified nanoparticles were also tested but rather increased wear due to abrasive agglomerates formation.

Most of these studies aimed to evaluate the intrinsic tribological properties of nanoparticles. Consequently, limited attention has been given to their compatibility with other common lubricant co-additives, such as antioxidants, detergents, or boundary additives. In this context, a new trend seems to arise from the finding of several synergistic effects between nanoparticles and traditional tribological additives.

1.3.4 Tribological Interaction between "Traditional Additives" and Nanoparticles

To incorporate an additive into a commercial oil formulation, it is essential to understand its interactions - both positive and negative - with other components already present in the blend. Recent studies have therefore investigated the tribological behavior of various nanoparticles in the presence of conventional additives such as ZDDP and MoDTC. These experiments suggest the emergence of synergistic effects between nanoparticles and traditional tribological additives, leading to enhanced tribological performance and improved nanoparticle suspension stability.

P. Deshpande *et al.* (2020) [26] demonstrated that the combination of MoDTC and 25 nm anatase TiO_2 nanoparticles showed better friction and wear reduction than each component used alone (Fig. 23).

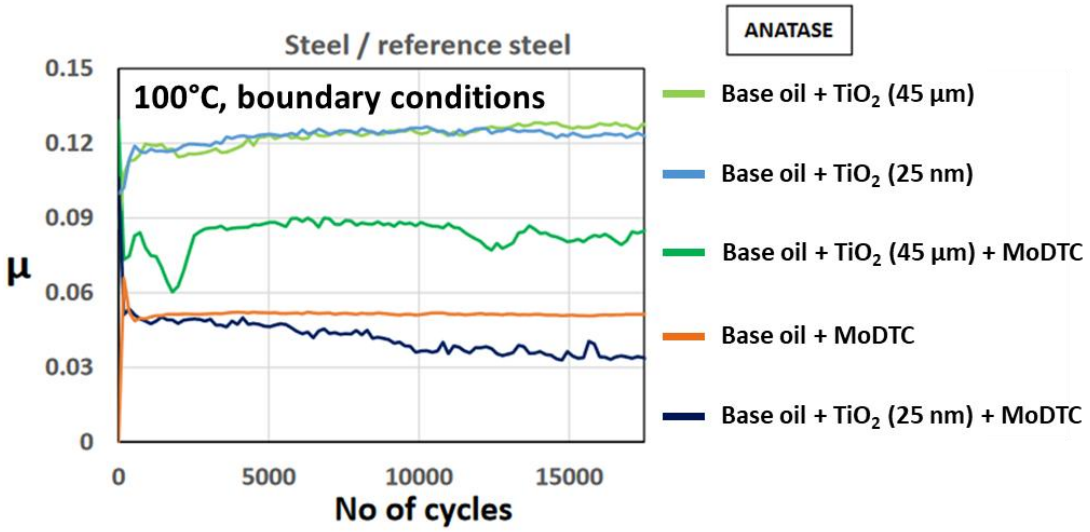

Fig. 23: Comparison of friction coefficients in a steel–steel contact for different lubricant solutions based on MoDTC or TiO_2 nanoparticles of anatase type (test duration: 1 h / 18,000 cycles). [46]

This effect was attributed to the tribo-catalytic properties of TiO_2, which promote MoS_2 sheets formation instead of tribologically inactive oxidated compounds like MoO_3 and sulfates (Fig. 24).

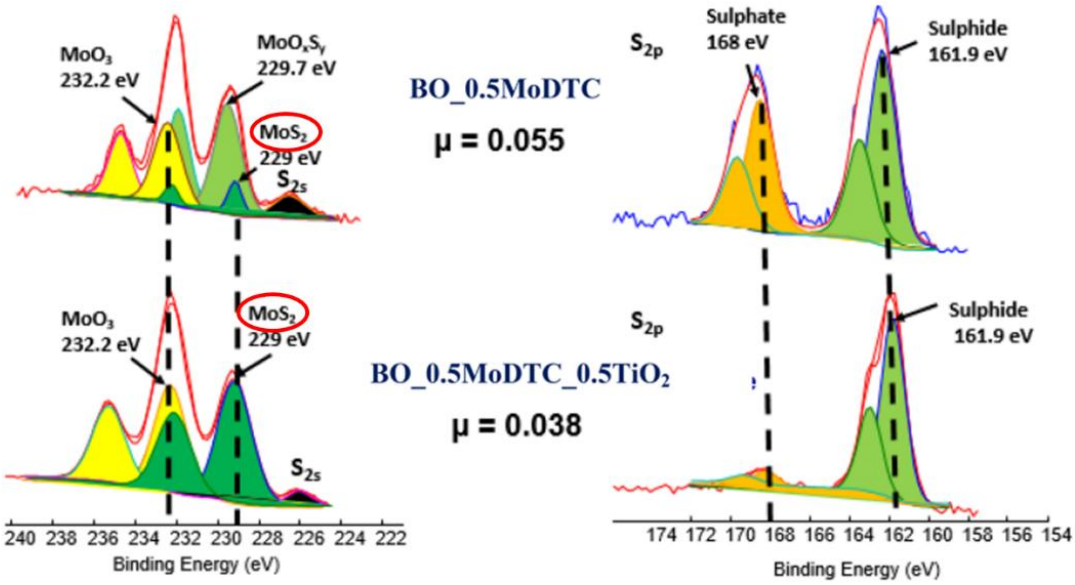

Fig. 24: High-resolution XPS spectra of tribofilms formed on steel–steel contacts using a lubricant containing MoDTC alone (top) and MoDTC combined with TiO_2 nanoparticles (anatase type, 25 nm) (bottom). [26]

It is noteworthy that in this study, TiO_2 nanoparticles were neither dispersed nor functionalized which caused them to quickly agglomerate. This effect was mitigated with the combination of the two additives, suggesting MoDTC's ability to improve nanoparticles dispersion. Given ZDDP's multifunctional role as an anti-wear, extreme pressure, and antioxidant additive [19], similar synergistic effects with nanoparticles may be achievable.

On this matter, X. Lei *et al.* (2021) [47] demonstrated that combining ZDDP with oleylamine-functionalized 5 nm CeO_2 nanoparticles creates a synergistic effect, enhancing friction and wear reduction as well as load-bearing capacity beyond what either additive achieves individually. The improved performance is attributed to the rapid formation of a nanocomposite tribofilm, where phosphate compounds from ZDDP decomposition act as a matrix and CeO_2 nanoparticles as reinforcing fillers. This nanocomposite nature enables the tribofilm to sustain higher loads and provides more effective wear protection under severe lubrication conditions, showcasing the potential of functionalized metal oxide nanoparticles in synergy with ZDDP to achieve superior tribological properties.

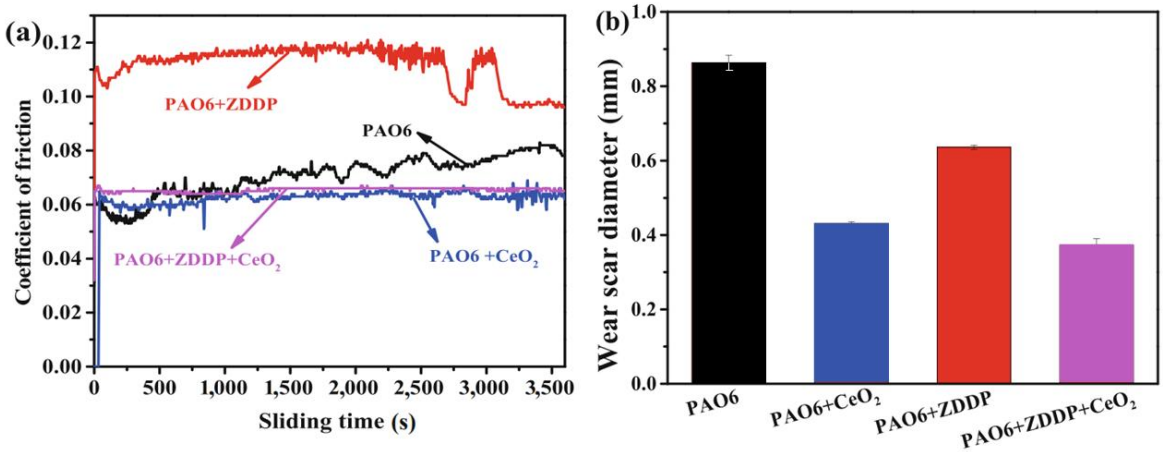

Fig. 25: Evolution of the friction coefficient in a steel–steel contact with different lubricants containing CeO_2 nanoparticles, ZDDP or a blend of both (a) and average wear scar diameter (b). Four-ball tribometer, 1200 RPM, 392 N, 75°C, 60 min.

The interaction between ZDDP and TiO_2 nanoparticles has also been studied, with particular focus on how TiO_2 surface characteristics impact its interaction with ZDDP. Sharma et al. (2019) [48] examined ZDDP interaction with both plasma-functionalized and unmodified 25 nm TiO_2 nanoparticles, observing that the unmodified nanoparticles displayed an antagonistic effect on friction and anti-wear properties when combined with ZDDP. This was attributed to the lack of chemical compatibility between unmodified TiO_2 surface and ZDDP, which hindered effective tribofilm formation. In contrast, plasma-functionalized TiO_2 nanoparticles showed better tribological properties when combined with ZDDP.

In a more recent study, Sharma et al. (2024) [49] explored this interaction further, testing a new protocol where ZDDP and unmodified 25 nm TiO_2 nanoparticles were added sequentially during tribological testing. This approach demonstrated that the sequence of additive introduction significantly affects tribological performance. When ZDDP was introduced first, followed by TiO_2, an antagonistic effect persisted. However, reversing the order led to a synergistic effect, suggesting that in the previous blend, ZDDP initially reacts faster, forming a tribofilm that competes with the TiO_2 nanoparticles rather than integrating with them. This could be explained by the abrasive nature of nanoparticles if they are not properly stabilized. The measurement of Electrical Contact Resistance (ECR) helps us visualize the formation of an insulating tribofilms and therefore the effect of using ZDDP or TiO_2 nanoparticles first. We can indeed see in Fig. 26 that an insulating tribofilm is formed only when TiO_2 NPs are introduced first (condition E versus C), which also leads to less wear (Fig. 27).

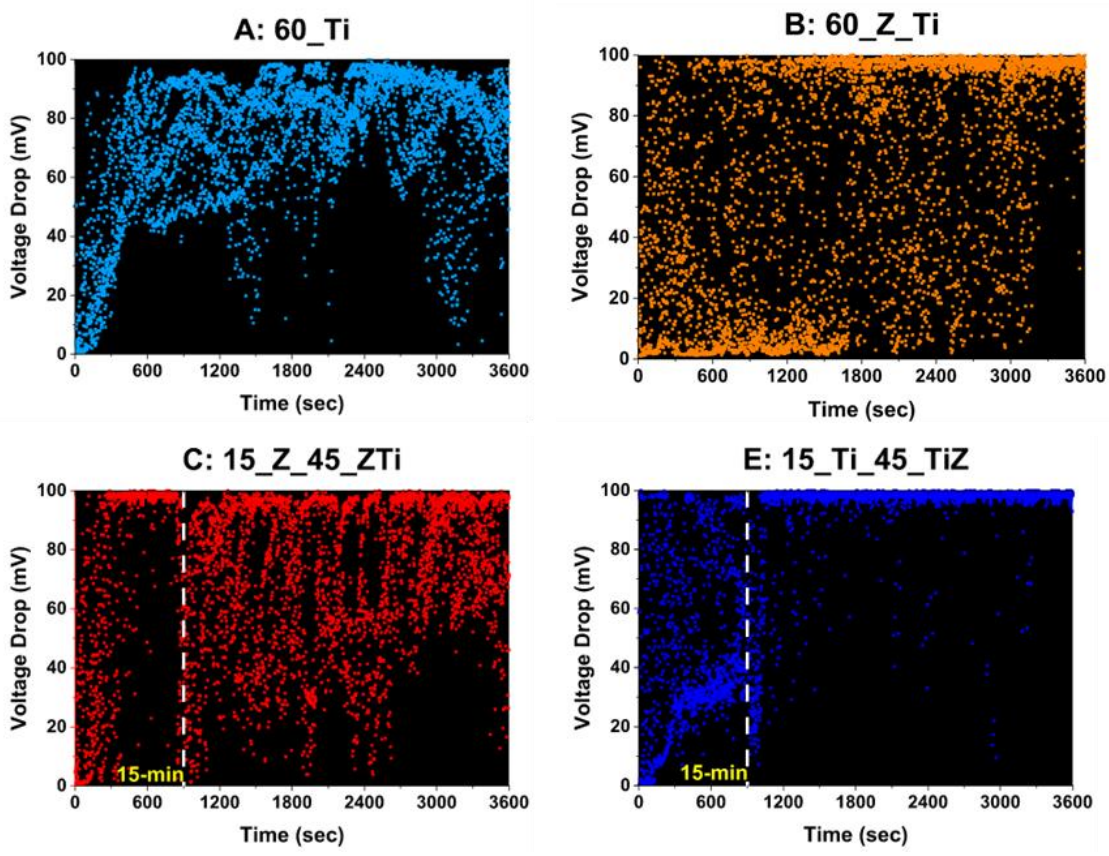

Fig. 26: Electrical Contact Resistance (ECR) plots showing voltage drop as function of time for tests - A: 60_Ti (TiO_2 NPs only); B: 60_Z_Ti (ZDDP + TiO_2 NPs); C: 15_Z_45_ZTi (ZDDP 15-min and then TiO_2 NPs addition); D: 30_Z_30_ZTi (ZDDP 30-min and then TiO_2); E: 15_Ti_45_TiZ (TiO_2 NPs 15-min and then ZDDP addition); F: 30_Ti_30_TiZ (TiO_2 NPs 30-min and then ZDDP addition). D and F conditions are not presented to improve legibility. [49]

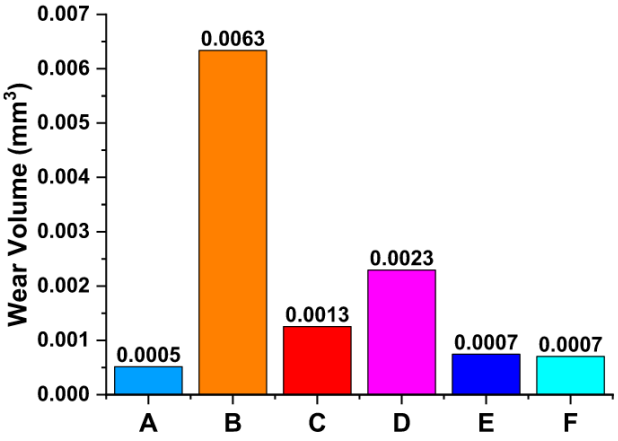

Fig. 27: Wear volume results for tests - A: 60_Ti (TiO_2 NPs only); B: 60_Z_Ti (ZDDP + TiO_2 NPs); C: 15_Z_45_ZTi (ZDDP 15-min and then TiO_2 NPs addition); D: 30_Z_30_ZTi (ZDDP 30-min and then TiO_2); E: 15_Ti_45_TiZ (TiO_2 NPs 15-min and then ZDDP addition); F: 30_Ti_30_TiZ (TiO_2 NPs 30-min and then ZDDP addition). [49]

The authors concluded that this competition between ZDDP and TiO_2 can result in antagonistic effects unless TiO_2 is introduced first to establish an initial layer that better promotes ZDDP decomposition and tribofilm formation.

Therefore, formulations combining nanoparticles with traditional tribological additives appear to be a promising approach for achieving superior tribological performance. As such, the investigation of these hybrid blends will represent a central focus of our study.

Another approach to addressing tribological challenges is to enhance the surface properties of materials in relative motion through functional coating. The following section provides a detailed discussion of this aspect.

1.4 Coatings for Tribological Applications

1.4.1 Designing Coatings for Tribological Applications

Material selection is always a complex process due to the multitude of constraints and requirements that must be met for a specific application. Key considerations include elastic strength, fatigue resistance, corrosion resistance, wear resistance, friction reduction, and manufacturing cost.

Among these constraints, many are directly or indirectly linked to surface-related issues. Fatigue behavior, for instance, is associated with the initiation and propagation of microcracks, which often originate at the material's surface. Corrosion involves electron exchange at the interface between two materials or environments and thus occurs at the surface. Wear and friction are governed by mechanical and chemical interactions between two surfaces in relative motion.

It becomes evident, therefore, that addressing many of these challenges involves focusing on surface engineering. This leads to the use of coatings, which offer the advantage of combining the beneficial properties of different materials - such as low cost, light weight, and ease of manufacturing for the bulk material - with surface-specific enhancements like hardness, wear resistance, low friction, and corrosion protection when a coating is used.

Tribological coatings are engineered surface layers designed to improve the performance of mechanical components under friction and wear conditions. In boundary lubrication regimes, where the lubricant film is too thin to fully separate surfaces, the coating's chemical and mechanical properties dominate contact behavior. By tailoring hardness, toughness, surface chemistry, and microstructure, coatings can significantly extend component life, reduce friction losses, and improve energy efficiency. [50]

Across industrial sectors, a wide range of tribological coatings are deployed to address specific performance requirements [51] [52]. Notable examples include:

- Physical Vapor Deposition (PVD) coatings such as TiN, CrN, and diamond-like carbon (DLC) for high hardness, wear resistance, and low friction.
- Chemical Vapor Deposition (CVD) coatings including carbides, nitrides, and polycrystalline diamond for extreme temperature stability and conformal coverage.
- Thermal spray coatings (for example plasma-sprayed Al_2O_3) for thick, durable protection against abrasion and erosion.
- Polymeric and composite coatings incorporating solid lubricants (PTFE, MoS_2, graphite) or hard fillers for low friction and corrosion resistance.
- Cold spray coatings for oxide-free, dense deposits of ductile metals and composites with minimal thermal degradation.

In addition to providing high hardness to prevent abrasive wear, coatings can be engineered to display tailored functionalities, such as chemical reactivity that enhances tribofilm formation from anti-wear additives, or electrical properties that modulate electro-tribological interactions. Their performance and suitability are strongly dependent on the operating conditions, including applied load, sliding velocity, lubrication regime, temperature, and environmental exposure.

Within this framework, composite coatings are of particular interest because they provide a versatile platform to combine distinct classes of materials - typically metallic, ceramic, or solid lubricant phases - into a single architecture. Such combinations enable the synergistic exploitation of individual properties: for instance, metallic matrices offer toughness and adhesion, ceramic reinforcements contribute hardness and wear resistance, and dispersed lubricating phases reduce friction through in situ tribofilm formation. By tuning the microstructure, composition, and distribution of these phases, composite coatings can be designed to withstand severe tribological environments, maintain low friction under variable lubrication conditions, and extend the service life of engineering components beyond the capabilities of monolithic coatings.

For example, Borgaonkar *et al.* (2021) [53] investigated a composite coating combining MoS_2 as a solid lubricant with TiO_2 nanoparticles to enhance mechanical support and hardness. The coating was applied on a pretreated substrate using a binder-assisted deposition method which involves mixing coating particles with a binder that adheres them to the substrate, which is then dried and cured. Dry sliding tests demonstrated that the composite exhibits a lower coefficient of friction and improved wear resistance compared to MoS_2 alone, provided the TiO_2 content is optimized as shown in Fig. 28 with the lowest CoF and wear rate obtained at 15 wt.% of TiO_2.

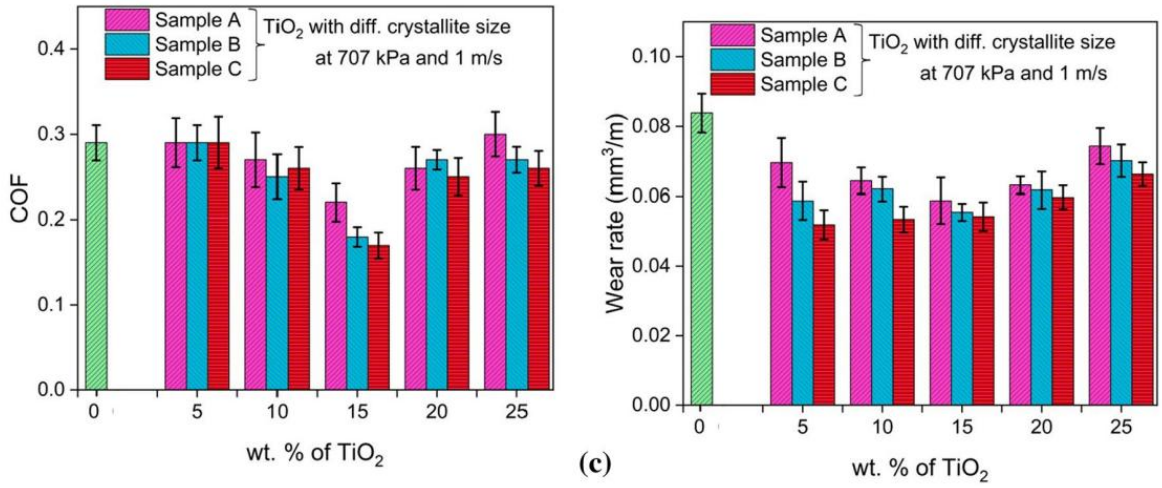

Fig. 28: Effect of addition of different wt.% of TiO_2 on COF and wear rate at 707 kPa contact pressure with 1 m/s sliding speed in dry test condition. [53]

The study concludes that TiO_2 reinforcement enhances the durability and tribological performance of the coating; however, excessive TiO_2 can lead to cohesion defects and microcracking, reducing the overall effectiveness.

Other studies have also reported that the incorporation of hard reinforcements in a metallic matrix can significantly reduce both the coefficient of friction and wear rate. Chandramouli *et al.* (2025) [54] investigated the tribological performance of iron-based composite coatings deposited via High Velocity Oxy-Fuel (HVOF) spraying, a technique in which powder particles are projected onto a substrate at supersonic speeds and elevated temperatures (~2800 °C). The study specifically evaluated the wear resistance and frictional behavior of these coatings under elevated temperature conditions, which are critical for aerospace and automotive applications. The results demonstrated that the inclusion of WC-Co and Cr_3C_2 carbides in a SS316L matrix increased the surface hardness of the steel substrate, leading to a substantial reduction in wear rate across a wide range of temperatures and applied loads (Fig. 29).

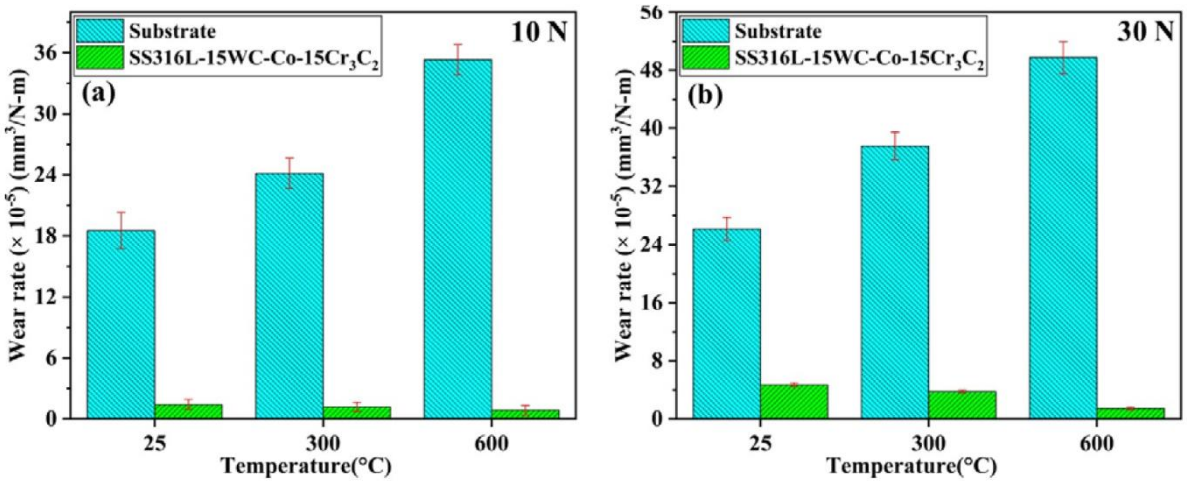

Fig. 29: Comparison of wear rate obtained with a composite coating and the substrate at various temperatures and loads in a dry test condition. [54]

Therefore, various fabrication methods exist to deposit composite coatings for enhancing the tribological performance of a material. Each technique presents specific advantages and limitations. For instance, in the case of MoS_2 and TiO_2 deposition using a binder-assisted method, excellent tribological performance can be achieved, but the adhesion to the substrate remains relatively low. In contrast, HVOF spraying provides strong adhesion and good tribological results; however, the high temperatures involved in the process can alter the structure and chemistry of the deposited mixture as well as the substrate, limiting its applicability to certain materials. For this reason, attention has turned to a similar technique that relies on supersonic particle deposition but at low temperatures: the Cold spray process.

1.4.2 Cold Spray Coatings Background and Principle

One surface engineering technique that has gained increasing attention in recent years is Cold spray deposition. Unlike traditional thermal spray processes (Fig. 30), Cold spray operates at relatively low temperatures, typically below the melting point of the materials being sprayed.

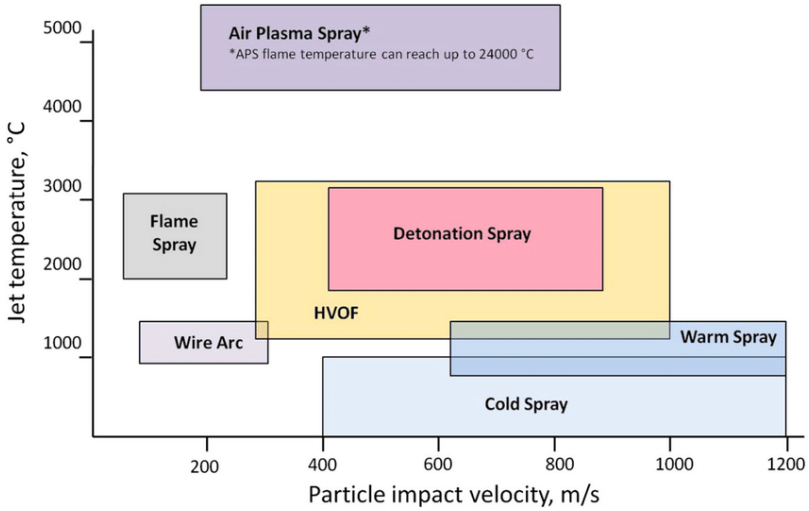

Fig. 30: Thermal spray family chart. [55]

In this process, fine powders are accelerated to supersonic velocities using high-pressure gas, and the particles bond to the substrate through plastic deformation upon impact as described in Fig. 31.

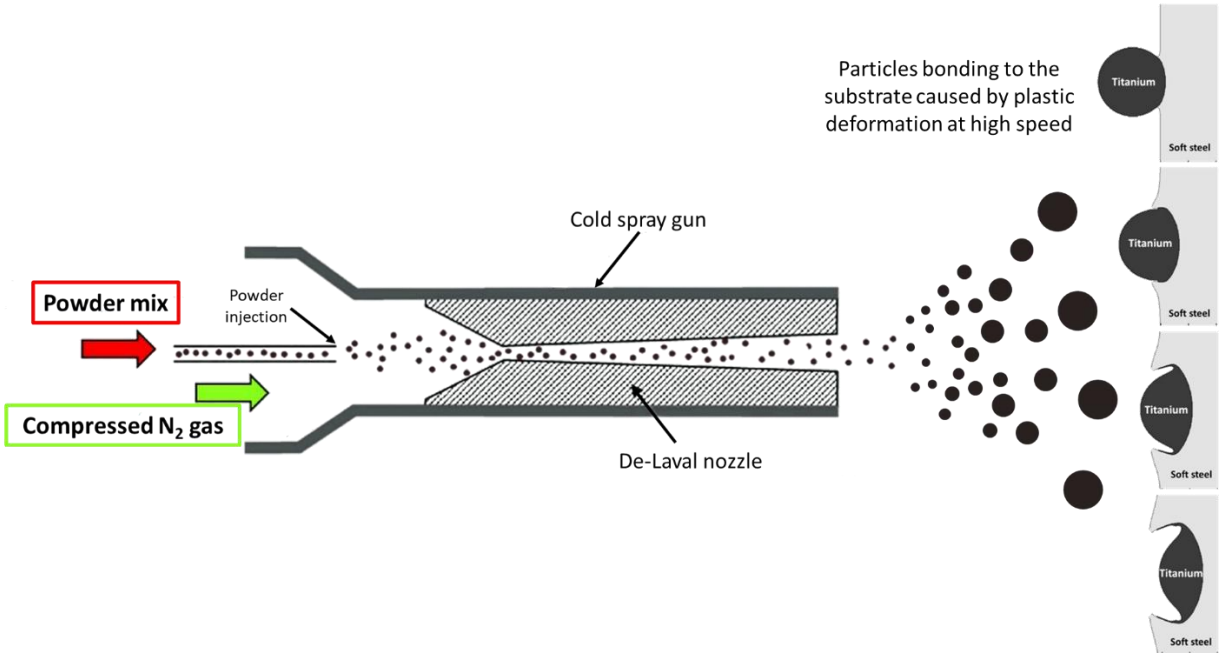

Fig. 31: Schematic principle of Cold spray deposition. [56]

This low-temperature approach offers several significant advantages:

- Wider material compatibility: Since the powders do not melt, cold spray is suitable for a broad range of materials, including metals, metal alloys, and some polymers, that might otherwise degrade or oxidize at high temperatures.

- Preservation of powder properties: The reduced thermal input minimizes oxidation and thermal degradation, allowing the intrinsic properties of the feedstock material to be retained in the final coating.

- Composite coatings: Cold spray allows powder blending, enabling the creation of composite or multi-phase coatings by mixing different powders prior to deposition. This opens the door to highly customizable surface properties.

- Thick coatings: The process enables the formation of relatively thick layers, reaching up to several millimeters, which is advantageous for wear-resistant or structural coatings.

A limitation lies in the powder material: in the case of a blend, at least one constituent must exhibit good plastic deformability to ensure the formation of a compact and robust coating. This will also influence adherence with the substrate that is overall not as good as with high temperature processes such as HVOF. It can however be optimized through surface preparation and is as well highly dependent on the substrate nature.

Thanks to these features, Cold Spray is particularly well-suited for applications requiring high-performance coatings with minimal thermal impact on the substrate and the initial powder, such as in aerospace and automotive industries. To achieve robust and durable coatings, careful selection of both the powder and the substrate material is essential, as their compatibility directly influences deposition efficiency and the resulting mechanical properties.

A good illustration of this material design strategy is provided by the work of Zhang et al. (2018) [57], who investigated the development of self-lubricating metal matrix composites (SLMMCs) produced by Cold spray. In their study, copper was selected as the matrix because of its excellent electrical conductivity, making it suitable for dry electrical contact applications. However, pure copper exhibits low hardness, which results in a high coefficient of friction and significant wear, thereby limiting component lifetime.

To address this, solid MoS_2 particles were sprayed together with copper powder on an aluminum substrate. MoS_2 is a well-known solid lubricant capable of reducing friction even under dry sliding conditions. The addition of MoS_2 indeed significantly decreased the CoF compared to pure copper coatings. Nevertheless, because the sliding contact remained dry and the matrix was still relatively soft, wear resistance was insufficient. To overcome this limitation, WC (tungsten carbide) particles were further introduced into the composite. The presence of WC increased the overall hardness of the coating, which not only improved wear resistance but also enhanced the lubricating effect of MoS_2, resulting in both lower CoF and reduced wear rates as illustrated in Fig. 32.

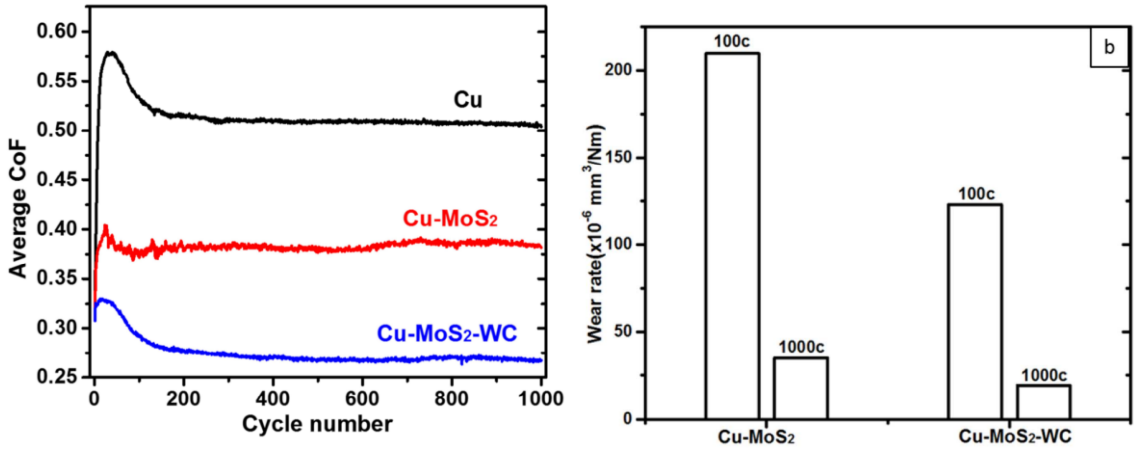

Fig. 32: Average coefficients of friction (CoFs) of Cu-MoS2, Cu-MoS2-WC, and pure Cu in dry nitrogen (left graph). Wear rates of Cu-MoS2 and Cu-MoS2-WC at 100 and 1000 cycles in dry nitrogen (right graph). [57]

This study highlights the relevance of Cold spray for producing multifunctional SLMMCs. Conventional manufacturing processes such as casting, laser cladding, powder metallurgy, or thermal spraying involve high temperatures, which can lead to the decomposition or phase transformation of solid lubricants like MoS_2, thereby degrading their tribological performance [58]. In contrast, cold spray enables the deposition of such composites at lower temperatures, preserving the structural integrity and lubricating capacity of MoS_2, while allowing the incorporation of hard reinforcements such as WC to achieve a well-balanced combination of low friction and high wear resistance.

Other studies have demonstrated the potential of cold spray to produce coatings with promising tribological performance under dry sliding conditions [59–61] but very few on lubricated contacts. The most significant contribution in this area is the doctoral thesis of L. Aubanel (2022) [62], which will serve as a key reference for the present work on composite cold sprayed coatings designed for lubricated applications.

1.4.3 Cold Spray Coatings in Lubricated Applications

In his thesis, L. Aubanel (2022) [62] investigates the influence of ICE cylinder material composition and surface texture on friction. The focus is exclusively on the top and bottom regions of the cylinder, where the lubrication regime is either boundary or mixed.

He therefore uses Cold spray technique in order to create a composite coating on a 6060 aluminum substrate. Different materials have been tested for the matrix as well as for the reinforcement.

For the matrix, the objective was to select a powder combining good deformability upon impact with sufficient flowability to ensure stable and homogeneous feeding of the cold spray nozzle. For this reason, single-component cold spray tests were carried out, and stainless steel 410L was retained and evaluated with different granulometries. The powders were produced by gas atomization under nitrogen, resulting in spherical morphologies generally favorable for both feeding and deposition.

Several particle size distributions were investigated in order to assess their influence on porosity, deposition efficiency, and coating thickness. Finer powders reached higher particle velocities during spraying, which improved deposition efficiency and reduced porosity (Fig. 33); however, their poor flowability led to unstable feeding conditions and inhomogeneous coatings. Consequently, powders in the 5-25 µm range were discarded. The granulometry 10-32 µm was identified as the most suitable, providing a balance between deposition efficiency and process stability. Under these conditions, cold sprayed 410L coatings exhibited a microhardness of approximately 380 HV.

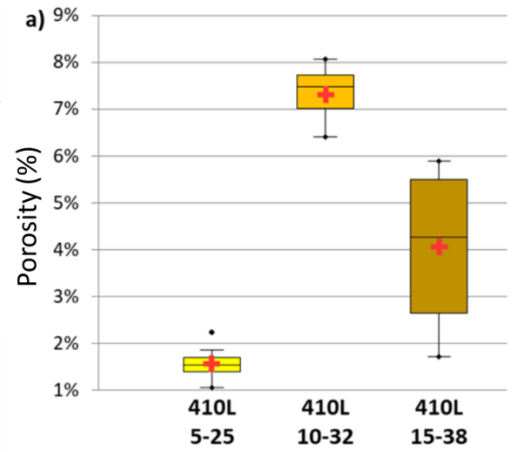

Fig. 33: Effect of 410L particle size distribution (5-25 µm; 10-32 µm and 15-38µm) on the porosity of the cold sprayed material. [62]

Cold spray tests were then conducted with the addition of a reinforcement. Two reinforcement powders were investigated, both produced by gas atomization to ensure spherical particle morphology. The first was M2 tool steel, characterized by a hardness of approximately 800 HV. The second was 420 stainless steel, with a lower hardness of around 700 HV.

Comparative analysis revealed that coatings reinforced with M2 particles exhibited both higher hardness and lower porosity than those reinforced with 420 stainless steel. Consequently, M2 was selected as the preferred reinforcement phase, as it enabled the composite to achieve a macro-hardness superior to that of the single-component 410L coating as well as the BSC (Bore Spray Coating) reference commonly used in cylinder applications (Fig. 34). The composite formulation ultimately retained for tribological testing consisted of a 410L matrix reinforced with 20 vol.% M2 particles, thereby combining the toughness and ductility of the stainless steel matrix with the hardness and wear resistance contributed by the tool steel reinforcement.

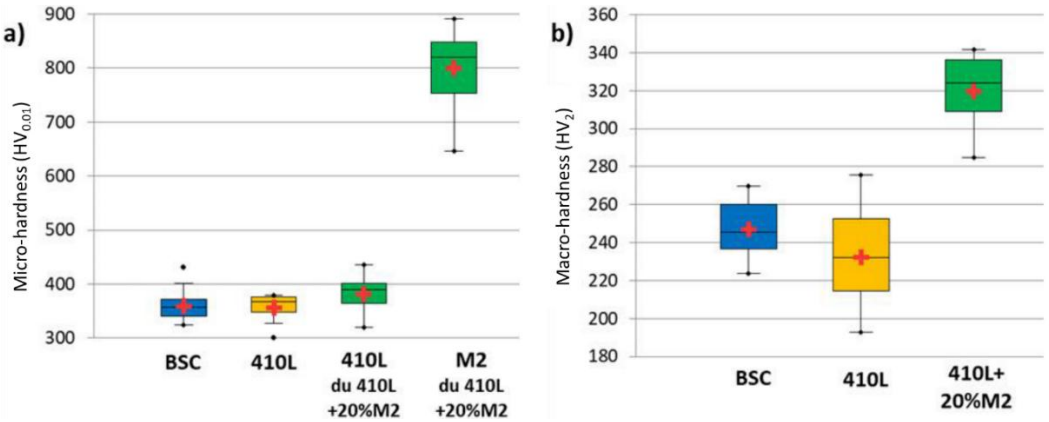

Fig. 34: Micro (a) and macro (b) hardness comparison between 410L and 410L+20%M2 cold spray coatings. BSC (Bore Sprayed Coating) is used as a reference for cylinder application. [62]

The composite cold-sprayed coatings were subsequently polished using different methods, namely SiC1200 abrasive paper, plateau honing, and OPS (Oxide Polishing Suspension) finishing. OPS corresponds to a colloidal silica suspension widely used in metallography to achieve mirror-like surfaces, effectively removing residual scratches and yielding a very smooth finish. In contrast, plateau honing is a finishing process designed to generate a surface consisting of load-bearing plateaus and lubricant-retaining valleys, a texture particularly relevant for cylinder bore applications.

It was observed that, except for the OPS treatment, polishing revealed a relief between the M2 reinforcement particles and the 410L matrix (Fig. 35). This feature may be advantageous for tribological applications, as the reinforcement phase is then more exposed and can support the majority of the applied load during sliding.

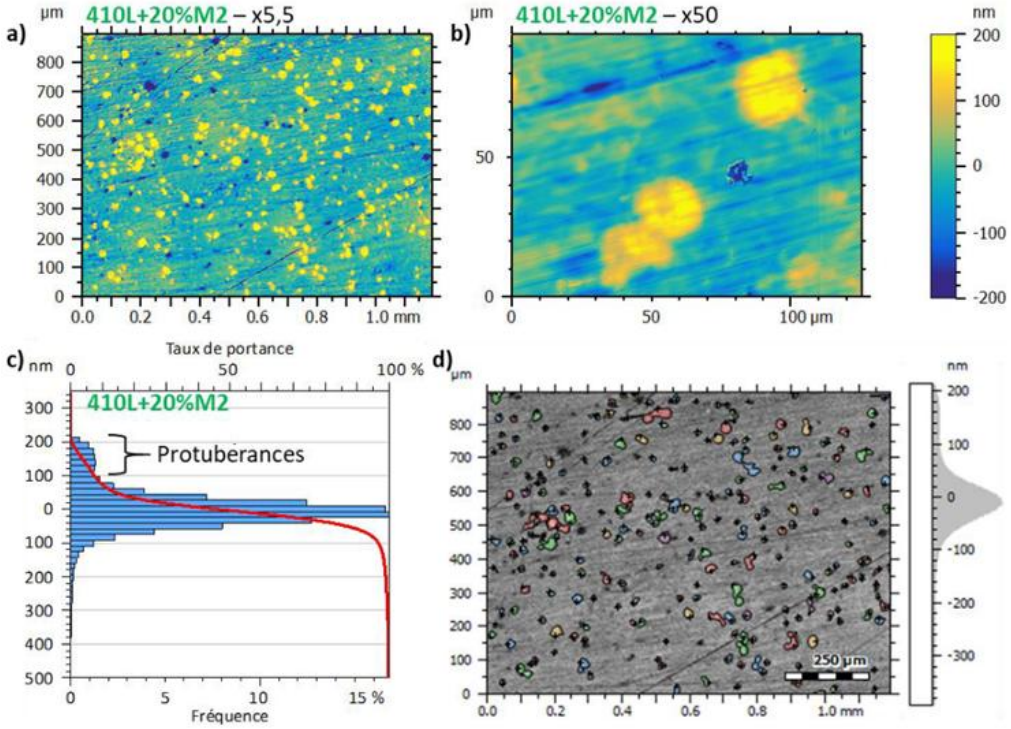

Fig. 35: Profilometric analyses performed by WLI (White light interferometry) on the surface after SiC1200 polishing of the composite 410L+20%M2 coating at a) ×5.5 magnification and b) ×50 magnification. c) Histogram of height distributions obtained from the WLI image at ×5.5 magnification, along with the Abbott curve. d) Identification of protuberances on the surface of the 410L+20%M2 coating by height thresholding, enabling their analysis. [62]

Tribological tests were conducted at 100 °C using a formulated oil containing ZDDP and MoDTC. The results showed that the single-component 410L coating exhibited the greatest friction reduction (Fig. 36), but its wear resistance was significantly lower (Fig. 37). In contrast, the 410L+M2 20 vol% composite demonstrated a moderate reduction in the coefficient of friction but notably provided excellent wear resistance compared to both the single-component coating and the reference process (BSC).

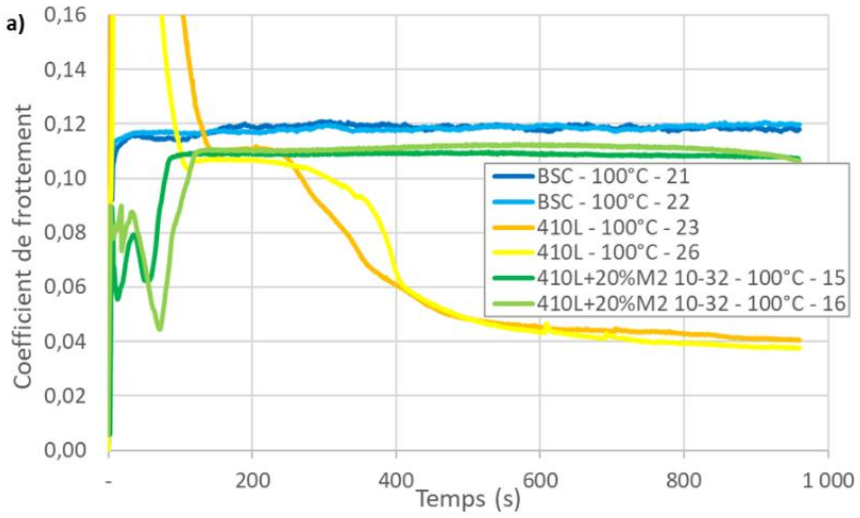

Fig. 36: Evolution of the friction coefficient of the 410L+20 vol% M2 composite coating compared to 410L and BSC coatings in a formulated engine oil at 100 °C. [62]

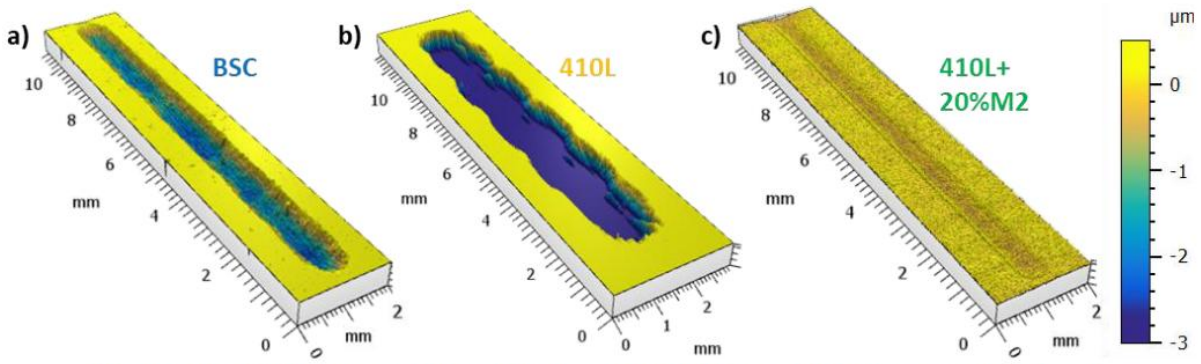

Figure 5-17 : Analyse topographique globale par WLI de la trace de frottement sur les différents revêtements, après l'essai tribologique à 100 °C : a) BSC, b) 410L et c) 410L+20%M2.

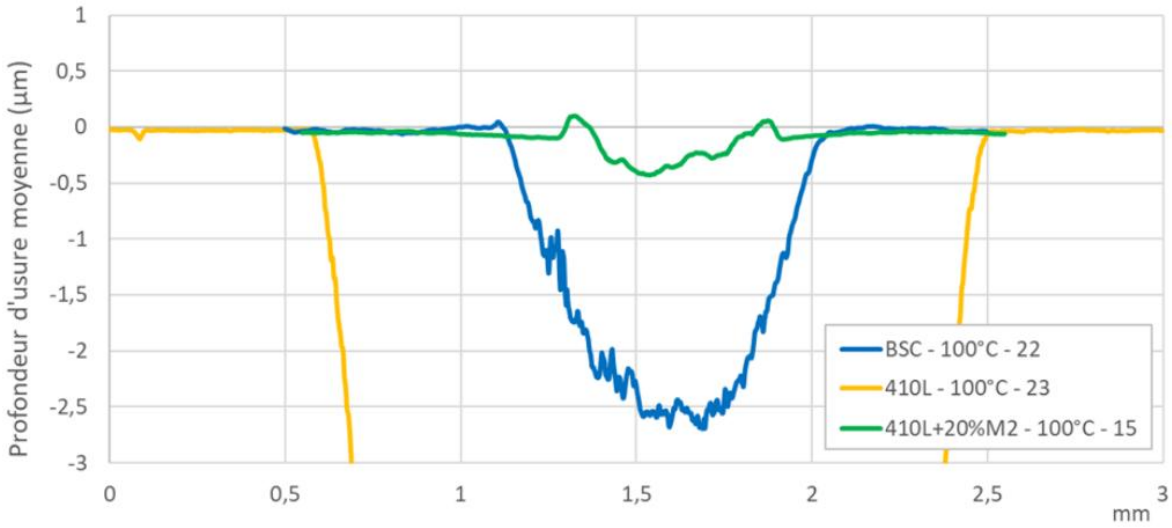

Fig. 37: Top: global profilometric analysis by WLI of the wear tracks on different coatings after tribological testing at 100 °C: (a) BSC (reference), (b) 410L, and (c) 410L+20 vol% M2.
Bottom: average wear profiles of the BSC (reference), 410L, and 410L+20 vol% M2 coatings after testing at 100 °C. [62]

Key findings include that the combination of tribofilm formation and asperity-rich topographies was essential to achieve a low coefficient of friction and negligible wear, even under extended test durations.

A mechanism for tribofilm evolution was proposed. At 100 °C, ZDDP decomposes to form an initial tribofilm on the protuberances and subsequently on the 410L matrix. This first layer, rich in iron compounds, stabilizes wear but corresponds to a relatively high friction plateau. As sliding progresses, the tribofilm on protuberances becomes thinner and changes in composition, while a second tribofilm layer forms on the matrix, enriched in zinc, sulfur, and molybdenum. Due to MoDTC decomposition, this second layer contains MoS_2 lamellae aligned parallel to the surface, which are most likely responsible for the sharp reduction in friction to low values.

It is likely that the combination of protuberances, which support part of the load and the formation of the tribofilm on the matrix enables the achievement of favorable tribological properties.

Finally, these results demonstrate the feasibility of engineering a composite coating by cold spray deposition for tribological applications under lubricated conditions. This approach could open the way to surface optimization for electric vehicles, whose mechanical components are less complex than those of internal combustion vehicles but are subjected to tribological stresses that can be significantly higher, as will be discussed in the following section.

1.5 New Challenges Brought by Electrification of Vehicles

Electric vehicles (EVs) have become a central element of the global strategy to reduce greenhouse gas emissions and urban air pollution. Their main advantage is the elimination of local exhaust emissions during use, which, when combined with low-carbon electricity, contributes significantly to climate targets. EVs also offer superior energy efficiency compared to internal combustion engines, owing to higher conversion efficiency and regenerative braking. From a technical perspective, powertrain architectures are often mechanically simplified, with fewer moving parts than conventional engines. However, electrification introduces new demands related to batteries, power electronics, and transmission systems.

The EV market has grown at an exceptional pace over the past years. In 2024, global sales reached about 17 million units, representing nearly 25% growth compared to 2023. Projections for 2025 exceed 20 million vehicles, confirming the acceleration of adoption. China remains the dominant market, while Europe continues its expansion under strong regulatory support and increasing competition from Asian manufacturers. These trends, reinforced by large-scale industrial investment, indicate that automotive electrification is not only established but accelerating. [63]

Electrification however introduces a range of new challenges across multiple domains, including thermal management, material compatibility, noise reduction, etc… as well as tribological considerations that remain critical, particularly in terms of lubrication which will be addressed in this section.

1.5.1 Increased Stress in the Drivetrain System

The integration of electric motors simplifies the complexity of vehicle drivetrains; it also imposes fundamentally different operating conditions on mechanical components compared to internal combustion engine systems. As described in Fig. 38, one of the most significant distinctions is the torque-speed profile of electric motors: they provide maximum torque from standstill and maintain it across a broad range of speeds. This characteristic enables most electric vehicles to operate with a single-speed transmission, eliminating the need for complex multi-ratio gearboxes.

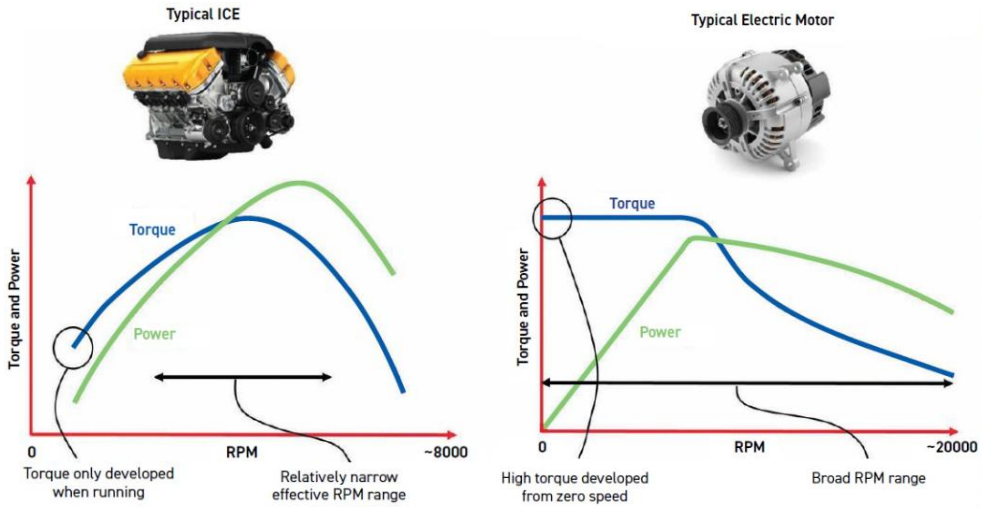

Fig. 38: Characteristics of internal combustion engines (left) and electric motors (right), showing torque and power as functions of rotational speed [12]

As a result, mechanical components such as gears and bearings must function efficiently across a wider speed range - from low shaft speeds (boundary/mixed lubrication regime) to very high rotational speeds (hydrodynamic regime). This dual requirement presents several tribological challenges:

- Increased load in the boundary regime: The high torque available at low speeds leads to elevated contact pressures in gear teeth and bearing surfaces during vehicle launch and low-speed operation. This intensifies wear and scuffing risks in the boundary lubrication regime, where the lubricant film is thin or absent.

- Severe mixed lubrication conditions: because a single gear ratio must accommodate the full driving spectrum, gear and bearing materials are exposed to frequent transitions between boundary, mixed, and hydrodynamic lubrication regimes, especially under acceleration and regenerative braking phases.

- High-speed operation and viscous losses: EV motors can operate at speeds exceeding 15 000 to 20 000 RPM. To limit viscous drag and churning losses at such speeds, low-viscosity lubricants are required. However, reducing viscosity further exacerbates the challenges in the boundary regime, where the lubricant must still prevent direct asperity contact under high loads.

For a Newtonian fluid (i.e., with constant viscosity under applied stress) that is incompressible and forms a fluid film between two solid surfaces, the following relationship applies:

$$\sigma_t = \eta\dot{\gamma}$$

where σ_t is the tangential or shear stress, η is the dynamic viscosity, and $\dot{\gamma}$ is the shear rate.

Therefore, reducing the viscosity η leads to a decrease in shear stress σ_t, and consequently, in friction μ since $\mu = \frac{\sigma_t}{\sigma_n}$, with σ_n the normal stress applied at the interface between the two surfaces [64].

This is the main reason why, in recent years, manufacturers have favored low-viscosity fluids [65]. However, this approach also reduces the thickness of the lubricating film, thereby accelerating the transition toward boundary and mixed lubrication regimes.

These operational constraints demand a new generation of gear and bearing lubricants - formulated with advanced base oils, optimized additive chemistry, and tailored rheological properties - to ensure adequate protection under both extreme pressure and high-speed conditions.

Another factor that can exacerbate tribological contact conditions in electric vehicles is the risk of stray electrical currents. In these systems, propulsion is typically delivered by a large alternating current (AC) induction motor or a permanent magnet synchronous motor, powered by a high-capacity direct current (DC) battery pack. The DC output is converted to three-phase AC by an inverter using high-frequency pulse-width modulation (PWM) to approximate a sinusoidal waveform. Although this method improves drive efficiency, the rapid switching transients inherent to PWM operation can induce local voltage spikes along the motor shaft, resulting in shaft voltages and associated stray currents [66]. Both DC and AC currents were evaluated by Peter Lee et al. (2023) [67] at amplitudes of 2 A and 4 A, respectively. These levels are regarded as extreme for an EV motor-gearbox system, based on measurements conducted at the Southwest Research Institute (SwRI). However, the corresponding in-field current values were not reported.

Several grounding paths exist for these currents, but the most common involves passage through the motor's rolling element bearings due to their proximity to the source of voltage generation. When the potential difference across the bearing exceeds the dielectric strength of the thin lubricating film separating the rolling elements from the raceways, dielectric breakdown occurs. This results in electrical discharge machining (EDM)-type events, which can induce localized melting, pitting, and surface erosion. These damages are readily observable without magnification, as shown in Fig. 39.

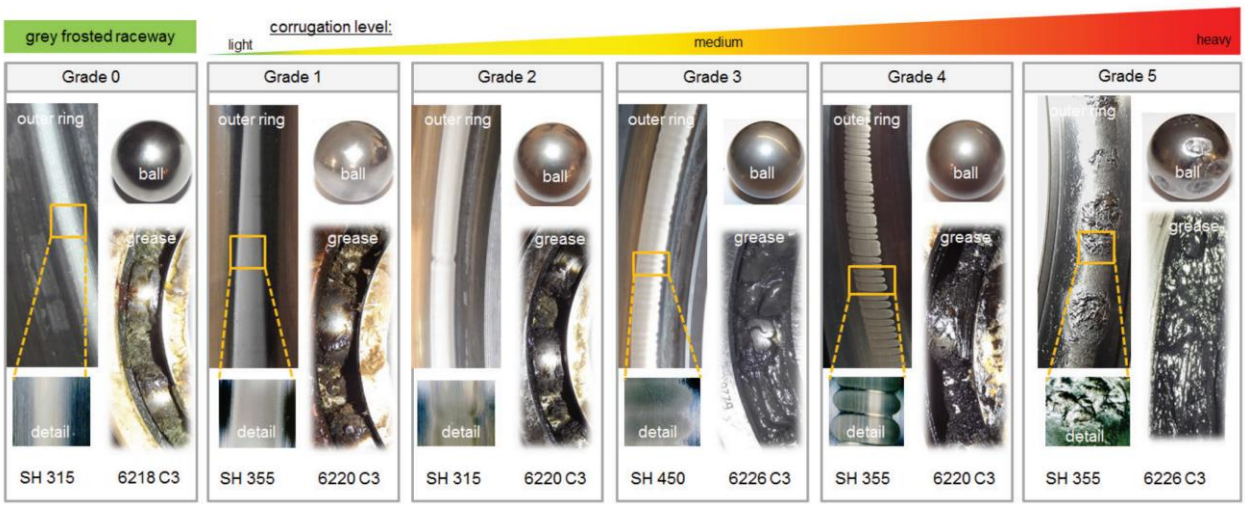

Fig. 39: Photographic examples of varying severity levels of electric discharge damage on ball bearings [68]

The effect of electric current on tribological contacts has already been extensively studied in the context of ball bearing optimization, particularly under hydrodynamic lubrication conditions. In such cases, the lubricating film is sufficiently thick to separate the contact surfaces, and the system can be electrically described as a capacitive circuit: the fluid film acts as a dielectric insulator, while the metallic surfaces on either side behave as electrodes accumulating electrical charge. When the accumulated charge reaches the breakdown voltage of the lubricant film, a dielectric breakdown occurs, resulting in an electrical discharge arc across the contact (Fig. 40). This arc can cause severe surface damage, including melting, pitting, and erosion [69,70].

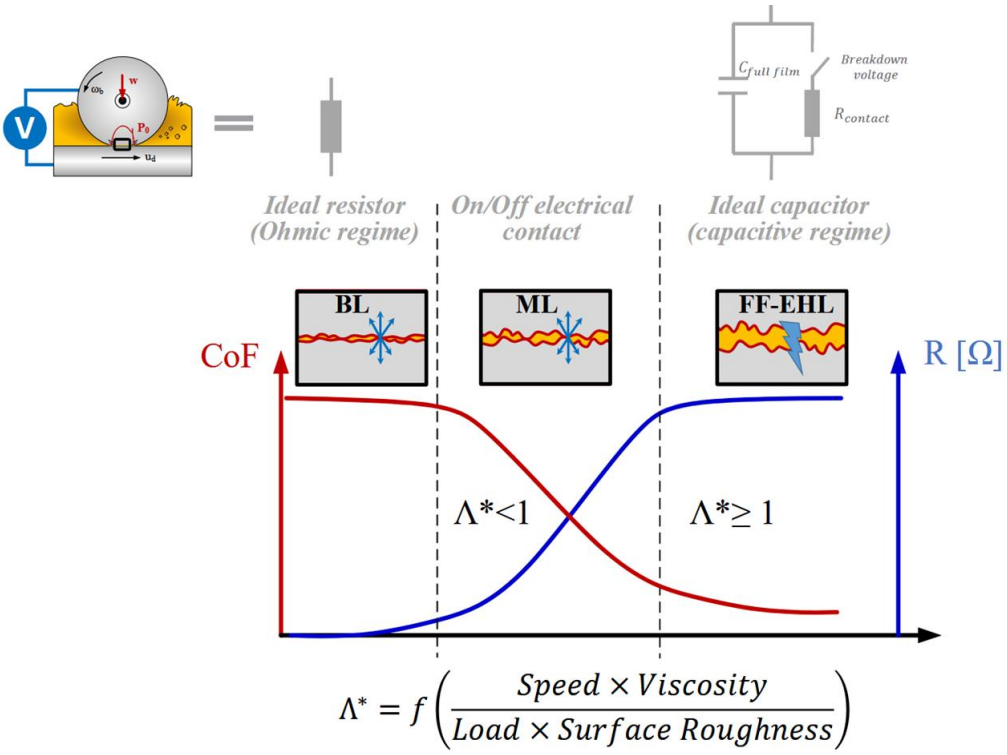

Fig. 40: Evolution of friction and electrical resistance across boundary, mixed, and full-film lubrication regimes based on the Stribeck curve [69]

In contrast, boundary and mixed lubrication - characterized by direct or near-direct contact between asperities - have traditionally been described as purely resistive systems, due to the continuous metal-to-metal contact. As such, they have received relatively little attention. However, emerging studies suggest that even in boundary regimes, electric current can hinder tribological performance [71,72].

Moreover, when anti-wear additives such as ZDDP are present, a tribochemical reaction can form an insulating tribofilm on the surface. This tribofilm introduces capacitive behavior into what would otherwise be a resistive system, thereby increasing the potential for charge accumulation and sudden discharge events.

Consequently, boundary contacts in EV drivetrains - already operating under more severe conditions due to high torque and thin lubricant films - may also be susceptible to stray current-induced damage. This underscores the need for further research into electro-tribological interactions in mixed and boundary regimes, particularly in the context of EV-specific lubricant formulations.

On this matter, recent articles pointed out the possible effects of electric current flowing through tribological contact in boundary or mixed lubrication regimes.

1.5.2 Wear and Friction under Electrified Conditions

The study of electrified tribological contacts for EVs has emerged as a rapidly expanding research field, driven by the increasing expansion of electric vehicles. As illustrated in Fig. 41, the number of publications has risen significantly in recent years, reflecting the growing scientific interest in understanding and optimizing lubrication and wear under electrical currents.

This graph was generated based on a Scopus search using the following query:

("lubrication" OR "tribology" OR "lubricant" OR "sliding contact" OR "rolling-sliding contact" OR "four-ball test") AND ("electric current" OR "electrical potential" OR electrotribology OR "electrified interface") AND (LIMIT-TO(EXACTKEYWORD, "Electric Vehicles"))

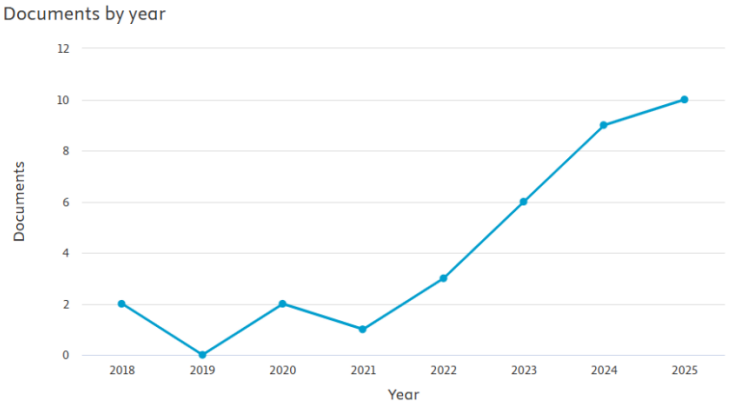

Fig. 41: Evolution of publications on electrified tribological interfaces in electric vehicles (2018–2025). Data source: Scopus.

This research topic has been notably addressed by four main research teams:

Ali Erdemir and its collaborators (Texas A&M University, USA) have been at the forefront of research on tribological contacts under electrified conditions. Their work focuses on understanding the influence of electrical currents on friction, wear, and lubricant. Specifically, Erdemir's group has conducted pioneering studies employing pure sliding configurations such as four-ball, pin-on-disk, and reciprocating tribometers, as well as rolling-sliding tests using a PCS Instruments MTM tribometer. Experiments were performed under DC and AC mode at fixed current levels, using both fully formulated lubricants (e.g., ATF) and individual additive solutions, including MoDTC and zinc ZDDP. [71,73–77]

Southwest Research Institute (SwRI, San Antonio, USA) appears to have worked closely with Ali Erdemir's group, complementing their fundamental studies with applied testing on electric vehicle driveline lubricants. Their work emphasizes the practical aspects of EV lubrication and the development of advanced experimental setups for studying electrified tribological contacts. Notably, SwRI has contributed to the electrification of the PCS Instruments MTM tribometer, enabling more representative laboratory test of electrified rolling-sliding conditions. [67,78]

Hugh Spikes and collaborators at Imperial College London focus on the fundamental mechanisms of tribofilm formation and electrochemical interactions under electrical potentials. Their studies are conducted using a PCS Instruments MTM tribometer operating in rolling-sliding conditions, where the influence of electrical current at a fixed potential on friction, surface damage, and tribochemical film formation is investigated. This research builds on earlier electrochemical investigations of lubricant additives, such as ZDDP, to better understand how imposed potentials affect additive reactivity and tribofilm growth under mixed lubrication regimes. [72,79,80]

Chinese research teams, including groups at Tsinghua University, Beijing Institute of Technology and Chinese Academy of Sciences focus on electrified interfaces in bearings and gears for electric vehicles. Their work explores electro-tribochemical mechanisms of lubricant additives under electrified conditions, conducting experiments with high electrical currents (up to 8 A) on base oils, ZDDP-containing formulations, and fully formulated lubricants. [81–83]

The majority of those experimental investigations converge on a key observation: the application of current leads to a severe increase in wear volume, especially at higher current densities (from 0.5 A to 3 A and more). In dry contacts, electrical current exacerbates abrasive and oxidative wear, often promoting the formation of third-body particles and oxide debris such as hematite (Fe_2O_3) and magnetite (Fe_3O_4), linked to flash temperatures and spark discharges in localized contact zones [74].

Even in lubricated conditions, wear increases significantly with current. This is typically attributed to tribofilm breakdown, electric discharge erosion, oxide formation and localized thermal degradation of the lubricant. For instance, in four-ball testing, wear diameter increases were recorded up to 150% for gear oils under 3 A [75].

Increased wear has also been reported with an electrified ball-on-disc tribometer setup, as shown in Fig. 42, which compares the wear volume under 0 A and 3 A for both the ball and the disc. The results clearly demonstrate that the effect of current strongly depends on the lubricant formulation. Base oils without additives (PAO2 and PAO10) exhibit a high increase in wear volume under 3 A, particularly on the disc. Fully formulated oils such as ATF (Automatic Transmission Fluid), Dexron (ATF), and a gear oil also show an increase in wear volume under 3 A, but the effect is significantly more moderate compared to base oils, suggesting that anti-wear and antioxidant additives play a key role in mitigating electro-tribological degradation. The relative increase in wear at 3 A is also higher on the disc (cathode) than on the ball (anode). In the case of the ATF oil, no increase in wear is observed on the ball when current is applied, whereas the wear on the disc increases by nearly a factor of seven.

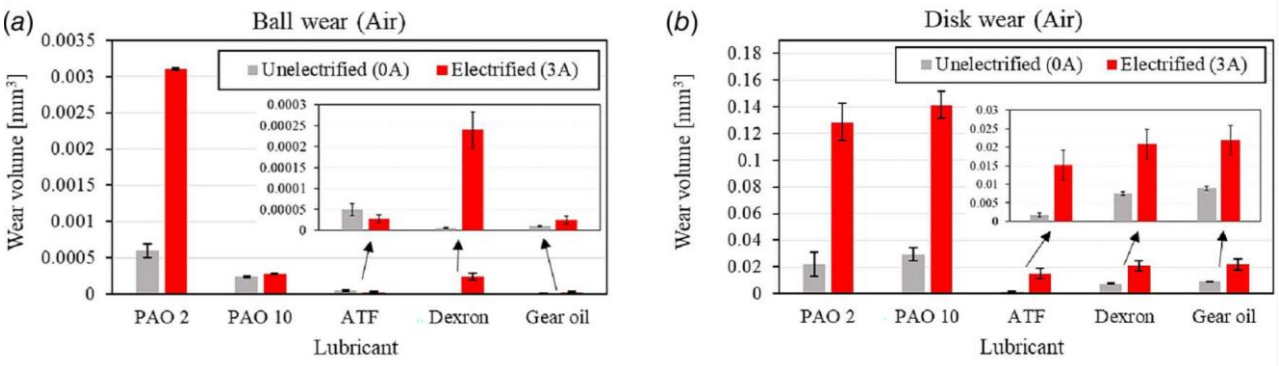

Fig. 42: Comparison of wear volumes of test pairs under unelectrified and electrified conditions in ambient air: (a) ball samples wear and (b) disk samples wear. [76]

Additional tests were performed under a 3 A current in a nitrogen gas environment (Fig. 43). Compared to previous tests conducted in ambient air, a significant reduction in wear was observed. This strongly suggests that the presence of oxygen in the environment promotes the formation of oxide particles, which, under electrified conditions, contribute to wear by acting as abrasive third bodies. In the absence of oxygen, these oxidative wear mechanisms appear to be greatly suppressed.

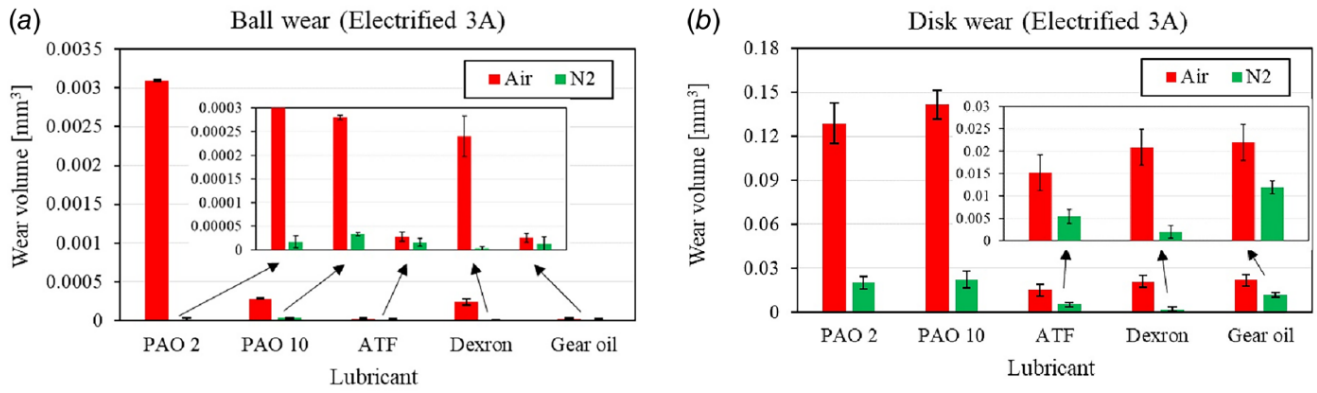

Fig. 43: Comparison of wear obtained for the different oils under electrified (3A) conditions in both ambient air and N2 gas: (a) ball samples wear and (b) disk samples wear. [76]

The same experiment has been conducted under unelectrified conditions in both ambient air and nitrogen gas (Fig. 44). We can see that in most cases the depletion of oxygen once again led to a decrease in wear. Therefore, it can be concluded that the application of current only accelerates this naturally occurring phenomenon.

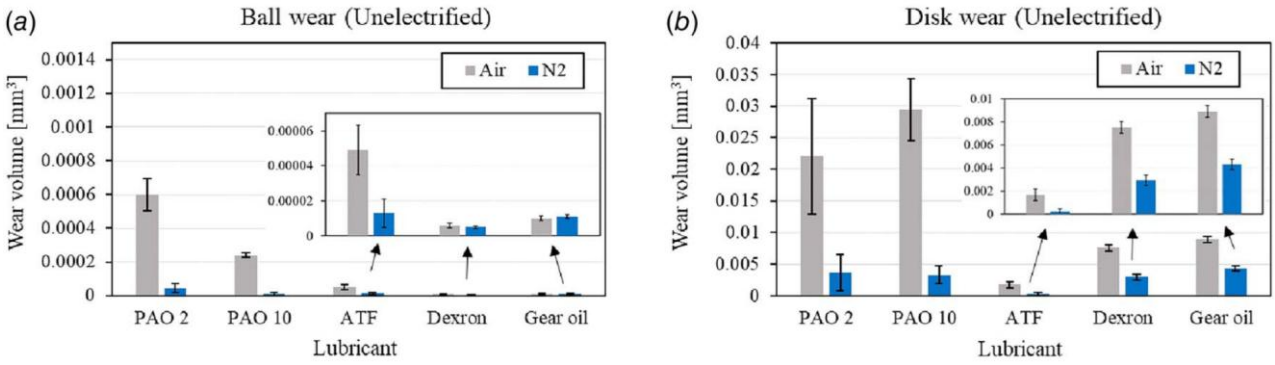

Fig. 44: Comparison of wear obtained for the different oils under unelectrified conditions in both ambient air and N2 gas: (a) ball samples wear and (b) disk samples wear. [76]

Concerning friction, the effect of electrification on its behavior in tribological contacts is complex and highly dependent on the nature of the lubricant, surface materials, and testing conditions. Across the literature, both increases and decreases in the coefficient of friction (CoF) have been reported under the influence of electric current or potential, reflecting competing mechanisms at play. In dry contacts, the application of electrical current generally leads to an increase in CoF, primarily due to intensified oxidative wear and third-body abrasion from electrically-induced oxide debris [74]. In these conditions, the absence of a lubricant film allows localized electric discharges to roughen the surface, thereby increasing friction.

In lubricated contacts, however, the effect of electrification on the CoF is more nuanced. Several studies have reported a slight reduction or stabilization of friction under current due to the rapid formation of oxide-based tribofilms or the reorientation of polar additive molecules under the electric field [75,84]. For instance, a phosphonium based ionic liquid (IL) used as an additive in an ATF showed lower friction than base oil formulations at 0 A and 0.5 A, attributed to the formation of black tribofilms. However, at higher current intensities (1 A or above), friction levels increased, suggesting degradation or disruption of the tribochemical film under harsher electrochemical conditions [84].

For example, we can see in Fig. 45b that the CoF is lower at 1.5 and 3 A than at 0 A for the base oil. However, this friction reduction does not necessarily correlate with reduced wear (Fig. 45a); on the contrary, it can coincide with increased surface damage, as observed through the formation of grooves, oxide layers, and abrasive third-body particles. This indicates that a lower CoF under electrified conditions is not always a reliable indicator of improved tribological performance.

Another parameter that likely influences both friction and wear behavior is the heat generated at the contact interface, which can be significantly higher under electrical current, as illustrated in Fig. 45c. The combined effect of frictional heating and Joule heating may accelerate lubricant degradation and surface oxidation, thereby amplifying wear and altering the stability of tribofilms.

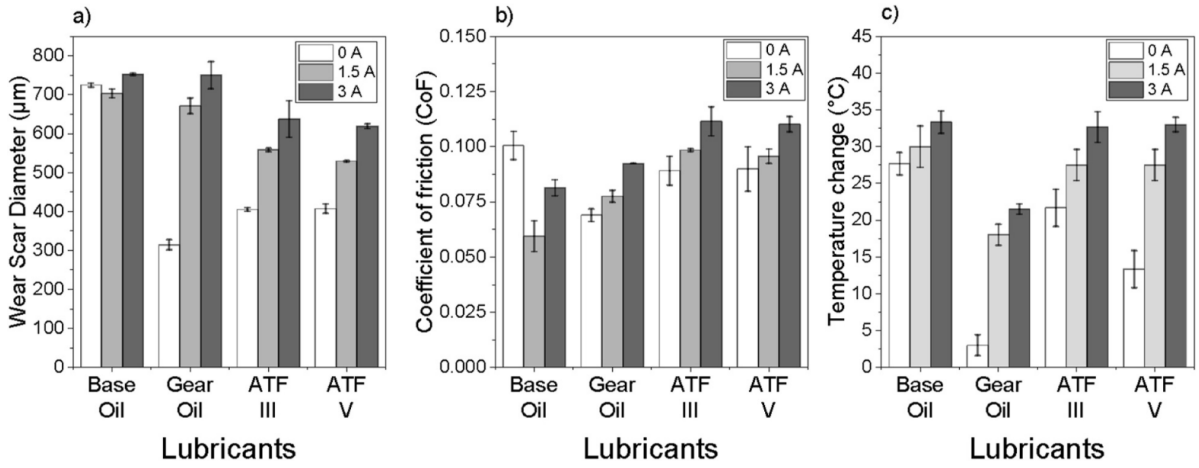

Fig. 45: Tribological characteristics of lubricants under unelectrified and electrified conditions: (a) Wear scar diameter; (b) coefficient of friction (CoF); (c) temperature change. [75]

High instability in the friction behavior is also reported and can be a good indicator for the wear induced by the application of current (Fig. 46)

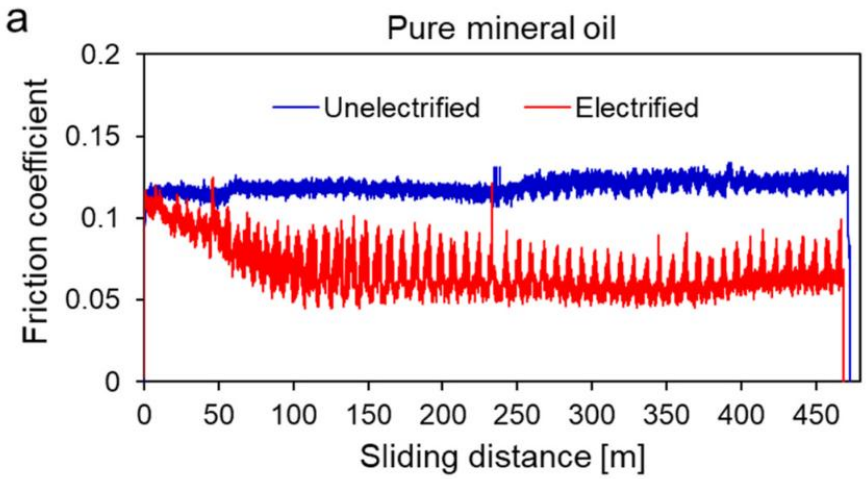

Fig. 46: Friction coefficient behavior obtained for unelectrified and electrified (1.5A with DC current) lubricated testing using a pure mineral oil [74]

In summary, the application of electric current or potential can lead to either reduction or increase in friction, depending on the lubricant formulation, additive chemistry, applied voltage/current, and electrode polarity. While electrification can enhance the formation of certain tribofilms that reduce friction, it may also destabilize or prevent their formation under more severe electrochemical conditions, resulting in higher and unstable friction and potential surface damage.

1.5.3 Effect of Electrification on Tribological Additives Performance

The tribological performance of widely used lubricant additives such as ZDDP and MoDTC is notably affected by the presence of electric current. Under non-electrified conditions, ZDDP forms robust phosphate-based anti-wear tribofilms and MoDTC contributes to friction reduction via MoS_2 formation. However, experimental studies demonstrate that the application of direct current at 1.5 A and 3 A can significantly reduce the effectiveness of these additives.

Electrified four-ball tribometer results showed that while ZDDP and MoDTC reduced both wear and friction at 0 A, their performance deteriorated under electrified conditions, with less stable friction and increased wear diameters behavior as shown in Fig. 47. The friction-reducing properties of MoDTC appear to be particularly affected, as shown by the PAO4+MoDTC and PAO4+ZDDP+MoDTC blends, which exhibit increases in CoF of approximately 60% and 30%, respectively, under a current of 1.5 A. Raman spectroscopy and XPS analyses indicated that electric current promotes the formation of iron oxides over additive-derived films, suggesting that electrochemical oxidation competes with tribochemical film formation. Although tribofilms were still detected under current, their protective capacity was hindered, with observations of film detachment, surface scratches, and areas without tribofilm coverage. This may stem from the breakdown of molecular precursors or the suppression of tribochemical reactions caused by localized heating or electron flow. [71]

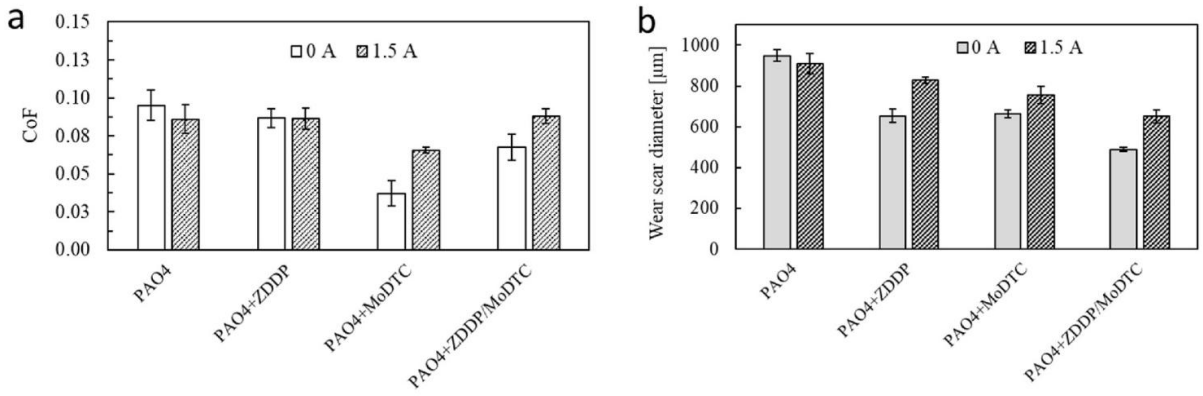

Fig. 47: Tribological characteristics of oils under non-electrified and electrified conditions: (a) coefficient of friction (CoF); and (b) wear scar diameter. [71]

Complementing these observations, Yousuf et al. (2025) [72] conducted a comprehensive study on the influence of applied electric potential in rolling-sliding contacts under mixed lubrication using PAO, ZDDP, and an ATF (Automatic Transmission Fluid). This time, the potential was fixed (5 V) instead of the current. Their results confirmed that electric potential significantly affects tribofilm behavior, particularly in ZDDP-containing lubricants. Under electrified conditions, ZDDP exhibited a distinct electrochemical polarity effect, where wear consistently localized on the anode, as shown in Fig. 48, while tribofilm preferentially formed on the cathode. This behavior was attributed to electrochemical oxidation of ZDDP-derived precursors at the anode, which inhibits protective film formation, while reductive environments at the cathode favor tribofilm growth. Surface analysis using SLIM (Spacer Layer Interferometry Method) and EDX revealed that the anodic regions had lower tribofilm coverage and higher sulfur/oxygen concentration, correlating with wear zones, while cathodic regions retained intact films.

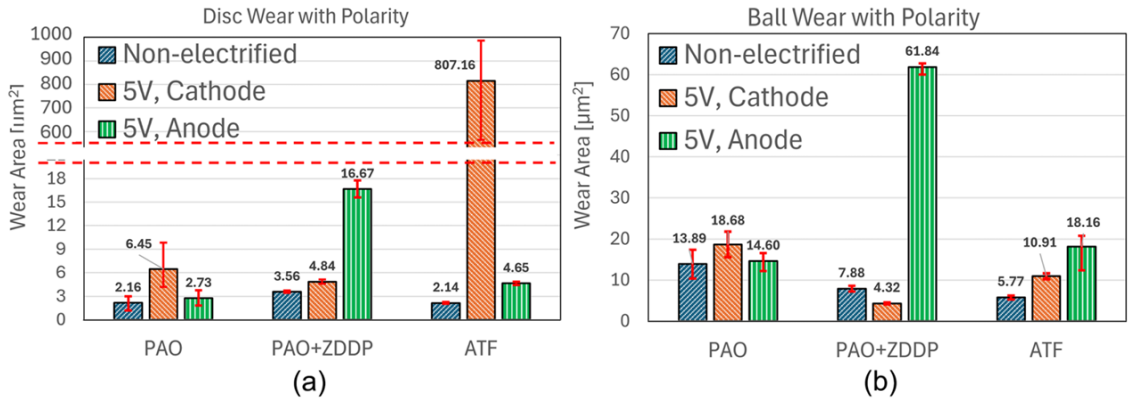

Fig. 48: (a) Disc wear in non-electrified and 5 V applied test with both polarities with each test oil. (b) Ball wear in non-electrified and 5 V applied test with both polarities with each test oil. Note difference in scales. [72]

This asymmetry is often attributed to the directionality of electron flow, redox reactions, and the fact that current preferentially passes through tribofilm-free regions, promoting localized discharge and erosion. The side that will undergo the largest amount of wear (anode or cathode) seems to depend on the chemical nature of the additive as the fully formulated ATF presents high wear in the cathode region contrary to the blend of PAO and ZDDP.

It must also be highlighted that wear under electrified conditions depends not only on the presence of current but also on the magnitude of the applied voltage, as shown in the comparison between 1 V and 5 V tests presented in Fig. 49. Indeed, for electrochemical (redox) reactions to occur, both an electric current and a sufficient electrochemical potential must be present - this potential must match or exceed the threshold for the specific redox couple involved at the interface [85]. At lower voltages (e.g., 1 V), redox activity may be limited or selective, leading to more stable tribofilm formation. In contrast, at higher voltages (e.g., 5 V), more aggressive oxidation or reduction reactions can be triggered, resulting in enhanced surface degradation, accelerated additive breakdown, and increased wear. This is likely the case for the PAO+ZDDP blend on the ball (anode), where the wear increase is much greater at 5 V than at 1 V (Fig. 49b), possibly due to the activation of redox reaction. In other cases, the increase in wear appears to be more directly proportional to the applied voltage. This highlights the importance of controlling both current intensity and voltage in tribological systems subjected to electrification.

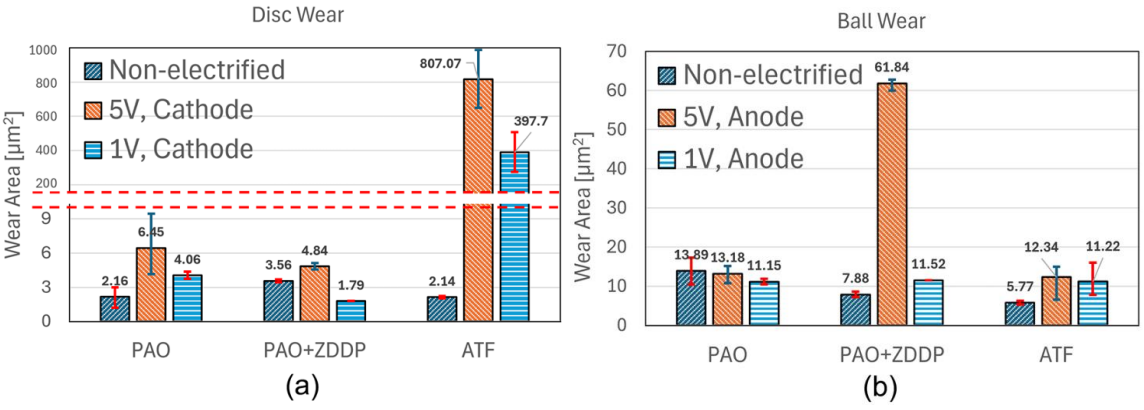

Fig. 49: (a) Disc wear in non-electrified, 5 V applied (disc being cathode), and 1 V applied (disc being cathode) tests with each test oil. (b) Ball wear in non-electrified, 5 V applied (ball being anode), and 1 V applied (ball being anode) tests with each test oil. [72]

Once again, wear could be mitigated under nitrogen atmosphere, indicating that oxidative degradation plays a central role in current-driven tribochemical failure. Although MoDTC was not directly evaluated in this study, the observed polarity-dependent degradation mechanisms are likely to affect other polar additive systems in similar ways. These results reinforce the notion that electrical potential not only accelerates wear but also disrupts the spatial uniformity of additive film formation, thereby challenging the conventional assumption that additives function uniformly under all conditions. This work highlights the need to consider electrode effects in lubricant formulation, particularly for electrically active systems such as those in EV transmissions.

The presence of electric current reduces the tribological efficacy of traditional additives like ZDDP and MoDTC, primarily by disrupting tribofilm formation and enhancing oxidative wear pathways. These findings underscore the importance of rethinking additive design for electrified lubrication environments, where tribo-electrochemical effects dominate and conventional tribo-chemistry may no longer be sufficient.

In summary, the application of electric current to tribological contacts:

- Increases wear, particularly due to oxidative and discharge-induced mechanisms.
- Alters friction behavior, often unpredictably.
- Affects the formation and stability of tribofilms, depending on the lubricant and polarity.
- Requires careful optimization of lubricant formulation, especially regarding additive chemistry (e.g., ZDDP, MoDTC)

These findings emphasize the complex interplay between mechanical, electrical, and chemical phenomena in electrified tribology, warranting further in-depth study to develop robust E-fluids and surface protection strategies for next-generation EV system

Conclusion

The review presented in this chapter demonstrates that mastering lubrication remains a cornerstone for ensuring the performance, efficiency, and durability of mechanical systems.

From a lubrication science standpoint, the Stribeck curve illustrates the role of the lubricant across different operating regimes. In the hydrodynamic lubrication regime, a continuous fluid film fully separates the contacting surfaces, and load support is provided primarily by the lubricant's viscosity, with minimal reliance on chemical additives. In contrast, in the mixed and boundary lubrication regimes, the film is too thin or discontinuous to prevent asperity contact, making the protective action of tribological additives critical to reducing friction and preventing wear. In real-world transmission systems, operating conditions often shift between these regimes, requiring lubricants to maintain sufficient viscosity for film formation at high speeds while ensuring optimal additive performance under thin-film conditions.

Conventional additives, such as zinc dialkyldithiophosphate (ZDDP) for anti-wear protection and molybdenum dithiocarbamate (MoDTC) for friction reduction, have historically proven highly effective. Their functionality is driven by the formation of protective tribofilms (polyphosphates glass in the case of ZDDP and low-shear molybdenum disulfide lamellae for MoDTC) that shield the substrate and reduce friction under load. However, the advent of electrified drivetrains introduces unique tribological challenges, including higher load, speed as well as stray electrical currents. These conditions fundamentally alter tribochemical pathways, destabilizing additive-derived films, promoting polarity-dependent degradation, and increasing oxidative wear. Under such circumstances, the performance of ZDDP and MoDTC can be greatly hindered, necessitating the exploration of alternative or hybrid lubrication strategies.

Nanoparticles have emerged as promising next-generation additives. Their nanoscale interactions allow for multiple protective mechanisms, such as rolling motion, asperity or crack filling, and tribofilm reinforcement. Furthermore, synergistic effects have been reported when combining nanoparticles with conventional additives, e.g., TiO_2 nanoparticles accelerating MoS_2 tribofilm formation from MoDTC, or CeO_2 nanoparticles enhancing the load-bearing capability of ZDDP-derived films supposedly through nanocomposite tribofilm formation. Nonetheless, their industrial adoption remains constrained by dispersion stability, chemical compatibility, and long-term performance reliability.

Beyond chemical strategies, tribological coatings offer a complementary approach to surface protection. By enabling the deposition of thick, oxidation-free metallic or composite layers without thermal degradation of the substrate, cold spray technology allows for the engineering of surfaces with tailored hardness, toughness, and tribochemical reactivity. In EV applications, where boundary and mixed regimes dominate under high torque and low viscosity lubrication, such engineered surfaces can substantially mitigate wear and extend component service life.

The findings presented here converge on several key research imperatives:

- **Formulation of EV-specific lubricants** integrating advanced additive packages, potentially hybridizing traditional chemistry with functional nanoparticles.
- **Incorporation of electro-tribological considerations** into additive design, ensuring that tribofilms remain stable under applied voltage/current and are resistant to polarity-dependent degradation.
- **Optimization of nanoparticle functionalization and dispersion strategies** to maintain their tribological efficacy in fully formulated oils.
- **Integration of surface engineering solutions**, such as cold spray coatings, into lubrication system design, creating multi-layered protection strategies.

Ultimately, the transition toward electrified powertrains demands a paradigm shift in tribology: moving from purely mechanical-chemical optimization toward a fully integrated *mechano–chemo–electrical* framework. Addressing the coupled effects of load, sliding, lubrication regime, additive chemistry, and electrical environment will be essential for the development of the next generation of lubricants and coatings. In addition, those lubricants could potentially be used as multipurpose fluids, therefore lubricating drivetrains but also acting as a coolant for the battery and the motor. They will therefore need to comply with sufficient thermal management capabilities as well as material compatibility.

These will not only ensure durability and efficiency but also contribute to global sustainability goals by reducing energy losses and emissions across transportation and industrial sectors.

Current State of the Art and Research Gaps

While the body of literature reviewed in this chapter provides a robust understanding of tribological fundamentals, additive chemistry, and emerging nanotechnology-based lubrication strategies, several critical gaps remain in the current state of the art. Addressing these will be essential for advancing tribology in the context of modern, electrified drivetrains.

First, the synergistic or antagonistic interactions between conventional tribological additives (ZDDP, MoDTC) and nanoparticles are still insufficiently understood at the mechanistic level. Although certain combinations have demonstrated improved performance in specific cases, the fundamental chemical and physical processes driving these interactions remain poorly understood. Key questions persist regarding how these species compete or cooperate at the surface, the stability of hybrid tribofilms, and the influence of dispersion strategy on tribological performance.

Concerning cold spray coatings, they have received minimal attention in the context of lubricated contacts. Most cold spray research has focused on wear and corrosion in dry conditions, leaving a significant knowledge gap regarding their behavior in boundary or mixed lubrication regimes, as well as their compatibility with lubricant additives.

The impact of electrical currents and potentials on tribofilm formation, chemistry, and durability remains incompletely understood, especially in boundary and mixed lubrication regimes relevant to EV gearboxes. Existing studies indicate that electrification can disrupt tribochemical pathways and promote oxidative wear, but it is not fully understood how it chemically affects the formation of a tribofilm nor how it affects their durability in the case of an already formed tribofilm.

At the moment, there is no study on the behavior of metallic oxide nanoparticles under electrical current. It is unknown whether they enhance or hinder tribofilm formation in electrified environments, how their surface chemistry interacts with electrochemical reactions, or whether they can provide specific protective effects under such conditions. This lack of knowledge significantly limits their rational integration into EV-specific lubricant formulations.

The present work attempts to address these interrogations through a systematic experimental approach. Dedicated test protocols will be implemented to evaluate the tribological behavior of selected additive-nanoparticle combinations, cold spray coatings, and their interaction under electrified conditions. These tests will be complemented by advanced surface and chemical analyses (e.g., Profilometry, SEM, EDX, XPS, TEM) to not only quantify performance but also to identify the underlying mechanisms responsible for the observed trends. By integrating tribological, chemical, and electrochemical perspectives, this research seeks to provide a coherent lab-scale framework for the design of next-generation lubrication and surface engineering solutions tailored to the operational realities of electrified mechanical systems.

Bibliography

[1] Brunetière N. Introduction à la tribologie. Institut Pprime, 2016.

[2] Holmberg K, Erdemir A. Influence of tribology on global energy consumption, costs and emissions. Friction 2017;5:263–84. https://doi.org/10.1007/s40544-017-0183-5.

[3] Matthews A, Franklin S, Holmberg K. Tribological coatings: contact mechanisms and selection. J Phys D: Appl Phys 2007;40:5463–75. https://doi.org/10.1088/0022-3727/40/18/S07.

[4] Blanc G. Les tribulations d'un (ex) astronome 2022. https://gblanc.fr/spip.php?page=forum&id_article=467&id_forum=2912 (accessed July 8, 2025).

[5] Corporation N. Base Oil Groups Explained n.d. https://www.machinerylubrication.com/Read/29113/base-oil-groups (accessed August 25, 2025).

[6] Polyalphaolefins Technology. Chevron Phillips Chemical n.d. https://www.cpchem.com/what-we-do/solutions/polyalphaolefins/technology (accessed August 27, 2025).

[7] Siqueira ALM, Beaumesnil M, Hubert-Roux M, Loutelier-Bourhis C, Afonso C, Pondaven S, Bai Y, Racaud A. Characterization of polyalphaolefins using halogen anion attachment in atmospheric pressure photoionization coupled to ion mobility spectrometry - mass spectrometry. The Royal Society of Chemistry 2018. https://doi.org/doi.org/10.1039/C8AN00920A.

[8] Noria Corporation. Polyalphaolefin (PAO) Lubricants Explained n.d. https://www.machinerylubrication.com/Read/31106/polyalphaolefin-pao-lubricants (accessed August 27, 2025).

[9] Berro H. A molecular dynamics approach to nano-scale lubrication. PhD dissertation. 2010.

[10] Stribeck Curve | About Tribology. Tribonet 2025. https://www.tribonet.org/wiki/stribeck-curve/ (accessed October 9, 2025).

[11] Mang T, Dresel W. Lubricants and lubrications. 2nd completely revised and extended ed. Weinheim: Wiley-VCH; 2007.

[12] Van Rensselar J. Lubrication and tribology trends and challenges in electric vehicles. Society of Tribologists and Lubrication Engineers - STLE 2020. https://www.stle.org/files/TLTArchives/2020/07_July/Webinars.aspx (accessed July 1, 2025).

[13] Spikes H. Mechanisms of ZDDP—An Update. Tribol Lett 2025;73:38. https://doi.org/10.1007/s11249-025-01968-3.

[14] Zhang J, Spikes H. On the Mechanism of ZDDP Antiwear Film Formation. Tribology Letters 2016;63:24. https://doi.org/10.1007/s11249-016-0706-7.

[15] De Feo M, Minfray C, De Barros Bouchet MI, Thiebaut B, Martin JM. MoDTC friction modifier additive degradation: Correlation between tribological performance and chemical changes. RSC Adv 2015;5:93786–96. https://doi.org/10.1039/C5RA15250J.

[16] Rudnick LR. Lubricant additives: chemistry and applications. CRC Press 2009.

[17] Morina A, Neville A, Priest M, Green JH. ZDDP and MoDTC interactions and their effect on tribological performance – tribofilm characteristics and its evolution. Tribol Lett 2006;24:243–56. https://doi.org/10.1007/s11249-006-9123-7.

[18] Spikes H. The History and Mechanisms of ZDDP. Tribology Letters 2004;17:469–89. https://doi.org/10.1023/B:TRIL.0000044495.26882.b5.

[19] Barnes AM, Bartle KD, Thibon VRA. A review of zinc dialkyldithiophosphates (ZDDPS): characterisation and role in the lubricating oil. Tribology International 2001;34:389–95. https://doi.org/10.1016/S0301-679X(01)00028-7.

[20] Shimizu Y, Spikes HA. The Influence of Slide–Roll Ratio on ZDDP Tribofilm Formation. Tribol Lett 2016;64:19. https://doi.org/10.1007/s11249-016-0738-z.

[21] Gosvami NN, Bares JA, Mangolini F, Konicek AR, Yablon DG, Carpick RW. Mechanisms of antiwear tribofilm growth revealed in situ by single-asperity sliding contacts. Science 2015;348:102–6. https://doi.org/10.1126/science.1258788.

[22] Fang L. Enabling ultra-low viscosity lubricants through fundamental understanding of zddps anti-wear additives and their tribofilm growth mechanisms: an in-situ study. University of Pennsylvania, 2022.

[23] Allum KG, Forbes ES. The Load-Carrying Properties of Metal Dialkyl Dithiophosphates: The Effect of Chemical Structure. Proceedings of the Institution of Mechanical Engineers, Conference Proceedings 1968;183:7–14. https://doi.org/10.1243/PIME_CONF_1968_183_273_02.

[24] Spikes H. Friction Modifier Additives. Tribol Lett 2015;60:5. https://doi.org/10.1007/s11249-015-0589-z.

[25] Onodera T, Morita Y, Suzuki A, Sahnoun R, Koyama M, Tsuboi H, Hatakeyama N, Endou A, Takaba H, Del Carpio CA, Deka RC, Kubo M, Miyamoto A. Tribochemical Reaction Dynamics of Molybdenum Dithiocarbamate on Nascent Iron Surface: A Hybrid Quantum Chemical/Classical Molecular Dynamics Study. J Nanosci Nanotech 2010;10:2495–502. https://doi.org/10.1166/jnn.2010.1399.

[26] Deshpande P, Dassenoy F, Minfray C, Jenei IZ, Le Mogne Th, Thiebaut B. Effect of Adding TiO2 Nanoparticles to a Lubricant Containing MoDTC on the Tribological Behavior of Steel/Steel Contacts Under Boundary Lubrication Conditions. Tribol Lett 2020;68:39. https://doi.org/10.1007/s11249-020-1278-0.

[27] Peeters S, Charrin C, Duron I, Loehlé S, Thiebaut B, Righi MC. Importance of the catalytic effect of the substrate in the functionality of lubricant additives: the case of molybdenum dithiocarbamates. Materials Today Chemistry 2021;21:100487. https://doi.org/10.1016/j.mtchem.2021.100487.

[28] Guimarey MJG, Villamayor A, López ER, Comuñas MJP. Performance and Antiwear Mechanism of 1D and 2D Nanoparticles as Additives in a Polyalphaolefin. Nanomaterials 2024;14:1101. https://doi.org/10.3390/nano14131101.

[29] Nasser KI, Liñeira Del Río JM, Mariño F, López ER, Fernández J. Double hybrid lubricant additives consisting of a phosphonium ionic liquid and graphene nanoplatelets/hexagonal boron nitride nanoparticles. Tribology International 2021;163:107189. https://doi.org/10.1016/j.triboint.2021.107189.

[30] Lahouij I, Vacher B, Martin J-M, Dassenoy F. IF-MoS2 based lubricants: Influence of size, shape and crystal structure. Wear 2012;296:558–67. https://doi.org/10.1016/j.wear.2012.07.016.

[31] Sgroi M, Gili F, Mangherini D, Lahouij I, Dassenoy F, Garcia I, Odriozola I, Kraft G. Friction Reduction Benefits in Valve-Train System Using IF-MoS_2 Added Engine Oil. Tribology Transactions 2015;58:207–14. https://doi.org/10.1080/10402004.2014.960540.

[32] Gulzar M, Masjuki HH, Kalam MA, Varman M, Zulkifli NWM, Mufti RA, Zahid R. Tribological performance of nanoparticles as lubricating oil additives. J Nanopart Res 2016;18:223. https://doi.org/10.1007/s11051-016-3537-4.

[33] Lahouij I, Carpick R, Jackson A, Khare H, Gosvami N, Demas NG, Erck RA, Greco AC, Fenske GR, Xu W, Cooper G, Chen Z. Nano-additives enabled advanced lubricants. US Patent 10,647,938, 2020.

[34] Dassenoy F, Jenei IZ, Pavan S, Galipaud J, Thersleff T, Wieber S, Hagemann M, Ness D. Performance and Lubrication Mechanism of New TiO_2 Nanoparticle-Based High-Performance Lubricant Additives. Tribology Transactions 2021;64:325–40. https://doi.org/10.1080/10402004.2020.1838678.

[35] Zhang L, Chen L, Wan H, Chen J, Zhou H. Synthesis and Tribological Properties of Stearic Acid-Modified Anatase (TiO2) Nanoparticles. Tribol Lett 2011;41:409–16. https://doi.org/10.1007/s11249-010-9724-z.

[36] Bogunovic L, Zuenkeler S, Toensing K, Anselmetti D. An Oil-Based Lubrication System Based on Nanoparticular TiO2 with Superior Friction and Wear Properties. Tribol Lett 2015;59:29. https://doi.org/10.1007/s11249-015-0557-7.

[37] Khare HS, Lahouij I, Jackson A, Feng G, Chen Z, Cooper GD, Carpick RW. Nanoscale Generation of Robust Solid Films from Liquid-Dispersed Nanoparticles via in Situ Atomic Force Microscopy: Growth Kinetics and Nanomechanical Properties. ACS Appl Mater Interfaces 2018;10:40335–47. https://doi.org/10.1021/acsami.8b16680.

[38] Lahouij I, Gould B, Demas N, Greco A, Chen Z, Cooper GD, Jackson A, Carpick RW. Inhibition of Micro-pitting by Tribofilm-Forming ZrO2 Nanocrystal Lubricant Additives: A Micro-pitting Rig and Transmission Electron Microscope Study. Tribol Lett 2022;70:13. https://doi.org/10.1007/s11249-021-01555-2.

[39] Hernandez Battez A, Fernandez Rico JE, Navas Arias A, Viesca Rodriguez JL, Chou Rodriguez R, Diaz Fernandez JM. The tribological behaviour of ZnO nanoparticles as an additive to PAO6. Wear 2006;261:256–63. https://doi.org/10.1016/j.wear.2005.10.001.

[40] Chen Y, Renner P, Liang H. Dispersion of Nanoparticles in Lubricating Oil: A Critical Review. Lubricants 2019;7:7. https://doi.org/10.3390/lubricants7010007.

[41] Rabaso P, Dassenoy F, Ville F, Diaby M, Vacher B, Le Mogne T, Belin M, Cavoret J. An Investigation on the Reduced Ability of IF-MoS2 Nanoparticles to Reduce Friction and Wear in the Presence of Dispersants. Tribol Lett 2014;55:503–16. https://doi.org/10.1007/s11249-014-0381-5.

[42] Rabaso P, Ville F, Dassenoy F, Diaby M, Afanasiev P, Cavoret J, Vacher B, Le Mogne T. Boundary lubrication: Influence of the size and structure of inorganic fullerene-like MoS2 nanoparticles on friction and wear reduction. Wear 2014;320:161–78. https://doi.org/10.1016/j.wear.2014.09.001.

[43] Khare HS, Gosvami NN, Lahouij I, Milne ZB, McClimon JB, Carpick RW. Nanotribological Printing: A Nanoscale Additive Manufacturing Method. Nano Lett 2018;18:6756–63. https://doi.org/10.1021/acs.nanolett.8b02505.

[44] Elinski MB, LaMascus P, Zheng L, Jackson A, Wiacek RJ, Carpick RW. Cooperativity Between Zirconium Dioxide Nanoparticles and Extreme Pressure Additives in Forming Protective Tribofilms: Toward Enabling Low Viscosity Lubricants. Tribol Lett 2020;68:107. https://doi.org/10.1007/s11249-020-01346-1.

[45] LaMascus P, Elinski MB, Delghandi D, Nautiyal P, Griffin J, Zheng L, Jackson A, Wiacek RJ, Carpick RW. Competition Between Growth and Removal in Zirconia Nanocrystal-Derived Tribofilms: The Role of Co-additives. Tribol Lett 2024;72:106. https://doi.org/10.1007/s11249-024-01905-w.

[46] Deshpande P. Interaction of MoDTC additive on TiO2 APS coating under mixed/boundary lubrication conditions: A tribocatalytic process. Thèse de Doctorat. L'Ecole centrale de Lyon, 2017.

[47] Lei X, Zhang Y, Zhang S, Yang G, Zhang C, Zhang P. Study on the mechanism of rapid formation of ultra-thick tribofilm by CeO2 nano additive and ZDDP. Friction 2022. https://doi.org/10.1007/s40544-021-0571-8.

[48] Sharma V, Timmons RB, Erdemir A, Aswath PB. Interaction of plasma functionalized TiO2 nanoparticles and ZDDP on friction and wear under boundary lubrication. Applied Surface Science 2019;489:372–83. https://doi.org/10.1016/j.apsusc.2019.05.359.

[49] Sharma V, Timmons RB, Erdemir A, Aswath PB. Synergistic and antagonistic interaction between ZDDP and TiO2 nanoparticles under boundary lubrication. Tribology International 2025;202:110299. https://doi.org/10.1016/j.triboint.2024.110299.

[50] Holmberg K, Matthews A. Coatings tribology: properties, mechanisms, techniques and applications in surface engineering. 2. ed. Amsterdam Heidelberg: Elsevier; 2009.

[51] Luo D. Selection of coatings for tribological applications. Thèse de Doctorat. L'Ecole centrale de Lyon, 2009.

[52] Grill A. Diamond-like carbon: state of the art. Diamond and Related Materials 1999;8:428–34. https://doi.org/10.1016/S0925-9635(98)00262-3.

[53] Borgaonkar A, Syed I. Friction and wear behaviour of composite MoS2–TiO2 coating material in dry sliding contact. J Braz Soc Mech Sci Eng 2021;43:51. https://doi.org/10.1007/s40430-020-02721-8.

[54] Chandramouli T V, Joladarashi S, Ramesh MR. Tribological characteristics of HVOF sprayed Fe-based composite coatings at elevated temperatures. Tribology - Materials, Surfaces & Interfaces 2025;19:54–69. https://doi.org/10.1177/17515831241309208.

[55] Řehořek L, Dlouhý I, Jan V. Cold gas dynamic spray deposition as additive manufacturing of architectured materials. Materials Engineering 2017.

[56] Tan AW-Y, Tham NYS, Chua YS, Wu K, Sun W, Liu E, Tan SC, Zhou W. Cold Spray of Nickel-Based Alloy Coating on Cast Iron for Restoration and Surface Enhancement. Coatings 2022;12:765. https://doi.org/10.3390/coatings12060765.

[57] Zhang Y, Epshteyn Y, Chromik RR. Dry sliding wear behaviour of cold-sprayed Cu-MoS2 and Cu-MoS2-WC composite coatings: The influence of WC. Tribology International 2018;123:296–306. https://doi.org/10.1016/j.triboint.2017.12.015.

[58] Kato H, Takama M, Iwai Y, Washida K, Sasaki Y. Wear and mechanical properties of sintered copper–tin composites containing graphite or molybdenum disulfide. Wear 2003;255:573–8. https://doi.org/10.1016/S0043-1648(03)00072-3.

[59] Li C, Ma K, Zhang Z, Ni L, Wen B, Yang Z, Shao R, Qu D. Microstructure and Tribological Properties of Cold-Sprayed Cu/B4C Composite Coating. Journal of Thermal Spray Technology 2025. https://doi.org/10.1007/s11666-025-02053-w.

[60] Jafari R, Cizek J, Lukac F, Cvrcek L, Buril M, Walter J, Honkanen M, Vippola M, Koivuluoto H. A Comparative Study on Wear Resistance of Cold-Sprayed Aluminum/Quasicrystal Composite Coatings. J Therm Spray Tech 2024;33:705–18. https://doi.org/10.1007/s11666-024-01758-8.

[61] Shockley JM, Descartes S, Vo P, Irissou E, Chromik RR. The influence of Al2O3 particle morphology on the coating formation and dry sliding wear behavior of cold sprayed Al–Al2O3 composites. Surface and Coatings Technology 2015;270:324–33. https://doi.org/10.1016/j.surfcoat.2015.01.057.

[62] Aubanel L. Étude du comportement tribologique en régime lubrifié de revêtements cold spray composites à base d'acier. Université PSL, 2022.

[63] Trends in electric car markets – Global EV Outlook 2025 – Analysis. IEA n.d. http://www.iea.org/reports/global-ev-outlook-2025/trends-in-electric-car-markets-2 (accessed September 30, 2025).

[64] Roussel J. Dynamique des fluides visqueux 2022. https://femto-physique.fr/mecanique_des_fluides/fluides-visqueux.php.

[65] Electric Vehicle Demand Spurs Lubricant Development Urgency. Tribology & Lubrication Technology 2022.

[66] Somani A, Gupta RK, Mohapatra KK, Mohan N. On the Causes of Circulating Currents in PWM Drives With Open-End Winding AC Machines. IEEE Trans Ind Electron 2013;60:3670–8. https://doi.org/10.1109/TIE.2012.2208430.

[67] Lee PM, Sanchez C, Frazier C, Velasquez A, Kostan T. Tribological evaluation of electric vehicle driveline lubricants in an electrified environment. Front Mech Eng 2023;9:1215352. https://doi.org/10.3389/fmech.2023.1215352.

[68] Tischmacher H. Bearing Wear Condition Identification on Converter-fed Motors. 2018 International Symposium on Power Electronics, Electrical Drives, Automation and Motion (SPEEDAM), Amalfi: IEEE; 2018, p. 19–25. https://doi.org/10.1109/SPEEDAM.2018.8445293.

[69] Hansen J. Fundamentals of Tribology in EVs. TriboNet 2023. https://doi.org/10.13140/RG.2.2.14685.28642/1.

[70] Notay RS. A Brief Review on the Tribological Effects of Electrically Induced Bearing Damage. Journal of Tribology 2025;147:051112. https://doi.org/10.1115/1.4067831.

[71] Farfan-Cabrera LI, Hernández-Peña A, Resendiz-Calderon CD, Lee P, Sanchez C, Lee S, Erdemir A. Electrified four-ball testing of ZDDP and MoDTC as additives in low-viscosity synthetic oil. Wear 2025:205835. https://doi.org/10.1016/j.wear.2025.205835.

[72] Yousuf A, Spikes H, Guo L, Kadiric A. Influence of Electric Potentials on Surface Damage in Rolling–Sliding Contacts Under Mixed Lubrication. Tribol Lett 2025;73:45. https://doi.org/10.1007/s11249-025-01977-2.

[73] Farfan-Cabrera LI, Lee P, Sanchez C, Lee S, Erdemir A. Alteration of the traction behavior of lubricants under electrified sliding-rolling conditions. Tribology International 2025;211:110833. https://doi.org/10.1016/j.triboint.2025.110833.

[74] Farfan-Cabrera LI, Erdemir A, Cao-Romero-Gallegos JA, Alam I, Lee S. Electrification effects on dry and lubricated sliding wear of bearing steel interfaces. Wear 2023;516–517:204592. https://doi.org/10.1016/j.wear.2022.204592.

[75] Aguilar-Rosas OA, Farfan-Cabrera LI, Erdemir A, Cao-Romero-Gallegos JA. Electrified four-ball testing – A potential alternative for assessing lubricants (E-fluids) for electric vehicles. Wear 2023;522:204676. https://doi.org/10.1016/j.wear.2023.204676.

[76] Farfan-Cabrera LI, Lee S, Skowron S, Erdemir A. Enhancing Lubrication of Electrified Interfaces by Inert Gas Atmosphere. Journal of Tribology 2025;147:051104. https://doi.org/10.1115/1.4066649.

[77] Deshpande P, Yelkarasi C, Lee S, Farfan-Cabrera LI, Erdemir A. Electrotribochemical formation of abrasive nano-carbon particles under electrified conditions on lubricated sliding contacts. Carbon 2024;228:119425. https://doi.org/10.1016/j.carbon.2024.119425.

[78] Lee P, Sanchez C, Moneer M, Velasquez A. Electrification of a Mini Traction Machine and Initial Test Results. Lubricants 2024;12:337. https://doi.org/10.3390/lubricants12100337.

[79] Oh J, Yousuf A, Spikes H, Kadiric A. The Influence of Lubricant Formulation on Surface Damage Under Electrified Rolling-Sliding Contact with Relevance to Electric Vehicle Drivetrain Applications. Tribol Lett 2025;73:126. https://doi.org/10.1007/s11249-025-02059-z.

[80] Spikes HA. Triboelectrochemistry: Influence of Applied Electrical Potentials on Friction and Wear of Lubricated Contacts. Tribol Lett 2020;68:90. https://doi.org/10.1007/s11249-020-01328-3.

[81] He F, Xie G, Luo J. Electrical bearing failures in electric vehicles. Friction 2020;8:4–28. https://doi.org/10.1007/s40544-019-0356-5.

[82] Ali MKA, Zhang C, Yu Q, Sun Y, Zhou F, Liu W. Do electrification-temperature effects deteriorate ZDDP tribofilms in electric vehicles transmission? Insights into antiwear mechanisms using low-SAPS oils. Wear 2025;564–565:205746. https://doi.org/10.1016/j.wear.2025.205746.

[83] Ali MKA, Zhang C, Yu Q, Sun Y, Zhou F, Liu W. Exploring tribo-electro-chemistry mechanisms of h-BNO@PDA as lubricant additives under electrified conditions for electrical vehicles powertrain. Tribology International 2024;200:110092. https://doi.org/10.1016/j.triboint.2024.110092.

[84] García Tuero A, Lee S, Hernández Battez A, Erdemir A. Tribological Performance of an Automatic Transmission Fluid Additized with a Phosphonium-Based Ionic Liquid Under Electrified Conditions. Lubricants 2025;13:209. https://doi.org/10.3390/lubricants13050209.

[85] Xu X, Brandon N, Spikes H. Study of zinc dialkyldithiophosphate using electrochemical techniques. Tribology Series, Elsevier; 2002, p. 175–81. https://doi.org/10.1016/s0167-8922(02)80019-0.

Chapter 2: Materials and Methods

Résumé en français :

Ce chapitre décrit les procédures expérimentales et les techniques de caractérisation employées dans le cadre de ce travail. Il présente d'abord les matériaux utilisés, notamment l'huile de base, les additifs conventionnels et les nanoparticules de TiO_2, ainsi que les protocoles de préparation des mélanges lubrifiants. Les dispositifs d'essais tribologiques sont ensuite détaillés, qu'ils soient réalisés avec ou sans sollicitation électrique.

Une attention particulière est portée aux techniques d'analyse employées pour caractériser les traces de frottement générées au cours des essais. Les approches mises en œuvre incluent l'imagerie en microscopie électronique à balayage (MEB), la spectroscopie à rayons X à dispersion d'énergie (EDX), la profilométrie, ainsi que la spectroscopie photoélectronique à rayons X (XPS) pour l'étude de la composition chimique des potentiels tribofilms formés.

Enfin, ce chapitre aborde l'élaboration des revêtements obtenus par Cold spray. Les différentes étapes du procédé sont décrites : préparation des surfaces, conditions de déposition et paramètres opératoires, suivies des méthodes de caractérisation des dépôts permettant d'évaluer leur microstructure, leur homogénéité et leurs propriétés fonctionnelles.

This chapter describes the experimental procedures and characterization techniques employed throughout this work. It first details the materials used, including the base oil, conventional additives, and TiO_2 nanoparticles, as well as the preparation and stability assessment of lubricant blends. The tribological testing setups, both under conventional and electrified conditions, are then presented to provide insight into the evaluation of friction and wear performance. Finally, the elaboration of cold sprayed coatings and the associated surface characterization methods are described.

2.1 Base oil, Tribological Additives and Nanoparticles

2.1.1 Traditional Boundary Additives

Zinc dialkyldithiophosphate (ZDDP) was selected as the anti-wear additive for this study, as it remains the most widely used and extensively characterized compound in this category. Its well-documented tribological behavior provides a robust reference framework for interpreting results, particularly in formulations involving blends with nanoparticles or subjected to electrified conditions. The specific compound used was zinc bis[O,O-bis(2-ethylhexyl)] bis(dithiophosphate) (supplied by DAYANG CHEM (Hangzhou), CAS: 4259-15-8), with a phosphorus content of 8.2 wt%. This molecule is classified as a primary ZDDP, which is known to form a tribofilm more slowly than secondary ZDDPs [1,2], but offers superior thermal stability. It was chosen based on a study that compared the tribological performance of several ZDDPs and this particular ZDDP performed the best regarding wear reduction [3]. The chemical structure of this additive is shown in Fig. 50.

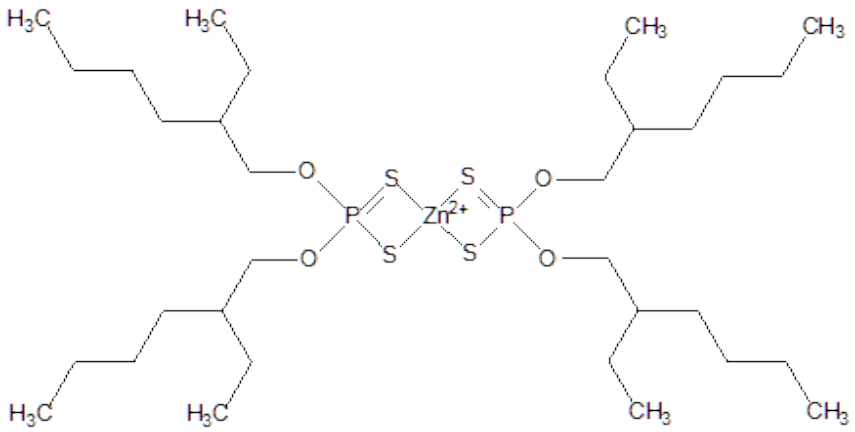

Fig. 50: Zinc bis[O,O-bis(2-ethylhexyl)] bis(dithiophosphate) chemical structure. [4]

Molybdenum dithiocarbamate (MoDTC) was selected as the friction modifier for this study due to its proven effectiveness in reducing friction under boundary lubrication conditions and its widespread use in modern engine oils. MoDTC is well-known for forming in-situ tribofilms containing molybdenum disulfide (MoS_2), a solid lubricant with a layered structure and exceptionally low shear strength between basal planes. MoDTC was also chosen based on a study by Deshpande et al. (2020) [5], which demonstrated a clear synergistic effect when it was combined with 25 nm anatase TiO_2 nanoparticles in a steel on steel contact. The specific compound used was molybdenum bis(N,N-ditridecyl carbamodithioate)di-μ-oxo, oxo-di-, sulfurized (CAS: 71342-89-7), supplied by Actylis. The chemical structure of the MoDTC molecule is illustrated in Fig. 2.

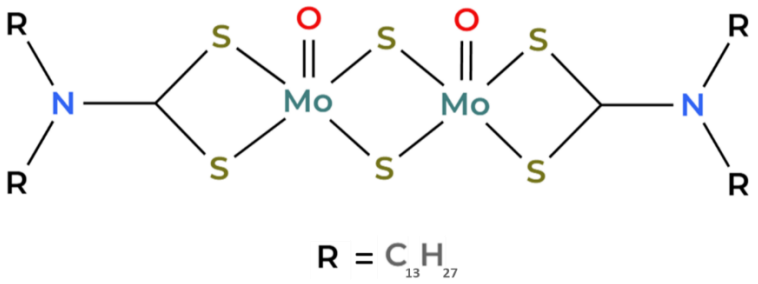

Fig. 51: Molybdenum bis(N,N-ditridecyl carbamodithioate)di-mu.-oxo oxo-di-,sulfurized chemical structure.

2.1.2 TiO_2 Nanoparticles and Stabilizing Methods

Dispersed TiO_2 nanoparticles

Several types of TiO_2 nanoparticles were evaluated in this study. Initially, commercial 5 nm Anatase nanoparticles in powder form were provided from us-nano.com. To be tribologically active, these nanoparticles required stabilization in the base oil using a dispersing agent, in this case, oleic acid (Fisher Sci, >95%, CAS: 112-80-1) (Fig. 52). This corresponds to a physical dispersion where the bonding is due to Van der Walls interactions between the carboxylic acid function of the dispersant and the surface of the TiO_2 nanoparticles [6]. The long carbon chain of oleic acid then ensures the stability in the apolar base oil media.

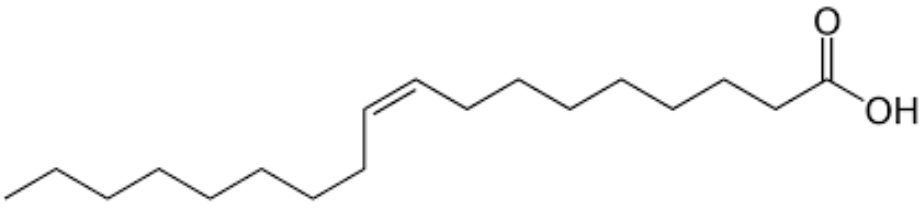

Fig. 52: Oleic acid chemical structure.

Grafted TiO_2 nanoparticles

To assess their performance comparatively, a second type of TiO_2 nanoparticle was introduced. These were stabilized using the same molecule, oleic acid, but this time using a functionalization process carried out by the company Ceranovis. As detailed in Chapter 1, surface functionalization typically enhances dispersion stability, although this sometimes occurs at the expense of tribological performance, an aspect this study aims to clarify. Additionally, the influence of functionalization on the interaction between nanoparticles and traditional tribological additives will be investigated. The synthesis protocol for the oleic acid-functionalized TiO_2 nanoparticles provided by Ceranovis is described below.

(i) Synthesis and surface modification of TiO_2 nanoparticles

TiO_2 nanoparticles were synthesized by a solvothermal method according to established protocols by Niederberger and co-workers using benzyl alcohol as solvent [7–9]. The titanium alkoxide precursor, eg Titanium (IV) Isopropoxide, was mixed with benzyl alcohol and transferred to a PTFE-lined pressure vessel (autoclave) and heated to 200-210°C. This temperature was maintained for several hours, and the autoclave was passively cooled to room temperature overnight. The as-synthesized TiO_2 nanoparticles were collected and purified by centrifugation. Centrifugation and redispersion was performed in an apolar solvent such as heptane or cyclohexane. The separated purified sediment containing the TiO_2 nanoparticles was redispersed in THF (Tetrahydrofuran) using the fatty acid, oleic acid, as surface modifying agent. The long carbon chains (C18) of the oleic acid molecules lend the TiO_2 excellent colloidal stability and enable compatibility of the TiO_2 nanoparticles with non-polar media such as hydrocarbon oils.

(ii) Transfer of the oleic acid-stabilized TiO_2 nanoparticles to PAO6 oil

The stable dispersion of oleic acid-functionalized TiO_2 nanoparticles in THF was mixed in the desired ratio with the polyalphaolefin PAO6 oil, resulting in a homogenous mixture without any sign of nanoparticle agglomeration or significant turbidity. The solvent THF was removed by distillation at 40 °C under reduced pressure using a rotary evaporator. The elimination of the solvent had no impact on the colloidal stability of the TiO_2 nanoparticles in the PAO6 oil. After complete solvent removal a slightly yellow homogenous dispersion of colloidally stable oleic acid-modified TiO_2 nanoparticles in the polyalphaolefin PAO6 in the desired concentration was obtained.

Nanoparticles size and stability

Dynamic light scattering (DLS) of the functionalized TiO_2 NPs shows a narrow particle size distribution, with an average NP size of 4.38 nm (D90vol = 5.34 nm). Transmission electron microscopy (TEM) observations (Fig. 53) confirm the presence of individual nanoparticles approximately 4–6 nm in size. The nanoparticle-blended suspension appears transparent with a slight milky hue to the naked eye and remains stable for several months, showing no signs of sedimentation. After those few months, the suspension starts to become cloudy, this is attributed to oxidation of oleic acid which then becomes unable to efficiently disperse nanoparticles.

In contrast, the particle size of the oleic acid-dispersed nanoparticles suspension was not measured; however, the solution appears opaque and forms sediment within a few hours because of the weak bonding between oleic acid and TiO_2 nanoparticles.

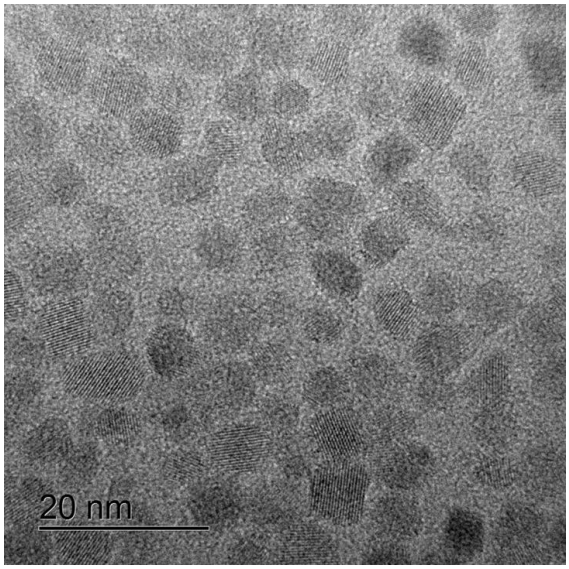

Fig. 53: TEM micrography of functionalized TiO_2 nanoparticles (Leibniz Institute for New Materials).

Based on the results obtained with those two suspensions, a third type of functionalized TiO_2 nanoparticle was developed by Ceranovis using a silane-based functionalizing agent (hexadecyltrimethoxysilane, CAS: 16415-12-6, see Fig. 54), resulting in significantly improved long-term colloidal stability (at least 11 months for now). The synthesis procedure used for these silane-functionalized nanoparticles was similar to that previously employed for oleic acid functionalization with the obtention of an optically clear, transparent suspension.

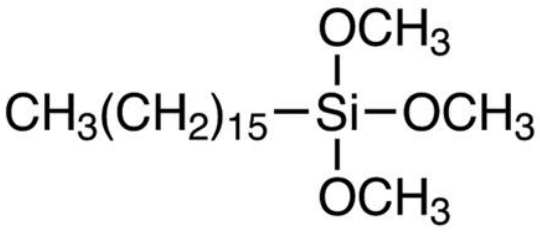

Fig. 54: Hexadecyltrimethoxysilane chemical structure.

Dynamic Light Scattering (DLS) of the silane-functionalized TiO_2 NPs shows once again a narrow particle size distribution, with an average NP size of 11.28 nm (D90vol = 15.20 nm).

2.1.3 Blends preparation

The base oil used for the experiments was a polyalphaolefin (PAO6) synthetic oil, with a reported kinematic viscosity of 5,9 cSt at 100 °C (PAO6 Durasyn166, CAS: 68037-01-4) provided by INEOS.

The lubricant blends were prepared in 5 g batches using 10 mL glass test tubes and stored at 20 °C, protected from ambient light with aluminum foil. The formulation process involved sequentially introducing the additives (MoDTC, ZDDP, oleic acid, or TiO_2 nanoparticles) into the test tube, followed by the addition of PAO6 base oil. When working with dry powdered TiO_2 nanoparticles, handling was carried out in a glove box to ensure safety until the base oil is added, as these materials pose a potential inhalation hazard only in their dry form [10].

The formulations are then blended using a vortex mixer and an ultrasonic bath (40 kHz, 120 W) for 30 minutes at room temperature to promote proper additives dissolution and nanoparticles stabilization. After sonication, the blends were visually inspected to confirm the absence of sedimentation or visible particle clusters. If necessary, additional sonication was applied to ensure colloidal stability. Prior to tribological testing, all formulations are once again blended using this method to ensure homogeneity and repeatability.

2.1.4 Blends stability

The stability of the nanoparticles suspensions was monitored visually. Suspensions prepared directly from nanoparticles powder were difficult to stabilize, even after prolonged ultrasonication. These suspensions sedimented almost immediately due to the presence of large agglomerates.

The addition of a dispersant (oleic acid) greatly improved the stability of the nanoparticles. However, the suspension remains unstable and sediments after a few days.

In contrast, nanoparticles supplied by Ceranovis are closer to ideal suspensions, with nanoparticles appearing non-agglomerated according to DLS measurements, for both oleic acid- and silane-based functionalization.

Nevertheless, these suspensions exhibit a certain sensitivity to oxidation, which accelerates aging, leading to nanoparticle agglomeration and subsequent sedimentation. Specifically, a portion of the oleic acid-functionalized nanoparticles stock solution was transferred into test tubes, and differences in stability duration were observed depending on whether the tubes were completely filled or not (Fig. 55). Partially filled tubes containing air showed accelerated suspension aging, whereas fully filled tubes, devoid of oxygen, maintained stability for a longer period.

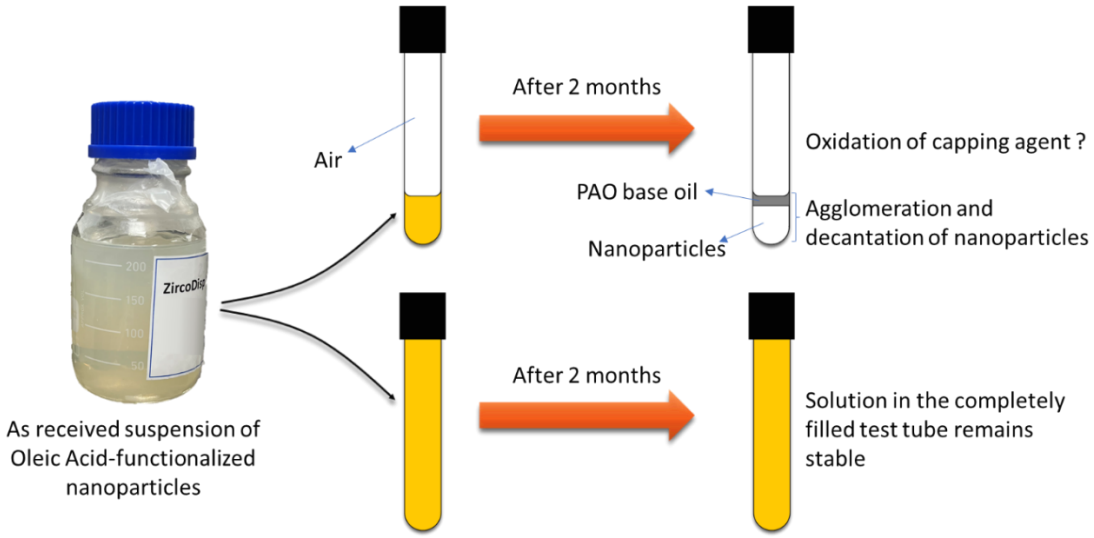

Fig. 55: Effect of oxygen exposure on suspension stability: oleic acid-functionalized nanoparticles stored in fully filled versus partially filled test tubes.

The same protocol was applied to silane-functionalized nanoparticles. In this case, no sedimentation was observed in either type of tube. However, suspensions in partially filled tubes exhibited a noticeable yellowing, while those in completely filled tubes remained perfectly transparent after 10 months. These observations suggest that, despite their excellent stability, silane-functionalized nanoparticles remain sensitive to oxidation, underscoring the importance of proper storage conditions for these formulations.

2.2 Tribological testing setup

2.2.1 Linear Ball-on-Disc Tribometer

All tribological tests were conducted using a linear reciprocating ball-on-disc tribometer (Anton Paar TRB^3) under boundary lubrication conditions. The configuration involved a steel ball sliding against a flat steel disc, generating a non-conformal contact. This setup is presented in Fig. 56.

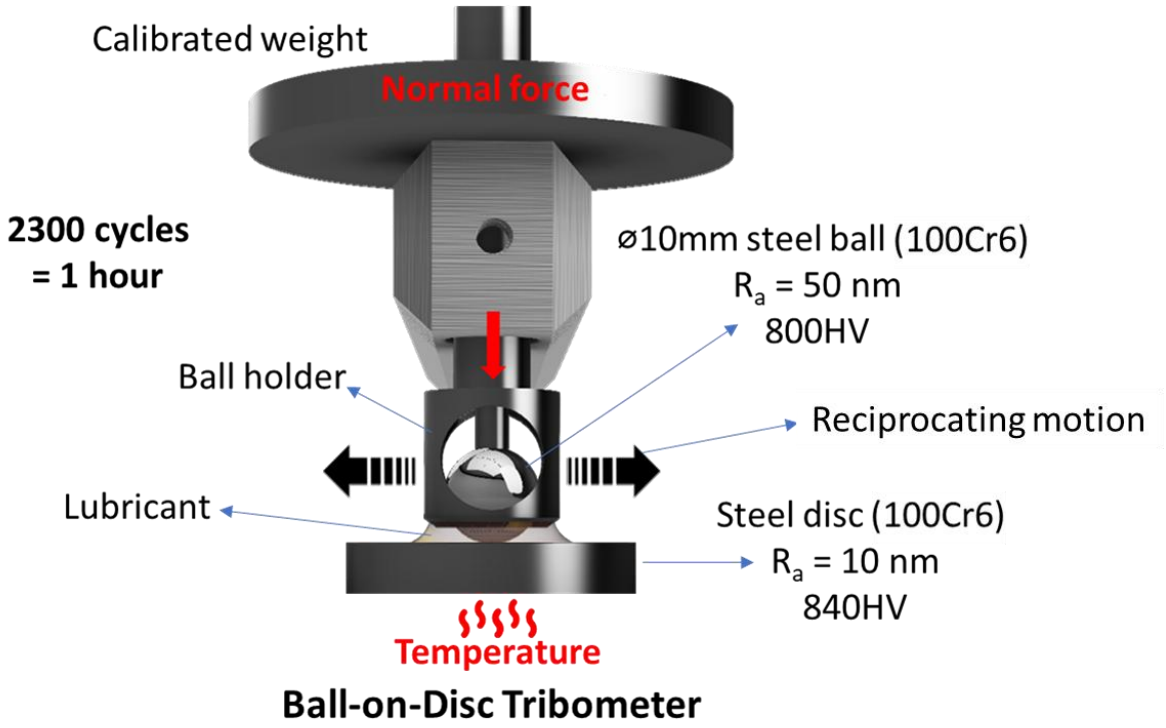

Fig. 56: Anton Paar TRB^3 ball-on-disc tribometer setup in a linear configuration.

Tribological conditions are presented in **Table *1***.

Temperature	100°C
Normal load	5.5 or 10.5 N
Ball diameter	10 mm
Maximum Hertzian contact pressure	0.83 or 1.03 GPa
Hertz Diameter	112 or 140 µm
Test duration / cycle number	3600 s / 2300 cycles
Test frequency	0.64 Hz
Stroke length	5 mm
Maximum linear speed	10 mm/s
Oil quantity	2 mL
Repetitions	3
Acquisition frequency	25 Hz
Plotted curves processing	Averaged over 8 points

Table 1: Tribological conditions

Boundary lubrication conditions were verified using Hamrock and Dowson formula [11]:

$$\frac{h_{centre}}{R} = 1.90(\gamma E^*)^{0.53}\left(\frac{\eta_0(V_1+V_2)}{2RE^*}\right)^{0.67}\left(\frac{F_n}{R^2E^*}\right)^{-0.067}$$

With h_{centre} corresponding to the central lubricant film thickness

R, the ball radius (in meters)

γ, the pressure-viscosity coefficient of the lubricant (in Pa^{-1}) (1.9 x 10^{-8} Pa^{-1} for PAO6 oil)

η_0, the lubricant viscosity (in Pa.s) (4.88 x 10^{-3} Pa.s for PAO6 oil)

F_n, the applied normal load (in newtons)

E*, the effective elastic modulus (in pascals), defined as:

$$\frac{1}{E^*} = \frac{1-\nu_{ball}^2}{E_{ball}} + \frac{1-\nu_{disc}^2}{E_{disc}}$$

E and ν correspond to the Young's modulus (210 GPa for 100Cr6 steel) and Poisson's ratio (0.3 for 100Cr6 steel), respectively, of the two contacting surfaces.

For 5.5N applied normal load, h_{centre} = 1.6 nm

For 10.5N applied normal load, h_{centre} = 1.5 nm

The h_{centre} value is then compared to the equivalent roughness of the contact such as:

$$\sigma_{eq} = \sqrt{\sigma_{ball}^2 + \sigma_{disc}^2}$$

with σ_{ball} corresponding to the ball roughness and σ_{disc} to the disc roughness.

In our case, σ_{eq} = 51 nm

Therefore, $h_{centre} << \sigma_{eq}$, which theoretically validates the boundary lubrication conditions for both applied normal loads.

It is important to note that, due to the nature of our linear tribological configuration, the sliding speed is not constant throughout the stroke. As shown in Fig. 57, the speed profile indicates that the maximum speed of 10 mm/s is reached only at the center of the track, over a distance of approximately 1 mm (linear position from -0.5 to +0.5 mm). For this reason, the coefficient of friction (CoF) vs cycles curve is generated by analyzing only this central region, where the sliding conditions are most stable.

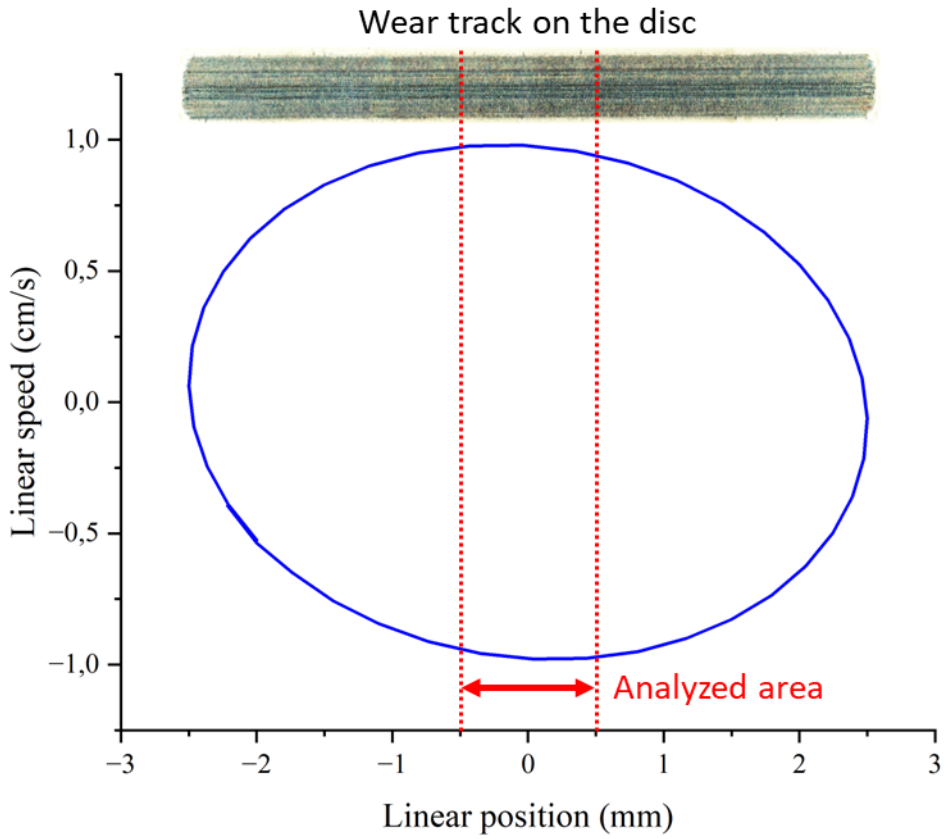

Fig. 57: Speed profile during one friction cycle on a linear configuration (Anton Paar TRB³), highlight on the analyzed area of the wear track on the disc.

2.2.2 Electrified Tribometer Setup

To enable electrified tribological testing, the tribological contact must first be electrically insulated from the tribometer's structural frame.

For the ball, this was achieved by replacing the original holder with a custom component provided by the instrument manufacturer. The modified ball holder incorporates two zirconia bushings, ensuring electrical insulation, as illustrated in Fig. 58.

For the disc, an insulating holder was specifically designed in-house and then manufactured by a CNC machining company (Final-Materials). The holder was manufactured from a 99.7% pure sintered alumina block, chosen for its good dielectric strength (17 kV/mm), high chemical inertness, and good thermal conductivity (30 W/m·K at 100 °C) [12]. These properties ensure both electrical isolation and efficient heat transfer (as the system is heated by a resistance under the disc holder), allowing for uniform thermal distribution and reduced heating time prior to tribological testing. The modified tribometer assembly is presented in Fig. 58.

It is also noteworthy that a new cooling platform (to evacuate excessive heat for prolonged tribological tests) was designed in-house to compensate for the overall height increase resulting from the introduction of the insulating disc holder.

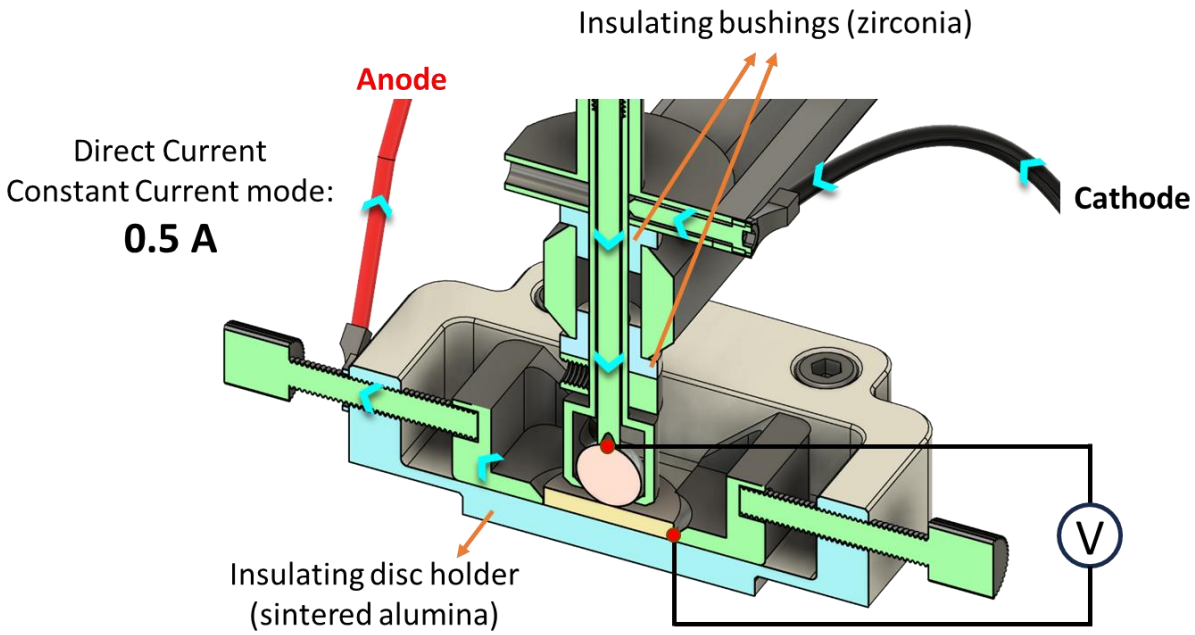

Fig. 58: Illustration of the modified Anton Paar TRB3 ball-on-disc tribometer for electrified tribological tests.

During all tribological tests, the direction of the current was kept the same, with the ball acting as the cathode (negative pole) and the disc as the anode (positive pole). The current was supplied using a Rigol DP811A programmable power supply, configured in Constant Current mode at 0.5 A. This setting was selected to replicate mild electrification conditions representative of those encountered in electric vehicle drivetrains, based on insights from the literature and a previous in-house study [13]. The normal force is also decreased from 10.5 N down to 5.5 N in order to anticipate the increase in wear caused by electrification.

The applied voltage was continuously recorded using a QuantumX HBM (MX440A) data acquisition system operating at 300 Hz.

The full set of experimental parameters used during electrified testing is summarized in **Table *2***.

Temperature	100°C
Normal load	5.5 N
Ball diameter	10 mm
Maximum Hertzian contact pressure	0.83 GPa
Hertz Diameter	112 µm
Test frequency	0.64 Hz
Stroke length	5 mm
Maximum linear speed	10 mm/s
Oil quantity	2 mL
Repetitions	3
CoF acquisition frequency	25 Hz
Current intensity	0.5 A in CC mode
Cathode (-)	Ball
Anode (+)	Disc
Voltage acquisition frequency	300 Hz

Table 2: Tribological conditions for electrified tests

Regarding the sequence of the tribological tests themselves:

- Voltage recording is initiated.
- The ball is brought into contact with the disc.
- The test is started.
- Immediately afterwards, the current is applied.

A few seconds before the end of the test, the current is switched off.

In order to study the effect of current, 3 kinds of tribological tests have been conducted and are presented in **Table 3**.

Condition	Electric current	
	0 to 2300 cycles	2300 to 3450 cycles
A	0A	
B	0.5A	
C	0A	0.5A

Table 3: Tribological test methods for electrified test campaign.

Condition A is conducted in order to assess the usual behavior of tribological additives.

For condition B, the current is applied at the beginning of the test, we can therefore evaluate the effect of electric current on tribofilm formation.

With condition C, the current is applied after a tribofilm has been formed, this way we can see if an already formed tribofilm can sustain the current flow.

Experimental repeatability is illustrated for ZDDP tested under an applied current of 0.5 A (Fig. 59), where both the coefficient of friction (CoF) and the voltage evolution are reported for each repetition.

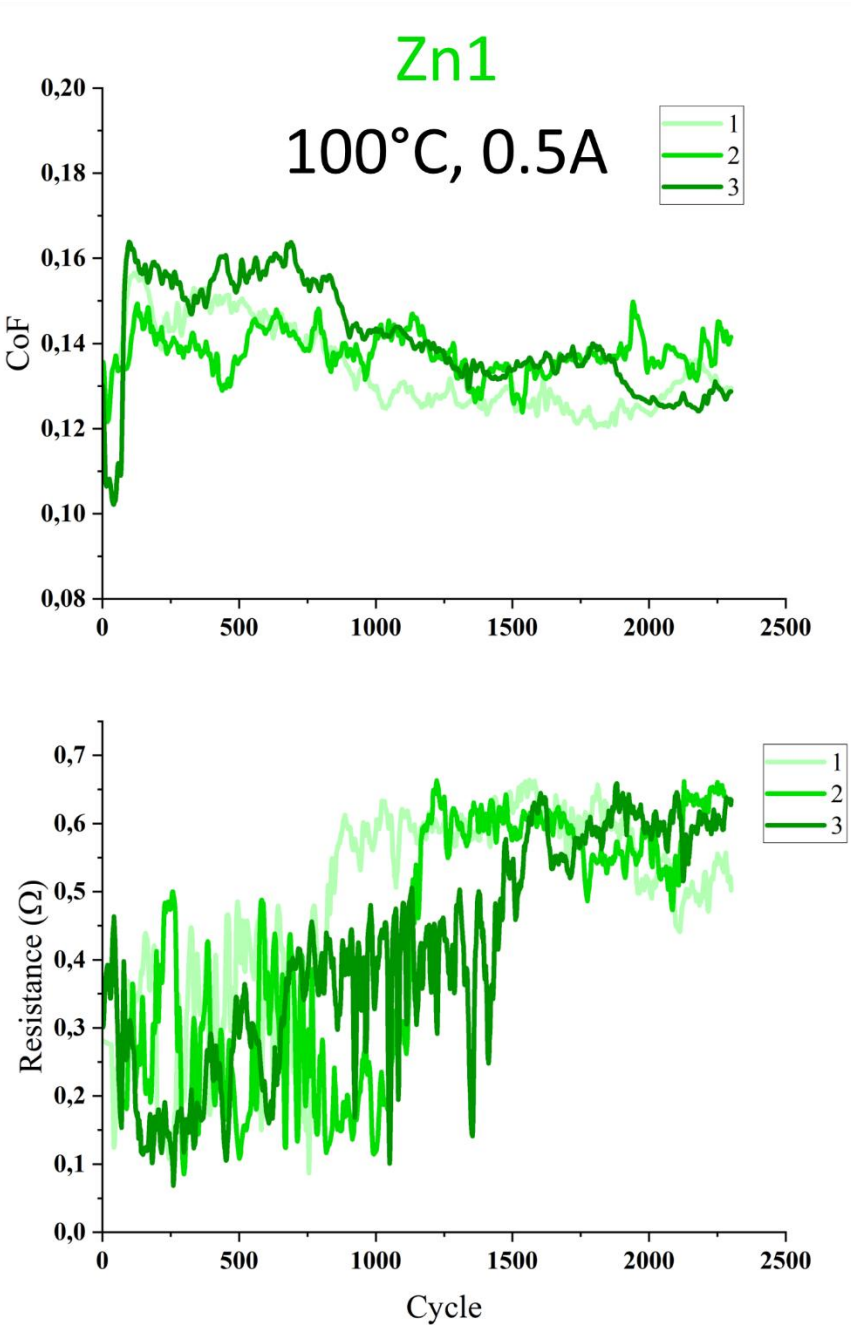

Fig. 59: Evolution of CoF (top) and Voltage (bottom) for the three tests acquired in the presence of a solution containing 1 wt.% of ZDDP (Zn1) in a PAO base oil, with an imposed current of 0.5A at 100°C.

In all three experiments, the CoF initially exhibits elevated values (~0.15) with pronounced fluctuations during the first 1000 cycles. This transient regime coincides with large instabilities in the measured voltage. Subsequently, the CoF decreases (~0.13) and displays reduced noise in some repetitions (e.g., repetition 3), which correlates with an increase and stabilization of the voltage (from 0.25 V to 0.40 V). These consistent trends across repetitions indicate good experimental repeatability.

The friction curves were plotted by averaging the values over eight points. Voltage was acquired at a much higher frequency of 300 Hz (**Table 2**) and required additional processing to extract measurements at the center of the track, following the same procedure applied to the CoF in the Anton Paar software. Since the two data streams are not synchronized, a custom algorithm was developed in Python with the assistance of AI (Artificial Intelligence) to identify the beginning and end of each cycle. This code automatically identifies the start and end of each cycle by detecting the half-cycles and matching them to the expected half-cycle frequency (0.64 Hz x 2). The detection was performed using signal-processing functions from the **SciPy** and **NumPy** libraries - particularly scipy.signal.find_peaks, which locates local maxima in the absolute voltage signal. The algorithm optimizes the peak-detection parameters (peak height and minimum peak distance) so that the number of detected cycles and their average frequency correspond to the expected mechanical oscillation frequency. Once the half-cycles are identified, the code averages the voltage values within the central portion of each cycle, corresponding to the displacement range of -0.5 mm to +0.5 mm on the experimental track.

It can be observed that during a cycle (when the ball is moving on the disc), the signal is very noisy, likely due to inhomogeneities in the contact resistance across the track. In contrast, when the ball remains static (at one end of the wear track), the signal is more stable and slightly higher in voltage. This behavior difference allows for clear identification of individual half-cycles.

Fig. 60 shows an example of cycle identification obtained with this code. The central values were then extracted and averaged over eight points before plotting.

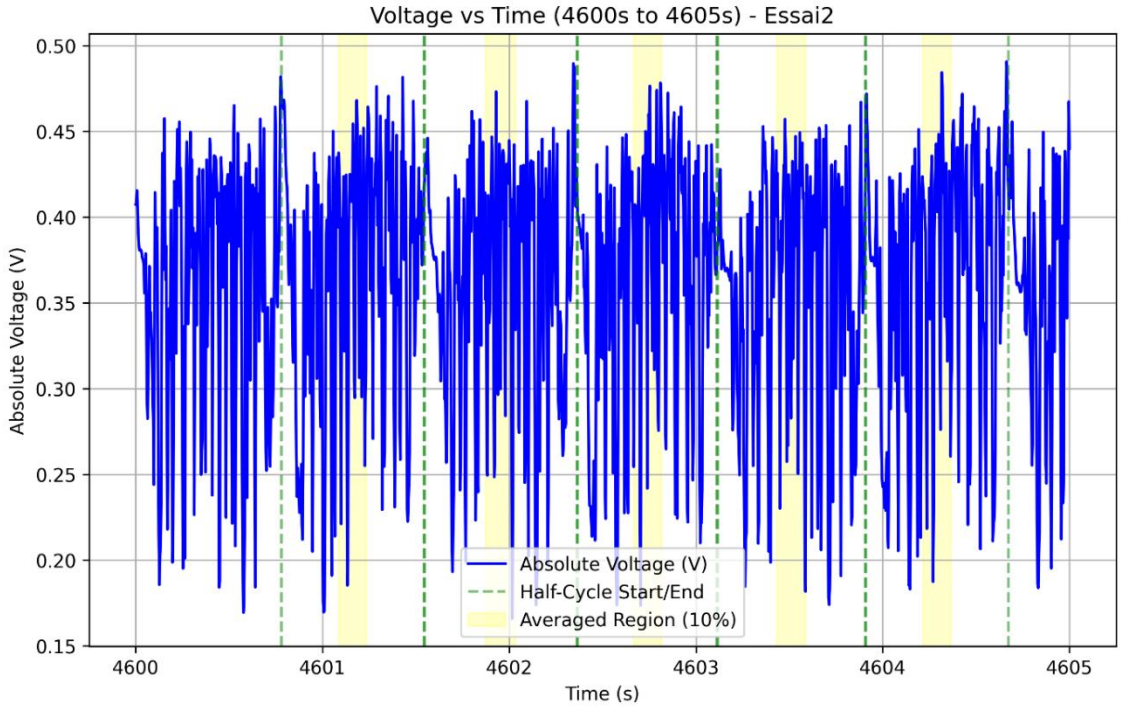

Fig. 60: Identification of the start and end of each half-cycle by peak detection, enabling extraction of the voltage at the track center. Each ~0.8 s segment of the signal corresponds to either the forward or backward stroke of the reciprocating ball-on-disc tribological test, that is, to one half-cycle of the sliding motion.

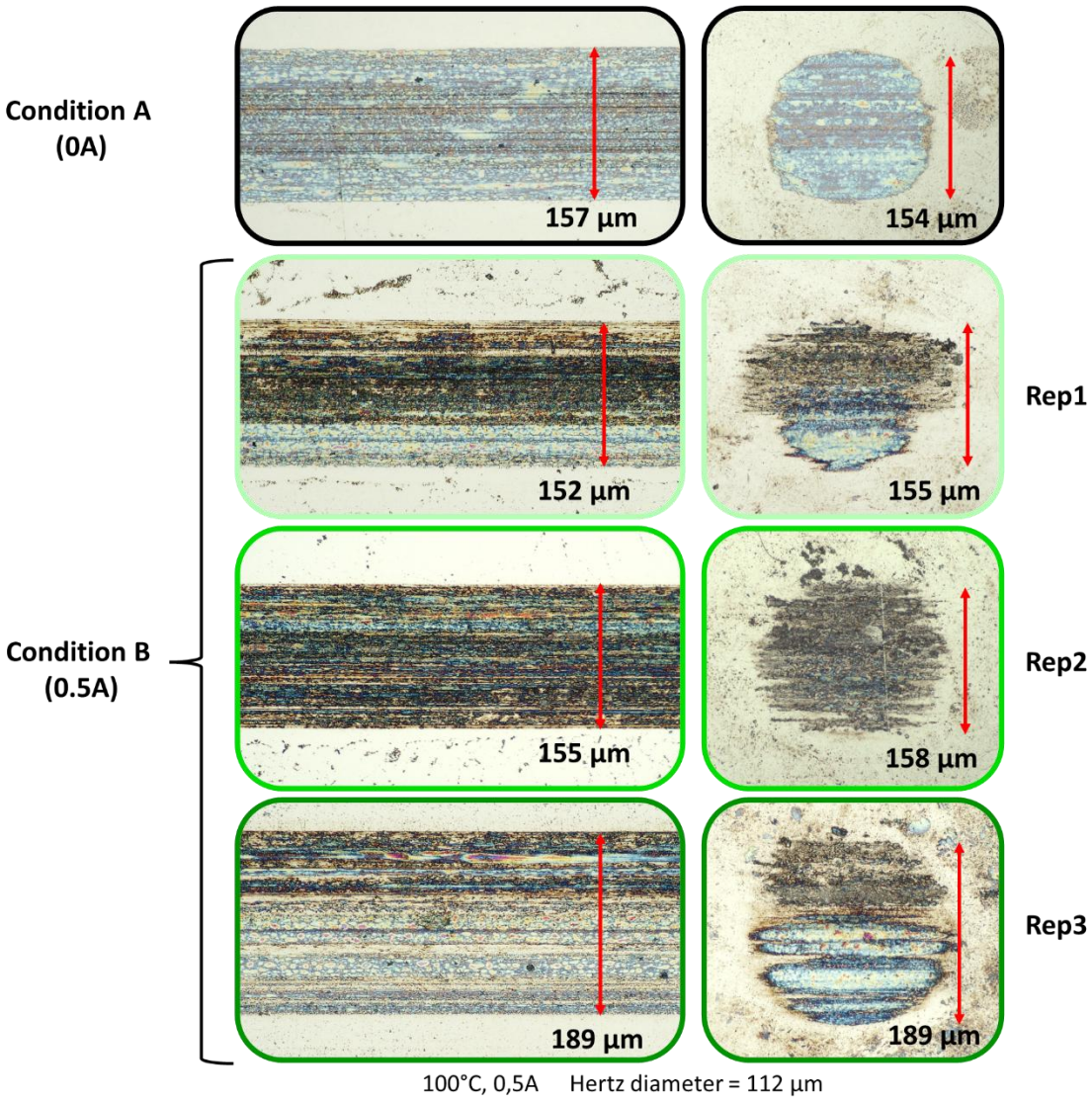

Fig. 61: Optical micrographs of wear tracks obtained for the solution containing 1 wt.% of ZDDP (Zn1) in a PAO base oil under applied current (0.5 A). A track obtained at 0A is also presented for comparison.

Analysis of the wear tracks (Fig. 61) reveals, in all cases, regions that appear to be covered by tribofilm (light blue), similar to the reference track obtained without electrical current. In addition, darker zones are observed, which may be attributed to wear. While the track widths remain very consistent across repetitions (~154 µm), the relative proportion of tribofilm-covered versus uncovered regions varies depending on the repetition.

Similar observations can be made for condition C and those results will be discussed in Chapter 5.

2.2.3 Ball and Disc Samples Preparation

The balls were purchased pre-hardened and polished from a commercial supplier (MARTIN & C°. SPA). The measured hardness is 800 HV (62 HRC), and the surface finish corresponds to grade G28 according to the ISO 3290 standard [14], which specifies a surface roughness of 50 nm (Ra).

The discs were initially supplied in an annealed and as-machined condition (20 mm in diameter and 4 mm in thickness). They were heat treated to achieve an 840 HV hardness. Then they were subsequently ground to ensure flatness and polished following the protocol detailed in **Table 4** with a Mecatech 334 polishing machine from PRESI. The measured surface roughness (Ra) after polishing is below 10 nm (STIL micromeasure2 3D noncontact surface measurement system based on a chromatic confocal sensor (CCS)).

SiC abrasive paper (FEPA)	Time (s)	Plate speed (RPM)	Head speed (RPM)	Normal load (N)	Lubricant
240	60	200 (CW)	100 (CW)	13	Water
320					
600					
1200					

Polishing cloths	Diamond suspension	Time (s)	Plate speed (RPM)	Head speed (RPM)	Normal load (N)	Lubricant
RAM (PRESI)	3 µm	80	180 (CW)	80 (CW)	13	Ethanol based 0,2mL / 10 sec
NT (PRESI)	1 µm					

Table 4: Polishing protocol and conditions for the 100Cr6 discs.

Prior to testing, both balls and discs were cleaned in an ultrasonic bath using the following solvents in sequence:

- 99% heptane: removes apolar compounds

- 99.5% acetone: removes residual heptane as well as some polar and apolar contaminants

- 99.5% isopropanol: eliminates remaining acetone and polar residues

After cleaning, specimens were hermetically stored in 99.8% absolute ethanol and dried with compressed air before each tribological test.

2.3 Characterization techniques

2.3.1 Tribofilm and wear characterization

After tribological testing, both the ball and the disc are cleaned using heptane followed by ethanol and then stored in 99.8% absolute ethanol prior to surface analysis.

First off, optical observations are performed using a Keyence VHX-7000 digital microscope. These observations serve multiple purposes: they allow measurement of the wear scar diameter on the ball and the friction track width on the disc, which can then be compared to the Hertzian contact diameter [11,15] (considered as the theoretical minimum wear diameter). In addition, they provide a first visual assessment of tribofilm formation and morphology (homogeneity in the sliding / transverse directions, patchy or continuous…).

Depending on the additive used, the tribofilm may appear either opaque (for TiO_2 nanoparticles based tribofilms for example) or transparent (for tribofilms derived from ZDDP decomposition for example). Therefore, tribofilms can be observed either thanks to their opacity or through light interference effects resulting from their thickness (~ 100 nm for ZDDP), which leads to the appearance of interference colors (generally bluish) from the white light spectrum.

In contrast, tribofilms formed from MoDTC additives are typically not optically detectable, due to their very low thickness (~10-20 nm), which is insufficient to produce visible light diffraction effects.

Additionally, a STIL micromeasure2 3D noncontact surface measurement system based on a chromatic confocal sensor (CCS) Prima is used to quantify the depth of friction tracks formed on the disc and the ball. Unless otherwise stated, the surface profile was acquired over a 1 mm × 0.5 mm region at the center of the friction track with an acquisition step of 2 µm in x and y axis. This corresponds to the same area of the wear track presented in Fig. 57.

For more precise information, both the ball and the disc are examined using a Scanning Electron Microscope (SEM) (Tescan MAIA3). Energy Dispersive X-ray (EDX) analysis is carried out using a QUANTAX detector (Bruker) for a semi-quantitative elemental analysis of the deposition and wear surfaces, the data was processed using Esprit software (Bruker). SEM observations are conducted with Secondary electron (SE) and Back-Scattered Electron (BSE) modes, a beam energy (BE) of 10 keV and a working distance (WD) of 9 mm. EDX analysis are conducted with SE mode, a BE of 10 keV and WD of 5 mm. High resolution (HR) mode is also used with a BE of 15 keV and a WD of 5 mm.

Chemical analysis is conducted using X-ray Photoelectron Spectroscopy (XPS) to determine the atomic composition and chemical nature of a potentially formed tribofilm. This technique is used because of its low analysis depth of 5-10 nm [16]. XPS analyses were initially performed using a K-ALPHA system, and subsequently a newly acquired NEXSA instrument, both from ThermoFisher Scientific with an AlKα monochromated source. A comparative study on selected tribofilms revealed no significant differences in atomic composition or chemical states between the two systems. The main advantage of the NEXSA lies in its more sensitive detector, which enables the use of a smaller spot size, offering improved spatial resolution.

The operating parameters for both instruments are detailed in **Table 5** (K-ALPHA) and **Table 6** (NEXSA). In-depth sputter profiling was performed with the K-ALPHA system, using a monoatomic Ar+ ion gun.

Peak analysis		Depth profile	
Source	Monochromatic Al Kα	Energy	2000 eV
Spot size	300 µm	Etching speed (on Ta_2O_3)	0.59 nm/s
Step size	0.1 eV		
Pass energy	40 eV	Total time	5000 s
Charge compensation	Low energy flood gun with an ion/electron dual beam		

Table 5: K-ALPHA parameters for XPS analysis

Peak analysis	
Source	Monochromatic Al Kα
Spot size	**50 µm**
Step size	0.1 eV
Pass energy	40 eV
Charge compensation	Low energy flood gun with an ion/electron dual beam

Table 6: NEXSA parameters for XPS analysis

The C1s peak (C-C bond) is calibrated at 284.8 eV, and peak decomposition is carried out using Avantage software (ThermoFisher). Elemental quantification was performed using Scofield sensitivity factors (ALTHERMO1 database) and a Smart (modified Shirley) background.

Finally, a Transmission Electron Microscope (TEM) was used to observe cross-sectional lamellae in order to measure the thickness and assess the microstructure of the tribofilm. The lamellae were prepared by Focused Ion Beam (FIB) at CIMAP (UMR6252) – ENSICAEN. Observations were carried out in STEM mode using the ThermoFisher Scientific SPECTRA 200 microscope operated at an acceleration voltage of 200 kV, located at the ACTEM platform.

2.4 Cold spray coating

The objective of this section is to present the methodology and tools used to produce a cold sprayed coating tailored for our application under boundary lubrication conditions.

The development of such a coating is structured around three main aspects:

1. **Substrate surface preparation**, to ensure good adhesion with the coating.
2. **Deposition process**, to achieve a dense and mechanically robust coating.
3. **Tribological performance**, to minimize friction and wear.

Each of these aspects involves multiple parameters that can significantly influence the mechanical and tribological properties of the resulting coating. For this reason, we adopted an iterative approach. Initially, we focused on the coating itself and its physico-mechanical properties, aiming to optimize these using a single-component coating (no reinforcement).

Following this initial optimization, composite coatings were produced and evaluated mechanically as well as tribologically. These results then guided a second round of deposition parameter adjustments to further improve friction reduction and wear resistance.

This iterative strategy is illustrated in Fig. 62.

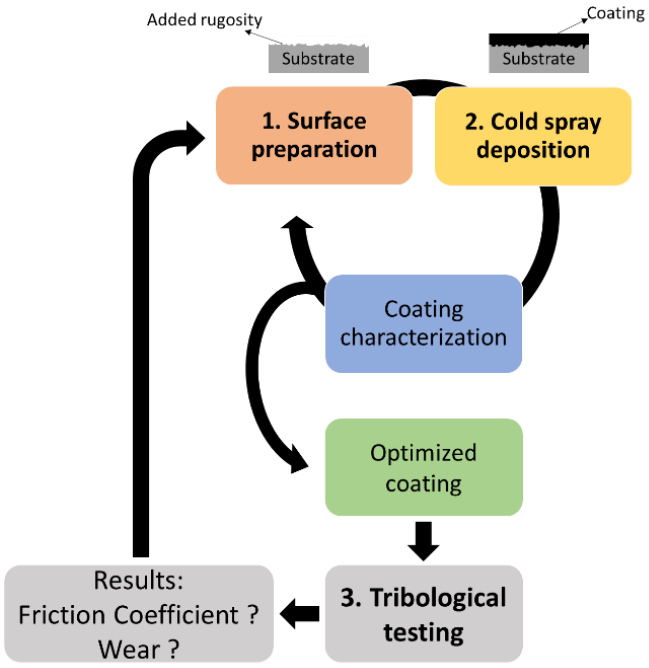

Fig. 62: Iterative optimization approach for cold spray coating development through: surface preparation, cold spray deposition, and tribological performance.

In the following sections, we will examine each of these three aspects in detail, describing the parameters we varied, and the measurements performed to assess their impact on coating performance.

2.4.1 Substrate Surface Preparation

The substrate selected for this study is a ferrito-perlitic low-carbon steel, grade ASTM S235 (AISI A570). Steel was chosen over aluminum mainly because of its higher Young's modulus as well as yield strength, which make it more suitable for applications subjected to high mechanical loads, such as transmission gears. One drawback of steel, however, is their higher hardness compared to aluminum alloys, which can make particle adhesion with cold spray more challenging. For this reason, a mild steel with a low carbon content and consequently a relatively low hardness such as S235 was selected as a compromise, combining sufficient mechanical strength with moderate surface hardness. Chemical composition of S235 is presented in **Table 7**.

Composition (wt.%)	C	Mn	P	S	N	Cu	Fe
ASTM S235 / AISI A570	0.17-0.20	≤ 1.40	≤ 0.035	≤ 0.035	≤ 0.012	≤ 0.55	Rem.

Table 7: Chemical composition (wt.%) of ASTM S235 / AISI A570 steel. *[17]*

S235 sheets were supplied as 100 × 40 mm plates with a macroscopic hardness of 192 ± 7 HV_{10} and microhardness of 235 ± 10 $HV_{0.1}$. The surfaces were ground to ensure good planarity and then thoroughly cleaned using heptane, acetone, and isopropanol to remove contaminants. The samples were subsequently sent to the CRITT - TJFU (Centres Régionaux d'Innovation et de Transfert de Technologie - Techniques Jet Fluide et Usinage) for surface preparation.

Three different surface treatments were investigated with the objective of increasing the surface roughness to enhance coating adhesion:

Water Jet Blasting

In this method, a high-pressure jet of water loaded with abrasive particles is directed onto the substrate surface. The kinetic energy of the abrasive particles induces localized plastic deformation and material removal, thereby increasing the surface roughness and promoting mechanical interlocking with the deposited coating. This technique can be considered intermediate between fluid line-jet polishing (FLJP) [18] and abrasive water-jet cutting [19], with the specific objective here of generating controlled surface roughness to enhance coating adhesion. [20]

Cryogenic Jet Blasting (Liquid Nitrogen Jet)

In this variant, pressurized liquid nitrogen is used instead of water as the carrier fluid, while maintaining the injection of abrasive particles. The much lower temperature of the nitrogen jet induces brittle behavior at the surface, facilitating material removal through micro-fracture rather than plastic deformation. This mechanism can generate higher roughness with limited work hardening of the near-surface region. [21,22]

Sandblasting

For comparison, conventional sandblasting was also tested. This process relies on the impact of dry abrasive particles propelled by compressed air, which plastically deform and erode the surface to generate roughness. However, in our case, sandblasting rapidly proved less effective in creating the desired roughness compared to the two fluid-jet methods and was therefore not further pursued.

A schematic comparison between the water-jet and liquid-nitrogen jet processes is shown in Fig. 63.

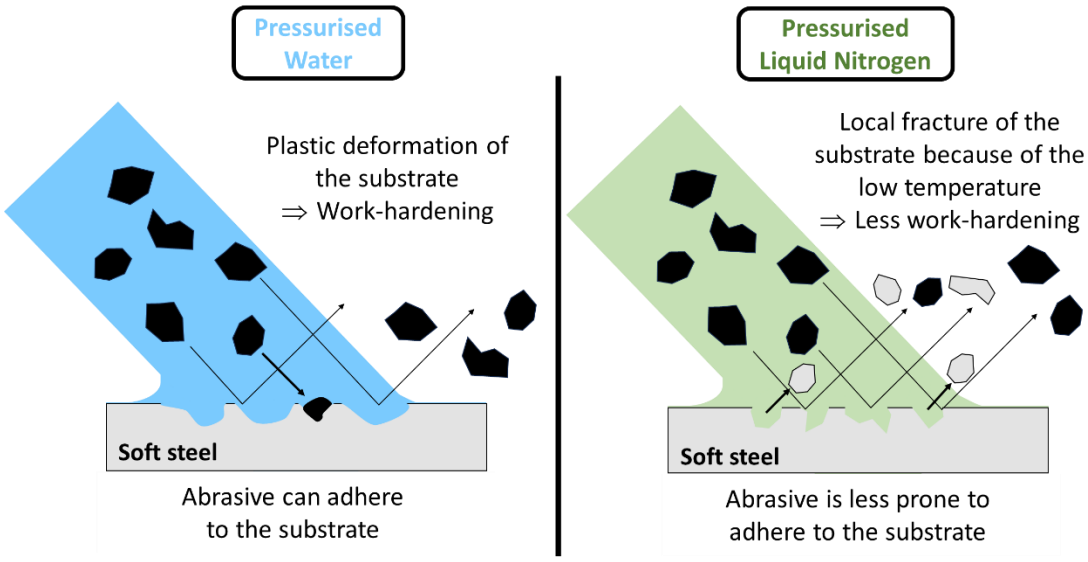

Fig. 63: Schematic representation and comparison of Water Jet (left) and Liquid Nitrogen Jet surface preparation principles

The surface preparation parameters for each method are summarized in **Table 8**.

Parameters	Surface preparation method		
	Water Jet	Liquid Nitrogen Jet	Sandblasting
Pressure	2000 bar	2000 bar	8 bars
Stand-off distance	120 mm	60 mm	~20 mm
Traverse speed	250 mm/s	167 mm/s	
Number of passes	1	1	
Abrasive size	80 mesh (177 µm)		
Abrasive feed rate	100 to 300 g/min		
Nozzle angle	45° or 90°		

Table 8: Parameters for each surface preparation methods.

For the fluid-jet processes, two parameters were adjusted to optimize surface topography while minimizing contamination:

- the **abrasive flow rate** (100, 150, and 300 g/min).
- the **nozzle angle** (90° and 45° relative to the substrate surface).

The treated surfaces were characterized as follows:

- **Surface roughness** was measured using a STIL micromeasure2 3D noncontact surface measurement system based on a chromatic confocal sensor (CCS) Prima.
- **SEM cross-sectional observations** were performed to evaluate the surface morphology, roughness, and possible incorporation of contaminants.
- **Microhardness measurements** were carried out using a Micromet 5124 from BUEHLER on cross-sections to assess the degree of surface work hardening induced by each treatment.

The results of these characterizations therefore provided feedback for optimizing the surface preparation parameters, allowing the selection of conditions that maximize roughness and adhesion while minimizing contamination.

Building on the optimized substrate preparation, we can now focus on refining the cold spray deposition parameters to achieve coatings with improved mechanical and tribological performance.

2.4.2 Cold Spray Coatings Deposition

The cold spray coatings were produced at CRITT-TJFU using an Impact Innovation 5/11 cold spray system, shown in Fig. 64. This setup can operate at pressures up to 50 bar and temperatures up to 1100 °C [23].

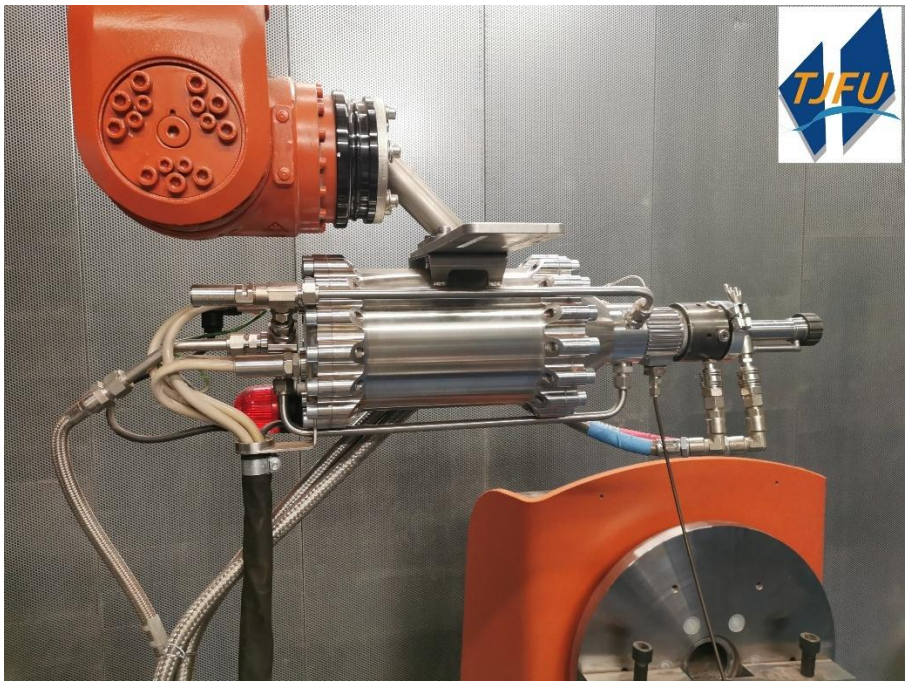

Fig. 64: Photography of Impact Innovation 5/11 cold spray gun

A schematic representation of this cold spray gun parts is presented in Fig. 65.

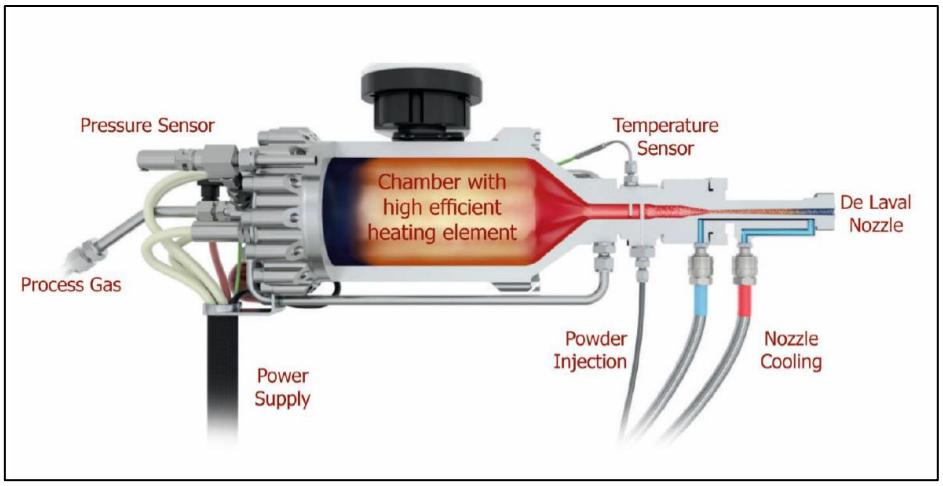

Fig. 65: Schematic representation of the different parts of Impact Innovation 5/11 cold spray gun.

Regarding materials for the coating, a pure titanium matrix was selected. Several reasons motivated this choice. First, from the perspective of its role as a matrix, the cold sprayed powder must exhibit good plastic deformability to ensure strong adhesion to the substrate and to form a cohesive coating. According to data provided by the manufacturer, pure titanium fulfills these criteria, showing a deposition efficiency of 98 % with the 5/11 system [24].

In addition, titanium offers excellent corrosion resistance, which is particularly advantageous for protecting the steel substrate used in this study. This property has also been demonstrated for Ti/TiO_2 composite coatings produced by cold spray, where the amount of TiO_2 reinforcement was found to significantly influence the corrosion behavior [25]. A powder mixture containing 20 wt.% TiO_2 appears to preserve the corrosion resistance of titanium while simultaneously enhancing dry wear resistance. The addition of more TiO_2 (40 to 60 wt.%), however, led to a decrease in wear resistance of the coating as well as in its corrosion protection towards the 316L stainless steel substrate. This is explained by the increase in porosity and the decrease in cohesivity [25].

For the choice of a titanium powder, the morphology and microstructure have a significant influence on the properties of the cold sprayed coating. According to Munagala et al. (2018) [26], spherical Ti-6Al-4V powders produced by gas atomization exhibit a martensitic α’ microstructure, which forms during the very rapid solidification of molten droplets in an inert gas atmosphere. In contrast, irregular powders fabricated via the Armstrong process - a chemical reduction of titanium tetrachloride ($TiCl_4$) by molten sodium - display an equiaxed α + β microstructure. This difference in microstructure strongly affects particle deformability during impact. Spherical Ti-6Al-4V particles, being harder and less ductile due to their martensitic structure, deform less upon impact, leading to higher coating porosity (Fig. 66). Additionally, these coatings exhibit a higher hardness loss, which reflects a lower inter-splat (flattened particles) cohesion, since hardness loss quantifies the reduction in hardness between small-scale and large-scale indentation tests (here with 25g to 500g hardness tests) and is directly related to the bonding quality between splats.

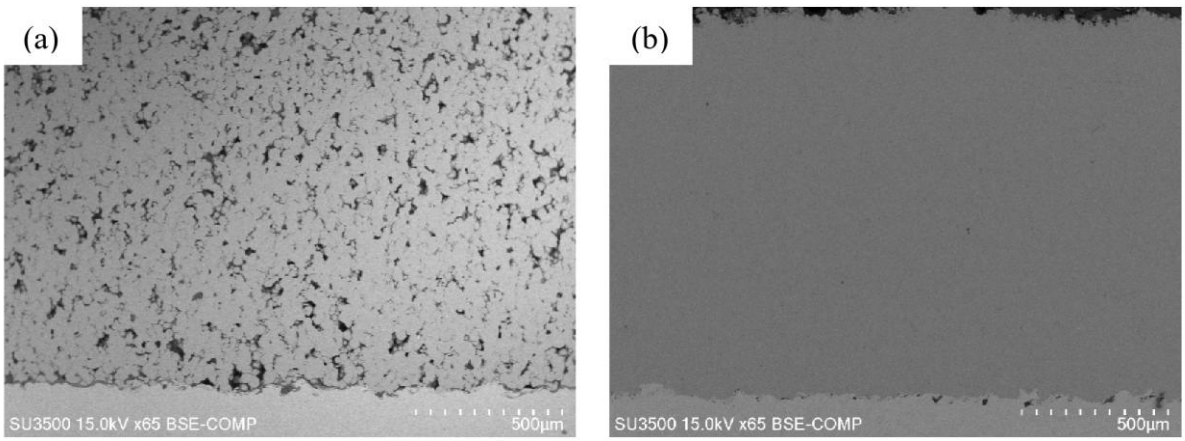

Fig. 66: Cross-section of Ti-6Al-4V coatings deposited using spherical (a) or irregular (b) powders. SEM micrographs in BSE mode. [26]

Based on these findings, our study focuses on two titanium powders of different morphologies: a spherical powder (forAM® CP-Ti G2 15–53 EG) and an irregular powder (Amperit® 155.086). Both powders consist of commercially pure titanium, which is α-stable up to 880°C [27] and does not form martensite upon rapid cooling. Therefore, a higher particle deformability and consequently denser, more cohesive coatings are expected compared to martensitic Ti-6Al-4V.

For clarity, **forAM® CP-Ti G2 15–53 EG** will hereafter be referred to as **Sph-Ti**, and **Amperit® 155.086** as **Irr-Ti**.

According to the manufacturer, Sph-Ti powder is produced by gas atomization and have a particle size distribution between 15 and 53 µm [28]. We verified this data by depositing a small quantity of powder on carbon tape and observing the particles using SEM (Fig. 67).

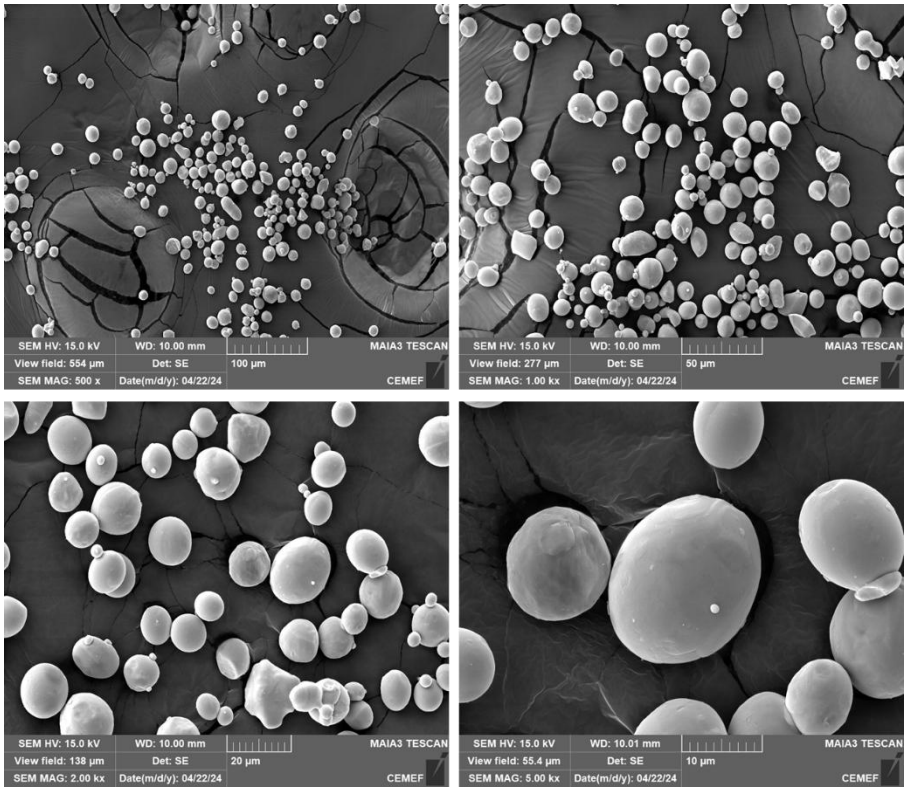

Fig. 67: SEM micrographs (SE mode) of Sph-Ti powder deposited on carbon tape.

To quantify the particle size distribution, ImageJ was used to identify particles based on their contrast with the carbon tape. A filter was then applied to remove agglomerated clusters and segmentation artefacts, which were identified by their low circularity (< 0.4), as illustrated in Fig. 68.

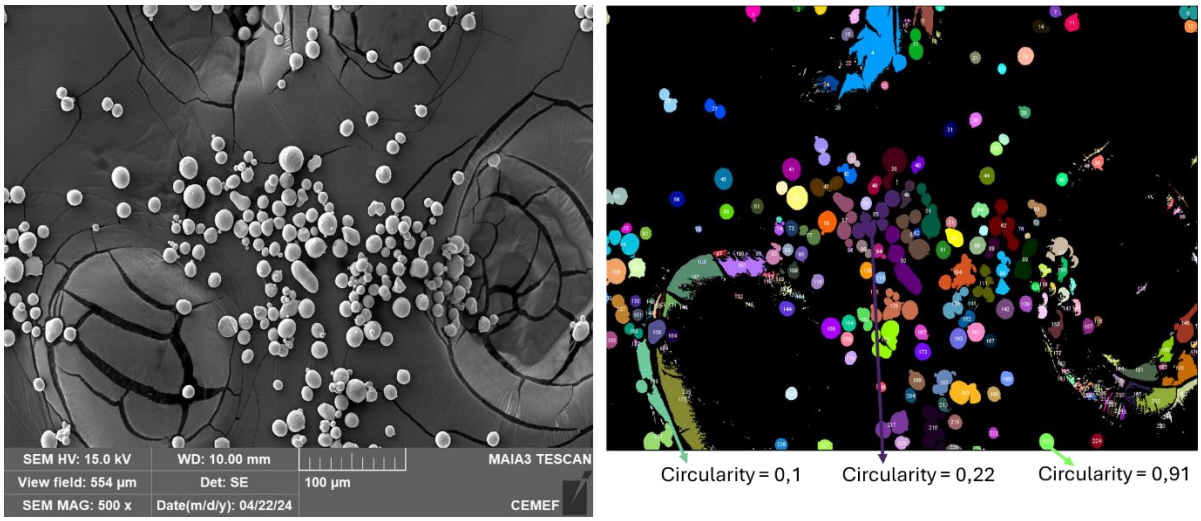

Fig. 68: Identification of spherical particles using a segmentation protocol with ImageJ on SEM micrographs.

The particle size was determined using the maximum Feret diameter, which corresponds to the distance between two parallel tangents on opposite sides of a particle (Fig. 69), effectively measuring its maximum caliper dimension.

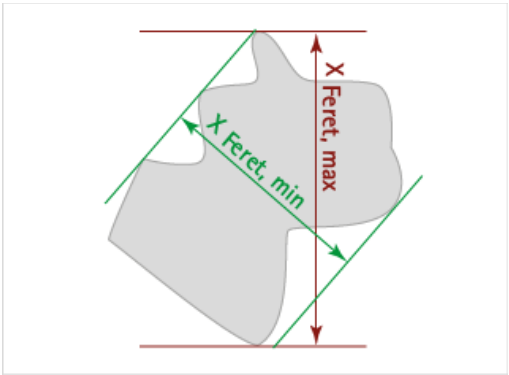

Fig. 69: Feret diameter measurement of a particle. [29]

Analysis of ten SEM images allowed the particle size distribution curve to be plotted, as shown in Fig. 70. The powder exhibits a Dv90 of 22.5 µm, meaning that 90 % of the powder volume consists of particles smaller than 22.5 µm. Hardness test on the cold spray coating with a 0.1 kg weight shows a mean value of 204 ± 6 $HV_{0.1}$.

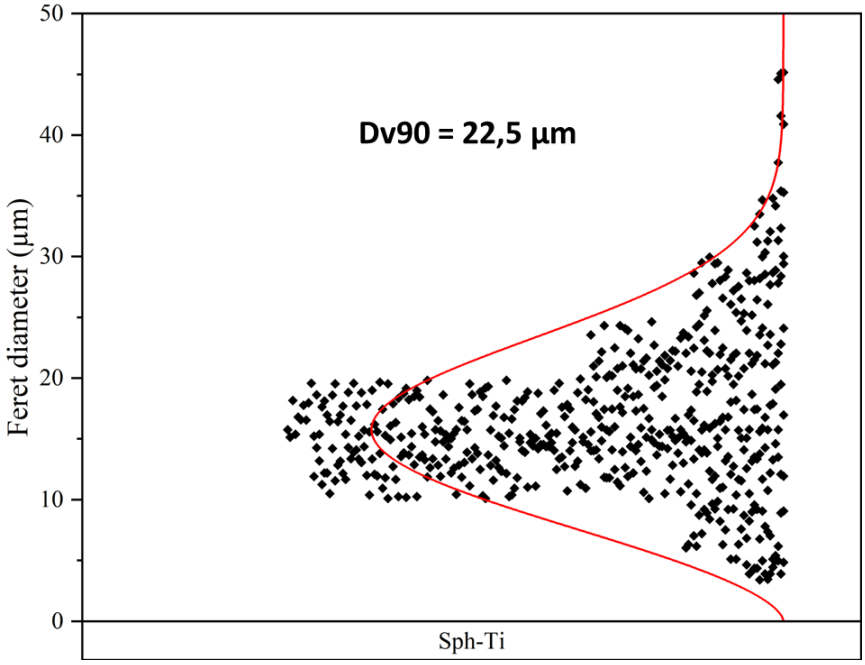

Fig. 70: Particle size distribution of Sph-Ti powder obtained using ImageJ on SEM micrographs.

Irr-Ti powder, on the other hand, are produced by a crushing process - where bulk titanium is mechanically crushed into fine particles - and have a particle size range between 0 and 63 µm. Although still composed of α-phase titanium, these particles have undergone significant mechanical deformation during crushing, likely resulting in a higher strain-hardened state compared to the Sph-Ti powder. The manufacturer does not report any stress-relief or annealing treatment applied after crushing.

SEM observations of Irr-Ti reveal that this powder tends to form agglomerates more easily than the spherical one, preventing reliable size quantification with ImageJ. Nevertheless, SEM imaging somehow confirmed the manufacturer's specifications: particle sizes range from less than 1 µm for the smallest debris (Fig. 71) up to approximately 85 µm (Fig. 72), depending on how the particle is measured. The broader particle size distribution compared with Sph-Ti likely results from the crushing step as well as the absence of a sieving step in the manufacturing process. Hardness test on the cold spray coating with a 0.1 kg weight shows a mean value of 222 ± 10 $HV_{0.1}$.

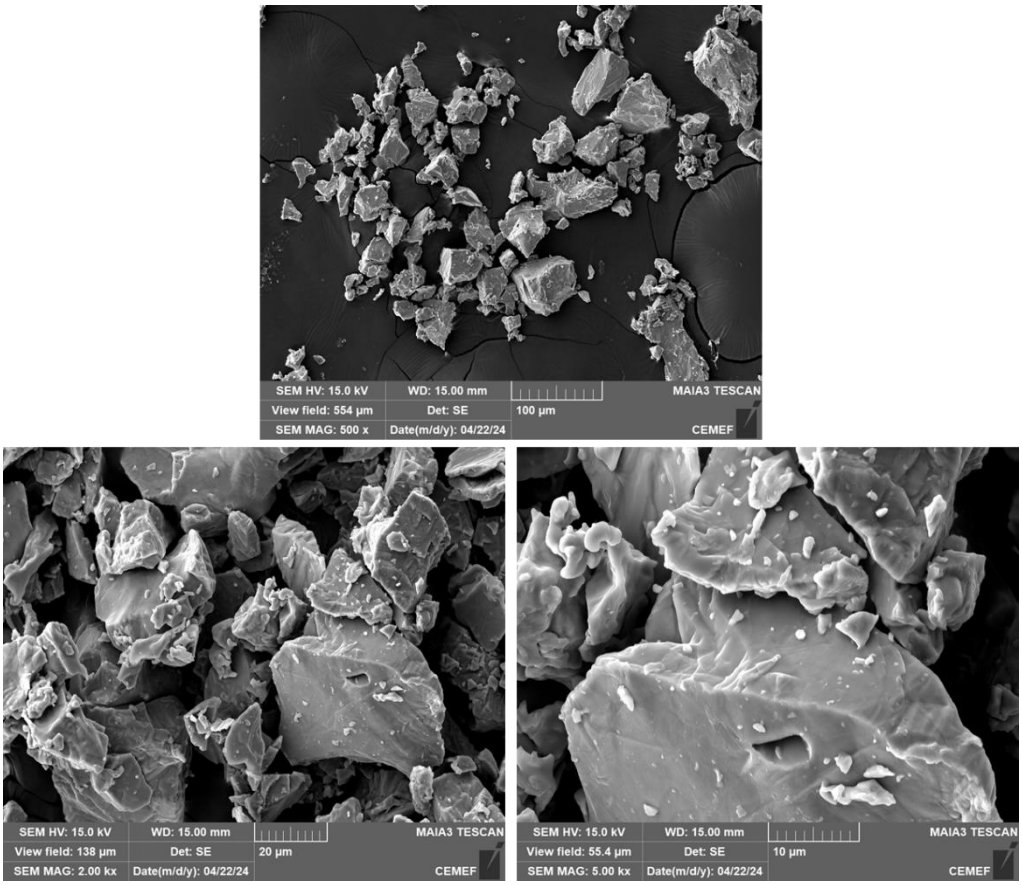

Fig. 71: SEM micrographs (SE mode) of Irr-Ti powder at different scales.

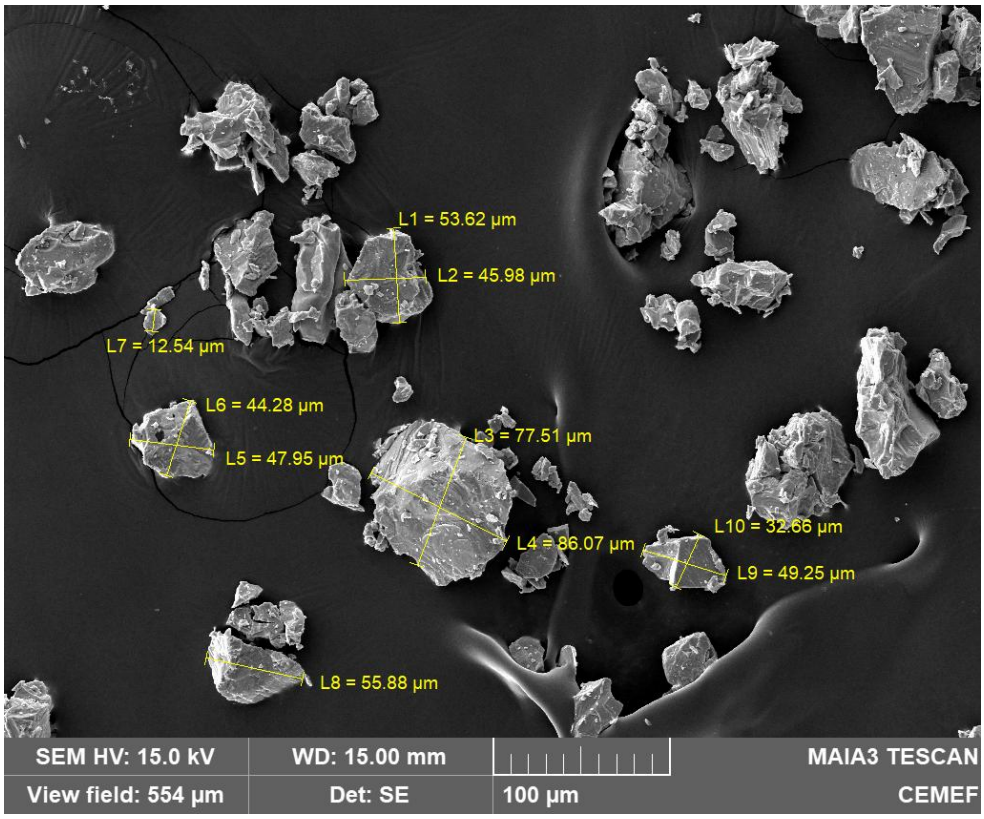

Fig. 72: Measurement of Irr-Ti powder particles size on a SEM micrograph (SE mode).

Interestingly, this wide distribution size could actually enhance coating densification during cold spraying. In addition to the plastic deformation induced by particle impact, powders with a broad size distribution can benefit from a granular packing effect - that is, smaller particles filling the voids between larger ones, improving the packing density and reducing coating porosity as shown in Fig. 73. This principle is well established in powder metallurgy, where optimizing particle size distribution increases bulk and coating density. A drawback, however, lies in the difficulty of feeding such powders into the cold spray gun, as they exhibit lower flowability due to increased interparticle interactions.

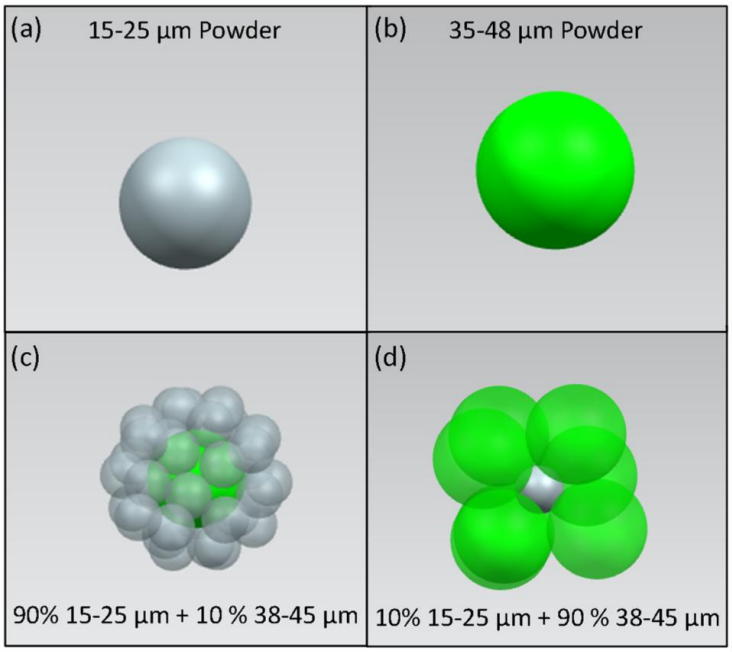

Fig. 73: A 3D representation of particle packing model. (a) 15–25 µm particles. (b) 38–45 µm particles. (c) 15–25 µm particles packed around a central 38–45 µm particle. (d) 38–45 µm particles packed around a central 15–25 µm particle. [30]

For the reinforcement, a TiO_x powder supplied by Saint-Gobain [31] was selected. TiO_x is a reduced form of TiO_2 whose crystallographic structure belongs to the Magnéli series (e.g., Ti_4O_7, Ti_5O_9, Ti_6O_{11}, etc…). According to the manufacturer, this powder exhibits a lower melting point than TiO_2, which could enhance its suitability for spray deposition techniques by allowing easier incorporation into the coating without fragmentation, notably in the case of cold spray.

Although the manufacturer does not specify an exact melting temperature, the Ti-O phase diagram (Fig. 74) suggests a range of 1675-1775°C, depending on the specific Magnéli composition, compared to ~1865 °C for TiO_2. This reduction in melting temperature is significant, as it implies lower thermal stresses during deposition and therefore a reduced risk of particle cracking or spallation.

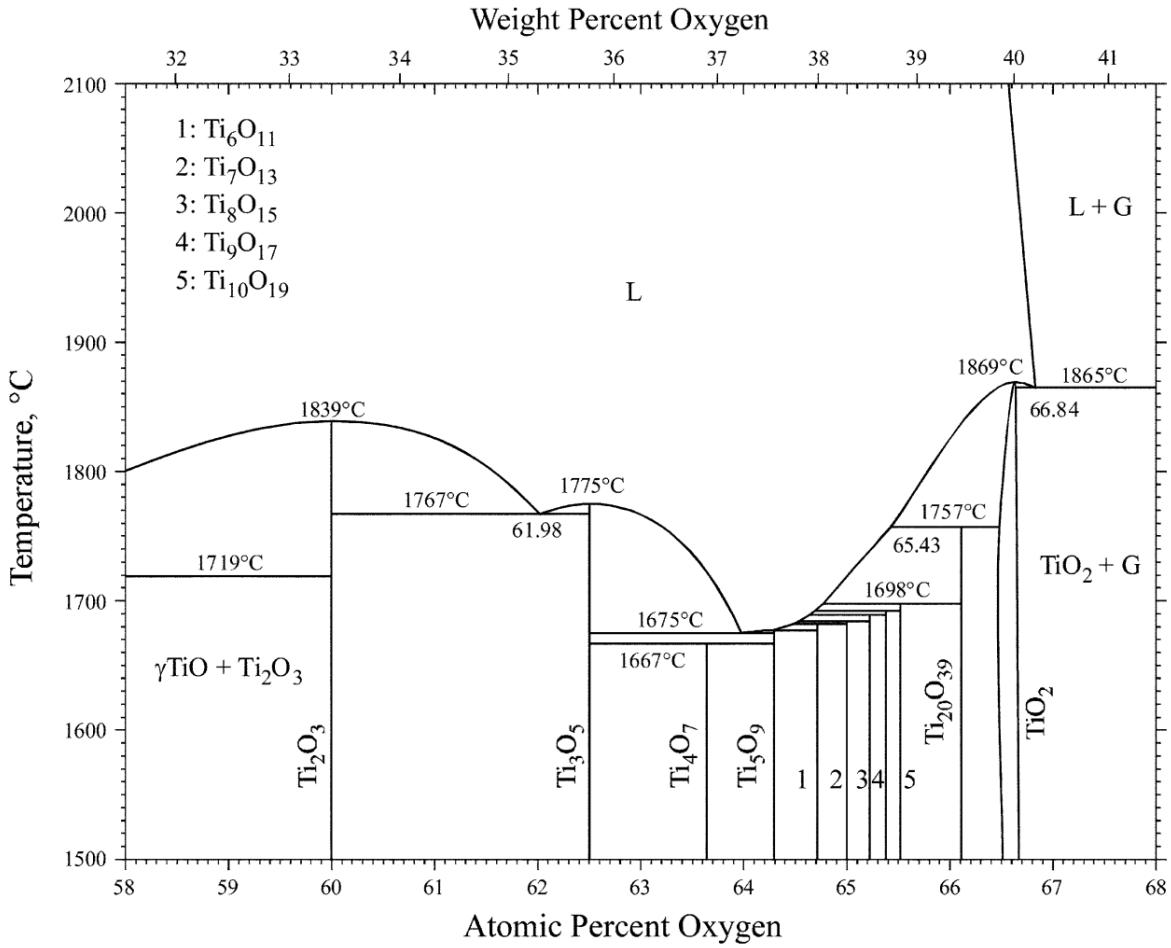

Fig. 74: High temperature Ti-O phase diagram from 58 to 68 at.% of oxygen. [32]

Saint-Gobain also claims that their TiO_x powder has solid-lubrication properties (dry lubrication), which could beneficially influence the tribological behavior of the coatings in our tests. Also, unlike TiO_2, TiO_x is electrically conductive, a feature that may be interesting to investigate under electrically loaded conditions such as in EVs drivetrains.

This TiO_x powder is produced by a crushing process, and according to the manufacturer it exhibits a particle size distribution between 15 and 45 µm. A distribution curve provided by Saint-Gobain is shown in Fig. 75. The stoichiometry parameter x corresponds to 1.81 and was determined by a mass re-oxidation test in air at 1000°C conducted by Saint-Gobain.

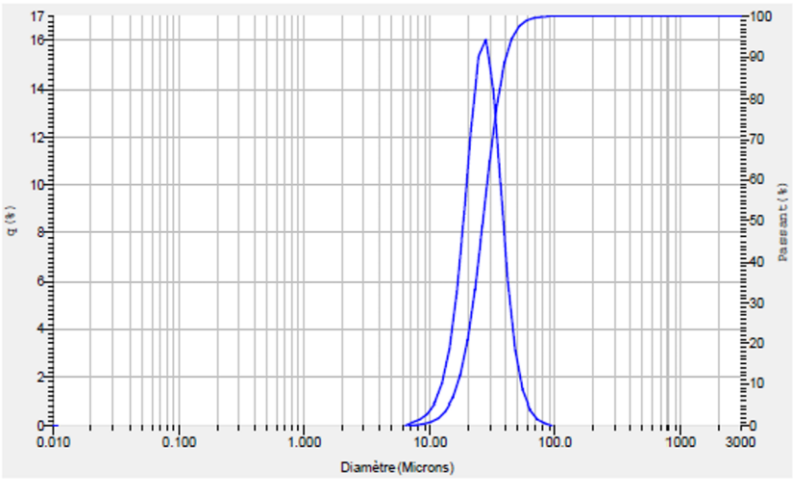

D10	D50	D90	D95
16.5µm	26.4µm	40.5µm	46µm

Fig. 75: Particle size distribution supplied by Saint-Gobain for the TiOx powder.

We performed SEM imaging of the TiO_x powder (Fig. 76), and observed a morphology similar to Irr-Ti, as expected from the crushing production process. However, fewer small debris were present, consistent with the narrower size distribution, which may be attributed to a sieving step in the manufacturing process.

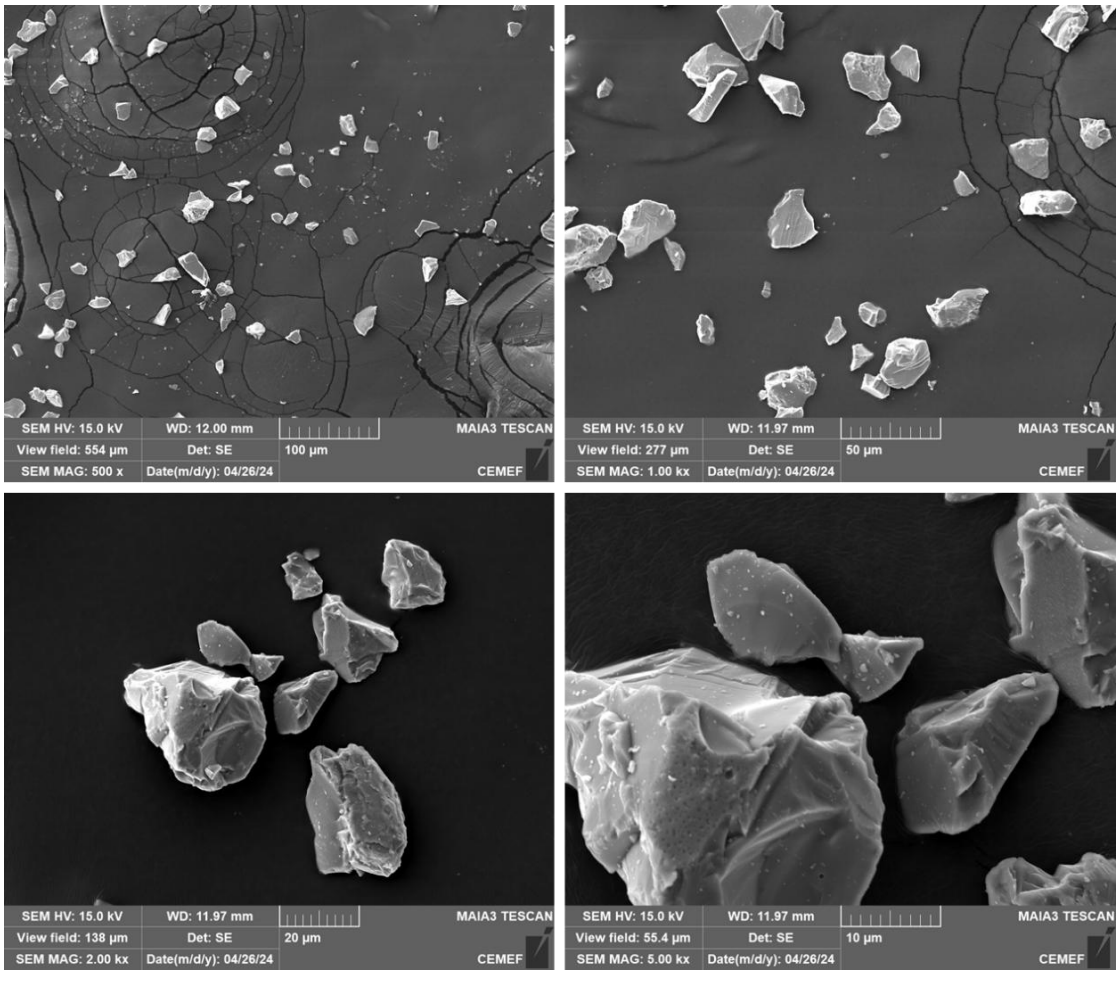

Fig. 76: SEM micrographs (SE mode) of TiO_x powder at different scales.

Because the particles did not strongly agglomerate, we attempted to measure their sizes and reconstruct our own particle size distribution curve (Fig. 77). We obtained a Dv90 of 30 µm, compared with 40.5 µm from the manufacturer's datasheet. This minor discrepancy is likely due to the limited number of particles visible in the SEM images. Hardness test on individual particles on the composite cold spray coating with a 0.01 kg weight shows a mean value of 1130 ± 200 $HV_{0.01}$, corresponding to 11.08 GPa which is close to the value that can be found in the literature [33].

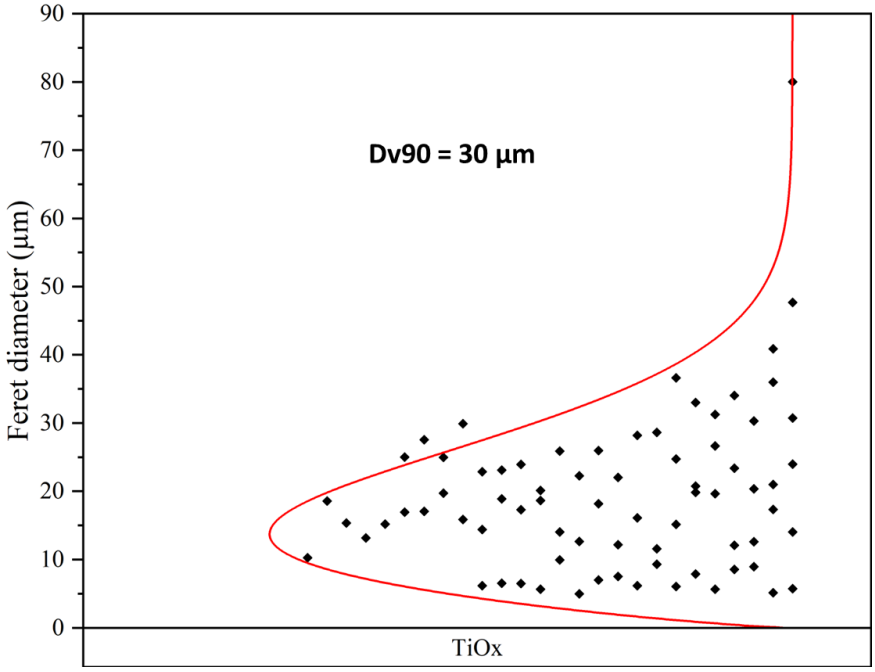

Fig. 77: Particle size distribution of TiOx powder obtained using ImageJ on SEM micrographs.

Concerning the deposition process itself, several parameters were adjusted in order to optimize the coating for tribological performance:

- Gas pressure: Increasing the deposition pressure results in higher particle velocities, which generally improves particle deformation and bonding. However, higher pressure also increases the operational cost, which must be considered for industrial-scale applications. Moreover, there exists an optimal deposition window: if the particle velocity is too low, the coating lacks cohesion, whereas excessive velocity causes erosion of the deposited layer, as illustrated in Fig. 78.
- Matrix powder: Two types of titanium powders were used, namely Sph-Ti and Irr-Ti, in order to evaluate the influence of powder morphology on coating quality.
- Reinforcement content: The TiO_x volume fraction was varied to investigate its effect on wear resistance. Up to a certain level, increasing the amount of reinforcement improves the coating's ability to withstand severe tribological conditions. Beyond this threshold, however, the coating tends to lose cohesion [34], indicating that an optimal balance must be found between hardness, toughness, and cohesion to achieve the desired performance.

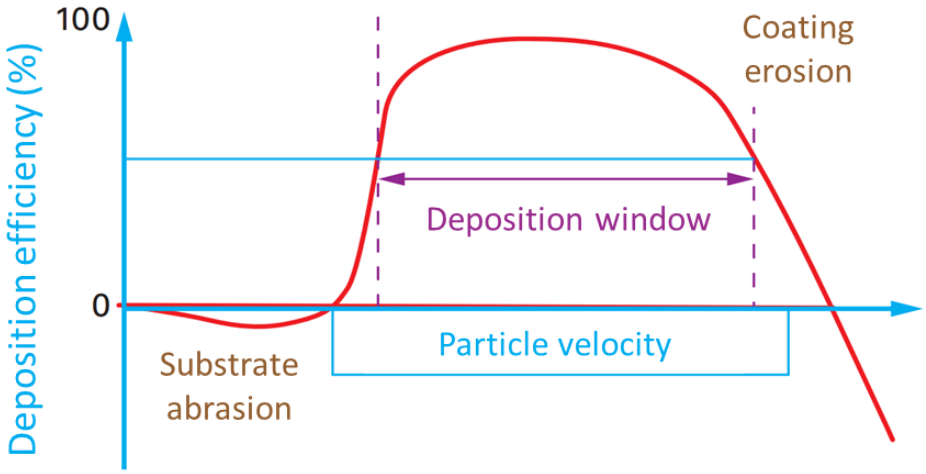

Fig. 78: Evolution of coating deposition efficiency with particle velocity (CRITT-TJFU).

Main cold spray deposition parameters are presented in **Table 9**.

Parameters	Cold Spray Deposition
Temperature	700°C
Stand-off distance	40 mm
Traverse speed	100 mm/s
Number of passes	4
Step size	4 mm
Pressure	15 to 50 bar
Matrix powder	Irr-Ti or Sph-Ti
Reinforcement fraction	0 to 50 v.%

Table 9: Cold spray deposition parameters

Following the deposition process, the coatings were characterized in order to refine and optimize the deposition parameters. The different characterization methods employed are presented in the next section.

2.4.3 Cold Spray Coatings Characterization

To characterize the cold spray deposits, both physico-mechanical and tribological measurements were carried out.

First, the cold spray samples were prepared as cross-sectional specimens to examine both the substrate and the coating. The cross-sections were then mounted in epoxy resin and polished to a mirror finish following the procedure summarized in **Table 10**.

SiC abrasive paper (FEPA)	Time (s)	Plate speed (RPM)	Head speed (RPM)	Normal load (N)	Lubricant
600	120	300 (CW)	150 (CW)	5	Water
1200	120	150 (CW)	150 (CW)	5	Water

Polishing cloths	Abrasive suspension	Time (s)	Plate speed (RPM)	Head speed (RPM)	Normal load (N)	Lubricant
OPS cloth	50% Colloidal silica suspension + H_2O_2	360	150 (CW)	150 (CW)	5	50% Colloidal silica suspension

Table 10: Polishing protocol for Cold sprayed samples for observation and characterization.

The coating thickness is measured using optical microscopy, and a matrix of hardness tests is then performed (Fig. 79). These measurements allowed characterization of the substrate work-hardening state (at -250 µm and -50 µm from the interface), indirect evaluation of the substrate-coating adhesion (interface), and assessment of the coating cohesion at different heights (50 µm, 250 µm, and 500 µm).

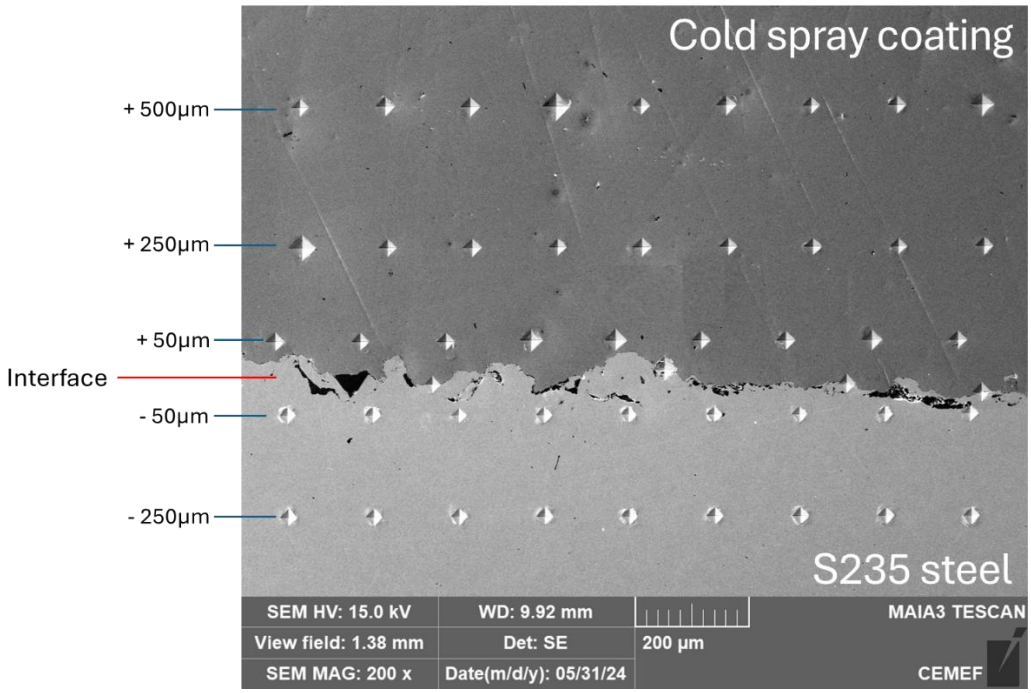

Fig. 79: Hardness test matrix of the cross section of the cold sprayed coating observed with a SEM (SE mode).

After these preliminary measurements, the samples are metallized for SEM observation. SEM imaging enabled detailed examination of both the coating and its interface with the substrate. The observations focused in particular on the presence of contaminants at the interface, which can be introduced during substrate surface preparation (Fig. 80). In addition, multiple images of the coating were acquired to quantify porosity and, where applicable, the reinforcement fraction, based on contrast differences using ImageJ software (Fig. 81).

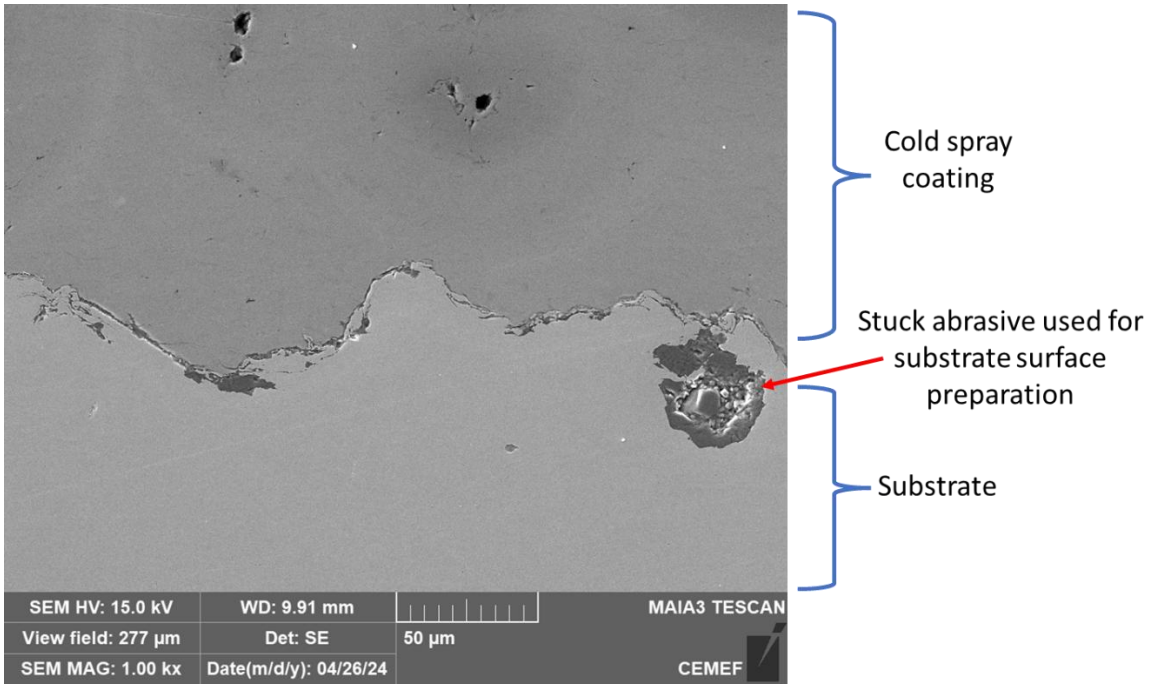

Fig. 80: SEM micrograph (SE mode) of the interface between the cold sprayed coating and the substrate.

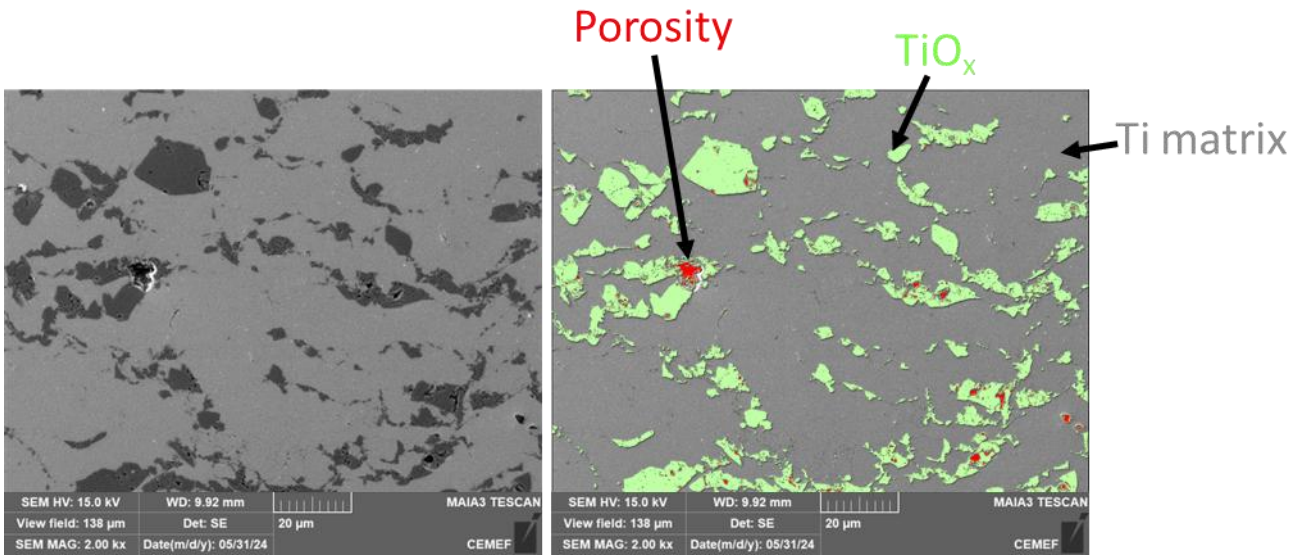

Fig. 81: SEM micrograph (SE mode) of a composite cold sprayed coating before (left) and after (right) being processed using ImageJ software.

In addition to the cross-sections, the same observations are also performed on the coating surface in order to identify any potential anisotropy. These surface samples were prepared following the same protocol described in **Table 10** and a slightly lower reinforcement content is measured compared with cross section samples. This could be due to the anisotropy of the sample, which may originate from the nature of the cold spray process, where particles can align preferentially along a specific direction during deposition.

For the tribological tests, new samples were prepared by sectioning 15 × 15 mm square specimens and polishing them according to the procedure described in **Table 11**.

SiC abrasive paper (FEPA)	Time (s)	Plate speed (RPM)	Head speed (RPM)	Normal load (N)	Lubricant
600	120	300 (CW)	150 (CW)	5	Water
1200	120	150 (CW)	150 (CW)	5	Water
2400	60	150 (CW)	100 (CW)	5	Water

Table 11: Polishing protocol for Cold sprayed samples for tribological tests.

Prior to testing, both balls and coated specimen were cleaned using the following solvents in sequence:

- 99% heptane: removes apolar compounds

- 99.5% acetone: removes residual heptane as well as some polar and apolar contaminants

- 99.5% isopropanol: eliminates remaining acetone and polar residues

After cleaning, the specimens were dried in an oven at 50 °C for several hours due to the porosity of some of the coatings.

The tribological tests were then performed using a ball-on-disc tribometer (Fig. 56) with the parameters summarized in **Table 12**.

Temperature	25 or 80°C
Normal load	4 N
Ball diameter	10 mm
Maximum Hertzian contact pressure	0.6 GPa
Hertz Diameter	108 µm
Test duration / cycle number	2300 or 4600 cycles (1 hour)
Test frequency	0.64 Hz
Stroke length	5 mm
Maximum linear speed	10 or 20 mm/s
Oil quantity	2 mL
Repetitions	3
Acquisition frequency	25 Hz
Plotted curves processing	Averaged over 8 points

Table 12: Tribological conditions used for Cold sprayed samples.

Finally, the characterization of the samples after the tribological tests was carried out using the same techniques presented in Section 2.3

Conclusion

In Chapter 1, the main tribological challenges encountered in modern drivetrains were discussed, particularly in the context of electric vehicles (EVs). These include higher operating torques and rotational speeds, which exacerbate boundary lubrication regimes, as well as the presence of electrical currents that can modify wear and tribofilm formation efficiency.

Building upon these considerations, the present chapter detailed the experimental methodologies established to reproduce and analyze these tribological conditions. A complete tribological framework was developed, combining boundary lubrication testing, controlled electrified testing with advanced surface and lubricant characterization techniques, ensuring reliable assessment of frictional and wear behavior under representative operating conditions.

Two complementary approaches were implemented to explore potential mitigation pathways. The first focuses on lubricant formulation, through the design of nanoparticle-based additives and optimized blends aimed at improving tribofilm formation under severe boundary conditions as well as their friction reduction and anti-wear properties. The second addresses surface engineering, through the development of cold sprayed coatings intended to enhance surface robustness and durability in demanding mechanical environments.

Together, these methodologies form a comprehensive experimental basis for evaluating the respective effectiveness of lubricant- and surface-oriented solutions in mitigating friction and wear in next-generation drivetrain systems.

Bibliography

[1] Spikes H. Mechanisms of ZDDP—An Update. Tribol Lett 2025;73:38. https://doi.org/10.1007/s11249-025-01968-3.

[2] Fang L. Enabling ultra-low viscosity lubricants through fundamental understanding of zddps anti-wear additives and their tribofilm growth mechanisms: an in-situ study. Thesis. University of Pennsylvania, 2022.

[3] Minfray C. Réactions tribochimiques avec le dithiophosphate de zinc. Thèse de Doctorat. L'Ecole centrale de Lyon, 2004.

[4] 4259-15-8 / 2-2185 n.d. https://www.nite.go.jp/chem/jcheck/detail.action?cno=4259-15-8&mno=2-2185&request_locale=en (accessed August 3, 2025).

[5] Deshpande P, Dassenoy F, Minfray C, Jenei IZ, Le Mogne Th, Thiebaut B. Effect of Adding TiO2 Nanoparticles to a Lubricant Containing MoDTC on the Tribological Behavior of Steel/Steel Contacts Under Boundary Lubrication Conditions. Tribol Lett 2020;68:39. https://doi.org/10.1007/s11249-020-1278-0.

[6] Chen Y, Renner P, Liang H. Dispersion of Nanoparticles in Lubricating Oil: A Critical Review. Lubricants 2019;7:7. https://doi.org/10.3390/lubricants7010007.

[7] Niederberger M. Nonaqueous Sol–Gel Routes to Metal Oxide Nanoparticles. Acc Chem Res 2007;40:793–800. https://doi.org/10.1021/ar600035e.

[8] Niederberger M, Garnweitner G. Organic Reaction Pathways in the Nonaqueous Synthesis of Metal Oxide Nanoparticles. Chemistry A European J 2006;12:7282–302. https://doi.org/10.1002/chem.200600313.

[9] Zhou S, Garnweitner G, Niederberger M, Antonietti M. Dispersion Behavior of Zirconia Nanocrystals and Their Surface Functionalization with Vinyl Group-Containing Ligands. Langmuir 2007;23:9178–87. https://doi.org/10.1021/la700837u.

[10] Belut E, Castaing G, Diers B, Hou A, Lanfranconi I, Lebreton R, Moncoq D, Oillic-Tissier C, Soyez A. Nanomatériaux. Prévention des risques dans les laboratoires. INRS 2012:58.

[11] Guay P. Lubrification élastohydrodynamique. Frottement, usure et lubrification 2015. https://doi.org/10.51257/a-v1-tri1540.

[12] FINAL Advanced Materials - Sintered Technical Ceramics data sheet. https://www.final-materials.com/gb/59-sintered-alumina n.d.

[13] Peng Z, Nassif A, Georgi F, Montmitonnet P, Lahouij I. Electric polarity: A key factor in lubricated wear of bearing steel. Tribology International 2025;209:110748. https://doi.org/10.1016/j.triboint.2025.110748.

[14] Grade de billes. CIMAP n.d. https://cimap.fr/billes/precision-et-qualite/grade-de-billes/ (accessed August 3, 2025).

[15] Brunetière N. Introduction à la tribologie. Institut Pprime, 2016.

[16] Siol S, Mann J, Newman J, Miyayama T, Watanabe K, Schmutz P, Cancellieri C, Jeurgens LPH. Concepts for chemical state analysis at constant probing depth by lab-based XPS/HAXPES combining soft and hard X-ray sources. Surface & Interface Analysis 2020;52:802–10. https://doi.org/10.1002/sia.6790.

[17] Acier S235. Masson's Steel n.d. https://massons-steel.com/acier/acier-s235/ (accessed October 6, 2025).

[18] Wang CJ, Cheung CF, Ho LT, Loh YM. Development of a fluid line-jet polishing process for rotational axisymmetric surfaces. Journal of Manufacturing Processes 2021;61:15–24. https://doi.org/10.1016/j.jmapro.2020.10.069.

[19] Jagadish, Gupta K. Abrasive Water Jet Machining of Engineering Materials. Cham: Springer International Publishing; 2020. https://doi.org/10.1007/978-3-030-36001-6.

[20] Buss L, Qi Y, Heidhoff J, Riemer O, Fritsching U. Towards an Understanding of Multiphase Fluid Dynamics of a Microfluid Jet Polishing Process: A Numerical Analysis. Fluids 2022;7:119. https://doi.org/10.3390/fluids7030119.

[21] Tazibt A, Ezo'o G, Khalsi Y, Yahiaoui M. Dry Surface Preparation Using Supercritical Cryogenic Nitrogen Jet Improves the Adhesion Strength of Cold Gas Sprayed Coatings (SCNCS). MSF 2018;941:1668–73. https://doi.org/10.4028/www.scientific.net/MSF.941.1668.

[22] Laribou H, Fressengeas C, Entemeyer D, Jeanclaude V, Pesci R, Tazibt A. Effects of the impact of a low temperature nitrogen jet on metallic surfaces. Proc R Soc A 2012;468:3601–19. https://doi.org/10.1098/rspa.2012.0241.

[23] Cold Spray Guns n.d. https://impact-innovations.com/en/portfolio-item/cold-spray-guns/ (accessed October 7, 2025).

[24] Ti | Impact Cold Spray System n.d. https://impact-innovations.com/en/materials/titanium/ (accessed October 7, 2025).

[25] Kumar A, Singh H, Kant R. Influence of Substrate Roughness and Ceramic Content on Deposition Characteristics of Cold-Sprayed Ti/TiO2 Deposits. Met Mater Int 2023;29:1669–83. https://doi.org/10.1007/s12540-022-01323-4.

[26] Munagala VNV, Akinyi V, Vo P, Chromik RR. Influence of Powder Morphology and Microstructure on the Cold Spray and Mechanical Properties of Ti6Al4V Coatings. J Therm Spray Tech 2018;27:827–42. https://doi.org/10.1007/s11666-018-0729-8.

[27] Dutta Majumdar J, Manna I. Laser surface engineering of titanium and its alloys for improved wear, corrosion and high-temperature oxidation resistance. Laser Surface Engineering, Elsevier; 2015, p. 483–521. https://doi.org/10.1016/B978-1-78242-074-3.00021-0.

[28] forAM CP-Ti G2 15-53 EG n.d. https://www.hoganas.com/en/powder-technologies/products/foram/foram-cp-ti-g2-15-53-eg/ (accessed October 7, 2025).

[29] Particle Shape. Sympatec | Analysers for Particle Size and Shape n.d. https://www.sympatec.com/en/particle-measurement/glossary/fundamentals-of-particle-characterisation/particle-shape (accessed October 7, 2025).

[30] Young Z, Qu M, Coday MM, Guo Q, Hojjatzadeh SMH, Escano LI, Fezzaa K, Chen L. Effects of Particle Size Distribution with Efficient Packing on Powder Flowability and Selective Laser Melting Process. Materials 2022;15:705. https://doi.org/10.3390/ma15030705.

[31] Titania Thermal Spray Powders | Titania Powders n.d. https://www.coatingsolutions.saint-gobain.com/products/thermal-spray/plasma-spray/powders/titania (accessed October 7, 2025).

[32] Okamoto H. O-Ti (Oxygen-Titanium). J Phase Equilib Diffus 2011;32:473–4. https://doi.org/10.1007/s11669-011-9935-5.

[33] Yang B, Richter N, Li H, Shang Z, He Z, Dou H, Shen J, Edwin García R, Bernstein N, Stephen Hellberg C, Wang H, Zhang X. Dislocation-enabled plasticity in rutile TiO_{2-x} at room temperature. Nanoscale 2025;17:20338–50. https://doi.org/10.1039/D5NR02684A.

[34] Wang Q, Spencer K, Birbilis N, Zhang M-X. The influence of ceramic particles on bond strength of cold spray composite coatings on AZ91 alloy substrate. Surface and Coatings Technology 2010;205:50–6. https://doi.org/10.1016/j.surfcoat.2010.06.008.

Chapter 3: Synergy between Traditional Additives and TiO_2 nanoparticles

Résumé en français :

La première partie de ce chapitre s'intéresse à la performance tribologique de nanoparticules de TiO_2 en fonction de leur méthode de stabilisation colloïdale. Il est notamment démontré que la stabilisation par ajout d'un simple dispersant ne permet pas d'obtenir une suspension durablement stable. À l'inverse, la fonctionnalisation de surface améliore fortement la stabilité, avec une efficacité dépendant de la nature de l'agent fonctionnalisant. Bien que les suspensions les plus stables aient été obtenues avec les nanoparticules fonctionnalisées avec un agent silane, ce sont les nanoparticules fonctionnalisées avec de l'acide oléique qui ont présenté les meilleures performances tribologiques. Dans ce dernier cas, on observe la formation d'un tribofilm stable constitué de TiO_2 compacté, dont le mode de formation le plus probable repose sur un mécanisme de tribo-frittage.

La seconde partie du chapitre traite des interactions entre nanoparticules de TiO_2 et additifs de lubrification conventionnels tels que le MoDTC et le ZDDP. Dans le premier cas, la nature des interactions dépend de la méthode de stabilisation : le mélange de nanoparticules non modifiées avec du MoDTC conduit à la formation d'un tribofilm TiO_2/MoS_2, générant un coefficient de frottement plus faible que celui obtenu avec le MoDTC seul, ce qui témoigne d'une relation synergique. En revanche, lorsque des nanoparticules fonctionnalisées sont utilisées, l'effet réducteur de frottement disparaît. Les analyses XPS confirment alors l'absence de MoS_2, suggérant que les agents fonctionnalisants bloquent l'accès du MoDTC à la surface du TiO_2, empêchant la réaction de décomposition. La synergie entre MoDTC et nanoparticules de TiO_2 semble donc être d'origine chimique. À noter que les meilleurs résultats en termes de réduction d'usure et de formation de tribofilm ont été obtenus avec les nanoparticules fonctionnalisées silane.

En ce qui concerne les mélanges entre nanoparticules de TiO_2 et ZDDP, une synergie est systématiquement observée : diminution du coefficient de frottement, du temps d'induction nécessaire à la formation du tribofilm, et formation d'un tribofilm plus épais que ceux générés par les additifs pris individuellement, et ce quelle que soit la méthode de stabilisation. Les meilleurs résultats sont cependant obtenus avec les nanoparticules les plus stables, c'est-à-dire celles fonctionnalisées à l'acide oléique ou au silane. Dans chaque cas, la formation du tribofilm résulte d'une complémentarité entre les mécanismes d'action des deux espèces :

- Les nanoparticules interagissent rapidement avec les surfaces en contact, formant un premier tribofilm protecteur par tribofrittage ;
- Cette barrière initiale laisse au ZDDP le temps de se décomposer sans usure des surfaces et de générer son propre tribofilm, tandis que les nanoparticules continuent de se déposer en parallèle ;
- Il en résulte la formation d'un tribofilm composite, probablement moins dur qu'un tribofilm purement céramique mais se formant aussi plus facilement, ce qui permet d'obtenir une meilleure couvrance.

La synergie entre TiO_2 et ZDDP repose donc sur une complémentarité des mécanismes de formation des tribofilms, plutôt que sur des interactions chimiques directes comme dans le cas du MoDTC.

This chapter focuses on the possible interactions between nanoparticles and tribological additives such as MoDTC and ZDDP. As highlighted in Chapter 1, several studies have demonstrated that such combinations can exhibit either synergistic or antagonistic effects. In this work, we will specifically investigate the interactions between TiO_2 nanoparticles and conventional lubricant additives, namely the friction modifier MoDTC and the anti-wear additive ZDDP.

To study these interactions, it is necessary to characterize the intrinsic lubricating properties of the nanoparticles. The first part of this chapter therefore addresses this aspect, with particular attention given to the influence of the stabilization method on the tribological behavior of the nanoparticles. After presenting their tribological properties, as well as the mechanisms involved in tribofilm formation, the second part will examine the interactions between TiO_2 nanoparticles and conventional additives. Special emphasis will be placed on how the nanoparticle stabilization route affects these interactions.

3.1 Lubricating Properties of TiO_2 Nanoparticles

This first section aims to establish an initial assessment of the tribological performance of TiO_2 nanoparticles prior to their combination with other tribological additives.

As highlighted by Y. Chen et al. (2019) [1], the stability of nanoparticles can directly influence their tribological behavior. Consequently, this work has been divided into two parts to investigate this influence:

- **Effect of dispersion method:** The first part examines how the dispersion method affects the tribological performance of TiO_2 nanoparticles. Oleic acid was selected as a dispersing agent and applied in two different ways. In the first approach, it was simply blended with nanoparticle in a base oil, thereby stabilizing the particles through physical interactions. In the second approach, oleic acid was chemically grafted onto the nanoparticle surface, ensuring stronger stabilization. **The key question here is how the stabilization method influences nanoparticles tribological properties.**
- **Effect of functionalizing agent.** The second part focuses on the role of the chemical nature of the functionalizing agent. The previously studied oleic acid-based functionalization is therefore compared with a silane-based functionalization. **The central question here is how the chemical nature of the functionalizing agent influences nanoparticles' tribological behavior.**

To answer those questions, tribological tests in boundary lubrication conditions were conducted with the parameters summarized in **Table *13***.

Temperature	100°C
Normal load	10.5 N
Ball diameter	10 mm
Maximum Hertzian contact pressure	1.03 GPa
Hertz Diameter	140 µm
Test duration / cycle number	3600 s / 2300 cycles
Test frequency	0.64 Hz
Stroke length	5 mm
Maximum linear speed	10 mm/s
Oil quantity	2 mL
Repetitions	3
Acquisition frequency	25 Hz
Plotted curves processing	Averaged over 8 points

Table 13: Tribological conditions

In both cases, after initial testing on a tribometer, the resulting samples were subsequently characterized using various analytical techniques, which allowed us to better understand the mechanisms governing the behavior of the different additives employed.

3.1.1 Effect of the Dispersion Method on Tribological Performance: The Case of Oleic Acid

First, in order to differentiate the effects of dispersion or functionalization from other possible interactions, an experimental design was carried out using the additives both individually and in combination.

Table 14 presents the formulations that were tribologically tested for this study. All experiments were repeated three times. Good repeatability has been found in all cases.

Composition	Name
PAO6	PAO6
PAO6 + 1 wt.% TiO_2 nanoparticles (NP) powder	Ti1
PAO6 + 1 wt.% oleic acid (OA)	OA1
PAO6 + 1 wt.% TiO_2 NP powder + 1 wt.% OA	Ti1_OA1
PAO6 + 1 wt.% oleic acid-functionalized TiO_2 NP	Tif(OA)1

Table 14: Composition and name of tribologically tested blends used to compare the effect of dispersion methods

Although the viscosity of the mixtures was not measured, it is expected to remain close to that of the base oil. Dassenoy *et al.* (2021) [2] showed an increase in viscosity of 4.7% at both 20°C and 100°C with the addition of 1 wt.% of TiO_2 nanoparticles in a group III base oil. Thrush *et al.* (2020) [3] also observed an increase in viscosity of 1.8% and 4.7% at 40°C and 100°C, respectively, with the addition of 1 wt.% of capped ZrO_2 nanoparticles in a PAO4 base oil. Such increases are not expected to have a significant impact on our results, as we designed the experimental conditions to operate in a severe boundary lubrication regime.

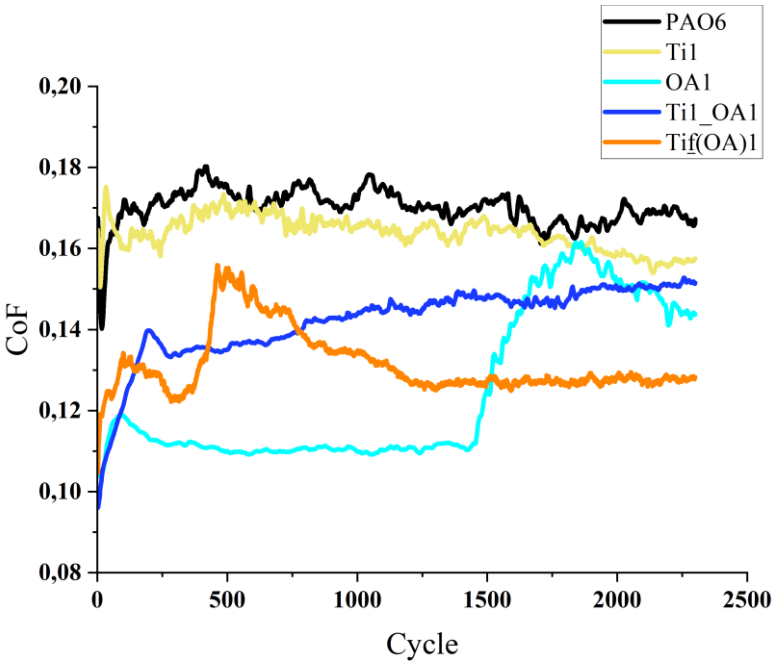

Fig. 82: Evolution of friction coefficient with cycles at 100°C for the samples containing TiO_2 nanoparticles (Ti1), oleic acid (OA1) or a combination of both (Ti1_OA1), compared with functionalized TiO_2 nanoparticles (Tif(OA)1), and PAO6 base oil used as a reference.

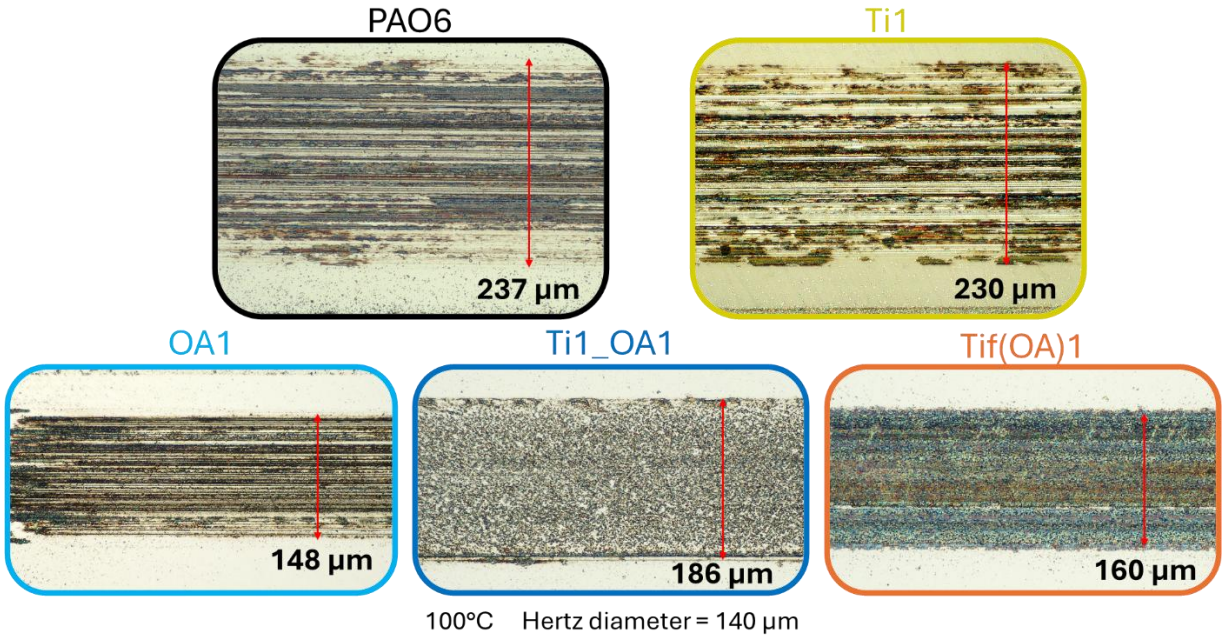

Fig. 83: Optical observations of wear tracks formed at 100°C on the discs in the presence of solutions containing TiO_2 nanoparticles (Ti1), oleic acid (OA1) or a combination of both (Ti1_OA1), compared with functionalized TiO_2 nanoparticles (Tif(OA)1), and PAO6 base oil used as a reference.

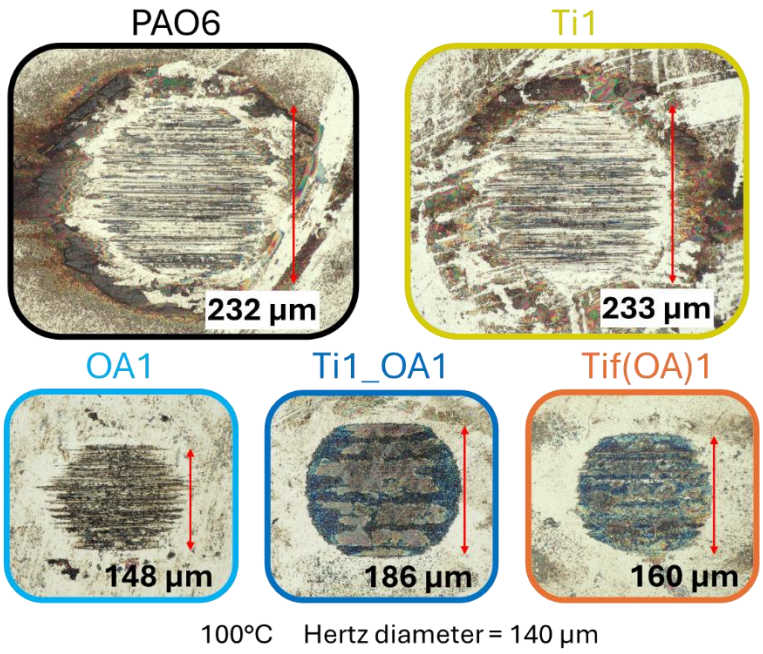

Fig. 84: Optical observations of wear scars formed at 100°C on the balls in the presence of solutions containing TiO_2 nanoparticles (Ti1), oleic acid (OA1) or a combination of both (Ti1_OA1), compared with functionalized TiO_2 nanoparticles (Tif(OA)1), and PAO6 base oil used as a reference.

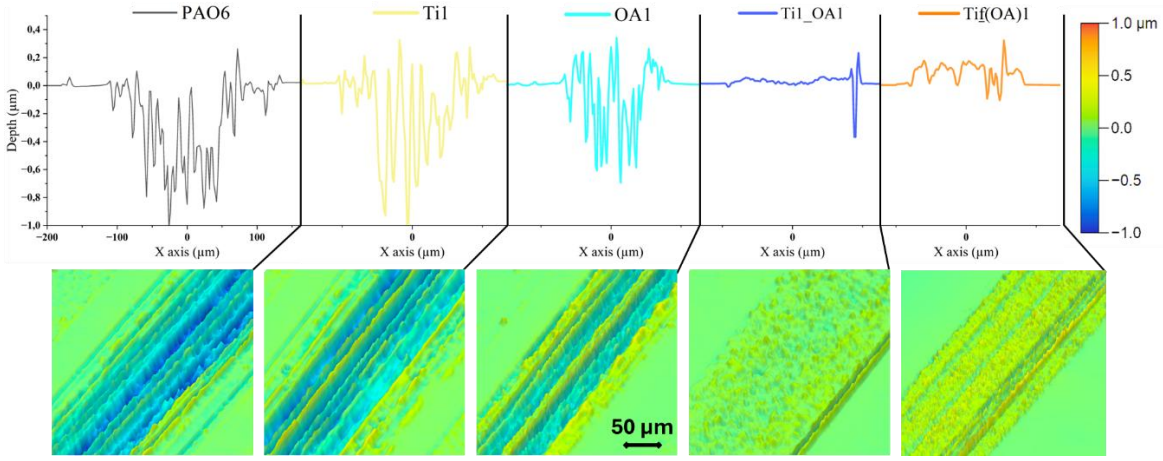

Fig. 85: Mean depth profiles and surface morphology of wear tracks formed at 100°C on the discs in the presence of solutions containing TiO_2 nanoparticles (Ti1), oleic acid (OA1) or a combination of both (Ti1_OA1), compared with functionalized TiO_2 nanoparticles (Tif(OA)1), and PAO6 base oil used as a reference.

Fig. 82 presents the evolution of the coefficient of friction (CoF) for lubricants containing TiO_2 nanoparticles, oleic acid or a combination of both, compared with functionalized TiO_2 nanoparticles. PAO6 is used as a reference. Plotted curves are averaged over 8 points.

Optical observations (Fig. 83 and Fig. 84) are used to measure friction track width and wear diameter and compare it to the Hertz diameter (140 µm). These optical observations also reveal the wear pattern; for instance, scratching is observed in the tracks formed with PAO6, Ti1, and OA1. In contrast, tracks formed with Ti1_OA1 or Tif(OA)1 show evidence of deposit formation. Therefore, optical observations alone cannot provide definitive conclusions regarding the proportion of wear versus deposit formation. For this reason, profilometric measurements are carried out. Mean profiles on 1 mm of the wear tracks are presented in Fig. 85.

Under the present conditions (~1.03 GPa, 100°C) and in the absence of seizure or major surface degradation, the PAO6 sample exhibits moderate friction levels throughout the test cycles, with a coefficient of friction (CoF) ranging between 0.16 and 0.18. This lubricant shows slight instability due to the absence of boundary additives. This friction behavior is linked to the wear of the disc and the ball during the sliding as observed with optical microscopy (Fig. 83 and Fig. 84) and profilometry (Fig. 85). Accumulation of debris and scratches can be observed as well as material removal.

Ti1 sample was formulated by adding 1 wt.% of TiO_2 nanoparticles to the base oil. This sample shows a similar behavior to PAO6 with marginal reduction of CoF and wear. This is probably due to the agglomeration of NPs that hinders their tribological activity and could potentially act as abrasive particles.

OA1 initially achieves a low CoF of about 0.1 due to the friction reduction properties of oleic acid caused by the formation of a thin physisorbed layer [4]. However, after approximately 1500 cycles under the present conditions, the CoF begins to increase steadily, reaching around 0.14-0.15. This rise is likely due to the breakdown of the thin adsorbed layer formed by the additive and was observed with the 3 repetitions but at different cycle numbers. With continuous friction and the associated heat generation during the test [5], this physisorbed layer may degrade, leading to an increase in friction. Another explanation could lie in the oxidation of oleic acid during the test [4]. Either way this increase in friction is caused by the initial test temperature as it was not observed when they were conducted at 25°C (Fig. 87).

Concerning wear, we can observe in Fig. 83 and Fig. 84 a friction track width and a wear diameter close to Hertz diameter. However, scratches can be observed and the mean profile (Fig. 85) confirms that they correspond to material removal.

The Ti1_OA1 formulation, a combination of TiO_2 nanoparticles and oleic acid, shows a more stable CoF profile than PAO6 or Ti1 formulations. It begins with a relatively low CoF ~0.10, ultimately achieving a lower CoF than Ti1 alone, at ~0.15. This result suggests that oleic acid enhances the dispersion of the TiO_2 nanoparticles, facilitating their entry into the contact interface and preventing agglomeration, thereby reducing possible abrasive effects. Indeed, the surface shows almost no scratches (Fig. 83 and Fig. 84) and even seems to form a protective film with a height of 50 to 80 nm from the surface (Fig. 85).

Finally, Tif(OA)1 represents TiO_2 nanoparticles that have been functionalized with oleic acid and diluted at 1 wt.% in PAO6. This sample demonstrates a low and steady CoF, maintaining consistent friction levels after an initial induction period of approximately 1000 cycles. As shown in Fig. 86, those results are repeatable regarding CoF values and variations, notably in the induction period where a spike in CoF value is observed, probably linked to the tribofilm formation mechanism. Tif(OA)1 therefore appears to have better friction reduction properties than its dispersed counterpart. It also seems to form a thicker film as suggested by profilometry measurements (Fig. 85).

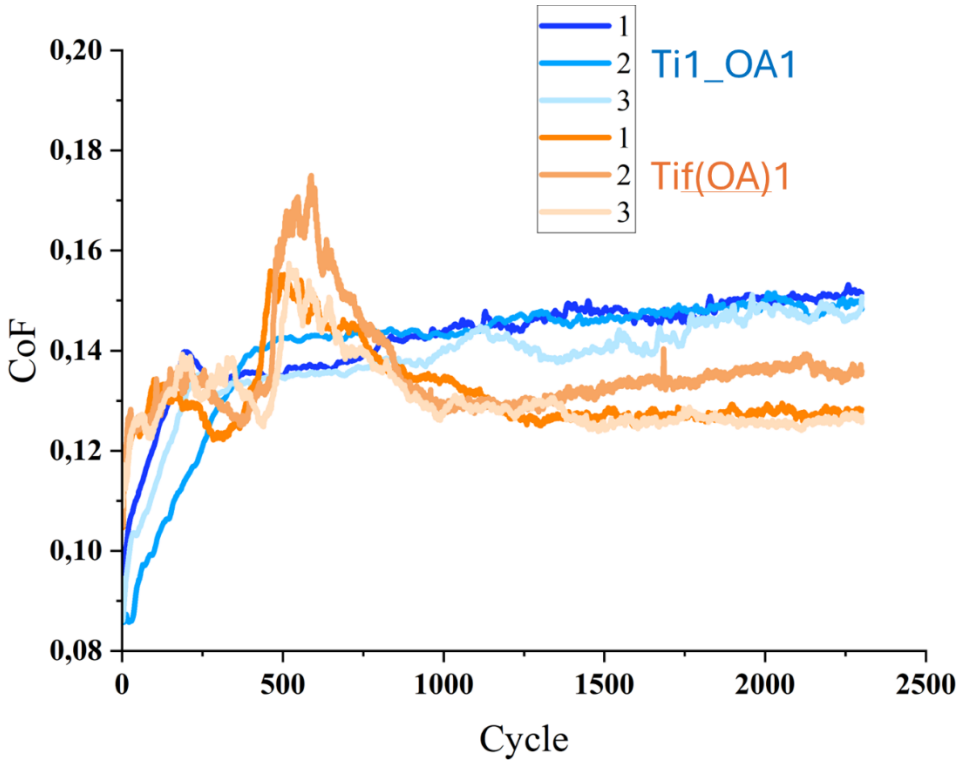

Fig. 86: Friction tests repeatability at 100°C for the samples containing dispersed (Ti1_OA1) or functionalized (Tif(OA)1) TiO_2 nanoparticles in PAO6. Three repetitions are carried out for each formulation.

These results collectively highlight the importance of stabilizing nanoparticles suspension, either with dispersion or functionalization.

- PAO6 shows moderate friction for a pure base oil but lacks stability without additives.
- Ti1 shows little improvement over base oil solution due to unstable dispersion.
- OA1 initially reduces friction effectively, but thermal effects cause degradation over time.
- Ti1_OA1 achieves a stabilized and moderate CoF as well as good anti wear properties, demonstrating the OA's role in improving nanoparticle dispersion.
- Tif(OA)1 provides the most consistent and low friction coefficient, confirming that oleic acid functionalization improves nanoparticle performance by preventing agglomeration and maintaining stability.

For both formulations containing dispersed and functionalized TiO_2 NPs, profilometry analyses (Fig. 85) indicate the formation of a tribofilm. However, the functionalized nanoparticles demonstrate superior performance in terms of friction reduction and anti-wear properties, primarily due to their ability to form a thicker tribofilm.

Compared to 100 °C, the tribological conditions at 25°C are less severe because of the higher viscosity of the base oil, which generally leads to a lower coefficient of friction (CoF) for most blends (Fig. 87). An exception is Ti1, where the unstabilized TiO_2 nanoparticles once again act as an abrasive third body, increasing friction. In contrast, Ti1_OA1 exhibits a lower CoF, improved wear reduction, and appears to form a more continuous tribofilm. Tif(OA)1 also shows a reduced CoF and comparable wear performance at both 25 °C and 100 °C, with tribofilm formation observed in both cases (Fig. 88 and Fig. 89). These results highlight the ability of nanoparticles to deliver favorable tribological properties even at 25 °C, a temperature at which ZDDP shows little efficiency.

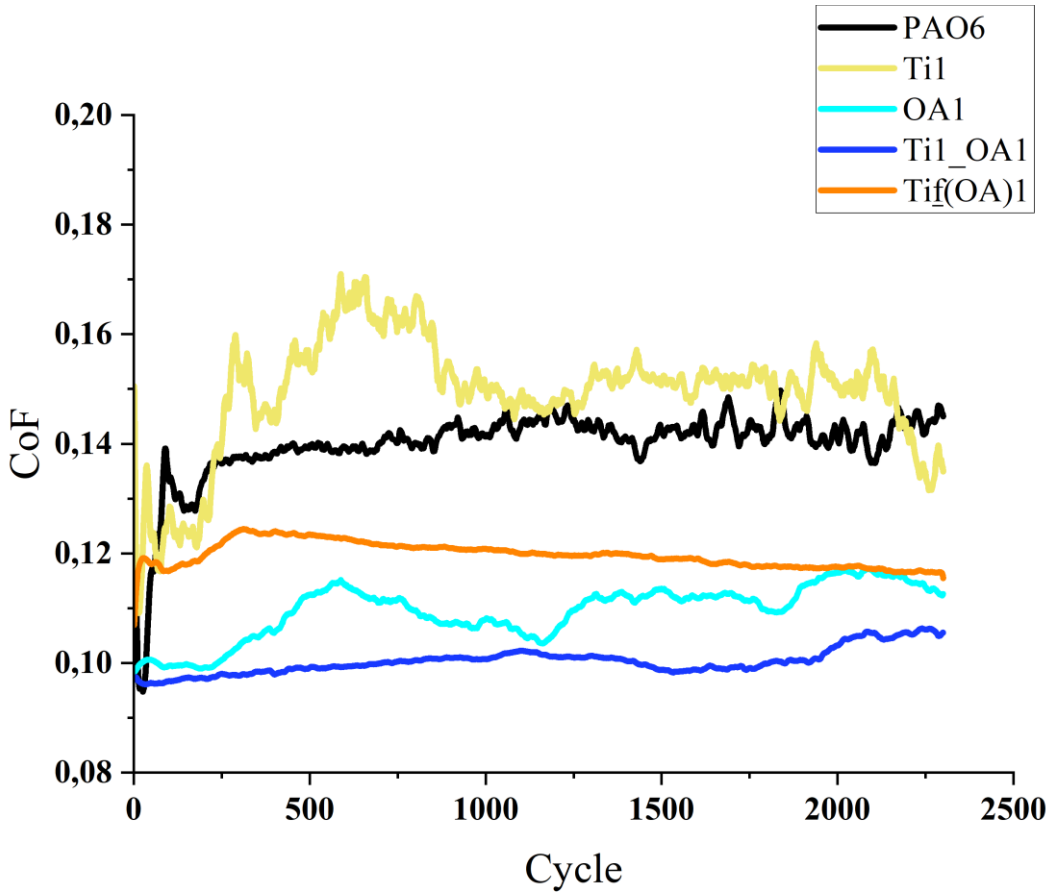

Fig. 87: Evolution of friction coefficient with cycles at 25°C for the samples containing TiO_2 nanoparticles (Ti1), oleic acid (OA1) or a combination of both (Ti1_OA1), compared with functionalized TiO_2 nanoparticles (Tif(OA)1), and PAO6 base oil used as a reference.

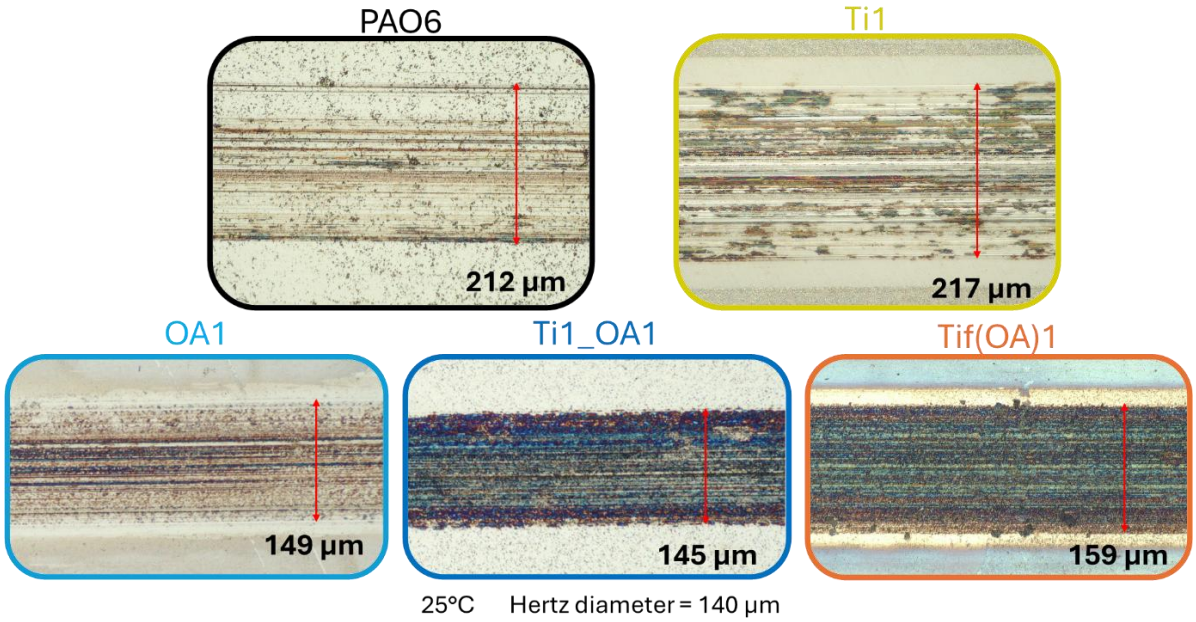

Fig. 88: Optical observations of wear tracks formed at 25°C on the discs in the presence of solutions containing TiO_2 nanoparticles (Ti1), oleic acid (OA1) or a combination of both (Ti1_OA1), compared with functionalized TiO_2 nanoparticles (Tif(OA)1), and PAO6 base oil used as a reference.

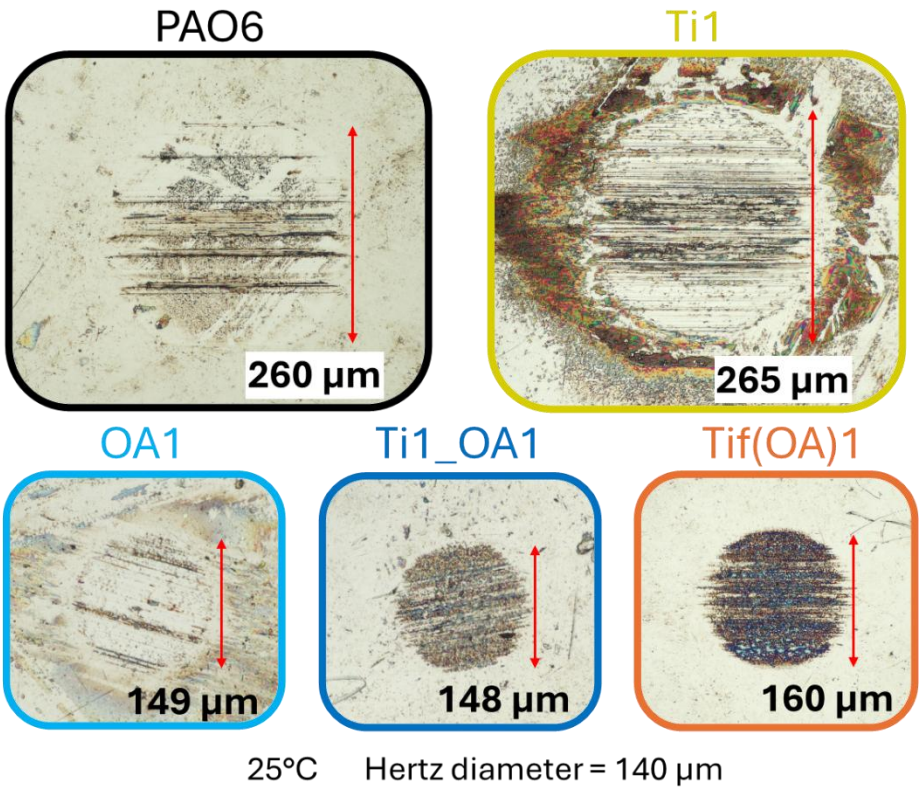

Fig. 89: Optical observations of wear scars formed at 25°C on the balls in the presence of solutions containing TiO_2 nanoparticles (Ti1), oleic acid (OA1) or a combination of both (Ti1_OA1), compared with functionalized TiO_2 nanoparticles (Tif(OA)1), and PAO6 base oil used as a reference.

SEM observations are presented for dispersed and functionalized suspensions. BSE mode images are presented first as the chemical contrast allows a better understanding of the tribofilm morphology at a low magnification. SE mode combined with EDX mapping (View Field of 30 µm) gives us the main elements composing the tribofilm and how they are distributed within the friction track. High resolution SE mode is then used to observe surfaces at a high magnification.

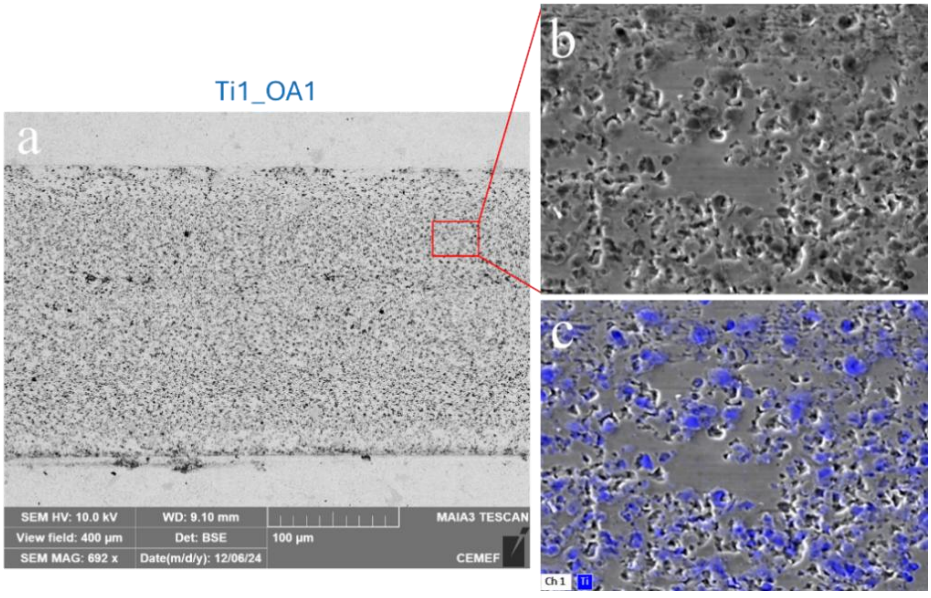

Fig. 90: SEM micrographs in BSE (a) and SE (b) modes with EDX mapping of titanium (Ti) (c) of a tribofilm formed on the disc in the presence of Ti1_OA1 solution at 100°C.

For Ti1_OA1 (Fig. 90), we observe small circular structures of 1-2 µm whose shape and distribution appear to not be influenced by the sliding direction. Dark areas are noticeable, corresponding either to the TiO_2 tribofilm or to holes, as indicated by the EDX mapping. TiO_2 rich structures are probably exposed to a contact stress much higher than maximum Hertzian pressure (1.03 GPa) as their height leads to a smaller contact area during sliding. This could promote local tribofilm formation as high pressure is required for NPs to bind in a cohesive way [6].

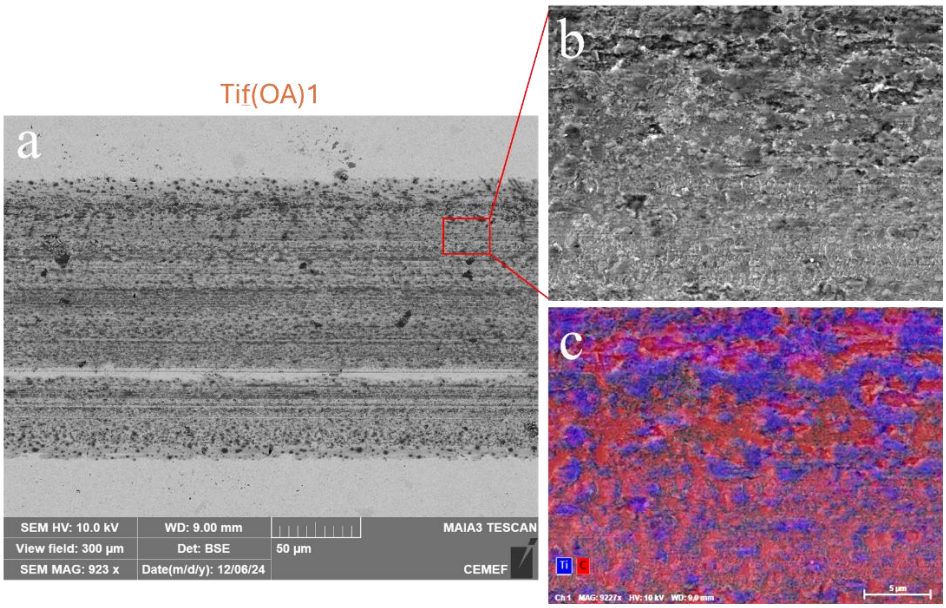

Fig. 91: SEM micrographs in BSE (a) and SE (b) modes with EDX mapping of carbon (C) and titanium (Ti) (c) of a tribofilm formed on the disc in the presence of Tif(OA)1 solution at 100°C (blue = Ti; red = C).

Concerning functionalized NPs (Fig. 91) we notice a tribofilm with greater coverage than the one formed in the presence of dispersed NPs. The structures are larger, ranging from 1 to approximately 5 µm, and seem to spread along the sliding direction. Very few holes are observed. Additionally, carbon is detected in areas less covered by the tribofilm, with 25-30 at.% of carbon, which was not observed for Ti1_OA1 (less than 5 at.% of carbon).

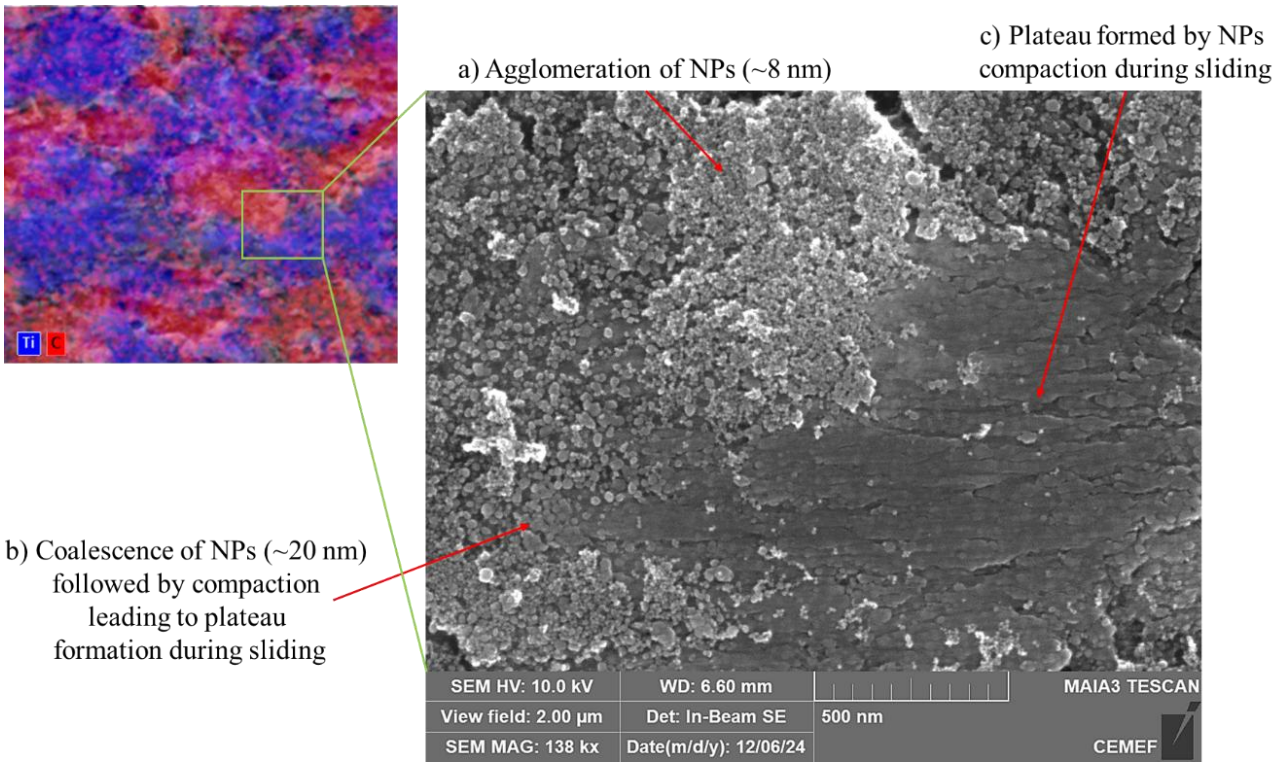

Fig. 92: High magnification SEM observation of a tribofilm formed on the disc in the presence of Tif(OA)1 solution at 100°C showing the formation of a plateau

The SEM image in Fig. 92 shows a close-up of the tribofilm formed by Tif(OA)1 and reveals a surface that appears to be covered by small, granular particles clustered in patches that correspond to the functionalized NPs. These nanoparticles are either small (6-8 nm) and densely packed (Fig. 92a) or bigger (~20 nm) and more dispersed (Fig. 92b). According to granulometry measurement of functionalized NPs solution, 90%vol of TiO_2 functionalized nanoparticles have a size below 5.34 nm. The bigger NPs observed could therefore be formed by coalescence of smaller NPs during tribological testing. The surface next to the nanoparticles forms a plateau with linear structures (Fig. 92c), likely resulting from the compaction of nanoparticles during sliding. Circular shapes of ~20 nm can still be seen in this structure, supporting this idea. Moreover, we can observe an area (Fig. 92b) where larger nanoparticles appear to be merging, forming the continuation of the observed plateau.

In addition, Fig. 92 shows that zone (a) corresponds to a carbon rich region (red) in the EDX mapping, while the plateau in zone (c) is associated with a titanium rich region (blue). This observation suggests that the nanoparticle agglomerates in zone (a) likely retain their capping agent (oleic acid), which appears to be removed during the formation of the plateau in zone (c). These findings support the hypothesis of tribofilm formation through a tribo-sintering process. To confirm this hypothesis, we would need to examine a TEM cross-section of the tribofilm, as performed by I. Lahouij *et al.* (2022) [7], who investigated a tribofilm formed by ZrO_2 nanoparticles. Their observations revealed a fully crystalline structure within the tribofilm. This finding further supported the tribosintering hypothesis proposed by Thrush *et al.* (2021) [8], which was based on the linear correlation between normal load and tribofilm formation rate, as well as on the measured Young's modulus, found to be close to that of bulk ZrO_2.

Regardless of the dispersion method, the growth of TiO_2 tribofilms likely occurs through a tribo-sintering process, facilitated by the small size of the nanoparticles used. However, in the first case with dispersed NPs, the resulting tribofilm appears thinner (Fig. 85) and less dense (Fig. 90). Moreover, the presence of circular holes suggests competition between tribofilm formation and wear of the steel surface, a phenomenon not observed with functionalized nanoparticles. The circular shape of these holes indicates that they are unlikely to have been caused by abrasive wear facilitated by TiO_2 agglomerates.

When comparing our nanoparticle-based formulations, functionalization yields better results than simple dispersion, demonstrating superior intrinsic potential. We also observed that a significant portion of the nanoparticles does not react to form a tribofilm but instead accumulates in the valleys, as suggested by the high carbon content in these regions (Fig. 91) and high magnification observations (Fig. 92). Those unreacted nanoparticles could therefore serve as a tribofilm reservoir.

XPS analyses were conducted to determine the chemical nature of previously formed tribofilms and to quantify the detected elements while minimizing substrate influence (as analysis depth is below 10 nanometers).

at.%	100°C	
	Ti1_OA1	**Tif(OA)1**
C 1s	**18.3**	**30.3**
Fe 2p	**14.5**	**12.6**
O 1s	**51.1**	**45.4**
Ti 2p	**15.9**	**11.1**
Ca 2p	**0.2**	**0.6**

Table 15: XPS chemical composition of tribofilms formed in the presence of solutions containing dispersed or functionalized TiO_2 nanoparticles at 100°C. Obtained with a K-ALPHA spectrometer.

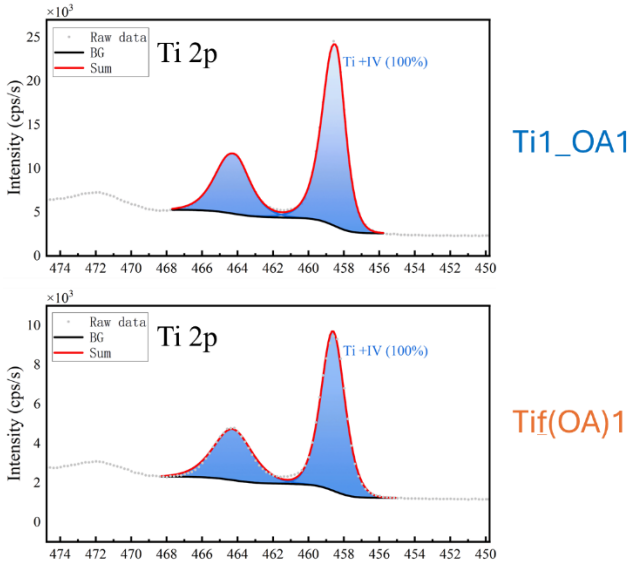

Fig. 93: Ti 2p XPS spectra of tribofilms formed at 100°C in presence of solutions containing dispersed or functionalized TiO_2 nanoparticles. Obtained with a K-ALPHA spectrometer.

For dispersed nanoparticles (Ti1_OA1), detected elements correspond to carbon, iron, titanium, and oxygen (**Table 15**). The Ti 2p peak shown in Fig. 93 corresponds to pure TiO_2, indicating that the TiO_2 content in the tribofilm is 47.7% atomic. This value is likely underestimated as this tribofilm presents poor coverage (Fig. 83 and Fig. 90) and therefore a lot of iron oxide from the steel substrate is also detected.

Tif(OA)1 tribofilm contains the same elements with higher carbon content and less titanium, which is also present in pure TiO_2 form (Fig. 93). As shown in Fig. 92, unreacted nanoparticles remain on the tribofilm which could explain the high carbon content corresponding to the functionalizing agent, oleic acid.

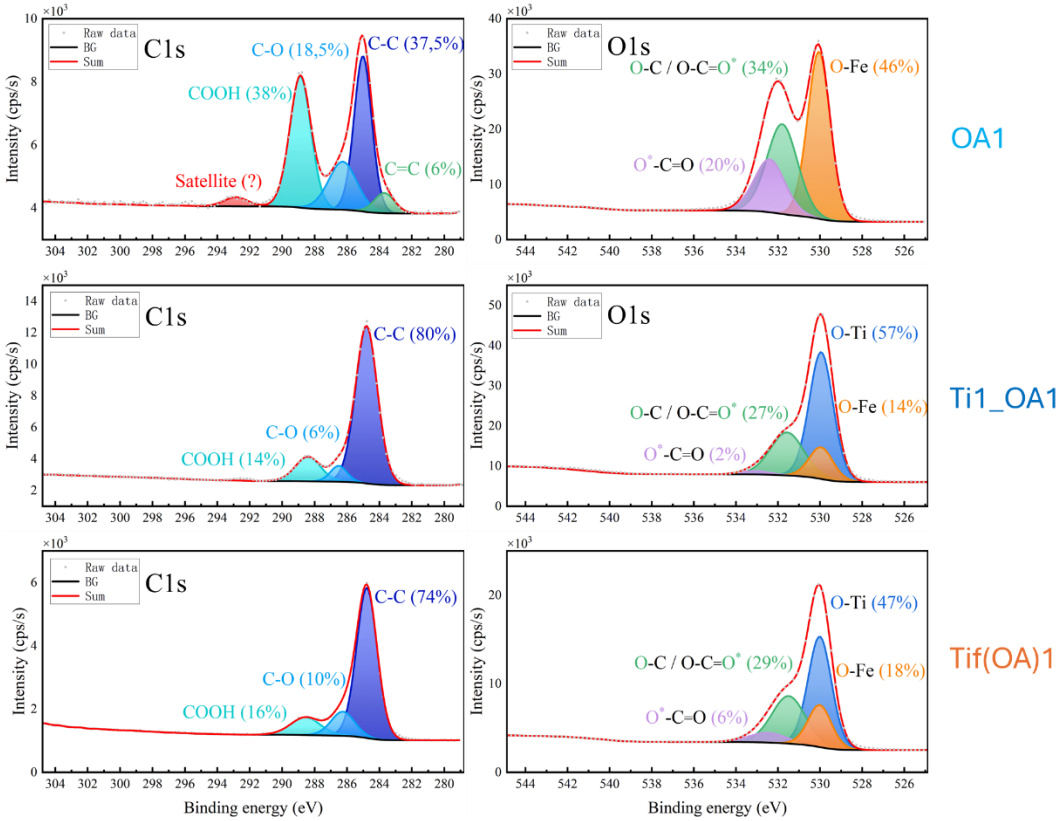

Fig. 94: C1s and O1s XPS spectra of tribofilms formed at 100°C in presence of blends containing oleic acid or dispersed or functionalized TiO_2 nanoparticles. Obtained with a K-ALPHA spectrometer.

For those two tribofilms, the decomposition of O1s spectra (Fig. 94) was made using 4 contributions: O-Ti (TiO_2) and O-Fe (iron oxide) both at 530 eV, O-C=O* / O*-C at 531.5 eV and O*-C=O at 532.5 eV (oleic acid and contaminants). Chemical percentages were used to adjust the decomposition, for example, O-Ti peak percentage corresponds to two times Ti at.% (pure TiO_2); O-C=O* / O*-C corresponds to the sum of C*OOH and C*-O percentages in C1s peak; O*-C=O corresponds to C*OOH percentage in C1s peak; the remaining oxygen left is attributed to iron oxide. We can see that compared to OA1, the oleic content (O*-C=O percentage) in Ti1_OA1 and Tif(OA)1 is low. Therefore, the discriminating factor between those two tribofilms is the total carbon content that is almost two times higher for Tif(OA)1 and must likely corresponds to capping agent of the nanoparticles.

Summary and Discussion

The disparity in performance between dispersed and functionalized nanoparticles stems from differences in their physical state within the lubricant. Dispersed NPs, derived from a dry powder, contained agglomerates, whereas functionalized NPs avoided this issue due to their synthesis method, which didn't include drying and subsequent agglomeration. This distinction was visually observed, with dispersed formulations appearing opaque, while functionalized ones were nearly transparent - indicating a higher proportion of individual NPs in the latter or at least smaller agglomerates.

Despite these differences, both types of nanoparticles appear to form a tribofilm through tribo-sintering mechanism. However, this tribofilm does not grow uniformly across the friction track. Instead, it seems to develop preferentially in certain areas, resulting in a patchy tribofilm. This localized growth could be driven by a nucleation process that initiates preferentially in areas with surface defects, as evidenced by Khare et al. [6].

It should be noted that although both physical dispersion and chemical functionalization enhance the stability of nanoparticle suspensions at ambient temperature, but agglomeration nevertheless occurs during tribological testing at 100 °C, as illustrated in Fig. 95.

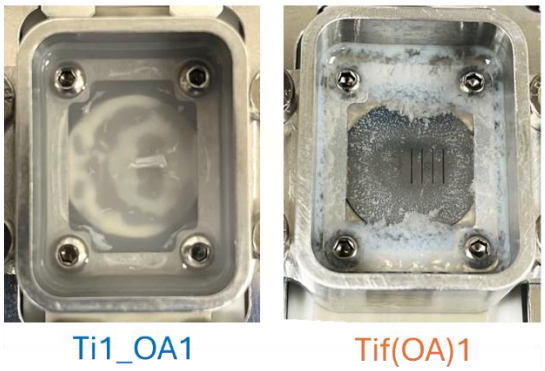

Fig. 95: Pictures of discs in their lubricant bath after tribological testing at 100°C in suspensions containing dispersed (Ti1_OA1) or oleic acid-functionalized (Tif(OA)1) TiO_2 nanoparticles.

This observation prompted us to explore strategies to further improve the stability of nanoparticle suspensions. Ceranovis company has demonstrated that this can be achieved by employing a silane-based functionalization instead of an oleic acid-based one, and they provided us with such material for tribological testing. Accordingly, the tribological performance of these two types of functionalized nanoparticles was compared, as detailed in the following section.

3.1.2 Influence of Functionalizing Agent Chemical Nature: Oleic Acid vs Silane

For this study, the tribologically tested formulations are presented in **Table 16**.

Composition	Name
PAO6	PAO6
PAO6 + 1 wt.% oleic acid-functionalized TiO_2 NP	Tif(OA)1
PAO6 + 1 wt.% silane-functionalized TiO_2 NP	Tif(Si)1

Table 16: Composition and name of tribologically tested blends used to compare the effect of the chemical nature of the functionalizing agent.

As previously mentioned, the silane-functionalized TiO_2 nanoparticles exhibit significantly improved colloidal stability. They can be stored for much longer periods without any alteration of their tribological properties, as shown in Fig. 96, and they also remain stable at elevated temperatures (Fig. 97).

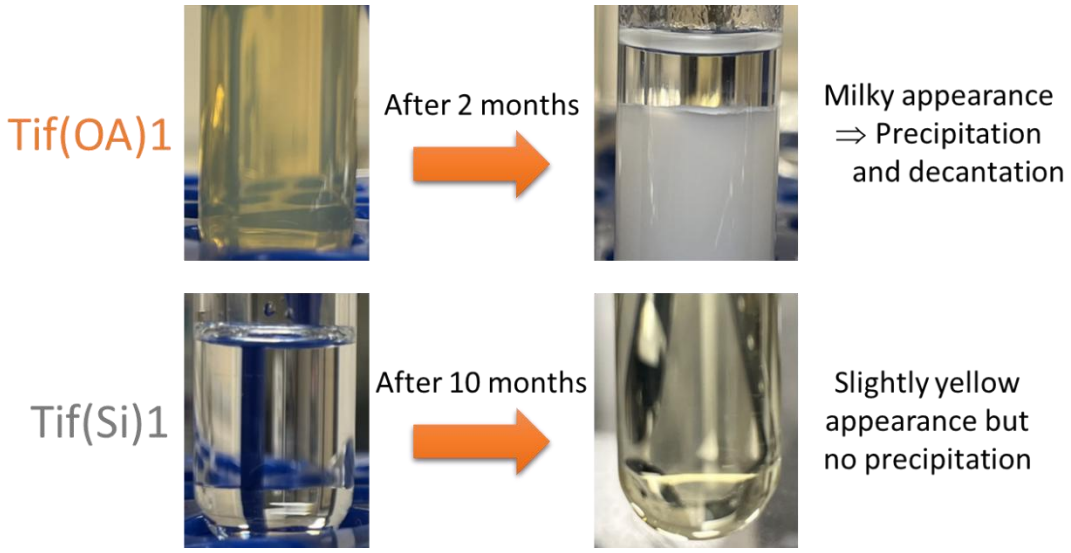

Fig. 96: Visual comparison of oleic acid-based (Tif(OA)1) and silane-based (Tif(Si)1) nanoparticles suspensions in their initial state and after respectively 2 and 10 months of storage at ambient temperature and protected from light.

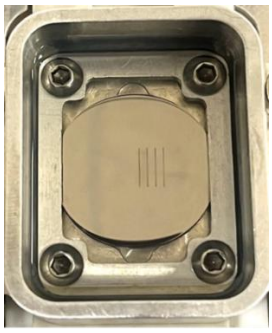

Fig. 97: Pictures of a disc in a lubricant bath after tribological testing at 100°C in a suspension containing dispersed silane-functionalized TiO_2 nanoparticles (Tif(Si)1).

Regarding tribological performance, the use of silane as a functionalizing agent leads to an increase in friction, which initially reaches 0.19 before stabilizing at 0.14 during testing, as shown in Fig. 98 . In fact, the actual friction is even higher. This is because our friction analysis protocol only accounts for the region where the sliding velocity is constant along the track (−0.5 to 0.5 mm at the center, see Chapter 2, 2.2.1). In this specific case (Tif(Si)1), friction is markedly higher at the edges of the track, as illustrated in Fig. 99 for one complete reciprocating cycle. This difference could come from the reciprocating nature of our tribometer with a difference in speed between the center of the track and its extremities. Therefore, Tif(Si)1 shows a high friction behavior at lower speed.

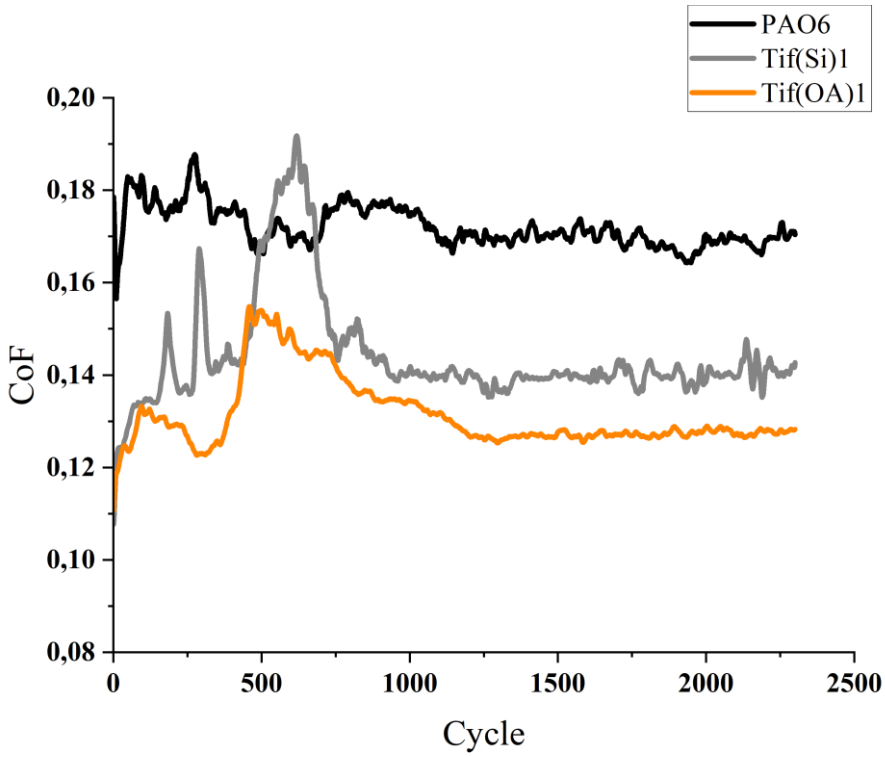

Fig. 98: Evolution of friction coefficient with cycles at 100°C for the samples containing oleic acid-functionalized (Tif(OA)1) or silane-functionalized (Tif(Si)1) TiO_2 nanoparticles. PAO6 base oil used as a reference.

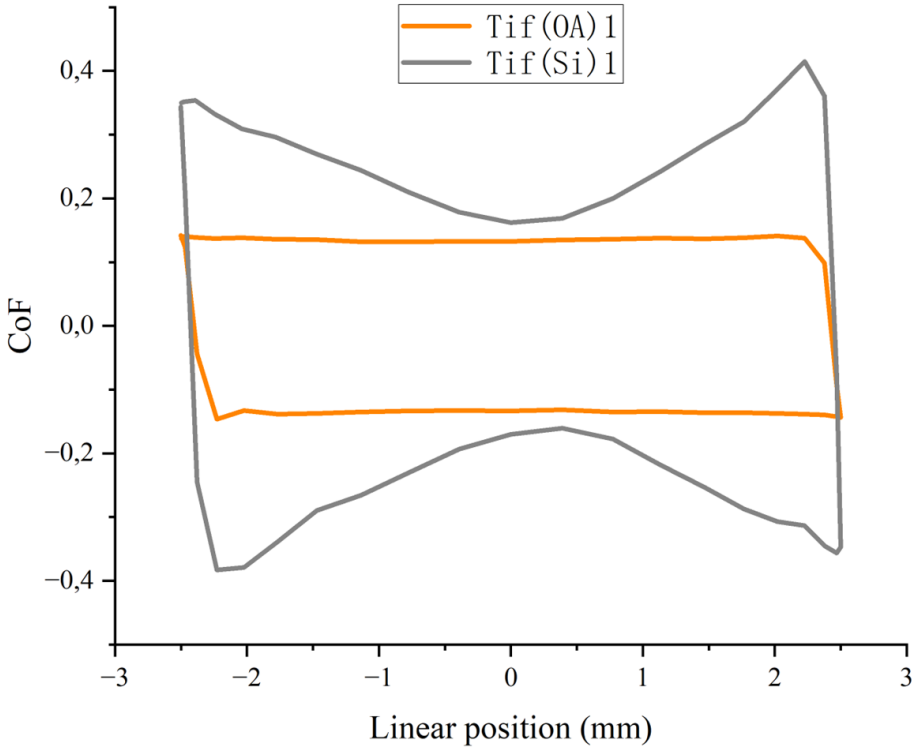

Fig. 99: Evolution of friction coefficient for the 700th cycle at 100°C for the samples containing oleic acid-functionalized (Tif(OA)1) or silane-functionalized (Tif(Si)1) TiO_2 nanoparticles.

The track width, however, is not affected, with a value of approximately 150 µm observed both on the ball and on the disk (Fig. 100 and Fig. 101). This is consistent with the Hertzian contact diameter and with the values previously obtained for oleic acid-functionalized nanoparticles.

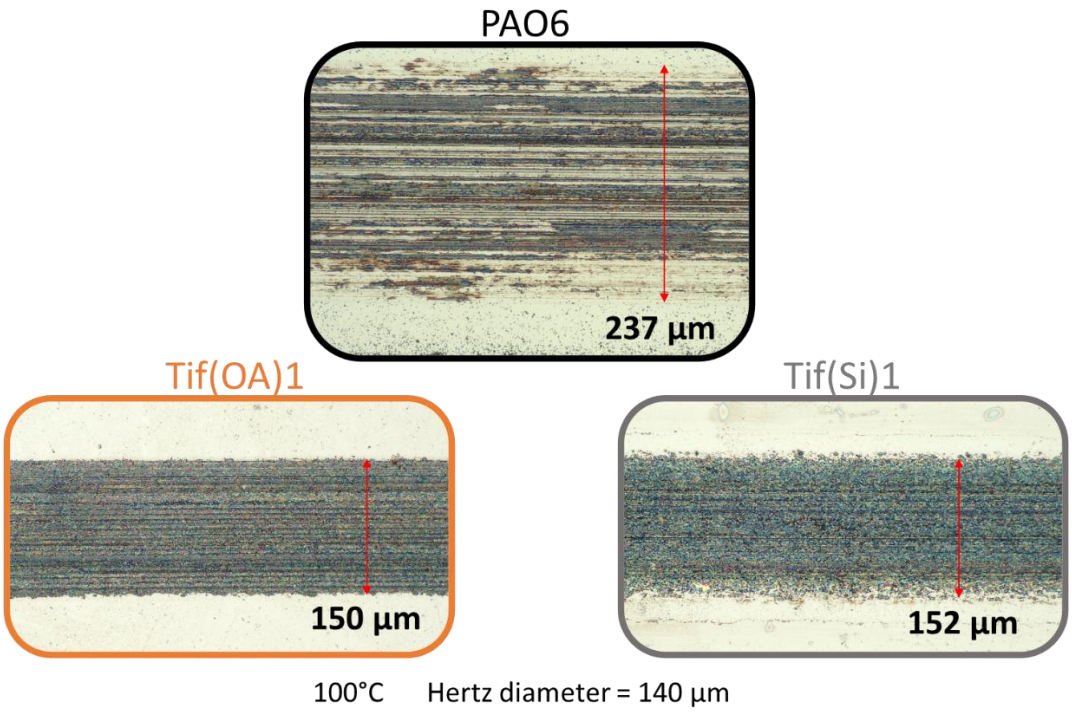

Fig. 100: Optical observations of wear tracks formed at 100°C on the discs in the presence of suspensions containing oleic acid-functionalized (Tif(OA)1) or silane-functionalized (Tif(Si)1) TiO_2 nanoparticles. PAO6 base oil used as a reference.

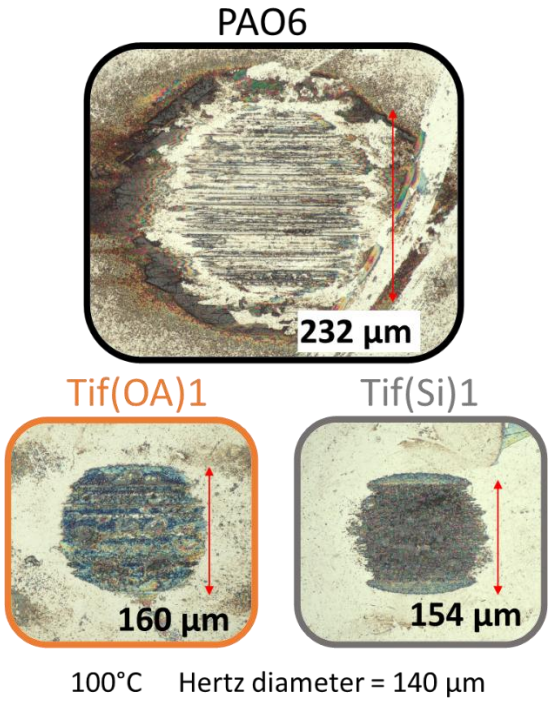

Fig. 101: Optical observations of wear scars formed at 100°C on the balls in the presence of suspensions containing oleic acid-functionalized (Tif(OA)1) or silane-functionalized (Tif(Si)1) TiO_2 nanoparticles. PAO6 base oil used as a reference.

Profilometric measurements nevertheless indicate that the tribofilm underwent significant wear, as shown in Fig. 102. The average height is even below the reference plane, indicating that the substrate itself experienced wear. Nonetheless, both nanoparticle suspensions achieve a significant reduction in wear compared to the PAO6 base oil. It appears that a competition occurs between tribofilm formation and tribofilm removal. In the case of oleic acid-functionalized nanoparticles, the equilibrium tends to favor tribofilm formation, unlike the silane-functionalized counterparts.

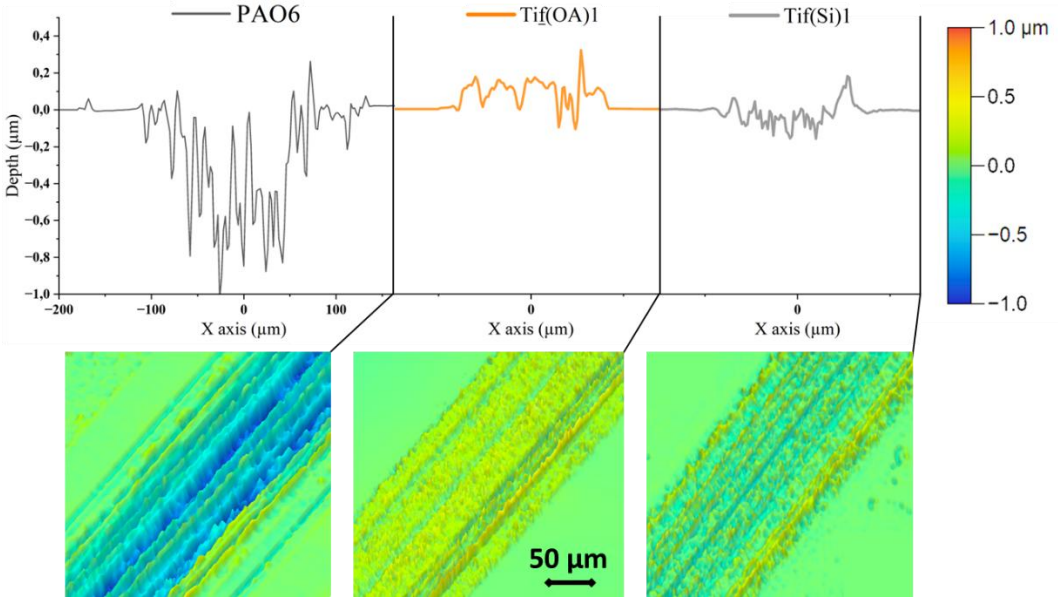

Fig. 102: Mean depth profiles and surface morphology of wear tracks formed at 100°C on the discs in the presence of suspensions containing oleic acid-functionalized (Tif(OA)1) or silane-functionalized (Tif(Si)1) TiO_2 nanoparticles. PAO6 base oil used as a reference.

Similar to the mentioned friction differences observed between the track center and its extremities, the tribofilm morphology of Tif(Si)1 also varies markedly between these regions, both in terms of optical appearance and profilometric height (Fig. 103). At the extremity of the wear track, a thick tribofilm appears to have formed, reaching up to 400 nm in height in certain areas. In contrast, at the center of the track, wear scratches are predominant, with depths ranging from 200 to 400 nm. Some regions at the center of the track, along the edges, exhibit a residual thickness of about 200-300 nm, which may correspond either to preserved tribofilm or to material that has been displaced toward the sides.

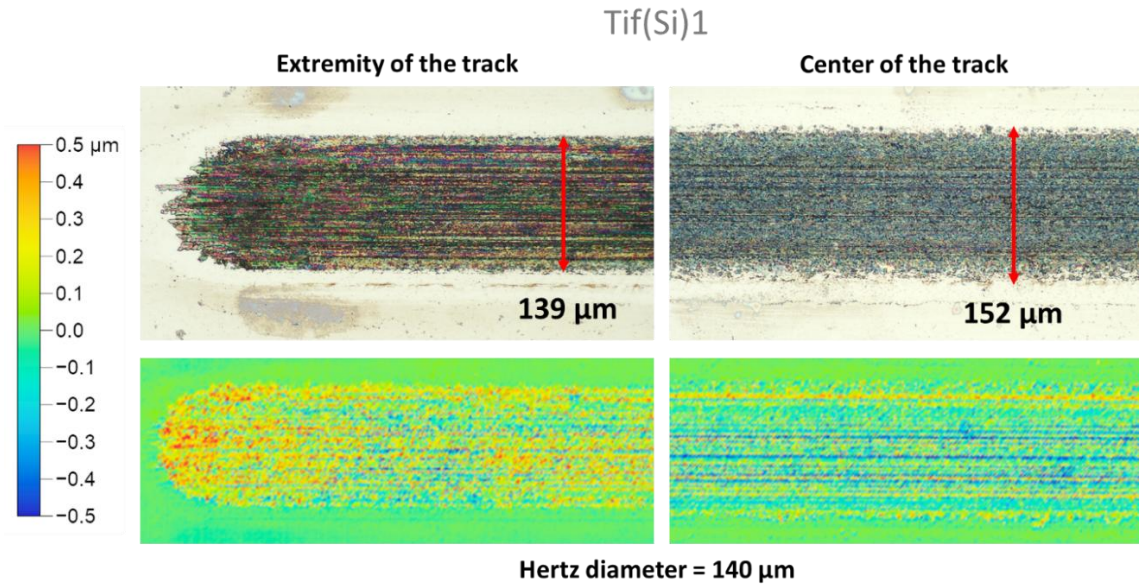

Fig. 103: Optical and profilometric characterization of wear tracks obtained at 100°C with silane-functionalized nanoparticles (Tif(Si)1). Comparison between the edge and the center of the track.

These results were systematically observed across the three tests, sometimes with one edge affected, sometimes both. The friction curves also behaved consistently (Fig. 104).

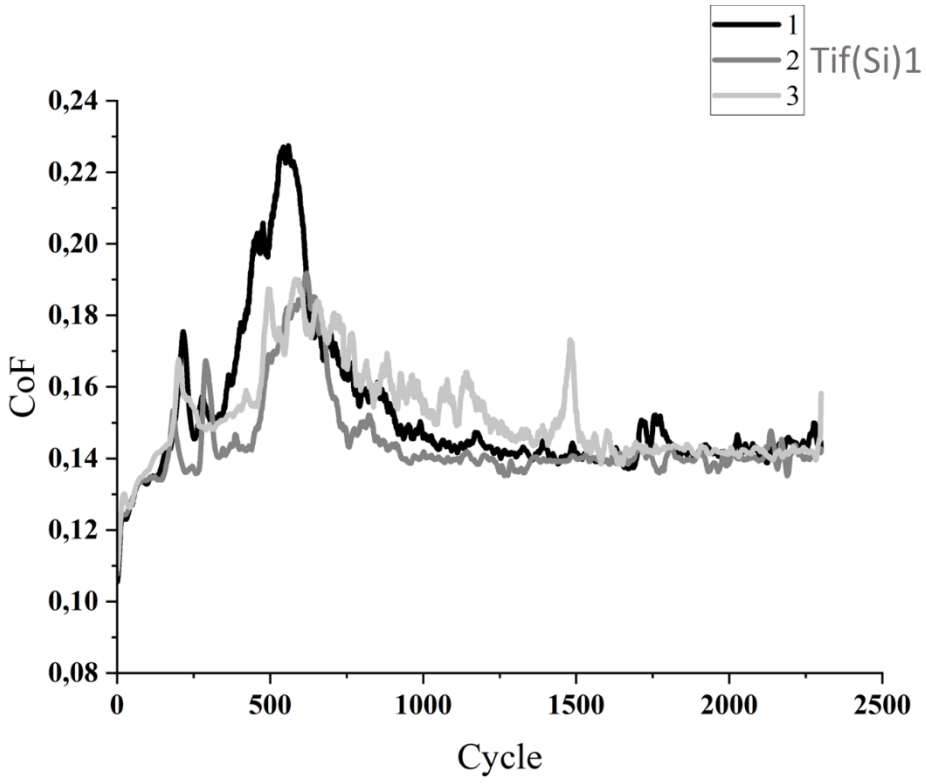

Fig. 104: Friction tests repeatability at 100°C for the samples containing silane-functionalized (Tif(Si)1) TiO_2 nanoparticles. Three repetitions were carried out for each blend.

To gain further insight into the mechanisms occurring during these tests, SEM observations and EDX analyses were carried out (Fig. 105). At low magnification in BSE mode, striations are observed that most likely correspond to exposed steel, highlighted by the scratches generated during sliding. The EDX mapping reveals that the tribofilm presents a patchy structure with tribofilm regions surrounded by Fe-rich regions that could correspond to the substrate.

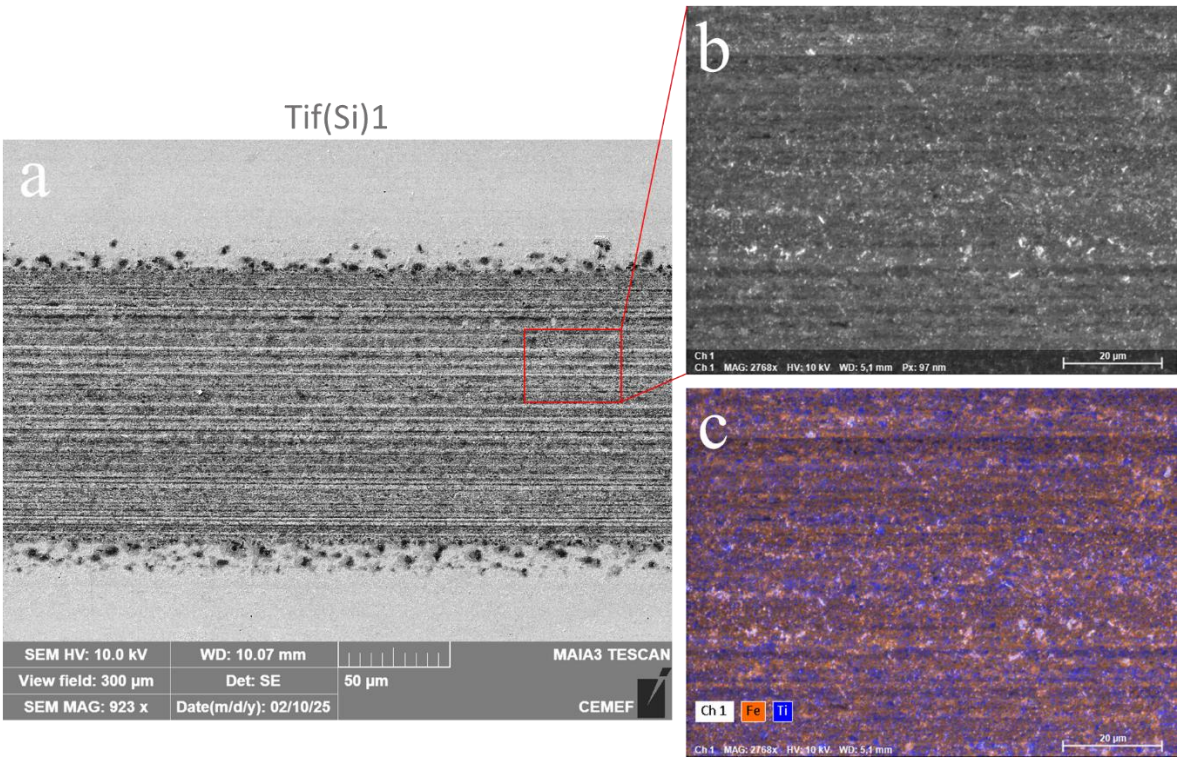

Fig. 105: SEM micrographs in BSE (a) and SE (b) modes with EDX mapping (c, d and e) of a tribofilm formed at 100°C on the disc in the presence of Tif(Si)1 solution (orange = Fe; blue = Ti).

High-magnification images were then acquired both at the center of the wear track (Fig. 106) and at its edges (Fig. 107). At the center, the tribofilm appears relatively smooth, although it contains numerous debris particles and microcracks within its structure. At the edges of the track (Fig. 107), the tribofilm appears rougher, less compact, and is likewise accompanied by debris and cracks. At the extreme edge, the tribofilm is even fragmented and severely cracked.

A close-up of one of the debris reveals that it consists of nanoparticle agglomerates. These agglomerates appear brittle and likely detach before being fully compacted into a denser and more robust tribofilm material.

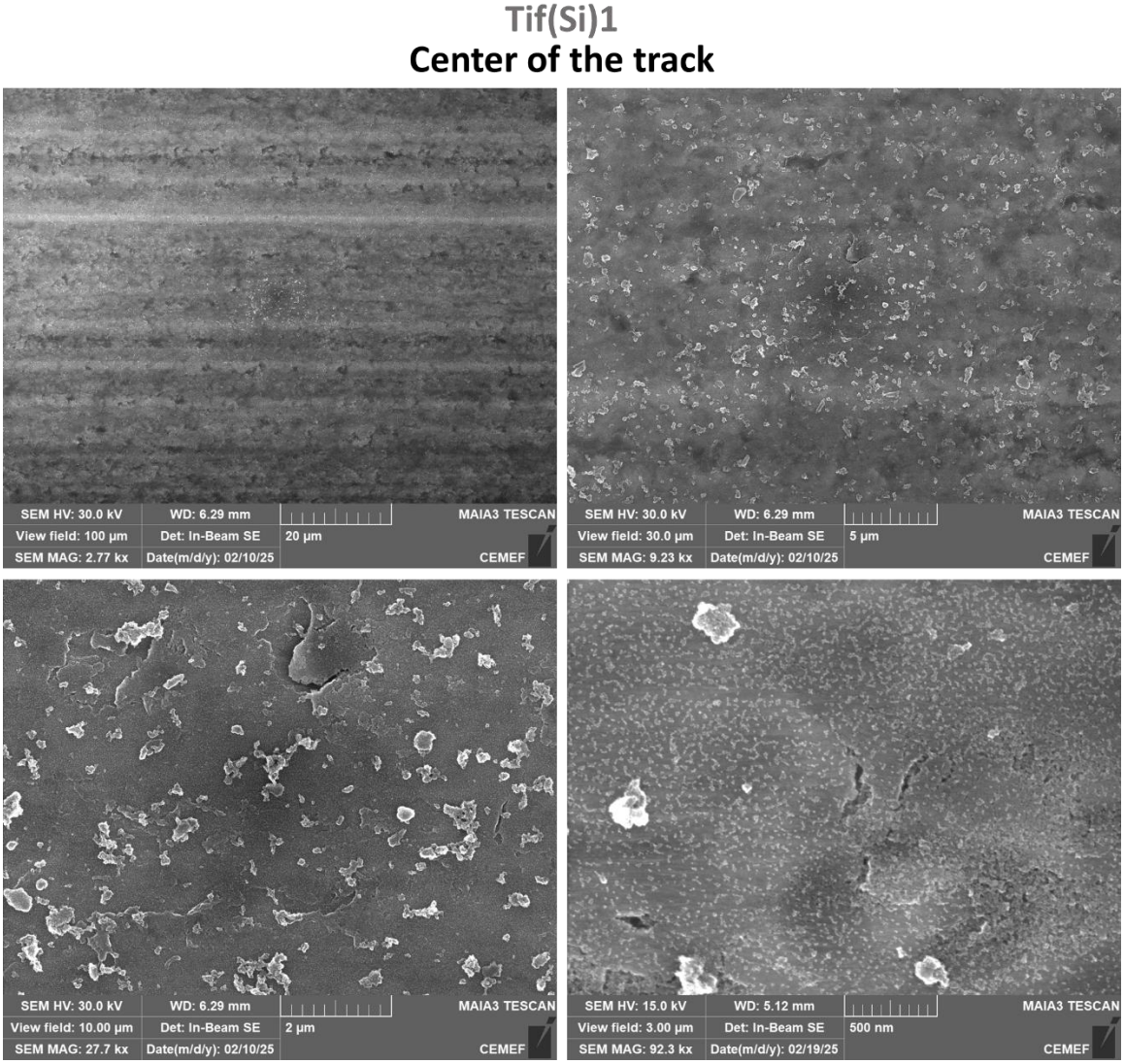

Fig. 106: High magnification SEM micrographs of the center of the wear track surface obtained at 100°C with silane-functionalized nanoparticles (Tif(Si)1) at different magnifications.

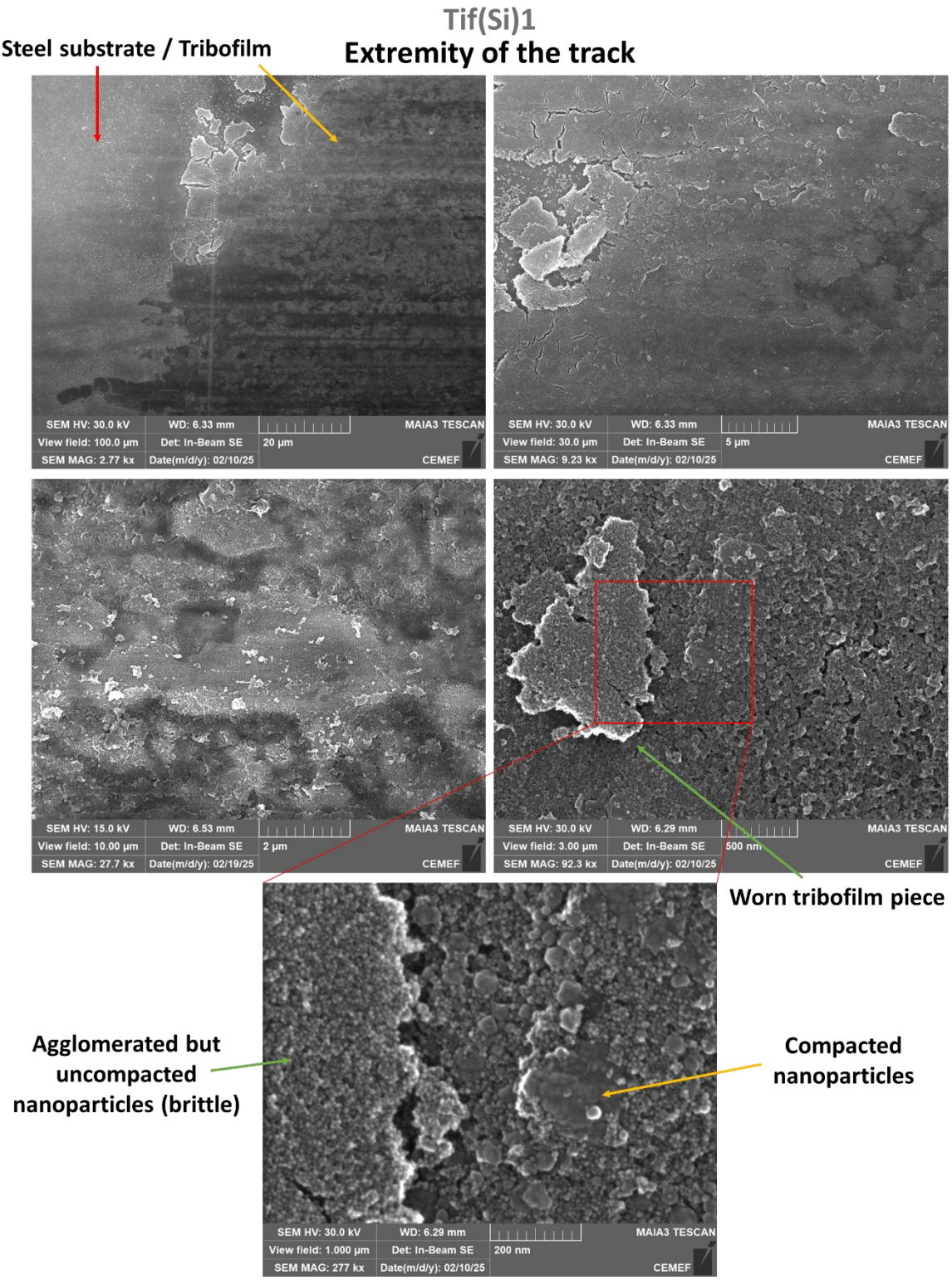

Fig. 107: High magnification SEM micrographs of the edge of the wear track surface obtained at 100°C with silane-functionalized nanoparticles (Tif(Si)1) at different magnifications.

A comparison with the tribofilm obtained using oleic acid functionalization clearly shows that changing the functionalizing agent for a silane one has a negative effect on the formation of a cohesive TiO_2 tribofilm. Indeed, well-compacted regions are both less numerous and smaller in size (Fig. 108). This is also accompanied by a significant presence of debris, likely abrasive, which could contribute to tribofilm wear and explain the higher friction coefficient.

It appears that with oleic acid, the tribofilm forms progressively: an initial compacted cluster initiates the reaction, and subsequent nanoparticles then fuse with it, that is probably why we observe either plateaus or agglomerated individual nanoparticles, but little to no intermediate structures. In contrast, with silane, numerous small compacted clusters (named tribofilm debris in Fig. 108) are formed, but they fail in merging together. A possible explanation could lie in the ligand removal step that is probably necessary to form a cohesive tribofilm. Overall, the silane nature of the capping agent led to the formation of a mechanically brittle tribofilm, making it prone to fracture and generating large abrasive debris within the contact which limits tribological performance.

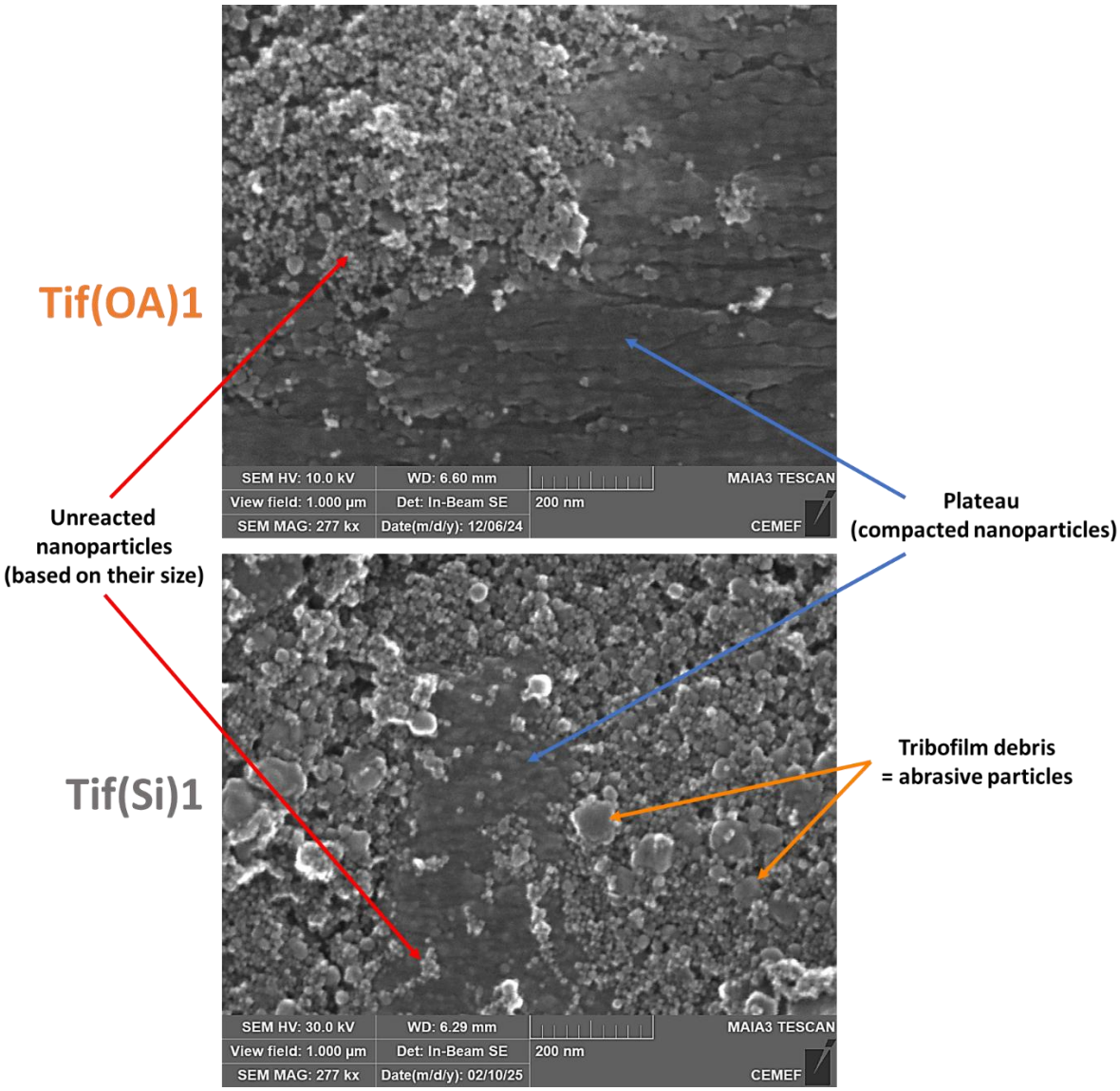

Fig. 108: High magnification SEM observations of tribofilms formed on the disc (center of the track) at 100°C in the presence of oleic acid-functionalized (Tif(OA)1) or silane-functionalized (Tif(Si)1) TiO_2 nanoparticles.

XPS analyses on the center as well as the extremity of the track were carried out and show that even though the tribofilm presents a more brittle structure, it contains more Ti and less carbon than the one formed with oleic acid-functionalized nanoparticles (**Table 17**). Almost similar values between the extremity and the center were found, therefore, only the results of the latter are presented.

This Ti is present in the form of pure TiO_2 as shown with the decomposition of the Ti2p peak in Fig. 109. Ti2p as well as C1s and O1s peaks were decomposed using the same method presented in 3.1.1 for Fig. 94. For the O1s peak, it should be noted that a satisfactory peak fitting could not be achieved without including the grey contribution, which is attributed to O-Si of the oxysilane group originating from the silane capping agent. This contribution is commonly found between 532 and 533 eV according to NIST (National Institute of Standards and Technology) XPS database as well as the literature [9] which corresponds to our measurement.

at.%	100°C	
	Tif(OA)1	**Tif(Si)1**
C 1s	**30.3**	**18.0**
Fe 2p	**12.6**	**2.7**
O 1s	**45.4**	**52.2**
Si2p	**0.0**	**2.1**
Ti 2p	**11.1**	**22.7**
Ca 2p	**0.6**	**2.4**

Table 17: XPS chemical composition of tribofilms formed at 100°C (center of the track) in the presence of solutions containing oleic acid-functionalized or silane-functionalized TiO_2 nanoparticles. Obtained with a K-ALPHA and a NEXSA spectrometer, respectively.

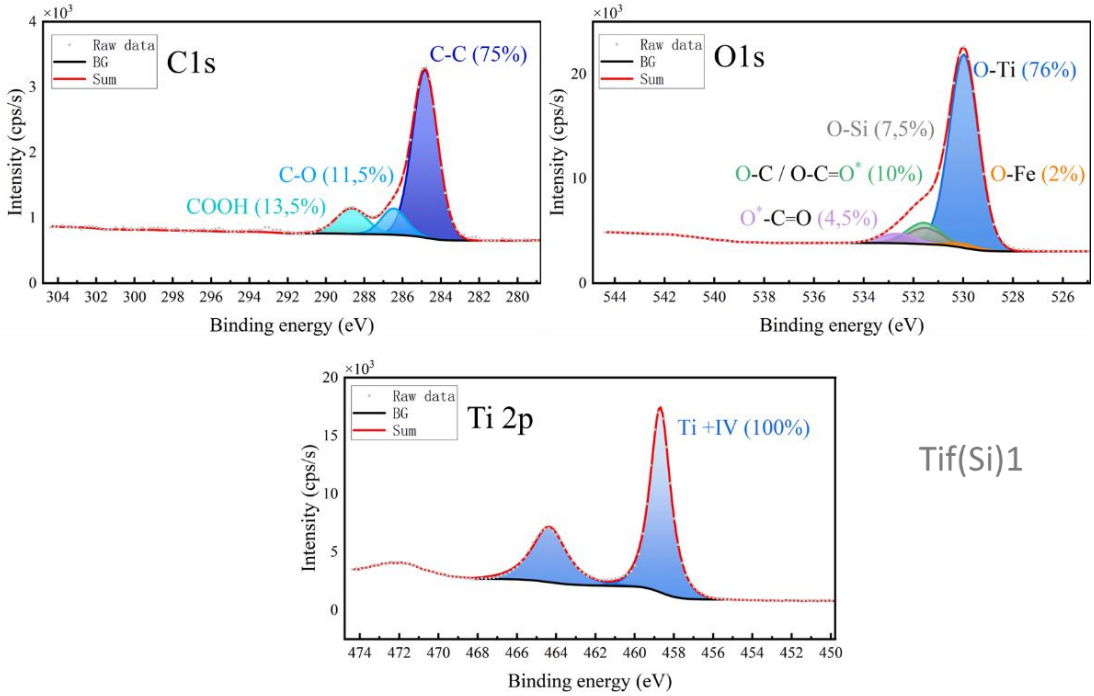

Fig. 109: C1s, O1s and Ti2p XPS spectra of a tribofilm formed at 100°C in presence of a silane-functionalized TiO_2 nanoparticles suspension.

The results highlight the strong influence of the functionalization method on the tribological behavior of TiO_2 nanoparticles. While silane functionalization greatly improves the colloidal stability of nanoparticle suspensions at both room and elevated temperatures, it negatively impacts tribofilm formation - not by preventing nanoparticles from entering the contact, but by compromising the structural integrity of the tribofilm. The resulting weakly bonded material appears brittle and is therefore prone to cracking and wear, leading to the detachment of small tribofilm fragments as well as abrasive debris formation. These phenomena are likely responsible for the elevated friction observed in Fig. 98 and the wear evidenced in Fig. 102. In addition, it can be inferred that debris generated from the worn central region of the track are displaced toward the edges, accounting for the thicker tribofilm and higher friction observed in these areas.

Overall, the findings emphasize a trade-off between suspension stability and tribofilm robustness: silane functionalization enhances storage and thermal stability but impairs the development of a protective and durable TiO_2 tribofilm.

In order to gain further insight into tribofilm formation, intermediate tests were performed. In these tests, wear tracks were generated up to a given number of cycles (10, 50, 100, 250, 500, 1000, or 2300 cycles). Each track was therefore produced independently, and the reliability of the results relies on the good repeatability of the suspensions. Two repetitions were carried out for each cycle count. The optical observations of the resulting wear tracks are presented in Fig. 110.

It should be noted that these experiments were performed under milder conditions (0.83 GPa instead of 1.03 GPa). No significant difference was observed between these two pressure levels, and this variation is therefore not expected to affect the results.

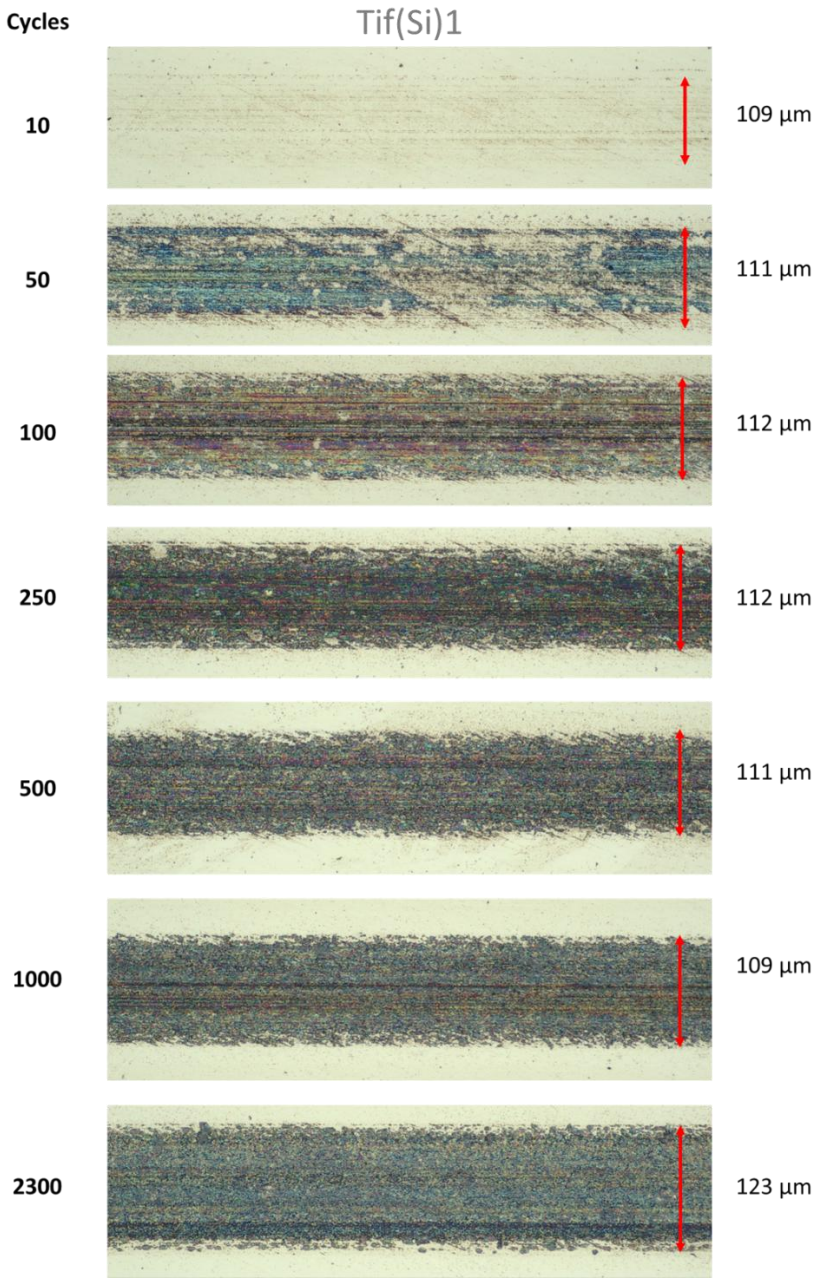

Fig. 110: Optical observations of wear tracks formed at 100°C on the disc at intermediate cycles in the presence of a solution containing silane functionalized TiO_2 nanoparticles (Tif(Si)1).

It can be observed that the tribofilm forms very rapidly. As early as 50 cycles, a tribofilm is already visible (bluish appearance). By 250 cycles, it appears to cover the entire contact area and to darken, showing an aspect similar to the one observed at the edges of the track in the previous tests (Fig. 103). From 500 cycles onwards, the tribofilm appears to lighten again, regaining a bluish aspect, probably linked to its thickness. This phenomenon intensifies up to 2300 cycles. The wear track width, meanwhile, remains relatively stable, close to the Hertzian diameter (112 µm), and increases only between 1000 and 2300 cycles.

This evolution was further quantified by profilometry (Fig. 111), which shows that the tribofilm reaches a maximum thickness between 250 and 500 cycles before subsequently decreasing. This suggests that the silane-functionalized nanoparticles are highly reactive, since they form a visible tribofilm as early as 50 cycles; however, due to its fragile structure, the tribofilm experiences partial degradation and lateral spreading under friction and load.

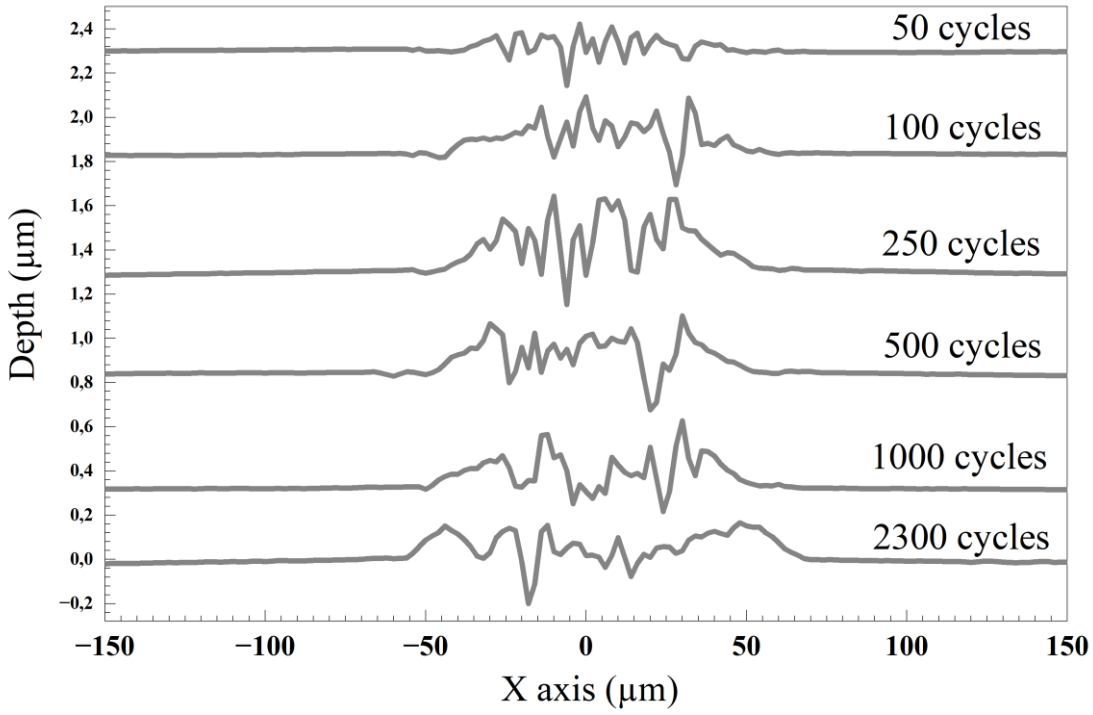

Fig. 111: Mean depth profiles of wear tracks (center) formed at 100°C on the disc at intermediate cycles in the presence of a solution containing silane functionalized TiO_2 nanoparticles (Tif(Si)1).

The tribofilm volume, shown in Fig. 112, confirms this trend: it reaches a maximum at 250 cycles, then drops sharply and continues to decrease between 1000 and 2300 cycles. At the same time, the first increases in the CoF are observed around 250 cycles (Fig. 104). Before this point, the system is likely dominated by tribofilm formation, whereas beyond it, the balance shifts and wear becomes the prevailing process.

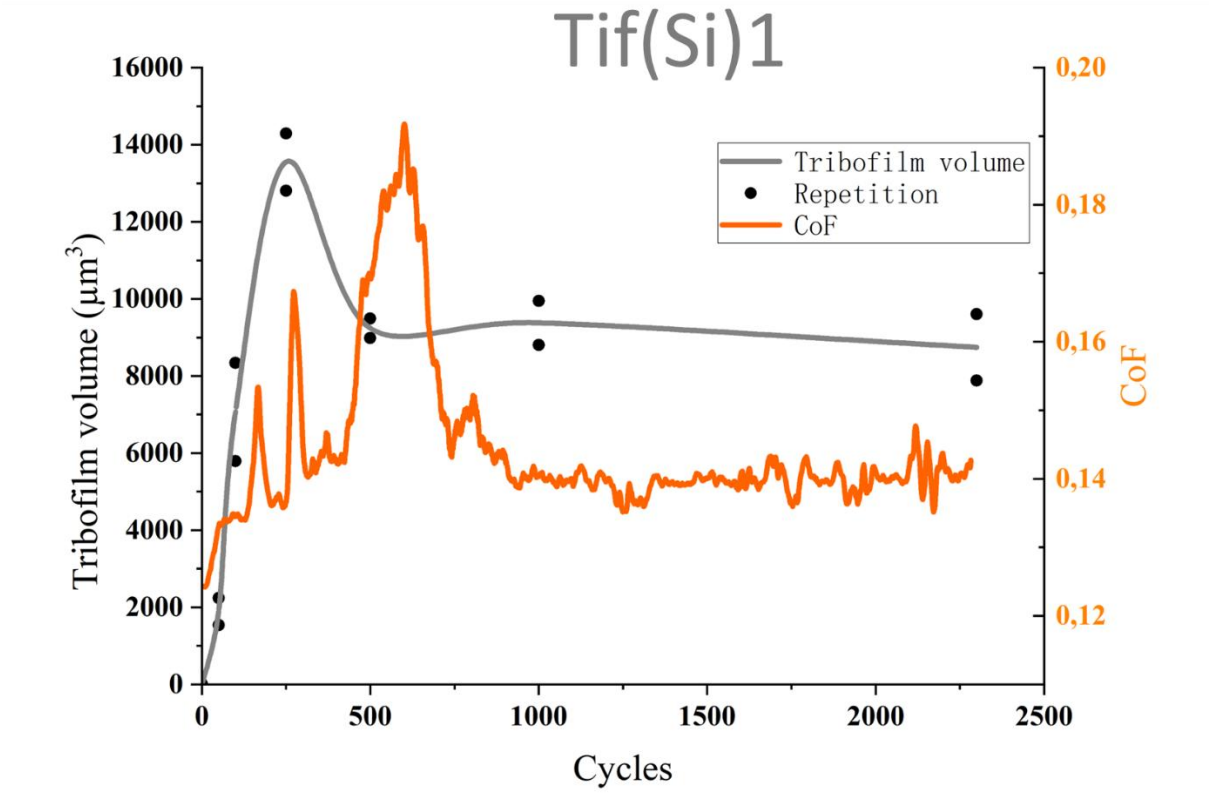

Fig. 112: Evolution of tribofilm growth volume with cycles (100°C) for silane-functionalized TiO_2 nanoparticles (Tif(Si)1) suspension.

Following figures present high magnification SEM micrographs conducted on the intermediate cycles tracks.

Even at 10 cycles (Fig. 113), preliminary structures composed mainly of agglomerated nanoparticles can already be observed, highlighting the high reactivity of these nanoparticles.

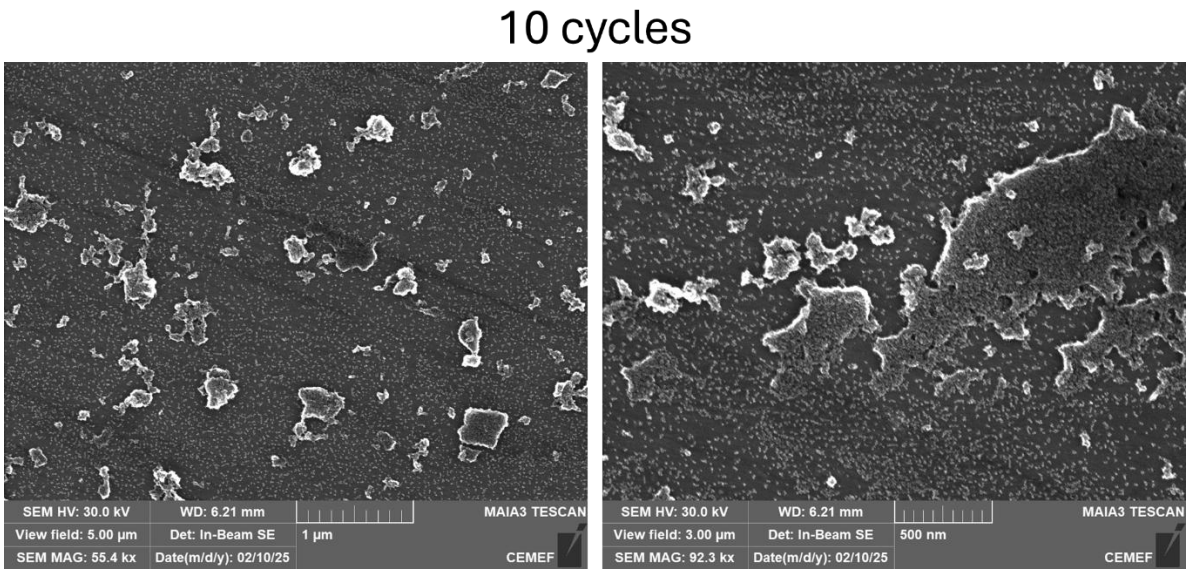

Fig. 113: SEM micrographs of the center of the track formed with silane-functionalized TiO_2 nanoparticles after 10 cycles.

Even larger structures can be observed at 50 cycles (Fig. 114) but still made from agglomerated NPs.

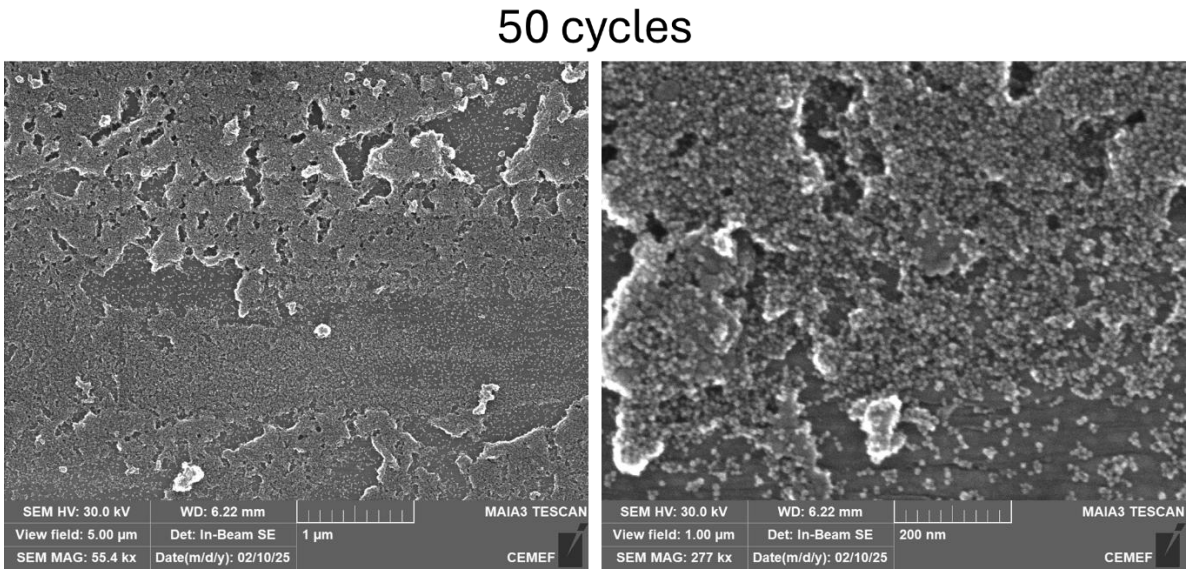

Fig. 114: SEM micrographs of the center of the track formed with silane-functionalized TiO_2 nanoparticles after 50 cycles.

At 100 cycles (Fig. 115), large fragments of tribofilm are observed, and the tribofilm itself displays a porous structure.

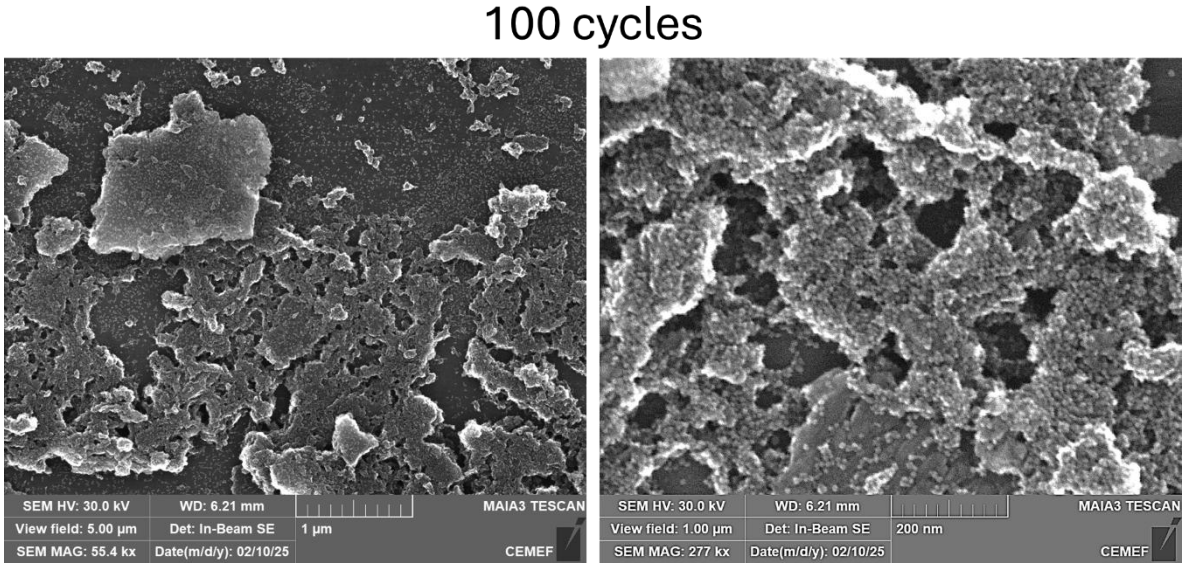

Fig. 115: SEM micrographs of the center of the track formed with silane-functionalized TiO_2 nanoparticles after 100 cycles.

Even larger fragments resulting from tribofilm cracking are observed at 250 cycles (Fig. 116). Although the overall appearance seems smoother, high-magnification observations reveal that the structure remains porous.

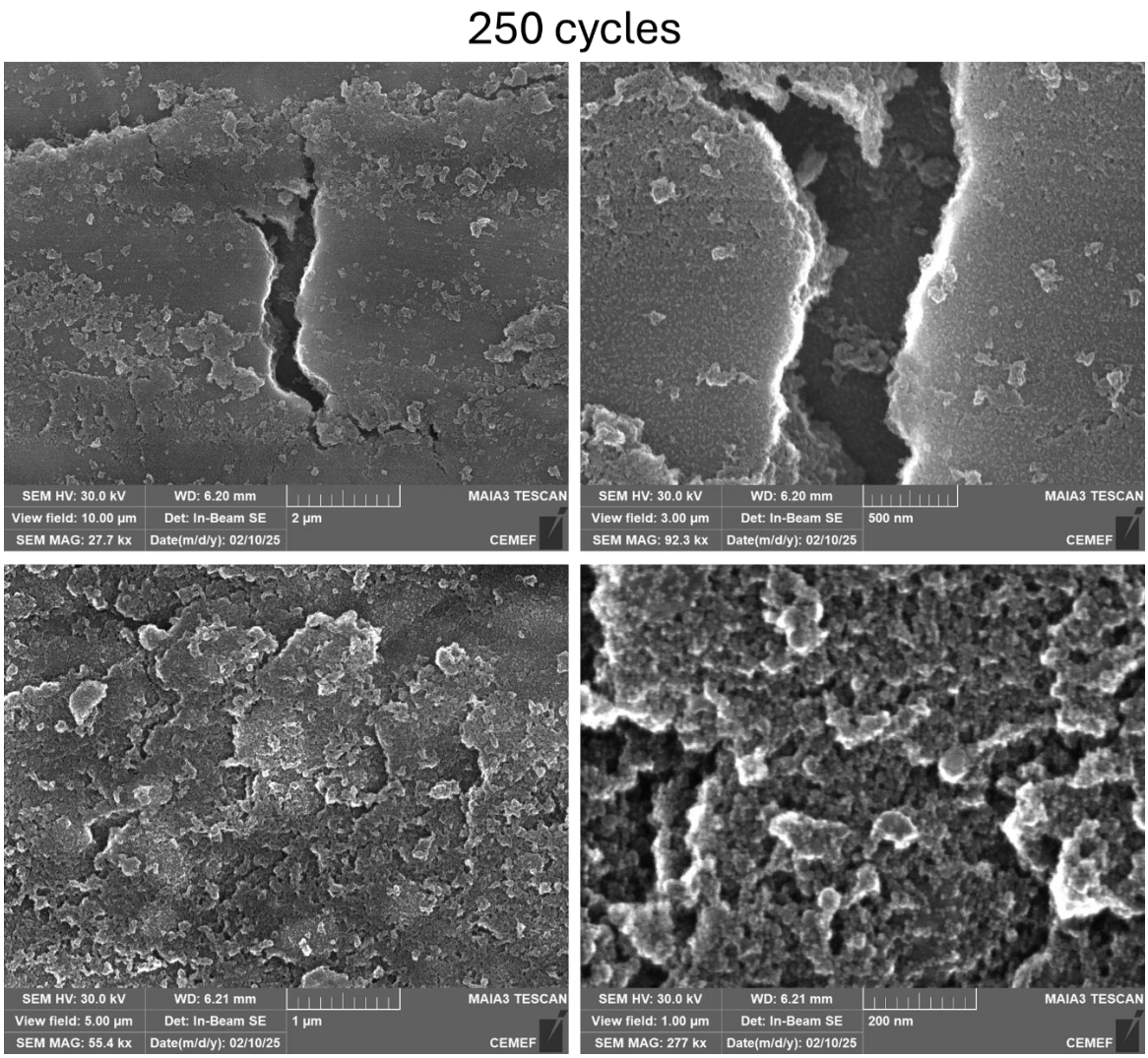

Fig. 116: SEM micrographs of the center of the track formed with silane-functionalized TiO_2 nanoparticles after 250 cycles.

The surface becomes even smoother at 500 and 1000 cycles (Fig. 117), which display a similar morphology. However, once again, high magnification observations show a porous structure. At this stage, it is composed of small compacted tribofilm fragments surrounded by nanoparticle agglomerates.

It is only at 2300 cycles that larger compact structures forming plateaus are observed (Fig. 108).

Across these figures, it appears that the patches progressively extend until they coalesce, while residual pores are gradually filled. The tribofilm thus becomes continuous at the microscale, yet remains nanoporous.

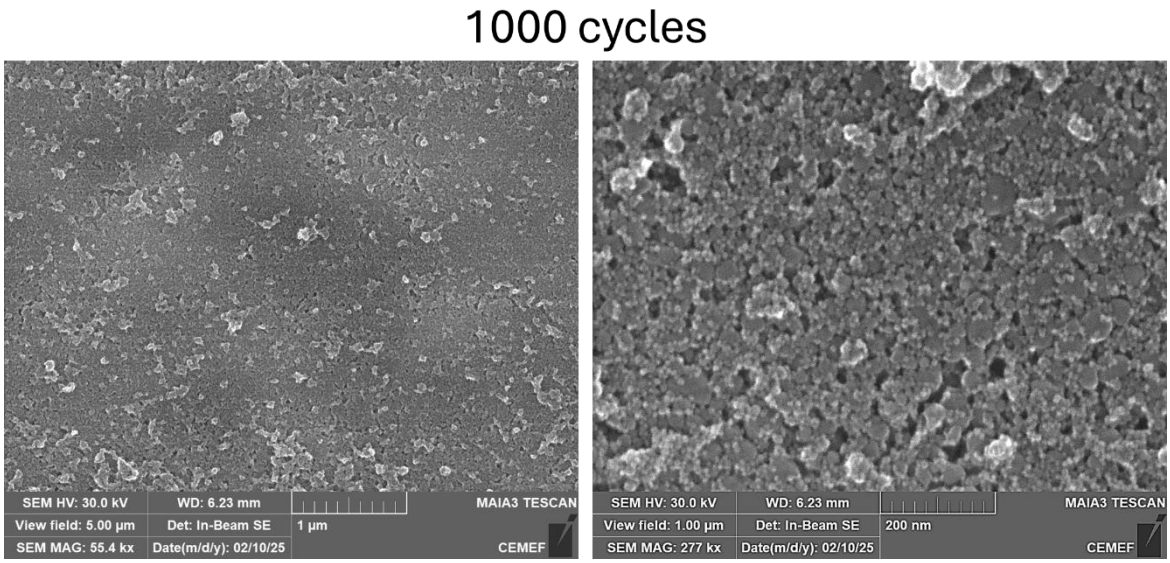

Fig. 117: SEM micrographs of the center of the track formed with silane-functionalized TiO_2 nanoparticles after 1000 cycles.

XPS analyses of the intermediate wear tracks are presented as a graph in Fig. 118, based on the data reported in **Table 18**.

These results once again confirm that the tribofilm forms very rapidly, with 9.9 at.% of Ti already detected after only 10 cycles. This value could, however, partly originate from remaining TiO_2 nanoparticles adhered to the surface at the end of the test. For this reason, an additional measurement was performed outside the wear track (**Table 18**), which indeed revealed the presence of residual TiO_2, but at a lower level of 5.7 at.%. The Ti content within the track then continues to increase and stabilizes at around 22 at.%. An increase in C content is observed at 250 cycles but its origin remains uncertain. This phenomenon may be related to the silane functionalizing agent or to an impurity present in the analyzed region. However, repetition of the analysis for the 250 cycles track on a different area shows that the increase in carbon persists, making the latter hypothesis less likely.

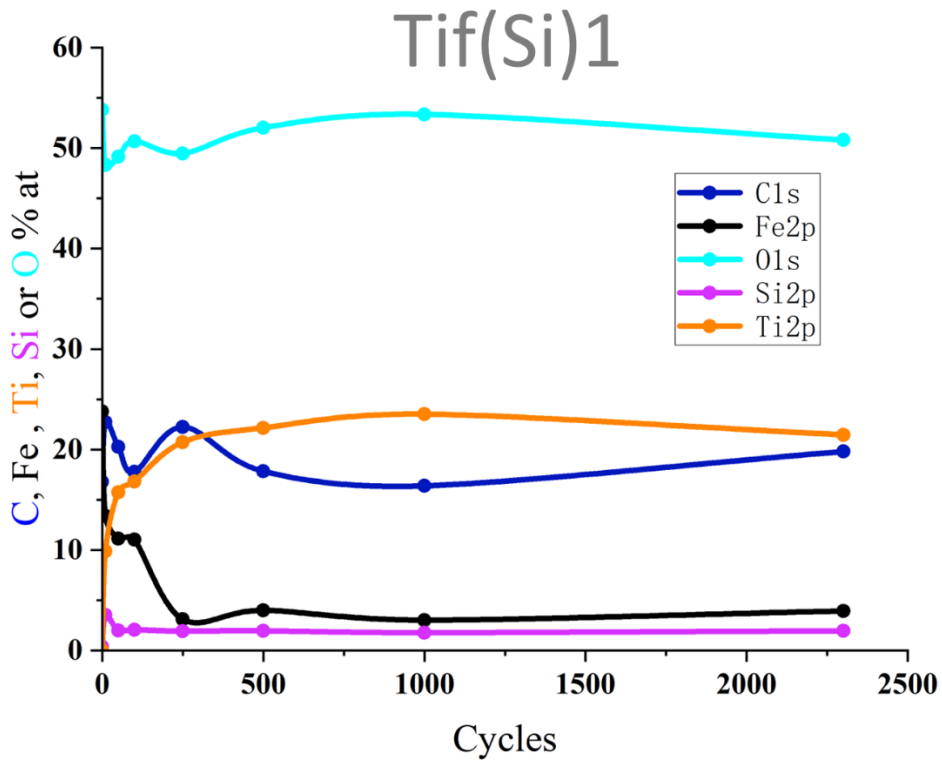

Fig. 118: Evolution of tribofilm at.% content (XPS analysis: C, Fe, O, Si and Ti) with cycles for silane-functionalized TiO_2 nanoparticles (Tif(Si)1) suspension (center of the track).

Cycles	Tif(Si)1					
	C1s	Fe2p	O1s	Si2p	Ti2p	Other
0	16,8	23,8	53,8	0,4	0,0	5,2
10	22,7	13,4	48,3	3,5	9,9	2,2
50	20,3	11,2	49,1	2,0	15,8	1,7
100	17,8	11,0	50,7	2,1	16,8	1,7
250	22,2	3,1	49,5	1,9	20,7	2,5
500	17,8	4,0	52,0	2,0	22,2	2,1
1000	16,4	3,0	53,3	1,8	23,5	2,0
2300	19,8	3,9	50,8	2,0	21,5	2,1
out	10,4	22,7	53,7	5,7	5,7	1,8

Table 18: Evolution of tribofilm at.% content (C, Fe, O, Si and Ti) with cycles for silane-functionalized TiO_2 nanoparticles (Tif(Si)1) suspension.

Fig. 119 presents the evolution of the fitted Ti 2p components between 10 and 250 cycles. Ti 2p peak is a doublet (Ti $2p_{3/2}$ and Ti$2p_{1/2}$) with contributions at 459.0 eV and 464.5 eV, respectively, for TiO_2. In this case, in addition to TiO_2, another contribution appears at 458.1 eV (Ti $2p_{3/2}$) at 10, 50 and 100 cycles, but it is absent in the subsequent cycles as well as in the final tribofilm formed after 2300 cycles (Fig. 109). Sharma *et al.* (2025) [10] investigated TiO_2 nanoparticles and reported, based on XANES (X-ray Absorption Near Edge Structure) analysis, the formation of iron titanate ($FeTiO_3$) within the tribofilm. Upon further verification, it appears that several studies indeed report the Ti $2p_{3/2}$ peak of iron titanate to occur between 458.0 and 458.2 eV [11,12] (adjusted to our C1s calibration at 284.8 eV). It is therefore likely that during the first cycles an iron titanate layer is formed followed by the compaction and eventual tribo-sintering of following TiO_2 nanoparticles.

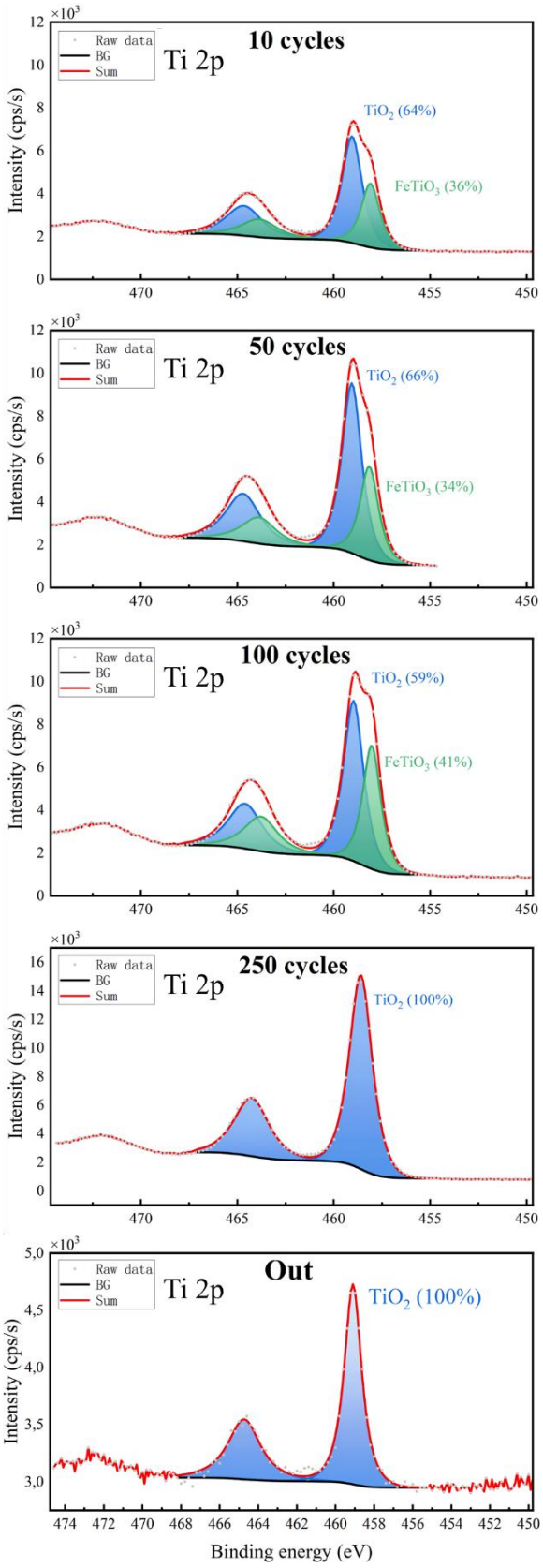

*Fig. 119: Evolution of Ti2p XPS spectrum of tribofilms formed in the presence of Tif(Si)1 for different cycles (10, 50, 100 and 250 cycles). The spectrum measured **outside of the track** Is also presented for comparison.*

Summary and Discussion

The interrupted tests provide important insights into the dynamics of tribofilm formation with silane-functionalized nanoparticles. The results confirm that tribofilm formation occurs very rapidly, with TiO_2 already detected after only 10 cycles partially in the form of iron titanate. Both optical and profilometric observations show that the film reaches its maximum thickness and volume at 250 cycles, before gradually decreasing under the effect of pressure and friction. This suggests that while the nanoparticles are readily available and able to nucleate tribofilm structures quickly, the weak cohesion of the material results in its progressive wear and spreading.

Morphological analyses reveal that although the tribofilm appears increasingly smooth with cycling, high magnification observations show that it remains nanoporous and fissured. At the edges of the wear track, the tribofilm is thicker and more compact than at the center, likely due to the lateral displacement and accumulation of debris originating from the central region. This non-uniformity reflects the difficulty of forming a continuous and stable layer across the whole contact.

Compared with oleic acid-functionalization, the silane-functionalized system produces fragmented compacted domains that fail to coalesce into a robust tribofilm. As a result, the tribofilm is discontinuous, brittle, and easily damaged. This structural weakness explains both the higher friction observed in the sliding tests and the significant wear of the tribofilm, further aggravated by the presence of abrasive debris.

The comparison between oleic acid and silane functionalization highlights a clear trade-off between colloidal stability and tribological performance. Oleic acid-functionalized nanoparticles display lower suspension stability, particularly at elevated temperatures, but promote the formation of a dense and cohesive TiO_2 tribofilm. This tribofilm develops through the progressive compaction and coalescence of nanoparticles, resulting in a more protective tribolayer as well as lower friction.

In contrast, silane functionalization greatly enhances suspension stability, enabling long-term storage and thermal stability. However, under tribological conditions, the resulting tribofilm is porous, discontinuous, and structurally fragile. Instead of coalescing into a compact layer, numerous small domains form but remain isolated, leading to crack propagation, debris formation, and ultimately higher friction and wear.

Overall, these findings demonstrate that the choice of functionalizing agent dictates not only the suspension stability but also the mechanisms and effectiveness of tribofilm formation. Oleic acid favors tribofilm robustness at the expense of colloidal stability, while silane ensures excellent suspension stability but hinders the development of a durable protective film.

3.2 Interactions Between Nanoparticles and Conventional Lubricant Additives

In lubricant formulations, nanoparticles are not intended to be used as stand-alone additives and must remain compatible with the complete additive package of a fully formulated oil. Their relevance therefore depends not only on their intrinsic tribological properties, but also on how they interact with other additives.

In this context, particular attention is given here to MoDTC and ZDDP, which are widely regarded as reference additives for friction reduction and anti-wear protection, respectively. The following section examines the interactions between TiO_2 nanoparticles and these two standards, in order to assess potential synergies or antagonisms in terms of friction behavior, wear protection, and tribofilm formation.

3.2.1 Synergetic Interactions Between MoDTC and TiO_2

We will first explore the synergistic interaction between MoDTC and unmodified TiO_2 nanoparticles, focusing on how these nanoparticles influence the additive's reactivity and tribological behavior.

In a second step, attention will be given to functionalized TiO_2 nanoparticles, with particular emphasis on how the chemical nature of the functionalizing agent modifies their interaction with MoDTC and impacts the resulting synergy.

3.2.1.1 Synergistic Interaction Between MoDTC and unmodified TiO_2 Nanoparticles

This synergy is described in work of Deshpande *et al.* (2017) [13], whose doctoral research partly focused on the use of MoDTC in combination with 25 nm unmodified TiO_2 nanoparticles. Their main observations were as follows:

- **Synergistic effect between MoDTC and TiO_2 nanoparticles.** The combination of the two additives exhibited superior tribological performance compared to each additive used individually, both in terms of friction reduction and wear protection.
- **Enhanced MoDTC-to-MoS_2 conversion.** XPS analyses of tribofilms formed with MoDTC alone and with the MoDTC-TiO_2 mixture reveal a higher proportion of MoS_2 in the latter case.
- **Improved stability of the mixture.** The blend also showed better temporal stability compared to TiO_2 nanoparticles dispersed alone in the base oil (PAO6). MoDTC appeared to act as a dispersing agent for the nanoparticles.

On this basis, we first sought to verify these findings using our own tribometer and formulations (MoDTC combined with unmodified TiO_2 nanoparticles). It should be noted that smaller nanoparticles (5 nm) were selected, as reducing particle size enhances surface reactivity and therefore promotes more efficient interaction during tribofilm formation.

It should be noted that this campaign was performed using 6 mm balls under a contact pressure of 0.83 GPa (full set of parameters presented in **Table 19**).

Temperature	100°C
Normal load	2 N
Ball diameter	6 mm
Maximum Hertzian contact pressure	0.83 GPa
Hertz Diameter	68 µm
Test duration / cycle number	3600 s / 2300 cycles
Test frequency	0.64 Hz
Stroke length	5 mm
Maximum linear speed	10 mm/s
Oil quantity	2 mL
Repetitions	3
Acquisition frequency	25 Hz
Plotted curves processing	Averaged over 8 points

Table 19: Tribological conditions for MoDTC and unmodified TiO_2 nanoparticles.

Blends used for this study are presented in **Table 20**. Ti0.5 formulation is not presented because of its poor tribological properties as illustrated in the previous section (3.1.1) with the Ti1 formulation.

Composition	Name
PAO6	PAO6
PAO6 + 0.5 wt.% MoDTC	Mo0.5
PAO6 + 0.5 wt.% MoDTC + 0.5 wt.% TiO_2 NPs	Mo0.5_Ti0.5

Table 20: Composition and name of tribologically tested blends used for the study of MoDTC and unmodified TiO_2 nanoparticles interactions.

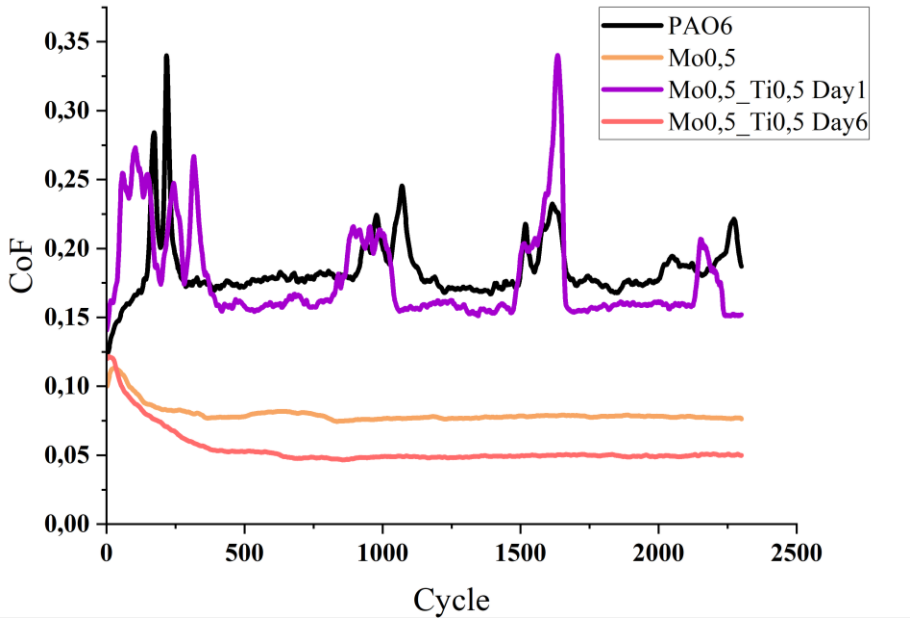

Fig. 120: Evolution of friction coefficient with cycles at 100°C for the samples containing MoDTC (Mo0.5) and a blend of MoDTC and unmodified TiO_2 nanoparticles (Mo0.5_Ti0.5) one day (Day1) and 6 days (Day6) after the blend was prepared. PAO6 base oil is used as a reference.

Fig. 120 shows the coefficients of friction (CoF) obtained with our formulations. As expected, MoDTC alone (Mo0.5) significantly reduces friction compared to the base oil, with a stabilized CoF of approximately 0.075. This low value is reached rather quickly, highlighting the ability of MoDTC to efficiently decompose and form MoS_2 lamellae.

A blend of MoDTC and TiO_2 nanoparticles (Mo0.5_Ti0.5) was then studied, and markedly different results were obtained depending on the timing of the tests. When the experiments were carried out one day after sample preparation, the mixture exhibited a very high friction level, comparable to that of the base oil (PAO6). However, when the same tests were repeated after a few days (six in our case), the results were completely different, the mixture exhibited a lower CoF than MoDTC alone (0.05 versus 0.08, respectively), corresponding to a 33% reduction.

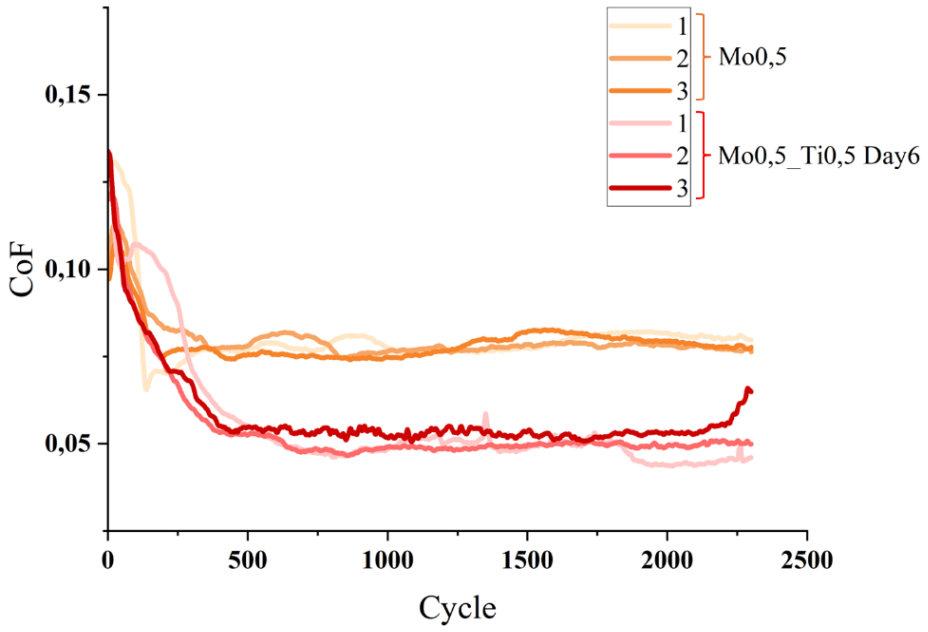

Fig. 121: Friction tests repeatability at 100°C for the samples containing MoDTC (Mo0.5) or a combination of MoDTC and unmodified TiO_2 nanoparticles (Mo0.5_Ti0.5). Three repetitions were carried out for each blend.

Furthermore, this result is repeatable, as demonstrated in Fig. 121.

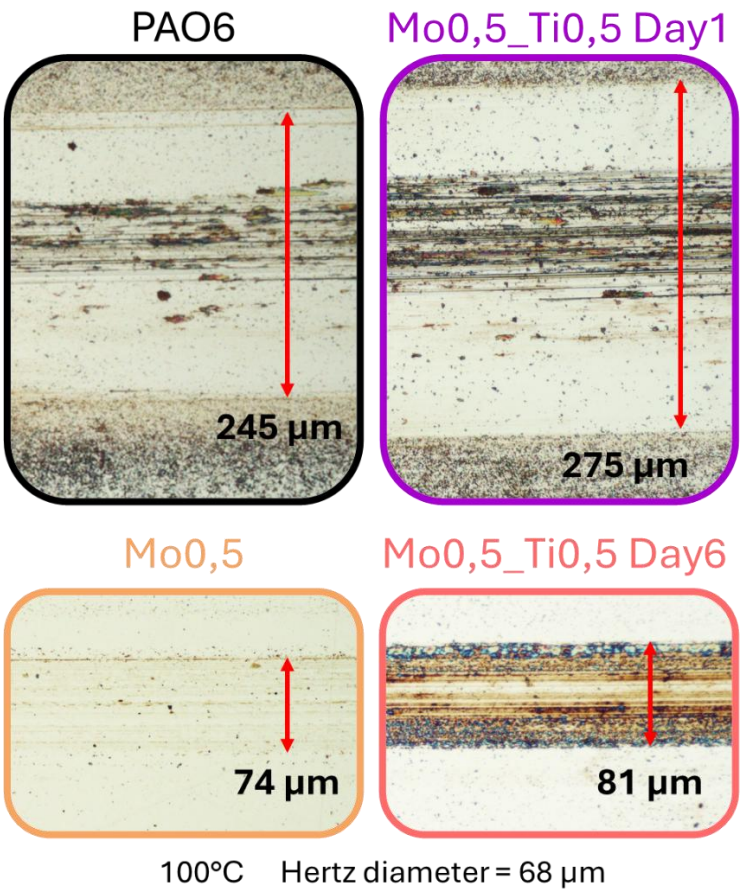

Fig. 122: Optical observations of wear tracks formed at 100°C on the discs in the presence of solutions containing MoDTC (Mo0.5) or a combination of MoDTC and unmodified TiO_2 nanoparticles (Mo0.5_Ti0.5) one day (Day1) and 6 days (Day6) after the blend was prepared.

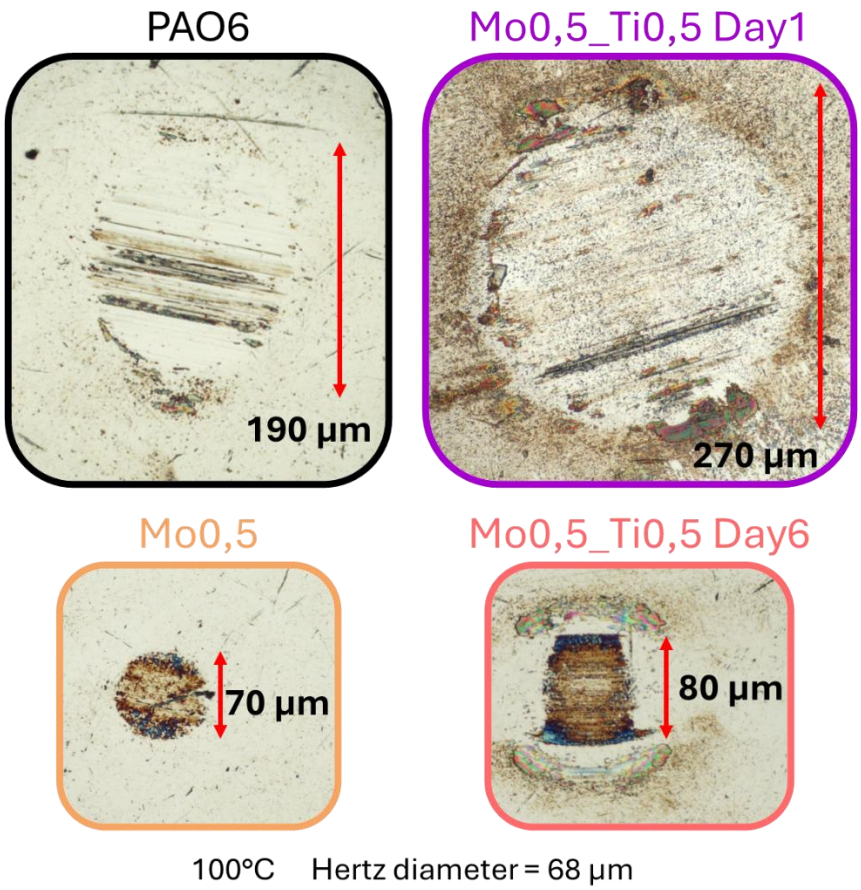

Fig. 123: Optical observations of wear tracks formed at 100°C on the balls in the presence of solutions containing MoDTC (Mo0.5) or a combination of MoDTC and unmodified TiO_2 nanoparticles (Mo0.5_Ti0.5) one day (Day1) and 6 days (Day6) after the blend was prepared.

Fig. 122 and Fig. 123 present the wear tracks observed on the discs and the balls. In addition to reducing friction, MoDTC also appears to limit wear, as the wear scar is barely distinguishable apart from tiny scratches and its width remains close to the Hertzian diameter. For the Mo0.5_Ti0.5 mixture tested one day after preparation (Day1), severe wear is observed, consistent with the high friction reported earlier. The wear even appears more pronounced than with PAO6 alone, which could be attributed to an abrasive effect of agglomerated nanoparticles.

After six days (Day6), however, the results are much more satisfactory: the wear scar width is about 80 µm, which is close to the Hertzian diameter (68 µm). In addition, what seems to be a tribofilm (bluish areas) is visible, forming mainly along the edges of the wear track, both on the disc and on the ball.

So far, we have successfully reproduced the behavior reported by Deshpande *et al.* (2017) [13], both in terms of enhanced friction reduction and wear mitigation. Furthermore, we observed that the temporal parameter strongly influences the tribological properties of the mixture which is completely ineffective if sufficient incubation time is not allowed. This result highlights an important mechanistic aspect: the synergy likely relies on the physicochemical interaction between MoDTC and TiO_2 in the base oil even before tribological contact occurs. This hypothesis is supported by the fact that, as noted by Deshpande and confirmed with our observations, suspensions of TiO_2 nanoparticles alone exhibit very poor stability (a few minutes), whereas the Mo0.5_Ti0.5 mixture remains stable for at least a few hours. Although stability remains limited, this observation emphasizes that MoDTC appears to act as a dispersing agent for the nanoparticles, suggesting at least a physical interaction between the two.

To understand the observed friction reduction, XPS analyses (**Table 21**) were performed on the tribofilms formed with Mo0.5 and Mo0.5_Ti0.5 (Day 6).

at.%	100°C	
	Mo0,5	**Mo0,5_Ti0,5**
C 1s	**22,2**	**18,8**
Fe 2p	**15,2**	**8,2**
O 1s	**45,4**	**46,3**
S 2p	**7,7**	**7,3**
Mo 3d	**8,9**	**6,2**
Ti 2p	**0,0**	**12,5**
Ca 2p	**0,7**	**0,8**

Table 21: XPS chemical composition of tribofilms formed in the presence of solutions containing MoDTC (Mo0.5) or a combination of MoDTC and unmodified TiO_2 nanoparticles (Mo0.5_Ti0.5) 6 days after the blend was prepared. Obtained with a K-ALPHA spectrometer.

We can clearly detect the presence of molybdenum, sulfur, and titanium in the case of the Mo0.5_Ti0.5 mixture, with titanium accounting for 12.5 at.% and present in the form of TiO_2 (Fig. 124).

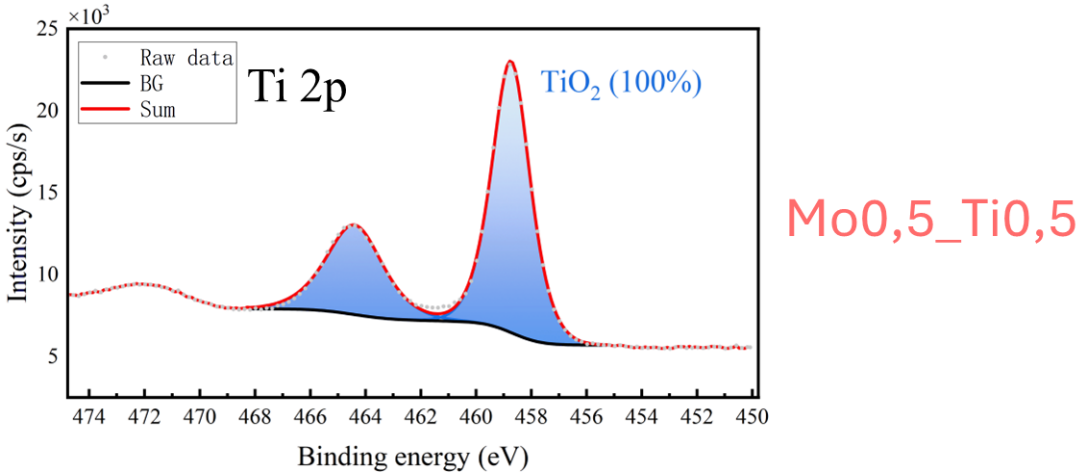

Fig. 124: Ti 2p XPS spectrum of tribofilm formed in presence of a blend containing MoDTC and unmodified TiO_2 nanoparticles (Mo0.5_Ti0.5) 6 days after the blend was prepared. Obtained with a K-ALPHA spectrometer.

When comparing the Mo and S contents in the two tribofilms, it appears that the film formed with the mixture contains a slightly lower relative amount of molybdenum (6.2 at.%) than the one formed with MoDTC alone (8.9 at.%). However, this difference is not necessarily contradictory to the improved friction performance. In this case, what matters most is the chemical state of Mo and S in the tribofilm.

To further investigate the chemical nature of Mo and S within the tribofilm, peak fitting of the Mo 3d and S 2p regions was performed.

Since these peaks can exhibit multiple contributions, a stepwise peak fitting approach was adopted. First off, the pure MoDTC additive was analyzed by depositing a drop onto a silicon wafer. The results are presented in Fig. 125.

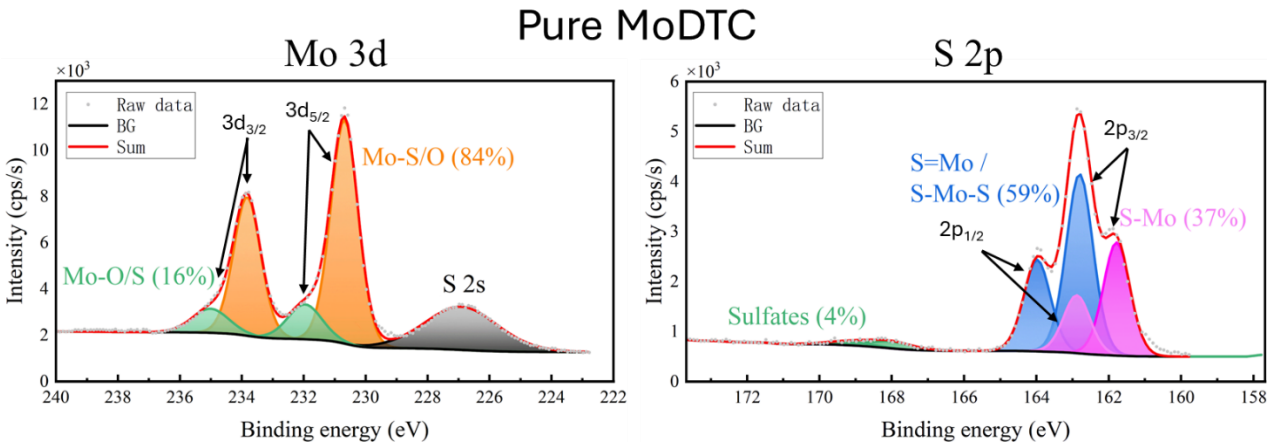

Fig. 125: Mo 3d and S 2p XPS spectra of pure MoDTC deposited as a drop on a silicon wafer. Obtained with a K-ALPHA spectrometer.

In the Mo3d region, three contributions are observed, from right to left:

- S 2s
- A doublet labeled Mo-S/O
- A doublet labeled Mo-O/S

To identify these contributions, the chemical structure of MoDTC was used (Fig. 126). Two possible isomers of MoDTC are presented, labeled (a) and (b). In isomer (a), the molybdenum atoms are bound to an oxygen atom via a double bond, whereas in isomer (b), this oxygen is replaced by a sulfur atom, also with a double bond. Therefore, isomer (a) is slightly more oxidized than (b) and appears further to the left in the Mo 3d peak. Accordingly, the Mo-O/S contribution corresponds to isomer (a), while Mo-S/O corresponds to isomer (b).

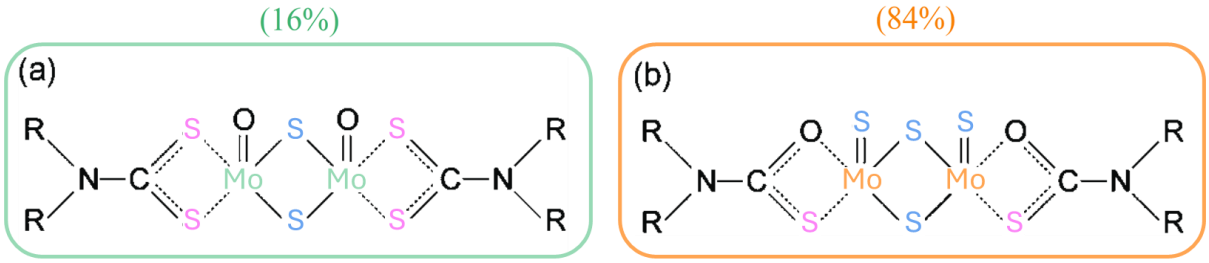

Fig. 126: Chemical structure of MoDTC isomers [14]

Using this approach, the relative ratio of the two isomers is determined: 16 at.% for isomer (a) and 84 at.% for isomer (b).

Based on this ratio, the origin of the two contributions around 163 eV in the S 2p peak (Fig. 125) could also be identified (the one around 168 eV corresponds to sulfates). Examining the structures of the MoDTC isomers once again, both contain two types of sulfur atoms:

- Sulfur bound to a molybdenum atom via a single covalent bond (S-Mo)
- Sulfur bound either to two molybdenum atoms or via a double bond to a molybdenum atom (S=Mo)

In isomer (a), four out of six sulfur atoms are S-Mo (pink), corresponding to 66.6 at.%. In isomer (b), only two out of six are S-Mo, corresponding to 33.3 at.%.

By multiplying the S-Mo fraction by the proportion of each isomer [(0.666 × 0.16) + (0.333 × 0.84)], we obtain 40 at.% of S-Mo and consequently 60 at.% of S=Mo (blue).

These values closely match the contributions observed in the 163 eV region of the S 2p peak with 59 at.% for S-Mo and 37 at.% for S=Mo, with the remaining 4% attributed to sulfates (Fig. 125).

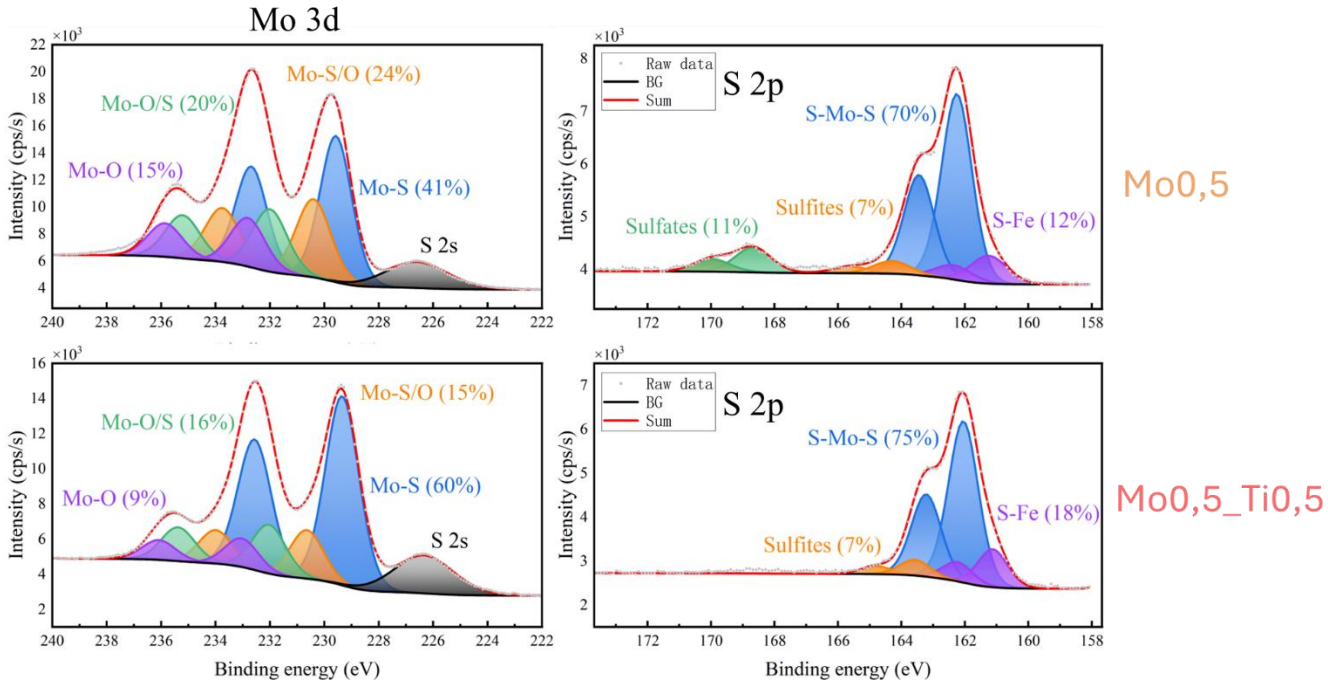

Fig. 127: Mo 3d and S 2p XPS spectra of tribofilms formed in presence of blends containing MoDTC (Mo0.5) or a combination of MoDTC and unmodified TiO_2 nanoparticles (Mo0.5_Ti0.5) 6 days after the blend was prepared. Obtained with a K-ALPHA spectrometer.

We then performed peak fitting for each contribution in the Mo 3d and S 2p spectra of the tribofilms formed with Mo0.5 and Mo0.5_Ti0.5 formulations, as shown in Fig. 127.

For the Mo 3d peak, the contributions previously identified as Mo-S/O and Mo-O/S were included; these may correspond either to unreacted MoDTC isomers present in the tribofilm or to intermediate species. In addition, the contribution associated with the formation of MoS_2 lamellae (Mo-S) was added at 229.3 eV, together with an oxidated decomposition product of MoDTC (Mo-O) appearing at 232.5 eV.

For the S2p peak, sulfates were identified around 168.5 eV, along with sulfites around 164 eV. A major doublet with its $2p_{3/2}$ component at 162 eV was assigned to sulfur atoms in MoS_2 lamellae (S-Mo-S). We must note that S-Mo-S peak position is lower than the one measured for pure MoDTC (162.8 eV). This may be caused by the fact that our MoDTC additive is a liquid which may influence results even after calibration using C1s peak (C-C). Another doublet at 161 eV was attributed to the possible presence of iron sulfide.

The results clearly show that the Mo-S contribution is higher when TiO_2 nanoparticles are present in the formulation (60 at.%) compared to MoDTC alone (41 at.%). Moreover, the presence of TiO_2 nanoparticles appears to suppress the formation of sulfates, and thus may partially inhibit MoDTC oxidation.

Areas outside the friction tracks formed during tribological testing were also analyzed and the results are presented in **Table 22**.

at.%	100°C	
	Mo0,5 out	**Mo0,5_Ti0,5 out**
C 1s	**1,9**	**1,9**
Fe 2p	**50,3**	**50,4**
O 1s	**46,5**	**47,1**
S 2p	**0,2**	**0,0**
Mo 3d	**0,7**	**0,0**
Ti 2p	**0,0**	**0,0**
Ca 2p	**0,4**	**0,6**

Table 22: XPS chemical composition of areas **outside of the tracks** formed in the presence of solutions containing MoDTC (Mo0.5) or a combination of MoDTC and unmodified TiO_2 nanoparticles (Mo0.5_Ti0.5) 6 days after the blend was prepared. Obtained with a K-ALPHA spectrometer.

The compositions outside the tracks are very similar for the two formulations, except for Mo, which is only detected when of MoDTC is used alone (Mo0.5). Peak fitting was therefore conducted to identify the chemical nature of this Mo, as shown in Fig. 128.

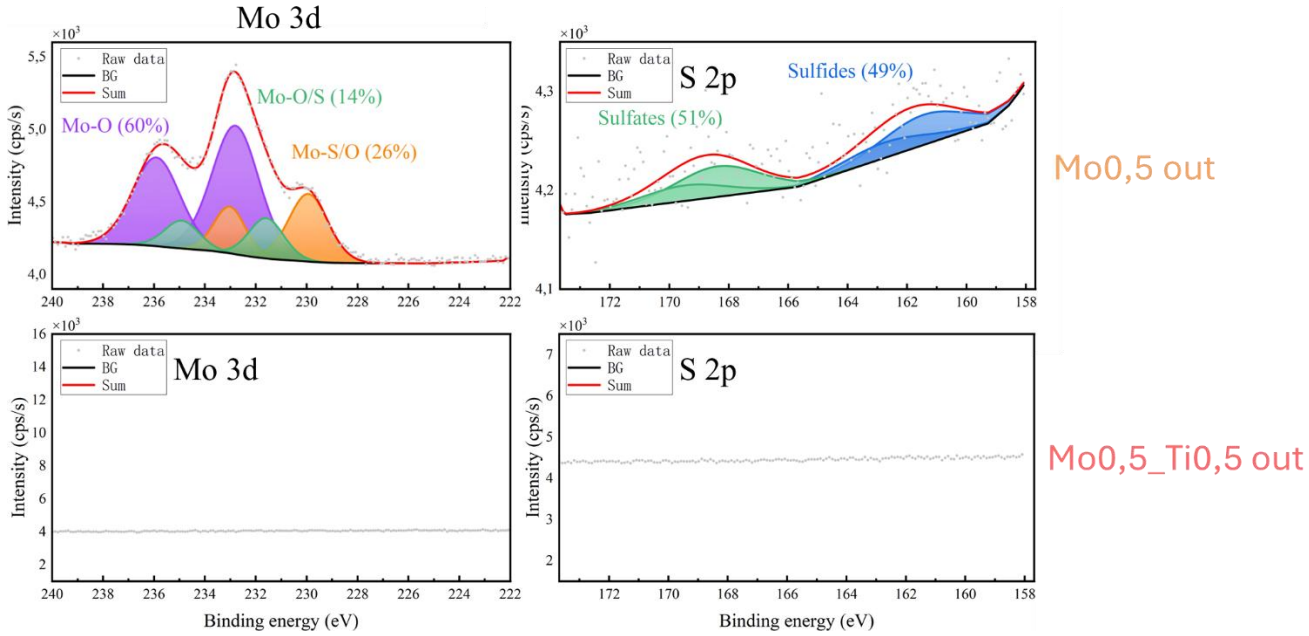

*Fig. 128: Mo 3d and S 2p XPS spectra of areas **outside of the tracks** formed in presence of blends containing MoDTC (Mo0.5) or a combination of MoDTC and unmodified TiO_2 nanoparticles (Mo0.5_Ti0.5) 6 days after the blend was prepared. Obtained with a K-ALPHA spectrometer.*

For the formulation containing only MoDTC (Mo0.5), molybdenum is detected despite the absence of a sliding contact, indicating that MoDTC can decompose on the steel surface under the effect of heat alone, leading in particular to the formation of molybdenum oxides. However, almost no sulfur was detected, confirming the absence of sulfur-containing species like MoS_2. In contrast, for the Mo0.5_Ti0.5 mixture, neither molybdenum nor sulfur was detected. The presence of TiO_2 thus seems to prevent MoDTC oxidation outside the tribological contact.

For Mo0,5, one might consider this oxide formation negligible (0.7 at.%). However, it must be taken into account that it occurs across the entire steel surface in contact with the lubricant, which represents a significant loss pathway for MoDTC under real operating conditions. This parasitic reaction consumes part of the additive and limits its ability to form effective tribofilms, thereby reducing its friction-reducing potential unless higher concentrations are used. The presence of TiO_2, on the other hand, helps to mitigate this undesirable reaction and allows MoDTC to express its full effectiveness.

In summary, the combination of MoDTC with TiO_2 nanoparticles leads to a greater reduction in the coefficient of friction, a slightly improved suspension stability, and a higher proportion of MoS_2 in the tribofilms compared to MoDTC alone.

Beyond this statement, our study also provides additional insights. Several lines of evidence indicate physical interactions occurring between MoDTC and TiO_2 nanoparticles, including the need for an incubation time before the formulations become effective, the improved - though still limited - colloidal stability of the mixture, and the absence of oxidized Mo species outside the wear tracks when nanoparticles are present. Together, these observations strengthen the hypothesis that the synergy relies on physicochemical interactions between the two additives occurring prior to tribological contact.

Moreover, a reduction in the total amount of molybdenum detected within the wear track was also observed with the mixture (Mo0.5_Ti0.5), suggesting that the improved tribological performance is achieved with a lower consumption of MoDTC. This implies that TiO_2 acts as a mediator that promotes a more targeted and controlled activation of MoDTC, effectively serving as a catalyst-like carrier or a vector for its conversion into MoS_2 within the tribological contact.

Taken together, these results demonstrate that TiO_2 nanoparticles can interact with MoDTC in a way that enhances friction reduction, improves stability, and promotes a more efficient use of the additive. However, the limited colloidal stability of unmodified nanoparticles remains a significant limitation, raising concerns about the robustness of such formulations under practical operating conditions.

To overcome this drawback, we next investigated whether similar synergies could be achieved with functionalized TiO_2 nanoparticles, which exhibit much higher colloidal stability. The following section therefore focuses on the interactions between MoDTC and TiO_2 nanoparticles functionalized with either oleic acid or with silane.

3.2.1.2 Influence of Functionalizing Agent Chemical Nature on the Synergistic Effects Between MoDTC and TiO_2 Nanoparticles

The experimental campaign for this section has been conducted using 10 mm balls with a contact pressure of 0.83 GPa.

Formulations studied in this section are presented in **Table 23.**

Composition	Name
PAO6	PAO6
PAO6 + 0.5 wt.% MoDTC	Mo0.5
PAO6 + 0.5 wt.% MoDTC + 0.5 wt.% oleic acid-functionalized TiO_2 NPs	Mo0.5_Tif(OA)0.5
PAO6 + 0.5 wt.% MoDTC + 0.5 wt.% silane-functionalized TiO_2 NPs	Mo0.5_Tif(Si)0.5

Table 23: Composition and name of tribologically tested blends used for the study of MoDTC and oleic acid- or silane-functionalized TiO_2 nanoparticles interactions.

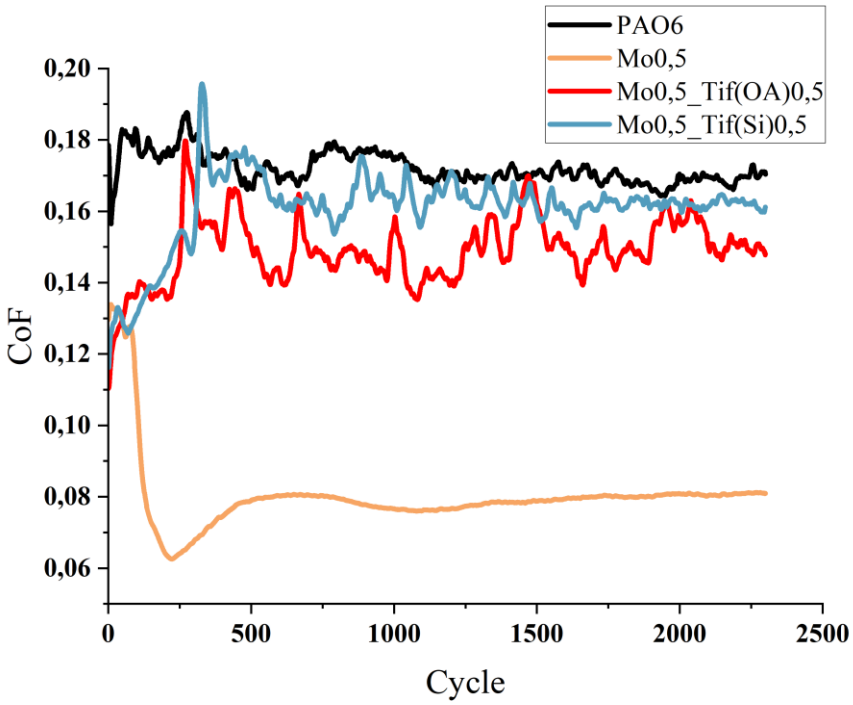

Fig. 129: Evolution of friction coefficient with cycles at 100°C and 0.83 GPa pressure for the samples containing MoDTC (Mo0.5) and a blend of MoDTC and either oleic acid- or silane-functionalized TiO_2 nanoparticles (Mo0.5_Tif(OA)0.5 and Mo0.5_Tif(Si)0.5, respectively). PAO6 base oil is used as a reference.

Fig. 129 shows the evolution of the coefficient of friction with sliding cycles. MoDTC alone behaves similarly to the tests performed with 6 mm balls (Fig. 120), with friction stabilizing around 0.08. However, in this case, the addition of functionalized TiO_2 nanoparticles - either with oleic acid or with silane - results in an increase of the CoF, reaching values close to that of the base oil (PAO6) and displaying even greater instability. As with unmodified nanoparticles, we conducted tribological tests 1 and 6 days after sample preparation but this time they did not show any improvement.

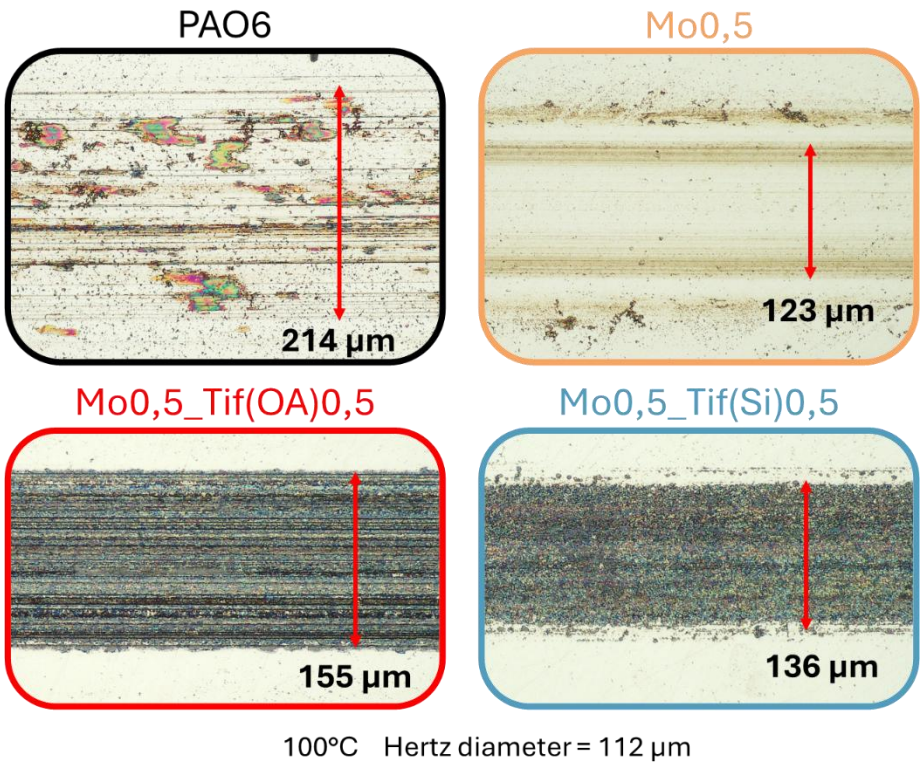

Fig. 130: Optical observations of wear tracks formed at 100°C on the discs in the presence of solutions containing MoDTC (Mo0.5) or a combination of MoDTC and either oleic acid- or silane-functionalized TiO_2 nanoparticles (Mo0.5_Tif(OA)0.5 and Mo0.5_Tif(Si)0.5, respectively). With PAO6 base oil used as a reference.

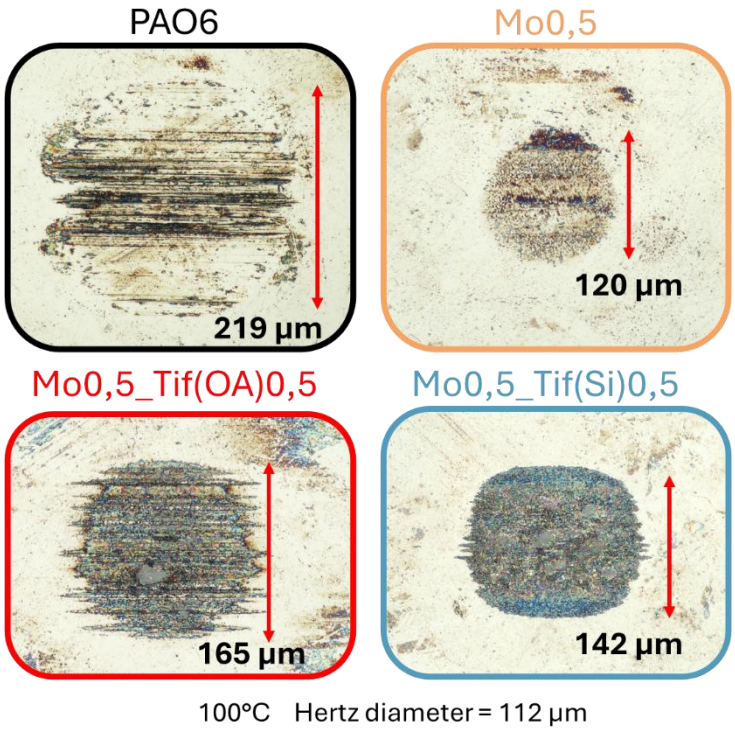

Fig. 131: Optical observations of wear tracks formed at 100°C on the balls in the presence of solutions containing MoDTC (Mo0.5) or a combination of MoDTC and either oleic acid- or silane-functionalized TiO_2 nanoparticles (Mo0.5_Tif(OA)0.5 and Mo0.5_Tif(Si)0.5, respectively). With PAO6 base oil used as a reference.

Regarding wear, MoDTC again exhibits a behavior similar to the one observed using 6 mm balls: the wear track width on both the disc (Fig. 130) and the ball (Fig. 131) is close to the Hertzian diameter (123 and 120 µm, respectively). For the mixtures containing functionalized nanoparticles, despite the high friction values, the wear track widths are significantly smaller than with PAO6. In addition, the formation of a tribofilm is observed on both the disc and the ball for nanoparticles functionalized with either oleic acid (Mo0.5_Tif(OA)0.5) or silane (Mo0.5_Tif(Si)0.5).

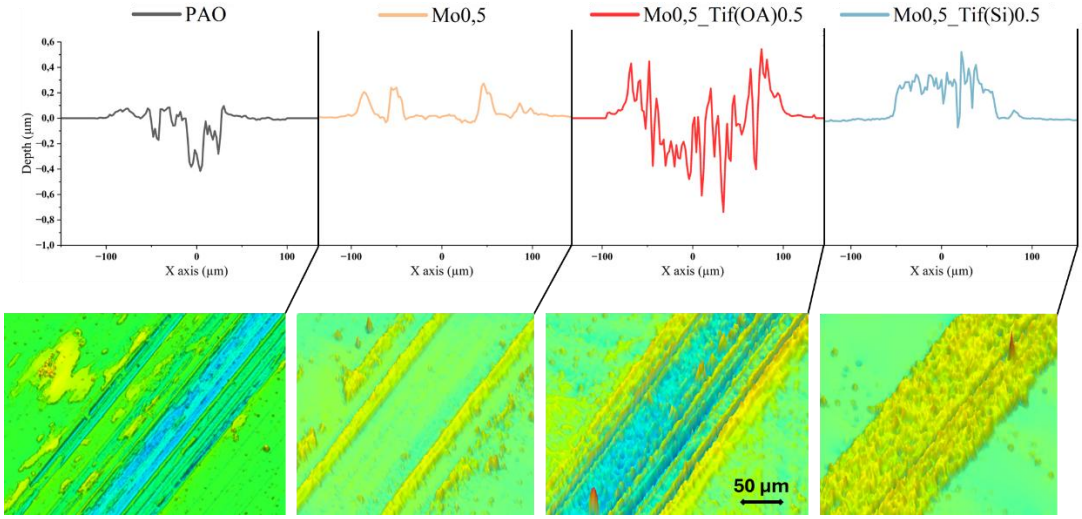

Fig. 132: Mean depth profiles and surface morphology of wear tracks formed at 100°C on the discs in the presence of solutions containing MoDTC (Mo0.5) or a combination of MoDTC and either oleic acid- or silane-functionalized TiO_2 nanoparticles (Mo0.5_Tif(OA)0.5 and Mo0.5_Tif(Si)0.5, respectively). With PAO6 base oil used as a reference.

Profilometric measurements (Fig. 132) nevertheless reveal severe wear for the MoDTC/oleic acid-functionalized nanoparticles mixture. This suggests that, although a tribofilm is formed, it does not provide sufficient protection, either because it forms too late or because it lacks mechanical robustness. The presence of MoDTC does not contribute to friction reduction in this case and appears to even diminish the previously established good anti-wear performance of oleic acid-functionalized nanoparticles (3.1.1). MoDTC used alone on the other hand does not induce any measurable wear and the tribofilm is not detectable either.

In contrast, for the mixture with silane-functionalized nanoparticles, the behavior is different. These nanoparticles were previously shown to form a tribofilm very quickly, although it eventually wore away and ceased to protect the surface (3.1.2). Here, while the addition of MoDTC does not lower the CoF either, the tribofilm formed is significantly thicker, ranging between 200 and 300 nm.

Overall, these results suggest that, although MoDTC does not contribute to a reduction in friction in this case, it can still influence the anti-wear performance of functionalized TiO_2 nanoparticles - sometimes beneficially, sometimes detrimentally depending on the nature of the functionalizing agent.

It should also be noted that, unlike unmodified nanoparticles, allowing the mixtures to rest for several days prior to testing does not lead to improved results. In the case of unmodified TiO_2, we previously hypothesized that this incubation time was necessary to enable physical interactions between MoDTC and the nanoparticles. For functionalized TiO_2, however, it is likely that the functionalizing agent hinders the access of MoDTC to the nanoparticle surface, thereby preventing the MoDTC/TiO_2 synergy from occurring. This observation further supports our hypothesis that the synergistic effect relies on interactions between the additives taking place prior to tribological contact.

at.%	100°C		
	Mo0,5	Mo0,5_Tif(OA)0,5	Mo0,5_Tif(Si)0,5
C 1s	23,3	16,5	25,6
Fe 2p	15,0	10,5	4,8
O 1s	45,8	53,2	48,0
S 2p	6,1	0,5	0,7
Mo 3d	8,6	0,3	0,6
Ti 2p	0,0	18,6	17,5
Si 2p	0,0	0,0	1,3
Ca 2p	1,3	0,4	1,4

Table 24: XPS chemical composition of tribofilms formed in the presence of solutions containing MoDTC (Mo0.5) or a combination of MoDTC and either oleic acid- or silane-functionalized TiO_2 nanoparticles (Mo0.5_Tif(OA)0.5 and Mo0.5_Tif(Si)0.5, respectively). Obtained with a NEXSA spectrometer.

XPS analyses were again performed on the wear tracks, as summarized in **Table 24**. For MoDTC alone (Mo0.5), the values are consistent with those obtained using 6 mm balls, with the exception of sulfur, which is slightly lower (6.1 vs. 7.7 at.%). As expected, in the case of formulations containing functionalized nanoparticles, low amounts of molybdenum and sulfur are detected (<1 at.%). In contrast, relatively high titanium contents are observed: 18.6 at.% for Mo0.5_Tif(OA)0.5 and 17.5 at.% for Mo0.5_Tif(Si)0.5.

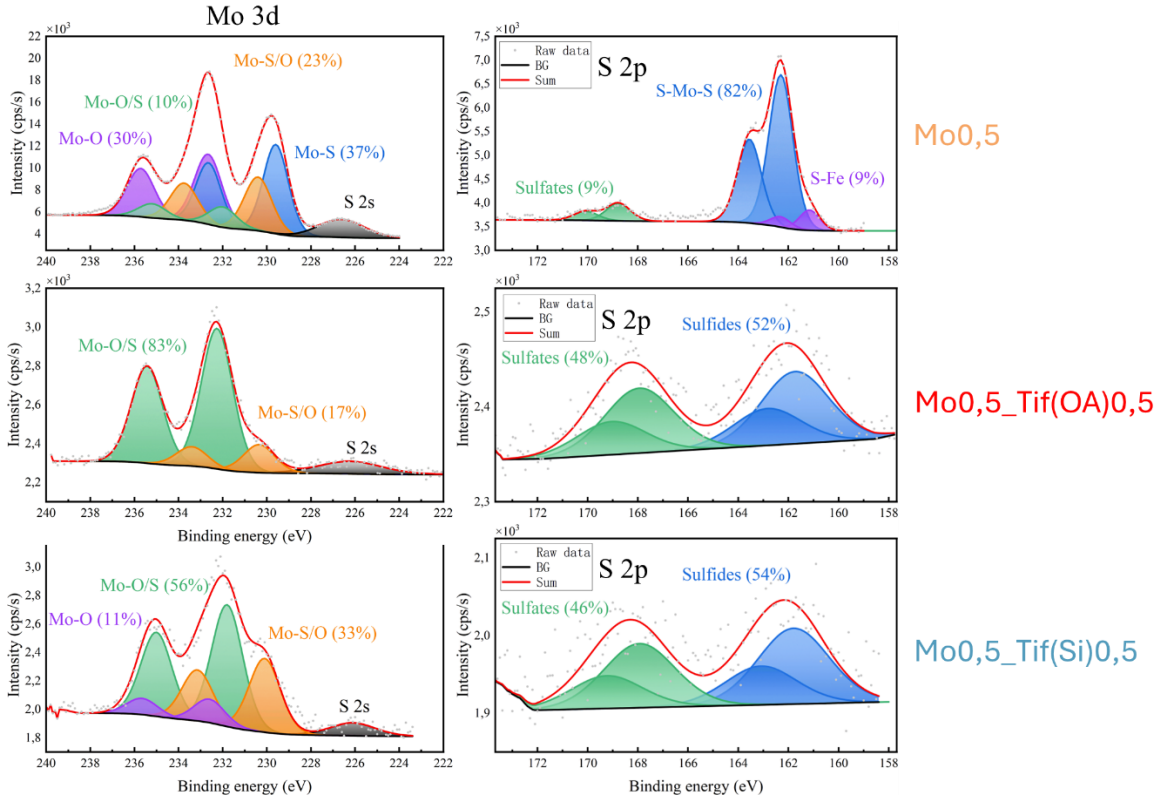

Fig. 133: Mo 3d and S 2p XPS spectra of tribofilms formed in presence of blends containing MoDTC (Mo0.5) or a combination of MoDTC and either oleic acid- or silane-functionalized TiO_2 nanoparticles (Mo0.5_Tif(OA)0.5 and Mo0.5_Tif(Si)0.5, respectively). Obtained with a NEXSA spectrometer.

The peak-fitting of Mo 3d and S 2p spectra (Fig. 133) confirm, on the one hand, that MoDTC alone decomposes to MoS_2 with a yield comparable to that obtained with 6 mm balls (37 and 41 at.%, respectively), and on the other hand, the absence of MoS_2 in the mixtures containing MoDTC and functionalized nanoparticles. In these cases, molybdenum is found predominantly in either fully or partially oxidized forms.

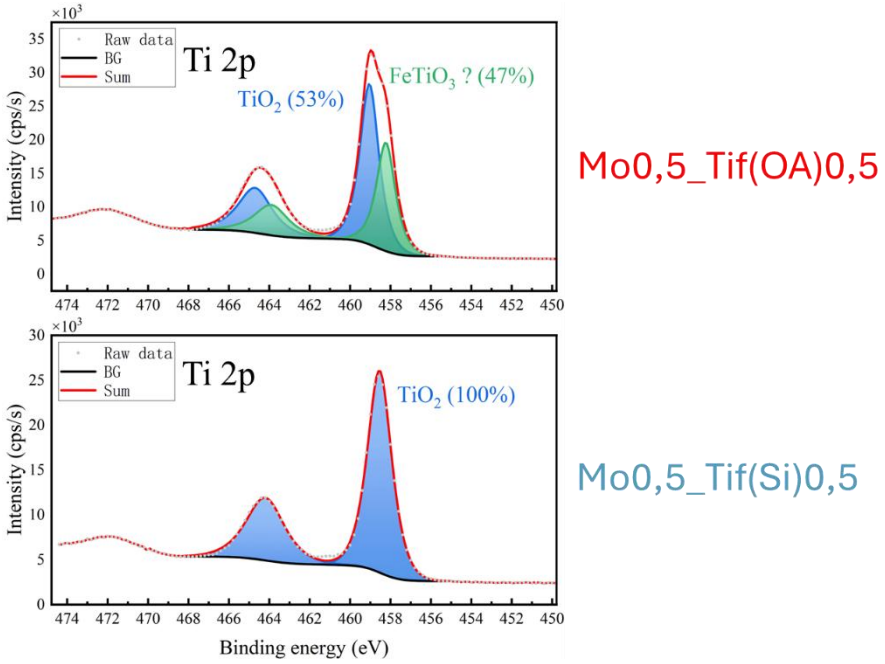

Fig. 134: Ti 2p XPS spectra of tribofilms formed in presence of blends containing MoDTC (Mo0.5) or a combination of MoDTC and either oleic acid- or silane-functionalized TiO_2 nanoparticles (Mo0.5_Tif(OA)0.5 and Mo0.5_Tif(Si)0.5, respectively). Obtained with a NEXSA spectrometer.

The Ti 2p region was also analyzed (Fig. 134). For the Mo0.5_Tif(OA)0.5 formulation, titanium is detected as a blend of TiO_2 and potentially iron titanate ($FeTiO_3$). In the previous section on silane-functionalized nanoparticles used alone (3.1.2), we showed that $FeTiO_3$ forms during the first sliding cycles and is therefore located on the steel substrate. It is therefore possible that a similar mechanism occurs with the tribofilm formed with oleic acid-functionalized nanoparticles, and that the wear observed in Fig. 132 exposes this underlying layer.

at.%	100°C		
	Mo0,5 out	**Mo0,5_Tif(OA)0,5 out**	**Mo0,5_Tif(Si)0,5 out**
C 1s	**16,3**	**15,4**	**15,6**
Fe 2p	**25,8**	**18,1**	**30,0**
O 1s	**53,4**	**55,3**	**50,2**
S 2p	**0,4**	**0,2**	**0,5**
Mo 3d	**2,7**	**0,1**	**0,1**
Ti 2p	**0,0**	**9,9**	**0,9**
Si 2p	**0,0**	**0,0**	**1,2**
Ca 2p	**1,4**	**1,1**	**1,4**

Table 25: XPS chemical composition of areas **outside of the tracks** formed in the presence of solutions containing MoDTC (Mo0.5) or a combination of MoDTC and either oleic acid- or silane-functionalized TiO2 nanoparticles (Mo0.5_Tif(OA)0.5 and Mo0.5_Tif(Si)0.5, respectively). Obtained with a NEXSA spectrometer.

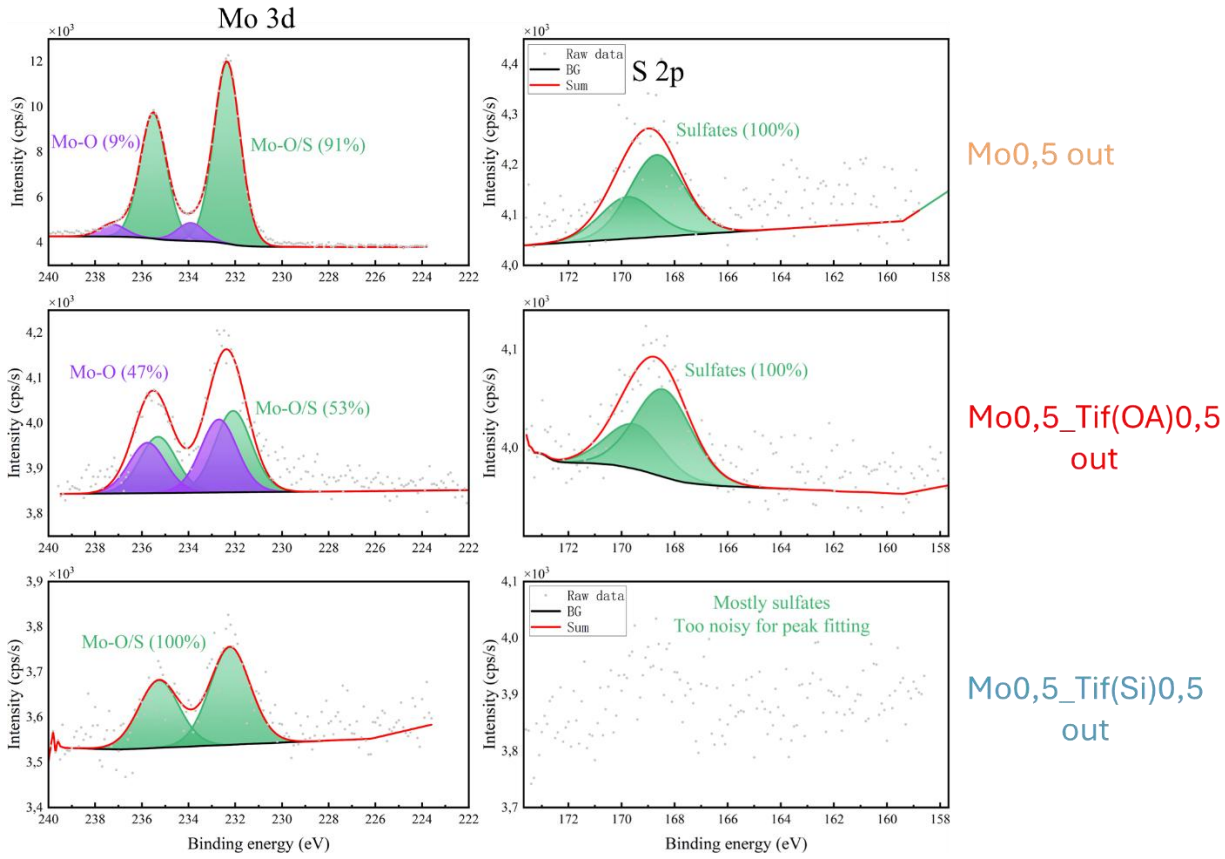

*Fig. 135: Mo 3d and S 2p XPS spectra of areas **outside of the tracks** formed in presence of blends containing MoDTC (Mo0.5) or a combination of MoDTC and either oleic acid- or silane-functionalized TiO_2 nanoparticles (Mo0.5_Tif(OA)0.5 and Mo0.5_Tif(Si)0.5, respectively). Obtained with a NEXSA spectrometer.*

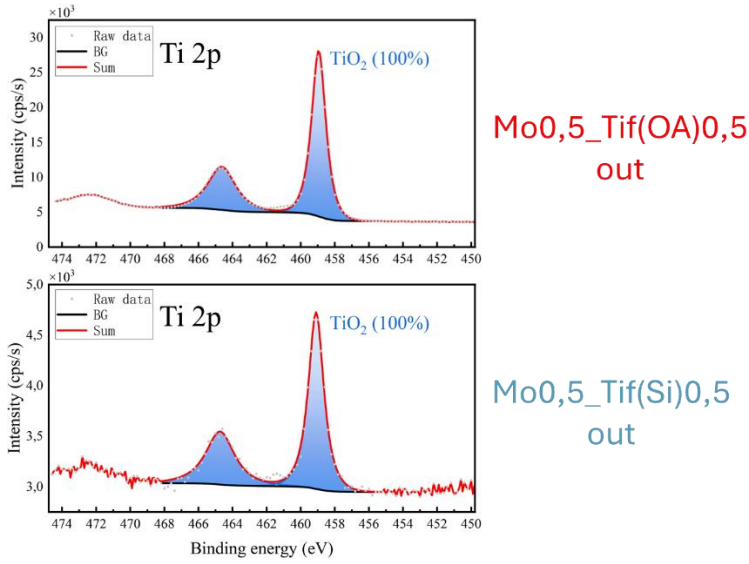

*Fig. 136: Ti 2p XPS spectra of areas **outside of the tracks** formed in presence of blends containing MoDTC (Mo0.5) or a combination of MoDTC and either oleic acid- or silane-functionalized TiO_2 nanoparticles (Mo0.5_Tif(OA)0.5 and Mo0.5_Tif(Si)0.5, respectively). Obtained with a NEXSA spectrometer.*

XPS analyses were also carried out on the discs outside the wear tracks (**Table 25**). For MoDTC alone, molybdenum is detected at 2.7 at.%, present in oxidized forms (Fig. 135). For the mixtures containing functionalized nanoparticles, only trace amounts of Mo are detected (0.1 at.%). In contrast, a significant amount of titanium is found for the oleic acid-functionalized nanoparticles (9.9 at.%) but not for silane-functionalized ones (0.9 at.%). Given the lower colloidal stability of the oleic acid functionalization, this is most likely due to nanoparticles precipitation under the effect of heat, followed by deposition on the disc surface. In both types of functionalized nanoparticles, titanium is present as TiO_2 (Fig. 136).

In summary, our results demonstrate that a synergy between MoDTC and TiO_2 nanoparticles is indeed possible, but that it strongly depends on their ability to interact physicochemically. When functionalized nanoparticles are used, the TiO_2 surface becomes inaccessible, and the synergy that enables a significant reduction in friction is no longer observed. Nevertheless, MoDTC still influences tribofilm formation, either positively or negatively depending on the nature of the functionalizing agent. Specifically, we observed a clear incompatibility with oleic acid-functionalized nanoparticles, whereas silane-functionalized nanoparticles not only avoided this incompatibility but even showed a beneficial effect on wear reduction.

A possible explanation for the degradation of MoDTC performance in the presence of functionalized nanoparticles could lie in their high surface reactivity. As shown in Section 3.1.2, Tif(Si)1 reacts very rapidly with the steel surface - within the first ten cycles. MoDTC also reacts quickly, but since the reduction in the coefficient of friction occurs only after about 100 cycles when used alone, its activation is probably slower. It is therefore plausible that the nanoparticles initially block MoDTC access to the steel surface by rapidly forming a tribofilm, thus preventing the early formation of MoS_2. In a later stage, because the nanoparticles are encapsulated by the functionalizing agent, MoDTC cannot interact with them as it does with non-functionalized nanoparticles, and consequently, it cannot be efficiently incorporated into the tribofilm.

Building on the insights gained from the study of MoDTC-TiO_2 interactions, it is equally important to investigate whether similar synergistic effects can be achieved with other lubricant additives. Among these, ZDDP is of particular interest, given its widespread use as an anti-wear additive in engine and transmission oils. Understanding how ZDDP interacts with TiO_2 nanoparticles could open new perspectives for enhancing both tribological performance and formulation stability.

3.2.2 Interactions Between ZDDP and TiO_2

This part of the work is therefore dedicated to the study of ZDDP–TiO_2 interactions and will be divided into two subsections. The first will examine the effect of the dispersion method of TiO_2 nanoparticles, comparing formulations where the particles are stabilized with oleic acid either through simple addition (physical dispersion) or through chemical grafting (functionalization). The second subsection will then focus more specifically on the role of functionalization, highlighting how the chemical nature of the grafting agent (oleic acid versus silane) influences the interaction between ZDDP and TiO_2 nanoparticles.

3.2.2.1 Influence of the Dispersion Method on the Interactions Between ZDDP and TiO_2 Nanoparticles

For this study, the tribological conditions are the same as the one used in section 3.1.1 presented in **Table *13*** with a 10 mm ball and a 1.03 GPa contact pressure.

Formulations studied in this section are presented in **Table 26**.

Composition	Name
PAO6	PAO6
PAO6 + 1wt.% TiO_2 NP powder + 1wt.% OA	Ti1_OA1
PAO6 + 1wt.% oleic acid-functionalized TiO_2 NP	Tif(OA)1
PAO6 + 1wt.% ZDDP (820 ppm of phosphorus)	Zn1
PAO6 + 1wt.% ZDDP + 0.5wt.% TiO_2 NP powder + 1wt.% OA	Zn1_Ti0.5_OA1
PAO6 + 1wt.% ZDDP + 0.5wt.% oleic acid-functionalized TiO_2 NP	Zn1_Tif(OA)0.5

Table 26: Composition and name of tribologically tested blends used for the study of ZDDP and oleic acid-functionalized TiO_2 nanoparticles interactions.

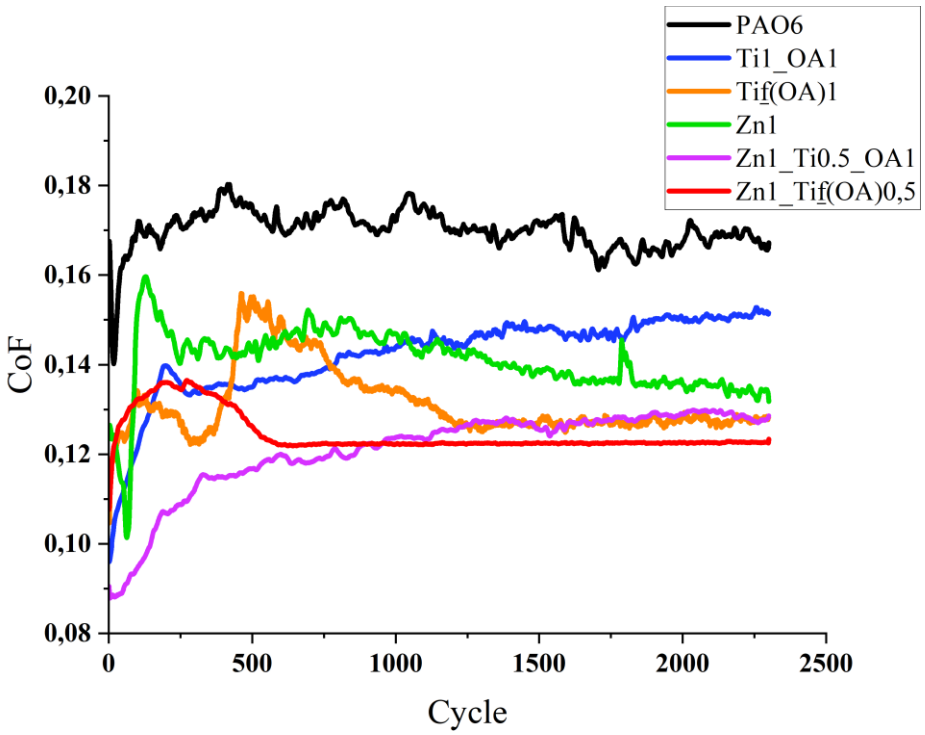

Fig. 137: Evolution of friction coefficient with cycles at 100°C for the samples containing ZDDP, dispersed TiO_2 nanoparticles, functionalized TiO_2 nanoparticles or a combination of ZDDP and dispersed or functionalized TiO_2 nanoparticles. With PAO6 base oil used as a reference.

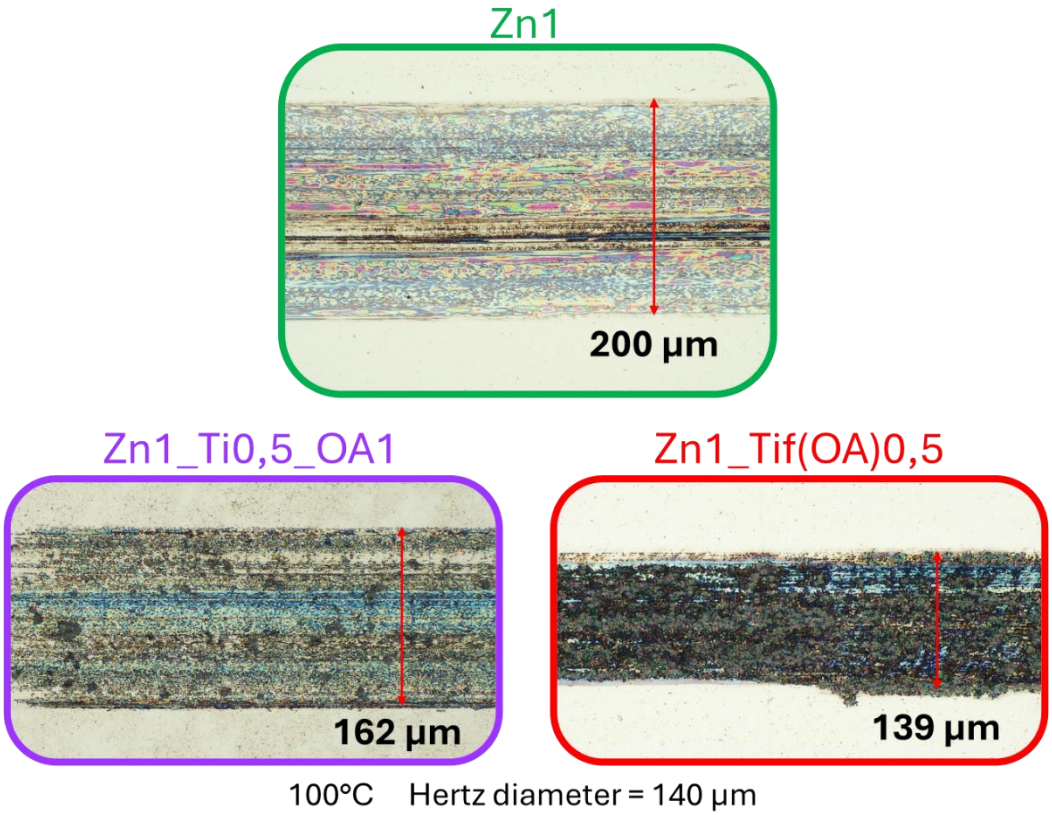

Fig. 138: Optical observations of wear tracks formed at 100°C on the discs in the presence of solutions containing ZDDP (Zn1) or a combination of ZDDP and dispersed (Zn1_Ti0.5_OA1) or functionalized (Zn1_Tif(OA)1) TiO_2 nanoparticles.

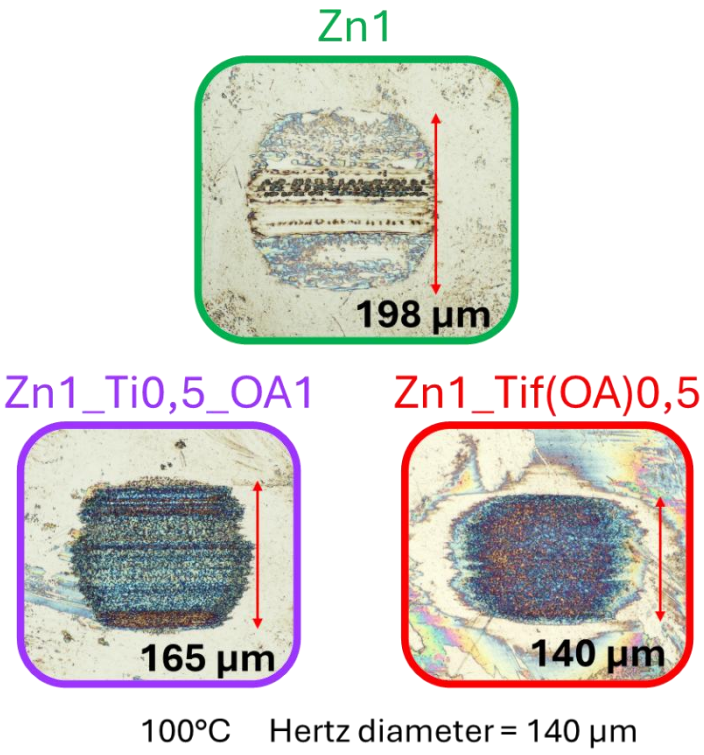

Fig. 139: Optical observations of wear tracks formed at 100°C on the balls in the presence of solutions containing ZDDP (Zn1) or a combination of ZDDP and dispersed (Zn1_Ti0.5_OA1) or functionalized (Zn1_Tif(OA)1) TiO_2 nanoparticles.

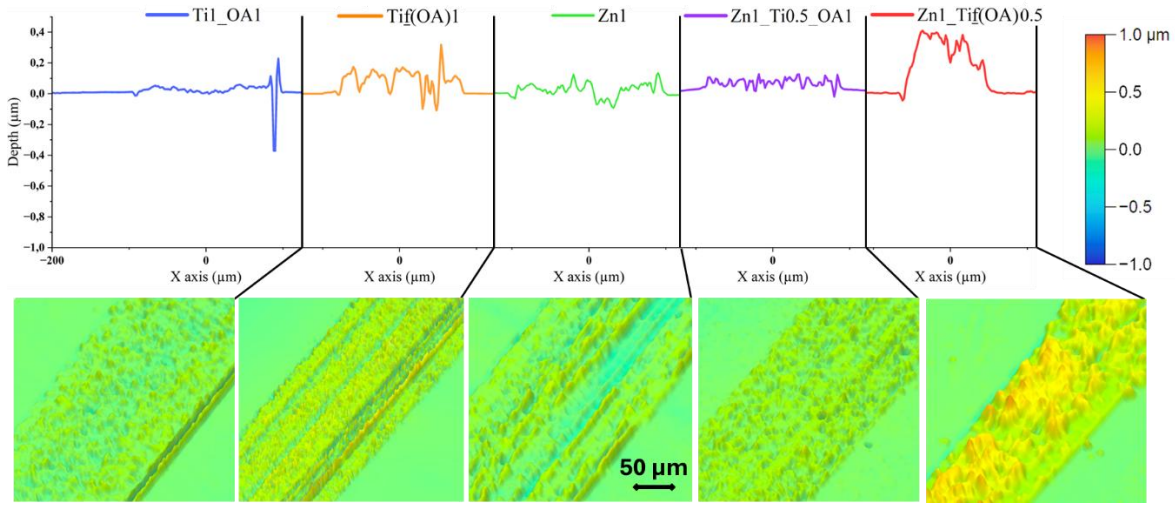

Fig. 140: Mean depth profiles and surface morphology of wear tracks formed at 100°C on the discs in the presence of solutions containing ZDDP (Zn1) or a combination of ZDDP and dispersed (Zn1_Ti0.5_OA1) or functionalized (Zn1_Tif(OA)1) TiO_2 nanoparticles.

Fig. 137 presents the CoF evolution for lubricants containing TiO_2 nanoparticles, previously introduced as Ti1_OA1 (dispersed nanoparticles with oleic acid) and Tif(OA)1 (functionalized nanoparticles with oleic acid), compared to our reference anti-wear additive, ZDDP (Zn1). With dispersed nanoparticles (Ti1_OA1), the CoF is more stable than with ZDDP (Zn1) but reaches higher values at the end of the test (0.15 and 0.13 respectively). On the other hand, the use of functionalized nanoparticles shows better friction reduction properties as CoF value decreases to 0.125 from 1200 cycles and remains stable until the end of the test. Interestingly, we can link the friction behavior with the wear observed in Fig. 138 and Fig. 139. For Zn1, the CoF initially reaches a relatively high value (~0.16) before decreasing. This behavior suggests that significant wear occurred early in the test, prior to the formation of a protective tribofilm. As a result, Zn1 exhibited a higher friction track width and a larger wear diameter at the end of the test compared to nanoparticles solutions containing oleic acid. The presence of OA facilitates effective friction reduction and wear protection at least during the first cycles, providing sufficient time for a tribofilm to form and stabilize.

We then combined ZDDP with these two types of nanoparticles suspension, resulting in the formulations Zn1_Ti0.5_OA1 and Zn1_Tif(OA)0.5.

First off, for dispersed NPs, when comparing Ti1_OA1 formulation to Zn1_Ti0.5_OA1 formulation, we observe that the addition of ZDDP leads to a lower CoF, stabilizing at 0.125. This highlights the synergistic effect of ZDDP and TiO_2 nanoparticles dispersed with oleic acid, which further reduces friction compared to either additive used alone. If we then compare Fig. 83 and Fig. 138, we can see that friction track width is lower with Zn1_Ti0.5_OA1 than with Ti1_OA1 (162 vs 186 µm) and the tribofilm also seems to have better coverage. Better anti-wear properties are confirmed in Fig. 140 with overall mean profiles, profile area and maximum height values that are greater with Zn1_Ti0.5_OA1.

A similar observation can be made with functionalized NPs when comparing Tif(OA)1 with Zn1_Tif(OA)0.5. Here, the addition of ZDDP not only decreases the CoF but also reduces the induction time from approximately 1200 cycles to 500 cycles. This reduction in induction time suggests faster tribofilm formation when ZDDP is combined with functionalized nanoparticles which ensure good wear protection as most of the wear is generated during this critical unprotected running-in phase. Furthermore, the resulting CoF is more stable, reflecting improved consistency in the lubrication process.

For anti-wear properties, as shown in Fig. 138, the friction track width closely approaches the theoretical minimum Hertz diameter (140 µm). Additionally, surfaces lubricated with the combination of Tif(OA)1 and ZDDP display significantly different facies morphologies compared to those with Tif(OA)1 alone (Fig. 2). Notably, very thick patches form across the track, as evidenced by profilometer analysis, showing a maximum deposit height of ~400 nm compared to ~200 nm for Tif(OA)1 alone. These findings confirm a synergistic effect between ZDDP and TiO_2 nanoparticles stabilized in PAO base oil.

Finally, comparing dispersed (Zn1_Ti0.5_OA1) and functionalized (Zn1_Tif(OA)0.5) nanoparticles mixed with ZDDP, we see that both achieve a low stabilized CoF of approximately 0.125 and 0.12, respectively. However, the mixture with functionalized nanoparticles (Zn1_Tif(OA)0.5) exhibits a more stable friction behavior, with less variation in the CoF over time. Moreover, the repeatability in CoF values and variations is better with Zn1_Tif(OA)0.5 as we can see in Fig. 141. This suggests that functionalized nanoparticles not only enhance friction reduction but also contribute to a more uniform tribological performance. We can see in Fig. 142 that contrary to Zn1_Ti0.5_OA1, the functionalized blend Zn1_Tif(OA)0.5 remains stable during tribological testing at 100C° which could explain the better consistency observed.

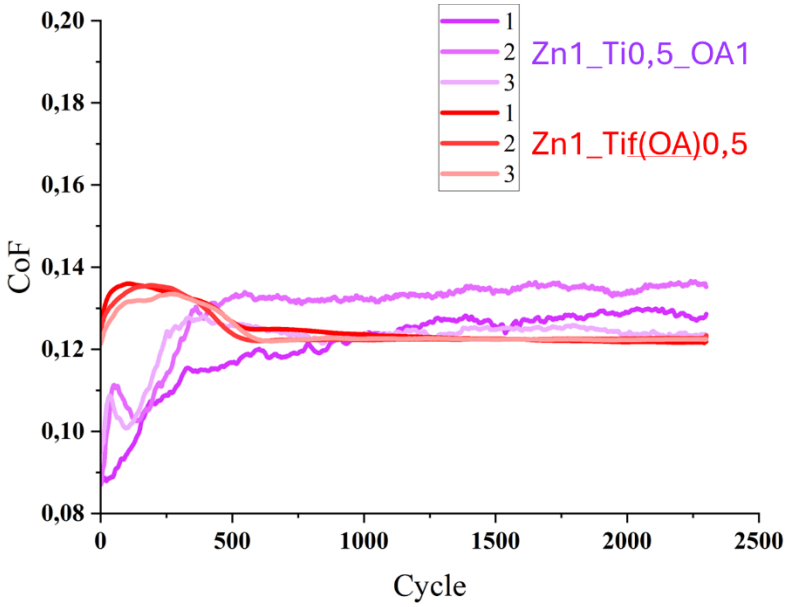

Fig. 141: Friction tests repeatability at 100°C for the samples containing a combination of ZDDP and dispersed (Zn1_Ti0.5_OA1) or functionalized (Zn1_Tif(OA)1) TiO_2 nanoparticles. Three repetitions were carried out for each blend.

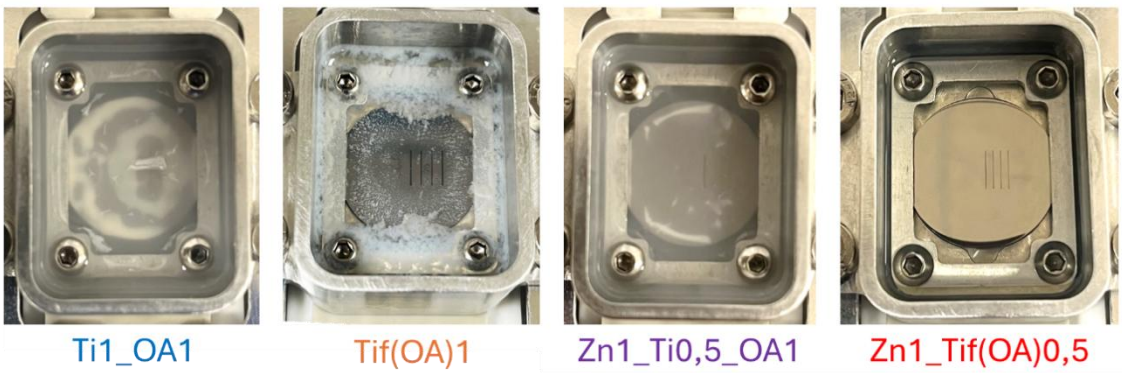

Fig. 142: Pictures of discs in their lubricant bath after tribological testing at 100°C in solutions containing dispersed (Ti1_OA1) or functionalized (Tif(OA)1) TiO_2 nanoparticles or a blend of ZDDP with dispersed (Zn1_Ti0.5_OA1) or functionalized (Zn1_Tif(OA)0.5) TiO_2 nanoparticles.

At 25 °C, ZDDP (Zn1) exhibits an initial friction coefficient of 0.13, which rapidly decreases to 0.10 after 400 cycles, before gradually increasing again to 0.14 by the end of the test (Fig. 143). In contrast, the addition of dispersed nanoparticles (Zn1_Ti0.5_OA1) reduces friction to around 0.11, likely due to the presence of oleic acid in the mixture. When oleic acid-functionalized nanoparticles are added (Zn1_Tif(OA)0.5), the friction coefficient initially rises to 0.13 but subsequently shows a downward trend, reaching a final value of 0.105 at the end of the test.

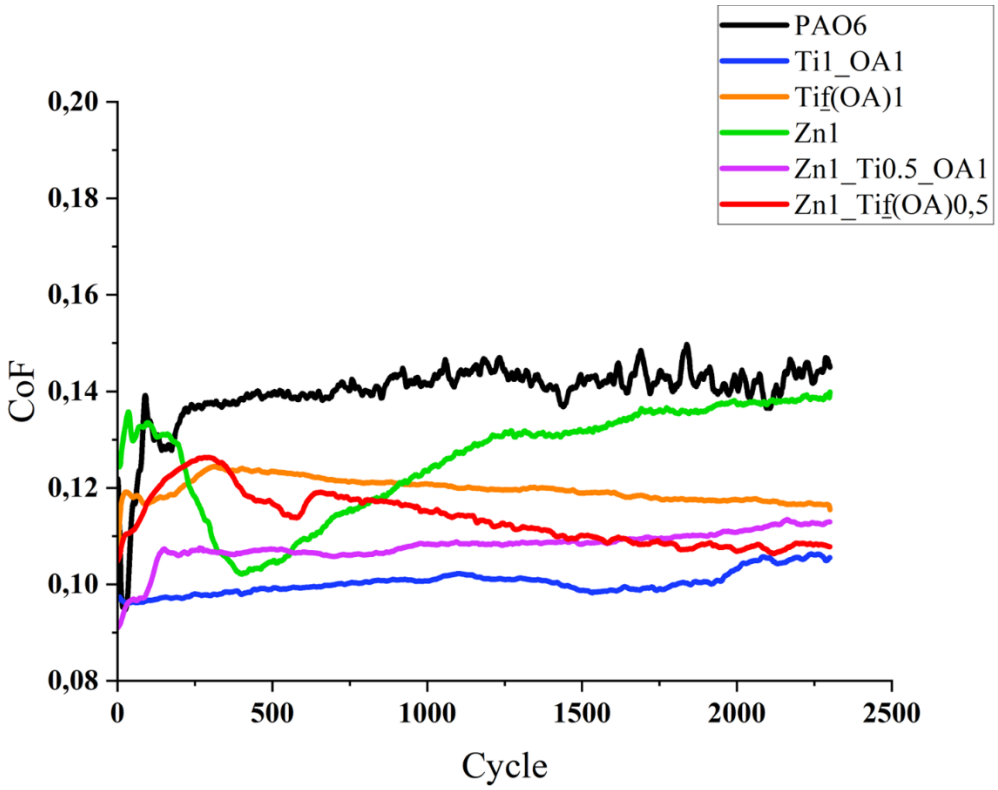

Fig. 143: Evolution of friction coefficient with cycles at 25°C for the samples containing ZDDP, dispersed TiO_2 nanoparticles, functionalized TiO_2 nanoparticles or a combination of ZDDP and dispersed or functionalized TiO_2 nanoparticles, with PAO6 base oil used as a reference.

Regarding wear, the only formulation that appears to form a thick tribofilm on the disc at 25°C is the mixture containing ZDDP and oleic acid-functionalized TiO_2 nanoparticles, as shown in Fig. 144. On the balls, however, a tribofilm is observed both with ZDDP / dispersed nanoparticles (Zn1_Ti0.5_OA1) and with ZDDP / oleic acid-functionalized nanoparticles (Zn1_Tif(OA)0.5) (Fig. 145).

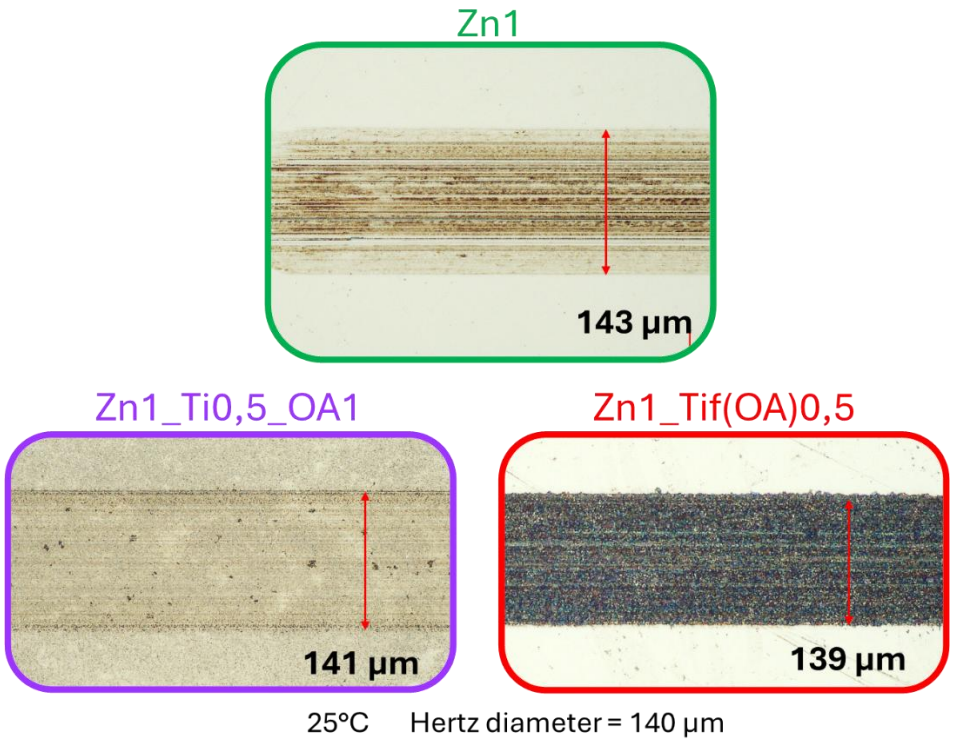

Fig. 144: Optical observations of wear tracks formed on the discs in the presence of solutions containing ZDDP (Zn1) or a combination of ZDDP and dispersed (Zn1_Ti0.5_OA1) or functionalized (Zn1_Tif(OA)0.5) TiO_2 nanoparticles.

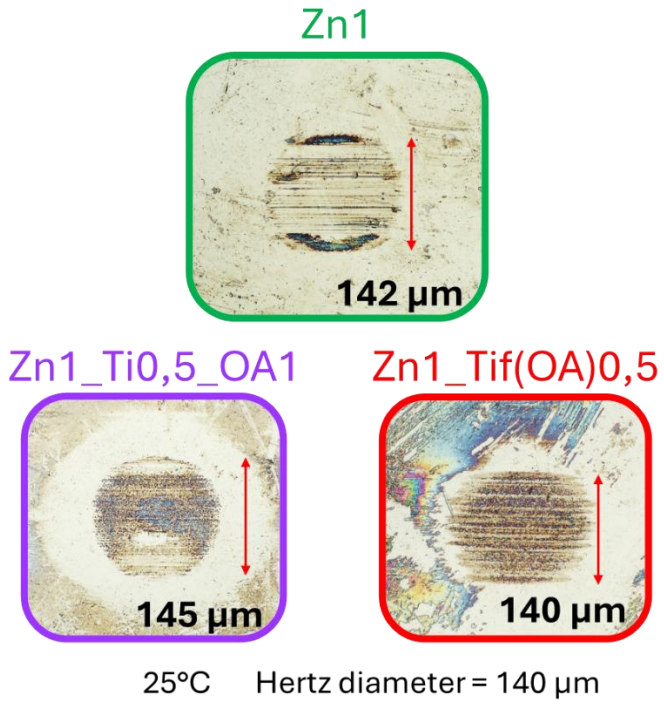

Fig. 145: Optical observations of wear tracks formed on the balls in the presence of solutions containing ZDDP (Zn1) or a combination of ZDDP and dispersed (Zn1_Ti0.5_OA1) or functionalized (Zn1_Tif(OA)0.5) TiO_2 nanoparticles.

With both dispersion methods, a synergy is observed between ZDDP and TiO_2 nanoparticles, but it is more prominent with the use of functionalized nanoparticles at 100°C as well as 25°C for both friction (Fig. 137, Fig. 143) and wear reduction properties (Fig. 138 to Fig. 140 and Fig. 144, Fig. 145).

SEM observations are presented for tribofilms formed at 100°C with ZDDP solution (Zn1) as well as the combination of ZDDP with dispersed (Zn1_Ti0.5_OA1) or functionalized NPs (Zn1_Tif(OA)0.5). BSE mode images are presented first as the chemical contrast allows a better understanding of the tribofilm morphology at a low magnification. SE mode combined with EDX mapping (View Field of 30 µm) gives us the main elements composing the tribofilm and how they are distributed within the friction track. High resolution SE mode is then used to observe surfaces at a high magnification.

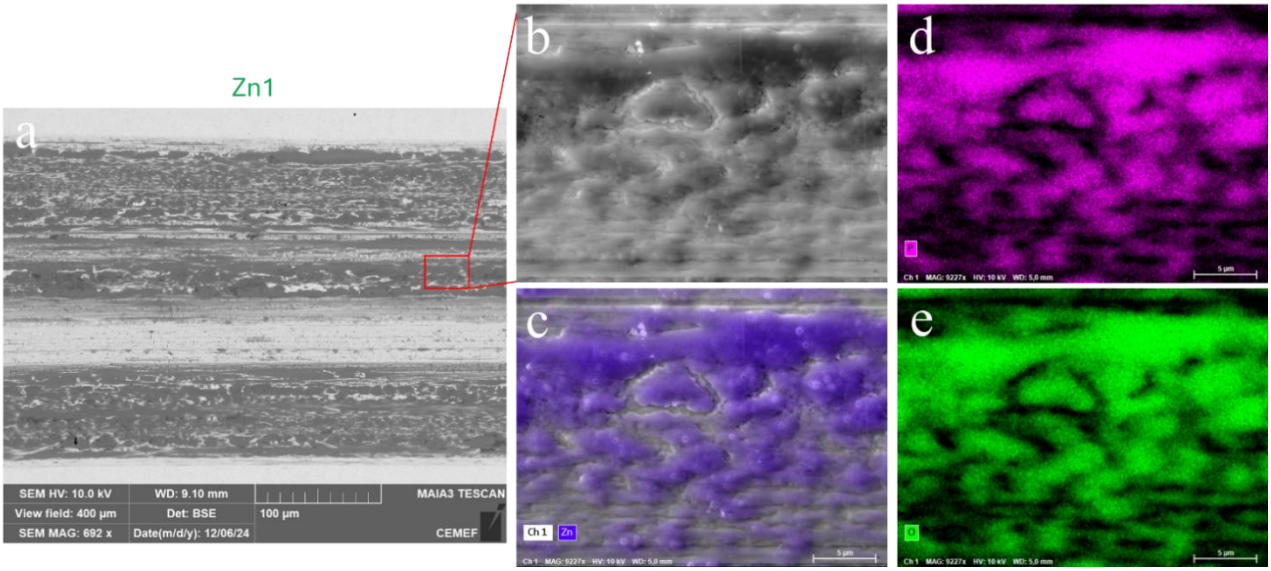

Fig. 146: SEM micrographs in BSE (a) and SE (b) modes with EDX mapping (c. d and e) of a tribofilm formed on the disc at 100°C in the presence of Zn1 solution (purple = Zn; pink = P; green = O).

Fig. 146 illustrates SEM and EDX analyses of the tribofilm formed in the presence of Zn1 (1wt% ZDDP). The tribofilm consists of elongated patches aligned with the sliding direction, ranging in width from 2 to 10 µm. These patches contain Zn, O, and P (indicative of phosphate glass), along with S (not shown here but presents the same distribution as P), with all elements distributed within the same regions (patches). These observations align well with descriptions and observations commonly found in the literature [15,16].

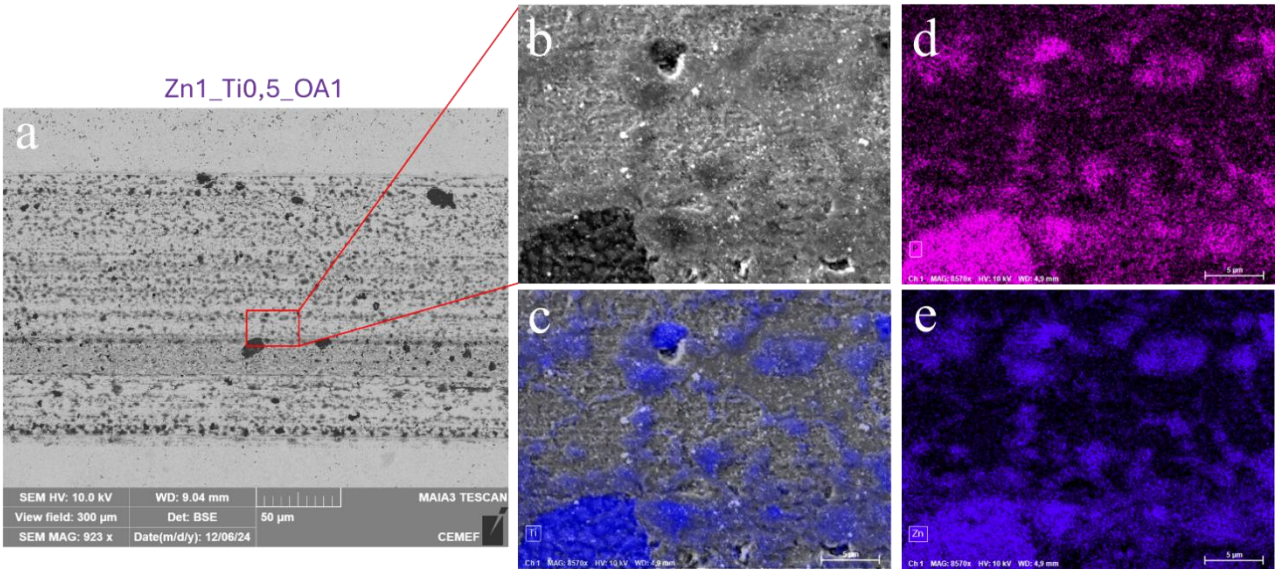

Fig. 147: SEM micrographs in BSE (a) and SE (b) modes with EDX mapping (c, d and e) of a tribofilm formed on the disc at 100°C in the presence of Zn1_Ti0.5_OA1 solution (blue = Ti; pink = P; purple = Zn).

Zn1_Ti0.5_OA1 SEM micrography (Fig. 147) shows a tribofilm with a structure similar to the one formed in the presence of Tif(OA)1 (Fig. 91) with patches thicker than for Ti1_OA1 (Fig. 90) and preferentially distributed in the sliding direction. Zn and P are detected in the same zones as Ti and O corresponding to thicker parts of the tribofilm. Very thick black patches can be observed, which was not the case with previous formulations.

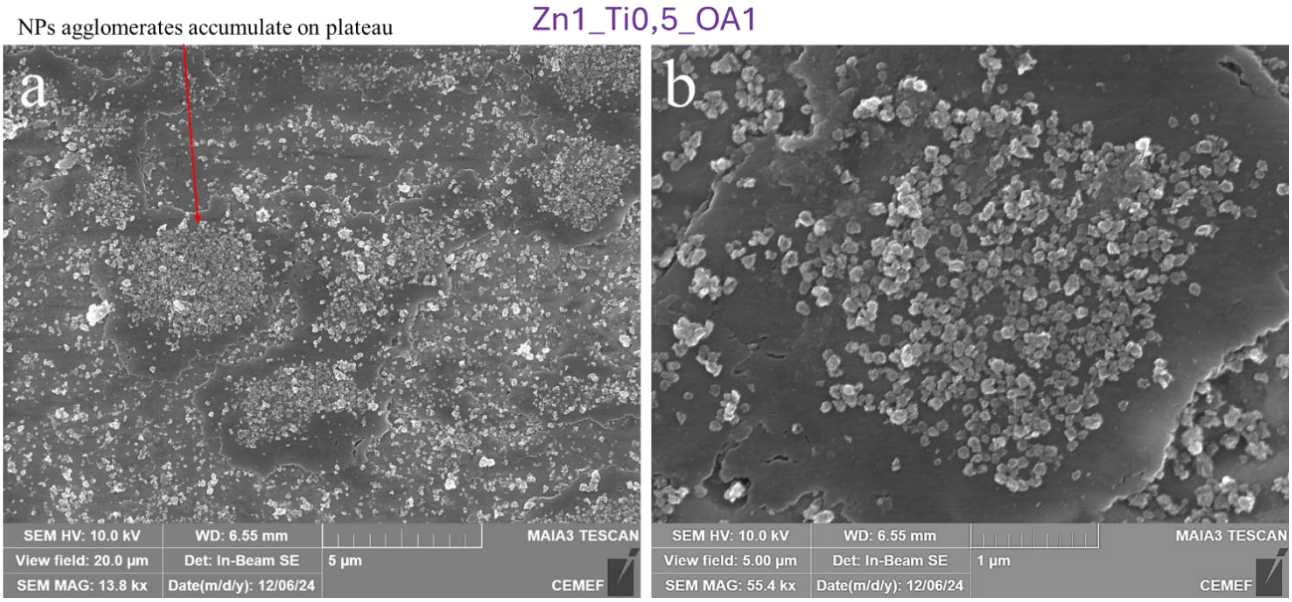

Fig. 148: High magnification SEM observations of a tribofilm formed on the disc at 100°C in the presence of Zn1_Ti0.5_OA1 solution showing the accumulation of NPs agglomerates on the plateau.

A close-up on the patches (Fig. 148) shows nanoparticles agglomerates that seem to accumulate on plateaus rather than valleys. A hypothesis could be that these NPs were partially crushed during sliding, causing them to adhere to the contact surface, which here corresponds to the observed plateaus, as their height leads to higher local pressure. With the following sliding cycles those NPs could form a structure corresponding to the observed plateaus, with what appears to be a smooth surface.

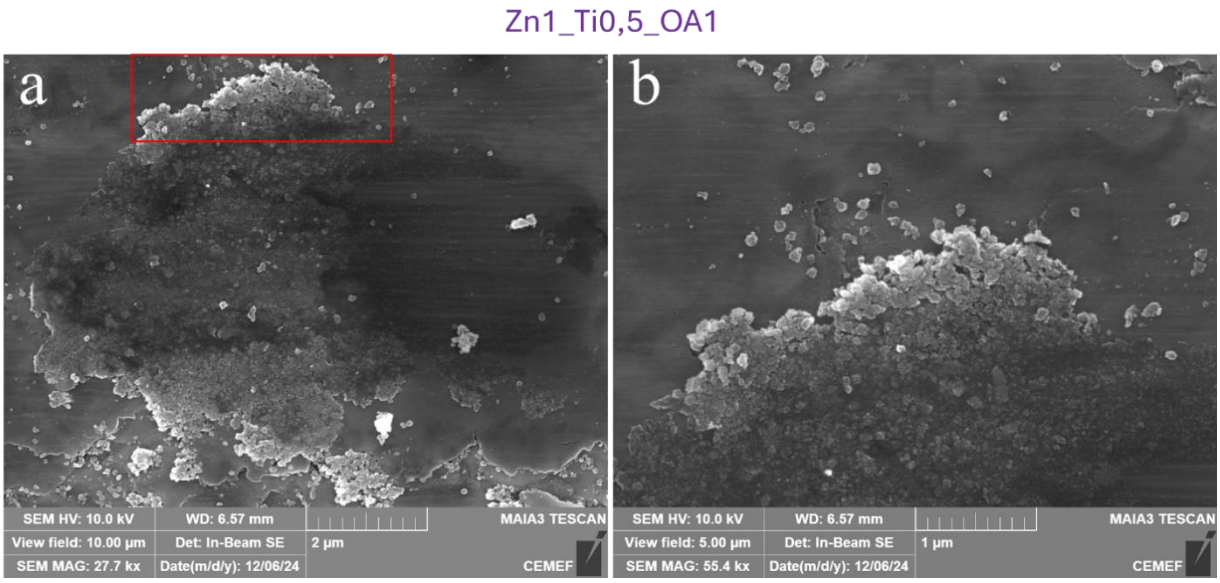

Fig. 149: High magnification SEM observations of a tribofilm formed on the disc at 100°C in the presence of Zn1_Ti0.5_OA1 solution showing the formation of a plateau.

Other areas with less debris were observed and confirmed this hypothesis. Fig. 149 shows a close-up on nanoparticles that have been crushed during sliding and are beginning to take on a plateau-like form.

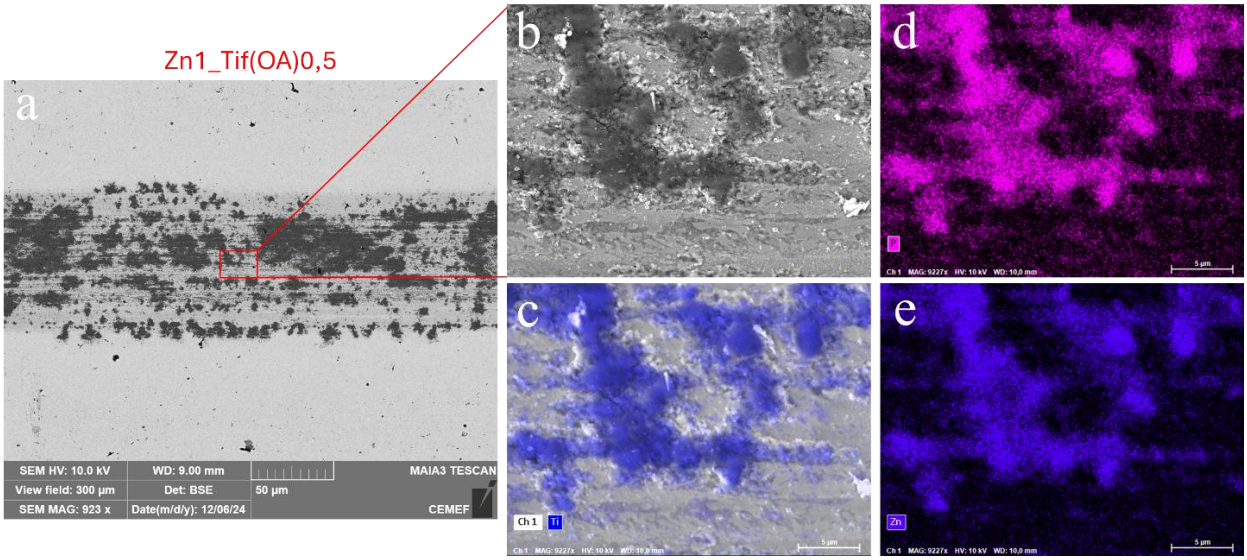

Fig. 150: SEM micrographs in BSE (a) and SE (b) modes with EDX mapping (c, d and e) of a tribofilm formed on the disc at 100°C in the presence of Zn1_Tif(OA)0.5 solution (blue = Ti; pink = P; purple = Zn).

Finally, for Zn1_Tif(OA)0.5 (Fig. 150), we observe a very different tribofilm aspect as it seems that very large patches have been formed, elongated in the sliding direction. The tribofilm appears continuous, with thick structures that are darker in contrast, and very thin ones that appear brighter but not as bright as the steel substrate in the BSE micrography, as the track boundaries are clearly distinguishable. EDX mapping confirms that the patches correspond to thick regions of the tribofilm, containing Ti, O, Zn and P, as well as S (not shown).

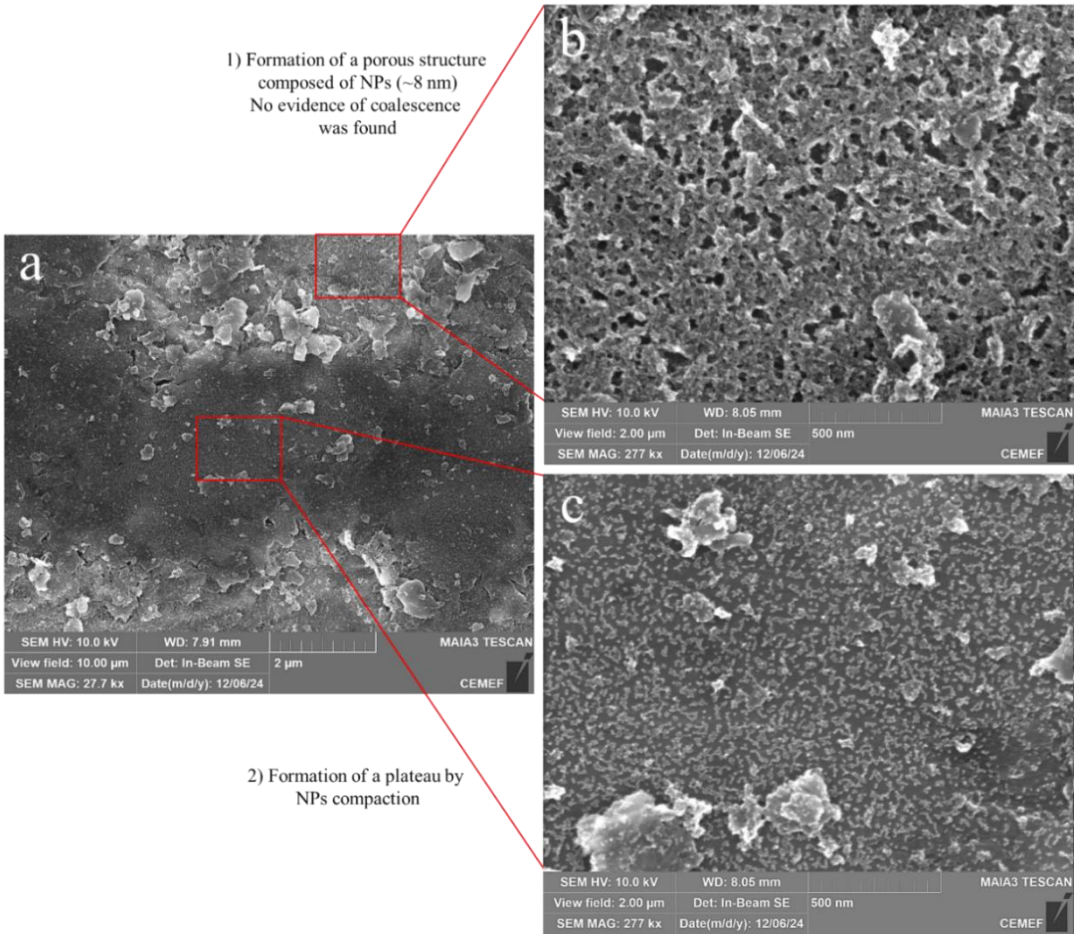

Fig. 151: High magnification SEM observations (a, b, c) of a tribofilm formed on the disc at 100°C in the presence of Zn1_Tif(OA)0.5 solution showing the formation of a porous structure in the valleys (b) and the accumulation of NPs agglomerates on the plateau (c).

Fig. 151 shows several close-ups of a transition zone between a plateau and a valley. We observe that the valley (Fig. 151b) has a porous structure formed by the aggregation of small nanoparticles (6–8 nm), likely due to the low pressure exerted in these regions. In contrast, in high-pressure areas, such as the plateau (Fig. 151c), a compact tribofilm appears to have been formed. Interestingly, nanoparticles are also deposited on the plateau. Unlike the Tif(OA)1 tribofilm, only small nanoparticles (6–8 nm) are visible, which raises questions about the influence of ZDDP on the stability of functionalized nanoparticles. This observation could also explain the tribological performance of this formulation, as preventing nanoparticles coalescence helps maintain a smaller nanoparticles size, enhancing their specific surface area and therefore their reactivity with the surface.

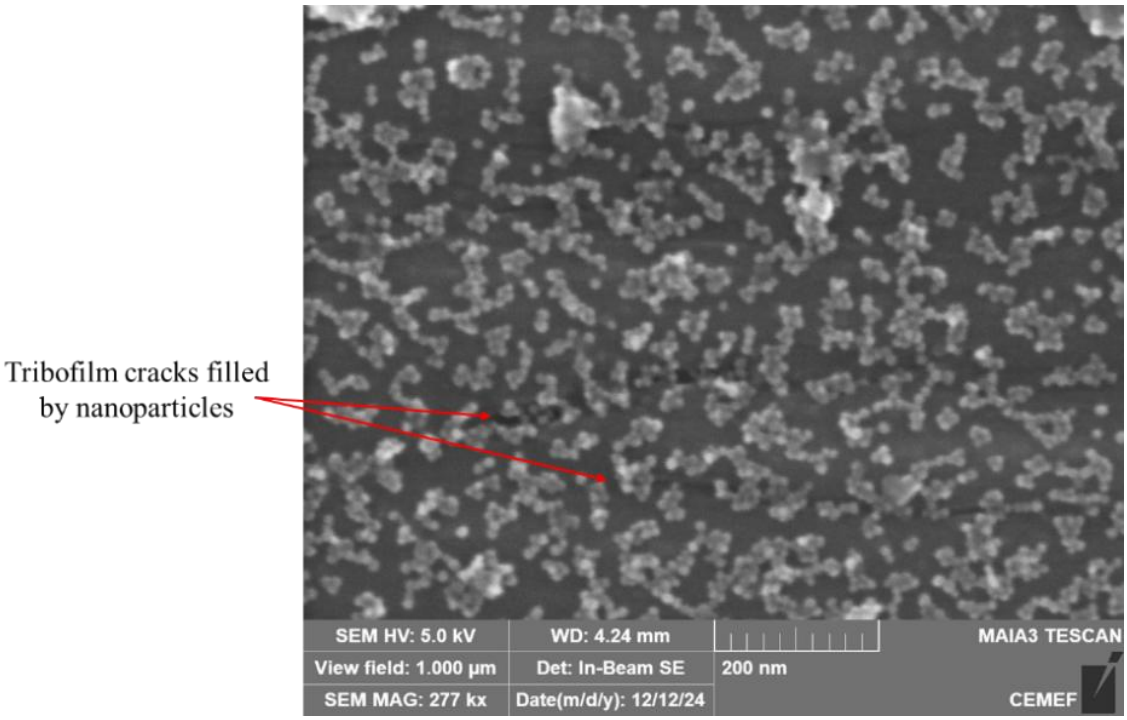

Fig. 152: High magnification SEM observation on tribofilm formed on the disc in the presence of Zn1_Tif(OA)0.5, showing the presence of cracks in the plateau region.

Another close-up of Fig. 151c is presented in Fig. 152, highlighting the presence of cracks within the tribofilm. These cracks may have formed during the tribofilm's development due to uneven compaction or may have resulted from wear. However, these defects appear to be filled with what seem to be unreacted nanoparticles, suggesting that the tribofilm exhibits self-healing properties.

When comparing our nanoparticle-based formulations, functionalization yields better results than simple dispersion, demonstrating superior intrinsic potential. However, the main drawback of using functionalized nanoparticles alone is that a significant portion of the nanoparticles does not react to form a tribofilm but instead accumulates in the valleys left by the tribofilm, as suggested by the high carbon content in these regions (Fig. 91).

The addition of ZDDP appears to mitigate this effect, likely due to its unique tribological properties. Unlike TiO_2 nanoparticles, ZDDP does not rely on direct solid-solid contact to form a tribofilm; instead, it requires only shear stress, as demonstrated by J. Zhang and H. Spikes (2016) [17]. These findings suggest that while TiO_2 nanoparticles form a tribofilm primarily through a tribo-sintering process when used alone, the incorporation of ZDDP results in a composite-like tribofilm. This tribofilm can form even under lower pressures, such as in the valleys, as it does not depend solely on contact stress. This supports the hypothesis of a trapping effect, where nanoparticles become embedded within the tribofilm formed in the valleys, as illustrated in Fig. 151b when compared to Fig. 92.

at.%	100°C				
	Ti1_OA1	Tif(OA)1	Zn1	Zn1_Ti0.5_OA1	Zn1_Tif(OA)0.5
C 1s	18.3	30.3	7.5	6.5	12.1
Fe 2p	14.5	12.6	3.4	12.2	4.7
O 1s	51.1	45.4	52.8	58.1	56.2
P 2p	0.0	0.0	13.8	2.1	3.9
S 2p	0.0	0.0	3.5	0.3	1.0
Zn 2p	0.0	0.0	18.7	1.7	2.3
Ti 2p	15.9	11.1	0.0	18.5	19.2
Ca 2p	0.2	0.6	0.4	0.6	0.6

Table 27: XPS chemical composition of tribofilms formed in the presence of solutions containing ZDDP or a combination of ZDDP and dispersed or functionalized TiO_2 nanoparticles. Obtained with a K-ALPHA spectrometer.

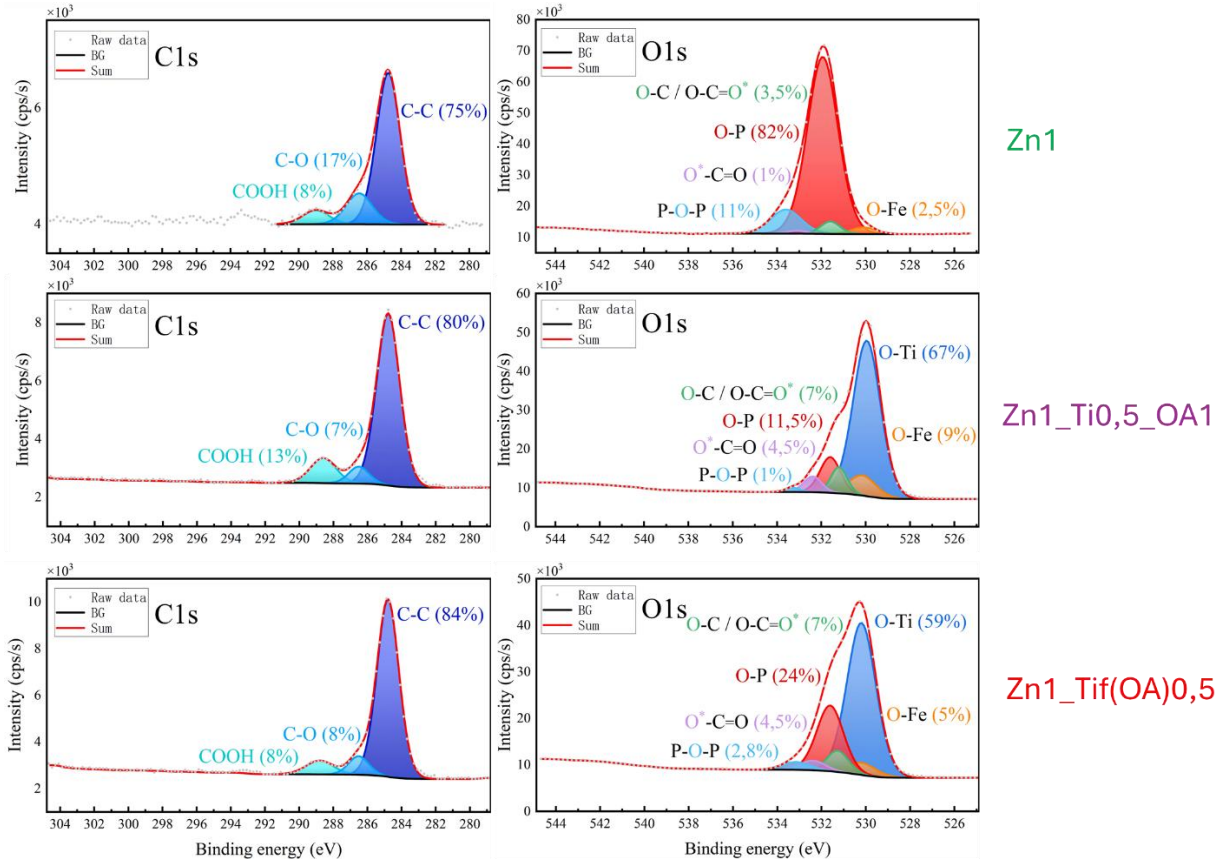

Fig. 153: C1s and O1s XPS spectra of tribofilms formed in presence of blends containing dispersed or functionalized TiO_2 blended with ZDDP. Obtained with a K-ALPHA spectrometer.

For the tribofilm Zn1 formed in the presence of ZDDP, there is an additional presence of P, S, and Zn. As expected, no Ti is detected. Carbon and iron contents are relatively low (7.5 at.% and 3.4 at.%, respectively), while zinc, phosphorus, and oxygen make up the characteristic phosphate glass formed during the decomposition of ZDDP. O1s peak decomposition (Fig. 153) was made using the same method used in 3.1.1, with the addition of O-P (non-bridging oxygen, called NBO) and P-O-P (bridging oxygen, called BO) peaks at 532 eV and 533.5 eV, respectively.

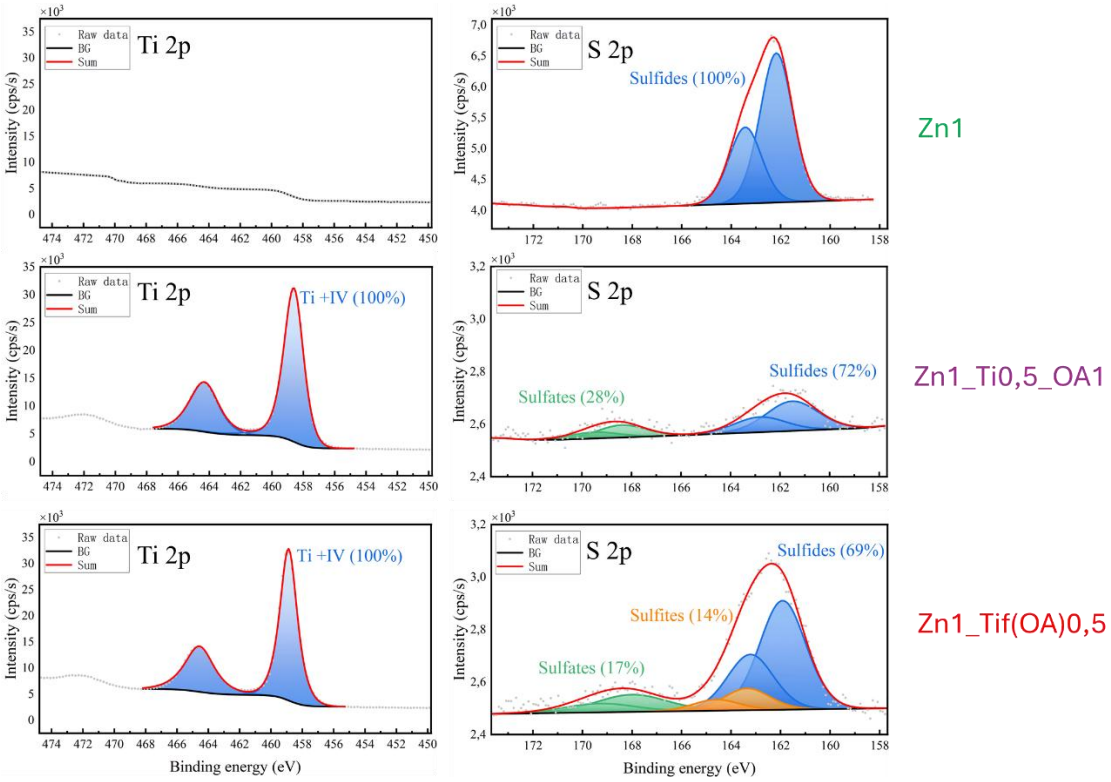

Fig. 154: Ti 2p and S 2p XPS spectra of tribofilms formed in presence of blends containing dispersed or functionalized TiO_2 blended with ZDDP. Obtained with a K-ALPHA spectrometer.

The presence of sulfur corresponds to the formation of a metal sulfide. presumably iron and zinc sulfides, as evidenced by S2p peak decomposition in Fig. 154.

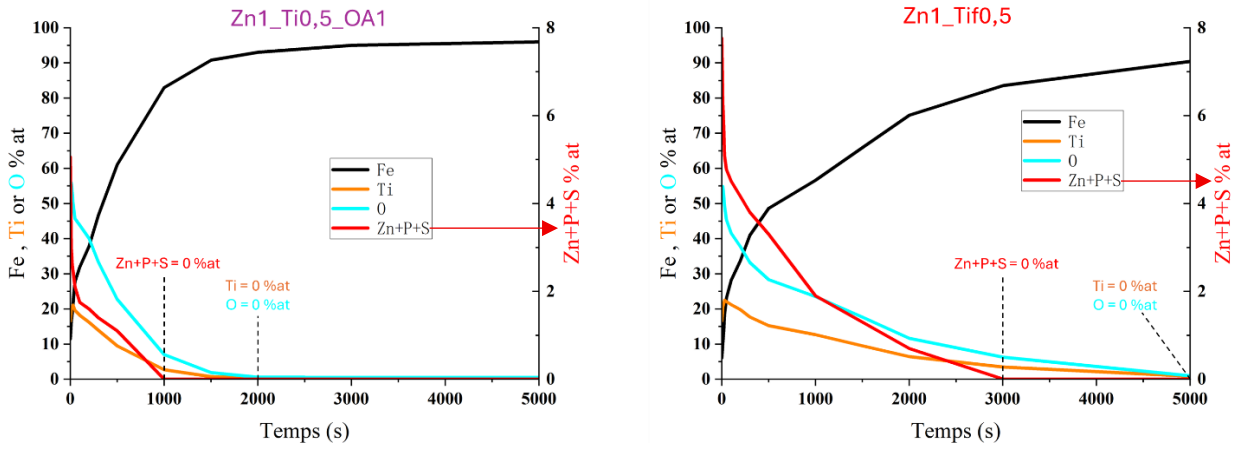

Fig. 155: Evolution of Fe, Ti, O and (Zn+P+S) content (at.%) with erosion time for tribofilms formed with formulations containing a blend of ZDDP with dispersed (Zn1_Ti0.5_OA1) or functionalized (Zn1_Tif(OA)0.5) TiO_2 nanoparticles. Obtained with a K-ALPHA spectrometer.

For Zn1_Ti0.5_OA1, the presence of ZDDP leads to a great increase in Ti content (18.3% atomic), which remains in the form of TiO_2 (Fig. 154), corresponding to a TiO_2 content of 54.9% atomic. However, TiO_2 nanoparticles appear to negatively impact ZDDP decomposition, as the derived elements of this additive (P, S, and Zn) are reduced by nearly a factor of ten compared to the tribofilm formed with Zn1 (**Table 27**).

Sulfur also reacts differently as oxidated species like sulphates are detected in addition to sulfides (Fig. 154). Nevertheless, this does not hinder tribological performance; rather, it improves it, as indicated by tribological testing.

A similar phenomenon occurs when functionalized nanoparticles (Zn1_Tif(OA)0.5) are used, showing lower P, S, and Zn content compared to the tribofilm formed with ZDDP alone, but slightly higher than with Zn1_Ti0.5_OA1, notably for phosphorus, whose O-P contribution in Fig. 153 is higher for Zn1_Tif(OA)0.5, which is consistent with this result. Sulfides species are once again detected but also intermediate species that could possibly correspond to sulfites. The iron content, however, is lower than with dispersed nanoparticles, showing improved coverage of this tribofilm. Additionally, the Ti content greatly increases to 19.2% atomic, corresponding to pure TiO_2 (Fig. 154), which means that the tribofilm is composed of 57.6% atomic of TiO_2.

XPS depth profiles (Fig. 155) show similar behavior for both formulations. With Zn1_Ti0.5_OA1, we can see a steep decrease in (Zn+P+S) content (from 5 at.% to 2 at.% at 100s) that is not observed for Ti (from 21 at.% to 19 at.% at 100s). With Zn1_Tif(OA)0.5 formulation, the same variation can be observed for (Zn+P+S) from 8 at.% to 5 at.% at 100s and for Ti from 23 at.% to 21 at.% at 100s. Those results suggest the coexistence of TiO_2 nanoparticles with ZDDP products within the depth of the tribofilm. Furthermore, considering that in both cases the signals from Zn, P and S elements disappear before Ti and O signals, we could assume the kinetic deposition of nanoparticles is faster than the chemical reaction of ZDDP within the surface (Fig. 155). This first layer could therefore correspond to the formation of titanate ($FeTiO_3$) as observed in the literature by X-ray absorption near edge spectroscopy (XANES) on a tribofilm formed with non-modified TiO_2 nanoparticles [10]. Another explanation could lie in the difference in erosion rate between those two materials, therefore ZDDP products could be washed away faster than TiO_2. A TEM observation of the cross section could help us better understand this result.

Concerning tribofilms thickness, we considered an erosion rate of 0.1 nm/s based on results obtained with ZDDP used alone and the hypothesis of a 100nm tribofilm based on the literature. With this hypothesis, Zn1_Tif(OA)0.5 forms the thicker tribofilm (~400-500 nm) followed by Zn1_Ti0.5_OA1 (~200 nm) and ZDDP (~100 nm), which is consistent with profilometry analysis (Fig. 140).

For both dispersed and functionalized nanoparticles, the presence of ZDDP enhanced their intrinsic tribofilm formation capabilities. Zn1_Tif(OA)0.5 therefore performed better because even without ZDDP, functionalized nanoparticles (Tif(OA)1) already formed a thicker tribofilm than dispersed ones (Ti1_OA1).

Summary and Discussion

To investigate the influence of the dispersion method (physical dispersion versus chemical functionalization) of 5 nm anatase TiO_2 nanoparticles on their synergy with ZDDP, tribological tests were conducted under boundary lubrication conditions. The wear tracks were subsequently characterized using optical microscopy, profilometry, SEM, EDX, and XPS analyses.

The results revealed a significant synergistic interaction between TiO_2 nanoparticles and ZDDP, leading to notable improvements in tribological performance compared to individual additives, particularly in friction and wear reduction, as well as tribofilm formation (induction time, thickness, and coverage). This synergy was observed for both dispersed and functionalized nanoparticles, with the latter demonstrating superior performance.

Effect of dispersion and functionalization methods on lubricating performances of TiO_2 NPs

The disparity in performance between dispersed and functionalized nanoparticles stems from differences in their physical state within the lubricant. Dispersed NPs, derived from a dry powder, contained agglomerates, whereas functionalized NPs avoided this issue due to their synthesis method, which didn't include drying and subsequent agglomeration. This distinction was visually observed, with dispersed formulations appearing opaque, while functionalized ones were nearly transparent - indicating a higher proportion of individual NPs in the latter or at least smaller agglomerates.

Despite these differences, both types of nanoparticles appear to form a tribofilm through tribo-sintering mechanism. However, this tribofilm does not grow uniformly across the friction track. Instead, it seems to develop preferentially in certain areas, resulting in a patchy tribofilm. This localized growth could be driven by a nucleation process that initiates preferentially in areas with surface defects, as evidenced by Khare et al. [6].

The addition of ZDDP enhanced the native tribological performance of both types of nanoparticles by promoting more uniform tribofilm coverage. This improvement is due to the complementary nature of the two additives: TiO_2 NPs rely on direct solid-solid contact and pressure to facilitate tribofilm growth, particularly within surface defects, while ZDDP can form a tribofilm even under elastohydrodynamic (EHD) conditions [17,18]. Together, they enhance the embedment of nanoparticles within the tribofilm, leading to improved performance. Indeed, the resulting phosphate glass can act as a binder for TiO_2 nanoparticles to form a tribofilm even without direct contact stress out of the thick patches.

XPS analysis revealed similar tribofilm compositions for the Zn1_Ti0.5_OA1 and Zn1_Tif(OA)0.5 blends (reduction of Zn, P and S content compared to Zn1), suggesting that the underlying chemical reactions during tribo-testing are consistent. The key difference once again lies in the physical characteristics of the NPs, such as size and agglomeration which will dictate the tribofilm structure (Fig. 157).

A separate blend of ZDDP with oleic acid in PAO6 (Zn1_OA1) was also tested (results not shown for brevity). This formulation produced a tribofilm with a composition identical to that of ZDDP used alone (Zn1), confirming that the observed reduction in Zn, P, and S content (**Table 27**) in the NPs and ZDDP blends is related to TiO_2 reactivity rather than oleic acid.

Antagonistic Effect and Mitigation

Interestingly, Sharma *et al.* (2024) [10] observed an antagonistic interaction between ZDDP and unmodified 25 nm TiO_2 NPs, specifically for anti-wear properties. They demonstrated that sequentially introducing the additives mitigates this issue, with optimal results achieved when TiO_2 NPs is applied first, allowing the formation of an initial titanate ($FeTiO_3$) layer through a reaction between TiO_2 and the steel substrate. This layer acts as a promoter for tribofilm growth. In contrast, introducing ZDDP first blocked the formation of this titanate layer, resulting in increased wear and altered tribofilm formation. Depth profile analysis in Fig. 155 are supporting this hypothesis as with both dispersed and functionalized nanoparticles, Ti and O elements are still detected when there is no Zn, P and S left. Moreover, although low cycle tests could not be performed on these formulations due to their restricted shelf life, it can reasonably be assumed that such a layer was formed, since a similar feature was observed in the previous section (3.1.2) for the formulation containing silane-functionalized TiO_2 nanoparticles (Fig. 119).

Our tests with a similar blend containing ZDDP and TiO_2 NPs (Zn1_Ti0.5) (not shown) corroborate these findings, showing increased wear and friction track width. However, the presence of oleic acid appeared to mitigate this issue by adsorbing rapidly onto the steel substrate surface before any mechanical or tribological stress is applied. This likely prevented ZDDP first layer reactions and facilitated NPs interaction with the surface, as illustrated in Fig. 156. Overall, excellent tribological performance appears to be achievable by combining fast-reacting agents, such as oleic acid, with slower ones that can form a robust tribofilm like TiO_2 nanoparticles. A similar observation was made by Elinski *et al.* (2020) [19] where extreme pressure additives adsorbed on the steel surfaces prevent early adhesive wear, letting time for ZrO_2 nanocrystals to form a protective tribofilm.

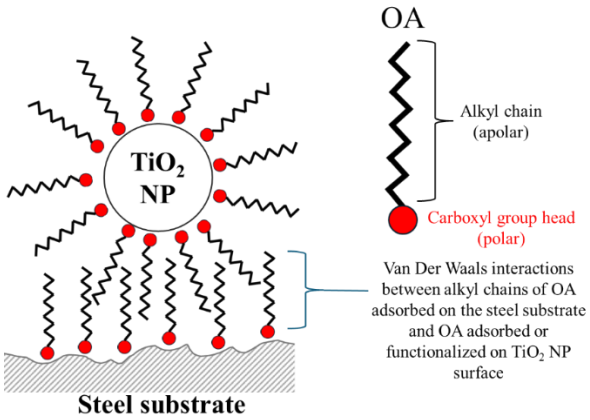

Fig. 156: Schematic representation of OA interaction between steel substrate and TiO_2 dispersed or functionalized nanoparticles.

Whatever the ZDDP-TiO_2 blends (dispersed NPs, or functionalized NPs), the resulting tribofilms consistently exhibited low levels of ZDDP-related elements (Zn, P, and S). Nevertheless, tribological performance was not compromised; rather, it was enhanced. These findings suggest that the synergistic or antagonistic relationship between ZDDP and TiO_2 NPs can be effectively controlled by employing an efficient dispersing agent, which improves nanoparticles behavior and compatibility within the lubricant system.

Tribofilm Formation Mechanisms

Functionalized 5 nm TiO_2 nanoparticles in PAO base oil led to the formation of a protective tribofilm. However, the tribofilm's growth appears uneven along the friction track, as evidenced by the patchy morphology observed in SEM images (Fig. 91). We propose that TiO_2 nanoparticles nucleate under tribological stress, preferentially within surface defects [6], driving the formation of a patchy tribofilm. In this scenario, the plateaus are exposed to higher contact stress compared to the valleys, which promotes greater tribofilm thickness on the plateaus while limiting tribo-sintering within the valleys. Consequently, individual nanoparticles tend to accumulate in the less-stressed valley regions.

Concerning functionalized nanoparticles and ZDDP blend, oleic acid seems to react with the substrate first. This interaction promotes TiO_2 nanoparticles deposition and hinders ZDDP products to form on the surface. This initial layer that could correspond to a titanate compound [10] acts as a promoter for tribofilm growth with both TiO_2 nanoparticles and ZDDP decomposition products.

The combination of functionalized TiO_2 nanoparticles with ZDDP then promotes the formation of a thicker and more uniform tribofilm by enhancing the trapping of nanoparticles within the tribofilm through two complementary mechanisms. First, a stress-assisted process facilitates the incorporation of nanoparticles, while the chemical decomposition of ZDDP further aids their embedment, particularly in areas of the contact that experience lower pressure.

Therefore, we could assume the formation of a composite-like tribofilm, with TiO_2 nanoparticles surrounded by a phosphate glass that acts as a binder. If the reaction with ZDDP is similar for dispersed and functionalized nanoparticles (same thickness of phosphate glass surrounding the nanoparticles), the amount of binder should be higher with smaller particles (higher surface to volume ratio) which would be seen in XPS results as a high concentration of binder, indicated by the amount of phosphorus in our case (**Table 27**). A schematic explanation is shown in Fig. 157.

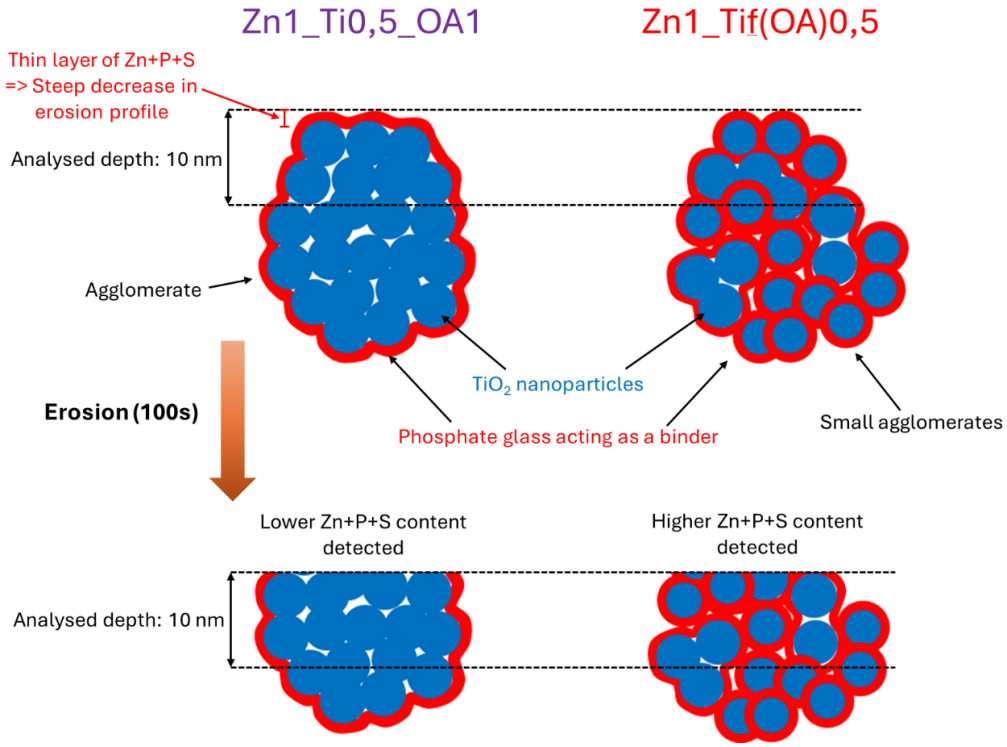

Fig. 157: Schematic representation of tribofilms structure formed in the presence of solutions containing dispersed or functionalized TiO_2 blended with ZDDP. Before (top) and after (bottom) 100s of erosion.

This hypothesis is supported by the fact that the EDX composition (**Table 28**) (measured over ~1 µm depth) on the thickest patches closely matches the XPS composition (measured over ~10 nm depth). This indicates, on one hand, that the tribofilm in some areas is sufficiently thick to minimize substrate influence in EDX analysis (Fe < 5 at.%), and on the other hand, that the surface composition corresponds to the overall composition of the tribofilm, therefore suggesting that it is formed by a mixture of TiO_2 NPs and products from ZDDP decomposition. This could also explain why the plateaus appear smoother with Zn1_Tif(OA)0.5 (Fig. 151) than with Tif(OA)1 (Fig. 92) as phosphate glass could fill the potential gaps between TiO_2 NPs. A similar observation was recently reported by LaMascus *et al.* (2024) [20] where the use of a S and P-based co-additives promoted a more polished final interface of the tribofilm formed with ZrO_2 nanocrystals.

at.%	Zn1_Tif(OA)0.5	
	EDX	XPS
C 1s	6.1	12.1
Fe 2p	7.1	4.7
O 1s	58.8	56.2
P 2p	3.3	3.9
S 2p	1.0	1.0
Zn 2p	2.1	2.3
Ti 2p	21.5	19.2
Ca 2p	0.1	0.6

Table 28: EDX and XPS chemical composition of a tribofilm formed in the presence of a solution containing a combination of ZDDP and functionalized TiO_2 nanoparticles (Zn1_Tif(OA)0.5). XPS analysis obtained with a K-ALPHA spectrometer.

These hypotheses could be further explored through complementary analyses, such as investigating the early stages of tribofilm formation during the initial cycles of tribological testing, along with TEM cross-section observations to more accurately assess the composition and morphology of the tribofilms.

Therefore, functionalized TiO_2 nanoparticles appear to be a better candidate for commercial use due to their strong synergistic effect with ZDDP in enhancing tribological properties, as well as for their higher stability. Additionally, Zn1_Tif(OA)0.5 is the only nanoparticle blend that remains stable at 100°C, as evidenced by the formulation maintaining optical clarity during tribological testing (Fig. 142).

Having examined the effect of the nanoparticle dispersion method on the interactions between ZDDP and TiO_2, the next step is to investigate the role of nanoparticle functionalization. In particular, the chemical nature of the functionalizing agent will be assessed to determine how it influences ZDDP - TiO_2 interactions and the resulting tribological performance.

3.2.2.2 Influence of Functionalizing Agent Chemical Nature on the Interactions Between ZDDP and TiO_2 Nanoparticles

This section examines the role of the ligand in the ZDDP / TiO_2 nanoparticles interaction by comparing mixtures containing ZDDP with either oleic acid- or silane-functionalized nanoparticles.

Formulations studied in this section are presented in **Table 29**.

Composition	Name
PAO6	PAO6
PAO6 + 1wt.% ZDDP (820 ppm of phosphorus)	Zn1
PAO6 + 1wt.% ZDDP + 0.5wt.% oleic acid-functionalized TiO_2 NP	Zn1_Tif(OA)0.5
PAO6 + 1wt.% silane-functionalized TiO_2 NP	Tif(Si)1
PAO6 + 1wt.% ZDDP + 0.5wt.% silane-functionalized TiO_2 NP	Zn1_Tif(Si)0.5

Table 29: Composition and name of tribologically tested blends used for the study of ZDDP and oleic acid- or silane-functionalized TiO_2 nanoparticles interactions.

For these tests, the applied pressure was reduced from 1.03 to 0.83 GPa.

3.2.2.2.1 Comparison between oleic- and silane-functionalized TiO_2 nanoparticles blended with ZDDP for enhanced tribological performance.

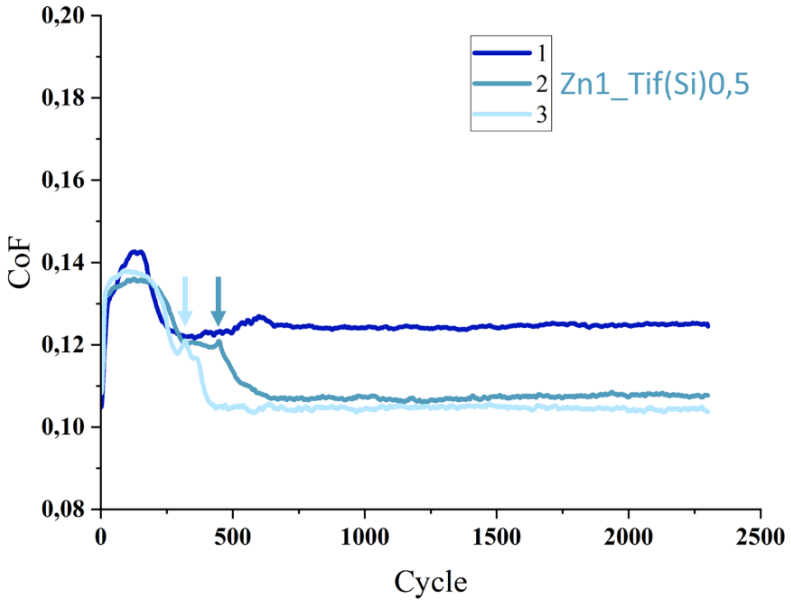

Fig. 158: Friction tests repeatability at 100°C for the samples containing a combination of ZDDP and silane-functionalized (Zn1_Tif(Si)0.5) TiO_2 nanoparticles. Three repetitions were carried out for each blend.

We first focus on the ZDDP / silane-functionalized TiO_2 nanoparticles mixture, as the oleic acid-functionalized system was already discussed in the previous section.

The repeatability tests on the friction coefficient (Fig. 158) reveal that for this blend different friction levels may be obtained, although the origin of this variation remains unclear. For instance, in the first repetition the CoF initially rises to 0.14 before decreasing and stabilizing at 0.125. In contrast, in the two subsequent repetitions, the CoF also increases to 0.14 but then stabilizes at a lower value of 0.105. Interestingly, in these latter cases the drop in friction is preceded by a small positive peak, highlighted by the arrows in Fig. 158.

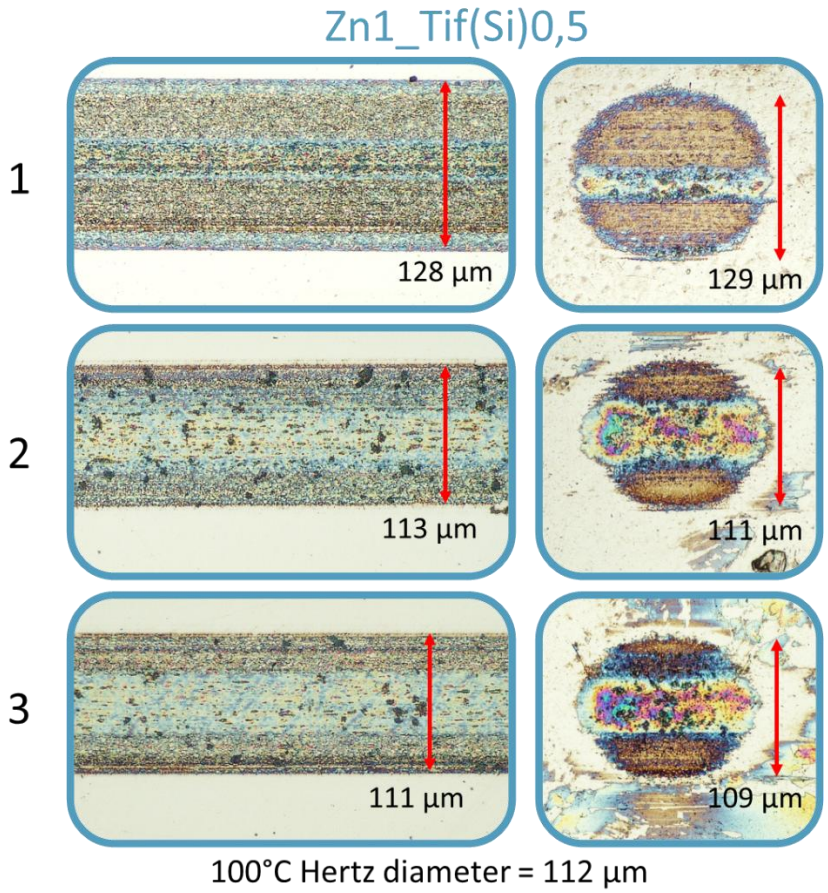

Fig. 159: Optical observations of wear tracks formed at 100°C for the samples containing a combination of ZDDP and silane-functionalized (Zn1_Tif(Si)0.5) TiO_2 nanoparticles. Three repetitions were carried out for each blend.

Fig. 159 highlights the correlation between friction and wear: the test with the highest CoF also shows the widest wear scar (128 µm vs. ~112 µm for the others). In all cases, the tribofilm exhibits a more vivid central region, particularly on the balls, suggesting a thicker or more compacted layer in the zone of highest contact pressure.

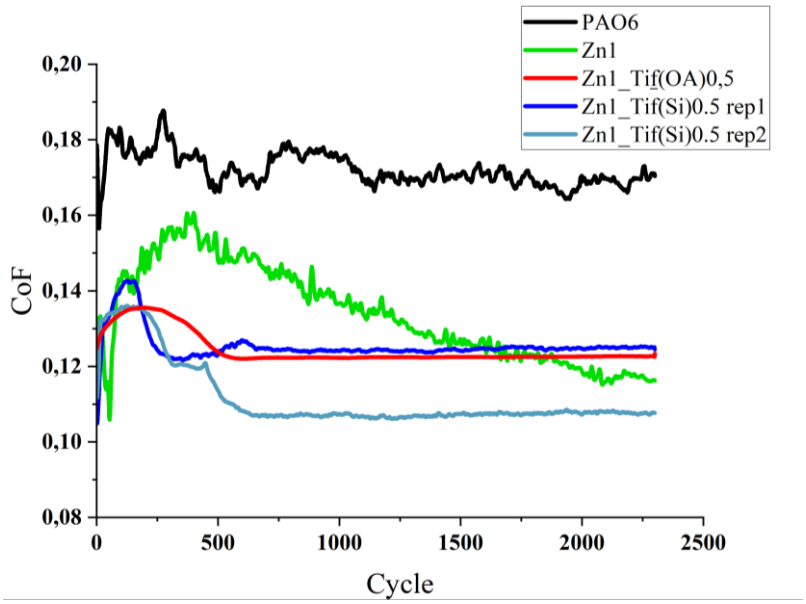

Fig. 160: Evolution of friction coefficient with cycles at 100°C for the samples containing ZDDP (Zn1), or a blend of ZDDP and either oleic acid-functionalized TiO_2 nanoparticles (Zn1_Tif(OA)0.5) or silane-functionalized TiO_2 nanoparticles (Zn1_Tif(Si)0.5). PAO6 base oil is used as a reference.

Fig. 160 compares the CoF obtained with ZDDP alone and with ZDDP combined with either oleic acid- or silane-functionalized nanoparticles. Both blends exhibit a rapid stabilization of friction with smoother, less noisy behavior, in contrast to ZDDP alone, which first shows an increase up to ~0.16 followed by a progressive decrease, reaching a minimum value of 0.115. The silane-functionalized system stabilizes either at a value similar to the oleic acid-functionalized case (~0.12) or at an even lower level (~0.105) depending on the repetition.

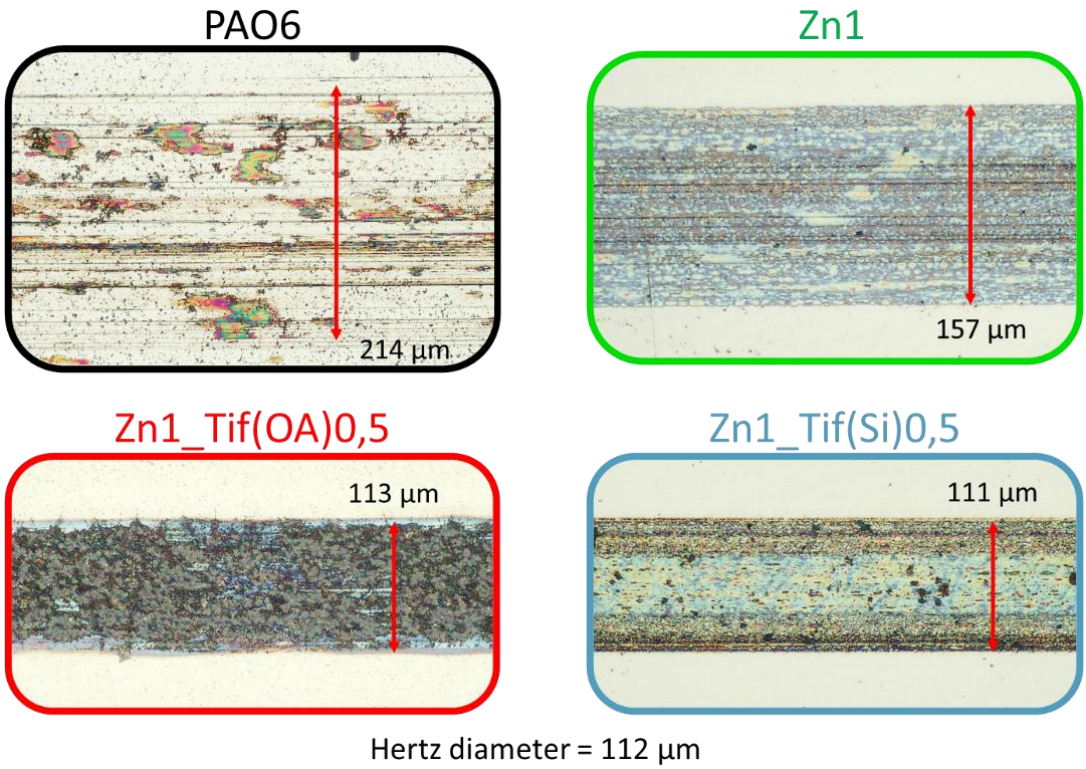

Fig. 161: Optical observations of wear tracks formed at 100°C on the discs in the presence of solutions containing ZDDP (Zn1) or a blend of ZDDP and oleic acid-functionalized TiO_2 nanoparticles (Zn1_Tif(OA)0.5) or silane-functionalized TiO_2 nanoparticles (Zn1_Tif(Si)0.5). PAO6 base oil is used as a reference.

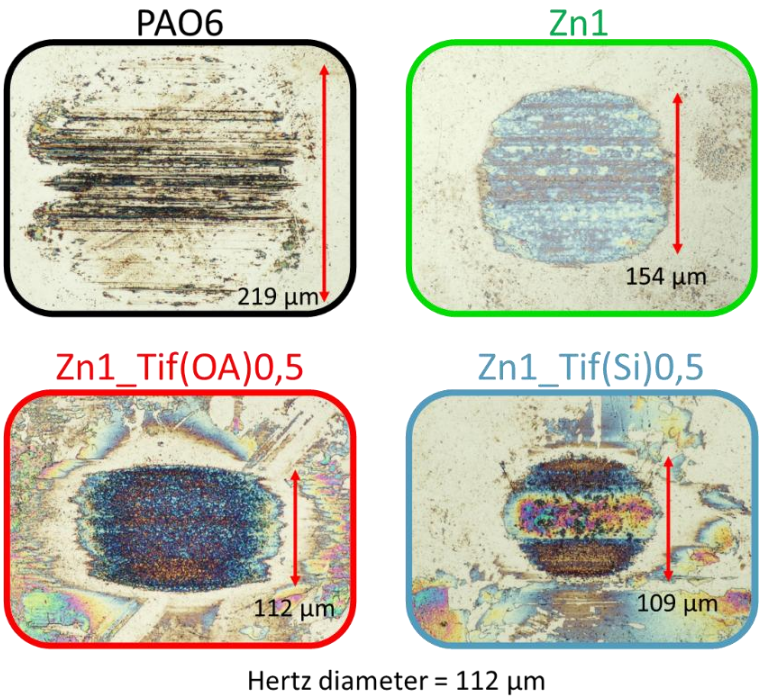

Fig. 162: Optical observations of wear tracks formed at 100°C on the balls in the presence of solutions containing ZDDP (Zn1) or a blend of ZDDP and oleic acid-functionalized TiO_2 nanoparticles (Zn1_Tif(OA)0.5) or silane-functionalized TiO_2 nanoparticles (Zn1_Tif(Si)0.5). PAO6 base oil is used as a reference.

Friction scar widths, measured on both the discs (Fig. 161) and the balls (Fig. 162), are consistently smaller for the blends than for ZDDP alone. In the best case, the scar width is close to the Hertzian diameter (112 µm), while even in the least favorable case with silane-functionalized nanoparticles (Fig. 159) it remains lower than with ZDDP (128 vs 157 µm). This coincides with the initially high friction that takes time to decrease, probably because the ZDDP tribofilm does not form rapidly, leaving the substrate vulnerable in contrast to the other two cases.

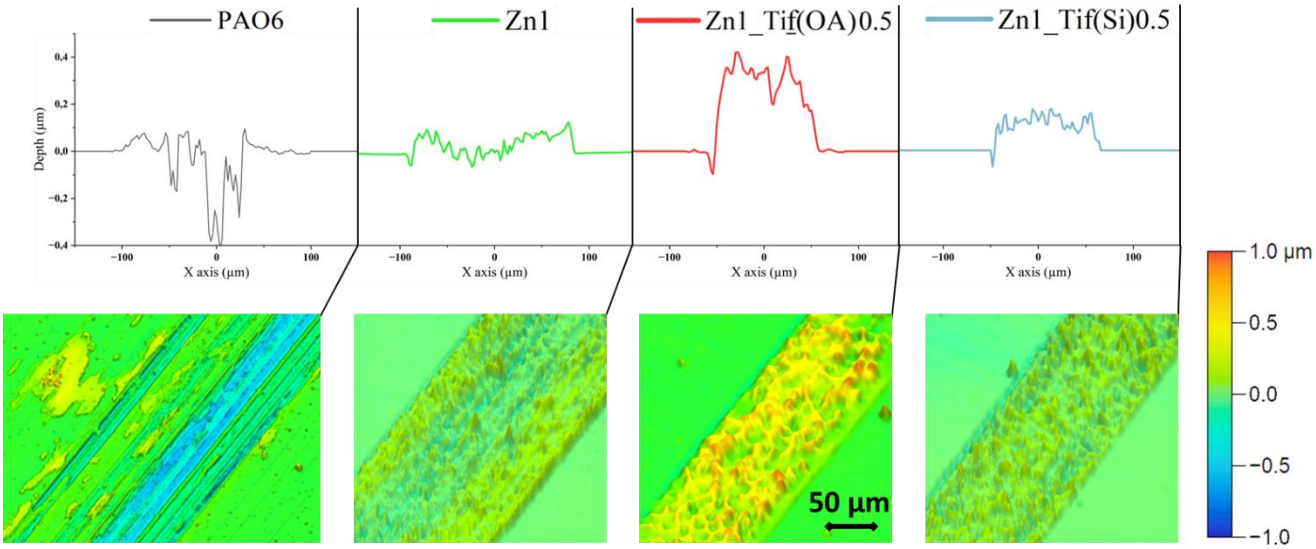

Fig. 163: Mean depth profiles and surface morphology of wear tracks formed at 100°C on the discs in the presence of solutions containing ZDDP (Zn1) or a blend of ZDDP and oleic acid-functionalized TiO_2 nanoparticles (Zn1_Tif(OA)0.5) or silane-functionalized TiO_2 nanoparticles (Zn1_Tif(Si)0.5). PAO6 base oil is used as a reference.

Profilometry (Fig. 163) further confirms that the mixtures outperform ZDDP in terms of tribofilm height and homogeneity. A clear advantage is observed for the oleic acid-functionalized nanoparticles blended with ZDDP (Zn1_Tif(OA)0.5), which produce a tribofilm of ~400 nm compared to ~150 nm for the silane-functionalized case (Zn1_Tif(Si)0.5).

at.%	100°C		
	Zn2	**Zn1_Tif(OA)0,5**	**Zn1_Tif(Si)0,5**
C 1s	**11.7**	**12.1**	**18.8**
Fe 2p	**1.8**	**4.7**	**1.1**
O 1s	**52.2**	**56.2**	**51.2**
P 2p	**14.8**	**3.9**	**8.6**
S 2p	**2.2**	**1.0**	**1.6**
Zn 2p	**17.0**	**2.3**	**4.6**
Si2p	**0.0**	**0**	**0.9**
Ti2p	**0.0**	**19.2**	**11.1**
Ca 2p	**0.4**	**0.6**	**2.2**

Table 30: XPS chemical composition of tribofilms formed in the presence of solutions containing ZDDP or a blend of ZDDP with either oleic acid- or silane-functionalized TiO_2 nanoparticles. Conducted using a K-ALPHA spectrometer for Zn1_Tif(OA)0.5 and a NEXSA for Zn1 and Zn1_Tif(Si)0.5.

In the previous section, it was shown that adding oleic acid-functionalized nanoparticles to ZDDP led to an increase in Ti content in the tribofilm, at the expense of ZDDP-derived elements (Zn, P, and S). The addition of silane-functionalized nanoparticles produces a similar, though less pronounced, effect. In this case, the Ti concentration reaches 11.1 at.% compared to 19.2 at.% for the oleic acid-functionalized system (**Table 30**). Likewise, the P content decreases to 8.6 at.% instead of 3.9 at.%. A small amount of silicon (0.9 at.%) is also detected, which likely corresponds to the presence of the functionalizing agent, either incorporated into or adsorbed onto the tribofilm. The very low Fe content observed for Zn1 and Zn1_Tif(Si)0.5 is due to the use of the NEXSA spectrometer, which enables measurements with a smaller spot size (50 µm) while maintaining a high signal-to-noise ratio. This allows analysis within the wear track without interference from the substrate on the edges. In contrast, the Zn1_Tif(OA)0.5 sample was analyzed with the K-ALPHA, which explains the higher Fe content detected.

Overall, it looks like silane-functionalized nanoparticles deposit less easily than oleic acid ones, allowing ZDDP derived elements to remain dominant. This reflects kinetic competition between the two additives in film formation. This suggests that the deposition rate of TiO_2 nanoparticles depends on the strength of its interaction with the capping agent: the stronger the interaction, the slower the deposition.

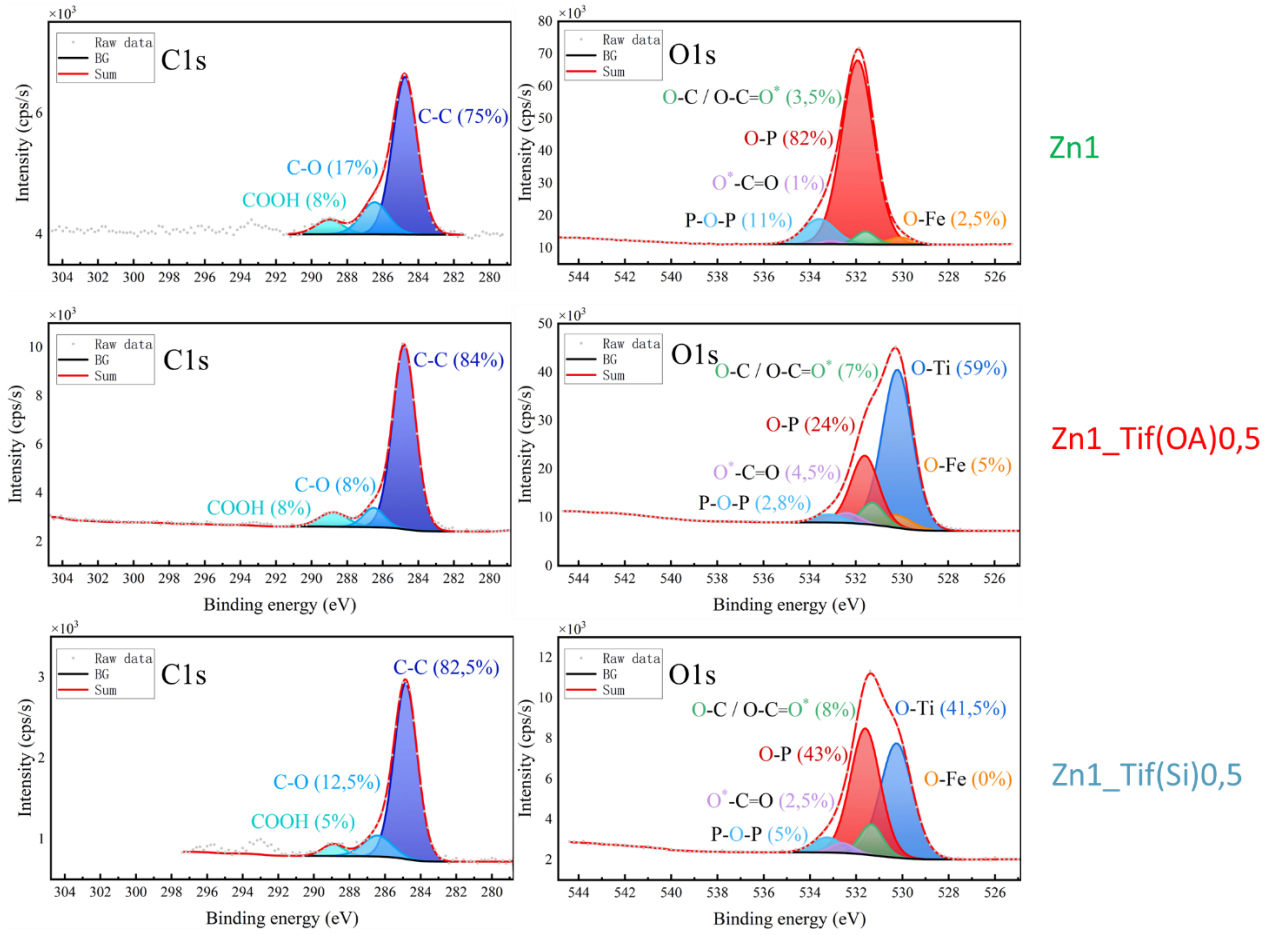

Fig. 164: C1s and O1s XPS spectra of tribofilms formed in presence of blends containing ZDDP (Zn1) or a mixture of ZDDP and either oleic acid-functionalized (Zn1_Tif(OA)0.5) or silane-functionalized TiO_2 nanoparticles (Zn1_Tif(Si)0.5).

This intermediate behavior for Zn1_Tif(OA)0.5, between ZDDP and Zn1_Tif(OA)0.5 composition, is further confirmed by peak fitting analysis, particularly the O1s peak (Fig. 164), processed using the same method described in 3.1.1 for Fig. 94. The O-P contribution, characteristic of phosphate glass formation, represents 82% of the signal for Zn1, 24% for Zn1_Tif(OA)0.5, and an intermediate value of 43% for Zn1_Tif(Si)0.5.

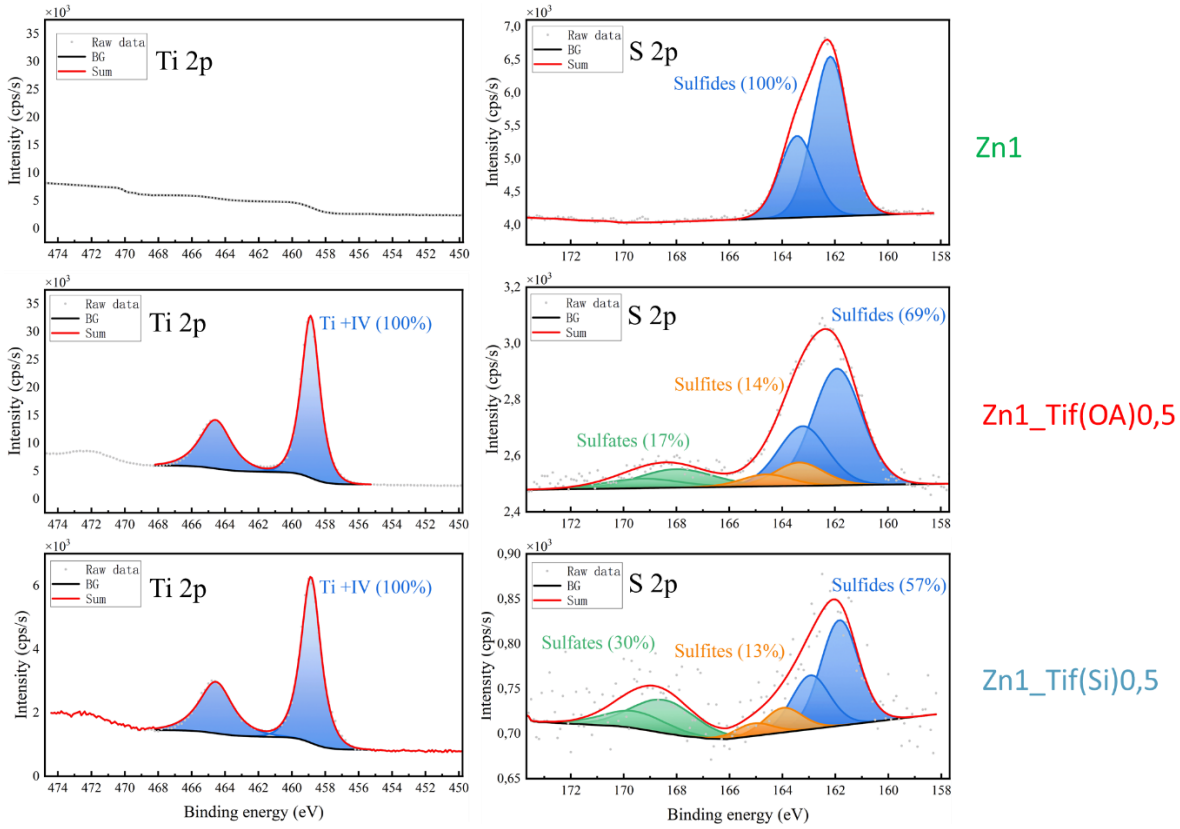

Fig. 165: Ti2p and S2p XPS spectra of tribofilms formed in presence of blends containing ZDDP (Zn1) or a mixture of ZDDP and either oleic acid-functionalized (Zn1_Tif(OA)0.5) or silane-functionalized TiO_2 nanoparticles (Zn1_Tif(Si)0.5).

Finally, Fig. 165 shows that in both nanoparticle-containing mixtures, Ti is present exclusively as TiO_2. In both cases, oxidized sulfur species also appear, whereas they are absent when ZDDP is used alone.

Overall, changing the functionalizing agent appears to modulate the relative contribution of ZDDP-derived elements and TiO_2 nanoparticles in the tribofilm, without clear evidence of new chemical reactions between ZDDP and the nanoparticles.

To gain further insight into the mechanisms of tribofilm formation, intermediate cycle tests were carried out.

3.2.2.2.2 Tribofilm growth rate study through intermediate cycle testing for silane functionalized TiO_2 nanoparticles and ZDDP blend.

In this section, the objective is to investigate tribofilm kinetic formation using intermediate tests. Results are presented for the Zn1 solution and the Zn1_Tif(Si)0.5 blend. As in 3.1.2, two repetitions were performed for each cycle value. Each track shown corresponds to a distinct experiment, carried out from 0 up to the selected final cycle. Therefore, the interpretation of the results relies on the good repeatability of our tests.

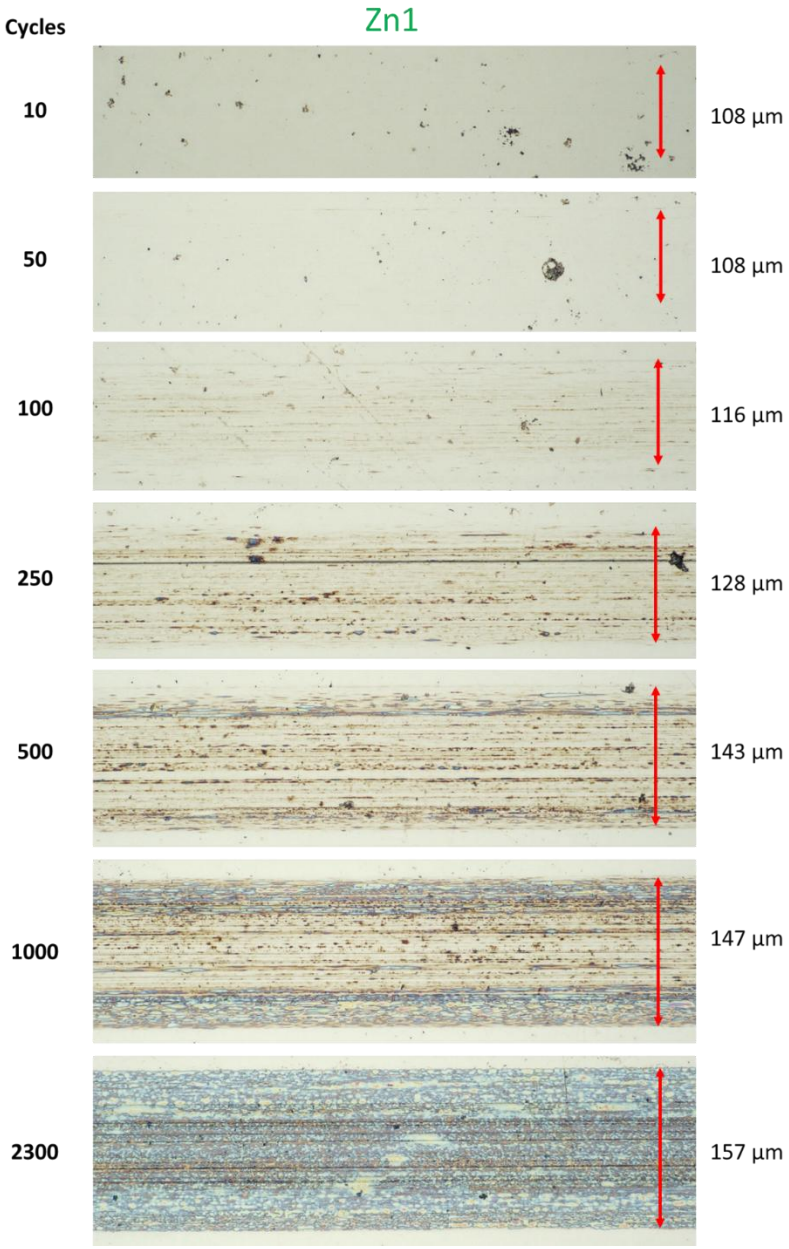

Fig. 166: Optical observations of wear tracks formed at 100°C on the disc at intermediate cycles in the presence of a solution containing ZDDP (Zn1).

Fig. 166 presents the evolution of the wear tracks obtained in the presence of ZDDP for different numbers of cycles. It can be observed that the tribofilm requires a certain induction time before fully covering the contact area. At 500 cycles, the tribofilm preferentially forms at the edges of the track, which are subjected to lower pressure compared to the central region. This observation is consistent with the friction coefficient curve shown in Fig. 160, where a decrease begins to appear around 400-500 cycles.

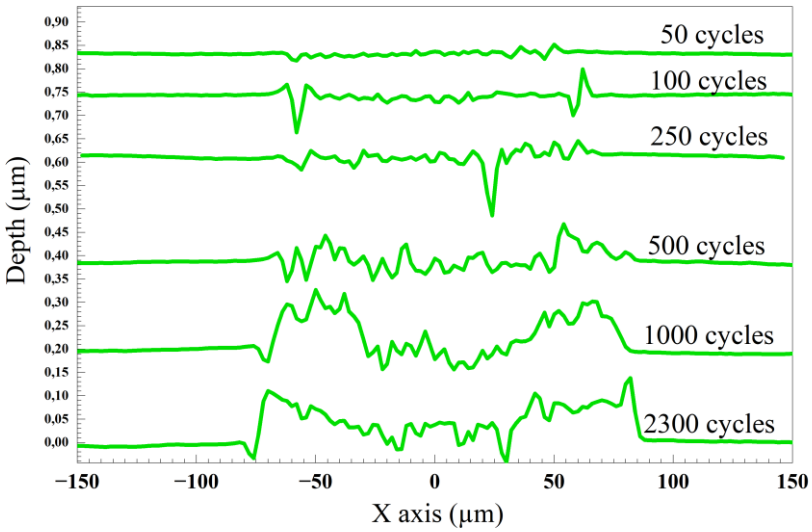

Fig. 167: Mean depth profiles wear tracks formed at 100°C on the disc at intermediate cycles in the presence of a solution containing ZDDP (Zn1).

Profilometry measurements (Fig. 167) clearly confirm these findings, showing a final tribofilm that is thicker at the edges than at the center. Furthermore, the substrate appears to undergo wear up to 250-500 cycles before being efficiently protected by the tribofilm.

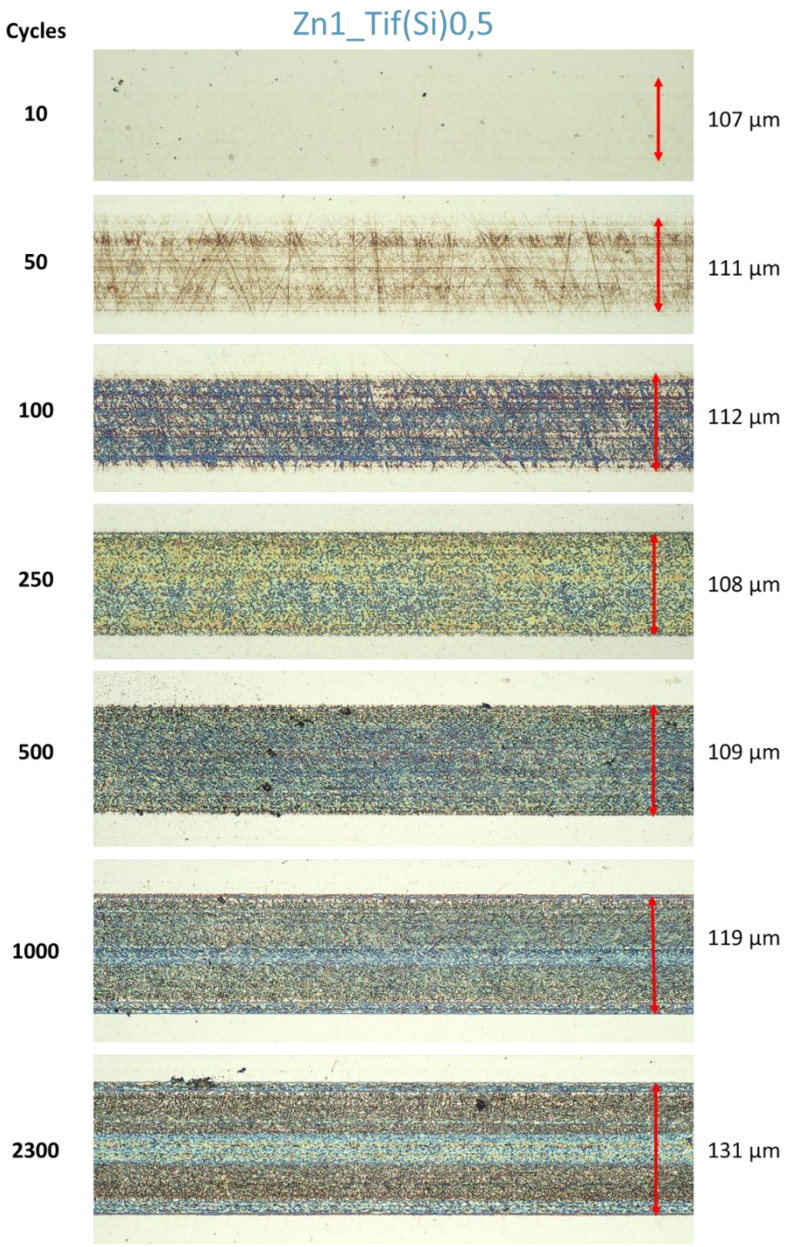

Fig. 168: Optical observations of wear tracks formed at 100°C on the disc at intermediate cycles in the presence of a solution containing a blend of ZDDP and silane functionalized TiO_2 nanoparticles (Zn1_Tif(Si)0.5).

For the ZDDP / silane-functionalized TiO_2 nanoparticle blend (Fig. 168), the tribofilm exhibits a behavior very similar to that of the nanoparticles used alone (Fig. 110). The tribofilm appears to form very rapidly and is already visible after only 50 cycles. As it highlights polishing marks on the substrate surface, it is likely that it starts to form in energetically favorable sites like scratches. By 250 cycles, the tribofilm seems to cover the entire contact area. From 500 cycles onward, the friction stabilizes (Fig. 160) and the wear track width remains almost unchanged until 1000 cycles, where the divergence between wider and narrower tracks - noted in Fig. 159 - becomes apparent.

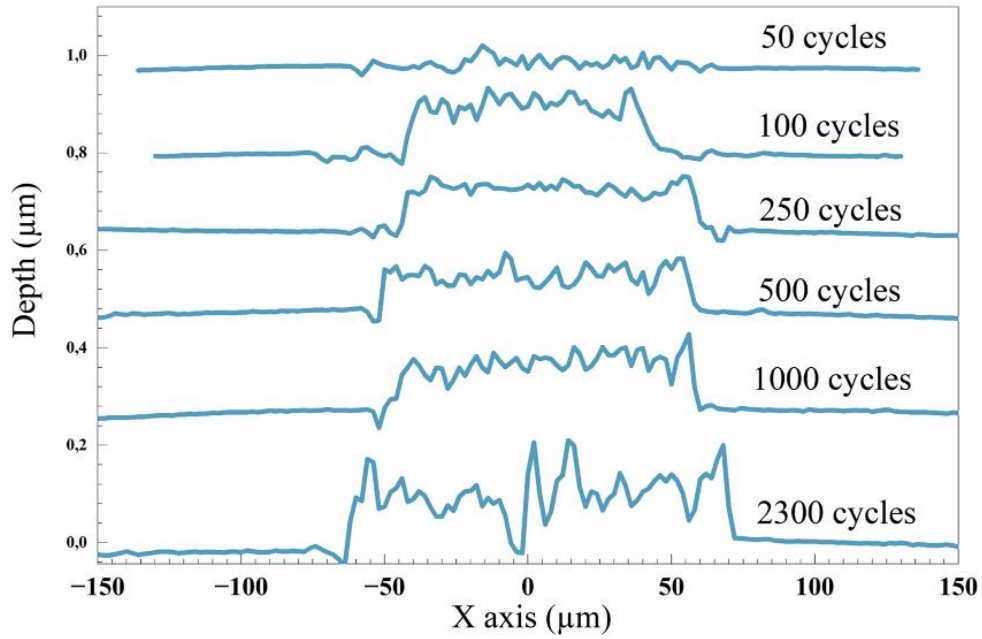

Fig. 169: Mean depth profiles wear tracks formed at 100°C on the disc at intermediate cycles in the presence of a solution containing a blend of ZDDP and silane functionalized TiO_2 nanoparticles (Zn1_Tif(Si)0.5).

The evolution of average wear track profiles is shown in Fig. 169. Once again, a rapid tribofilm formation is observed, with a thickness that appears stable as early as 250 cycles. Only at the final stage does the profile either widen or remain narrow (Fig. 161), depending on the test.

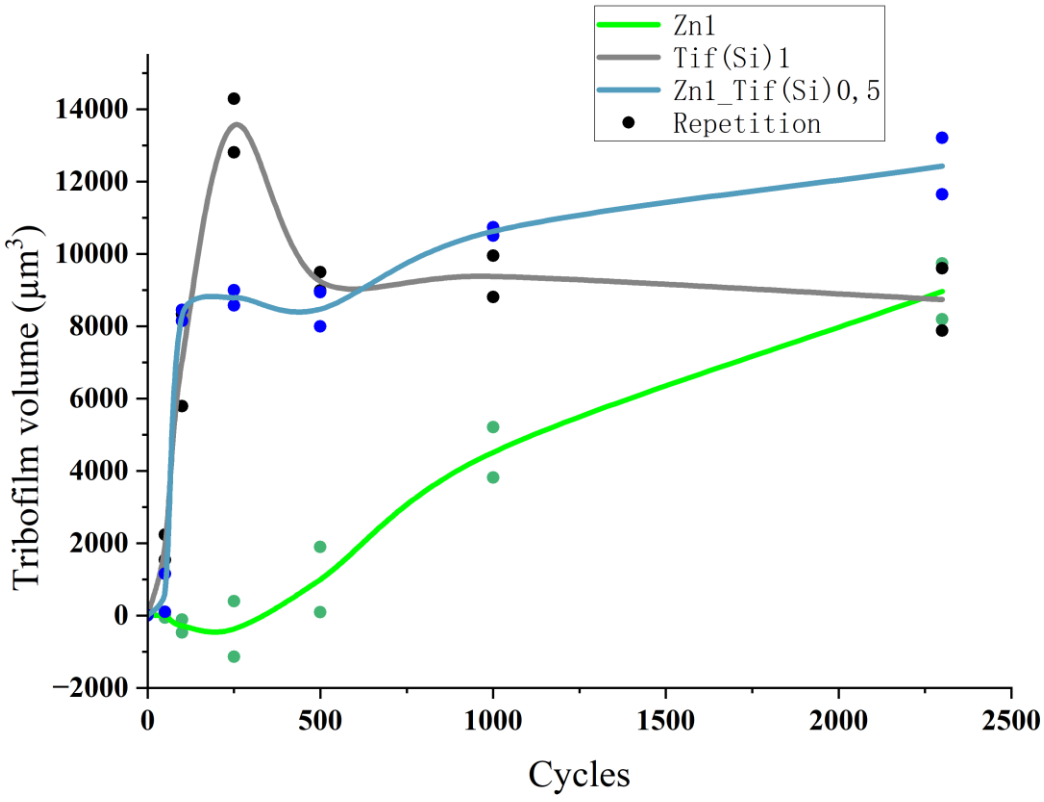

Fig. 170: Evolution of tribofilm growth volume with cycles for ZDDP solution (Zn1), silane-functionalized TiO_2 nanoparticles suspension (Tif(Si)1) and a blend containing ZDDP and silane-functionalized TiO_2 nanoparticles (Zn1_Tif(Si)0.5).

The evolution of the volume of tribofilm formed with ZDDP (Zn1) as well as with the ZDDP / silane-functionalized TiO_2 nanoparticle blend is presented in Fig. 170. For comparison, the previously obtained result with nanoparticles alone (Tif(Si)1) is also included. It can be observed that ZDDP alone requires more time to establish a protective tribofilm, which results in noticeable substrate wear during the early stages (0–250 cycles), before catching up at later stages. In contrast, the ZDDP / TiO_2 blend displays a behavior closely resembling that of nanoparticles alone, with comparable tribofilm growth rates between 0 and 100 cycles (150 and 105 μm^3/cycle, respectively). This suggests that the nanoparticles within the blend retain their high reactivity, enabling them to deposit first on the substrate. After this initial rapid growth phase, the tribofilm formation rate decreases significantly for the blend, suggesting that a different mechanism comes into play. It is likely that, once the nanoparticles have quickly been deposited on the surface, the subsequent consolidation of the tribofilm is ensured by a contribution of both ZDDP and silane-functionalized TiO_2 nanoparticles.

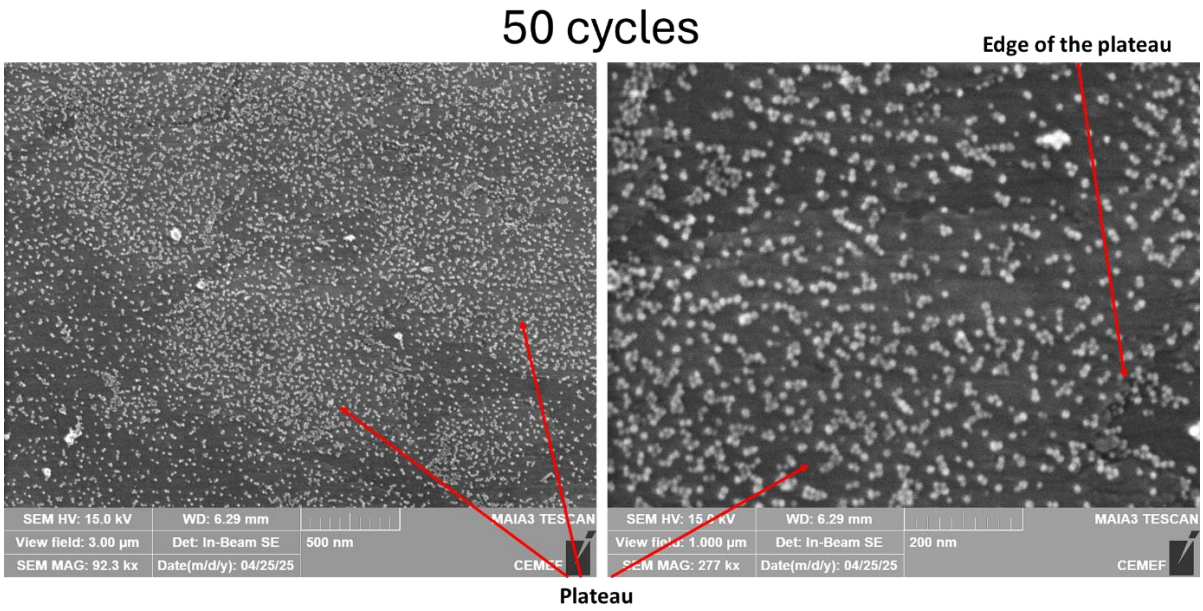

Fig. 171: SEM micrographs of the track formed with a blend of ZDDP and silane-functionalized TiO_2 nanoparticles (Zn1_Tif(Si)0.5) after 50 cycles.

SEM observations were also performed on these intermediate tracks. Although not easily visible, Fig. 171 shows that for the Zn1_Tif(Si)0.5 blend, plateaus are already visible after only 50 cycles and appear to result from the coalescence of nanoparticles. In comparison with the nanoparticles used alone (Fig. 114), no partially consolidated agglomerates are observed, suggesting that the presence of ZDDP modifies the way nanoparticles react on the surface and with each other from the very beginning.

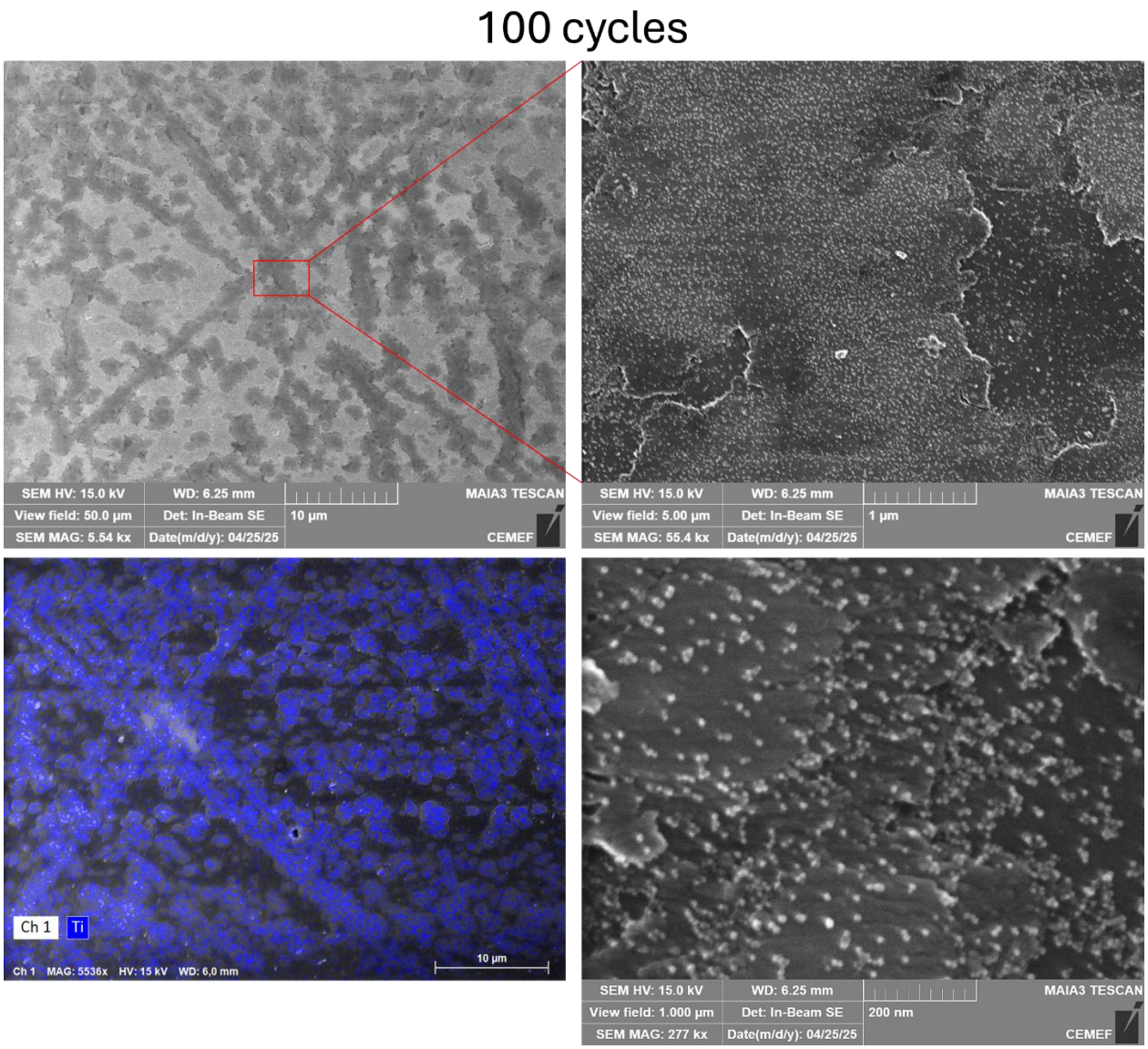

Fig. 172: SEM micrographs of the track formed with a blend of ZDDP and silane-functionalized TiO_2 nanoparticles (Zn1_Tif(Si)0.5) after 100 cycles. Accompanied by an EDX mapping of the tribofilm for Ti element.

At 100 cycles (Fig. 172), the tribofilm clearly develops preferentially within the polishing grooves of the substrate, as further confirmed by EDX mapping. High magnification images reveal once again the formation of well-defined plateaus, in continuity with the morphology observed at 50 cycles.

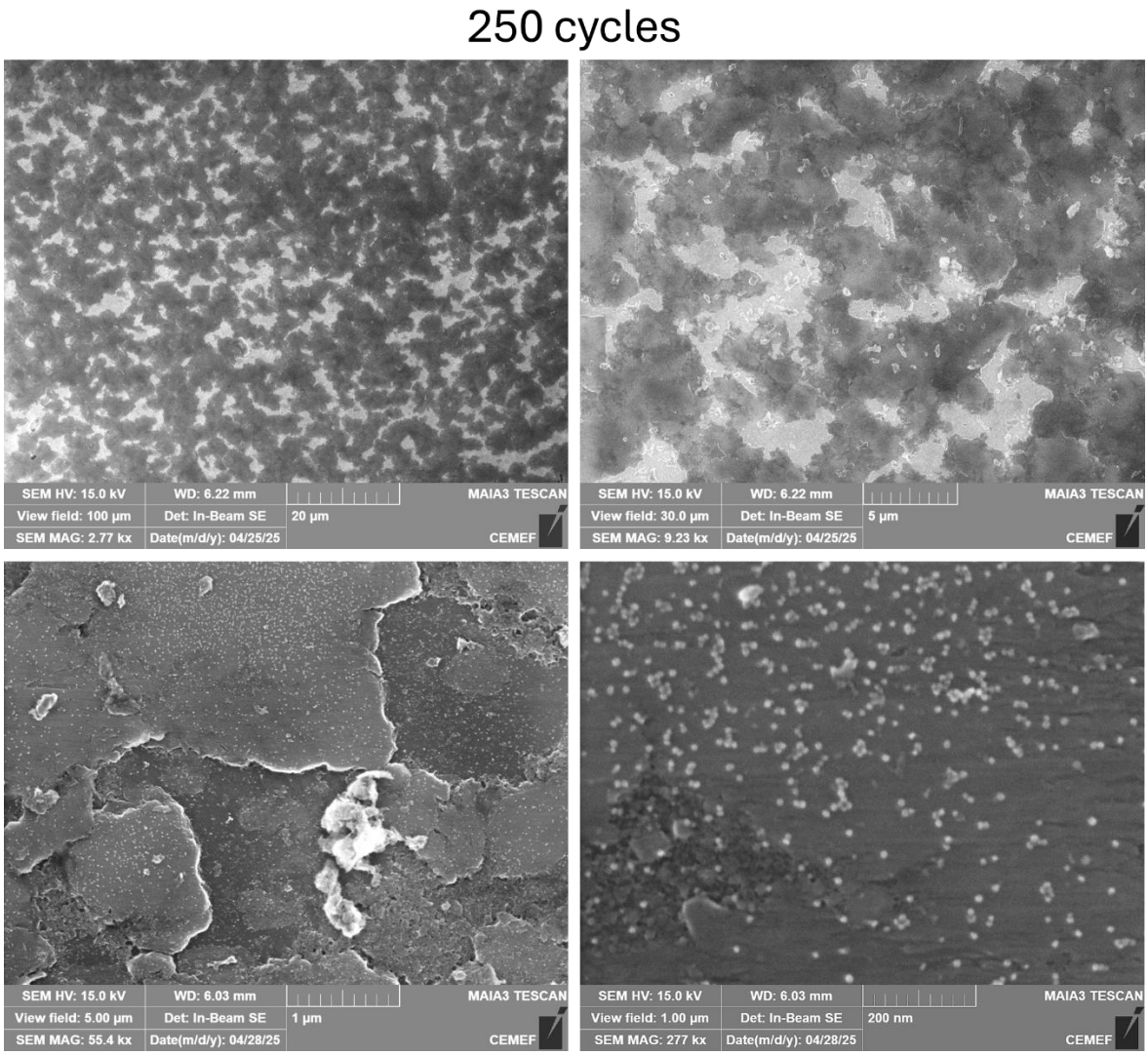

Fig. 173: SEM micrographs of the track formed with a blend of ZDDP and silane-functionalized TiO_2 nanoparticles (Zn1_Tif(Si)0.5) after 250 cycles.

From 250 cycles onwards, the tribofilm starts covering the entire track. The plateaus grow higher and exhibit a smoother surface, while only few debris are observed - contrasting with what was previously reported for nanoparticles alone (Fig. 116).

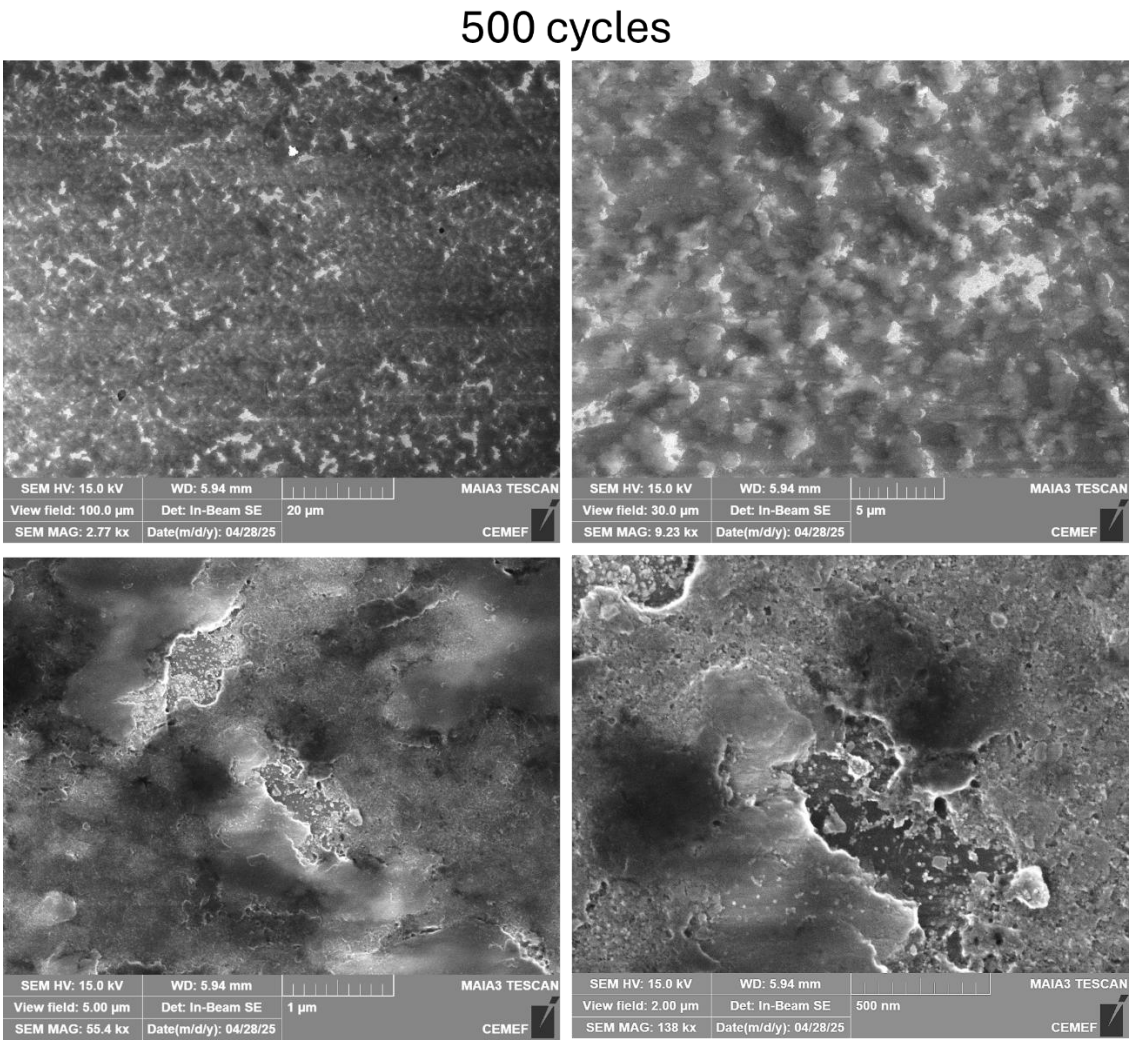

Fig. 174: SEM micrographs of the track formed with a blend of ZDDP and silane-functionalized TiO_2 nanoparticles (Zn1_Tif(Si)0.5) after 500 cycles.

At 500 cycles (Fig. 174), observations taken in the central region of the track reveal a continuous tribofilm with still distinguishable plateaus and valleys. The substrate seems to be fully covered by the tribofilm.

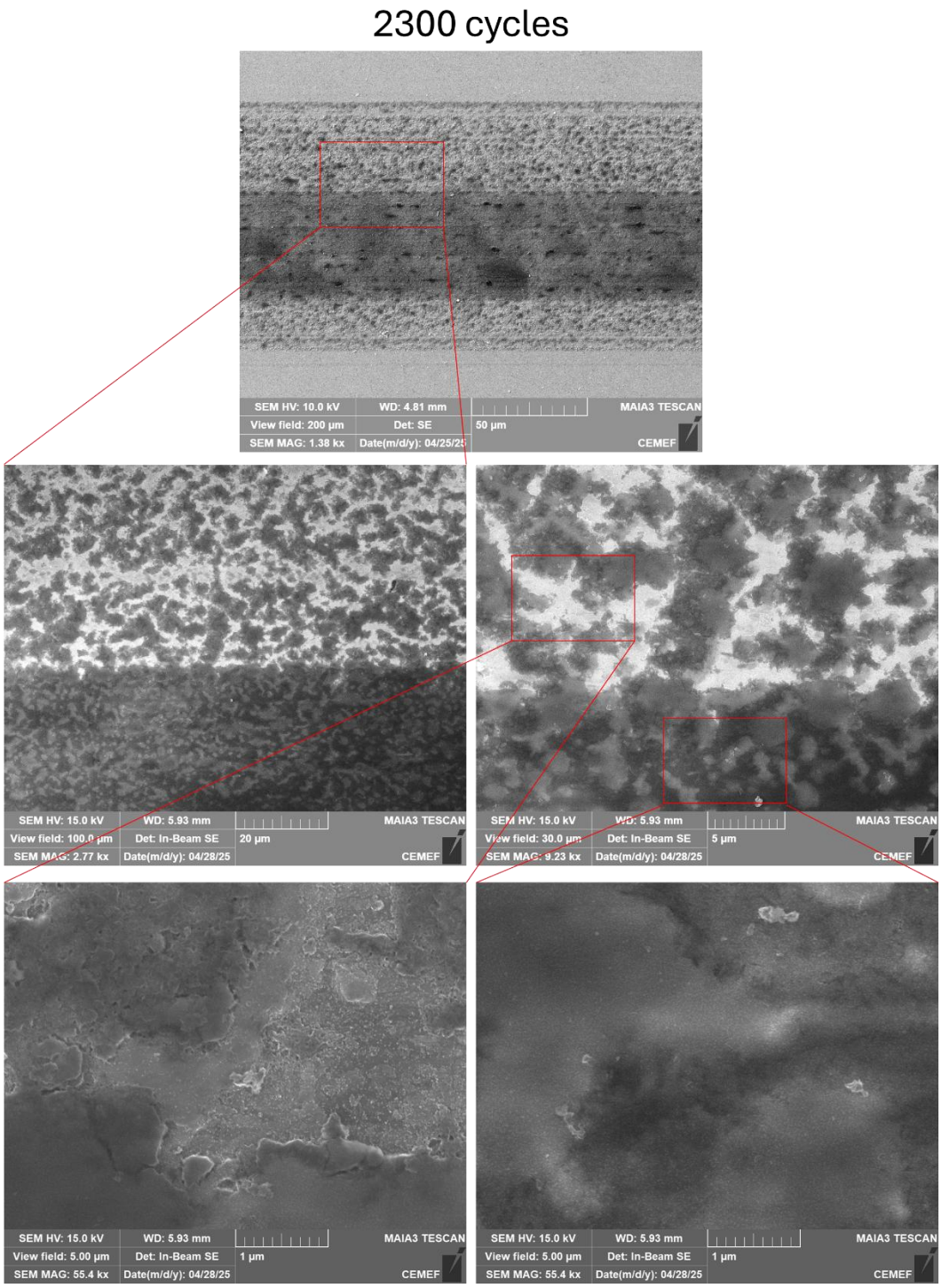

Fig. 175: SEM micrographs of the track formed with a blend of ZDDP and silane-functionalized TiO_2 nanoparticles (Zn1_Tif(Si)0.5) after 2300 cycles.

Finally, at 1000 and 2300 cycles (Fig. 175), the central zone appears more compacted compared to the peripheral regions of the tribofilm, consistent with optical images (Fig. 159). However, the contrast is somewhat misleading: the central region seems to consist solely of tribofilm, while the periphery seems to alternate between tribofilm and exposed substrate. However, high magnification images confirm that both areas are indeed fully covered by tribofilm. The difference lies in the plateau-valley relief, which is much less pronounced in the central zone, making plateaus and valleys nearly indistinguishable. These results suggest that once a certain tribofilm thickness is reached (Fig. 169),

further evolution proceeds primarily through consolidation rather than additional thickening as observed in the case of the blend with ZDDP and oleic acid-functionalized nanoparticles (Fig. 140 and Fig. 151).

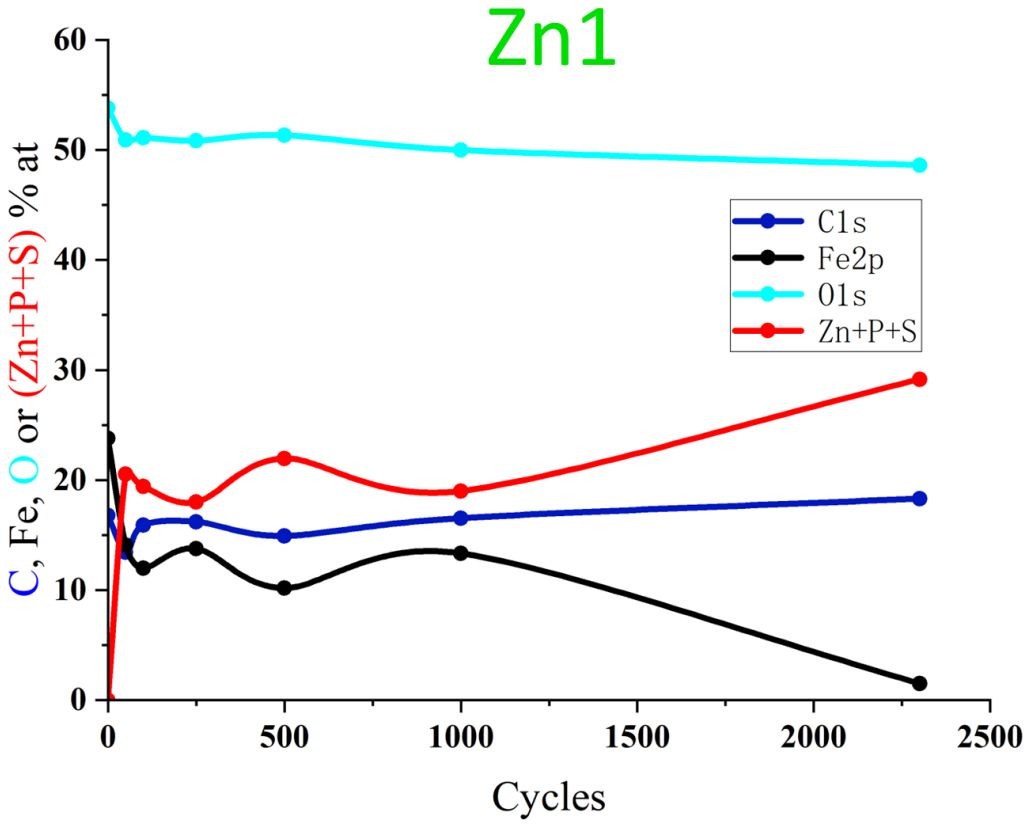

Fig. 176: Evolution of tribofilm at.% content (XPS analysis: C, Fe, O and (Zn+P+S)) with cycles for ZDDP solution (Zn1).

XPS analyses were also conducted on these intermediate tracks, and their evolution is presented in Fig. 176. A rapid increase in ZDDP-derived elements (Zn, P, and S) is detected as early as 50 cycles, but with a significant amount of Fe still present (14.1 at.%), indicating that the tribofilm formed at this stage remains either thin or with limited coverage (patchy). Only after 2300 cycles does the Fe content decrease to 1.8 at.% while Zn, P, and S become dominant.

Cycles	Zn1								
	C1s	Fe2p	O1s	Si2p	Ti2p	Zn2p	P2p	S2p	Other
0	16.8	23.8	54.8	0.4	0	0.7	0	0.2	4.3
50	13.5	14.1	50.9	0.0	0.0	5.5	11.0	4.0	1.0
100	15.9	12.0	51.1	0.0	0.0	6.2	9.6	3.6	1.6
250	16.2	13.8	50.8	0.0	0.0	4.6	9.5	3.9	1.2
500	14.9	10.2	51.3	0.0	0.0	8.1	10.6	3.3	1.6
1000	16.5	13.3	50.0	0.0	0.0	5.0	10.4	3.7	1.2
2300	11.7	1.8	52.2	0.0	0.0	17.0	14.8	2.2	0.4
out	20.9	22.6	51.9	0.0	0.0	1.4	1.7	0.0	1.5

Table 31: Evolution of tribofilm content (C, Fe, O, Si, Ti, Zn, P and S in at.%) with cycles for ZDDP solution (Zn1).

Table 31 reports the corresponding data used to plot Fig. 176, this time separating the contributions of Zn, P, and S. It can be seen that sulfur remains around 3.5 at.% between 50 and 1000 cycles before decreasing to 2.2 at.% at 2300 cycles, while Zn and P increase from ~6 and ~10 at.% to 17 and 14.8 at.%, respectively. These results are consistent with the state of the art, which suggests that the thick phosphate glass tribofilm formed by ZDDP is preceded by the formation of a thin iron sulfide layer [17,21]. This initial stage, extending from 0 to 500-1000 cycles, therefore corresponds to an induction phase during which this primary sulfide layer develops. It is then progressively covered by a phosphate-based tribofilm that grows on top of it, thereby ensuring the long-term protection of the substrate.

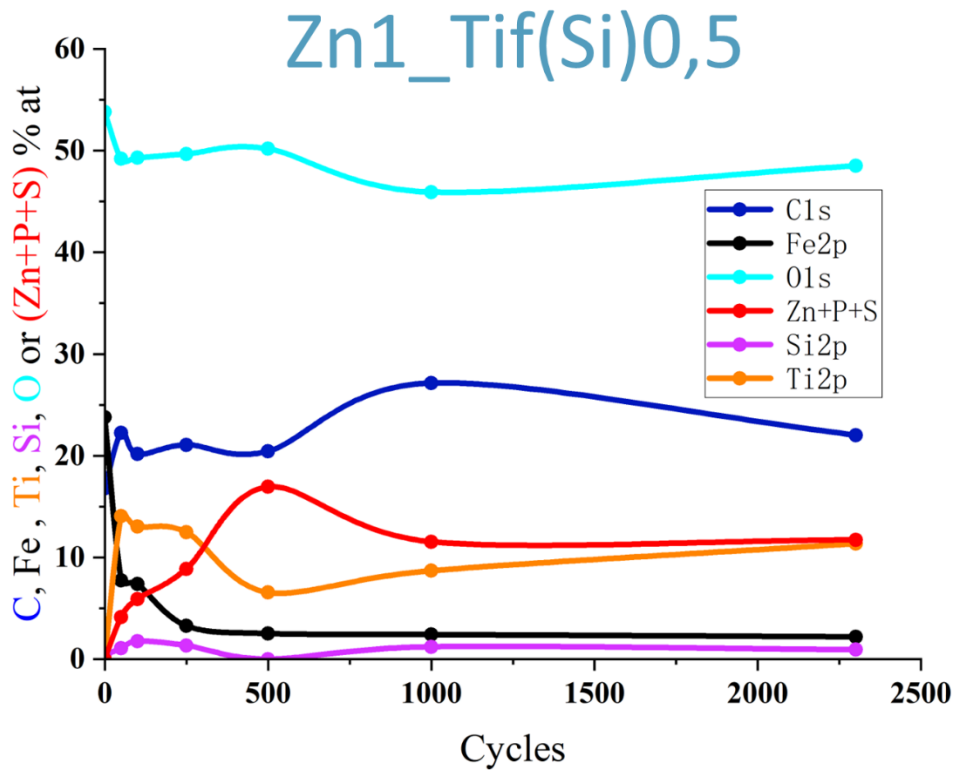

Fig. 177: Evolution of tribofilm at.% content (XPS analysis: C, Fe, O, Si and Ti) with cycles for the blend containing ZDDP and silane-functionalized TiO_2 nanoparticles (P_Zn1_Tif(Si)0.5).

For the blend, Fig. 177 shows that the first element detected during the early stages of tribofilm formation is Ti, which rapidly increases to 14.1 at.% after only 50 cycles (**Table 32**). Elements associated with ZDDP are also present but in much smaller amounts, with phosphorus being the most significant at 2.7 at.%. This supports the previous observations that nanoparticles within the blend tend to react first with the surface. Moreover, the Ti 2p peak at this stage already matches that of the final tribofilm (Fig. 165), indicating that Ti must be present exclusively as TiO_2, unlike what was observed for nanoparticles alone (Fig. 119) where $FeTiO_3$ is detected. The presence of ZDDP therefore appears to influence the way nanoparticles react.

Cycles	Zn1_Tif(Si)0,5								
	C1s	Fe2p	O1s	Si2p	Ti2p	Zn2p	P2p	S2p	Other
0	16.8	23.8	54.8	0.4	0	0.7	0	0.2	4.3
50	22.3	7.8	49.2	1.1	14.1	0.9	2.7	0.5	1.6
100	20.2	7.4	49.3	1.8	13.0	1.0	3.9	0.9	2.4
250	21.1	3.3	49.7	1.3	12.5	1.7	6.2	1.1	3.3
500	20.4	2.5	50.2	0.0	6.6	3.9	11.4	1.6	3.4
1000	27.2	2.4	45.9	1.2	8.7	2.2	8.3	1.1	3.1
2300	22.0	2.2	48.5	0.9	11.4	2.3	8.0	1.4	3.3
out	16.3	29.6	50.3	0.0	1.0	0.7	0.7	0.0	1.4

Table 32: Evolution of tribofilm content (C, Fe, O, Si, Ti, Zn, P and S in at.%) with cycles for the blend containing silane-functionalized TiO_2 nanoparticles (Zn1_Tif(Si)0.5) suspension.

Overall, the superior performance of the blend with ZDDP and silane-functionalized TiO_2 nanoparticles compared to the individual additives appears to arise not only from physicochemical interactions between ZDDP and TiO_2 nanoparticles, but also from their complementary reactivity. The nanoparticles, due to their high reactivity, deposit first on the surface and provide effective protection during the earliest cycles, thereby allowing ZDDP sufficient time to decompose and subsequently take over, most likely leading to the formation of a composite tribofilm.

This hypothesis was subsequently confirmed through TEM observations performed on a cross-sectional sample of the tribofilm formed at the center of the wear track. These analyses were conducted using a ThermoFisher Scientific SPECTRA 200 microscope operated at an acceleration voltage of 200 kV, located at the ACTEM platform.

Fig. 178 first presents the cross-section with a measured thickness of approximately 202 nm in the analyzed area, which is consistent with the profilometric measurements previously obtained (Fig. 163).

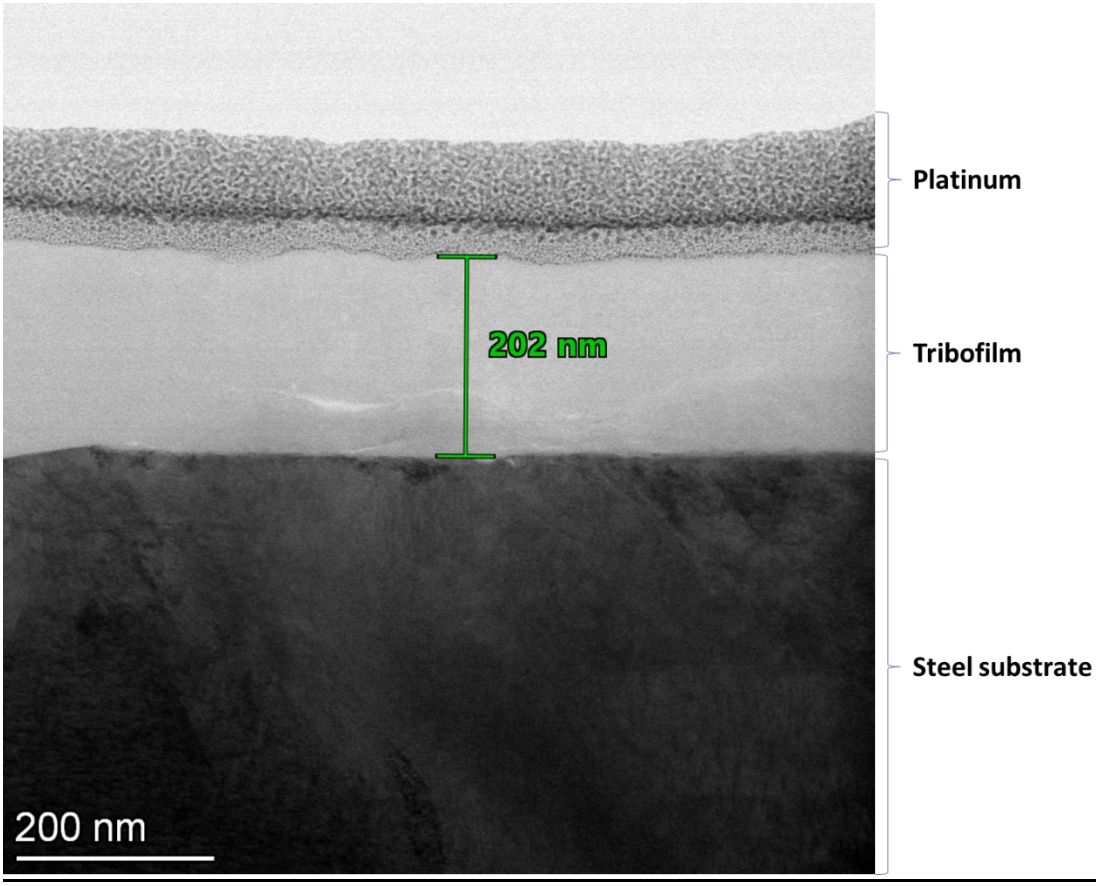

Fig. 178: TEM cross-section of the Zn1_Tif(Si)0.5 tribofilm formed at the center of the wear track.

An EDX mapping was then performed (Fig. 179), revealing that in the central region, a first Ti-rich tribofilm formed directly at the steel interface, followed by a second tribofilm this time rich in both phosphorus and titanium. It is noteworthy that the first tribofilm does not completely cover the substrate surface, unlike the second one. This observation is consistent with the fact that the ZDDP-derived tribofilm can form under shear conditions [17], whereas the TiO_2 nanoparticle-based tribofilm develops only in areas of direct mechanical contact.

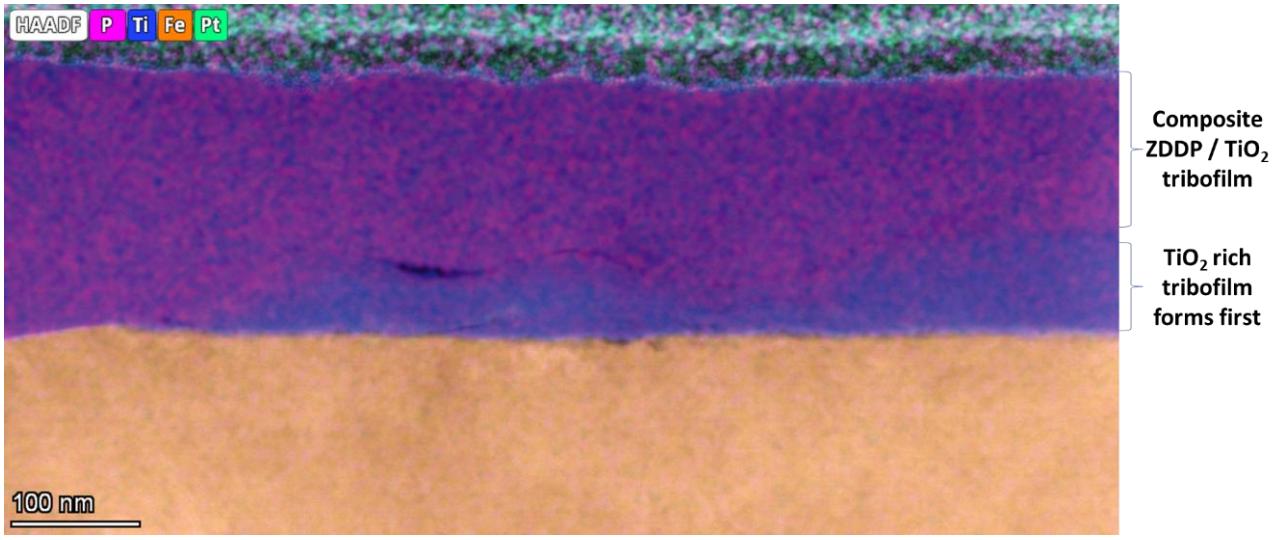

Fig. 179: EDX mapping of the Zn1_Tif(Si)0.5 tribofilm cross-section revealing a Ti-rich basal layer and a P–Ti-rich overlayer.

The chemical composition of these tribofilms is detailed in Fig. 180. The first layer (Area 2) is highly enriched in titanium and depleted in ZDDP-derived elements (Zn, P, and S). However, a non-negligible amount of iron is also detected. This iron may originate from the formation of iron titanate ($FeTiO_3$), as proposed in Section 3.1.2. Although the measured Fe/Ti/O ratios does not exactly match that of pure $FeTiO_3$, it likely corresponds to a mixture of $FeTiO_3$ and TiO_2 phases.

The second tribofilm (Area 3) contains a mixture of titanium (13.4 at.%) and ZDDP-derived elements (Zn + P + S = 15.5 at.%), confirming its composite nature.

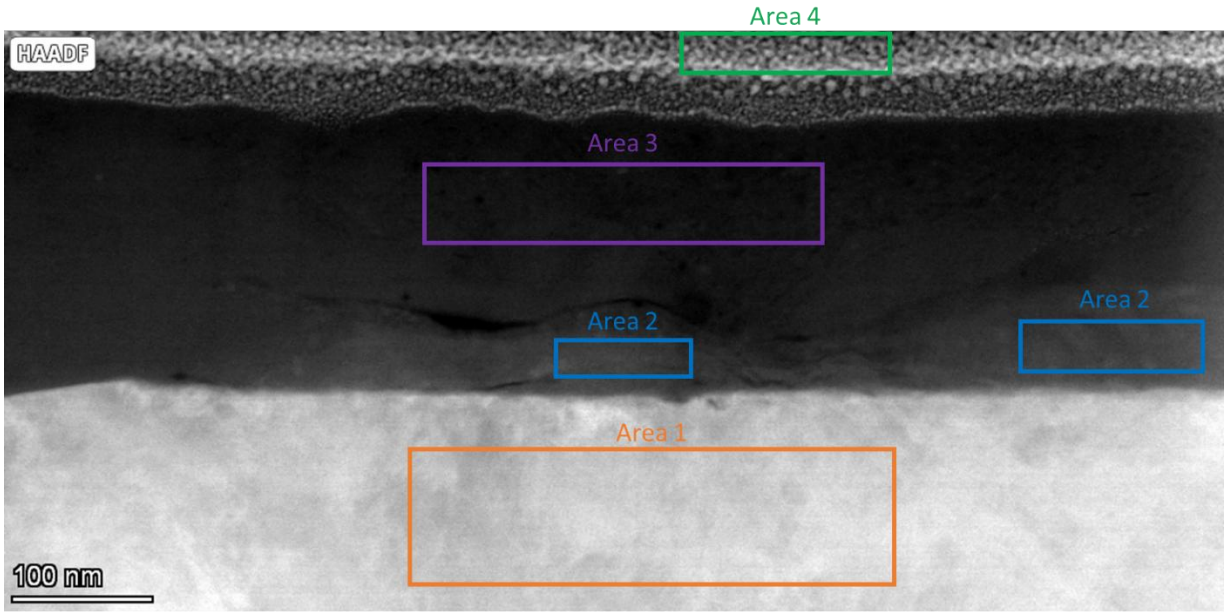

at.%	Area 1	Area 2	Area 3	Area 4
C	3.2	2.2	4.3	55.9
Fe	87.7	6.2	0.9	4.1
O	8.0	61.6	65.2	7.7
P	0.0	2.7	8.9	0.5
S	0.1	0.7	1.7	0.7
Zn	0.2	1.5	4.9	0.1
Si	0.6	1.2	0.6	0.7
Ti	0.2	23.8	13.4	0.6
Pt	0.0	0.1	0.2	29.7

*Fig. 180: EDX chemical composition of areas of Zn1_Tif(Si)0.5 tribofilm cross-section: **Area 1**: steel substrate, **Area 2**: Ti-rich tribofilm at the steel interface, **Area 3**: upper composite tribofilm containing Ti and ZDDP-derived elements, and **Area 4**: protective platinum layer deposited prior to FIB preparation.*

Finally, it is worth noting that the EDX composition measured in Area 3 of the TEM cross-section is very similar to the surface composition obtained by XPS analysis on the wear track (**Table 33**).

.at%	Zn1_Tif(Si)0.5	
	XPS	EDX TEM (Area 3)
C	18.8	4.3
Fe	1.1	0.9
O	51.2	65.2
P	8.6	8.9
S	1.6	1.7
Zn	4.6	4.6
Si	0.9	0.6
Ti	11.1	13.4
Other	2.2	0.2

Table 33: Comparison between the composition (at.%) obtained by XPS analysis on the wear track surface and by EDX analysis in Area 3 of the TEM cross-section for Zn1_Tif(Si)0.5 tribofilm.

Taken together, these results validate the proposed tribofilm formation mechanism:

TiO_2 nanoparticles, being more reactive, are the first to interact with the steel surface, leading to the formation of a TiO_2 and $FeTiO_3$ layer. This initial reaction acts as a transient interfacial stage, allowing sufficient time for ZDDP activation. Once activated, ZDDP contributes to the development of a composite tribofilm containing both ZDDP-derived compounds and Ti-based species. This latter film exhibits improved surface coverage, as it can form not only in zones of direct contact, but also in regions experiencing shear stresses without intimate asperity contact.

Summary and Discussion

The results obtained for ZDDP and its blends with TiO_2 nanoparticles functionalized either with oleic acid or silane clearly demonstrate that the functionalization route strongly influences both the chemical composition and the tribological performance of the resulting tribofilms.

When combined with oleic acid-functionalized nanoparticles, ZDDP exhibits a significant enrichment in Ti within the tribofilm, at the expense of ZDDP-derived elements (Zn, P, S). This composition leads to the formation of a thick tribofilm, which provides excellent friction reduction and wear protection. In contrast, the blend with silane-functionalized nanoparticles results in an intermediate behavior: the Ti contribution is lower, ZDDP-derived elements remain more prevalent, and the tribofilm formed is thinner but still provides a low friction as well as good anti-wear properties.

These results appear to depend strongly on the stability of the nanoparticles, and therefore on the strength of the interaction between the ligand and the nanoparticle surface:

- In the case of oleic acid-functionalized nanoparticles, the interaction between the ligand and the TiO_2 surface is relatively weak, leading to partial ligand desorption under tribological conditions. This promotes a rapid deposition kinetics of the nanoparticles onto the steel surface, occurring much faster than the decomposition and activation of ZDDP. As a result, the tribofilm formation process is dominated by the Ti-containing species, explaining both the high Ti enrichment and the reduced contribution of ZDDP-derived elements.

- Conversely, for silane-functionalized nanoparticles, the stronger chemical bonding between the silane ligand and the nanoparticle surface hinders nanoparticle deposition. This slower deposition rate allows ZDDP to decompose and react more effectively, leading to the formation of a more balanced composite tribofilm in which both additives contribute synergistically. This is consistent with the more uniform thickness and homogeneous morphology observed for the tribofilm formed with the blend containing ZDDP and silane-functionalized nanoparticles.

Despite these differences, both blends systematically outperform ZDDP alone in terms of friction stability, wear scar dimensions, and tribofilm coverage and thickness. Optical and SEM observations as well as profilometry and XPS analysis on the intermediate cycles suggest that this enhanced performance originates from a dual mechanism: nanoparticles deposit first, protecting the surface during the initial stages, while ZDDP subsequently decomposes and consolidates the tribofilm, likely leading to the development of a composite structure comprised of both TiO_2 and ZDDP derived elements.

In the case of silane-functionalized nanoparticles, which have been studied more thoroughly thanks to intermediate cycle tests, this mechanism helps to compensate for the individual limitations of the two additives when used separately. Silane-functionalized nanoparticles can rapidly form a tribofilm, but only in high-pressure regions where direct asperity contact occurs. However, their high colloidal stability limits further reactivity, which in turn compromises the long-term robustness of the resulting tribofilm.

On the other hand, ZDDP is capable of forming a tribofilm even in low-pressure regions subjected primarily to shear stress, but its slower decomposition kinetics cause an initial wear of the substrate before a protective film is fully established. Moreover, due to its glassy phosphate nature, the ZDDP-derived tribofilm is more prone to wear and must be continuously regenerated to maintain protection.

When both additives are combined, a synergistic tribofilm formation sequence is achieved: an initial ceramic Ti-based tribofilm forms rapidly but locally in the regions of highest contact pressure, followed by the growth of a composite tribofilm that develops more homogeneously over the entire area. This glass and ceramic composite film is likely less wear-resistant than a fully ceramic layer, yet it remains significantly more durable than the pure phosphate glass film formed by ZDDP alone.

Overall, ZDDP and TiO_2 nanoparticles appear to react independently on the steel surface. It is unlikely that direct chemical reactions occur between these two additives that could explain the observed tribological behavior. Rather, the synergistic effect arises from the complementary nature of their deposition kinetics, deposition mechanisms, and mechanical properties. The combination of these distinct but cooperative processes ultimately leads to enhanced performance of the lubricant blend.

Conclusion and Perspectives

This chapter has highlighted the crucial role of both the dispersion method and the nature of the functionalizing agent on the tribological performance of TiO_2 nanoparticles, as well as on their interactions with conventional additives.

First, the use of unmodified nanoparticles without a proper dispersion strategy leads to unstable suspensions and poor tribological efficiency, with agglomerates even acting as abrasive third bodies. By contrast, the use of oleic acid, either as a dispersing co-additive or chemically grafted onto the nanoparticle surface, significantly improves suspension stability and promotes the formation of thick and cohesive tribofilms. Oleic acid functionalization has proven particularly effective, both for enhancing suspension stability and for improving tribological performance. These tribofilms provide friction reduction and effective wear protection.

Silane functionalization, on the other hand, provides remarkable colloidal stability, even at high temperatures and over long storage periods. However, it can compromise the robustness of the tribofilms, which appear fragmented, porous, and prone to wear. Interrupted tests confirmed the very high initial reactivity of silane-functionalized nanoparticles, but also the fragility of the resulting structures, which are gradually worn under friction and load. Thus, a clear trade-off emerges between tribofilm performance and suspension stability, with oleic acid favoring tribofilm robustness and silane favoring dispersion stability.

When combined with MoDTC, the interactions with TiO_2 nanoparticles reveal additional mechanistic insights. With unmodified nanoparticles, a strong synergistic effect is observed, leading to a significant reduction in friction, moderate wear, and a higher proportion of MoS_2 compound in the tribofilm. This synergy depends on the ability of MoDTC to interact physically and chemically with the nanoparticle surface, which requires an incubation period of a few days. In contrast, when functionalized nanoparticles are used, the TiO_2 surface is partially or fully blocked, preventing the formation of this synergy and the associated friction reduction. Nevertheless, MoDTC still influences tribofilm formation, either positively or negatively depending on the functionalizing agent: oleic acid-functionalized nanoparticles show incompatibility, with poor tribofilm efficiency and wear protection, while silane-functionalized nanoparticles benefit from a thicker tribofilm, despite the lack of friction reduction.

When nanoparticles are combined with an anti-wear additive such as ZDDP, synergistic effects arise as well. The results show that nanoparticles provide rapid surface protection during the earliest cycles, while ZDDP gradually decomposes to form its characteristic tribo-products represented by Zn, P, and S. Their combination leads to the formation of composite tribofilms that are thicker and more homogeneous than those obtained with either additive alone. In contrast to MoDTC, the synergy between ZDDP and TiO_2 nanoparticles appears to arise primarily from a cooperative effect during tribofilm formation, rather than from modifications of reaction products through chemical reactions between additives. This explains why the synergistic effect is observed regardless of the level or type of nanoparticle functionalization.

Specifically, the comparison between oleic acid- and silane-functionalized nanoparticles in blends with ZDDP further illustrates the possibility of tuning tribofilm composition and structure. Oleic acid promotes the formation of TiO_2-rich tribofilms, expected to provide superior wear resistance, while silane functionalization, although less effective in tribofilm growth, offers an attractive compromise between suspension stability and very good tribological performance, due to a higher chemical bond with the nanoparticles.

In summary, this chapter demonstrates that the choice of functionalization agent and dispersion strategy not only governs suspension stability but also controls tribofilm growth mechanisms, chemical composition, structural properties, and synergies with conventional additives. For MoDTC in particular, these results highlight that the tribological benefit strongly depends on the accessibility of the nanoparticle surface and the nature of the functionalizing agent. In contrast, for ZDDP, the observed synergy with TiO_2 nanoparticles primarily arises from cooperativity between the two additives, which results in faster growth rate of tribofilms and higher thickness regardless of the nanoparticle functionalization. Together, these findings represent a key step toward the rational integration of TiO_2 nanoparticles into fully formulated lubricants, while carefully balancing stability, performance, and compatibility with the additive package.

Bibliography

[1] Chen Y, Renner P, Liang H. Dispersion of Nanoparticles in Lubricating Oil: A Critical Review. Lubricants 2019;7:7. https://doi.org/10.3390/lubricants7010007.

[2] Dassenoy F, Jenei IZ, Pavan S, Galipaud J, Thersleff T, Wieber S, Hagemann M, Ness D. Performance and Lubrication Mechanism of New TiO_2 Nanoparticle-Based High-Performance Lubricant Additives. Tribology Transactions 2021;64:325–40. https://doi.org/10.1080/10402004.2020.1838678.

[3] Thrush SJ, Comfort AS, Dusenbury JS, Xiong Y, Qu H, Han X, Schall JD, Barber GC, Wang X. Stability, Thermal Conductivity, Viscosity, and Tribological Characterization of Zirconia Nanofluids as a Function of Nanoparticle Concentration. Tribology Transactions 2020;63:68–76. https://doi.org/10.1080/10402004.2019.1660017.

[4] Kumar V, Wani MF, Mannekote JK, Kailas SV. Tribological Properties of Some Fatty Acids. J Phys: Conf Ser 2019;1240:012133. https://doi.org/10.1088/1742-6596/1240/1/012133.

[5] Blok H. The flash temperature concept. Wear 1963;6:483–94. https://doi.org/10.1016/0043-1648(63)90283-7.

[6] Khare HS, Lahouij I, Jackson A, Feng G, Chen Z, Cooper GD, Carpick RW. Nanoscale Generation of Robust Solid Films from Liquid-Dispersed Nanoparticles via in Situ Atomic Force Microscopy: Growth Kinetics and Nanomechanical Properties. ACS Appl Mater Interfaces 2018;10:40335–47. https://doi.org/10.1021/acsami.8b16680.

[7] Lahouij I, Gould B, Demas N, Greco A, Chen Z, Cooper GD, Jackson A, Carpick RW. Inhibition of Micro-pitting by Tribofilm-Forming ZrO2 Nanocrystal Lubricant Additives: A Micro-pitting Rig and Transmission Electron Microscope Study. Tribol Lett 2022;70:13. https://doi.org/10.1007/s11249-021-01555-2.

[8] Thrush SJ, Comfort AS, Dusenbury JS, Han X, Wang X, Qu H, Barber GC. Study of pressure dependence on sinterable zirconia nanoparticle tribofilm growth. Tribology International 2021;154:106683. https://doi.org/10.1016/j.triboint.2020.106683.

[9] Zhou Q, Xu S, Zhu C, Cao B, Kausar F, Xu A, Yuan WZ, Zhang Y. Towards high-performance hybrid hydrophilic membranes: chemical anchoring of hydroxyl-rich nanoparticles on PVDF membranes via a silane coupling agent. J Mater Sci 2017;52:11737–48. https://doi.org/10.1007/s10853-017-1313-1.

[10] Sharma V, Timmons RB, Erdemir A, Aswath PB. Synergistic and antagonistic interaction between ZDDP and TiO_2 nanoparticles under boundary lubrication. Tribology International 2025;202:110299. https://doi.org/10.1016/j.triboint.2024.110299.

[11] Fujii T, Takada Y, Nakanishi M, Takada J, Kimura M, Yoshikawa H. Electronic structure of stoichiometric and non-stoichiometric epitaxial $FeTiO_{3+\delta}$ films. J Phys: Conf Ser 2008;100:012043. https://doi.org/10.1088/1742-6596/100/1/012043.

[12] Gambhire AB, Lande MK, Rathod SB, Arbad BR, Vidhate KN, Gholap RS, Patil KR. Synthesis and characterization of $FeTiO_3$ ceramics. Arabian Journal of Chemistry 2016;9:S429–32. https://doi.org/10.1016/j.arabjc.2011.05.012.

[13] Deshpande P. Interaction of MoDTC additive on TiO_2 APS coating under mixed/boundary lubrication conditions: A tribocatalytic process. Thèse de Doctorat. L'Ecole centrale de Lyon, 2017.

[14] Onodera T, Morita Y, Suzuki A, Sahnoun R, Koyama M, Tsuboi H, Hatakeyama N, Endou A, Takaba H, Del Carpio CA, Deka RC, Kubo M, Miyamoto A. Tribochemical Reaction Dynamics of Molybdenum Dithiocarbamate on Nascent Iron Surface: A Hybrid Quantum Chemical/Classical Molecular Dynamics Study. J Nanosci Nanotech 2010;10:2495–502. https://doi.org/10.1166/jnn.2010.1399.

[15] Tsai AE, Komvopoulos K. Wear Mechanisms, Composition and Thickness of Antiwear Tribofilms Formed from Multi-Component Lubricants. Materials 2024;17:2324. https://doi.org/10.3390/ma17102324.

[16] Morina A, Neville A, Priest M, Green JH. ZDDP and MoDTC interactions and their effect on tribological performance – tribofilm characteristics and its evolution. Tribol Lett 2006;24:243–56. https://doi.org/10.1007/s11249-006-9123-7.

[17] Zhang J, Spikes H. On the Mechanism of ZDDP Antiwear Film Formation. Tribology Letters 2016;63:24. https://doi.org/10.1007/s11249-016-0706-7.

[18] Fang L, Korres S, Lamberti WA, Webster MN, Carpick RW. What stress components drive mechanochemistry? A study of ZDDP tribofilm formation. Faraday Discuss 2023;241:394–412. https://doi.org/10.1039/D2FD00123C.

[19] Elinski MB, LaMascus P, Zheng L, Jackson A, Wiacek RJ, Carpick RW. Cooperativity Between Zirconium Dioxide Nanoparticles and Extreme Pressure Additives in Forming Protective Tribofilms: Toward Enabling Low Viscosity Lubricants. Tribol Lett 2020;68:107. https://doi.org/10.1007/s11249-020-01346-1.

[20] LaMascus P, Elinski MB, Delghandi D, Nautiyal P, Griffin J, Zheng L, Jackson A, Wiacek RJ, Carpick RW. Competition Between Growth and Removal in Zirconia Nanocrystal-Derived Tribofilms: The Role of Co-additives. Tribol Lett 2024;72:106. https://doi.org/10.1007/s11249-024-01905-w.

[21] Spikes H. Mechanisms of ZDDP—An Update. Tribol Lett 2025;73:38. https://doi.org/10.1007/s11249-025-01968-3.

Chapter 4: Cold Sprayed Ti/TiO_x Composite Coatings: from Elaboration to Tribological Properties

Résumé en français :

Ce chapitre étudie l'amélioration des surfaces par l'application d'un revêtement composite Ti/TiO_x obtenu par Cold spray. Il se divise en deux parties : l'optimisation des conditions de projection, puis l'étude tribologique des revêtements développés.

Dans la première partie, différentes méthodes de préparation de surface ont été évaluées pour assurer une bonne adhésion du revêtement au substrat. Le jet d'eau s'est avéré plus efficace que le jet d'azote liquide, car il crée une rugosité suffisante tout en limitant l'incrustation de contaminants. Ensuite, les paramètres de projection du titane pur ont été optimisés en faisant varier la pression et la morphologie des poudres. Une pression d'environ 35 bars permet d'obtenir des revêtements denses et peu poreux. Les particules irrégulières adhèrent mieux à faible pression, tandis que les particules sphériques permettent d'obtenir une porosité plus faible à haute pression. L'ensemble montre que la performance du revêtement dépend de l'équilibre entre préparation de surface, pression et morphologie des particules.

La seconde partie utilise ces conditions optimisées pour élaborer des revêtements composites. Les essais ont montré que les poudres sphériques subissent plus d'usure adhésive, ce qui a conduit à retenir les particules irrégulières comme matrice métallique. La pression de 35 bars précédemment déterminée s'est révélée insuffisante pour mener à bien les essais tribologiques (usure excessive) et celle-ci a finalement été augmentée à 50 bars. Un mélange contenant 50 % vol. de poudre irrégulière de titane et 50 % vol. de TiO_x donne après projection un composite enrichi à environ 16 % vol. de renforts, présentant un frottement stable et une usure faible comparé aux revêtements monocomposants. En présence d'additifs lubrifiants, le revêtement montre une bonne compatibilité : le ZDDP génère un tribofilm épais et protecteur qui se forme seulement sur la matrice métallique, tandis que le MoDTC réduit efficacement le frottement grâce à la formation de MoS_2.

Globalement, le revêtement composite Ti/TiO_x obtenu par Cold Spray combine bonne adhésion entre les particules et avec le substrat, faible usure et compatibilité avec les additifs conventionnels, ce qui en fait une solution prometteuse pour l'amélioration des performances tribologiques des surfaces.

In the previous chapter, the enhancement of tribological performance under boundary lubrication was achieved by modifying the lubricant itself through the incorporation of nanoparticles combined with conventional additives (ZDDP and MoDTC). This formulation-based approach aimed to improve surface protection by optimizing the chemical and physical behavior of the lubricant.

In the present chapter, the focus shifts toward an alternative route to tribological improvement: acting directly on the surfaces. Among the various available surface engineering techniques, the Cold Spray process was selected for its ability to produce dense, adherent coatings while maintaining the intrinsic properties of the sprayed materials. As a solid-state deposition method, Cold Spray accelerates powder particles to high velocities, causing them to plastically deform and bond upon impact. Unlike conventional thermal spraying or other high-temperature deposition techniques, Cold Spray operates below the melting point of the materials, thereby preserving, to a certain extent, the initial microstructure and chemical composition of the powders when parameters are properly optimized.

In mechanical contacts such as gears, axles or transmission shafts, hard coatings are typically employed to resist wear and limit plastic deformation under high contact pressures. However, the Cold Spray process is poorly suited for depositing such hard, brittle materials, as it relies on the plastic deformation of particles upon impact to ensure adhesion and cohesion. To overcome this limitation, a composite approach is proposed.

This chapter focuses on the development and optimization of titanium-based composite coatings produced by the Cold Spray technique. The objective is to elaborate dense, adherent, and mechanically robust coatings combining a ductile metallic matrix with a hard ceramic reinforcement. Titanium (Ti) was selected as the matrix material due to its excellent mechanical properties, corrosion resistance, and suitability for Cold Spray processing. Titanium oxide (TiO_x) was chosen as the reinforcement phase to maintain full chemical compatibility with the metallic matrix. Moreover, TiO_x was considered with the objective of exploring whether it can interact synergistically with lubricant additives to enhance surface protection and mitigate wear, by analogy with the demonstrated ability of TiO_2 nanoparticles to improve the performance of boundary lubrication additives in the previous chapter.

This approach - combining a metal with its own oxide - minimizes risks of interfacial reactivity or poor adhesion that may arise from mismatched chemistries, thermal expansion coefficients, or surface energies typically encountered in heterogeneous metal-ceramic systems. As a result, it ensures a coherent and stable composite architecture, favorable to efficient load transfer and enhanced tribological durability.

The composite coating concept thus provides an optimized compromise between the process constraints of Cold Spray, which necessitate particle ductility for efficient deposition, and the tribological requirements of mechanical components, which demand hardness and long-term wear resistance. This strategy paves the way for the development of functional coatings that can simultaneously satisfy processability constraints and deliver high performance under frictional and wear conditions.

The chapter primarily focuses on the preparation and optimization of the Ti/TiO_x composite coating, including the adjustment of process parameters and microstructural analysis to achieve optimal deposition quality. The final section presents the tribological evaluation of the optimized coating under lubricated conditions, demonstrating promising results that highlight the potential of this approach for high-performance tribological applications.

This chapter is organized as follows:

- Section I presents the optimization of a single-component coating, focusing on the preparation of the substrate surface to promote adhesion, as well as on the optimization of deposition parameters to enhance inter-particle bonding and coating cohesion.
- Section II addresses the optimization of the composite coating, in which the deposition parameters are tuned to improve the physical and mechanical properties of the coating, and the resulting system is further evaluated in terms of its tribological performance.

4.1 Elaboration of the Titanium Matrix Coating

4.1.1 Enhancing Interfacial Adhesion with the Substrate

Achieving strong adhesion between the substrate and the coating is crucial to ensure reliable performance, prevent delamination, and enhance the overall durability of the coated system. To this end, we have identified several parameters that can influence the adhesion quality related to surface preparation parameters:

- Three types of abrasive-based surface preparation methods were investigated: water jetting, liquid nitrogen jetting, and sandblasting.
- The amount of abrasive used can be adjusted.
- The projection angle of the abrasives can also be varied.

In order to assess the effect of the different surface preparation techniques, samples were first prepared using each of the methods mentioned above with a 90° nozzle angle and a 300 g/min abrasive feed rate (described in Chapter 2). Their respective surface roughness (Ra) was then measured, as shown in Fig. 181.

It can be observed that the fluid-jet techniques resulted in the highest roughness values, with Ra = 10.5 µm for the water jet and Ra = 11.5 µm for the liquid nitrogen jet. In contrast, sandblasting produced a much lower roughness of only 2 µm. Considering that the as-received specimens exhibited a ground surface finish with an initial Ra of approximately 0.6 µm, all three preparation techniques effectively increased the surface roughness of the samples.

It can also be observed that the surface prepared using liquid nitrogen appears to have been more deeply impacted, with surface peaks reaching up to approximately 85 µm in height, compared to about 50 µm for the water-jet-prepared surface.

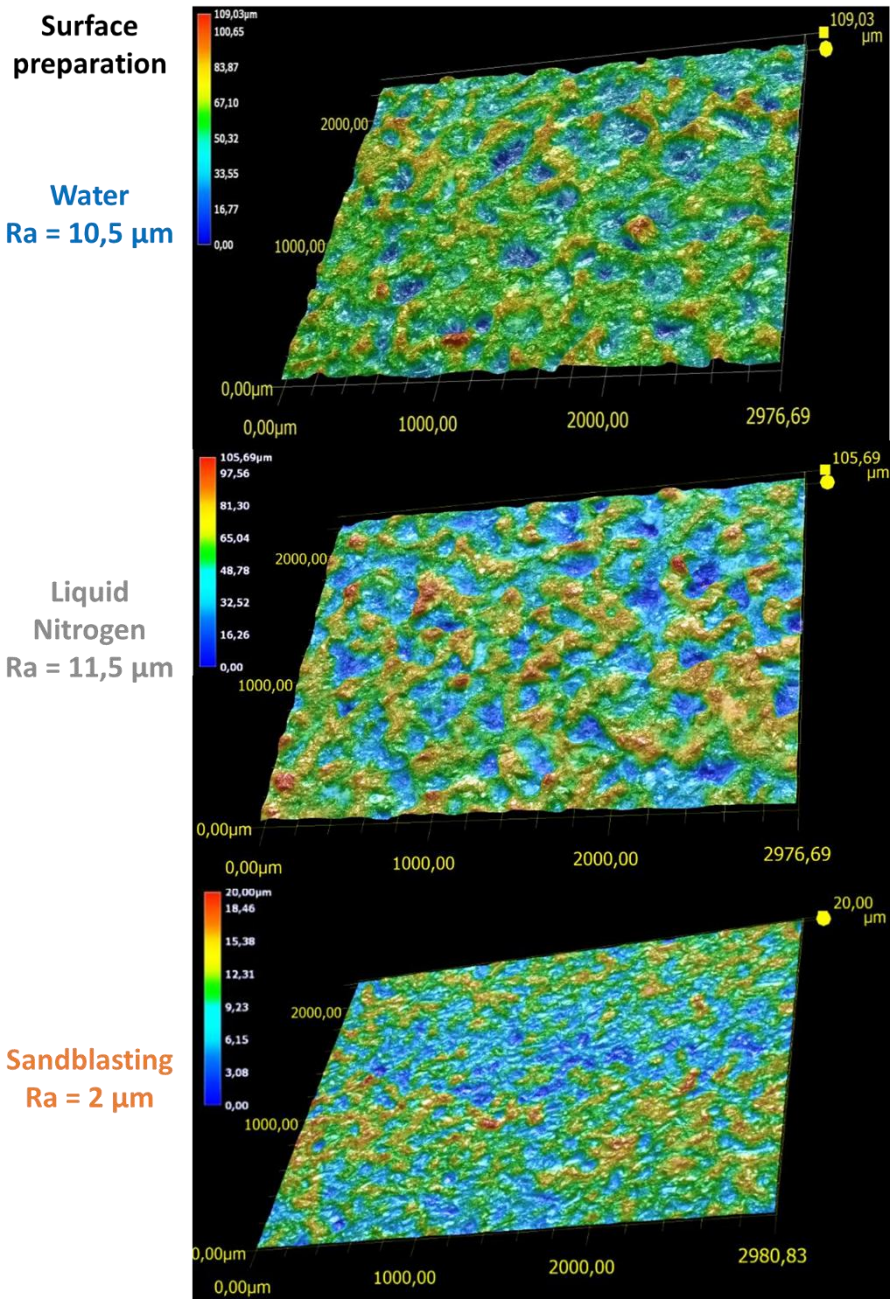

Fig. 181: Surface topography of S235 specimens prepared using Water Jet, Liquid Nitrogen Jet and Sandblasting. Overview of a 3 x 3 mm area.

Based on the roughness measurements, the fluid-jet preparation methods were selected for the following analyses, as surface roughness plays a key role in coating adhesion to the substrate. Nevertheless, coatings were also sprayed onto sandblasted samples, despite their lower roughness, to evaluate their adhesion behavior. However, no proper bonding was achieved below 35 bar deposition pressure. Fig. 182 clearly illustrates this issue, showing that the coating is delaminated from the substrate.

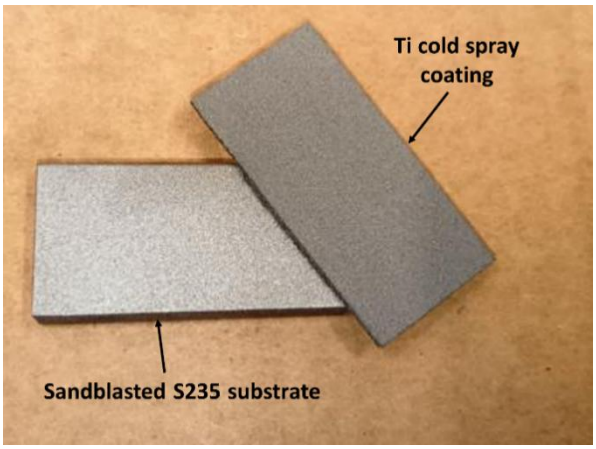

Fig. 182: Cold spray deposition at 30 bar on a sandblasted substrate showing coating delamination.

The fluid-jet methods were therefore investigated in more detail. Cross-sectional samples were prepared to perform microhardness tests in order to compare the degree of work hardening near the surface. These measurements were carried out at depths of 250 µm (unaffected area) and 50 µm (referred to as -250 and -50, respectively) below the surface, as shown in Fig. 183.

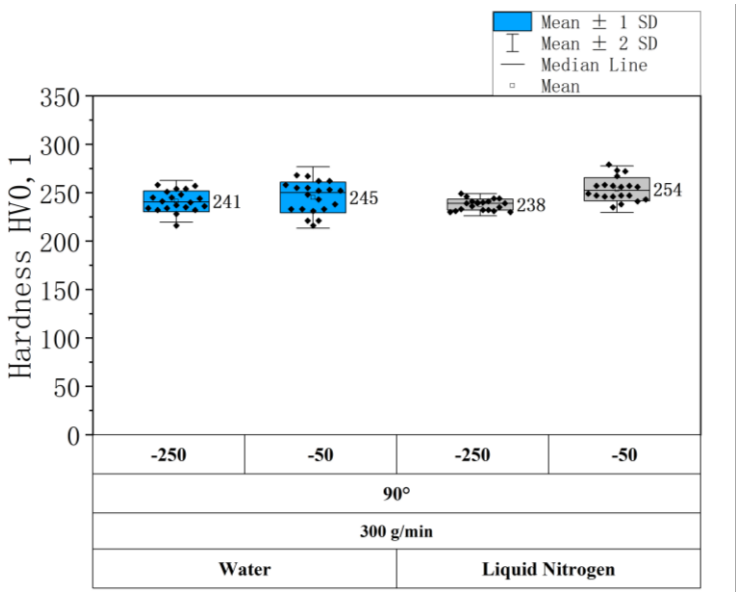

Fig. 183: Microhardness measurements performed at -250 µm and -50 µm below substrates surface prepared using either water or liquid nitrogen jet surface preparation.

For the water-jet preparation, the hardness measured at -50 µm showed no significant difference compared to the reference value at -250 µm. This suggests either that little or no work hardening occurred, or more likely that the region located 50 µm below the surface was not mechanically affected by the surface preparation. In contrast, for the liquid nitrogen-jet preparation, a slight increase in hardness was observed at -50 µm, which is consistent with the deeper grooves previously observed in Fig. 181.

The coatings were then deposited at different pressures in order to evaluate their adhesion to the water- and liquid nitrogen-jet prepared substrates. To this end, microhardness tests were again performed at the coating–substrate interface.

Two types of behaviors were observed: in cases of good adhesion, the hardness indentations were small and well defined, whereas poor adhesion led to localized delamination of the coating during indentation, resulting in much larger imprints. The objective here was therefore not only to measure hardness, but also to assess the variability induced by the presence of weakly bonded regions at the interface. An example of typical indentations obtained in both types of regions is shown in Fig. 184.

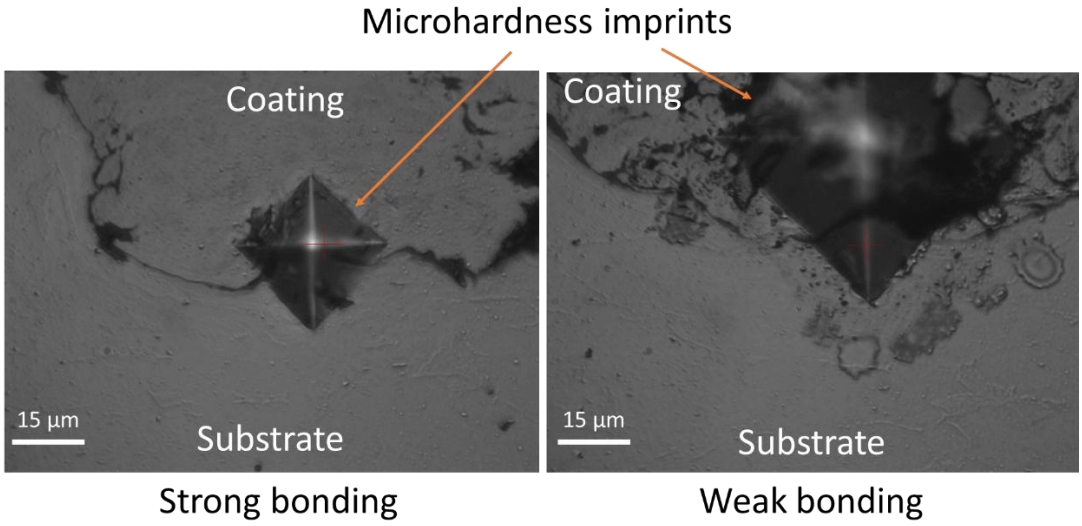

Fig. 184: Optical micrographs of microhardness imprints in well-adhered (left) and poorly-adhered (right) areas.

Cold spray depositions were carried out on both types of prepared surfaces (water-jet and liquid nitrogen-jet) using the two types of powders - Irregular (Irr-Ti) and Spherical (Sph-Ti) Ti particles - at deposition pressures ranging from 15 to 40 bar.

For the irregular powder (Irr-Ti) (Fig. 185), very low hardness values were obtained at the lowest pressure (15 bar), with an average of about 130 HV for the water-jet prepared surface and 85 HV for the liquid nitrogen-jet surface. From 25 bar onward, both preparation methods showed an increase in hardness, and therefore in adhesion. At 30 bar and above, the average hardness values were slightly higher for the water-jet prepared samples, although the large dispersion of the data makes it difficult to draw a definitive conclusion.

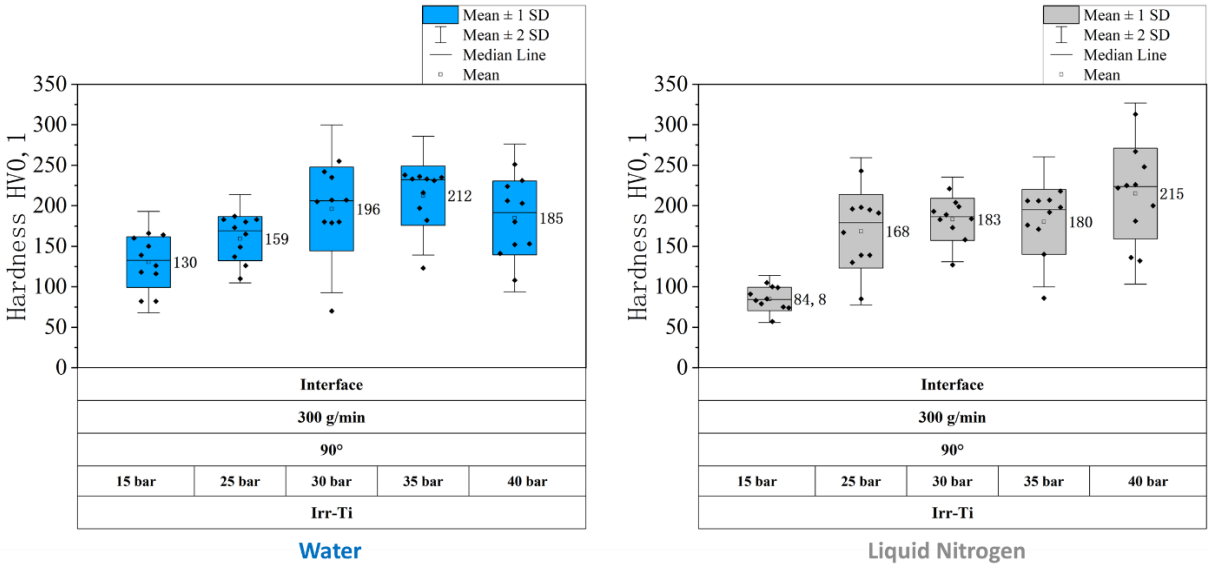

Fig. 185: Microhardness at the coating-substrate interface (100% Irr-Ti) for deposition pressures between 15 and 40 bar with a substrate surface prepared with either water-jet or liquid nitrogen-jet.

The results obtained with the spherical powder are presented in Fig. 186. It can clearly be seen that this powder exhibits greater difficulty in forming a strong bond with the substrate. The average hardness values between 15 and 35 bar remained around 130 HV for the water-jet preparation and approximately 160 HV for the liquid nitrogen-jet preparation. A significant increase in hardness, and therefore in adhesion, was only observed at 40 bar for both surface preparation methods.

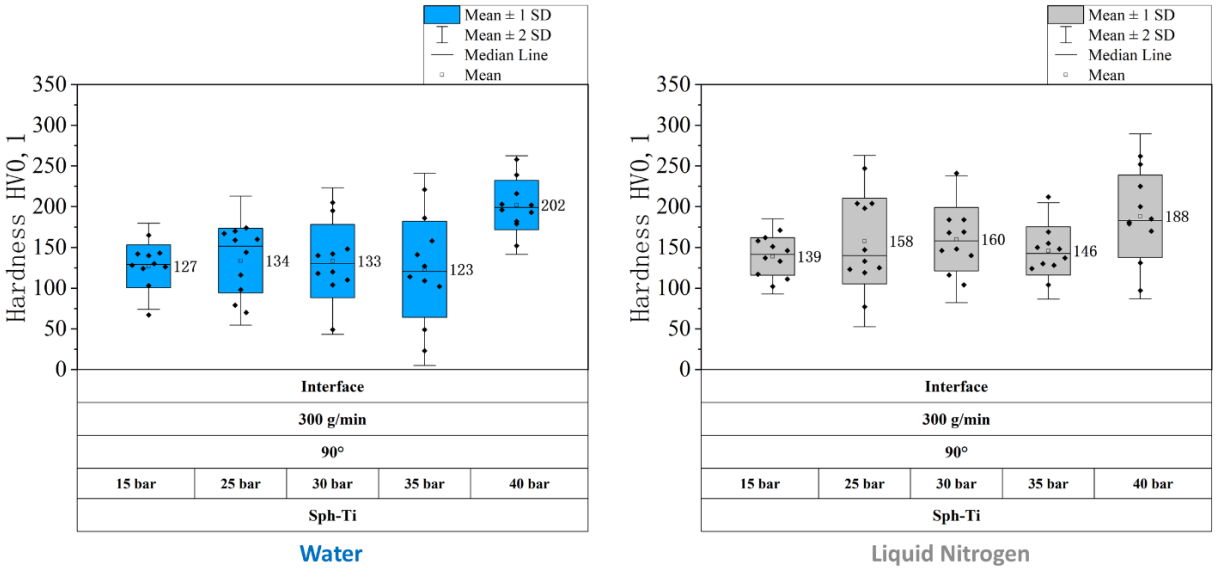

Fig. 186: Microhardness at the coating-substrate interface (100% Sph-Ti) for deposition pressures between 15 and 40 bar with a substrate surface prepared with either water-jet or liquid nitrogen-jet.

Therefore, irregular Ti powder more easily achieves strong bonding with the substrate, while the spherical powder requires higher pressures to reach similar adhesion levels. The effect of surface preparation is noticeable but remains less significant than that of deposition pressure and powder morphology.

However, since the operational cost of the cold spray process is strongly dependent on the deposition pressure, surface preparation plays an important economic role, as it can allow the use of lower deposition pressures while maintaining comparable adhesion levels at the substrate interface.

In order to better understand the factors influencing adhesion at the substrate interface, SEM observations and EDX mapping were performed on the cross-sections of the deposited coatings. They revealed the presence of abrasive particles embedded at the coating-substrate interface (Fig. 187). These hard particles are likely to weaken the interfacial bonding, as their brittleness and high hardness can locally hinder proper adhesion between the coating and the substrate.

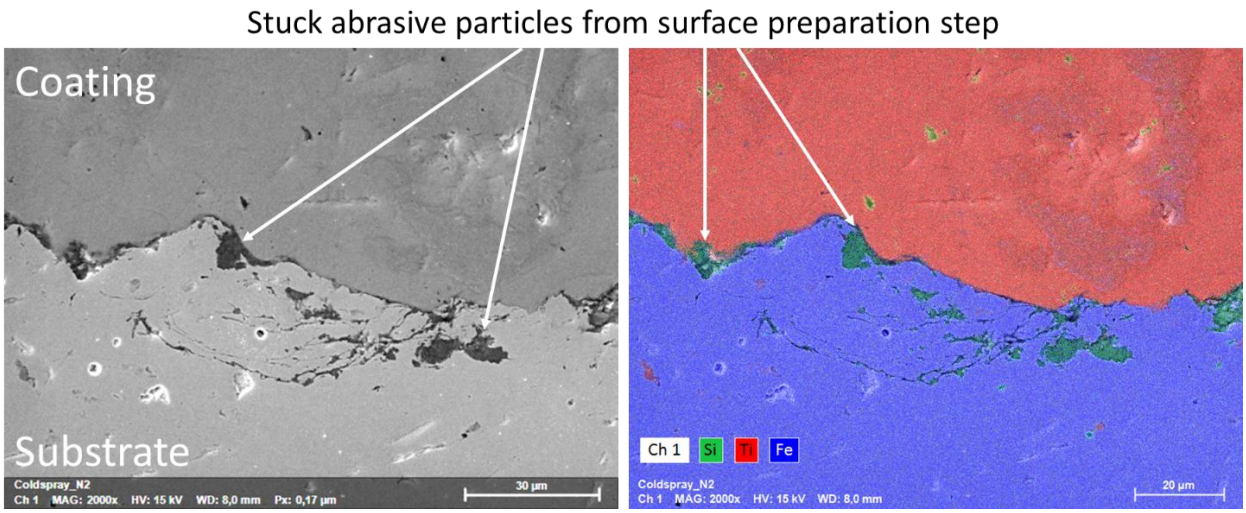

Fig. 187: SEM micrograph (SE mode) and EDX mapping of the coating-substrate interface (100% Irr-Ti) for a deposition pressure of 35 bar, showing abrasive particles stuck in the substrate surface. (green = Si; red = Ti; blue = Fe).

SEM close-up micrographs (Fig. 188) further show that these particles can cover relatively large surface areas and may act as stress concentrators, promoting local fracture initiation due to their high hardness and poor deformability.

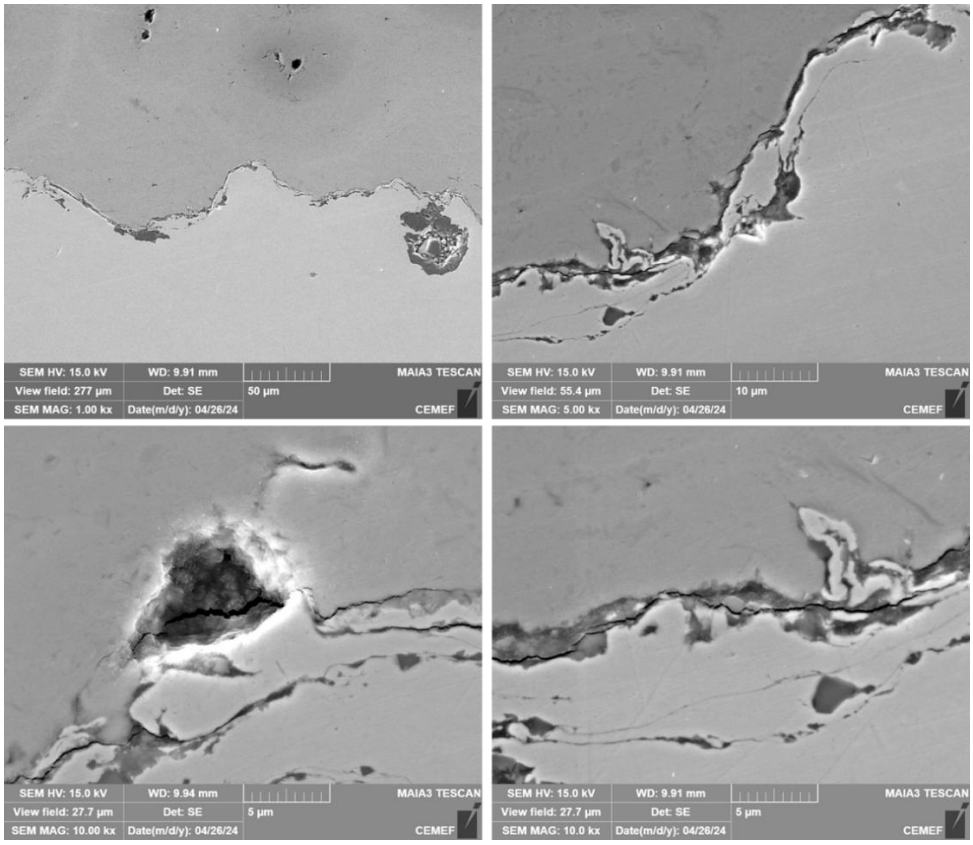

Fig. 188: SEM micrographs showing abrasive particles trapped at the interface as well as the initiation of cracks in the abrasive particles.

To improve the adhesion between the coating and the substrate, it is therefore necessary to drastically reduce the number of abrasive particles trapped at the interface while maintaining a sufficiently high surface roughness. This can be achieved by adjusting both the quantity of projected abrasive and the angle of incidence during surface preparation.

This study was carried out using only the spherical powder, as it exhibits poor adhesion compared to irregular powder, especially at deposition pressures below or equal to 35 bar. Tests were therefore performed at 35 bar using lower abrasive feed rates of 150 and 100 g/min, compared to the initial 300 g/min.

The hardness measured at the coating-substrate interfaces is presented in Fig. 189. A clear improvement in adhesion is observed for the water-jet preparation, with higher and less scattered hardness values obtained for both 150 and 100 g/min feed rates. For the liquid nitrogen-jet preparation, a slight increase in hardness is also observed, though the improvement is less significant.

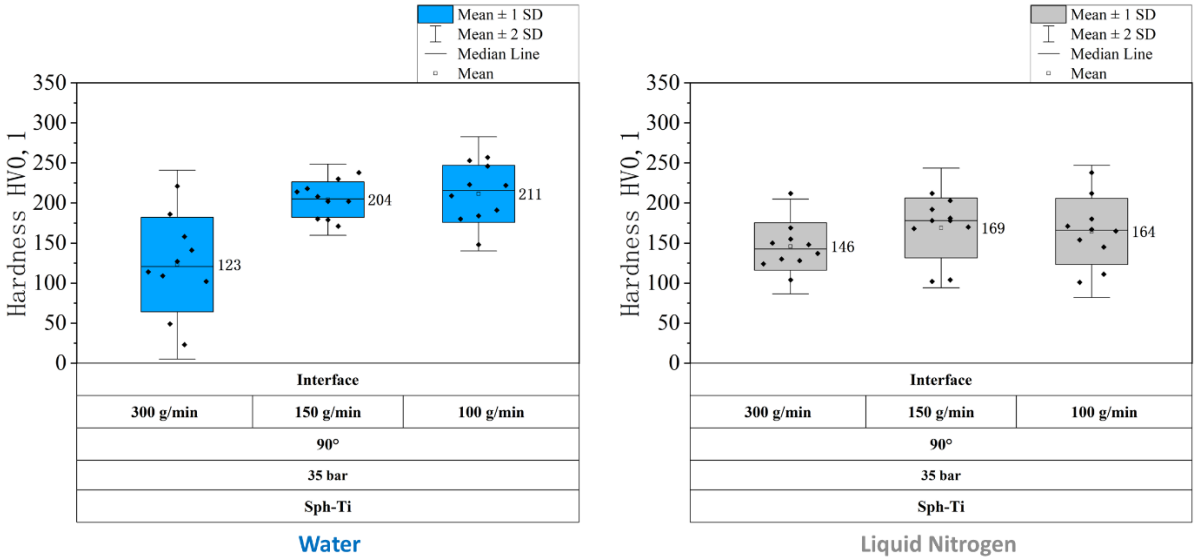

Fig. 189: Microhardness at the coating-substrate interface (100% Sph-Ti) for a deposition pressure of 35 bar with a substrate surface prepared with either water-jet or liquid nitrogen-jet using various abrasive feed rates.

SEM observations for the samples prepared using the water-jet are presented in Fig. 190. Surfaces prepared with lower abrasive feed rates of 150 and 100 g/min exhibit noticeably cleaner interfaces. Although a few defects remain, the number of trapped abrasive particles is significantly reduced compared to the initial condition at 300 g/min.

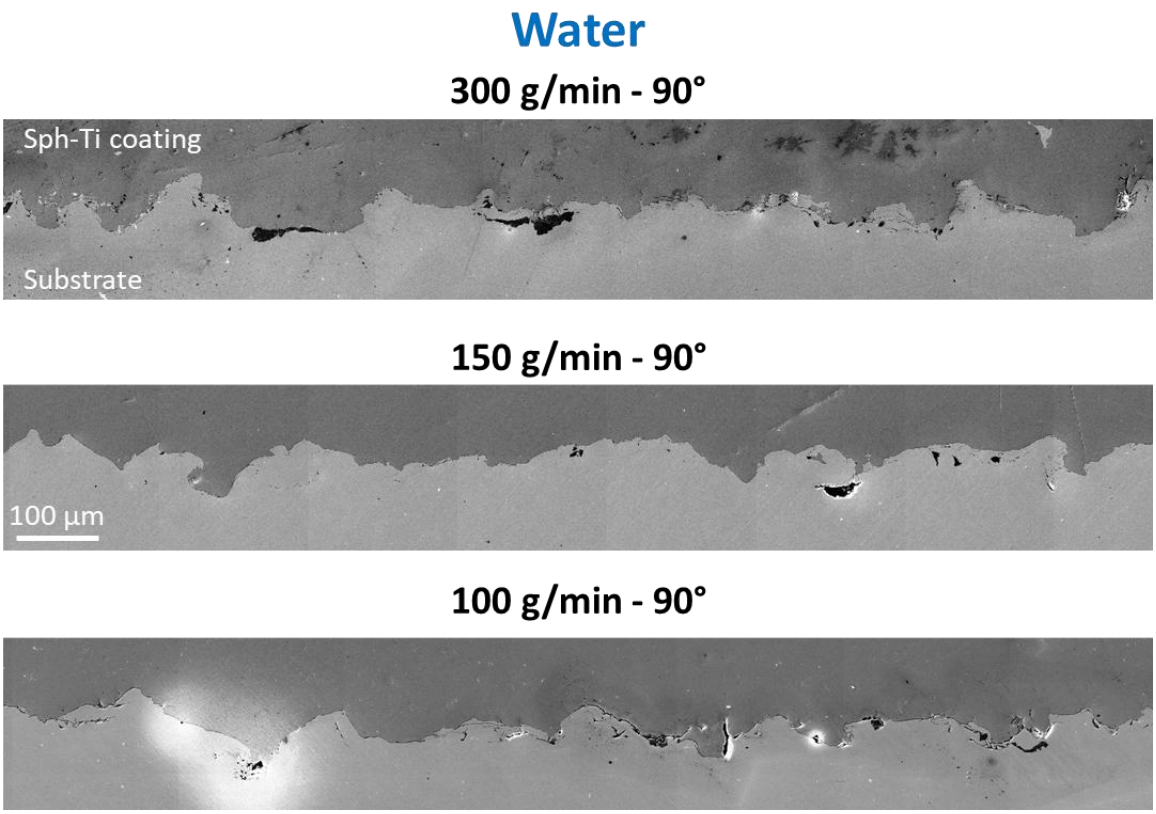

Fig. 190: SEM observations of cross-sections showing coating and substrate interface with water-jet preparation method with different abrasive feed rates.

Close-up SEM images of the interface (Fig. 191) further confirm this trend, showing a much lower concentration of abrasive residues at the interface under the reduced feed rate conditions, and therefore no cracks.

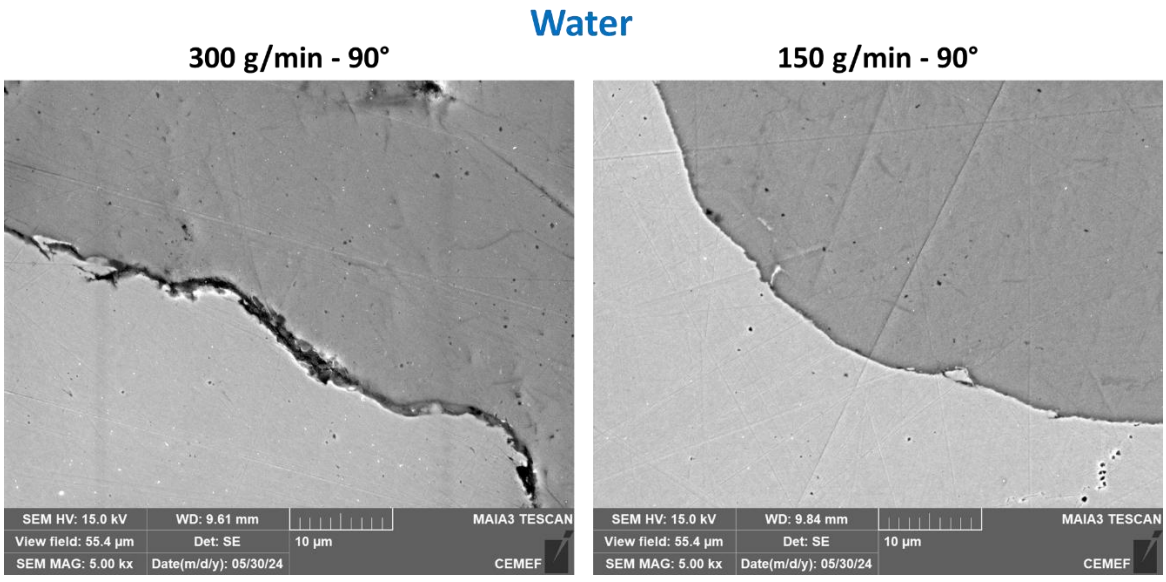

Fig. 191: SEM micrographs close up on the coating-substrate interface at 300 and 150 g/min abrasive feed rates.

For the substrates prepared using the liquid nitrogen-jet (Fig. 192), a similar improvement is observed when decreasing the feed rate; however, a considerable number of abrasive particles still remains embedded at the interface. This explains the lower hardness and, consequently, the weaker adhesion measured for these samples compared to those prepared with the water-jet.

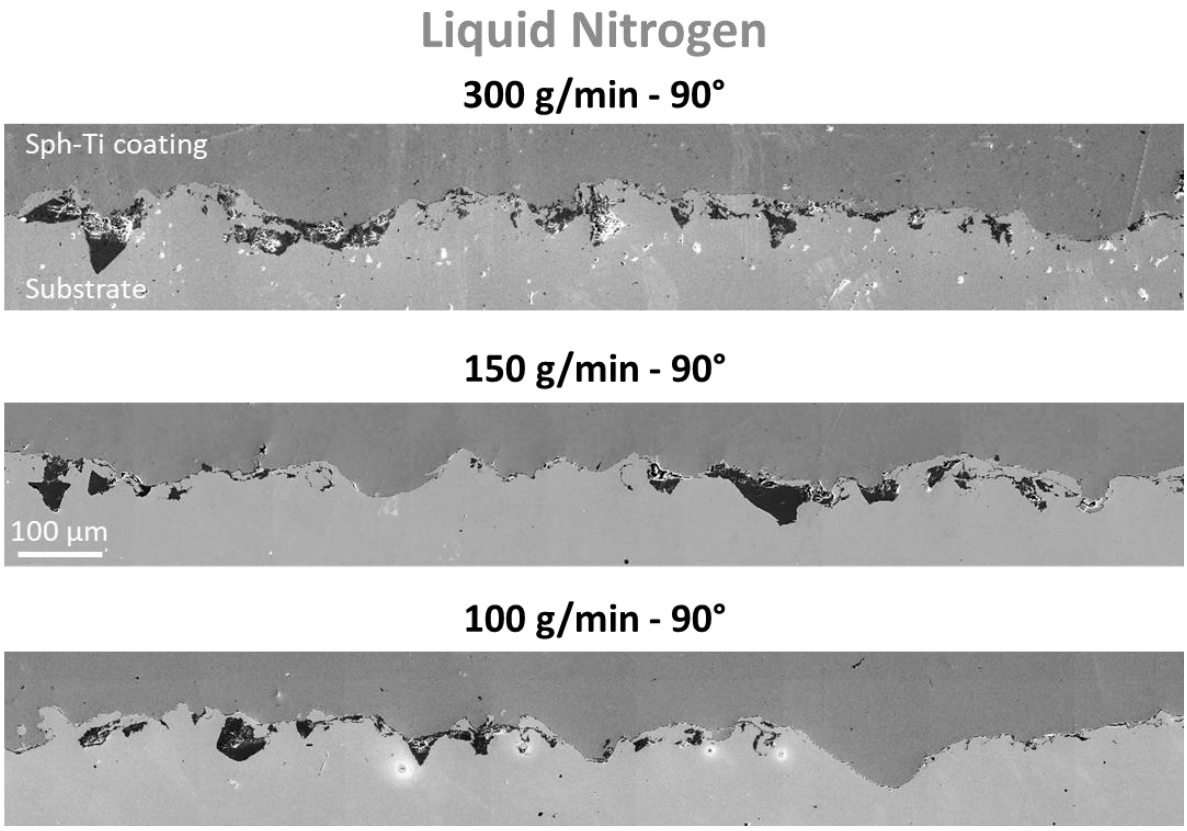

Fig. 192: SEM observations of cross-sections showing coating and substrate interface with liquid nitrogen-jet preparation method with different abrasive feed rates.

This behavior may be attributed to the very low temperature of the liquid nitrogen, which makes the abrasive particles extremely brittle. Instead of deforming the substrate surface and rebounding upon impact, these particles are likely to fracture, leading to their entrapment within the interface.

In order to further reduce the phenomenon of particle embedding, the incidence angle of the abrasive particles was modified. The initial angle of 90° was lowered to 45°, with the objective of promoting particle rebound rather than penetration and fragmentation into the substrate. The corresponding interfacial hardness results are shown in Fig. 193.

For the surfaces prepared using the water-jet, the average hardness values obtained at 90° and 45° were very similar around 200 HV, although a slightly higher dispersion was observed for the 45° condition. In contrast, for the liquid nitrogen-jet prepared surfaces, no noticeable difference between the two incidence angles was detected.

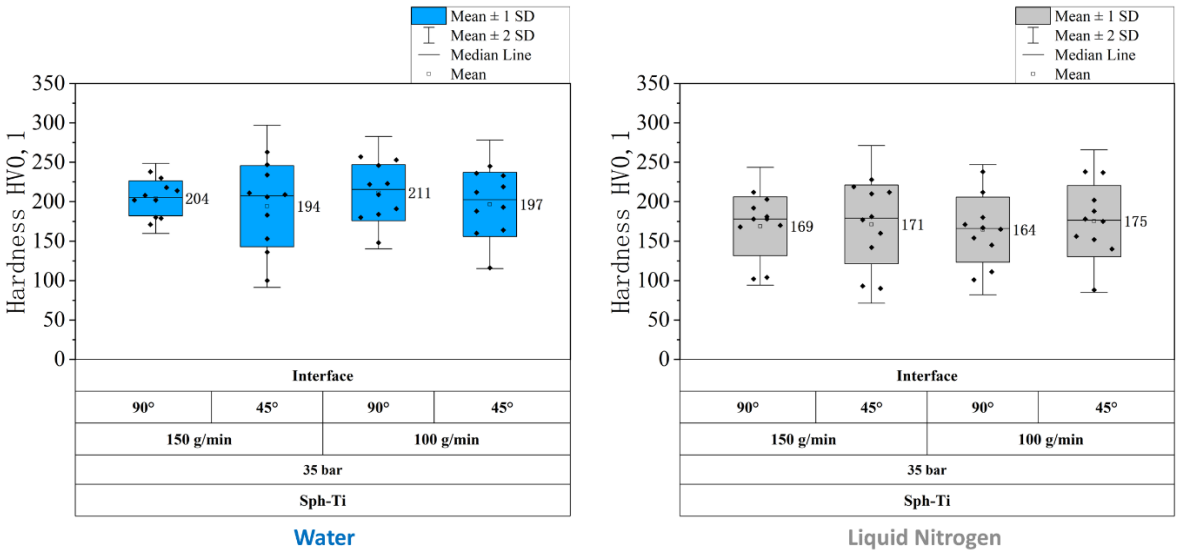

Fig. 193: Microhardness at the coating-substrate interface (100% Sph-Ti) for a deposition pressure of 35 bar with a substrate surface prepared with either water-jet or liquid nitrogen-jet with different abrasive feed rates and impingement angles.

SEM observations (Fig. 194) of surfaces prepared using water-jet with a 150 g/min feed rate reveals no significant difference between samples prepared at 90° and 45°. However, for the 100 g/min condition, the 45° samples appear less clean and exhibit more interfacial defects. Nevertheless, higher-magnification images did not reveal any clear distinguishing features.

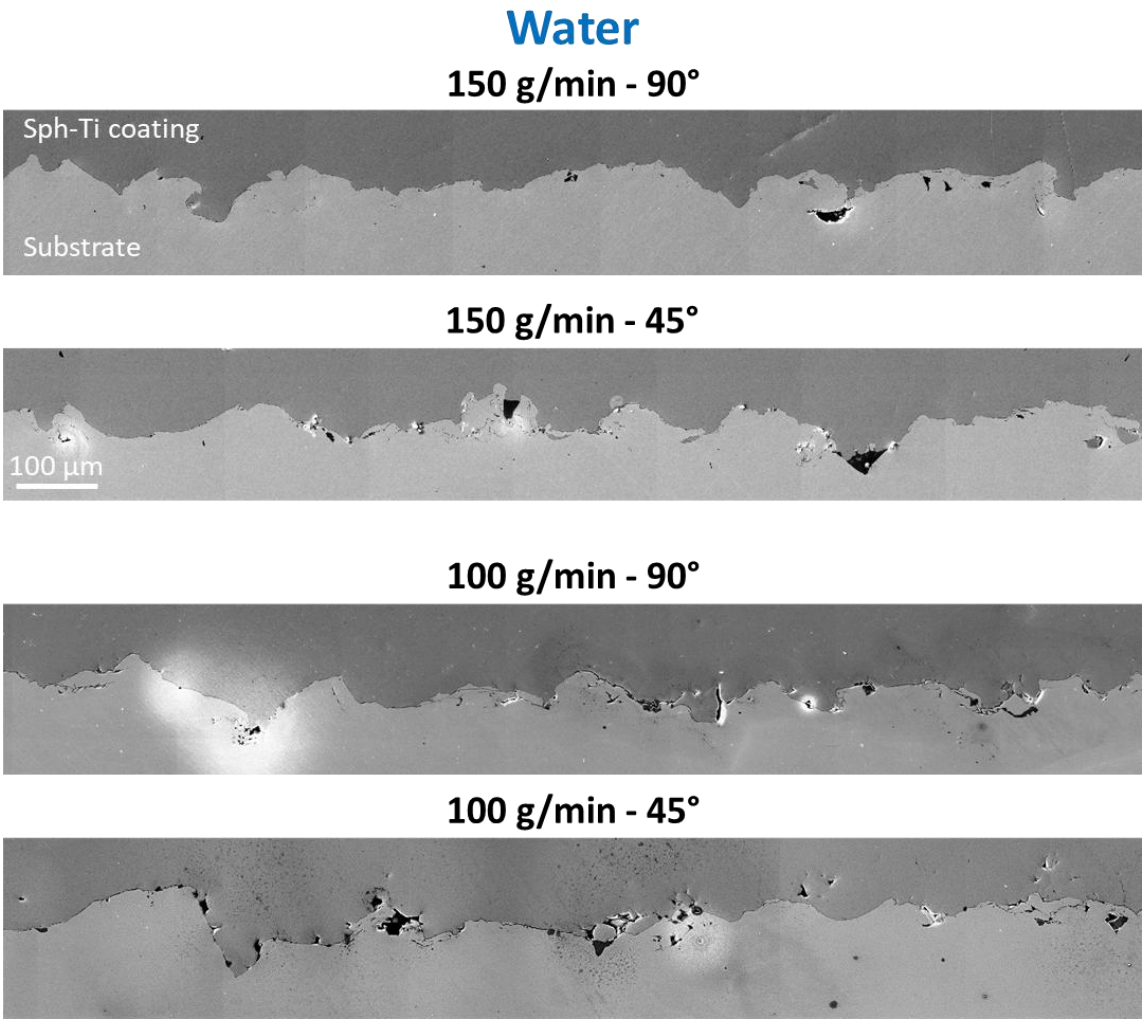

Fig. 194: SEM observations of cross-sections showing coating and substrate interface with water-jet preparation method with different abrasive feed rates and impingement angles.

For the liquid nitrogen-jet prepared surfaces (Fig. 195), the situation is different. For both feed rates, using an incidence angle of 45° considerably reduced the number of abrasive particles trapped at the interface. However, this did not translate into higher hardness values and therefore improved adhesion between the coating and the substrate.

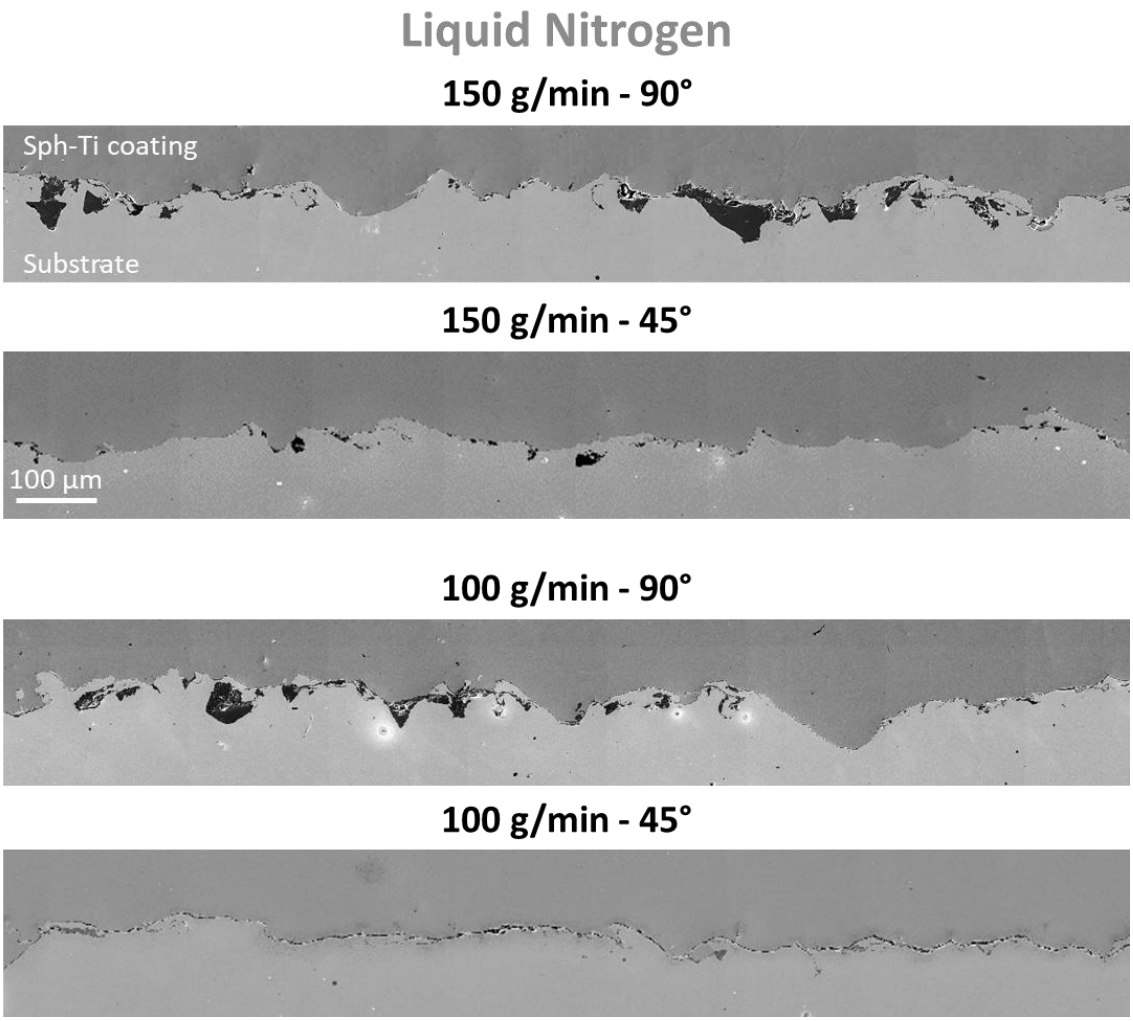

Fig. 195: SEM observations of cross-sections showing coating and substrate interface with liquid nitrogen-jet preparation method with different abrasive feed rates and impingement angles.

Close-up SEM images (Fig. 196) showed that the coating and substrate were still separated by abrasive particles which, although fewer and smaller, tended to spread over larger interfacial areas. It can therefore be concluded that while the 45° angle effectively promotes particle rebound, it does not completely prevent particle fragmentation or subsequent embedding into the substrate.

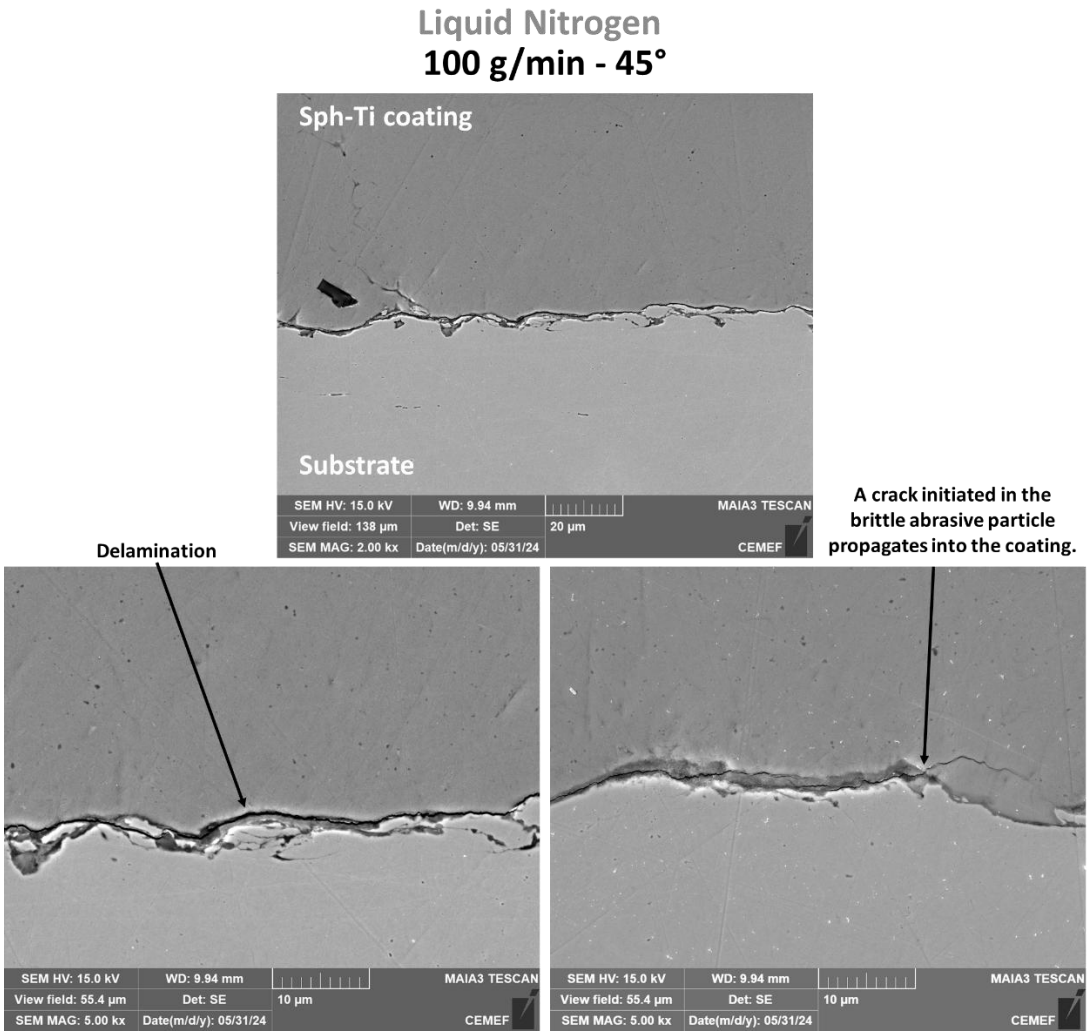

Fig. 196: SEM micrographs showing abrasive particles trapped at the interface as well as the initiation of cracks in the abrasive particles causing delamination. Substrate prepared using liquid nitrogen-jet method with a 100 g/min feedrate and a 45° impingement angle.

In addition, the surfaces prepared at 45° appeared less rough than those prepared at 90°, based on SEM observations - particularly for the liquid nitrogen-jet samples. To quantify this effect, a Python script was developed to automatically identify the titanium-steel interface based on contrast differences. The roughness measurement is then simulated by considering only the portion of the surface that would be visible from a top-down view, as illustrated in Fig. 197. The Ra is calculated according to the ISO 21920-3 [1] standard, using a cutoff wavelength (λc) of 8 mm.

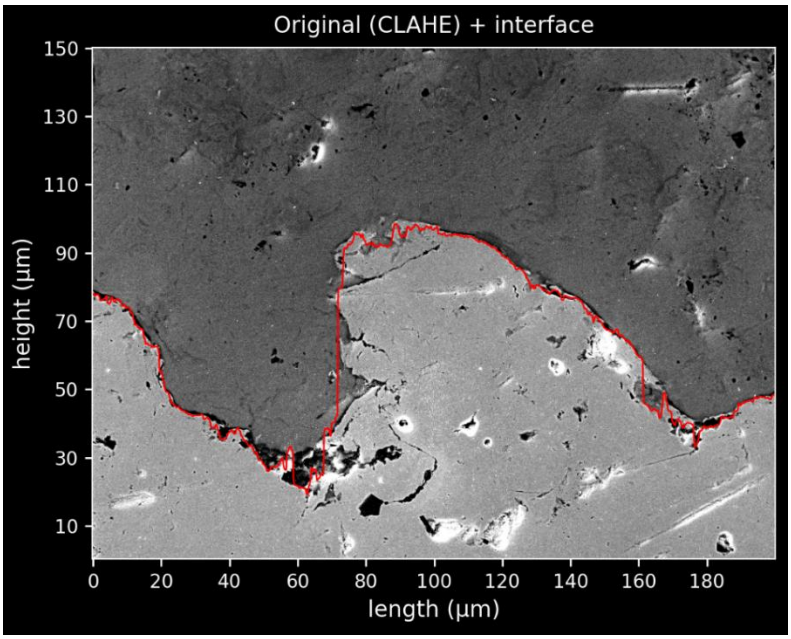

Fig. 197: Modified SEM micrographs obtained using a Python code to reproduce roughness-like data for the substrate.

Stitched SEM images covering a total surface length of 5 mm were then used to obtain reliable and statistically significant roughness measurements. The validity of the method was verified by ensuring that the simulated Ra values were consistent with those obtained by profilometry on cross-sections of the substrates prior to coating deposition: a deviation of less than ± 1 µm is obtained.

Afterward, the coatings were deposited and the Ra was measured again using SEM cross-section technique. As illustrated in Fig. 198, the Ra seem to increase after deposition (here around 17.3 µm), which is considerably higher than the pre-deposition value of 11.5 µm for the liquid nitrogen-jet prepared surface. This indicates that the cold spray process itself induces significant substrate deformation due to the high-velocity impact of the titanium particles.

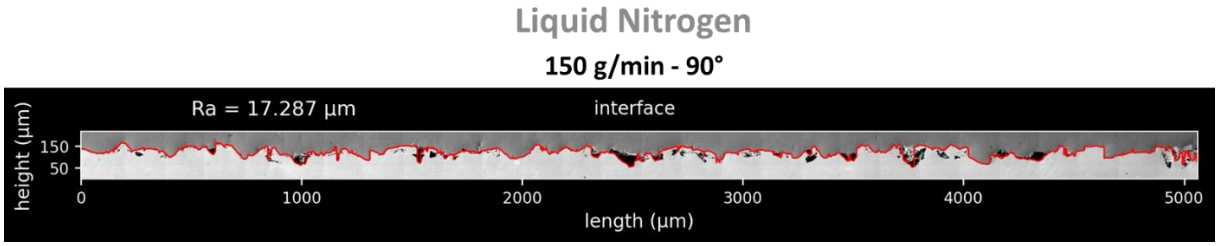

Fig. 198: Modified SEM images assembly obtained using a Python code to reproduce roughness-like data for the substrate.

The results obtained before deposition (reference) and after coating deposition are summarized in **Table *34***. For all conditions, the measured Ra values after coating deposition are higher than the reference values obtained before deposition, which is consistent with previous observations. This increase in roughness confirms that the cold spray process itself induces additional surface deformation due to the high-velocity impact of the titanium particles.

When comparing the different incidence angles, it is clear that the 45° projection angle systematically results in a lower surface roughness than the 90° condition, regardless of the feed rate or the surface preparation method (water- or liquid nitrogen-jet). This reduction in Ra can be attributed to the more glancing impact of abrasive particles at lower incidence angles, which promotes partial rebound and reduces the depth of the surface grooves formed during preparation.

Preparation methods	Pressure (bar)	Powder	Angle	Feed rate (g/min)	Ra before coating deposition (µm)	Ra after coating deposition (µm)
Water	35	Sph-Ti	90°	300	12	17,3
				150	10,7	16,7
				100	11,3	17,0
			45°	150	9,2	13,7
				100	8,7	13,9
Liquid nitrogen			90°	300	10,5	19,4
				150	11,1	17,3
				100	11,3	19,0
			45°	150	7,8	13,2
				100	8,2	13,2

Table 34: Influence of surface preparation parameters on roughness (Ra) before and after cold spray deposition of Sph-Ti coatings at 35 bar.

Based on the results obtained, the following parameters were selected for surface preparation: an abrasive feed rate of 150 g/min and a 90° incidence angle. This combination was found to maintain a high surface roughness while minimizing the amount of trapped abrasive particles at the interface, resulting in improved adhesion between the substrate and the coating. Despite the superior performance of the water jet surface preparation methods, it was decided to maintain a comparison with the liquid nitrogen jet during the cold spray deposition optimization, to determine whether this parameter could affect the coating deposition behavior.

Furthermore, it was observed that increasing the coating deposition pressure enhances adhesion, as higher impact velocities promote stronger interfacial bonding. This means that poor surface preparation can be partly compensated by using higher deposition pressures. However, achieving an optimized surface preparation remains advantageous, as it allows for lower deposition pressures to be used without compromising adhesion quality, thereby reducing the operational energy cost of the cold spray process.

Having established the adhesion behavior between the coating and the substrate, attention can now be directed to the characterization of the coating's own properties.

4.1.2 Influence of Deposition Parameters on Coating Properties

The focus is now shifted toward the intrinsic characteristics of the deposited coatings. In this part, the coating thickness, porosity, and microhardness are analyzed to assess the bonding quality between the deposited particles.

Particular attention is given to the influence of the deposition pressure and the powder morphology (irregular vs. spherical particles) on these properties, as they play a key role in determining the coating's density, cohesion, and overall mechanical performance. These coatings were deposited on substrates prepared using either the water-jet or the liquid nitrogen-jet techniques, which - as will be shown - can influence the coating's final characteristics.

Fig. 199 presents coatings thickness obtained by cold spray at different deposition pressures on water-jet prepared substrates, using the optimized surface preparation parameters defined in the previous section (150 g/min of abrasive feed rate at a 90° impingement angle). The thickness measurements were performed on cross-sections 10 mm long, with measurements taken every 1 mm to obtain an average over ten points. Except for the coatings deposited at the lowest pressure (15 bar), the samples show good uniformity with a low standard deviation of about 50 µm.

For the irregular powder, the coating thickness remains nearly constant (around 1000 µm) and tends to slightly decrease with increasing pressure. This trend can be attributed to enhanced particle compaction at higher impact velocities. In contrast, the spherical powder exhibits a much thinner coating at 15 bar (~680 µm) but reaches a very high thickness at 25 bar (~2100 µm). This behavior can be explained by the poor initial adhesion of spherical particles at low pressures, which limits deposition efficiency during the first passes. Above 25 bar, the pressure is sufficient to ensure proper particle anchoring from the start, resulting in thicker coatings.

When increasing the deposition pressure beyond 25 bar, the coating thickness decreases noticeably - from about 2000 µm at 25 bar to 1750 µm at 40 bar. This reduction is likely to result from progressive densification and compaction of the particles, resulting in a denser and less porous coating. Another possible explanation could be a low deposition efficiency due to particle rebound. This phenomenon is less pronounced for the irregular powder, probably due to its broader particle size distribution, which allows smaller particles to fill the gaps between larger ones, improving packing efficiency [2].

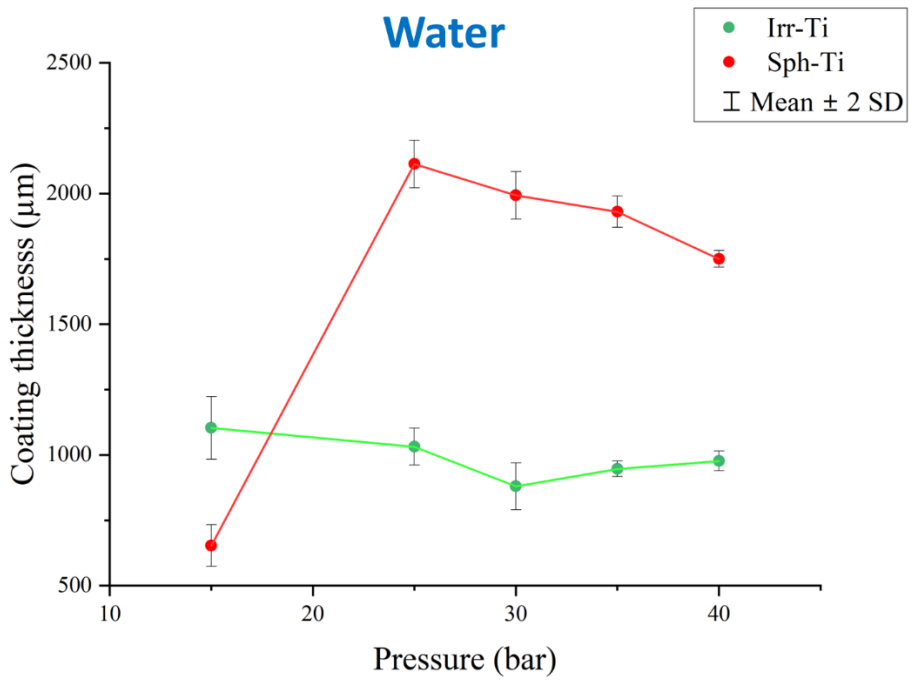

Fig. 199: Coating thickness as a function of deposition pressure for water-jet prepared substrates (comparison between irregular (Irr-Ti) and spherical (Sph-Ti) Ti powders). Obtained from cross-section samples.

Overall, relatively thick coatings were obtained under all conditions. Considering that four passes were applied, this corresponds to roughly 250 µm per pass for Irr-Ti powder and 450 µm per pass for Sph-Ti powder at 40 bar. While coating thickness is an interesting indicator, the mechanical robustness of the coating is the main factor governing its performance. For this reason, porosity is also evaluated.

Porosity results are shown in Fig. 200. Measurements were performed on the same cross-sections, within 500 × 500 µm regions, starting from the coating-substrate interface, with 5 repetitions per cross-section to obtain representative values.

As expected, the highest porosity is observed at the lowest deposition pressure, regardless of the powder morphology. From 15 to 25 bar, the porosity drastically decreases - from about 2.5% to 0.5% on average. For the irregular powder, porosity continues to decrease up to 30 bar (0.26%), as a local increase is observed at 35 bar (0.74). This anomaly is likely due to a non-representative cross-section, as porosity values dropped again to 0.16% at 40 bar.

For the spherical powder, the trend is more consistent: porosity stabilized at around 0.27% between 25 and 30 bar, then decreased further to about 0.07% at 35 and 40 bar.

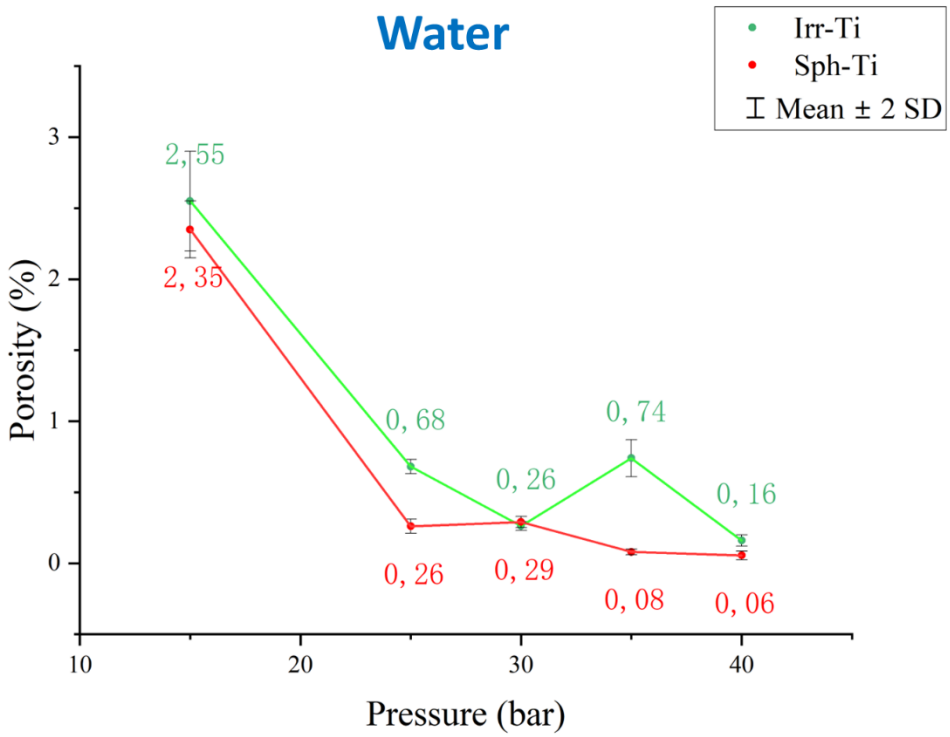

Fig. 200: Porosity of cold-sprayed coatings as a function of deposition pressure for water-jet prepared substrates (comparison between irregular (Irr-Ti) and spherical (Sph-Ti) Ti powders). Obtained from cross-section samples.

The spherical particles therefore appear to have a greater ability to fill voids, likely due to their lower initial work hardening state and consequently higher plastic deformability during impact. However, this observation should be interpreted with caution: as seen for the irregular powder at 35 bar, additional measurements on multiple cross-sections would be necessary to reduce statistical uncertainty and confirm these trends.

Fig. 201 presents SEM observations of coatings formed at 15, 30, and 40 bar using the irregular Ti particles (Irr-Ti). At 15 bar, the measured porosity partly originates from voids left by particle pull-outs, likely caused during sample polishing, and partly from intergranular porosity. At 30 bar, the porosity mainly results from inter-particle voids, and the same trend is observed at 40 bar, although the porosity becomes much less apparent.

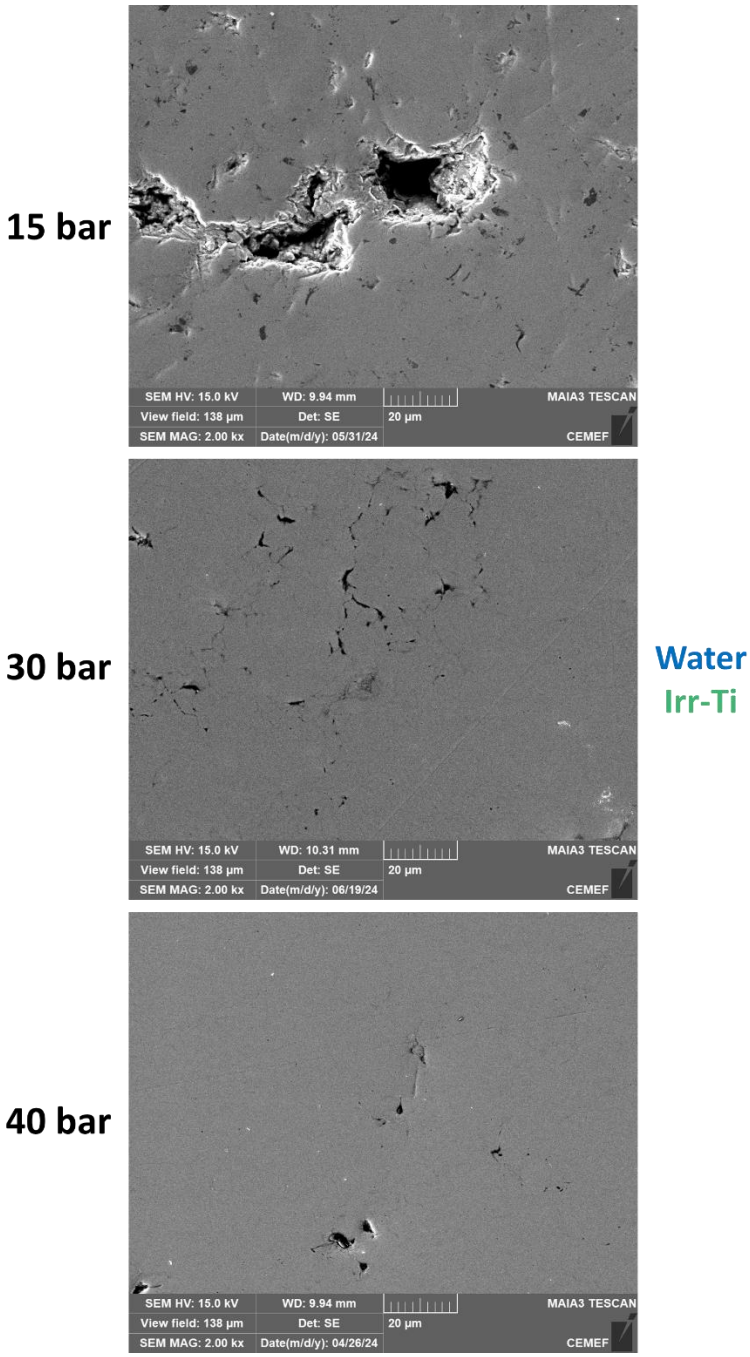

Fig. 201: SEM cross-sectional observations of coatings formed at 15, 30, and 40 bar using irregular Ti powder (Irr-Ti) for water-jet prepared substrates.

Similarly, Fig. 202 shows SEM observations for coatings formed with the spherical Ti particles (Sph-Ti). A comparable situation is observed at 15 bar, with the presence of pull-out holes and a more pronounced inter-particle porosity, probably because the deposition pressure is too low to effectively deform the particles. At 30 bar, the particle cohesion is sufficient to significantly reduce the number of pull-out voids, and inter-particle porosity becomes dominant. Individual spherical particles are distinguishable, and most of them retain their original rounded morphology. At 40 bar, however, individual particles are no longer distinguishable, and very few defects remain visible, indicating improved densification of the coating.

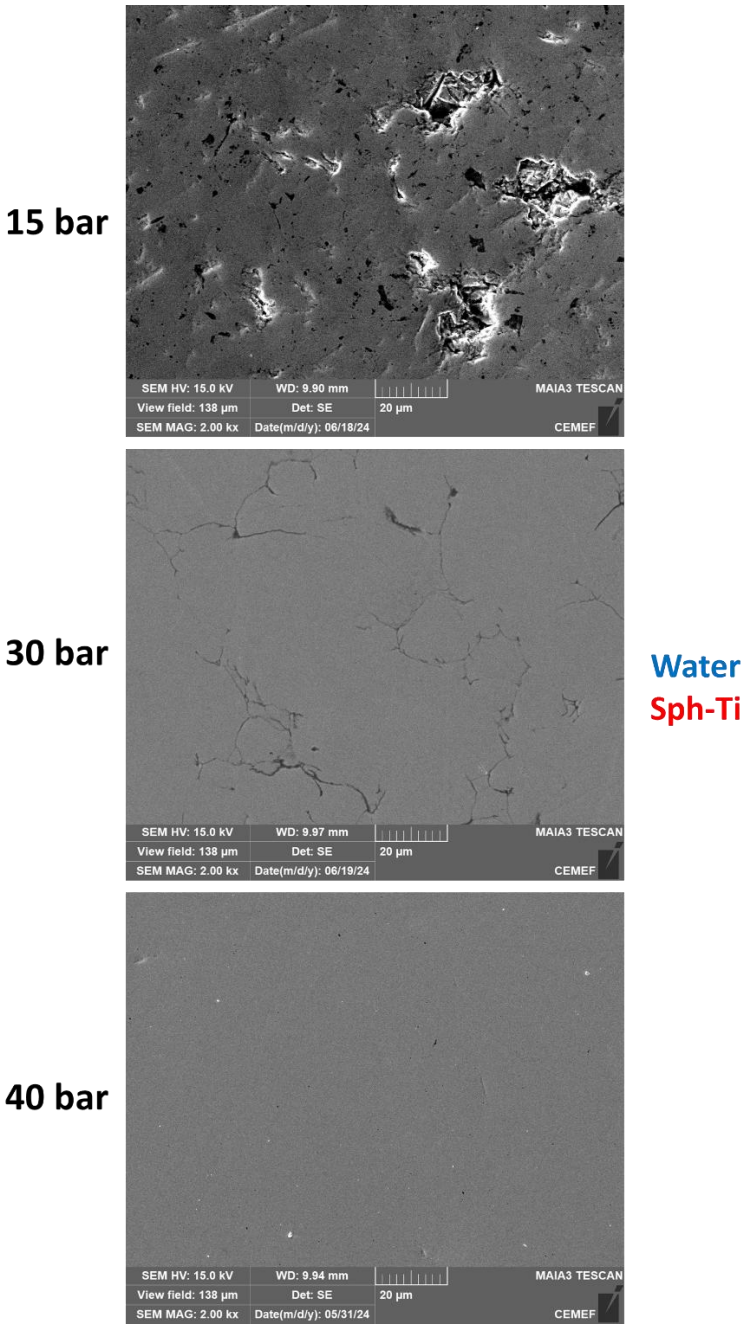

Fig. 202: SEM cross-sectional observations of coatings formed at 15, 30, and 40 bar using spherical Ti powder (Sph-Ti) for water-jet prepared substrates.

Microhardness tests are also performed on the coatings in order to indirectly assess inter-particle cohesion. Measurements are taken at 50, 250, and 500 µm above the coating-substrate interface to determine whether any gradient in cohesion may be present through the coating thickness.

Fig. 203 shows the average hardness values obtained for both irregular and spherical powders at different deposition pressures, with all depths combined (50, 250, and 500 µm) in order to determine whether a global trend can be identified. As expected, coatings formed at 15 bar exhibit the lowest hardness values. For Irr-Ti, a slight improvement appears at 25 bar (~148 HV), but from 30 bar onward, the hardness stabilizes at around 180 HV. Only a minor decrease is observed at 35 bar, which correlates with the higher porosity previously measured and is therefore likely due to local cross-sectional variability.

For Sph-Ti, a similar trend is observed, but the hardness only increases significantly from 35 bar, reaching 181 HV at 40 bar. This confirms that spherical particles require higher deposition pressures to achieve a dense coating with good inter-particle cohesion. The increased pressure provides more kinetic energy, enabling the particles to deform upon impact, either filling residual pores (reducing porosity) or enhancing contact and bonding with neighboring particles.

Therefore, although spherical powders yield lower porosity, this does not necessarily imply better cohesion within the coating compared to irregular powders, which deform less but appear to bond more effectively with one another.

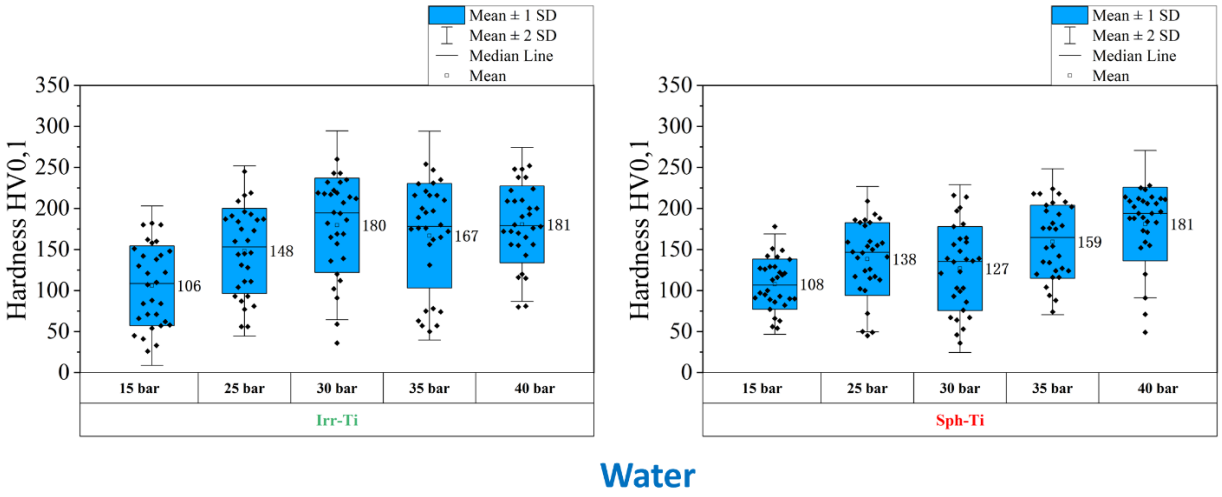

Fig. 203: Evolution of average microhardness with pressure of coatings produced with irregular (left) and spherical (right) particles for water-jet prepared substrates.

Fig. 204 presents hardness measurements distinguished by the three tested depths (50, 250, and 500 µm above the substrate-coating interface). No clear trend is observed: the particles deposited first (closer to 50 µm) are not systematically more or less cohesive than those deposited later (250 and 500 µm). For example, at 15 bar, no noticeable hardness difference is found for either Irr-Ti or Sph-Ti coatings. At 30 bar for Irr-Ti, slightly higher and less scattered hardness values are measured at 50 µm compared to 250 and 500 µm, whereas the opposite trend is observed for Sph-Ti at 40 bar. These observations make it difficult to draw definitive conclusions about potential gradients in cohesion through the coating thickness.

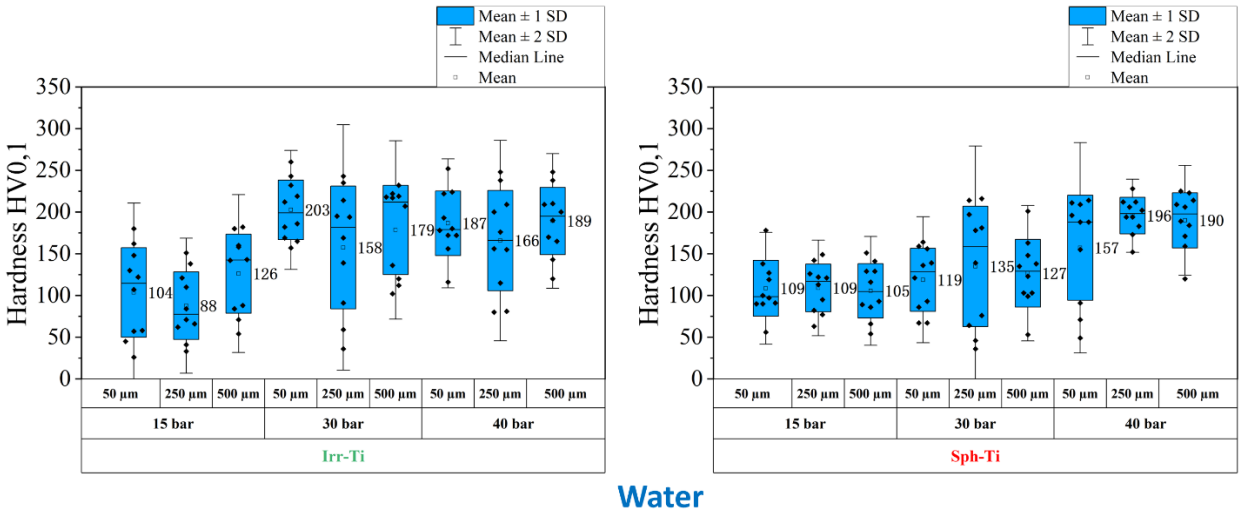

Fig. 204: Microhardness values measured at different depths (50, 250, and 500 µm above the substrate-coating interface) for coatings produced with irregular (left) and spherical (right) powders. Comparison between 15, 30 and 40 bar for coatings deposited on water-jet prepared substrates.

The combined analysis of coating thickness, porosity, and microhardness provides a comprehensive understanding of the cold spray deposition behavior for both irregular and spherical Ti powders. Increasing the deposition pressure generally enhances coating density and inter-particle cohesion, as reflected by the simultaneous decrease in porosity and increase in hardness. However, this effect tends to plateau beyond 30-35 bar, suggesting that a critical impact energy is reached for efficient particle bonding.

Now, the effect of using substrates prepared with the liquid nitrogen jet is examined to determine whether this surface preparation method influences the coating characteristics.

We begin once again with the measurement of coating thickness (Fig. 205). The overall behavior is very similar to that observed for the water-jet-prepared substrates (Fig. 199): coatings produced with irregular Ti particles display a relatively stable thickness across the tested pressures, while those obtained with spherical Ti particles (Sph-Ti) initially show low thickness values (at 15 bar) that sharply increase at intermediate pressure (25 bar), followed by a gradual decrease as pressure continues to rise.

Although the general trend remains the same, some differences are noticeable in the absolute coating thicknesses. For instance, coatings produced with Sph-Ti on liquid nitrogen-jet prepared substrates reach only about 1000 µm at 40 bar, compared to 1750 µm for those deposited on water-jet prepared substrates. Overall, the thickness values for Sph-Ti coatings are 200 to 700 µm lower for liquid nitrogen-jet preparation methods across comparable deposition pressures.

Two explanations can account for this difference. The first would be a further decrease in porosity, which would imply a denser coating. However, this is unlikely, since at 40 bar the measured porosity for Sph-Ti is already extremely low (0.06%, Fig. 200). Even if porosity dropped to 0%, such a reduction would not be sufficient to nearly halve the coating thickness.

The second explanation is therefore more plausible and is consistent with the differences previously observed between the two surface preparation methods (Section 4.1.1). As shown earlier, adhesion tends to be weaker for liquid nitrogen-jet prepared substrates, since the abrasive particles tend to shatter upon impact, leaving brittle residues that weaken the interface. Those results also showed that acceptable adhesion could still be achieved by increasing the deposition pressure. It is therefore likely that, at higher pressures, the first particles impact the substrate but do not fully adhere to the surface - instead, they help clean the substrate by removing remaining abrasive debris. This could explain why coatings appear thinner for this preparation method, particularly with spherical particles, which inherently adhere less efficiently than irregular ones.

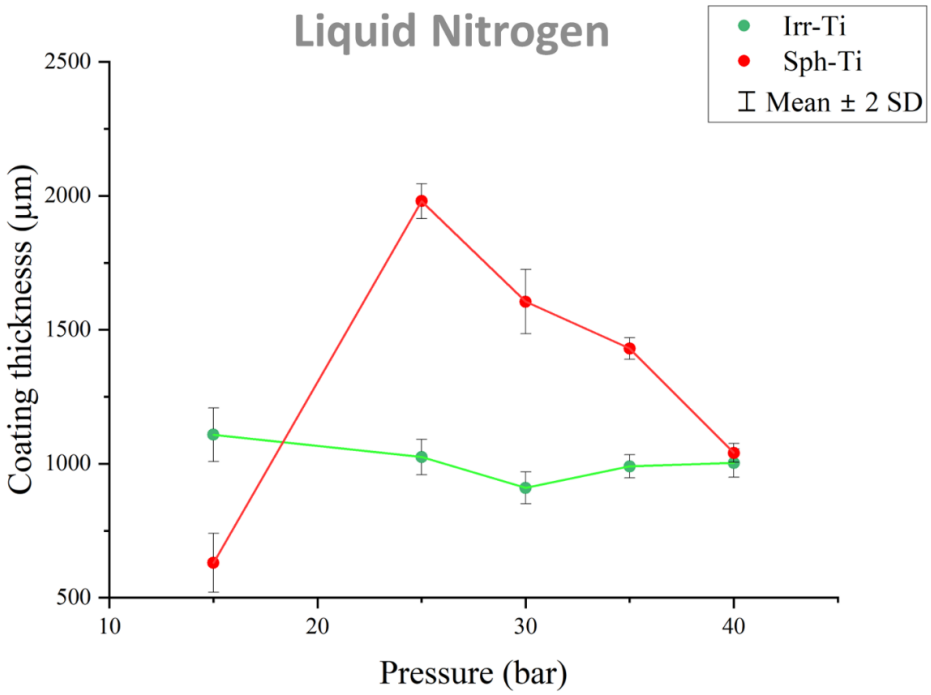

Fig. 205: Coating thickness as a function of deposition pressure for liquid nitrogen-jet prepared substrates (comparison between irregular (Irr-Ti) and spherical (Sph-Ti) Ti powders). Obtained from cross-section samples.

The porosity values (Fig. 206) are indeed identical at 40 bar to those obtained on the water-jet prepared substrates (0.06%), and a similar trend is observed: porosity decreases with increasing deposition pressure for both powder types. Moreover, coatings produced with Sph-Ti consistently show lower porosity than those made with Irr-Ti, as previously observed.

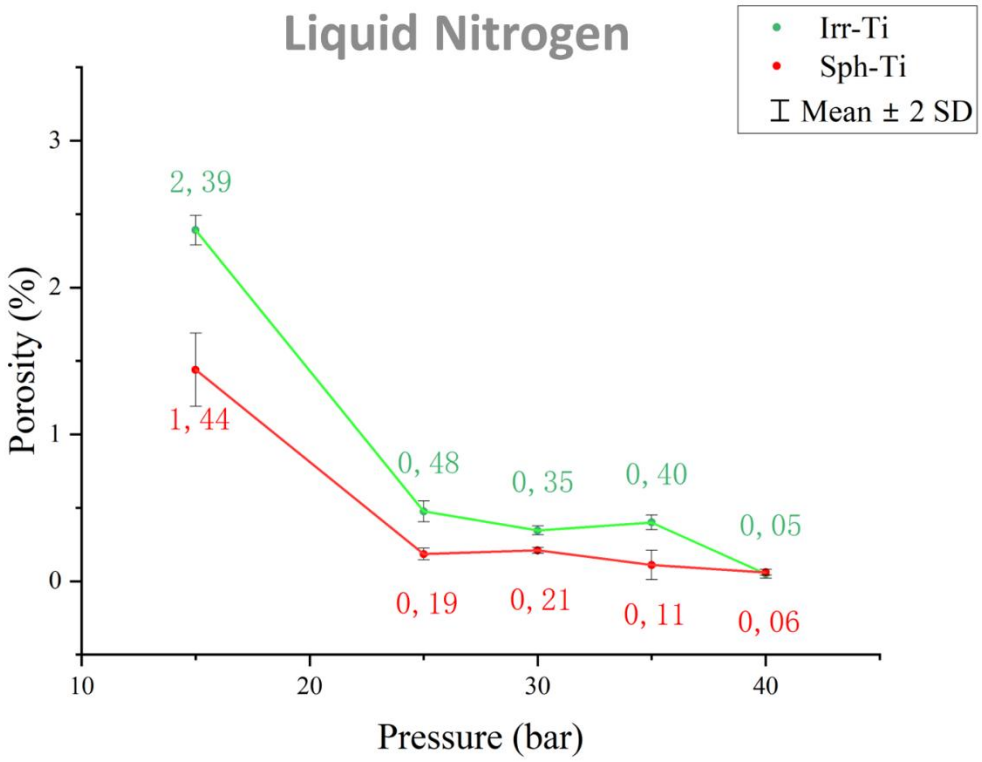

Fig. 206: Porosity of cold-sprayed coatings as a function of deposition pressure for liquid nitrogen-jet prepared substrates (comparison between irregular (Irr-Ti) and spherical (Sph-Ti) Ti powders). Obtained from cross-section samples.

SEM observations show that the same overall trends are obtained as with the water-jet prepared substrates, for both irregular and spherical Ti particles (Fig. 207). At low deposition pressure (15 bar), the coatings exhibit high porosity, mainly due to particle pull-outs during polishing. At higher pressures (30 and 40 bar), the remaining porosity is primarily intergranular, with the 40 bar samples showing very few visible surface defects, indicating improved densification.

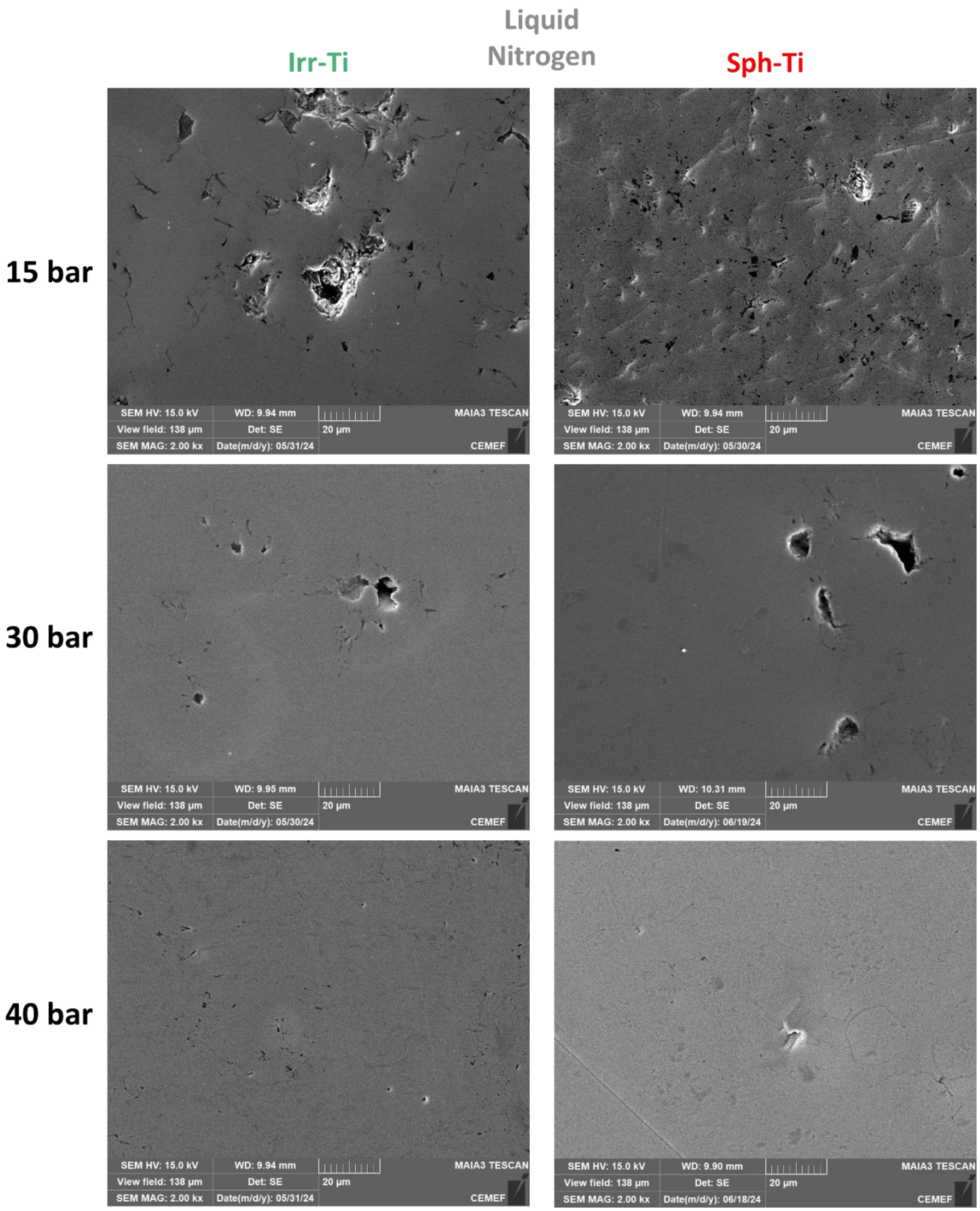

Fig. 207: SEM cross-sectional observations of coatings formed at 15, 30, and 40 bar using irregular Ti powder (left) or spherical Ti (right) for liquid nitrogen-jet prepared substrates.

From these observations, it can be anticipated that using liquid nitrogen-jet prepared substrates instead of water-jet ones does not influence inter-particle cohesion. This assumption is confirmed by the average hardness results (values averaged over 50, 250, and 500 µm tests) presented in Fig. 208. For Irr-Ti, hardness becomes high and stable (around 190 HV) only from 30 bar onward, consistent with the results obtained on water-jet prepared substrates (Fig. 203). For Sph-Ti, the hardness plateau is reached earlier, at 25 bar instead of 35–40 bar for the water-jet method, with an average value of approximately 170 HV.

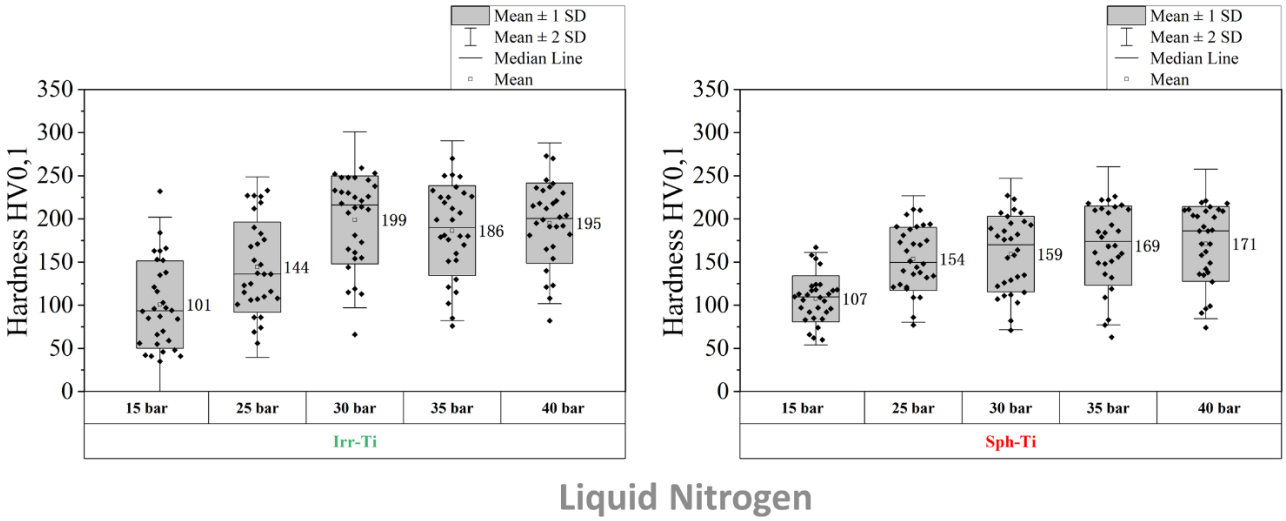

Fig. 208: Evolution of average microhardness with pressure of coatings produced with irregular (left) and spherical (right) particles for liquid nitrogen-jet prepared substrates.

Regarding the hardness gradient through the coating thickness (measured at 50, 250, and 500 µm above the substrate - coating interface) presented in Fig. 209, no significant variation is observed. The hardness values remain comparable at all depths, indicating a uniform intergranular cohesion throughout the coating.

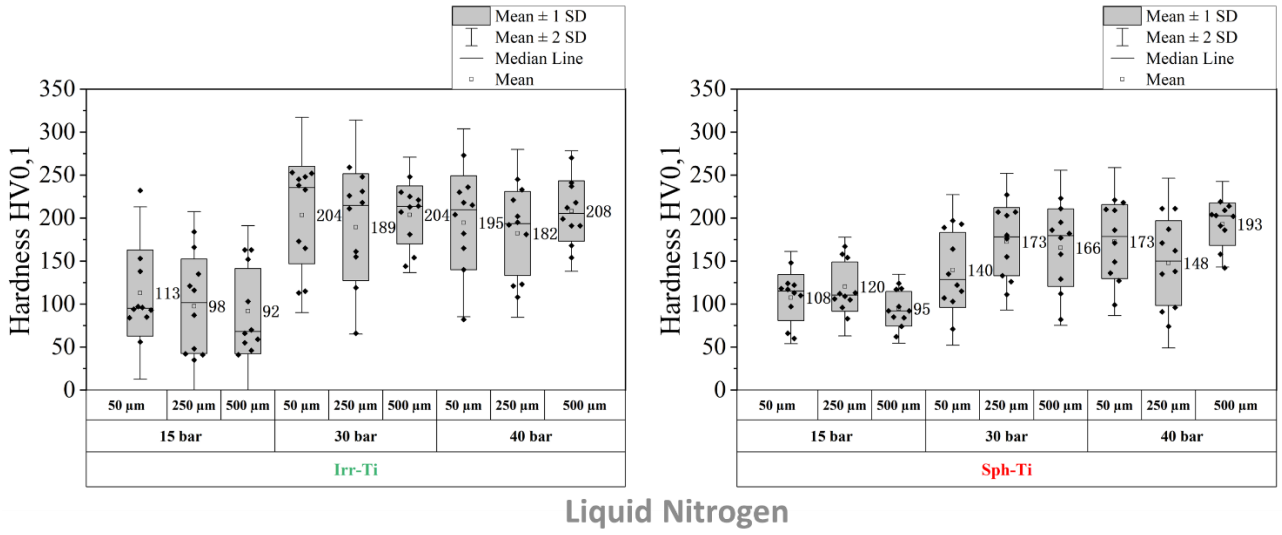

Fig. 209: Microhardness values measured at different depths (50, 250, and 500 µm above the substrate-coating interface) for coatings produced with irregular (left) and spherical (right) powders. Comparison between 15, 30 and 40 bar for coatings deposited on liquid nitrogen-jet prepared substrates.

In summary, the surface preparation method, whether by water-jet or liquid nitrogen-jet, does not affect the coating porosity or inter-particle cohesion. Its influence is mainly limited to the deposition efficiency, since better-prepared surfaces promote faster initial adhesion of the coating to the substrate, improving the overall buildup rate without changing the intrinsic microstructural quality of the deposit.

The results obtained from this study highlight the key parameters governing the formation and mechanical integrity of cold-sprayed titanium coatings.

First, **deposition pressure** plays a major role in both **adhesion** and **cohesion**. Increasing the pressure enhances particle impact energy, promoting plastic deformation and improving bonding between particles and with the substrate. A pressure around **35 bar** appears sufficient to achieve dense coatings with stable hardness values and low porosity.

The **powder morphology** also strongly influences coating behavior. Irregular particles (Irr-Ti) tend to bond more effectively at lower pressures thanks to their angular geometry and broader size distribution, which favor mechanical interlocking and efficient packing. Conversely, spherical particles (Sph-Ti) require higher impact velocities to achieve similar levels of cohesion and density, but they ultimately yield coatings with lower residual porosity due to their enhanced deformability once proper adhesion is achieved.

Regarding surface preparation, both water-jet and liquid nitrogen-jet methods produce coatings of comparable porosity and cohesion. However, the water jet provides slightly better initial adhesion, likely because it avoids the embedding and fracturing of abrasive particles observed with the liquid nitrogen-jet. Consequently, coatings deposited on water-jet prepared substrates exhibit higher deposition efficiency translated through greater coating thickness under identical conditions.

Overall, optimizing the surface preparation allows the use of lower deposition pressures while maintaining strong adhesion and coating integrity, thus reducing the operational energy cost of the cold spray process. A proper balance between substrate roughness, powder morphology, and deposition pressure is therefore essential to obtain dense, well-adhered, and mechanically robust titanium coatings.

Having characterized the single-component cold spray behavior, the next step is to examine the composite cold spray system and its tribological performance.

4.2 Optimization of a Ti/TiO_x Composite Cold Spray Coating

For this section, all substrates were prepared using the optimized surface preparation parameters established in the previous section: **water-jet preparation with an abrasive feed rate of 150 g/min and a 90° impact angle**.

The primary objective of this section is to characterize and optimize the composite cold spray coatings in terms of tribological performance. The results obtained will make it possible to identify the most suitable titanium powder (irregular or spherical) to be used as the matrix material, as well as to determine the optimal reinforcement content to achieve the best overall coating performance.

4.2.1 Influence of Matrix Powder Type on Composite Coatings Characteristics

Both composites formed using irregular and spherical Ti powders are compared in this study. The reinforcement content is here fixed at 20 vol.% of TiO_x, based on the results previously obtained by L. Aubanel (2022) [3].

Regarding the deposition pressure, although 35 bar seems sufficient to ensure good adhesion, a higher pressure of 40 bar is selected in order to anticipate potential cohesion issues related to the addition of the ceramic reinforcement [4].

As for the single-component coatings, coating thickness and porosity are measured and summarized in **Table 35**. In addition, for the composite coatings, the actual reinforcement content is quantified based on contrast differences between the matrix, porosity, and reinforcement phases using ImageJ analysis.

When using an Irr-Ti matrix, the coating thickness remains almost unchanged with or without reinforcement, while the porosity slightly increases from 0.16% to 0.27%. The deposition efficiency of the TiO_x reinforcement reaches 32.9%, which is slightly higher than the value obtained by L. Aubanel (2022) [3] when spraying a 410L stainless steel/TiO_2 blend (27% efficiency).

For the Sph-Ti matrix, the addition of TiO_x leads to a reduction in coating thickness - from 1750 µm to 1133 µm - which may result from poorer adhesion to the substrate and therefore a decrease in global deposition yield. The porosity also increases, from 0.06% to 0.13%, while the reinforcement deposition efficiency is slightly higher than for Irr-Ti, reaching 37.7%.

Matrix	Nominal TiO_x Content (v. %)	Measured TiO_x Content (v. %)	TiO_x Deposition Efficiency (%)	Coating Thickness (µm)	Porosity (%)
Irr-Ti	0	0		1012 ± 42	0,16 ± 0,04
	20	6,6 ± 0,2	32,9	970 ± 53	0,27 ± 0,03
Sph-Ti	0	0		1750 ± 60	0,06 ± 0,03
	20	7,5 ± 0,1	37,7	1133 ± 50	0,13 ± 0,04

Table 35: Comparison of composite cold spray coatings produced with irregular (Irr-Ti) and spherical (Sph-Ti) powders at different TiO_x reinforcement contents (0 and 20 v.%). Coatings prepared using a 40 bar deposition pressure.

In both cases, an increase in porosity is observed. This rise is mainly attributed to the fragmentation and pull-out of the ceramic reinforcement particles, as shown in Fig. 210.

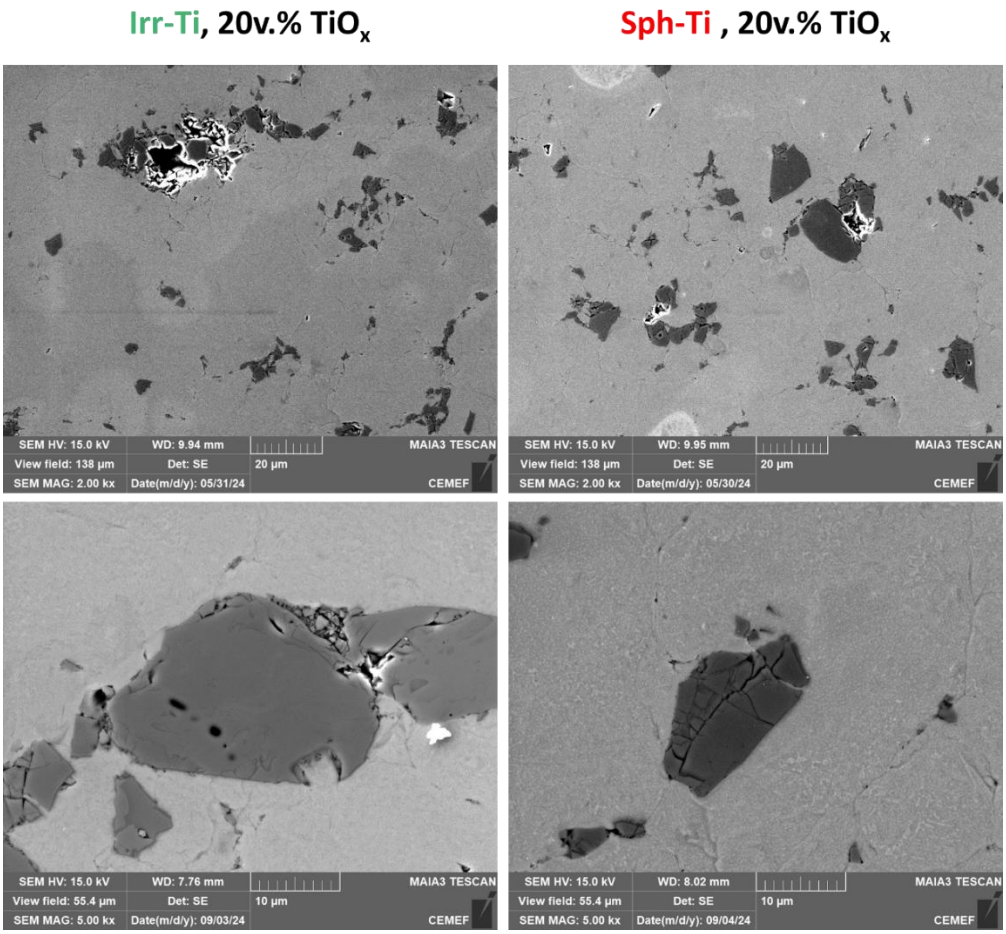

Fig. 210: SEM cross-sectional observations of composite coatings formed in a Irr-Ti (left) or Sph-Ti (right) matrix showing fragmentation and pull-out of TiO_x reinforcement particles.

The adhesion between the coating and the substrate does not appear to be affected by the addition of reinforcement particles, as evidenced by the microhardness measurements performed at the interface (Fig. 211).

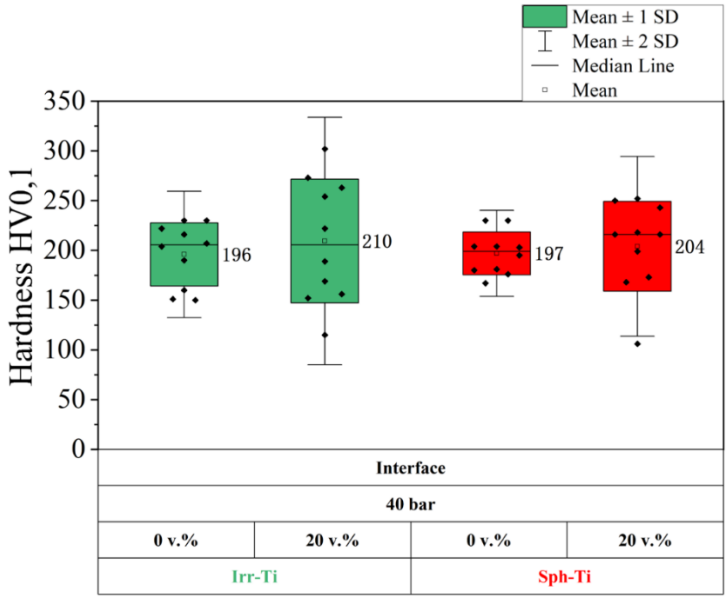

Fig. 211: Microhardness measurements at the substrate-coating interface for composite coatings produced with irregular (Irr-Ti) or spherical (Sph-Ti) matrix and either 0 or 20 v.% of TiO_x.

Regarding inter-particle cohesion, it remains unchanged with the addition of reinforcement in the Irr-Ti matrix but slightly increases for the Sph-Ti matrix (Fig. 212). It should be noted that the indentation tests are conducted in areas between reinforcement particles, not directly on them.

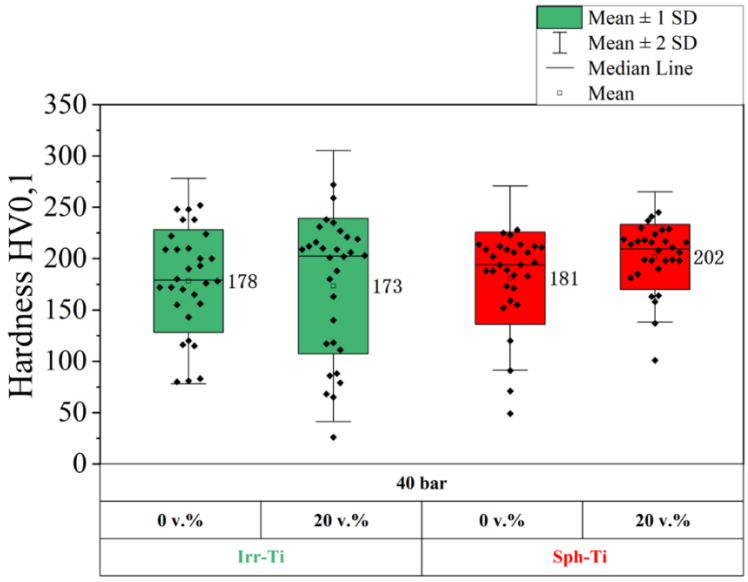

Fig. 212: Average microhardness within the coating matrix (Irr-Ti or Sph-Ti) for coatings with (20 v.%) and without TiO_x reinforcement.

The detailed hardness measurements through the coating thickness - at 50, 250, and 500 µm above the substrate-coating interface - are presented in Fig. 213. These results confirm that higher and less dispersed hardness values are obtained for coatings based on Sph-Ti matrix. As with the previous results at 35 bar (Fig. 204 and Fig. 209), it remains difficult to clearly identify a hardness gradient within the coating thickness.

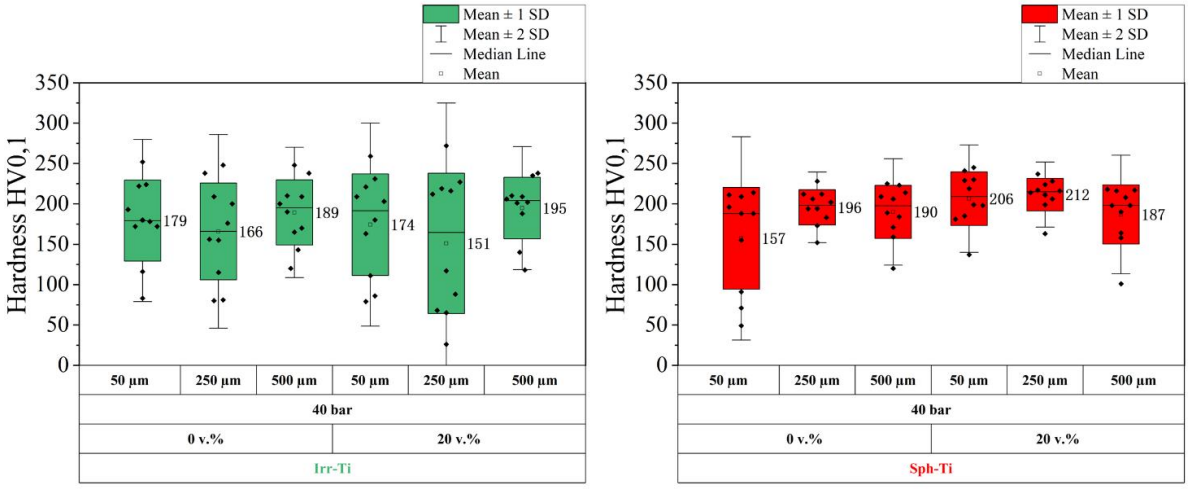

Fig. 213: Microhardness values measured at different depths (50, 250, and 500 µm above the substrate-coating interface) for coatings produced with irregular (left) and spherical (right) particles and a TiO_x content of either 0 or 20 v.%.

Based on the previous results, the Sph-Ti coatings appear to exhibit slightly better intrinsic properties than the Irr-Ti ones: they show lower porosity, a higher actual reinforcement content, and better inter-particle cohesion.

However, before definitively selecting the powder to be used as the matrix material, tribological tests were conducted. These tests were performed with a low viscosity transmission oil at 25 °C, with a maximum sliding speed of 20 mm/s.

Fig. 214 presents the coefficients of friction obtained for coatings without reinforcement deposited using either Irr-Ti or Sph-Ti powders. The tests are successful only for the coatings produced with irregular particles, showing stable friction around 0.115. In contrast, the coatings made with spherical particles exhibit a rapid increase in friction between 500 and 1000 cycles, leading to premature test failure.

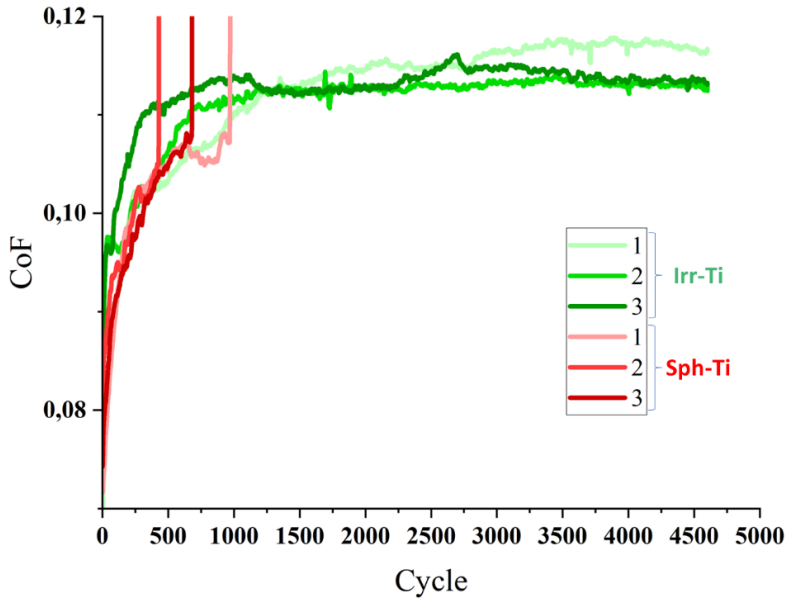

Fig. 214: Coefficient of friction (CoF) of unreinforced coatings produced with irregular (Irr-Ti) and spherical (Sph-Ti) particles at 40 bar. Tests conducted with a low viscosity gear oil at 25°C.

With the addition of reinforcement (Fig. 215), the CoF obtained for the Irr-Ti matrix decreases slightly, from 0.115 to just below 0.11. For the Sph-Ti matrix, a slight improvement is also observed, as one full test was successfully completed without seizure, unlike the unreinforced Sph-Ti coating. However, when attempting to reproduce these results using an additional sample, all 3 repetitions tests failed. This means that only one out of six tests reached completion, with a CoF value comparable to that of the Irr-Ti coatings.

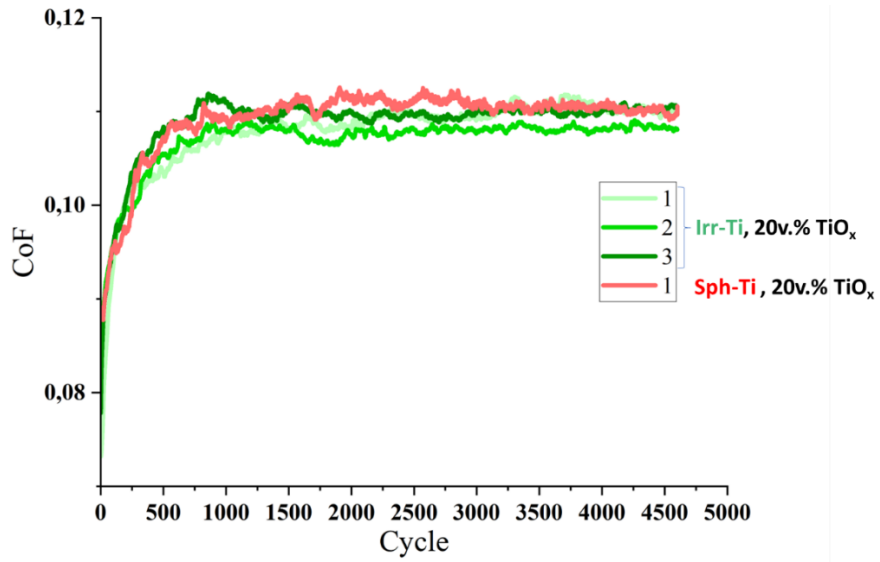

Fig. 215: Coefficient of friction (CoF) of reinforced coatings (20 v.% of TiO_x) produced with irregular (Irr-Ti) and spherical (Sph-Ti) particles at 40 bar. Tests conducted with a low viscosity gear oil at 25°C.

Fig. 216 shows the wear tracks obtained from these tests. For the successful tests, a brownish layer can be observed along the track. Moreover, the coatings containing reinforcement display narrower wear tracks (~130 µm) compared to those without reinforcement (~155 µm). The tests interrupted due to the sudden increase in friction (Sph-Ti coatings) show heavily scratched surfaces.

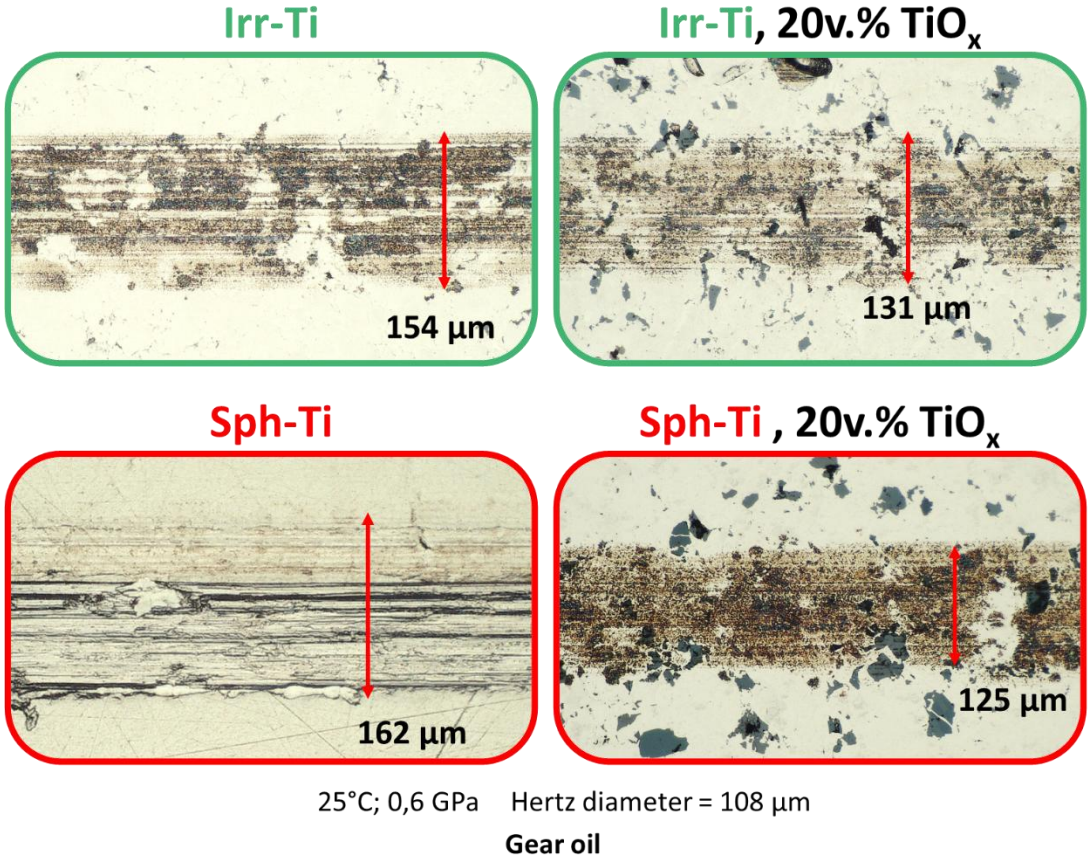

Fig. 216: Optical micrographs of wear tracks on the discs obtained after tribological tests on coatings with and without reinforcement produced with irregular (Irr-Ti) or spherical (Sph-Ti) powders at 40 bar. Tests conducted with a low viscosity gear oil at 25°C.

As shown in Fig. 217, for the Sph-Ti sample, titanium material adhered to the steel ball, which then scratched the coating surface, leading to the sharp rise in friction. This behavior is typical for pure titanium that is known to be prone to adhesive wear [5]. The fact that this is observed only with Sph-Ti could be due to their slightly lower hardness (200 HV) compared to Irr-Ti particles (220 HV). For the other tests, a tribofilm appears to have formed on the steel balls, exhibiting a characteristic bluish coloration.

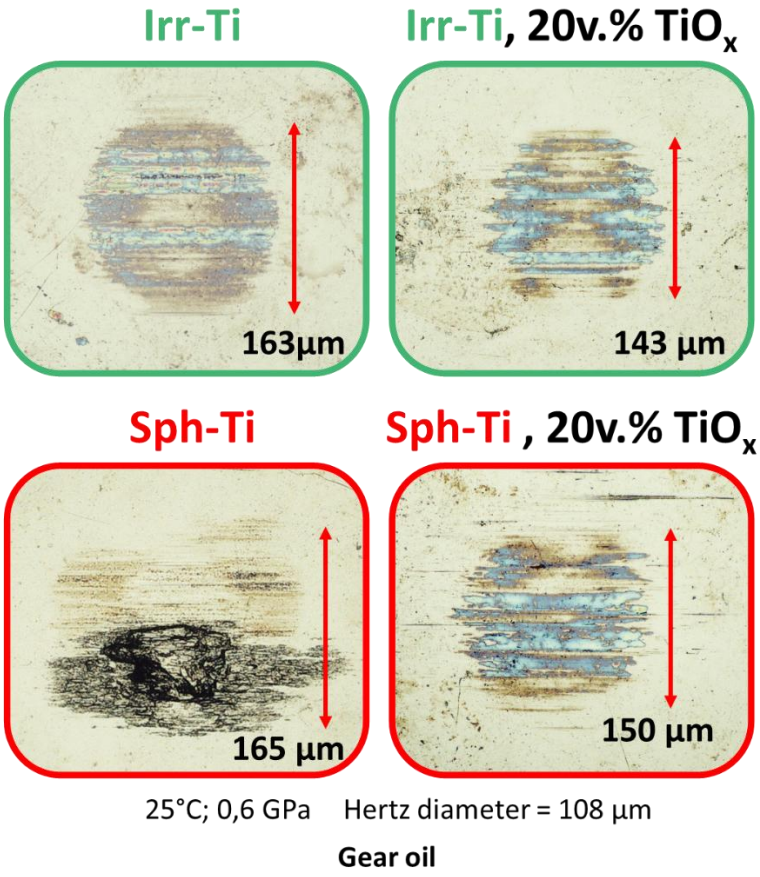

Fig. 217: Optical micrographs of wear tracks on the balls obtained after tribological tests on coatings with and without reinforcement produced with irregular (Irr-Ti) or spherical (Sph-Ti) powders at 40 bar. Tests conducted with a low viscosity gear oil at 25°C.

Fig. 218 presents an optical micrograph of the wear track obtained for the Sph-Ti + 20 % TiO_x coating, where the test was stopped early due to very high friction at the beginning. The image reveals a dragged titanium particle along the track, responsible for the scratch and the abrupt friction increase.

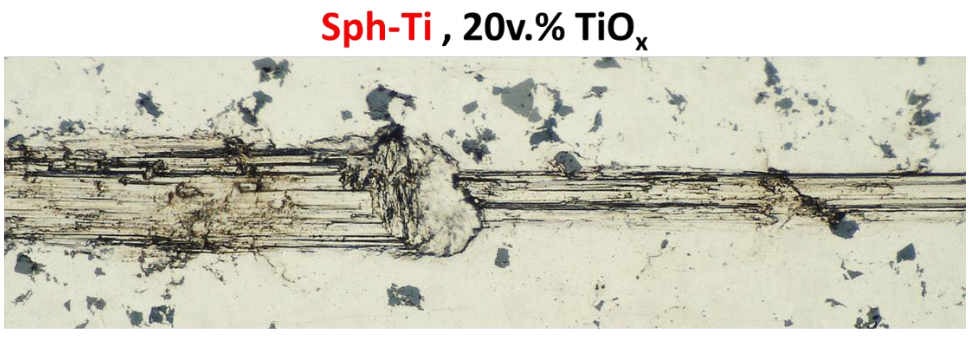

Fig. 218: Optical micrograph of the wear track from a failed tribological test at 25°C with a low viscosity gear oil on Sph-Ti + 20 vol.% TiO_x coating.

Concerning wear behavior, Fig. 219 compares the wear tracks profilometric measurements of coatings with and without reinforcement produced using the Irr-Ti matrix. No clear reduction in overall wear is observed, although the composite coating exhibits more homogeneous and shallower wear, with less localized damage. This behavior is likely due to the insufficient actual reinforcement content (6,6 v.% of TiO_x).

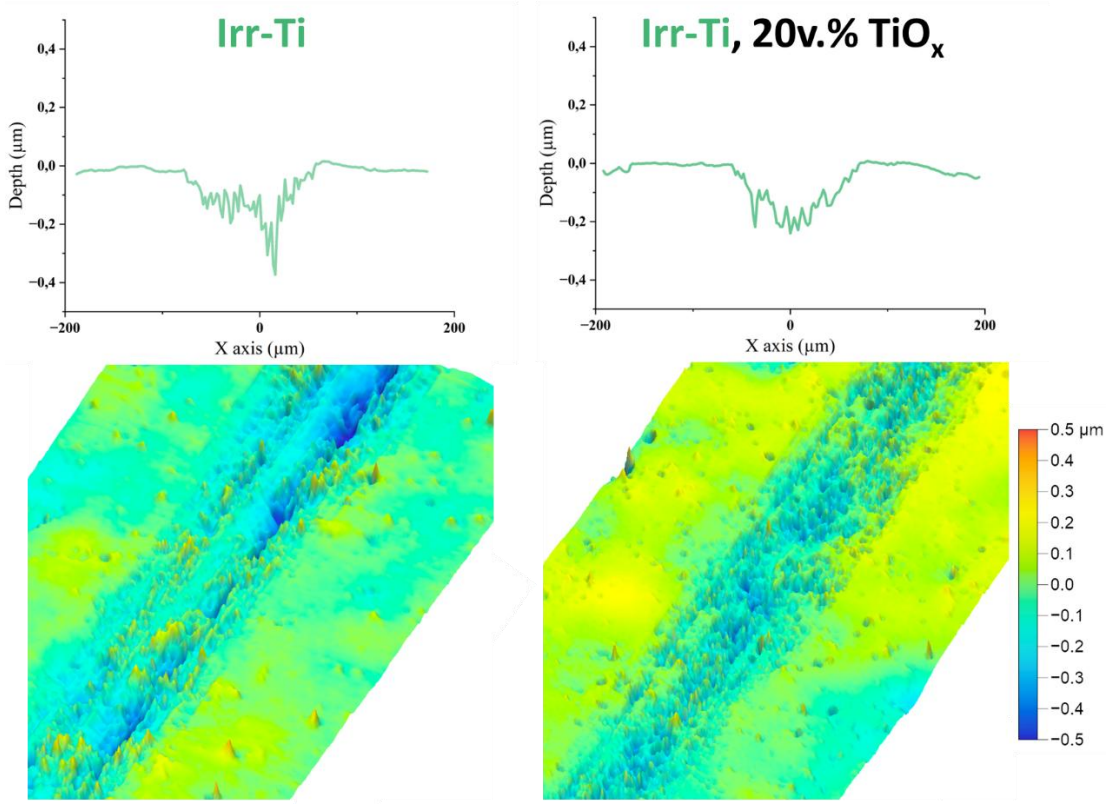

Fig. 219: Mean depth profiles and surface morphology of wear tracks formed on the discs at 25°C with a low viscosity gear oil on coatings with and without reinforcement produced with irregular (Irr-Ti) at 40 bar.

The addition of TiO_x reinforcement slightly increases the porosity of the coatings but does not significantly affect their adhesion to the substrate or inter-particle cohesion. Tribological testing shows that coatings based on irregular Ti particles (Irr-Ti) offer the most stable and reproducible friction behavior, whereas coatings with spherical particles (Sph-Ti) tend to fail prematurely due to titanium's well-known adhesive behavior. Consequently, Irr-Ti was selected as the matrix material for the following stage of the study, with an increased reinforcement content from 20 v.% to 50 v.% TiO_x to further enhance wear resistance.

4.2.2 Optimized Cold Spray Composite Coating

4.2.2.1 Mechanical and Morphological Characterization of the Coatings

As for the previous coatings, the main characteristics of these deposits are measured and summarized in **Table 36**. These coatings are produced at the maximum achievable deposition pressure (50 bar) for the cold spray gun used at CRITT-TJFU, in order to anticipate a possible reduction in cohesion due to the addition of a higher amount of reinforcement.

The coating thicknesses obtained are similar to each other and comparable to those formed previously at lower pressure (**Table 35**) with Irr-Ti. For the unreinforced coating, the measured porosity is minimal (0.03%). With the addition of reinforcement, the porosity increases significantly, reaching 0.74%. The deposition efficiency of the reinforcement is 32.6%, comparable to the value obtained for the 20 v.% TiO_x composite coating deposited at 40 bar.

Powder Type	Nominal TiOx Content (v. %)	Measured TiOx Content (v. %)	TiOx Deposition Efficiency (%)	Coating Thickness (µm)	Porosity (%)
Irr-Ti	0	0		985±31	0,03±0,02
	50	16,3±0,1	32,6	971±46	0,74±0,10

Table 36: Comparison of composite cold spray coatings produced with irregular (Irr-Ti) and spherical (Sph-Ti) powders at different TiO_x reinforcement contents (0 and 50 v.%). Coatings prepared using a 50 bar deposition pressure.

SEM observations of both coatings are presented in Fig. 220. The single-component coating shows a clean surface with very few defects, whereas the composite coating exhibits higher porosity mainly caused by pull-out of the reinforcement particles, as previously observed.

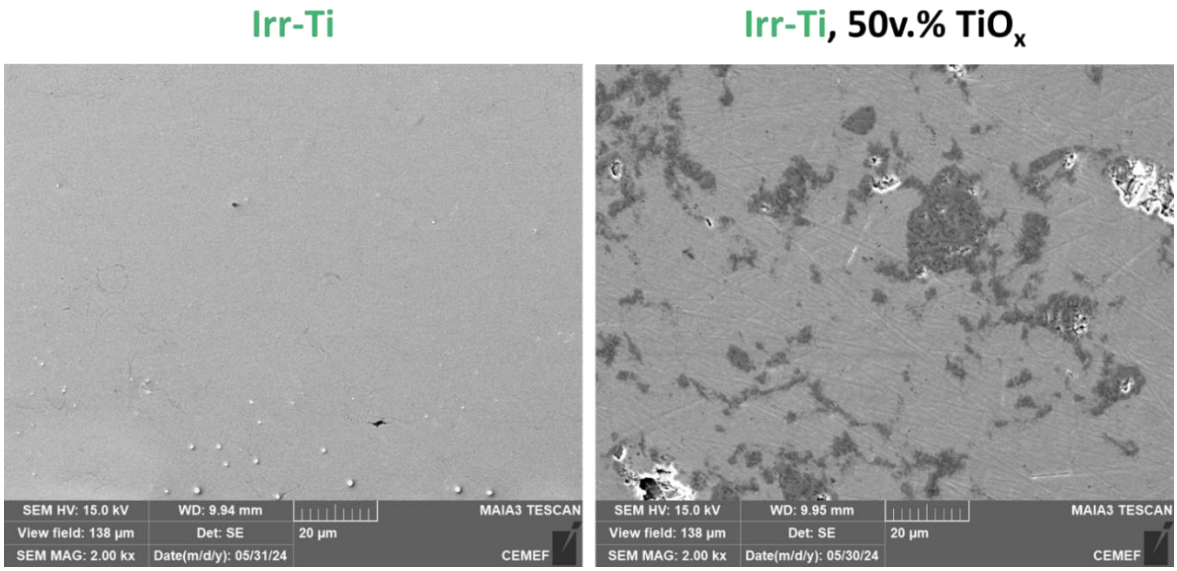

Fig. 220: SEM observations of coatings deposited at 50 bar with and without 50 v.% TiO_x reinforcement.

Regarding adhesion to the substrate (Fig. 221), very good results are obtained for the unreinforced coating, likely due to the high deposition pressure. The average microhardness measured for the composite coating is even higher, which suggests good integration of the reinforcement into the matrix without a detrimental effect on coating-substrate bonding. However, this increase in hardness is probably not directly related to better adhesion, but rather to an overall increase in the coating's intrinsic hardness.

These indentation tests are performed in areas free of visible reinforcement particles, but subsurface reinforcement could still influence the results. The hard particles may also locally enhance plastic deformation of the Ti matrix, thereby increasing its hardness. This highlights the limitations of using microhardness testing alone to evaluate coating-substrate adhesion. Ideally, standardized adhesion tests such as the ISO 14916:2017 [6] pull-off test should be performed to quantitatively assess interfacial strength.

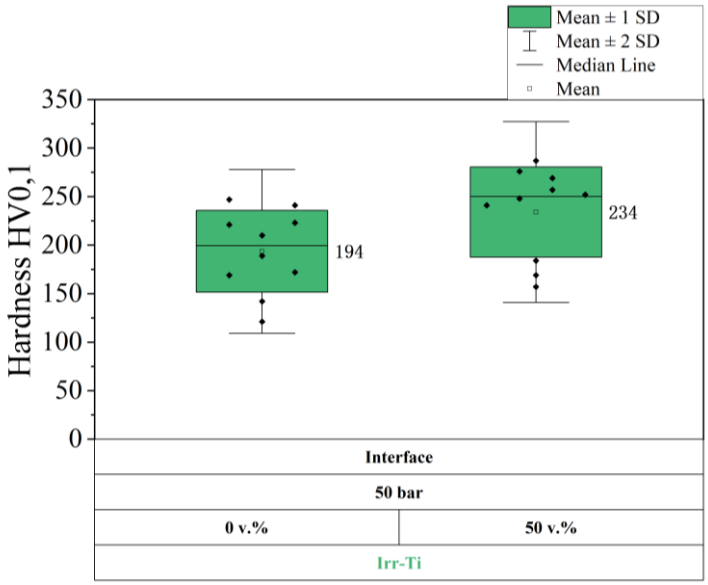

Fig. 221: Microhardness measurements at the substrate-coating interface for composite coatings produced with irregular (Irr-Ti) matrix and either 0 or 50 v.% of TiO_x.

As for the overall microhardness of the coatings (Fig. 222), higher values are obtained for the composite coating (218 HV) compared to the unreinforced one (184 HV), consistent with previous statement.

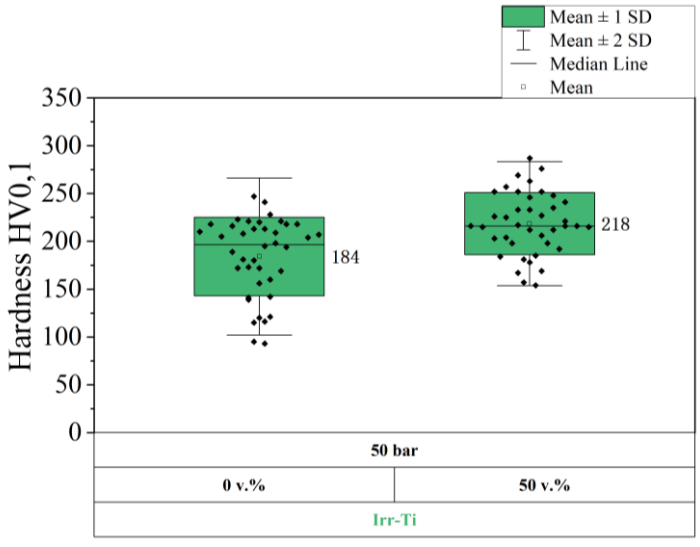

Fig. 222: Average microhardness within the coating matrix (Irr-Ti) for coatings with (50 v.%) and without TiO_x reinforcement.

When considering hardness across the depth of the coatings (Fig. 223), the composite coating shows both a higher mean hardness and lower data dispersion, indicating a more stable and homogeneous mechanical behavior across its thickness, with no apparent gradient.

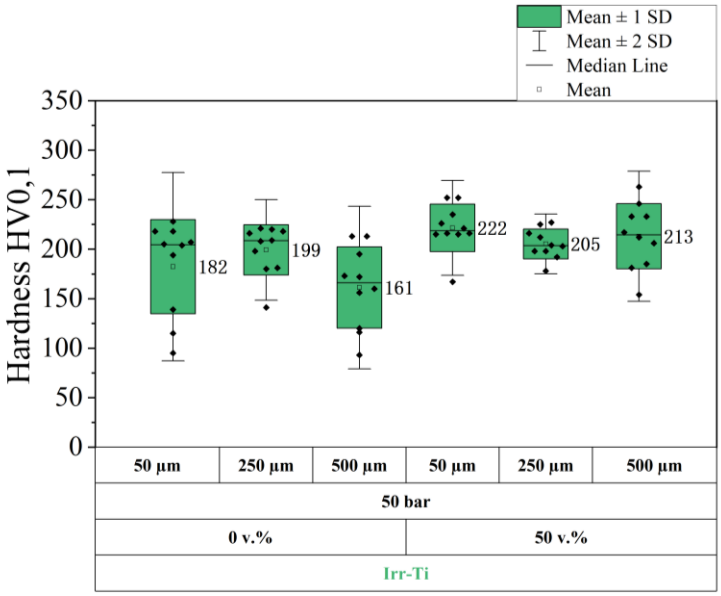

Fig. 223: Microhardness values measured at different depths (50, 250, and 500 µm above the substrate-coating interface) for coatings produced with irregular particles and a TiO_x content of either 0 or 50 v.%.

Compared to the 20 v.% TiO_x blend, the 50 v.% one exhibit a higher porosity but also an increase of 19% in hardness, suggesting effective incorporation of the ceramic phase within the titanium matrix. This increase in porosity is expected, as it mainly originates from the presence of the ceramic reinforcement particles; adding a larger amount of TiO_x inevitably introduces more voids within the coating structure. Despite this, no deterioration of substrate adhesion is observed, and the coating displays stable and homogeneous mechanical behavior throughout its thickness.

These findings confirm that the reinforcement is well integrated and contributes to overall strengthening, although the higher porosity could influence the surface durability. To further assess the functional impact of this high reinforcement content, tribological tests were subsequently carried out under lubricated conditions.

4.2.2.2 Coatings Tribological Properties

Tribological tests were carried out again using low viscosity transmission oil, this time at 25°C and 80°C, with a lower maximum sliding speed of 10 mm/s (compared to 20 mm/s previously) in order to slightly increase the severity of the testing conditions. It should be noted that the pressure of 0.6 GPa was calculated using the Young's modulus of pure titanium and is therefore likely slightly underestimated.

4.2.2.2.1 Composite Cold spray coating performance with a fully formulated gear oil

Despite the higher deposition pressure used for the single-component coating, the harsher boundary lubrication conditions caused by the reduced sliding speed led to excessive wear in all repetitions. This already provides a first indication of the superior performance of the composite coating. Therefore, only the results obtained with the composite coating are presented here.

Coefficient of friction evolution at 25°C and 80°C are presented in Fig. 224. For both tested temperatures, good repeatability is observed. The steady state friction is higher at 80 °C (0.14) than at 25 °C (0.115). The higher temperature reduces the oil viscosity, thereby worsening the lubrication regime and explaining the higher friction values. The temperature rise also activates the anti-wear and extreme-pressure additives present in the oil. This may compensate for this effect, but it does not seem to be the case here.

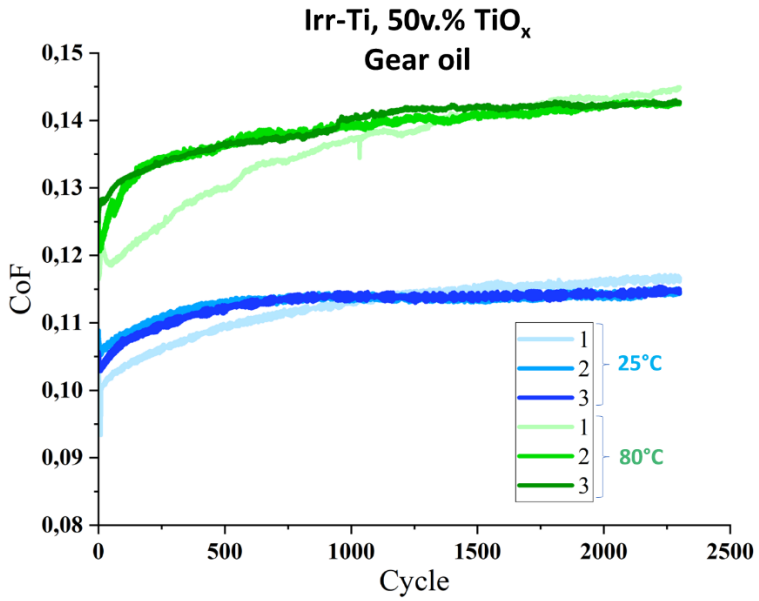

Fig. 224: Coefficient of friction (CoF) of reinforced coating (50 v.% of TiO_x) produced with irregular (Irr-Ti) particles at 50 bar. Tests conducted with a low viscosity gear oil at 25°C and 80°C.

Optical observations of the wear tracks at 25 °C are shown in Fig. 225. On the discs coated with the composite coating, the friction marks are barely visible, with a width close to the Hertzian contact diameter (108 µm). The 100Cr6 steel balls show slight surface markings, with a noticeably larger wear mark diameter than the track width on the discs.

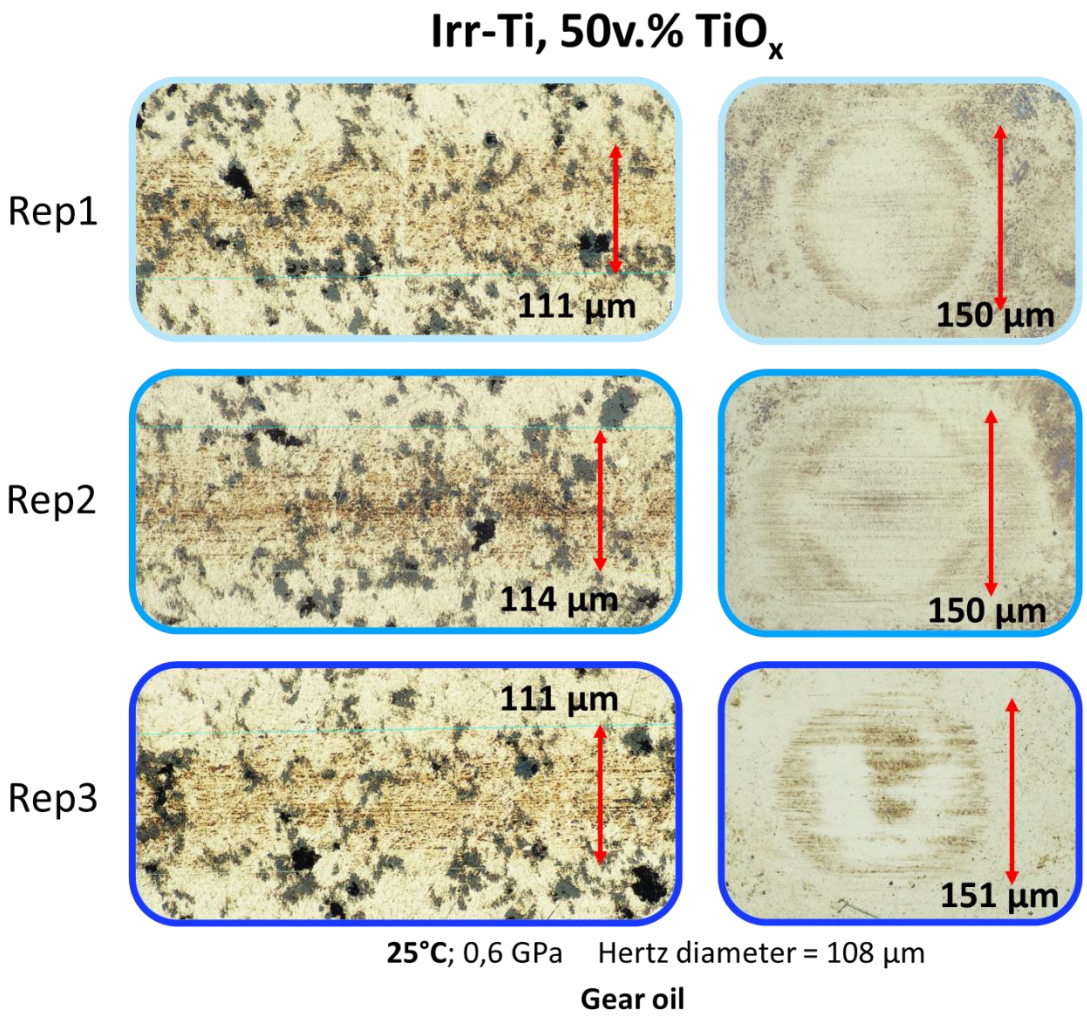

Fig. 225: Optical micrographs of wear tracks on the discs and balls obtained after tribological tests on coatings with 50 v.% reinforcement produced with irregular (Irr-Ti) particles at 50 bar. Tests conducted with a low viscosity gear oil at 25°C.

At 80 °C (Fig. 226), the friction tracks on the discs are even less visible, still with a width close to the Hertzian diameter. Conversely, the wear marks on the steel balls are more pronounced and show a slightly bluish appearance, indicating the potential formation of a tribofilm – clearer at 80°C than at 25°C.

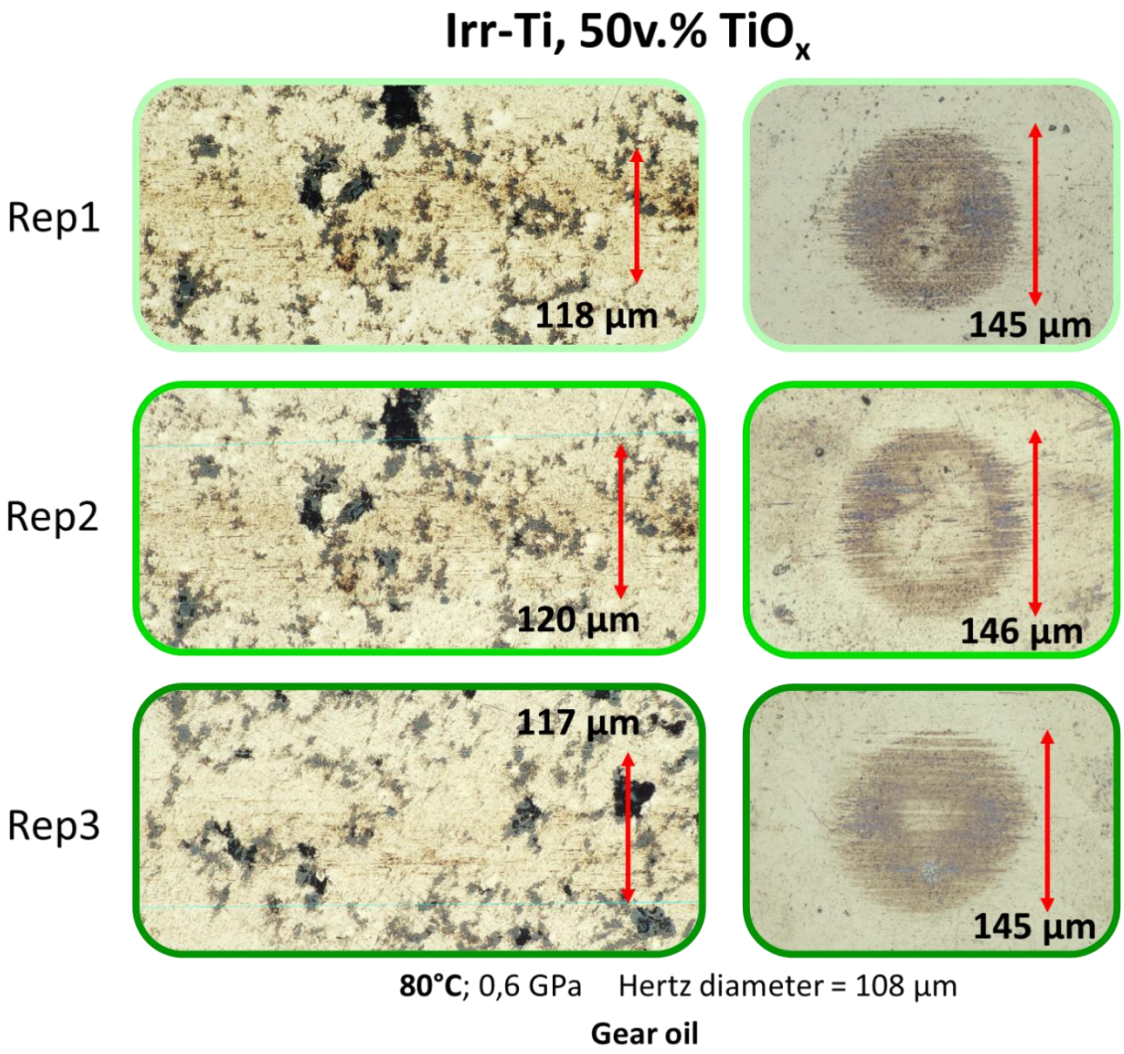

Fig. 226: Optical micrographs of wear tracks on the discs and balls obtained after tribological tests on coatings with 50 v.% reinforcement produced with irregular (Irr-Ti) particles at 50 bar. Tests conducted with a low viscosity gear oil at 80°C.

Profilometry results (Fig. 227) show that a tribofilm appears to have formed at 25 °C, while no such film is detected at 80 °C. Nevertheless, the wear depth remains undetectable at both temperatures, which is encouraging compared to the results previously obtained with the 20 v.% TiO_x composite coatings (Fig. 219).

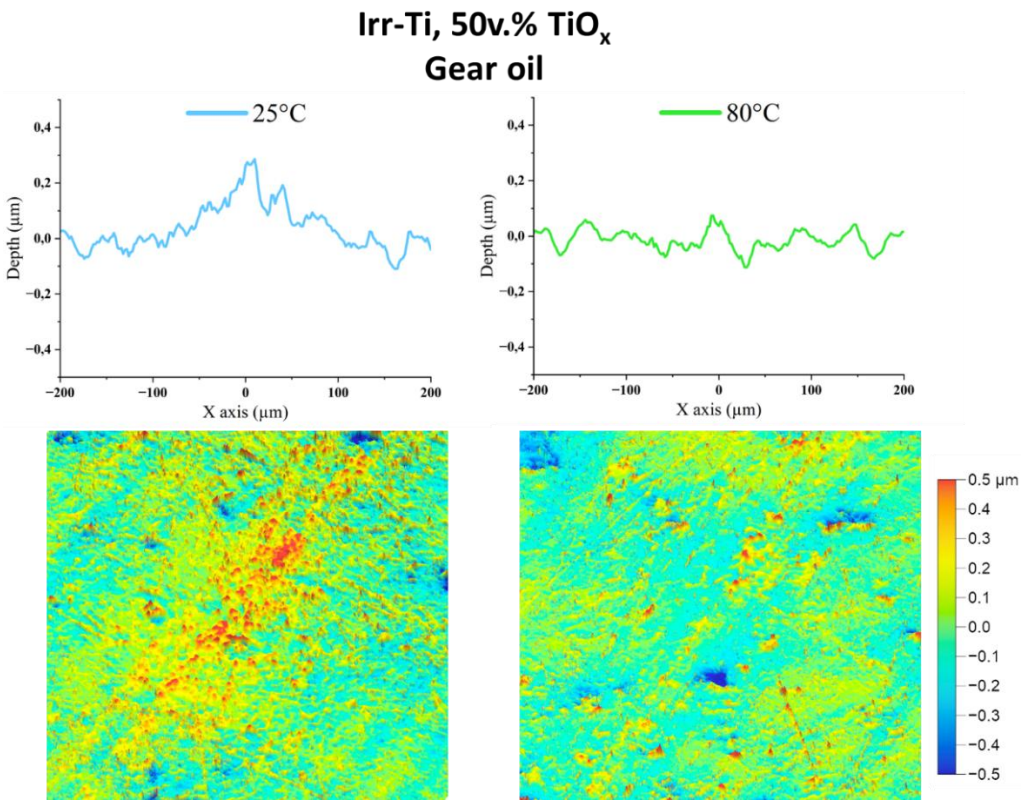

Fig. 227: Mean depth profiles and surface morphology of wear tracks formed on the discs at 25°C and 80°C with a low viscosity gear oil on coatings with 50 v.% reinforcement produced with irregular (Irr-Ti) at 50 bar.

Following the encouraging results obtained with the fully formulated transmission oil, additional tests are carried out using a base oil (PAO6) at 25°C and 80°C, with the aim to access the intrinsic ability of the coating to handle the stress applied to the contact. As shown in Fig. 228, these tests are not conclusive, exhibiting excessive friction levels around 0.45. At 25 °C, the CoF increases sharply after approximately 100 cycles, while at 80 °C, the rise occurs even earlier (after about 20 cycles), most likely due to enhanced adhesive interactions of titanium at higher temperature.

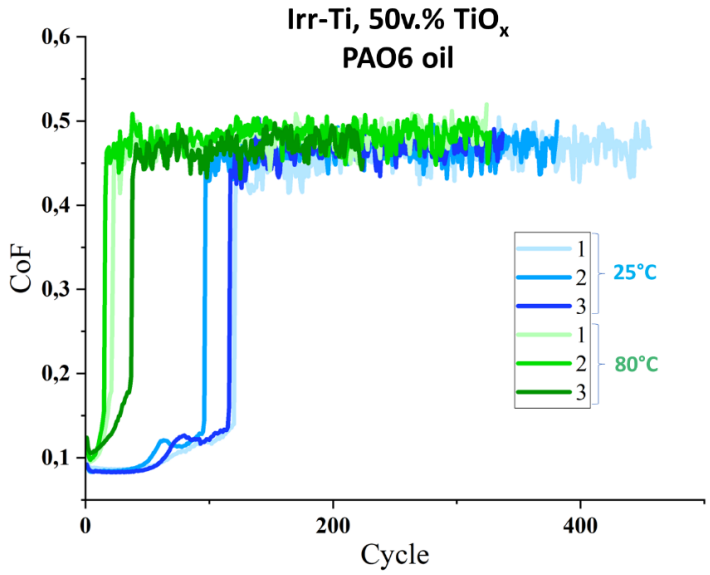

Fig. 228: Coefficient of friction (CoF) of reinforced coating (50 v.% of TiO_x) produced with irregular (Irr-Ti) particles at 50 bar. Tests conducted with a PAO6 base oil at 25°C and 80°C.

As shown in Fig. 229, the coating surface is severely damaged, with deep ploughing marks and a significant amount of transferred material adhering to the steel ball.

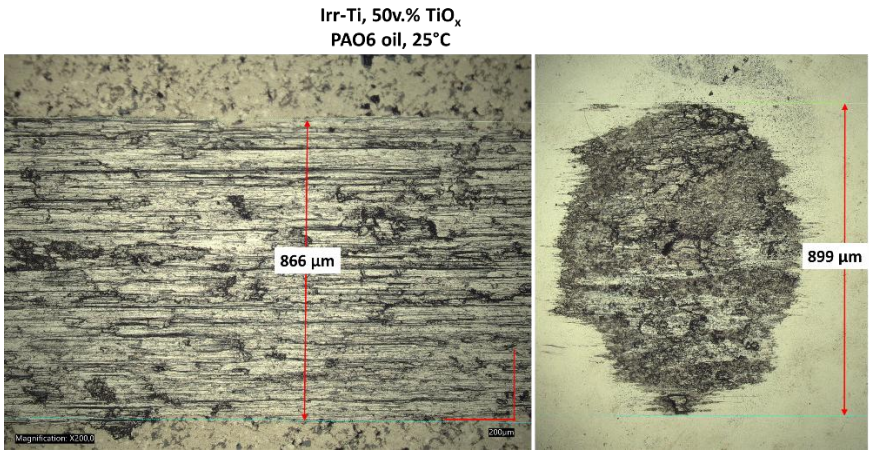

Fig. 229: Optical micrographs of wear tracks on composite-coated disc (left) and 100Cr6 steel ball (right) after tribological testing with PAO6 base oil at 25°C.

Since PAO6 is technically not a lubricant, as it lacks intrinsic lubricating properties - unlike ester-based oils for example - these results are not surprising, considering both the particulate nature of the coating and the intrinsic stickiness of titanium. However, the previous tests clearly demonstrated that the use of a fully formulated oil successfully prevented such adhesive wear phenomena. Therefore, subsequent experiments focus on characterizing the coating's behavior in the presence of individual lubricant additives. To better assess the interaction between the coating and boundary additives, we chose to focus on ZDDP and MoDTC, the same additives that were used in Chapter 3.

4.2.2.2.2 Tribological properties of composite Cold spray coating lubricated with ZDDP additive

First, Fig. 230 presents the evolution of the coefficient of friction obtained using a solution of 1 wt.% ZDDP in PAO6. At 25 °C, the friction tends to increase gradually without fully stabilizing within the duration of the test, with an average CoF of about 0.13. At 80 °C, the CoF starts at a higher value (0.14) but quickly decreases to around 0.12, with a somewhat noisy behavior. This initial phase resembles the friction evolution previously observed in Chapter 3 for ZDDP in a steel-steel contact, though over a shorter sliding window (0-1000 cycles for the coating instead of 0-2300 cycles for steel-steel contact). A second phase follows, characterized by a brief increase in friction (~0.14) before stabilizing again near 0.12. These trends are consistent across the three repetitions.

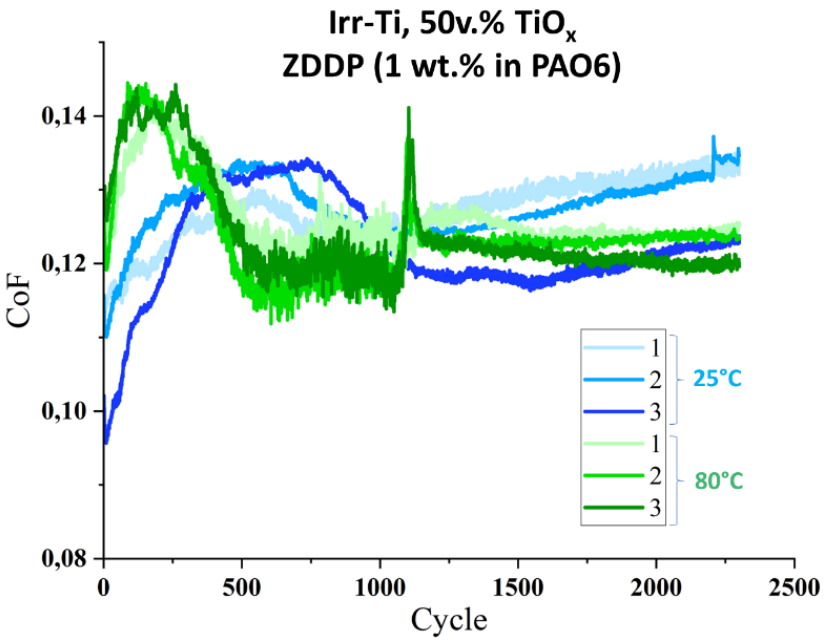

Fig. 230: Coefficient of friction (CoF) of reinforced coating (50 v.% of TiO_x) produced with irregular (Irr-Ti) particles at 50 bar. Tests conducted with a 1 wt.% ZDDP solution at 25°C and 80°C.

Regarding wear, Fig. 231 shows optical observations of the wear tracks obtained at 25 °C. The tracks are barely visible on both the discs and the balls. The track width and wear scar diameter are slightly larger than those observed with the fully formulated oil, which is expected since ZDDP forms a tribofilm more efficiently at elevated temperature.

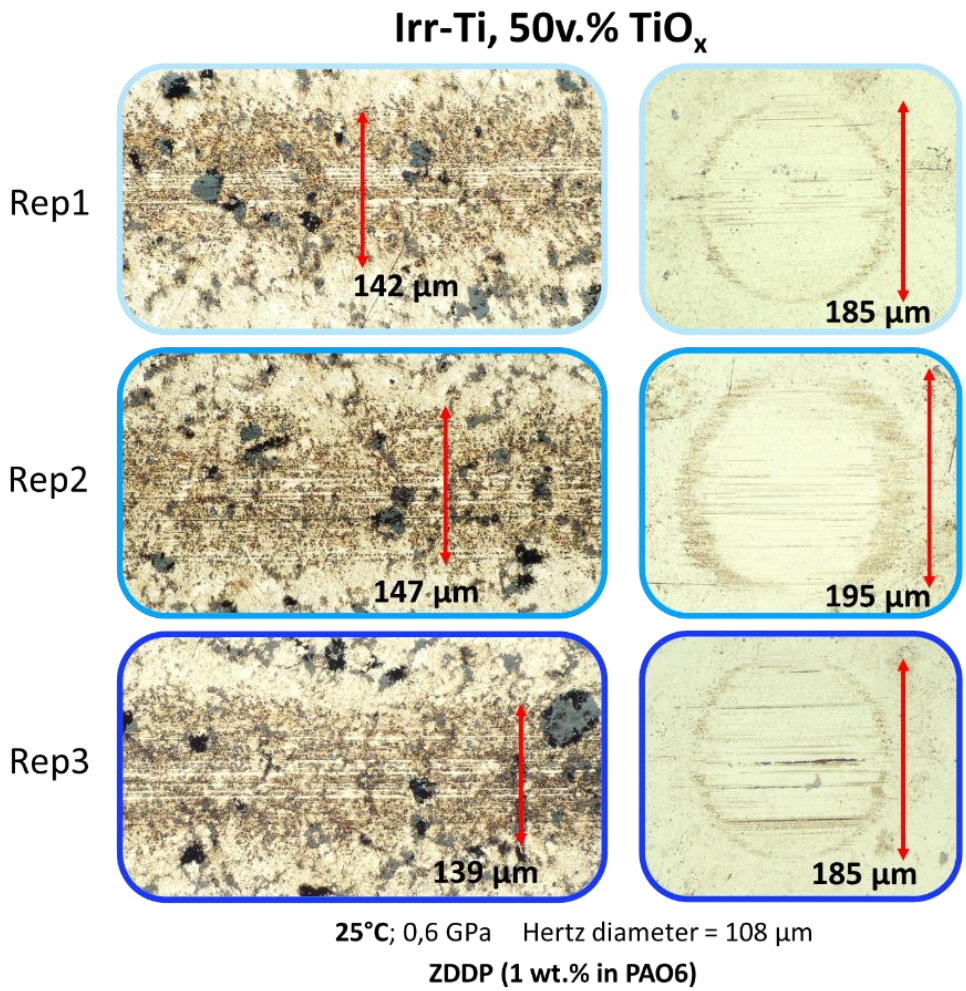

Fig. 231: Optical micrographs of wear tracks on the discs and balls obtained after tribological tests on coatings with 50 v.% reinforcement produced with irregular (Irr-Ti) particles at 50 bar. Tests conducted with a 1 wt.% ZDDP solution at 25°C.

At 80 °C, Fig. 232 reveals that a tribofilm has formed on both the composite-coated disc and the steel ball, as evidenced by the change in color and surface texture.

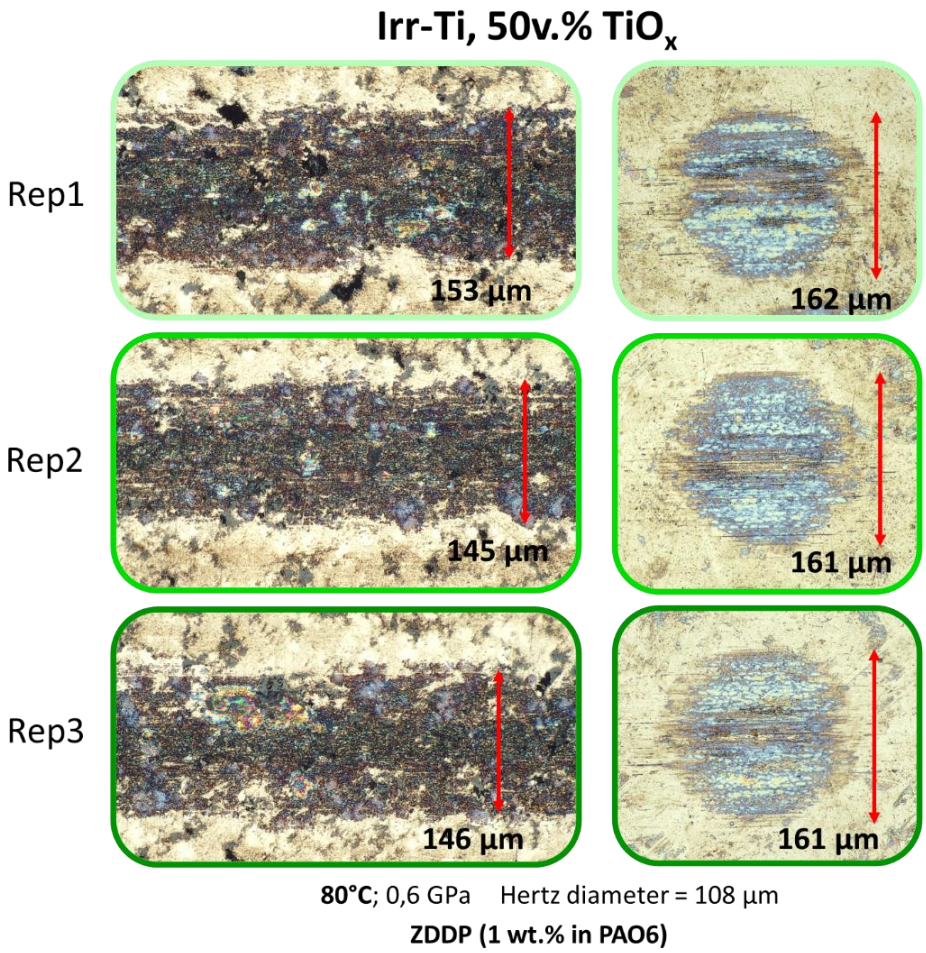

Fig. 232: Optical micrographs of wear tracks on the discs and balls obtained after tribological tests on coatings with 50 v.% reinforcement produced with irregular (Irr-Ti) particles at 50 bar. Tests conducted with a 1 wt.% ZDDP solution at 80°C.

Finally, profilometry results (Fig. 233) confirm the presence of tribofilms at both 25°C and 80°C. In both cases, the films exhibit a thickness greater than 200 nm, but the film formed at 80°C is more homogeneous and continuous. Interestingly, it appears thicker and more uniformly distributed than the films observed under steel-steel contact conditions in Chapter 3.

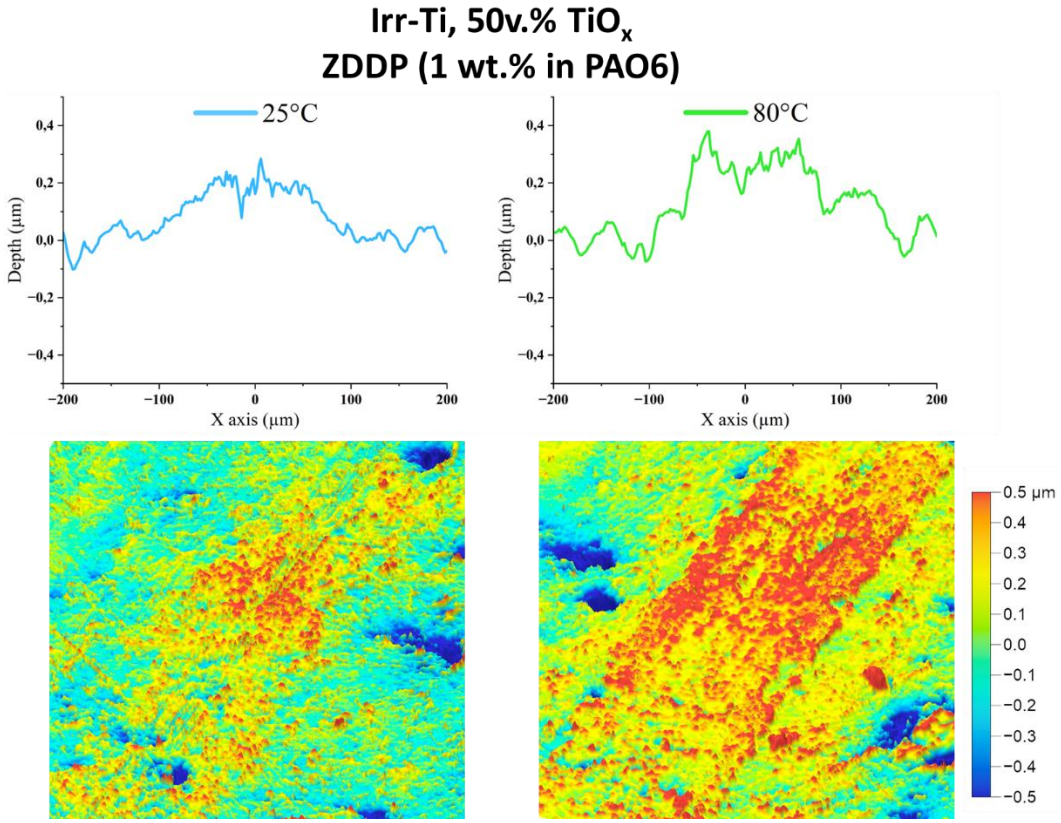

Fig. 233: Mean depth profiles and surface morphology of wear tracks formed on the discs at 25°C and 80°C with 1 wt.% ZDDP solution on coatings with 50 v.% reinforcement produced with irregular (Irr-Ti) at 50 bar.

To better understand the nature of the formed tribofilm, EDX mapping was performed on the disc surface (Fig. 234). This reveals the presence of the typical elements associated with ZDDP decomposition products - namely Zn, P, S, and O. No iron is detected within the wear track. It is well known that ZDDP initially reacts with the substrate to form metal sulfides [7]. Therefore, the observed tribofilm could result either from an initial reaction with the titanium-based substrate or from the interaction with wear particles originating from the steel ball. Since iron is not detected, it can be assumed that either a very thin, undetectable layer of iron sulfide formed at the interface, or that ZDDP effectively reacted with the titanium surface instead. We can also see that TiO_x particles do not seem to react with ZDDP as Zn, P and S elements are not detected in those areas.

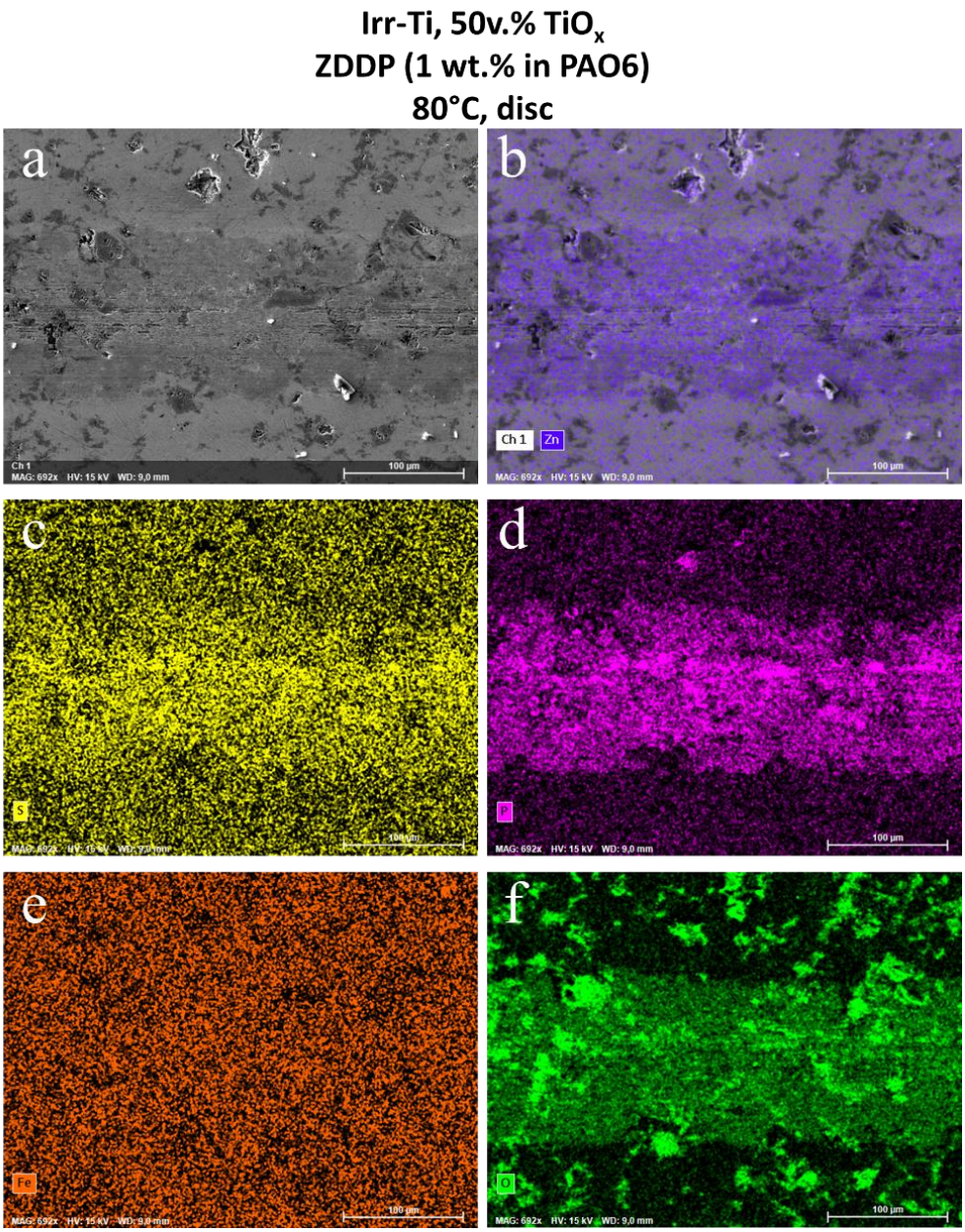

Fig. 234: SEM micrographs in SE (a) mode with EDX mapping (b, c, d, e and f) of a tribofilm formed on the composite-coated disc after testing with 1 wt.% ZDDP in PAO6 at 80 °C (purple = Zn; yellow = S; pink = P; orange = Fe; green = O).

High-magnification SEM observations (Fig. 235) show the coating morphology inside and outside the wear track, as well as on both the matrix and the reinforcement particles. A clear patchy-like tribofilm is visible on the matrix within the wear track, while it is absent outside of it. Notably, no tribofilm formation is observed on the reinforcement particles, either inside or outside of the track, suggesting that ZDDP does not react with metal oxides, which could explain this selective coverage.

In the case of composite coatings studied by L. Aubanel (2022) [3], a tribofilm was observed over the entire surface, first forming on the reinforcements with a small thickness, and then on the matrix with a larger thickness. The difference between Aubanel's results and ours can be attributed to the chemical nature of the reinforcement: metallic in Aubanel's study, whereas it is ceramic (TiO_x) in our case.

In Aubanel's system, both the matrix and the reinforcement were steels - one harder and one softer - showing the typical reactivity of ferrous materials toward ZDDP, which readily forms tribofilms on such metallic surfaces. In contrast, our system combines metallic titanium, which appears to react favorably, with titanium oxide, a chemically inert ceramic, for which tribofilm formation is much less likely.

As shown by Ueda et al. (2020) [8], while tribofilm formation on ceramic materials is possible, it strongly depends on their chemical nature and often results in poor adhesion to the substrate. It is therefore not surprising that no tribofilm was detected on the oxide regions in our samples.

If we consider Pearson's Hard and Soft Acids and Bases (HSAB) theory [9], chemical interactions between species can be rationalized based on their relative hardness or softness. In this framework, hard acids (small, highly charged, and weakly polarizable cations) preferentially interact with hard bases (small, highly electronegative, and weakly polarizable anions), while soft acids and soft bases tend to associate with each other through more covalent interactions.

The phosphate anion (PO_4^{3-}), derived from ZDDP decomposition, is considered a hard base and thus reacts preferentially with hard acids, such as Fe^{3+} - as demonstrated for iron oxides [10]. Following the same principle, a preferential reaction can also occur with Ti^{4+}, which is likewise classified as a hard acid. This could explain why a tribofilm readily forms on metallic titanium, which, in practice, is covered by a thin, native oxide layer (amorphous TiO_2) that still allows such acid-base interactions at the interface.

In contrast, for TiO_x coatings, the situation may differ. Either a very thin tribofilm formed - similar to what was reported by L. Aubanel (2022) with his steel reinforcement - and thus remained undetectable in SEM observations, or the Magnéli-type TiO_x phase present in the coating possesses less available Ti^{4+} sites, which would reduce its reactivity toward phosphate species and consequently limit tribofilm formation.

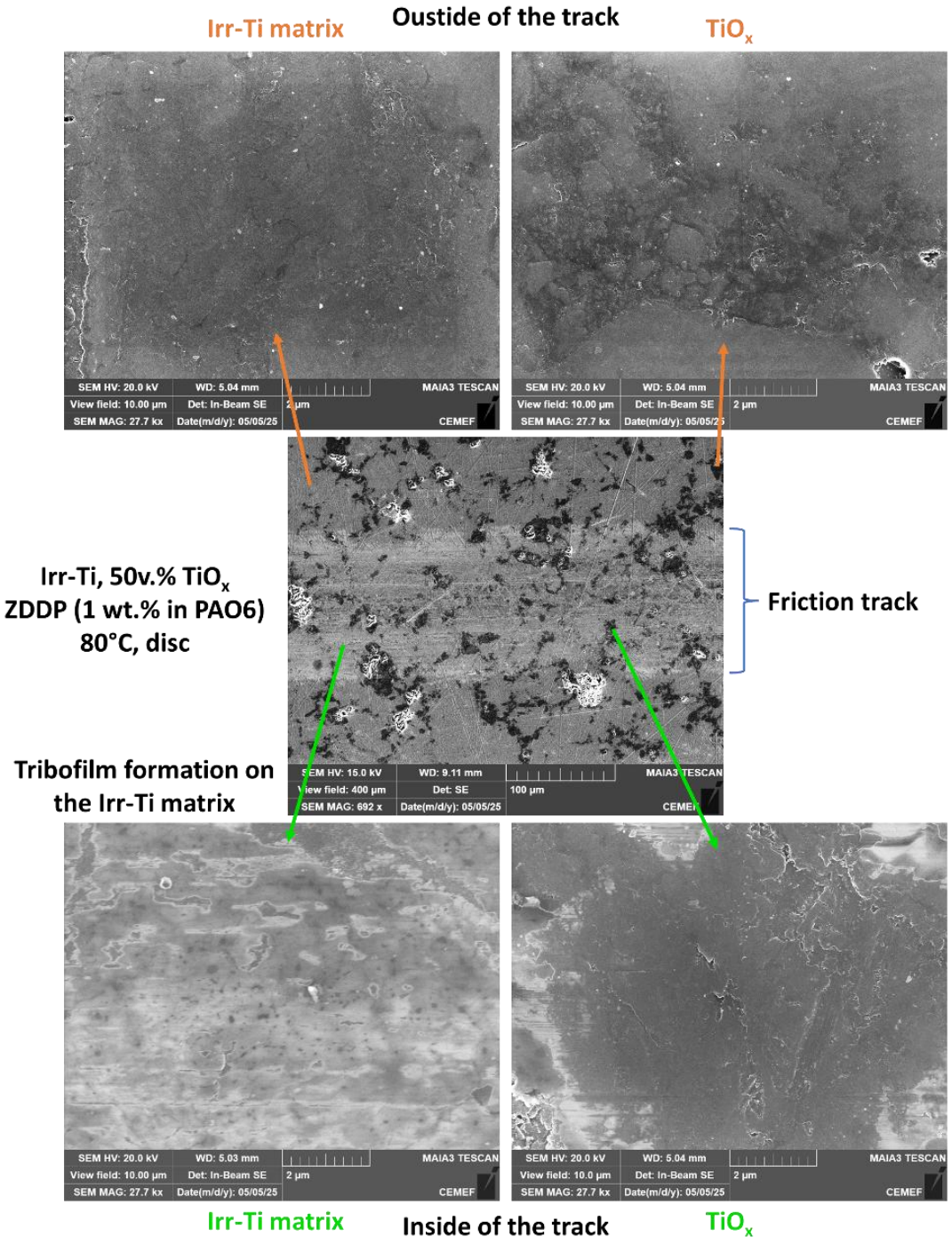

*Fig. 235: High-magnification SEM micrographs showing close ups inside and **outside the wear track** formed on the composite coating surface after testing with 1 wt.% ZDDP in PAO6 at 80 °C.*

An EDX mapping was also carried out on the steel ball (Fig. 236), revealing once again a tribofilm rich in Zn, P, S, and O. Similarly to the disc, which shows no evidence of iron transfer from the ball, the ball surface itself contains no detectable titanium, indicating that no significant material transfer occurred between the two counterparts during the test.

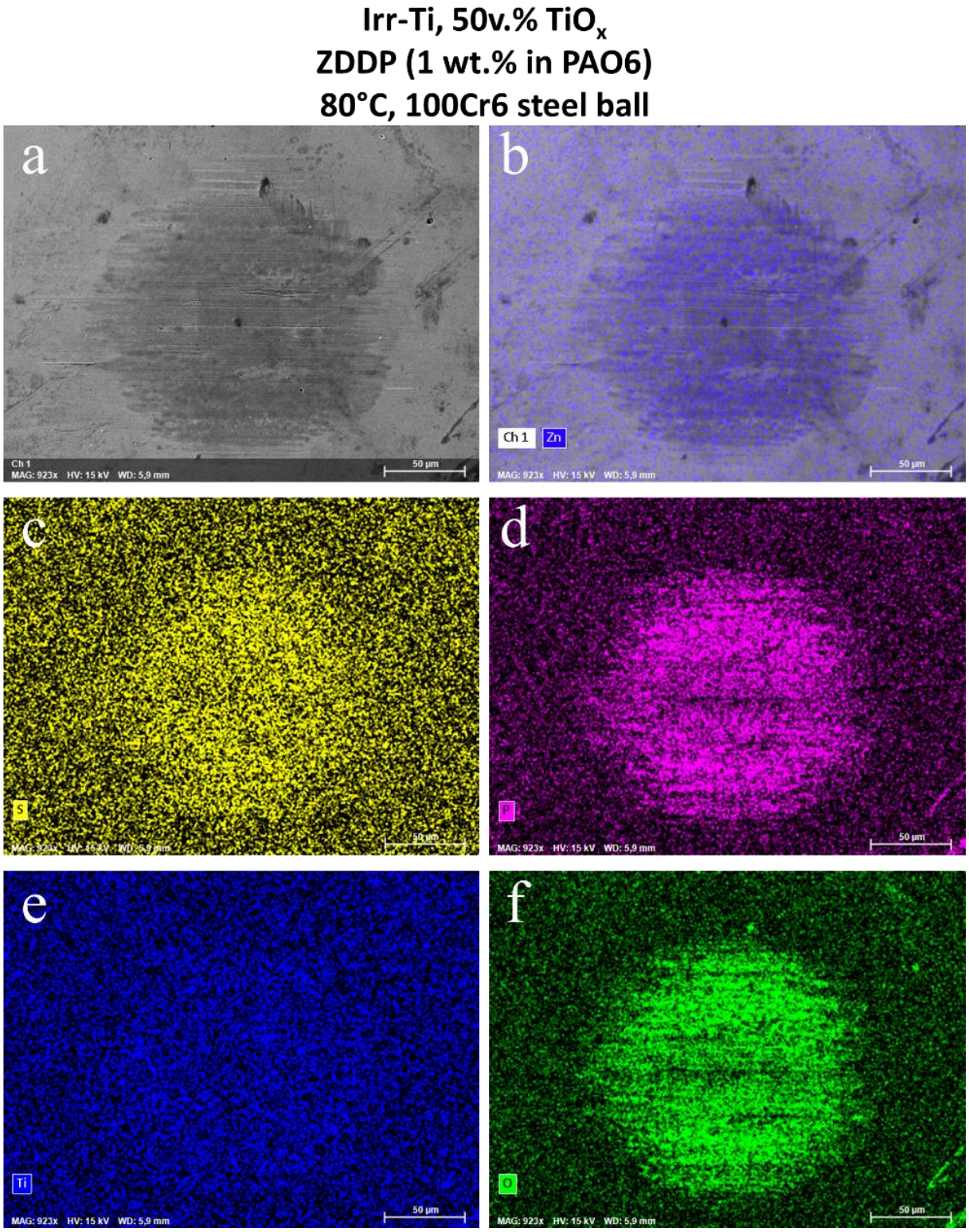

Fig. 236: SEM micrographs in SE (a) mode with EDX mapping (b, c, d, e and f) of a tribofilm formed on the 100Cr6 ball after testing with 1 wt.% ZDDP in PAO6 at 80 °C (purple = Zn; yellow = S; pink = P; orange = Fe; green = O).

The results obtained demonstrate that ZDDP can effectively form a protective tribofilm on the titanium-based composite coating, even though the chemical environment differs significantly from conventional steel-steel contacts. The tribofilm formed under these conditions is rich in Zn, P, S, and O, confirming the typical decomposition pathway of ZDDP additives.

The film appears on the metallic titanium matrix, while it seems to be absent on the TiO_x reinforcement particles, suggesting that ZDDP preferentially reacts with metallic titanium rather than titanium oxides.

As a result, the matrix is protected by the ZDDP-derived tribofilm, which prevents the adhesive phenomena typically associated with metallic titanium, while the ceramic reinforcement remains unaffected by wear thanks to its intrinsically high hardness. Together, these two effects ensure stable friction and minimal damage under lubricated contact.

After examining the behavior of the composite coating in the presence of an anti-wear additive such as ZDDP, the next step is to investigate its performance with a friction modifier, here MoDTC, under similar testing conditions.

4.2.2.2.3 Tribological properties of composite Cold spray coating lubricated with MoDTC additive

The friction behavior obtained with MoDTC is shown in Fig. 237. A relatively low coefficient of friction is already achieved at 25 °C, stabilizing around 0.085. At 80 °C, the friction decreases further and stabilizes near 0.065. This indicates that MoDTC successfully reacts on the composite coating surface, likely forming MoS_2, with a more pronounced effect at higher temperature, as expected from this additive [11].

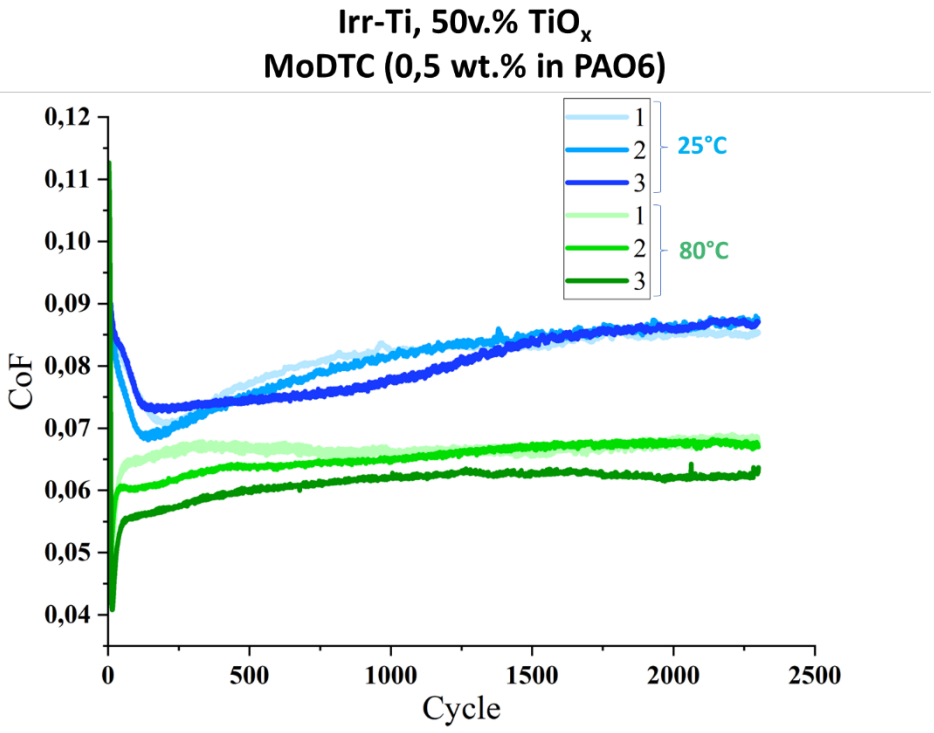

Fig. 237: Coefficient of friction (CoF) of reinforced coating (50 v.% of TiO_x) produced with irregular (Irr-Ti) particles at 50 bar. Tests conducted with a 0.5 wt.% MoDTC solution at 25°C and 80°C.

Optical observations at 25 °C (Fig. 238) once again show barely visible wear tracks, with an average width of about 135 µm on the discs and a wear scar diameter of about 150 µm on the balls.

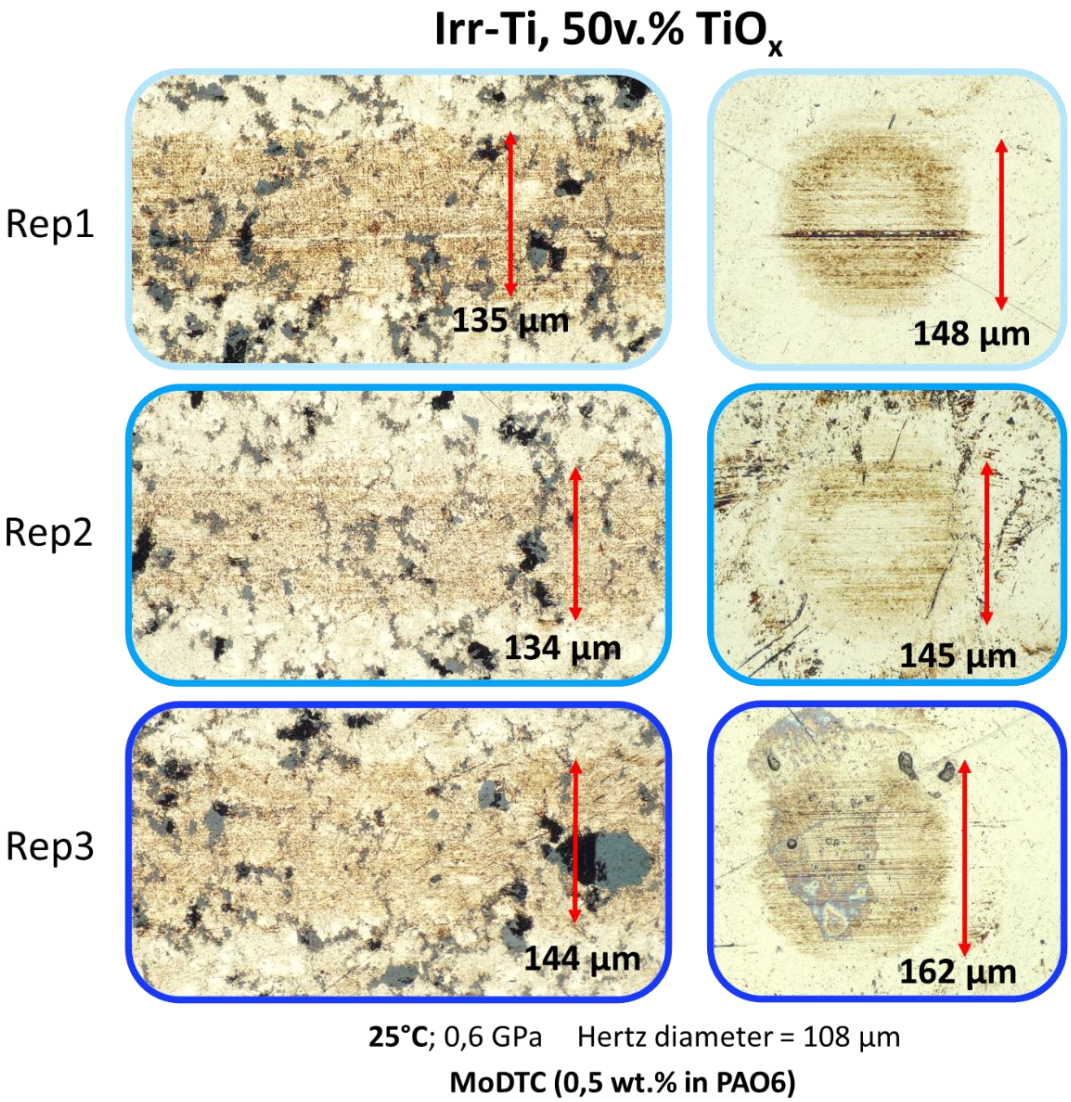

Fig. 238: Optical micrographs of wear tracks on the discs obtained after tribological tests on coatings with 50 v.% reinforcement produced with irregular (Irr-Ti) particles at 50 bar. Tests conducted with a 0.5 wt.% MoDTC solution at 25°C.

At 80 °C (Fig. 239), the friction tracks on the discs become even less visible, with a width of approximately 140 µm. In contrast, the tracks on the steel balls are more distinct and show a bluish coloration, suggesting the formation of a tribofilm. The wear scar diameter increases slightly to around 160 µm.

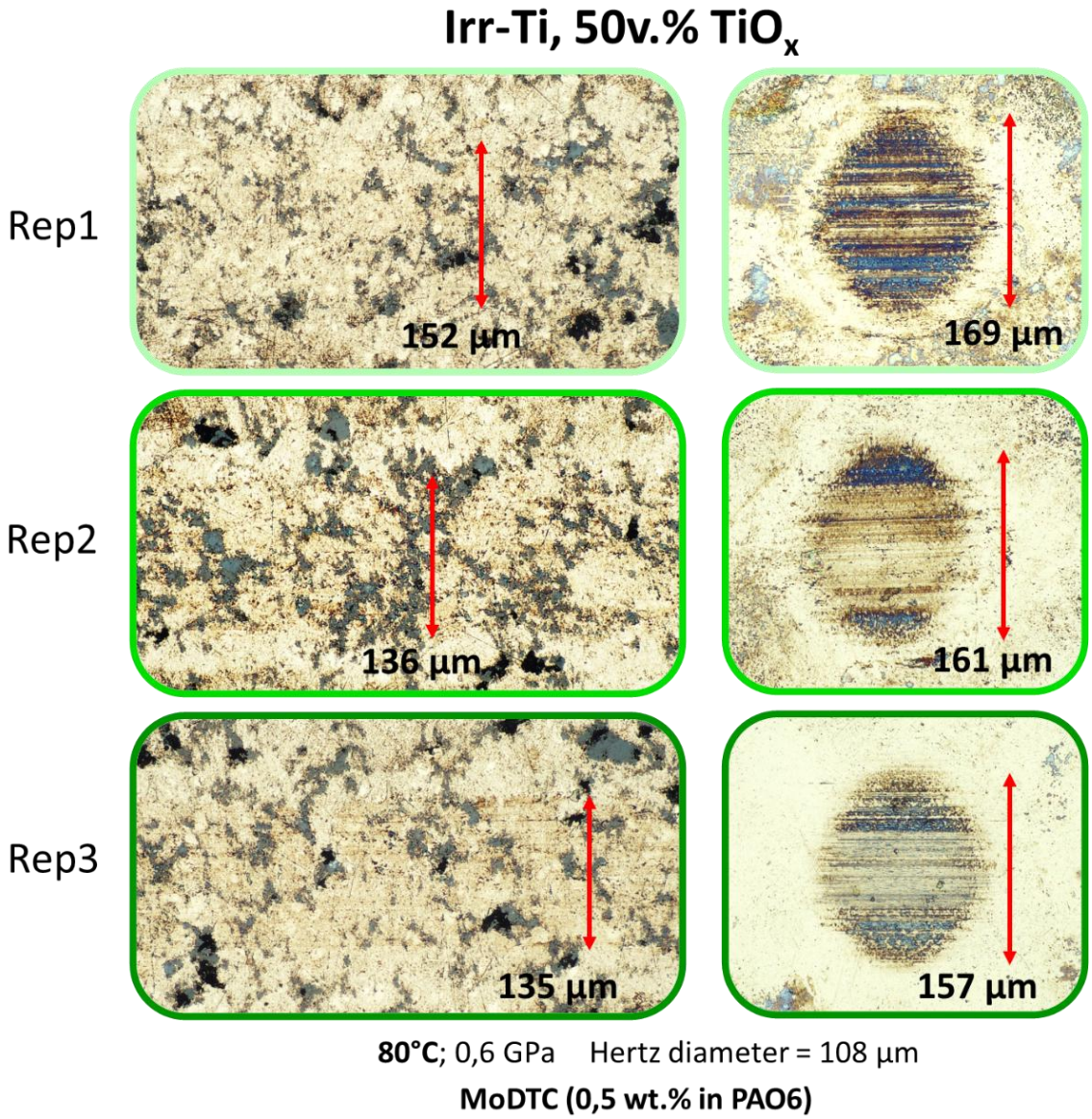

Fig. 239: Optical micrographs of wear tracks on the discs obtained after tribological tests on coatings with 50 v.% reinforcement produced with irregular (Irr-Ti) particles at 50 bar. Tests conducted with a 0.5 wt.% MoDTC solution at 80°C.

Profilometry measurements (Fig. 240) show that the wear tracks are barely distinguishable, especially at 25 °C. At 80 °C, a slight surface elevation is observed, which could correspond to the MoDTC-derived tribofilm, although this cannot be confirmed with certainty. Given that MoDTC tribofilms formed in steel-steel contacts typically have a thickness around 10 to 20 nm [12], their detection by profilometry is unlikely. Nevertheless, no signs of wear are observed at either temperature, which further confirms the protective nature of the additive.

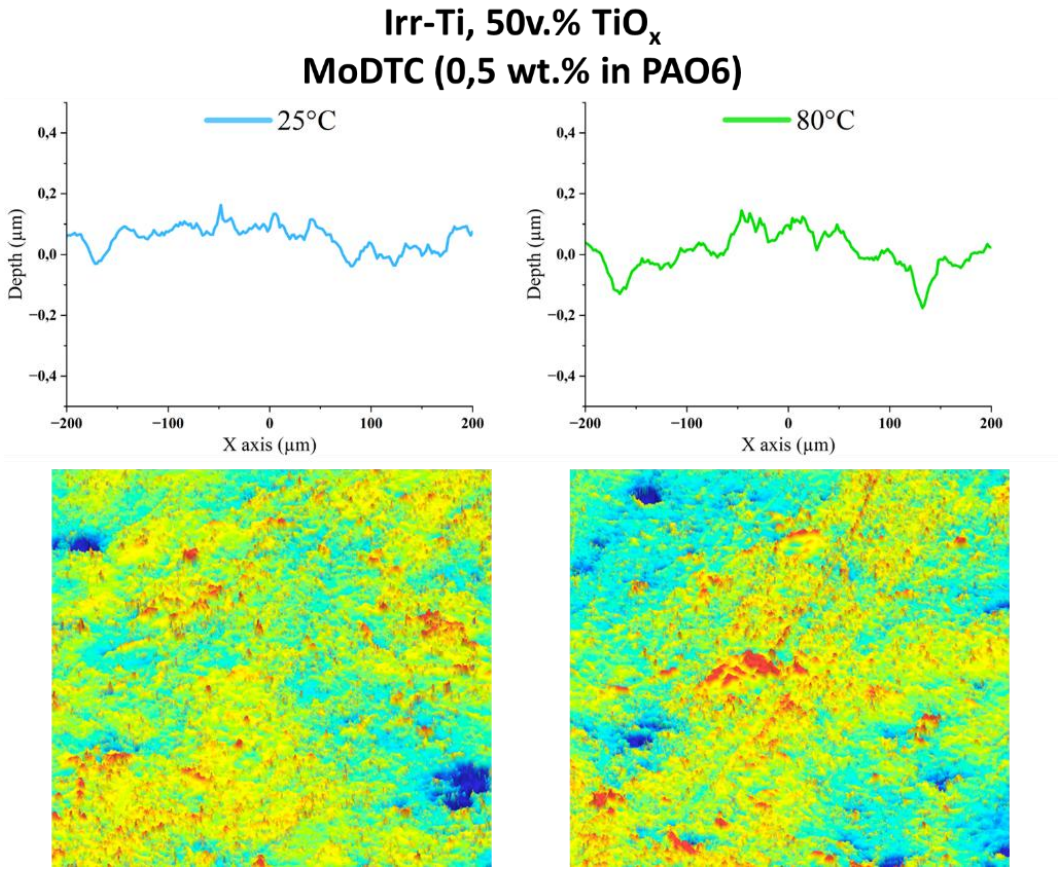

Fig. 240: Mean depth profiles and surface morphology of wear tracks formed on the discs at 25°C and 80°C with 0.5 wt.% MoDTC solution on coatings with 50 v.% reinforcement produced with irregular (Irr-Ti) at 50 bar.

To better characterize the formed tribofilm at 80°C, XPS analyses were carried out on the disc surface, both inside and outside the wear track. The Mo 3d spectrum reveals the presence of Mo-S bonds within the wear track, confirming the formation of MoS_2 nanosheets, consistent with the low CoF values measured. The Mo-S proportion is even higher than the one obtained with steel-steel contacts (60% vs 40%). In addition, oxidation products such as sulfates are also detected in the S 2p peak, like for steel-steel contact as shown in Chapter 3. Outside the wear track, no Mo-S species are detected; only oxides and oxysulfides are present, along with sulfates in the S 2p spectra.

Deshpande et al. (2017) [12] showed that a TiO_2 coating deposited by Atmospheric Plasma Spraying (APS) undergoes partial reduction during the process, leading to the formation of Magnéli phases.
These sub-stoichiometric oxides contain a higher concentration of reactive Ti^{3+} sites, which in turn facilitate the tribochemical decomposition of MoDTC into MoS_2.

This mechanism could explain both the low friction levels and the high MoS_2 conversion rate observed in our study.

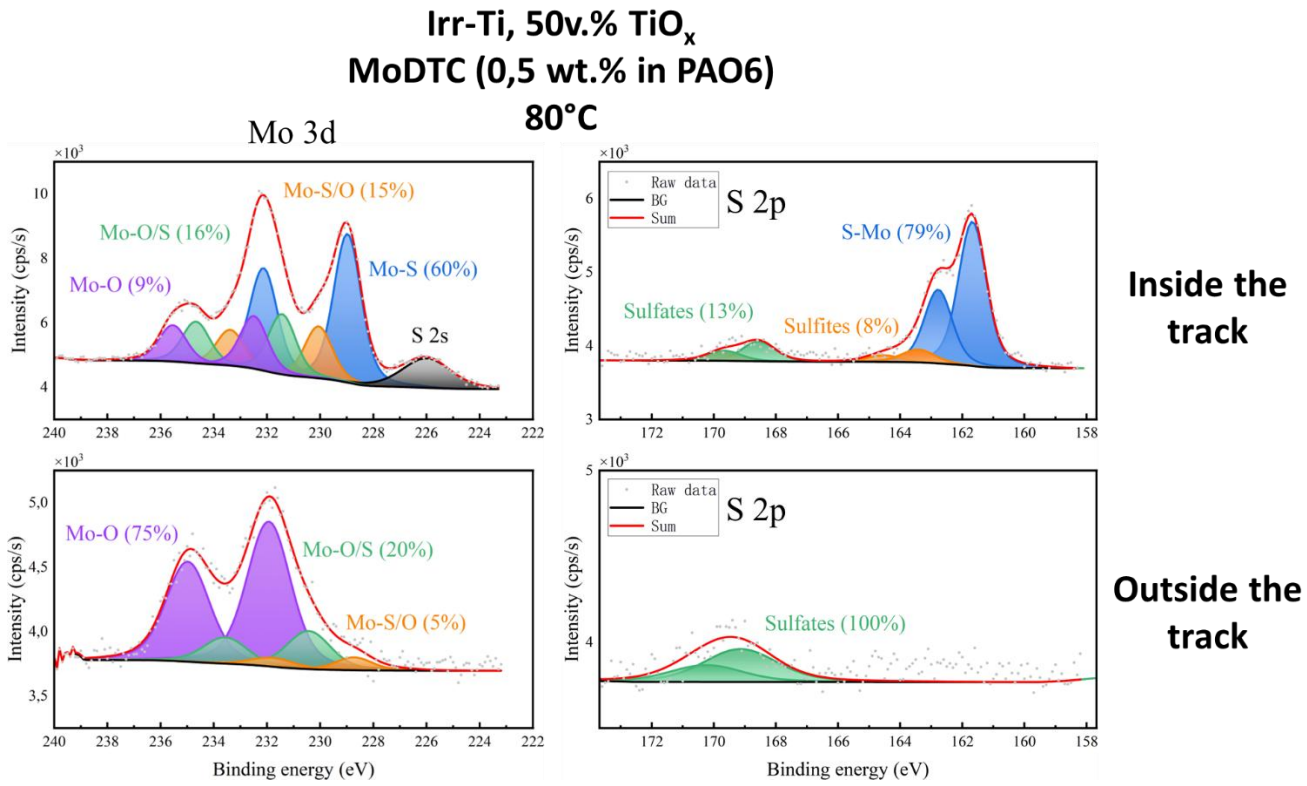

Fig. 241: Mo 3d and S 2p XPS spectra of tribofilm formed in presence of 0.5 wt.% MoDTC solution at 80°C on a coating with 50 v.% reinforcement produced with irregular (Irr-Ti) at 50 bar. Obtained with a NEXSA spectrometer.

These results demonstrate that MoDTC is effective in reducing friction on the Ti/TiO_x composite coating. Stable and low CoF values - 0.085 at 25 °C and 0.065 at 80 °C - indicate the successful formation of MoS_2 tribofilm, especially at elevated temperature, as confirmed by XPS analysis. Similarly to ZDDP, no chemical incompatibility with titanium is observed; on the contrary, MoDTC appears to interact favorably with the titanium surface, promoting the formation of a stable lubricating tribofilm.

Conclusion and Perspectives

This study provides a comprehensive understanding of the elaboration, optimization, and tribological behavior of titanium-based coatings produced by the cold spray process.

In the first part, the influence of deposition parameters and surface preparation on the substrate-coating adhesion is investigated. Increasing deposition pressure is shown to enhance both inter-particle cohesion and adhesion to the substrate, while surface preparation played a crucial role in reducing the required deposition pressure. Among the tested methods, water-jet preparation with a 150 g/min abrasive feed rate and a 90° impact angle provided the best balance between surface roughness and cleanliness, minimizing embedded abrasive particles and improving coating adhesion.

The second part focuses on composite cold spray coatings reinforced with TiO_x particles. The addition of reinforcement increases porosity due to TiO_x fragmentation, as expected from its ceramic nature, but doesn't hinder adhesion with the substrate and inter-particle cohesion. After optimization of deposition parameters, both Irr-Ti and Sph-Ti powders produce coatings with good cohesion, adhesion to the substrate, and low porosity, with slightly better results obtained using the spherical particles. However, preliminary tribological tests revealed that these spherical particles are more prone to adhesive wear than the irregular ones, likely due to their slightly lower hardness. This led to the choice of Irr-Ti for the matrix of the optimized reinforced coating.

Finally, the tribological evaluation of the composite coating reveals the beneficial effects of lubricant additives on the composite coating's performance. Under lubricated conditions with fully formulated oil, the coating exhibited low and stable friction with no observable wear. When tested with individual additives, ZDDP forms a protective anti-wear tribofilm on the titanium matrix, effectively preventing adhesive interactions, while the ceramic reinforcement remained intact due to its high hardness.

When comparing the composite coating with the results obtained using TiO_2 nanoparticles combined with ZDDP (Chapter 3), a similar trend can be observed regarding the chemical reactivity between ZDDP and the ceramic phase. As a reminder, with the TiO_2 - ZDDP mixtures, a composite tribofilm was indeed formed; however, this film did not result from a direct chemical reaction between the two additives leading to a single, co-reacted layer. Instead, it was produced through the simultaneous deposition of TiO_2 nanoparticles and decomposition of ZDDP.

A comparable behavior is observed here with the TiO_x composite coating, where no tribofilm formation is detected on the TiO_x particles themselves. This observation suggests a lack of direct chemical reactivity between ZDDP-derived species and the TiO_x reinforcement, consistent with the behavior previously reported for TiO_2 nanoparticles. Another possibility is that a tribofilm is formed but it's not thick enough to be detected by SEM high magnification observations.

In the present case, the formation of MoS_2 nanosheets on TiO_x particles could not be directly demonstrated, but this mechanism remains plausible. A similar phenomenon was reported by Deshpande et al. (2017) [12], who observed the formation of MoS_2 layers by TEM cross-sectional analysis on steel samples coated with TiO_2 deposited by Atmospheric Plasma Spraying (APS). In his work, the TiO_2 coatings contained Magnéli phases (Ti_nO_{2n-1}), which form during the plasma spraying process due to partial reduction of TiO_2. These sub-stoichiometric oxides are more electrically conductive and contain a higher density of reactive Ti^{3+} sites, which can facilitate the tribochemical decomposition of MoDTC and the subsequent growth of MoS_2 at the interface.

This demonstrates the chemical compatibility of those tribological additives with this composite coating.

Overall, this work demonstrates that the combination of a well-optimized cold spray process and the appropriate lubricant chemistry can yield titanium-based composite coatings with good mechanical integrity and tribological performance.

The perspectives of this work are multiple.

From a process standpoint, narrowing the particle size distribution of the TiO_x reinforcement could help prevent particle fragmentation during deposition. A sieving step to remove the larger particles, which are more prone to fracture than smaller ones, should be considered to further improve coating homogeneity and mechanical integrity.

Comparative hardness measurements were performed to provide an indirect estimation of the coating-substrate adhesion. However, a quantitative evaluation based on standardized adhesion tests such as pull-off testing (ASTM C633) [13] or progressive load scratch testing (ASTM C1624) [14] would provide more reliable data on interfacial strength and failure mechanisms.

From a tribological perspective, further investigations should be conducted under electrified conditions to evaluate the coating's behavior when subjected to combined mechanical and electrical stresses. Such tests would assess the electrical influence on tribofilm formation, wear mechanisms, and overall coating durability - key factors for future applications in electrified drivetrains.

It would also be of interest to perform rolling-sliding tests in order to evaluate the resistance of the coating to surface fatigue.

Complementary surface analyses using localized XPS analysis will be performed directly on specific areas of the wear track, targeting either the titanium matrix or individual TiO_x reinforcement particles. This spatially resolved approach aims to confirm whether tribofilm formation occurs exclusively on the metallic matrix and not on the oxide reinforcement. Demonstrating that tribochemical reactions are confined to the titanium phase would provide strong evidence that the TiO_x particles remain chemically inert during sliding, thereby clarifying the respective roles of the matrix and reinforcement in the overall tribological behavior of the composite coating.

Together, these studies will strengthen the understanding of the electro-tribological response of Ti/TiO_x coatings and their potential for integration into high-performance mechanical components operating under electrically stressed environments.

Bibliography

[1] Geometrical product specifications (GPS) — Surface texture: Profile - ISO 21920-3:2021 n.d.

[2] Young Z, Qu M, Coday MM, Guo Q, Hojjatzadeh SMH, Escano LI, Fezzaa K, Chen L. Effects of Particle Size Distribution with Efficient Packing on Powder Flowability and Selective Laser Melting Process. Materials 2022;15:705. https://doi.org/10.3390/ma15030705.

[3] Aubanel L. Étude du comportement tribologique en régime lubrifié de revêtements cold spray composites à base d'acier. Université PSL, 2022.

[4] Wang Q, Spencer K, Birbilis N, Zhang M-X. The influence of ceramic particles on bond strength of cold spray composite coatings on AZ91 alloy substrate. Surface and Coatings Technology 2010;205:50–6. https://doi.org/10.1016/j.surfcoat.2010.06.008.

[5] Liu Y, Al-Shan M, Bailey R, Sun Y. Effect of Counterbody Material on the Boundary Lubrication Behavior of Commercially Pure Titanium in a Motor Oil. Lubricants 2024;12:439. https://doi.org/10.3390/lubricants12120439.

[6] Thermal spraying - Determination of tensile adhesive strength - ISO-14916-2017 n.d.

[7] Spikes H. Mechanisms of ZDDP—An Update. Tribol Lett 2025;73:38. https://doi.org/10.1007/s11249-025-01968-3.

[8] Ueda M, Kadiric A, Spikes H. ZDDP Tribofilm Formation on Non-Ferrous Surfaces. Tribology Online 2020;15:318–31. https://doi.org/10.2474/trol.15.318.

[9] Pearson RG. The HSAB Principle — more quantitative aspects. Inorganica Chimica Acta 1995;240:93–8. https://doi.org/10.1016/0020-1693(95)04648-8.

[10] Martin JM. Antiwear mechanisms of zinc dithiophosphate: a chemical hardness approach n.d.

[11] Khaemba DN, Neville A, Morina A. New insights on the decomposition mechanism of Molybdenum DialkyldiThioCarbamate (MoDTC): a Raman spectroscopic study. RSC Adv 2016;6:38637–46. https://doi.org/10.1039/C6RA00652C.

[12] Deshpande P. Interaction of MoDTC additive on TiO2 APS coating under mixed/boundary lubrication conditions: A tribocatalytic process. Thèse de Doctorat. L'Ecole centrale de Lyon, 2017.

[13] B08 Committee. Test Method for Adhesion or Cohesion Strength of Thermal Spray Coatings n.d. https://doi.org/10.1520/C0633-13R21.

[14] C28 Committee. Test Method for Adhesion Strength and Mechanical Failure Modes of Ceramic Coatings by Quantitative Single Point Scratch Testing n.d. https://doi.org/10.1520/C1624-22.

Chapter 5: Effects of Electric Current on the Tribological Performance of Boundary Additives

Résumé en français :

Ce dernier chapitre étudie l'influence du courant électrique sur les performances tribologiques de trois formulations contenant du ZDDP, des nanoparticules de TiO_2 fonctionnalisées silane, ou leur mélange. Deux configurations expérimentales ont été considérées. Dans la première, le courant est appliqué dès le début de l'essai, ce qui permet d'analyser son effet sur la formation du tribofilm. Dans la seconde, le courant est appliqué uniquement après l'établissement d'un tribofilm, afin d'évaluer sa stabilité et les mécanismes de dégradation induits par l'électrification.

Lorsque le courant est appliqué pendant la formation du tribofilm, chaque formulation présente un comportement distinct. Le ZDDP seul montre une formation de tribofilm perturbée : le frottement devient plus bruité, des débris s'accumulent dans le contact et une augmentation localisée de l'usure est constatée. À l'inverse, les nanoparticules de TiO_2 fonctionnalisées silane bénéficient de l'apport d'énergie du courant, qui favorise leur tribo-frittage et conduit à la formation d'un tribofilm plus dense et compact qu'en absence de courant. Cependant, l'usure du substrat reste bien plus importante que pour les essais sans courant avec la présence de rayures profondes le long de toute la trace. On observe également la génération de dépôts épais et de débris abrasifs, responsables d'une usure localisée de la surface. Avec le mélange ZDDP + nanoparticules de TiO_2 fonctionnalisées silane, le comportement se rapproche de celui du ZDDP, avec un tribofilm endommagé de manière localisée mais de façon plus prononcée que pour le ZDDP utilisé seul. Dans tous les cas, la formation de débris abrasifs épais sur la bille, qui viennent rayer la surface du disque, est constatée. Cette asymétrie est due au sens du courant imposé, la bille étant la cathode et le disque l'anode.

Lorsque le courant est appliqué sur un tribofilm déjà formé, on observe encore une fois la formation de dépôts épais sur la bille, qui viennent ensuite rayer l'anode et provoquer une usure accrue. L'origine de ces dépôts n'est pas entièrement déterminée. Ils pourraient être issus de l'accumulation de débris d'usure métalliques ou bien se former à la suite de la formation d'arcs électriques. Avec le ZDDP, ces dépôts sont très riches en soufre, suggérant que seules les premières étapes de la formation du tribofilm ont pu se dérouler sur les surfaces fraîchement exposées, sans progression vers la phase phosphate protectrice. Dans le cas des nanoparticules TiO_2-silane, les dépôts observés sont plus larges et plus épais : la forte réactivité des nanoparticules avec l'acier mis à nu conduit à la formation rapide d'un tribofilm épais, mais sans empêcher la production continue de nouveaux débris, générant un cycle d'usure amplifié.

Concernant la tenue des tribofilms formés, il est montré qu'avec le ZDDP, le tribofilm préalablement formé peut localement rompre sous l'effet du courant, exposant l'acier nu et entraînant une usure excessive du disque dans la zone rompue. Avec le mélange ZDDP + nanoparticules TiO_2-silane, le tribofilm reste globalement intact, mais le courant réussit néanmoins à circuler via les zones périphériques non protégées. Ces zones fraîchement mises à nu conduisent de nouveau à la formation d'un dépôt sur la bille, qui vient rayer l'anode et dégrader la surface du disque. Dans les deux cas, l'endommagement provient donc du même mécanisme central : la croissance d'un dépôt sur la cathode, qui agit ensuite comme un abrasif transporté dans le contact.

Un essai complémentaire a été réalisé en formant un tribofilm avec le mélange ZDDP + TiO_2-silane, puis en remplaçant le lubrifiant par de la PAO sans additifs avant d'appliquer le courant. Dans ces conditions, le tribofilm reste dans la plupart des cas intact, et le nombre ainsi que la taille des amas présents sur la bille sont fortement réduits. Ce résultat confirme que ces amas se forment vraisemblablement à partir de débris d'usure initialement générés dans le contact ou à la suite de phénomènes d'arcs électrique, puis qui grossissent par réactions successives avec les additifs encore présents dans le lubrifiant - un phénomène particulièrement amplifié par la capacité des nanoparticules fonctionnalisées à former rapidement des tribofilms épais.

In the previous chapters, two main strategies for surface protection under severe tribological conditions were studied: Chapter 3 examined the potential of TiO_2 nanoparticles to enhance the performances of addition of boundary additives and nanoparticles to lubricants, while Chapter 4 investigated the cooperativity between cold-spray composite coatings reinforced with titanium oxide and boundary additives.

The present study, however, does not address the effect of electrical current on these composite coatings. Before analyzing such complex systems, it was necessary to establish a reference framework by first examining how current affects lubricant additives in conventional steel-steel contacts. This step is essential, as the coatings themselves exhibited effective wear protection only when used in combination with additives such as ZDDP or MoDTC. The electrification of tribological contacts with composite coatings will therefore be investigated outside the scope of this thesis.

On this basis, the present chapter focuses on the effect of electrical current on the performance of boundary additives on steel-steel contacts. Particular attention is devoted to three systems: ZDDP, the global benchmark anti-wear additive, silane-functionalized TiO_2 nanoparticles, and their blend. As shown in Chapter 3, the hybrid ZDDP/NPs system exhibited excellent colloidal stability while maintaining the rapid formation of a protective tribofilm, which may help mitigate wear effects associated with electrification.

Tribological conditions for electrified tests are reminded in **Table *37*.**

Temperature	100°C
Normal load	5.5 N
Ball diameter	10 mm
Maximum Hertzian contact pressure	0.83 GPa
Hertz Diameter	112 µm
Test frequency	0.64 Hz
Stroke length	5 mm
Maximum linear speed	10 mm/s
Oil quantity	2 mL
Repetitions	3
CoF acquisition frequency	25 Hz
Current intensity	0.5 A in CC mode
Cathode (-)	Ball
Anode (+)	Disc
Voltage acquisition frequency	300 Hz

Table 37: Tribological conditions for electrified tests

Since tribofilm growth and stability are key factors for wear protection, the influence of current is investigated at two distinct stages. The first part of this chapter addresses the effect of electrical current on tribofilm formation, with a direct comparison between ZDDP / silane-functionalized TiO_2 nanoparticles systems. The second part focuses on the effect of current on an already established tribofilm, again comparing those systems to provide insight into the stability of these films under electrified contacts.

This structure is based on the experimental conditions (B and C) presented in Chapter 2 and reminded in **Table 38**.

Condition	Electric current	
	0 to 2300 cycles	2300 to 3450 cycles
A	0A	
B	0.5A	
C	0A	0.5A

Table 38: Tribological test methods for electrified test campaign.

Through this two-step approach, this chapter aims to distinguish between the effect of current during tribofilm nucleation and growth (condition B), and its influence on the durability of the protective film (condition C), while enabling a direct comparison between ZDDP and nanoparticle-enhanced systems.

5.1 Effect of Electrical Current on Tribofilm Formation

5.1.1 Effect of Current on ZDDP Tribofilm Formation

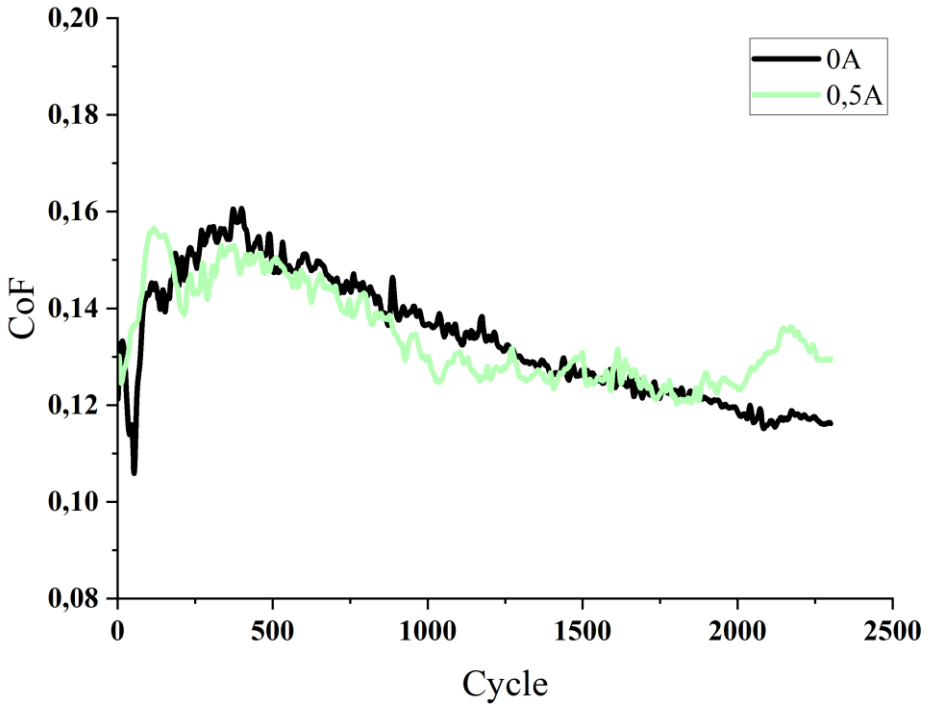

Fig. 242: Evolution of friction coefficient with cycles at 100°C for the sample containing ZDDP with an applied current of either 0A (reference) or 0.5A.

First off, it can be observed that applying a current of 0.5A during tribofilm formation does not necessarily lead to a significant increase in friction compared with the reference condition without current (Fig. 242). However, the coefficient of friction appears noisier, exhibiting more abrupt variations.

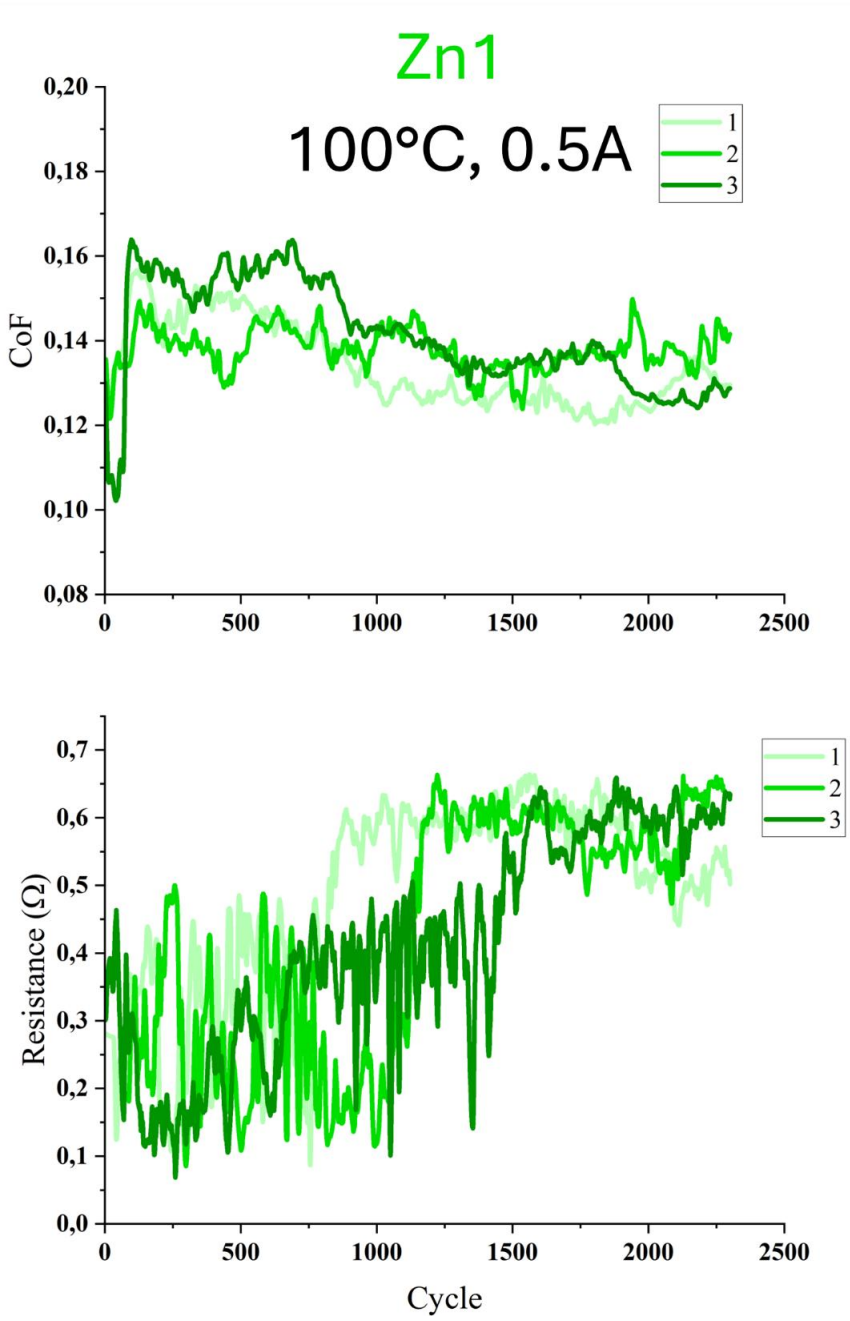

Fig. 243: Repeatability at 100°C for the sample containing ZDDP (Zn1) with an applied current of 0.5A. Top graph represents the evolution of friction coefficient and bottom part the evolution of contact resistance with cycles.

The three repetitions carried out under these conditions are presented in Fig. 243 and confirm these observations. The voltage was measured during the tests and divided by the applied current to obtain the evolution of the contact resistance. The same trend is observed for all three repetitions: an initial stage with low contact resistance (~0.1 to 0.4 Ω), likely corresponding to the induction period prior to the formation of an insulating tribofilm by ZDDP. A second stage follows, in which the resistance gradually increases and stabilizes at ~0.6 Ω, most probably coinciding with the development of the tribofilm. These increases in resistance occur between 500 and 1000 cycles, coinciding with the beginning of ZDDP tribofilm formation observed in Chapter 3. The contact does not become fully insulating, indicating that at least part of the track remains subject to metal-metal contact.

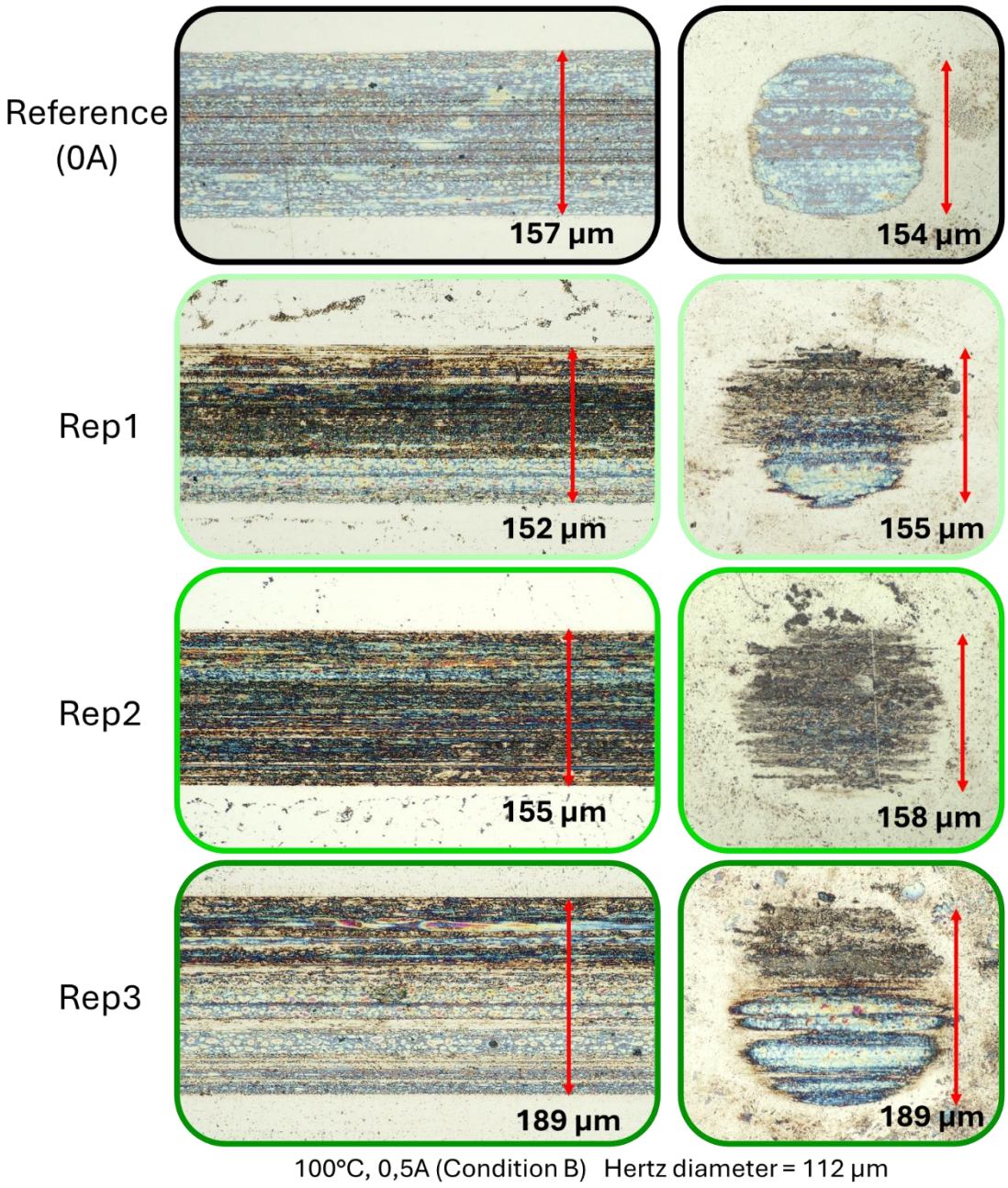

Fig. 244: Optical observations of wear tracks formed at 100°C on the discs and the balls under a 0.5A current for the sample containing ZDDP (Zn1). Three repetitions were carried out. Test at 0A is used as a reference.

This interpretation is supported by optical observations (Fig. 244), which reveal that under 0.5A applied current, dark regions appear that likely correspond to wear scars, while other areas display the characteristic appearance and bluish coloration of a ZDDP-derived tribofilm. These features are visible on both the disc and the ball.

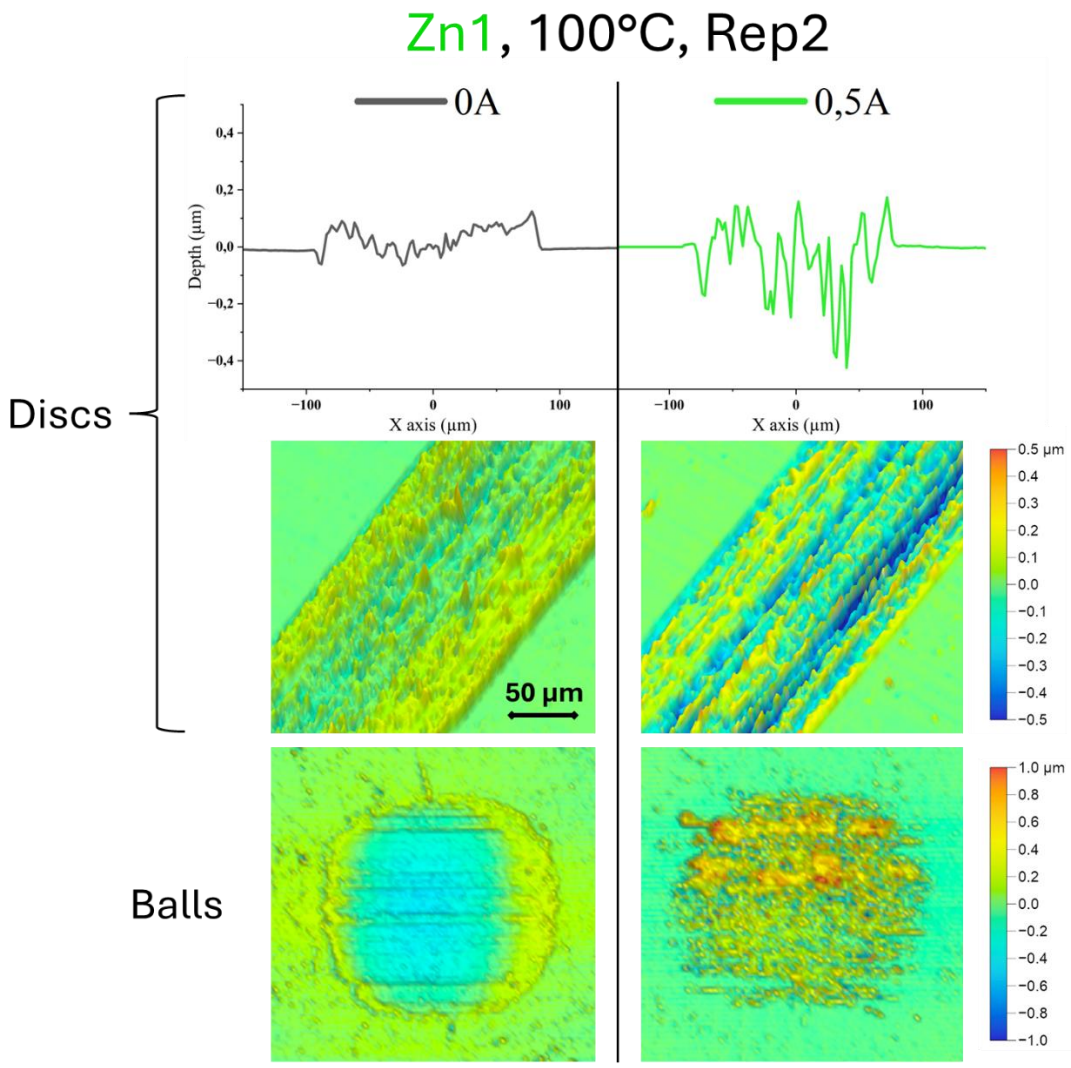

Fig. 245: Mean depth profiles and surface morphology of wear tracks formed at 100°C on the discs and the balls under a 0.5A current in the presence of solution containing ZDDP (Zn1). Test at 0A is used as a reference.

Profilometric measurements (Fig. 245) further confirm significant wear on the disc compared to the 0A reference condition. Additional measurements were also performed on the corresponding ball, after correcting its spherical geometry to a plane in order to better visualize the results. Without current, the ball already exhibits noticeable wear relative to the disc track. This is partly due to the slightly lower hardness of the balls compared with the discs (800 HV vs. 840 HV, respectively), but also to the nature of the test configuration, since the ball remains in constant contact with the same location, whereas the disc distributes wear over a 5 mm track length.

When a current of 0.5A is applied, a deposit up to 1 µm thick is formed. This phenomenon has already been reported in the literature for similar configurations (DC current). Steel wear debris particles appear to accumulate on the cathode - here, the ball - under the influence of the current [1]. This deposit is therefore most likely responsible for the severe wear observed on the disc.

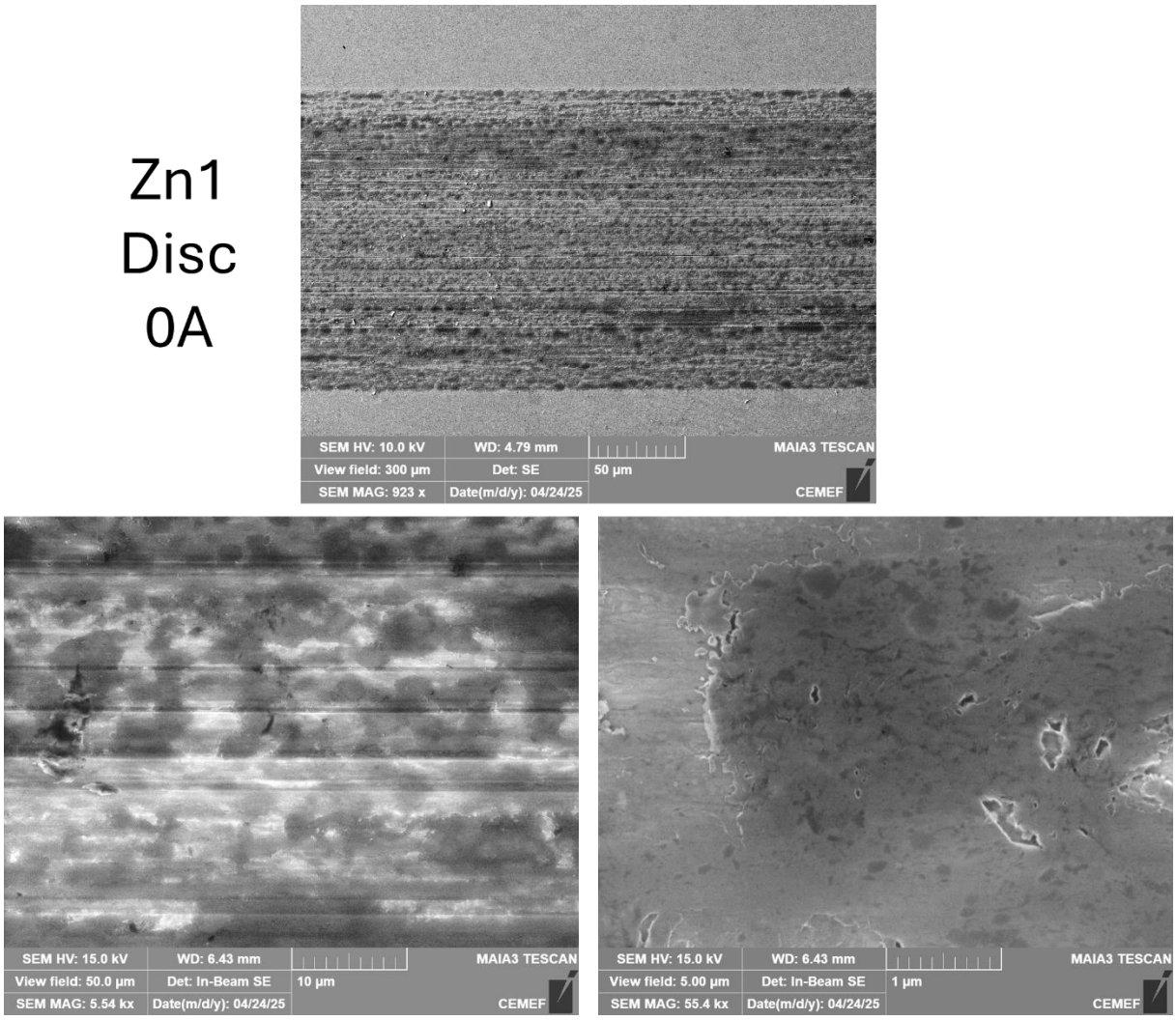

Fig. 246: High magnification SEM observations of a tribofilm formed on the disc at 100°C with no current exposure in the presence of Zn1 solution showing the formation of a patchy-like tribofilm.

SEM observations were also carried out. For the 0A reference condition (Fig. 246), the disc surface reveals a patchy-like tribofilm with some scratches but a relatively smooth morphology.

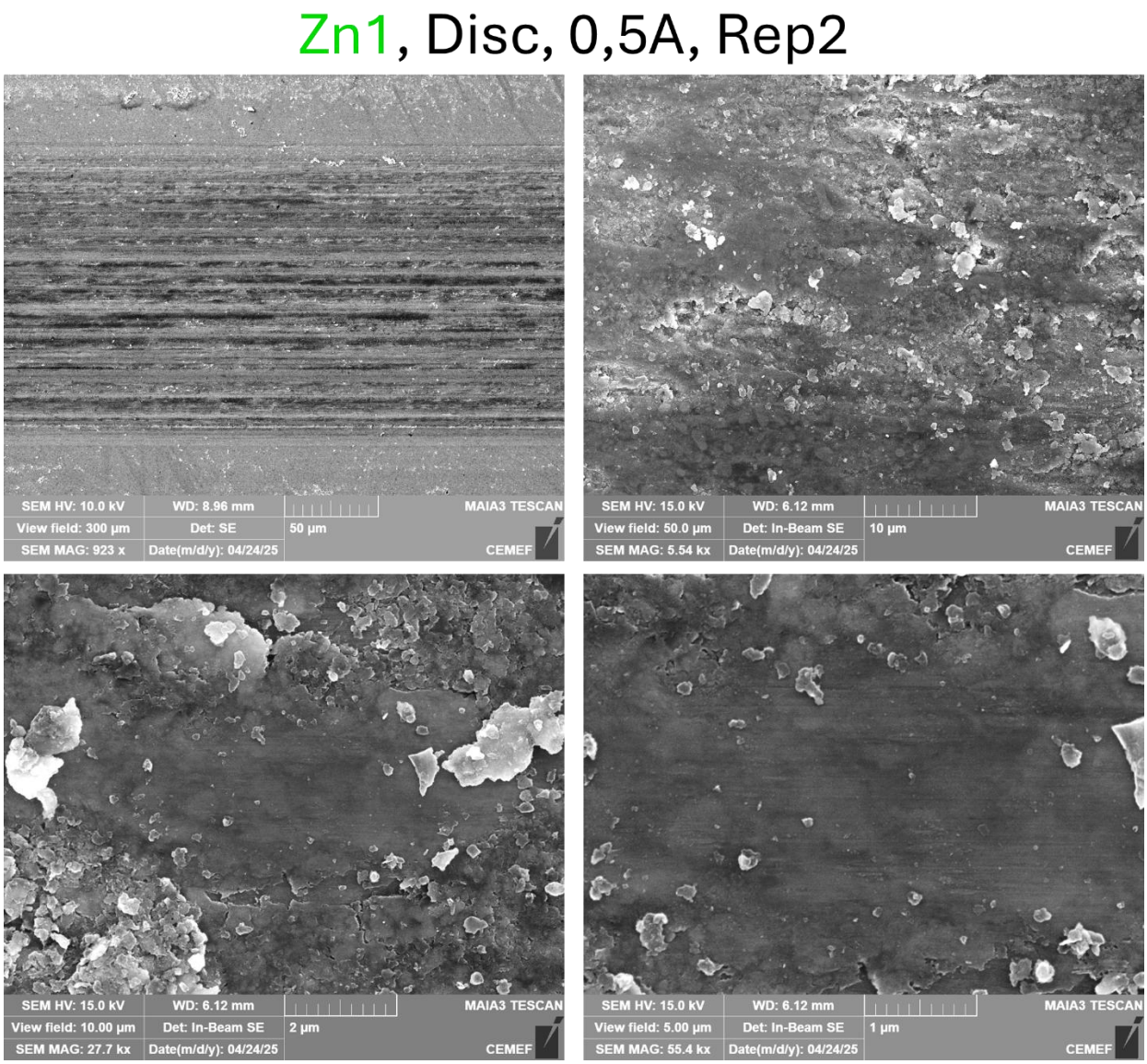

Fig. 247: High magnification SEM observations of a tribofilm formed on the disc at 100°C under a 0.5A current in the presence of Zn1 solution.

Under applied current (Fig. 247), however, the tribofilm morphology changes markedly. Smooth plateaus, which appear even thicker at higher magnification than at 0A, can be observed but are accompanied by a large amount of wear debris, which may account for the more unstable friction behavior.

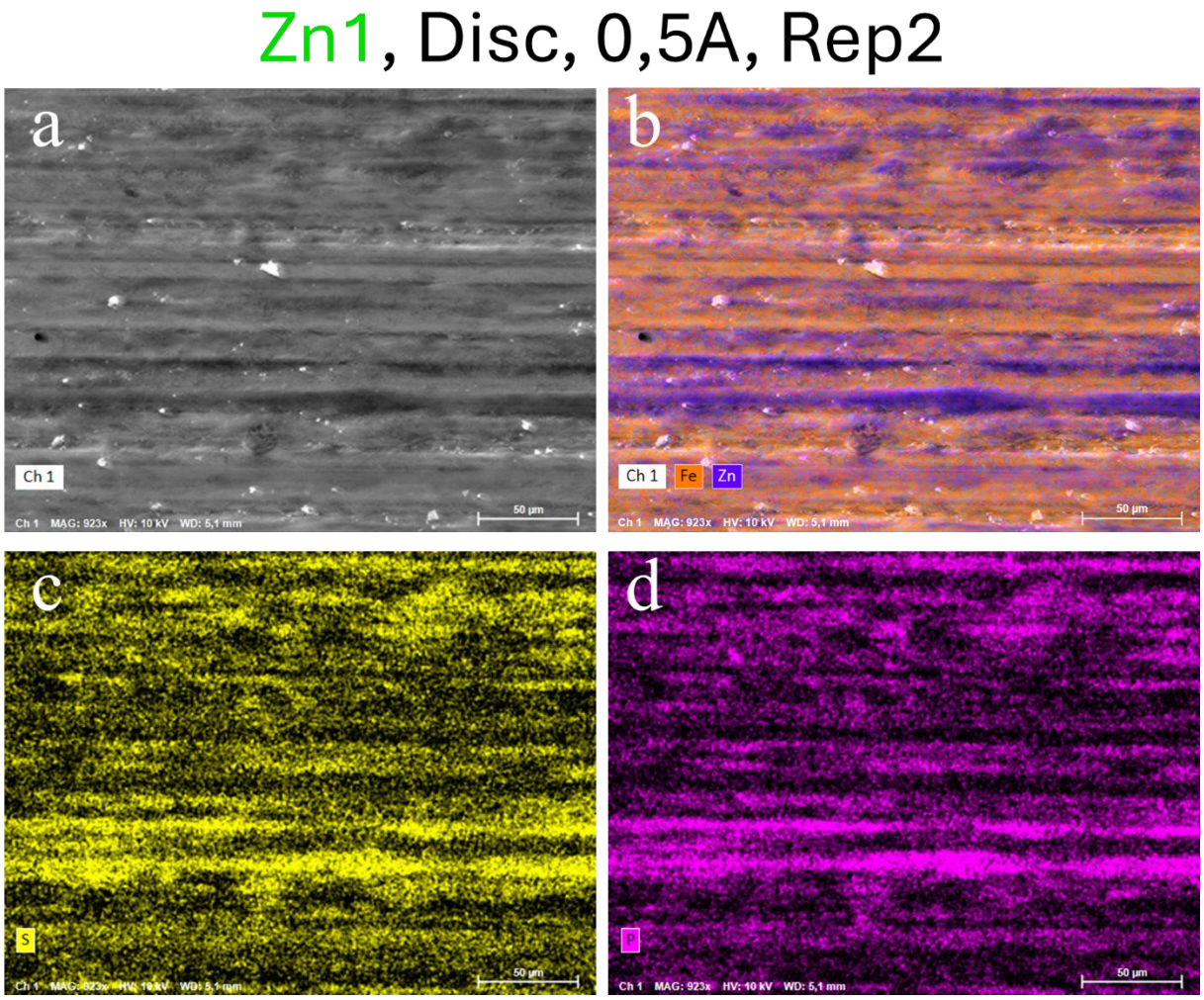

Fig. 248: SEM micrographs in SE (a) mode with EDX mapping (b, c and d) of a tribofilm formed on the disc at 100°C under a 0.5A current in the presence of Zn1 solution (orange = Fe; purple = Zn; yellow = S; pink = P).

EDX mapping (Fig. 248) confirms tribofilm formation through the detection of characteristic ZDDP-derived elements (Zn, P, and S). Nevertheless, the tribofilm does not appear to cover the entire wear track and seem to be more elongated in the sliding direction than with the reference condition at 0A.

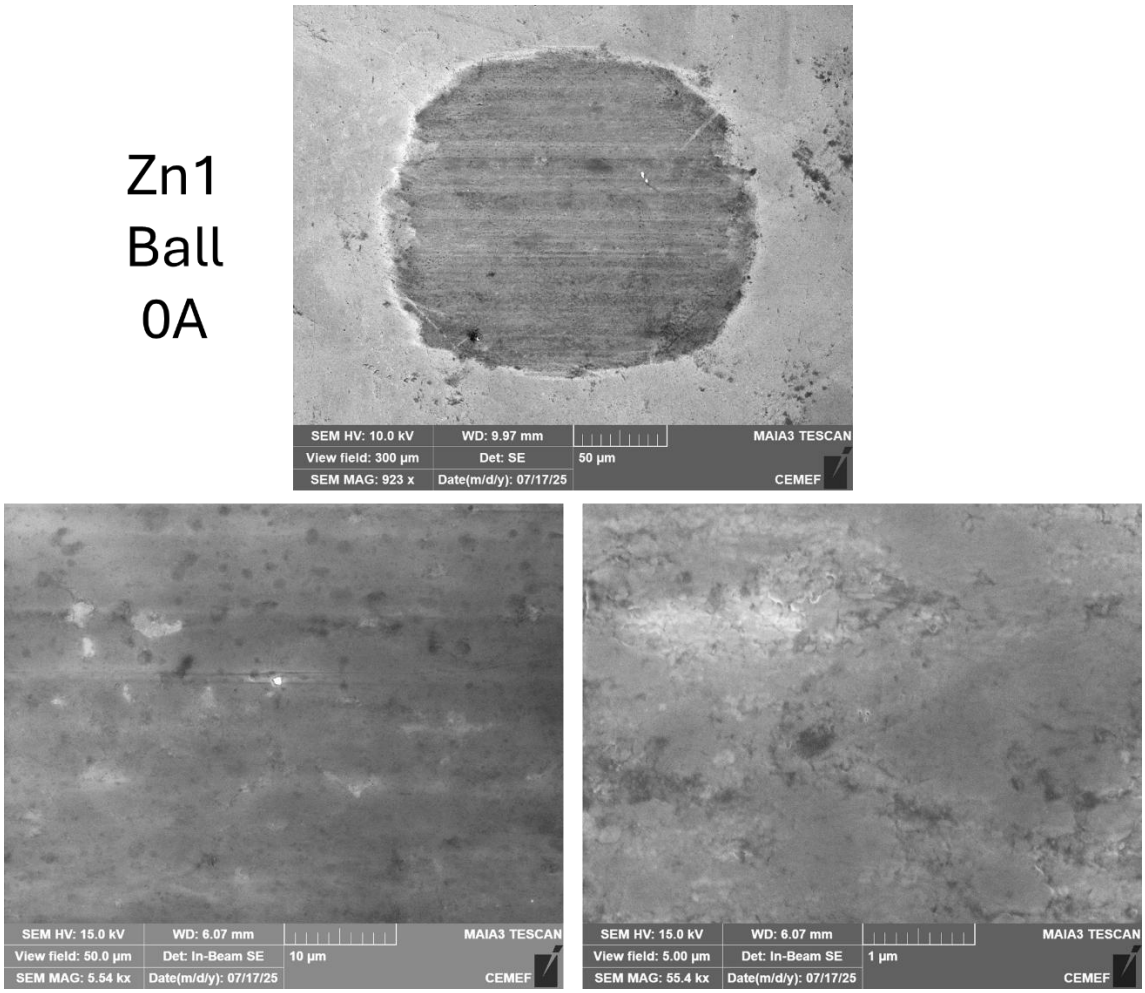

Fig. 249: High magnification SEM observations of a tribofilm formed on the ball at 100°C with no current exposure in the presence of Zn1 solution.

The wear scar on the ball was also examined. Without applying current (Fig. 249), a tribofilm forms in a manner similar than on the disc, but the patches are spatially closer, giving the impression of a nearly continuous film rather than a patchy-like coverage. This can be explained by the fact that the same surface of the ball remains in constant contact with the disc track, allowing more time for the tribofilm to develop.

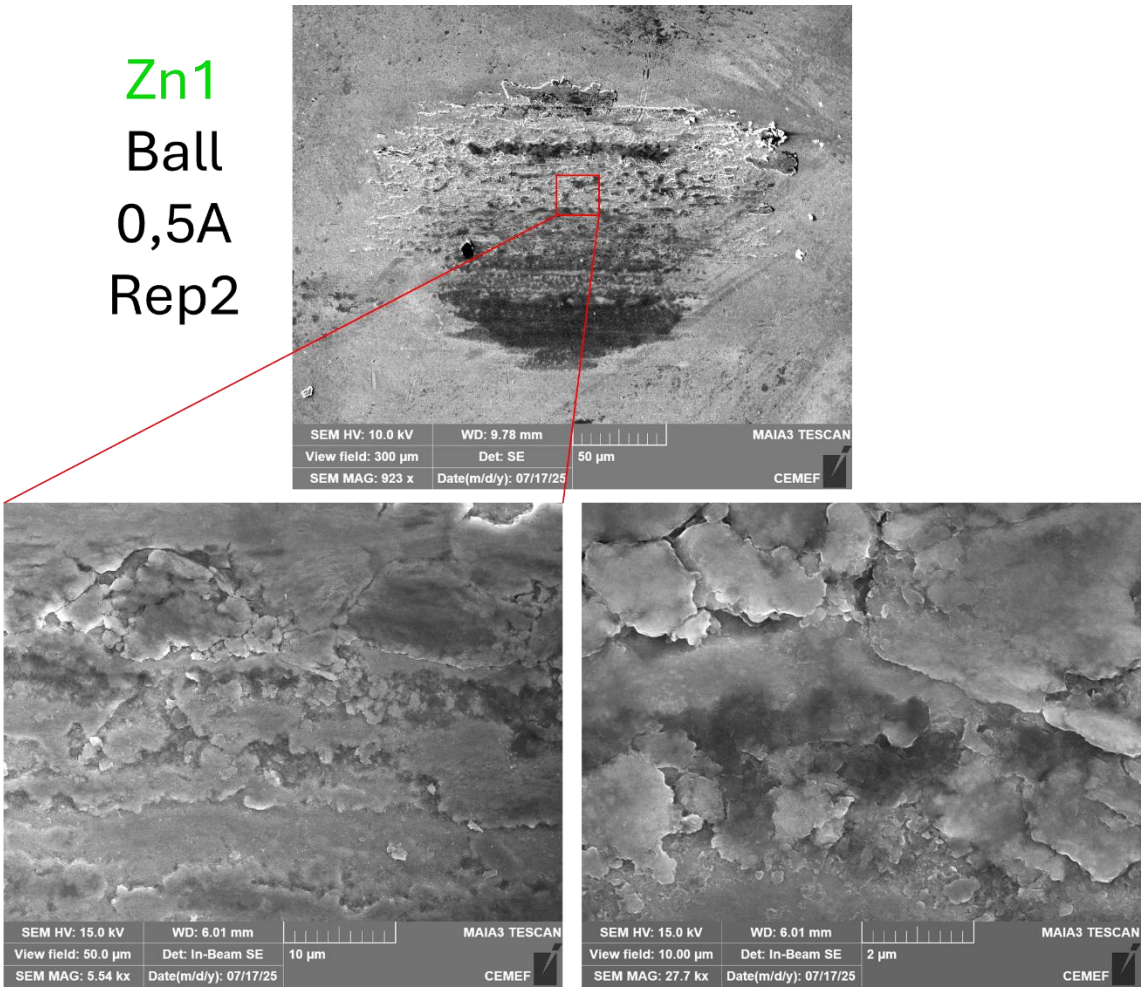

Fig. 250: High magnification SEM observations of a tribofilm formed on the ball at 100°C under a 0.5A current in the presence of Zn1 solution.

With the application of current (Fig. 250), a distinct contrast emerges between the lower and upper regions of the wear scar. The lower region displays a tribofilm similar to the current-free condition (Fig. 249), but with more wear debris. In contrast, the upper region (red square) appears brighter in SE mode and is more strongly affected by the current, with the formation of very thick plateaus stacked upon one another. These features likely result from the accumulation of wear particles that agglomerate and are subsequently compacted under the combined influence of electrical current and sliding.

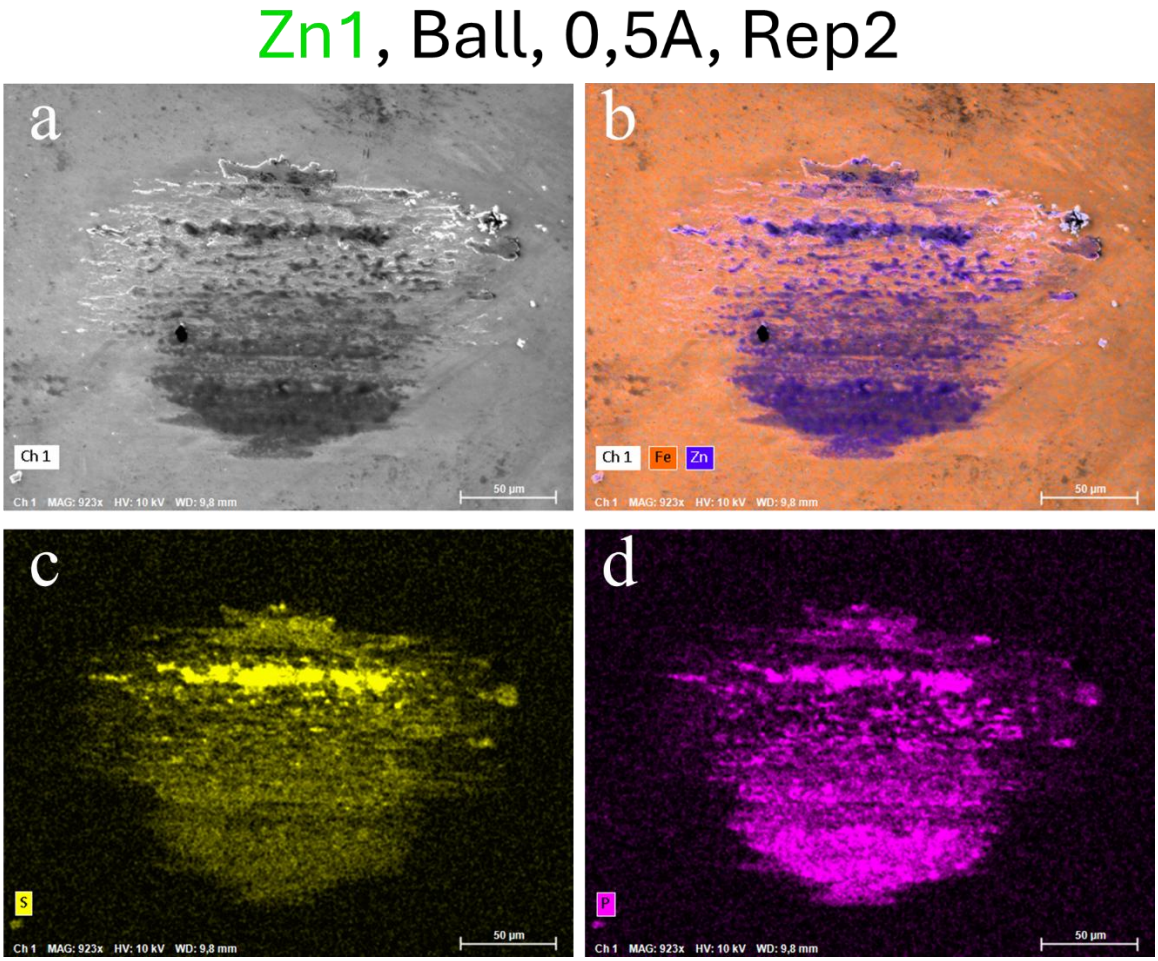

Fig. 251: SEM micrographs in SE (a) mode with EDX mapping (b, c and d) of a tribofilm formed on the ball at 100°C under a 0.5A current in the presence of Zn1 solution (orange = Fe; purple = Zn; yellow = S; pink = P).

EDX mapping (Fig. 251) reveals a zone in the upper part of the scar with a high sulfur concentration. A similar sulfur enrichment was observed at the cathode side by Z. Peng et al. (2025) [1] during tests at 2A with a fully formulated transmission lubricant containing 2 wt.% of ZDDP.

L. I. Farfan-Cabrera *et al.* (2025) [2] also realized EDX mappings on sample that underwent tribological testing with a 4-ball tribometer at 0A and 0.5A with a PAO4 + ZDDP (1 wt.%) solution. They also saw that Sulfur and Phosphorus are not present in the same areas.

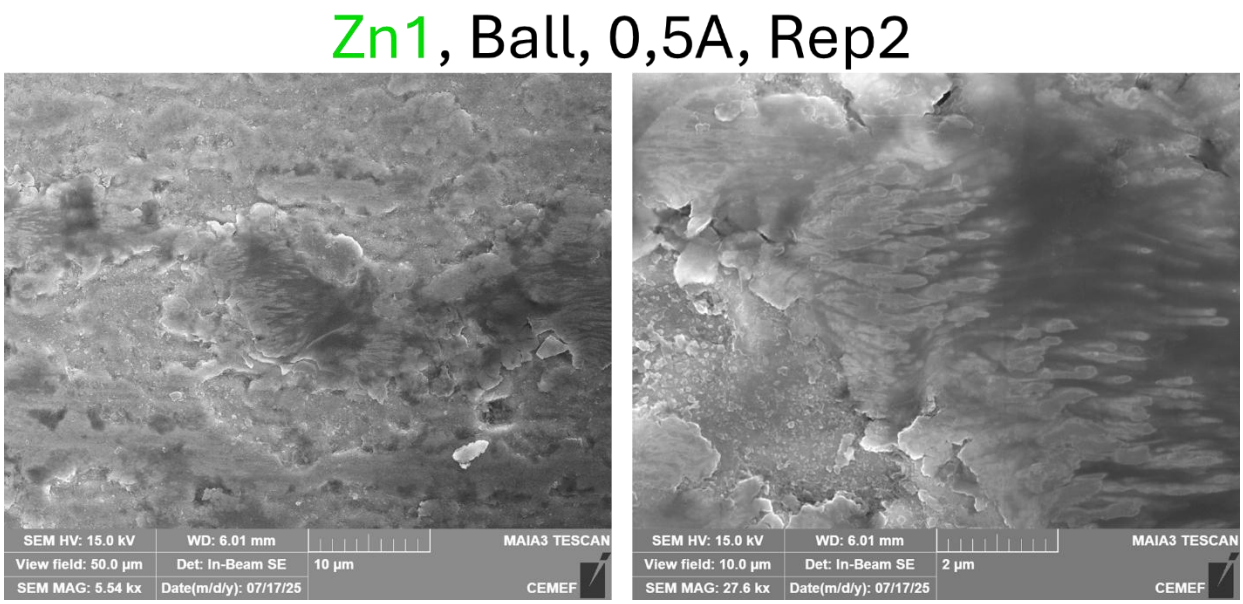

Fig. 252: High magnification SEM observations of a tribofilm formed on the ball at 100°C under a 0.5A current in the presence of Zn1 solution. Close-up on an asperity formed due to the application of current (sulfur rich area in Fig. 251).

A closer inspection of this sulfur-rich region (Fig. 252) shows the presence of very thick, smooth plateaus covered by a thin dark deposit. However, this deposit may correspond to cleaning solvent residues, which could have left carbon-rich residues upon evaporation.

at.%	Zn1 100°C	
	0A	**0,5A**
C 1s	**11,7**	**12,1**
Fe 2p	**1,8**	**8,6**
O 1s	**52,2**	**52,4**
P 2p	**14,8**	**13,0**
S 2p	**2,2**	**3,4**
Zn 2p	**17,0**	**9,2**
Ca 2p	**0,4**	**1,3**

Table 39: XPS chemical composition of tribofilms formed in the presence of a solution containing ZDDP (Zn1) with an applied current of either 0A or 0.5A. Conducted using a NEXSA spectrometer.

XPS analyses (**Table 39**) reveal a decrease in Zn content, from 17 at.% at 0A to 9.2 at.% at 0.5A, accompanied by an increase in Fe from 1.8 at.% to 8.6 at.%. Phosphorus also shows a slight decrease, whereas sulfur increases significantly, from 2.2 at.% without current to 3.8 at.% under 0.5A, which confirms previous EDX mapping observations.

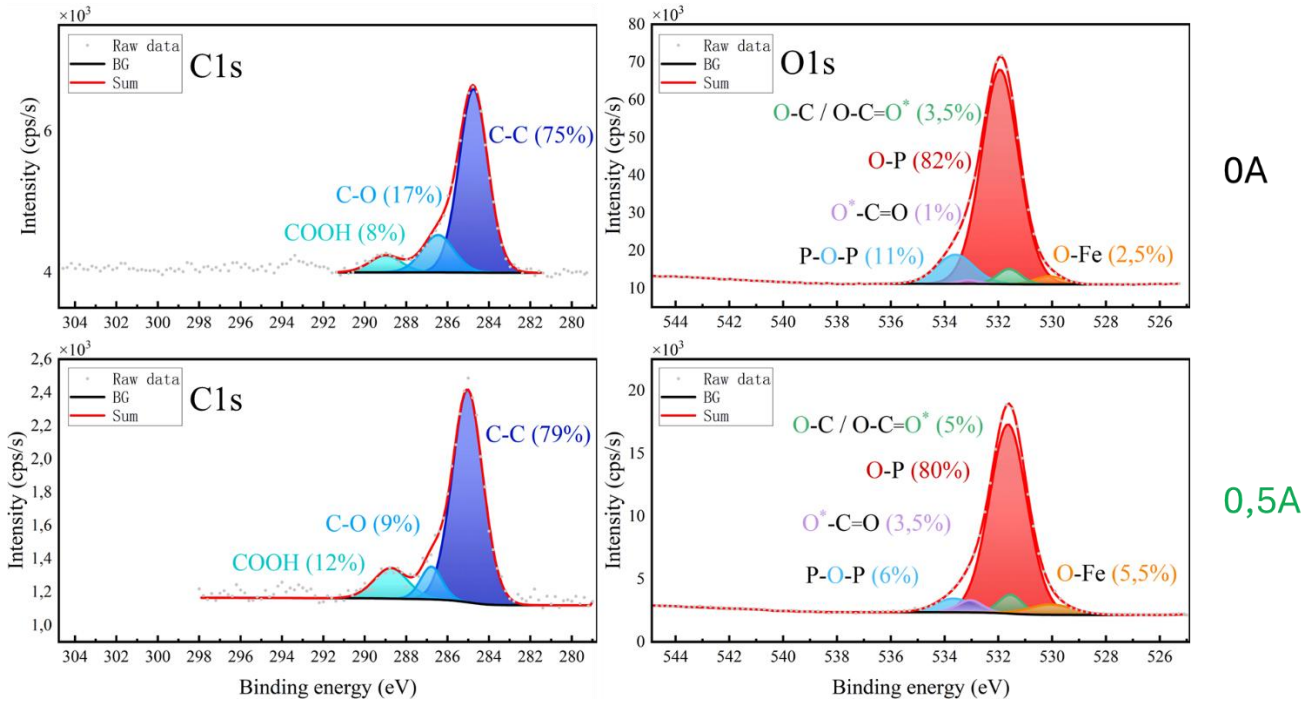

Fig. 253: C1s and O1s XPS spectra of tribofilms formed in presence of Zn1 solution with either a 0A or 0.5A applied current.

The carbon and oxygen spectra (Fig. 253) are broadly similar between the 0A and 0.5A conditions. A slight increase in iron oxide is detected, but this does not account for the full increase in Fe total concentration in electrified condition. It is likely that part of the Fe originates from metallic iron, associated with the significant generation of wear debris under electrified sliding, some of which subsequently oxidizes. Another portion of the Fe detected may correspond to the formation of iron sulfides (FeS_2), which could explain the higher sulfur content.

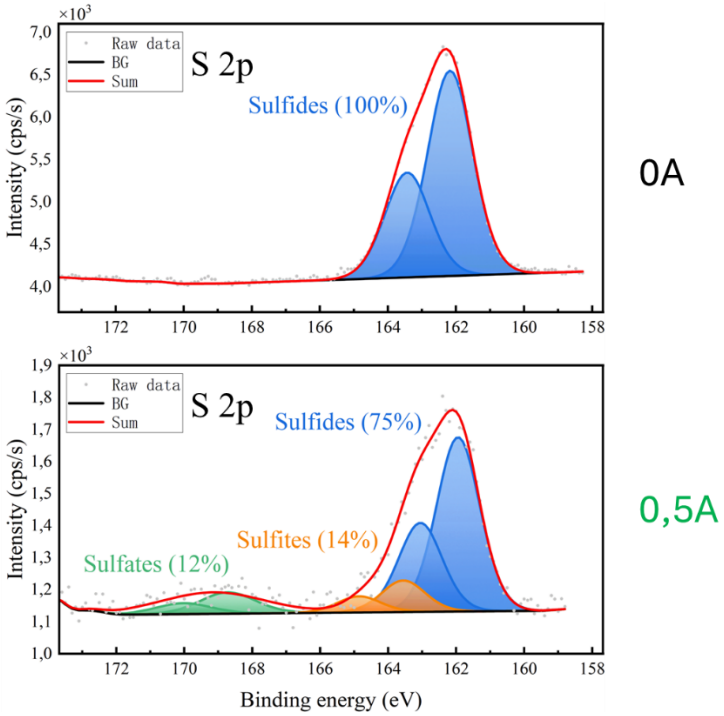

Fig. 254: S2p XPS spectrum of tribofilms formed in presence of Zn1 solution with either a 0A or 0.5A applied current.

Fig. 254 presents the sulfur (S2p) spectrum, showing that under applied current, oxidized sulfur species such as sulfites and sulfates are formed. However, distinguishing between zinc sulfide and iron sulfide remains challenging with this analysis technique.

In summary, the application of an electrical current during sliding significantly modifies the formation and characteristics of the ZDDP-derived tribofilm. While the tribofilm still develops, it appears less homogeneous and is accompanied by the accumulation of large amounts of wear debris. The current promotes the formation of thick plateaus on the ball surface, likely resulting from agglomerated and compacted steel wear particles, which correlates with the more unstable friction behavior observed. Chemical analyses confirm that the tribofilm formed under current is chemically altered: Zn and P contents decrease, while Fe and S increase, suggesting the incorporation of wear particles and the formation of iron oxides as well as oxidized sulfur species. This observation is consistent with results obtained by L. I. Farafan-Cabrera et al. (2025) [3] which showed that the use of an inert atmosphere during tribological testing prevents oxide formation and subsequent wear. A. Yousuf et al. (2025) [4] also observed similar results for ZDDP with the use of an inert gas but with a constant voltage setup. Overall, these results indicate that electrical current hinders the development of a continuous protective tribofilm and instead promotes heterogeneous layer growth and increased wear through metallic debris and oxides formation.

Having established the influence of electrical current on the formation of ZDDP-derived tribofilms, the next section examines whether similar effects are observed when using functionalized TiO_2 nanoparticles. In particular, the role of silane-modified TiO_2 nanoparticles in tribofilm development under electrified conditions will be investigated.

5.1.2 Effect of Current on Silane-functionalized TiO_2 Nanoparticles Tribofilm Formation

Fig. 255 compares the evolution of the CoF with and without current. In contrast to ZDDP, the application of current leads to a reduction and improved stability of the CoF, which remains around 0.15. Notably, no abrupt increases in friction are observed under 0.5A, unlike the current-free condition.

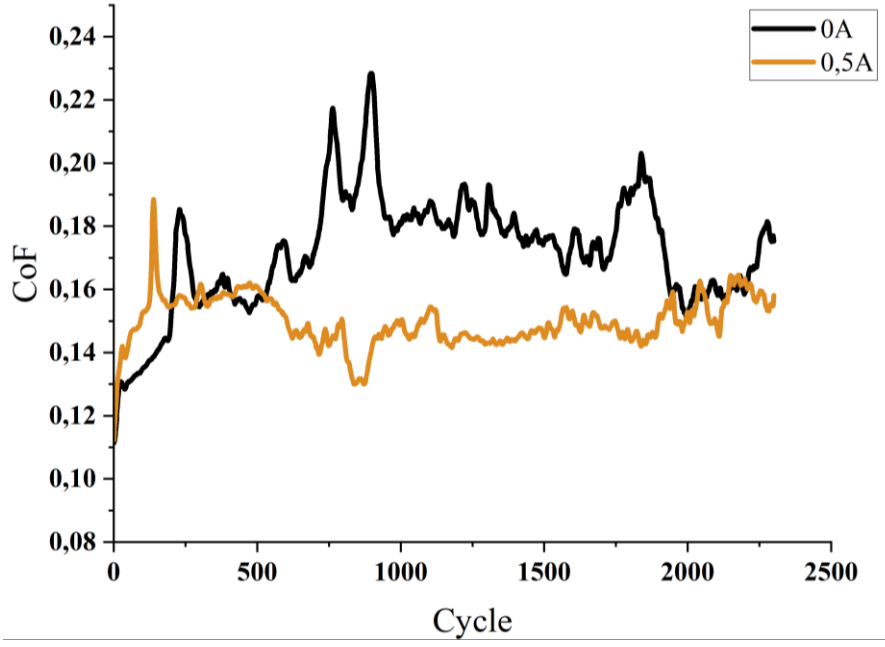

Fig. 255: Evolution of friction coefficient with cycles at 100°C for the sample containing silane-functionalized TiO_2 NPs (Tif(Si)1) with an applied current of either 0A (reference) or 0.5A.

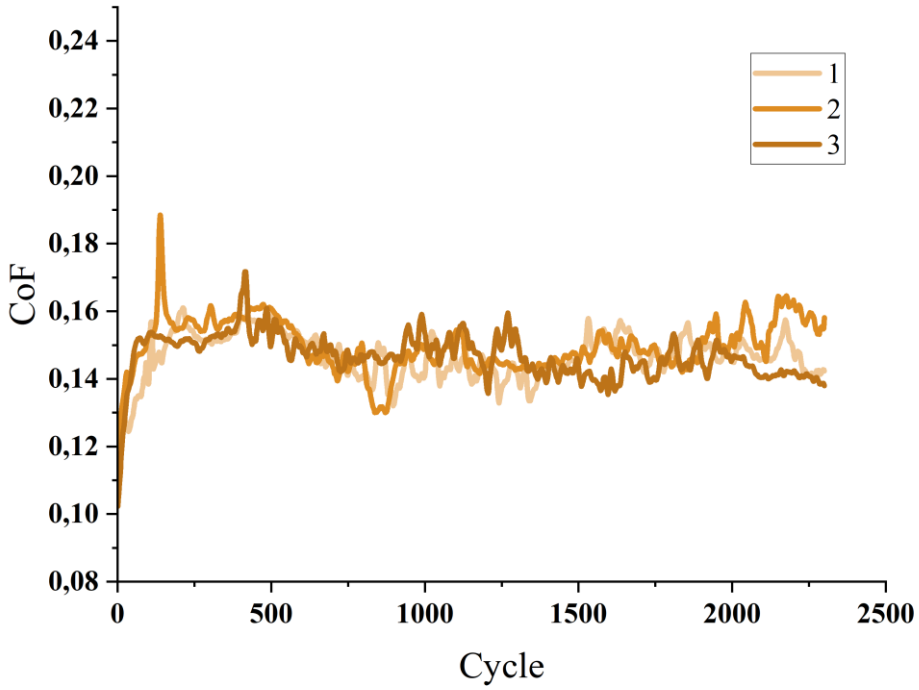

Fig. 256: CoF repeatability at 100°C for the sample containing silane-functionalized TiO_2 NPs (Tif(Si)1) with an applied current of 0.5A.

Fig. 256 demonstrates the good repeatability of the electrified tests, with the CoF consistently stabilizing around 0.15.

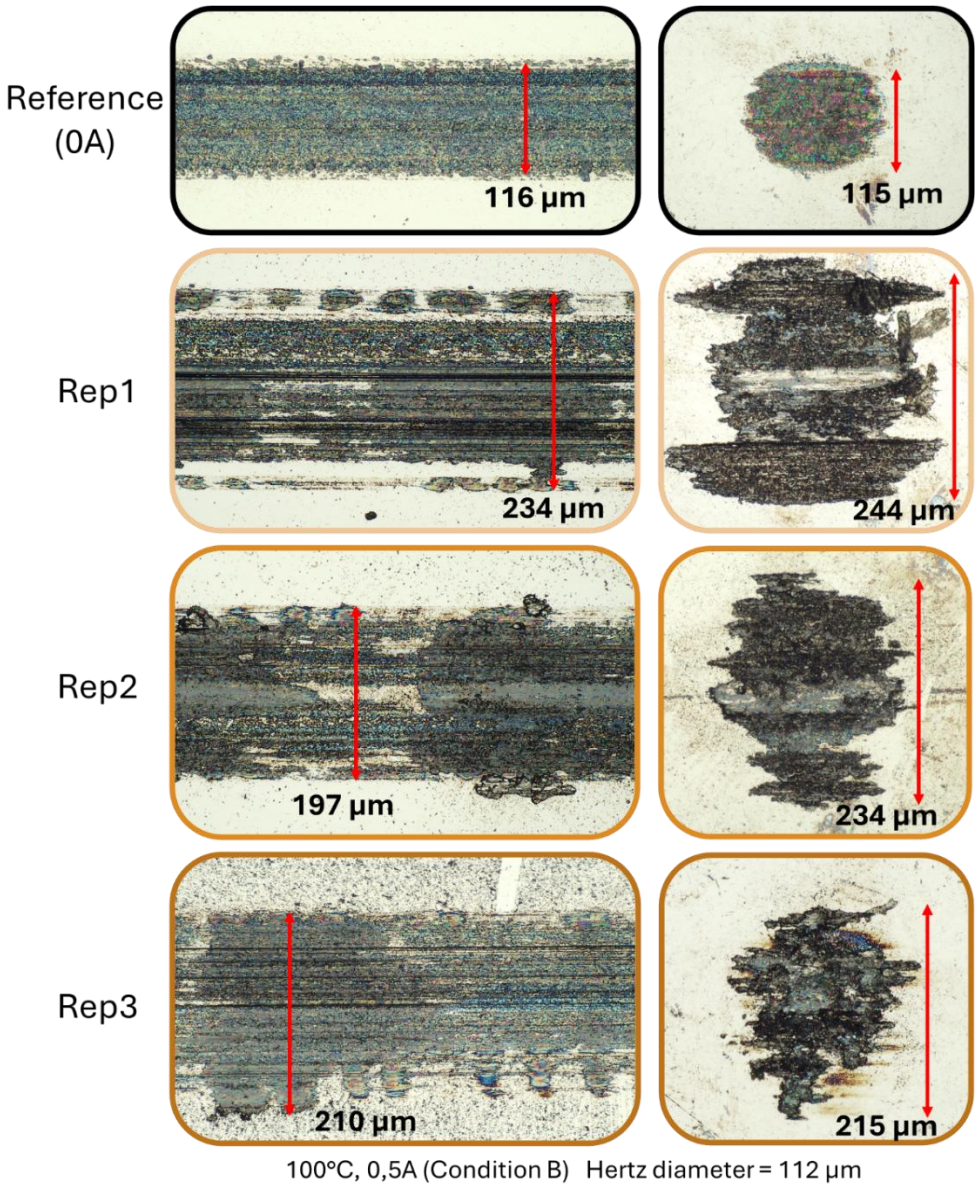

Fig. 257: Optical observations of wear tracks formed at 100°C on the discs and the balls under a 0.5A current for the sample containing silane-functionalized TiO_2 NPs (Tif(Si)1). Three repetitions were carried out. Test at 0A is used as a reference.

Although friction is lower with the application of a 0.5A current, Fig. 257 shows that the wear tracks are considerably wider (~215 µm at 0.5A vs. 116 µm at 0 A). Darkened regions are also observed on both the discs and the balls, similar to the features described for ZDDP in the previous section.

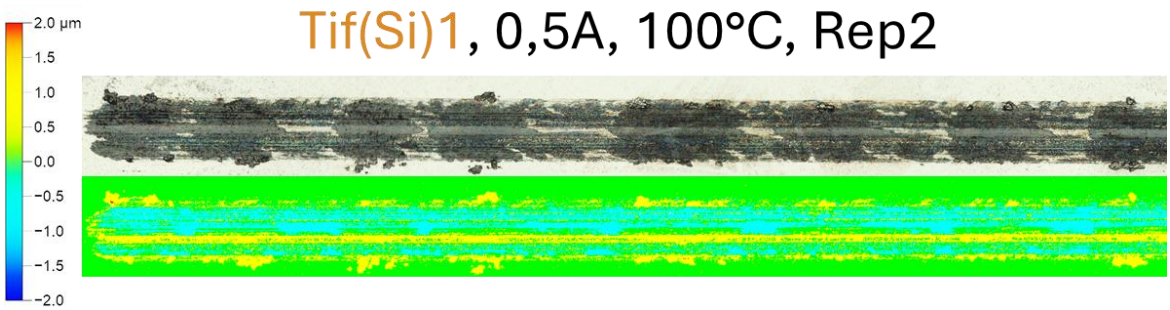

Fig. 258: Optical and profilometric observations of half a wear track formed at 100°C on the disc under a 0.5A current in the presence of a solution containing silane-functionalized TiO_2 NPs (Tif(Si)1).

An alternation between bright and dark zones is evident across the three repetitions (Fig. 258). The bright regions correspond to worn areas (below the reference plane), while the dark regions are at the reference level but were likely worn and subsequently covered by a deposit. The origin of this alternation remains uncertain: it could result from machine-related factors (e.g., arm vibration), although this is unlikely given that the phenomenon was not observed on other samples. Another possibility is related to surface topography, such as a local waviness of the disc. Alternatively, the behavior may be linked to the insulating effect of the nanoparticles, allowing the contact to behave like a capacitor. In this scenario, the alternation between bright and dark zones would correspond to charge-discharge cycles.

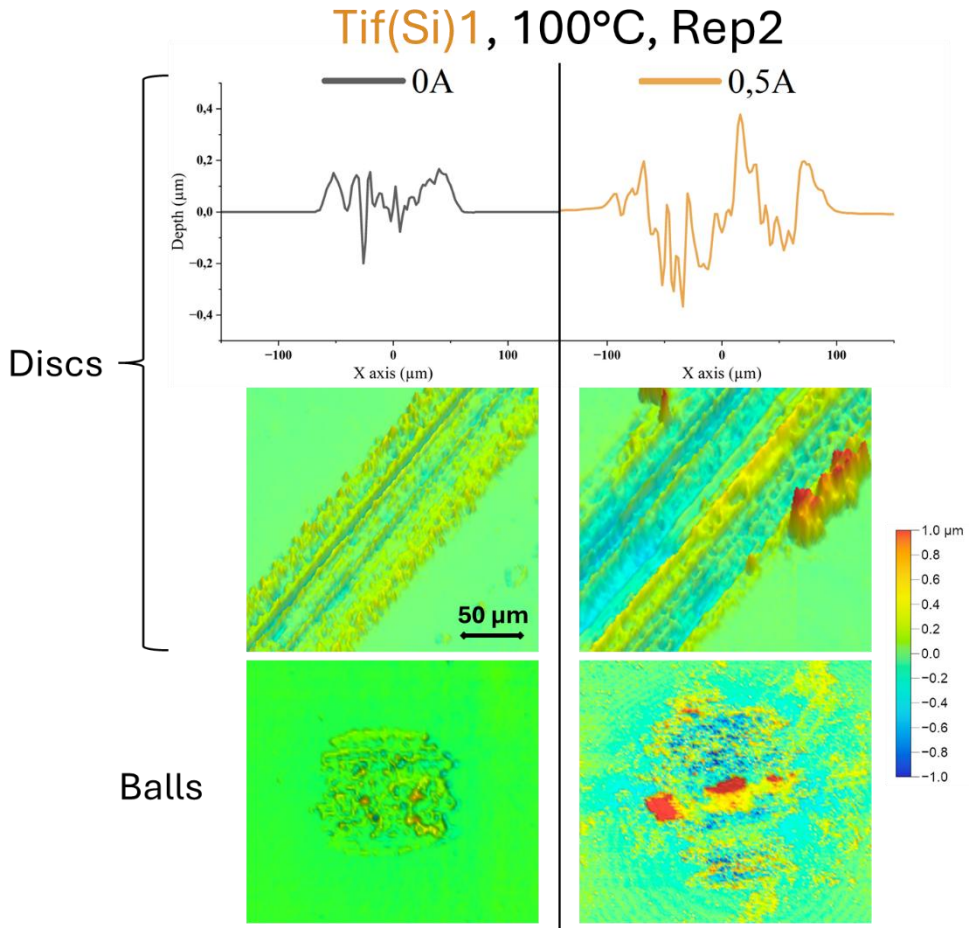

Fig. 259: Mean depth profiles and surface morphology of wear tracks formed at 100°C on the discs and the balls under a 0.5A current in the presence of a solution containing silane-functionalized TiO_2 NPs (Tif(Si)1). Test at 0A is used as a reference.

Profilometric measurements are detailed in Fig. 259 and confirm that disc wear is significantly increased under current. In addition, very thick deposits, up to ~1 µm, are found at the edges of the wear track which was not the case for ZDDP tests. On the ball, both localized wear scars and very thick, extended deposits are detected. These findings suggest that, similar to ZDDP, the application of current promotes the adhesion of wear particles; however, in this case the phenomenon is not restricted to the ball but also affects the disc.

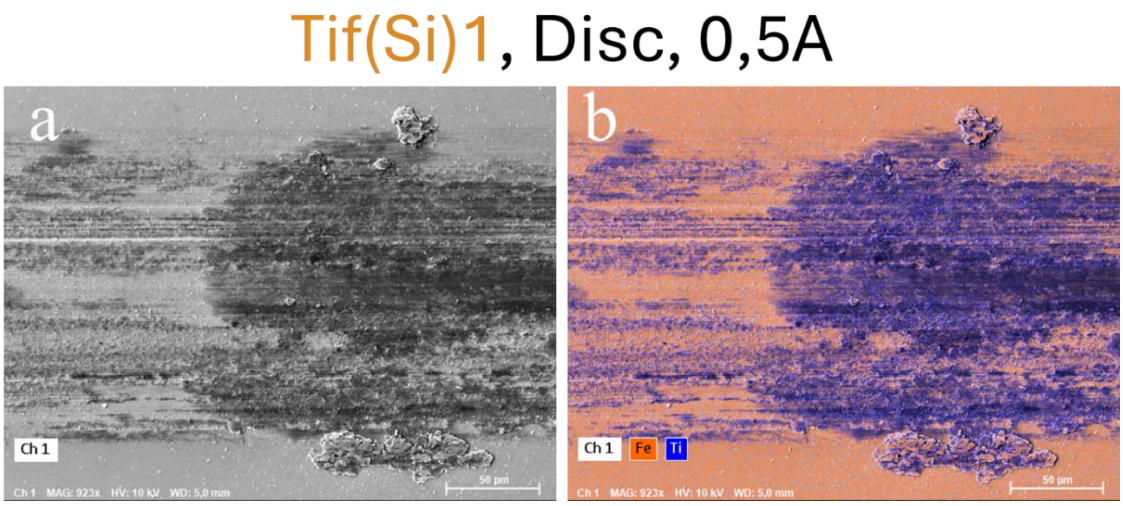

Fig. 260: SEM micrograph in SE mode (a) with EDX mapping (b) of a tribofilm formed on the disc at 100°C under a 0.5A current in the presence of silane-functionalized TiO_2 NPs solution (Tif(Si)1) (orange = Fe; blue = Ti).

Fig. 260 presents SEM observations combined with EDX mapping on a transition region between bright and dark zones. The bright area corresponds primarily to the steel substrate, whereas the dark region is rich in Ti. Thick agglomerates are observed at both edges of the wear track close to the dark region, containing both Fe and Ti.

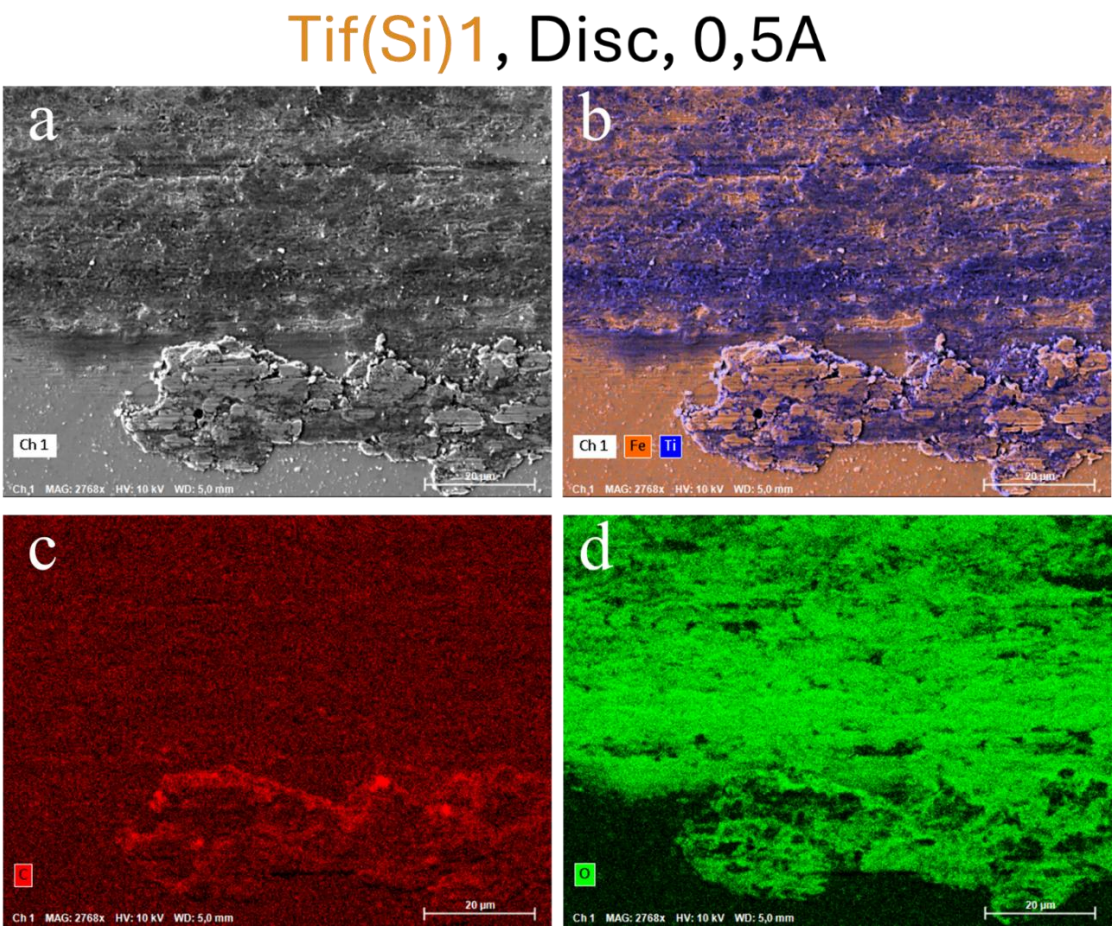

Fig. 261: SEM micrographs in SE (a) mode with EDX mapping (b, c and d) of a tribofilm formed on the disc at 100°C under a 0.5A current in the presence of silane-functionalized TiO_2 NPs solution (Tif(Si)1) (orange = Fe; blue = Ti; red= C; green = O).

A magnified view of the lower-edge agglomerate (Fig. 261) shows Fe-rich zones surrounded by Ti-rich regions, which coincide with oxygen-rich areas and are therefore most likely TiO_2 tribofilm. Compared with the rest of the wear scar, these agglomerates also exhibit a higher carbon concentration, which may be linked to unreacted nanoparticles.

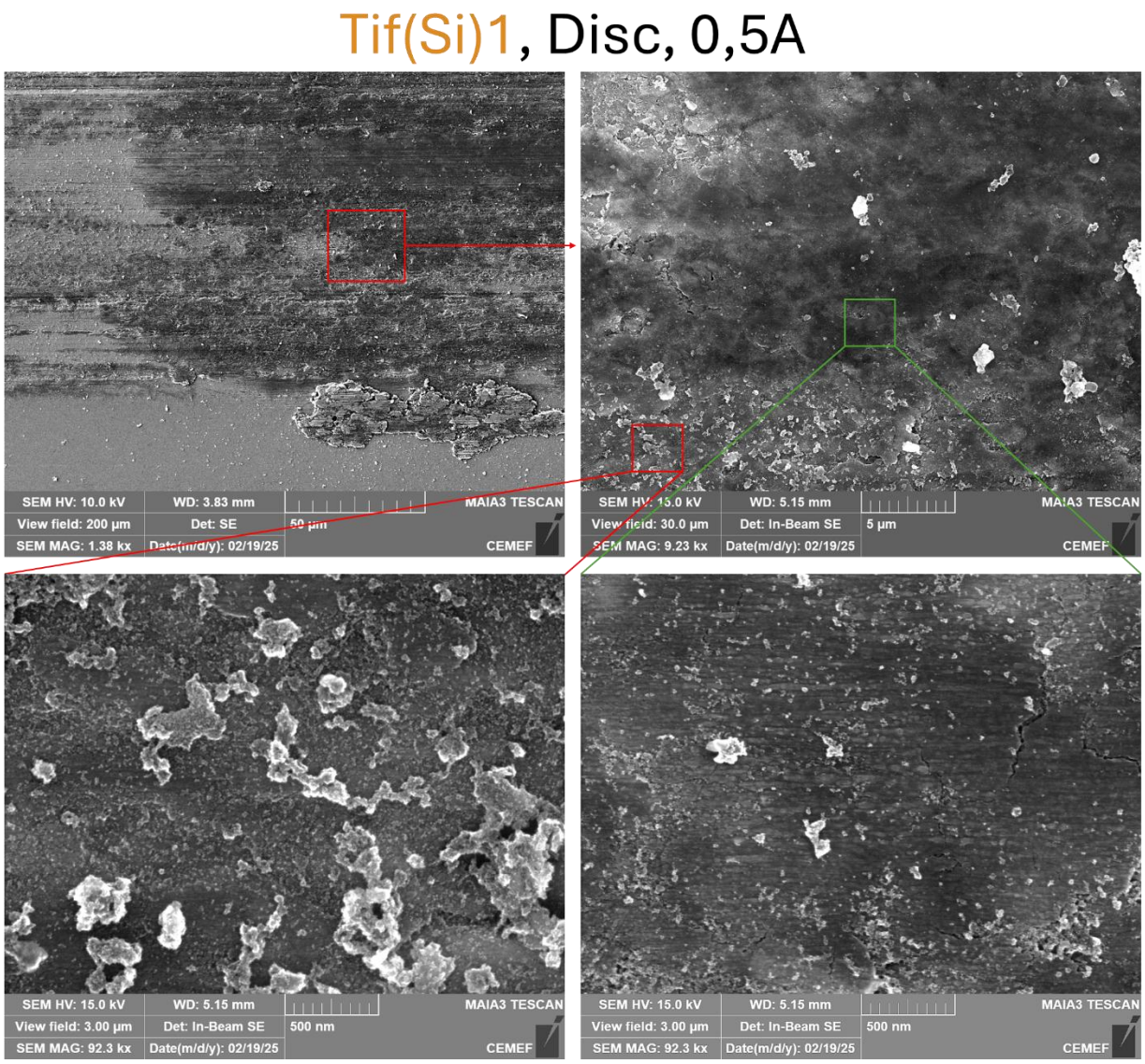

Fig. 262: High magnification SEM observations of a tribofilm formed on the disc at 100°C under a 0.5A current in the presence of silane-functionalized TiO_2 NPs solution (Tif(Si)1).

High-magnification SEM observations were then carried out to clarify these features. In a transition area between bright and dark zones (Fig. 262), the dark areas correspond to a smooth, compact tribofilm forming plateau-like structures. In contrast, the bright regions also contain tribofilm, but it appears thinner, less elevated, forming valley-like structures and with a large amount of debris.

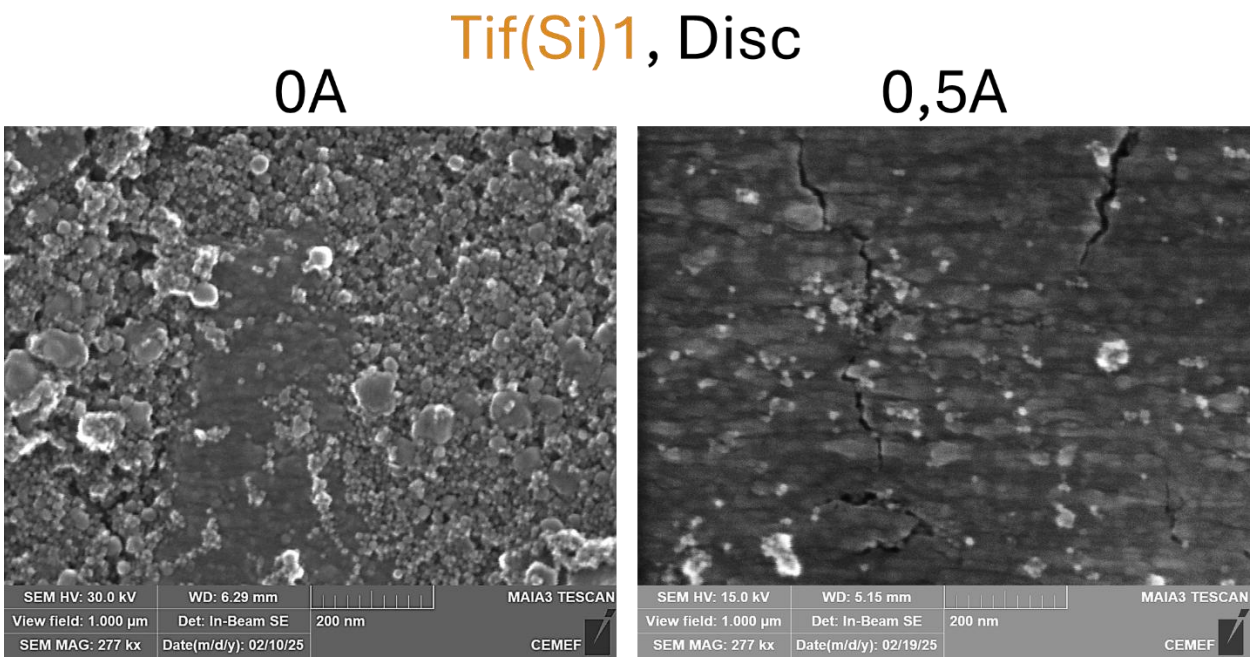

Fig. 263: Comparison of high magnification SEM observations of tribofilms formed on the disc at 100°C with either 0A or 0.5A applied current in the presence of silane-functionalized TiO_2 NPs solution (Tif(Si)1).

A closer inspection of the tribofilm (Fig. 263) shows that under 0.5A, the film is more compact than in the current-free condition, which may explain the lower and more stable friction observed earlier (Fig. 255). The applied current likely provides the energy required for tribo-sintering of the nanoparticles, resulting in the formation of a dense tribofilm. However, the presence of numerous cracks suggests that this tribofilm may be less mechanically robust than the one formed with oleic acid-functionalized TiO_2 nanoparticles studied in Chapter 3.

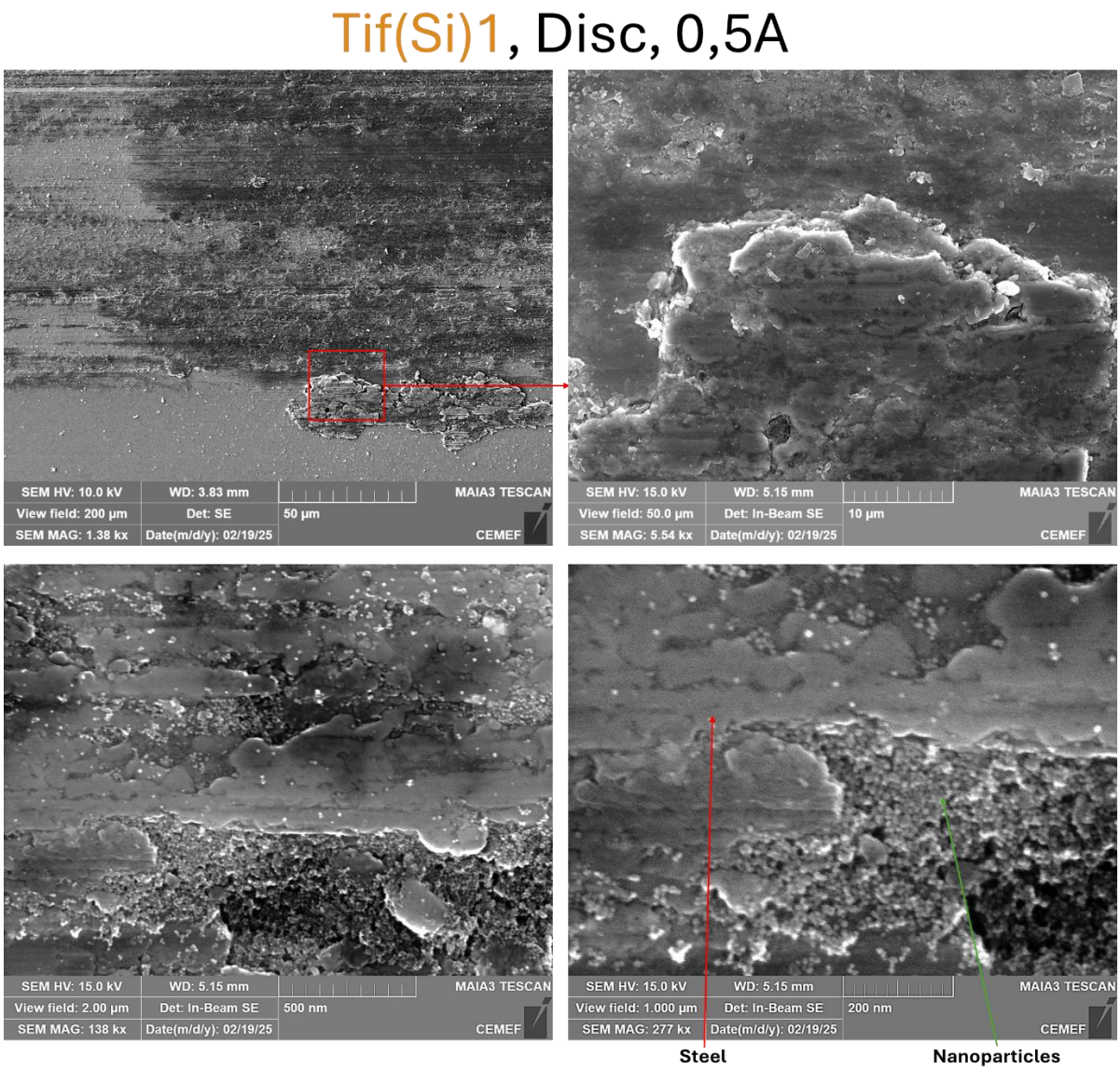

Fig. 264: High magnification SEM observations of a tribofilm formed on the disc at 100°C under a 0.5A current in the presence of silane-functionalized TiO_2 NPs solution (Tif(Si)1). Close up on agglomerated steel debris.

When focusing on the agglomerates at the wear track edges (Fig. 264), they appear to be a mixture of steel wear particles, nanoparticles, and tribofilm. The smooth metallic part displays an unusual morphology, as if folded, flattened and welded together under the combined effect of current and mechanical loading.

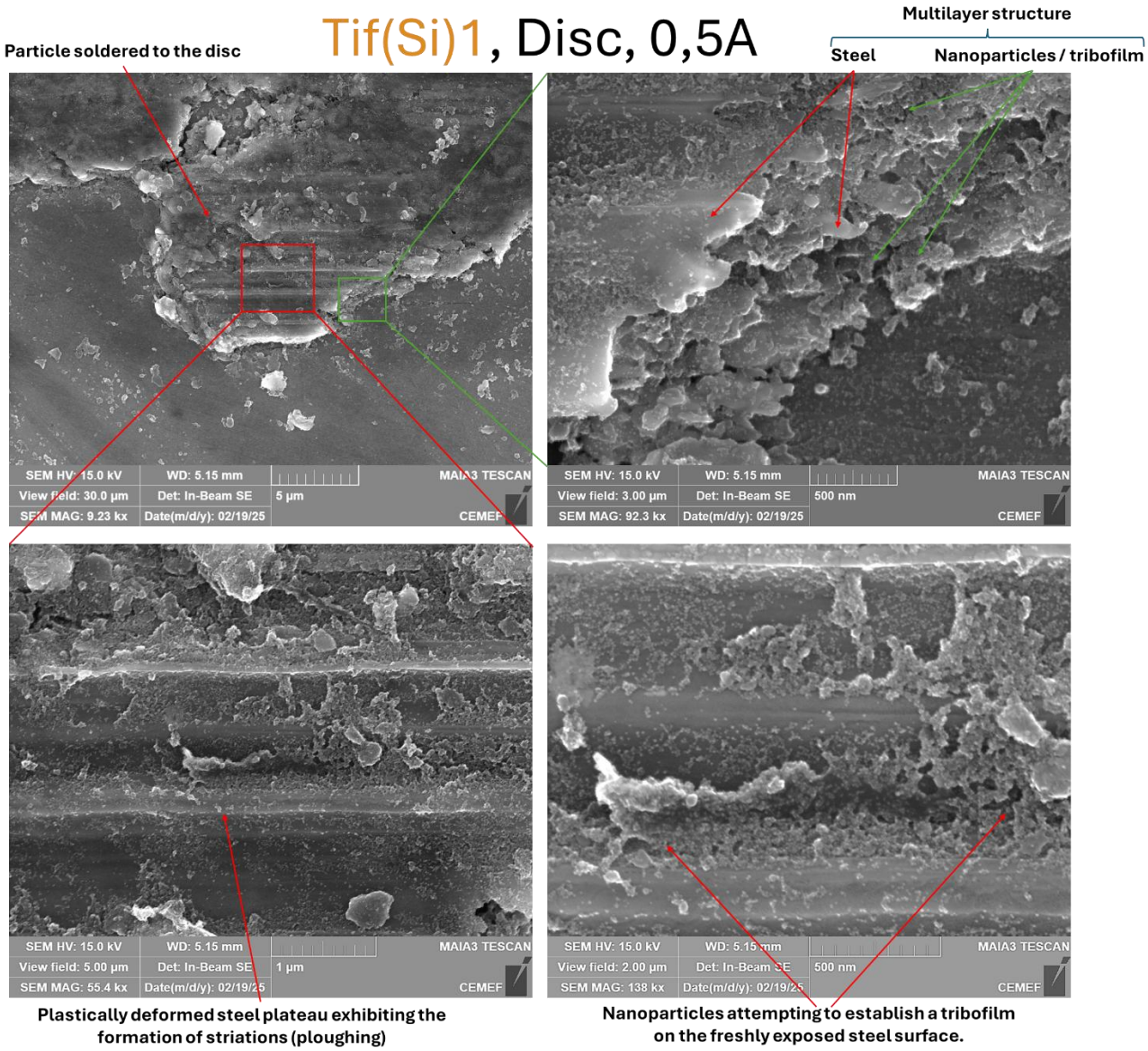

Fig. 265: High magnification SEM observations of a tribofilm formed on the disc at 100°C under a 0.5A current in the presence of silane-functionalized TiO_2 NPs solution (Tif(Si)1). Close up on agglomerated steel debris and the edge of this structure.

Fig. 265 provides a closer view of the same agglomerate, moving toward the outermost region. Within the inner zone (red box), smooth and homogeneous steel appears plastically deformed and ploughed by the sliding ball, leading to the formation of grooves. Nanoparticles are observed within these grooves, apparently agglomerating in the sliding direction and probably initiating tribofilm formation on the freshly exposed steel surface. At the extreme edge (green box), stacked layers can be distinguished, composed predominantly of steel intermixed with nanoparticles and tribofilm. We hypothesize that under current, wear particles from the steel substrate fuse with the surface, creating high-pressure asperities. These asperities in turn promote tribofilm formation by the nanoparticles, which increases their height and therefore enhances wear. New wear particles are then generated, adhere to the asperity, and again contribute to tribofilm formation. This cyclic process leads to the development of very thick (~1 µm) abrasive structures. Such behavior is likely associated with the highly reactive nature of these nanoparticles, which rapidly interact with the steel substrate as already demonstrated in Chapter 3.

The application of current markedly modifies the behavior of silane-functionalized TiO_2 nanoparticles during tribofilm formation. Under electrified conditions, a denser and more compact tribofilm is produced, which correlates with lower and more stable friction. However, SEM/EDX analyses also reveal large amounts of wear debris, agglomerates on the edges of the track corresponding to layered structures of steel debris and TiO_2 tribofilm. These observations suggest a cyclic mechanism in which steel wear particles fuse with the substrate under current, leading to tribofilm growth, asperity thickening, and further wear. This process results in the formation of thick (~1 µm), abrasive tribofilm structures, reflecting both the high reactivity of the nanoparticles and the dual role of current in enhancing tribofilm density while simultaneously accelerating wear.

Having examined the individual effects of electrical current on ZDDP and on silane-functionalized TiO_2 nanoparticles, the next section focuses on their combined action. Under non-electrified conditions, this mixture had previously yielded the best tribological performance compared with either additive alone. Here, we investigate how electrical current influences tribofilm formation when both ZDDP and functionalized nanoparticles are present, in order to assess if their synergistic relationship still prevails in an electrified contact.

5.1.3 Effect of Current on the lubricating properties of ZDDP / Silane-functionalized TiO_2 Nanoparticles Blend

Fig. 266 presents the evolution of friction for tests performed with and without current in the presence of the ZDDP/silane-functionalized TiO_2 nanoparticle mixture. As a reminder, two possible behaviors had been observed for this mixture under non-electrified conditions: in the first case, the CoF stabilizes around 0.125, while in the second it reaches a lower value near 0.11. In both cases, a transient increase to 0.14 is followed by a decrease before stabilization. The application of current does not fundamentally alter this trend, although the initial rise is slightly higher (0.15 instead of 0.14). The tests with 0.5A current also display greater instability but tend to stabilize around 0.13.

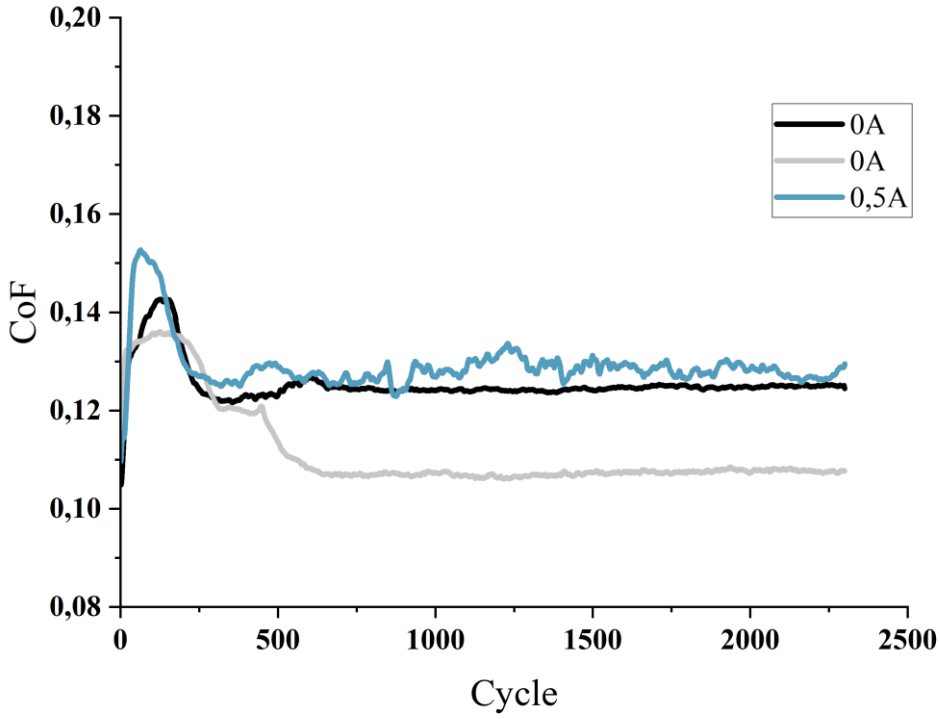

Fig. 266: Evolution of friction coefficient with cycles at 100°C for the sample containing a blend of ZDDP and silane-functionalized TiO_2 NPs (Zn1_Tif(Si)0.5) with an applied current of either 0A (references) or 0.5A.

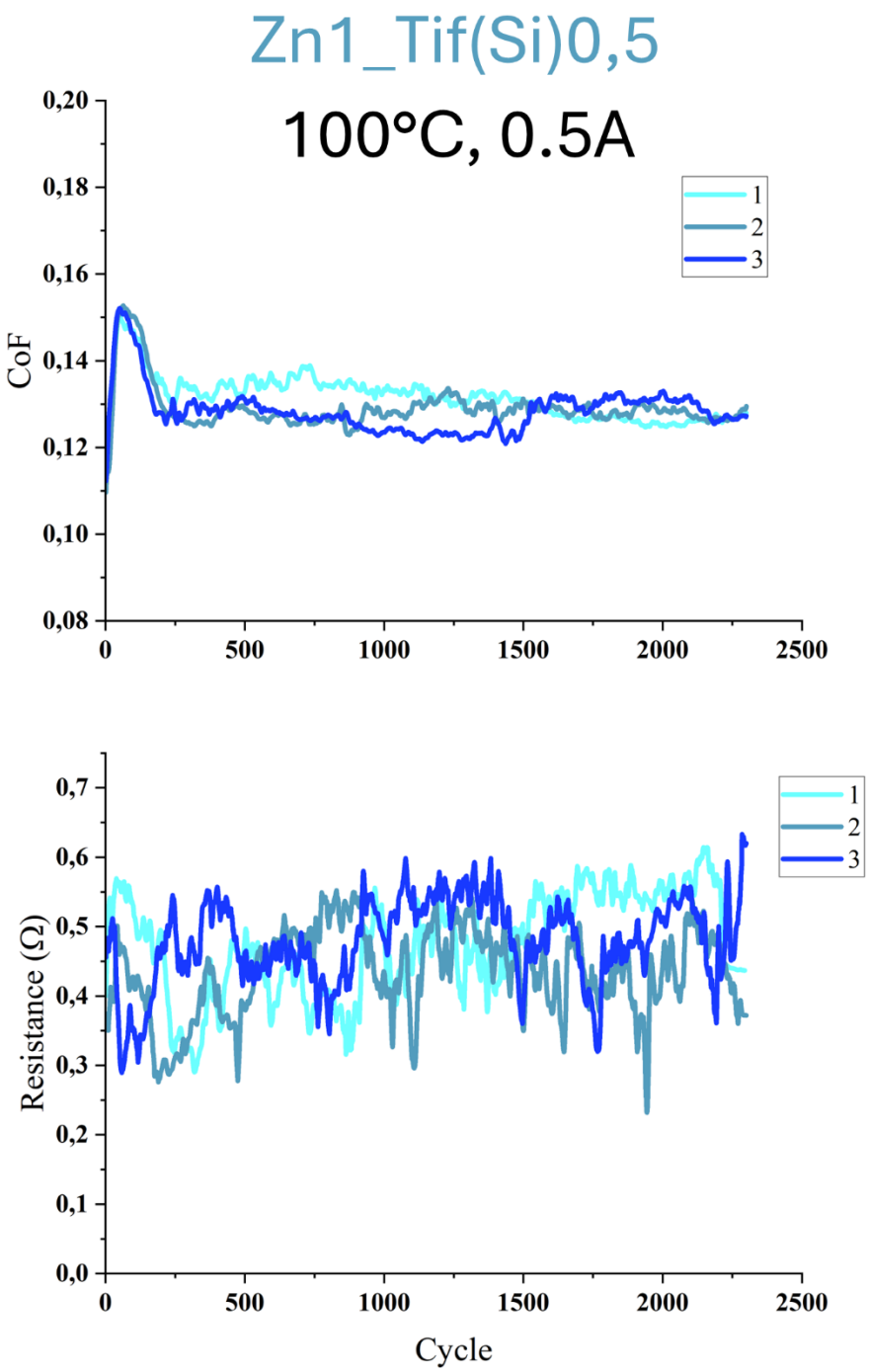

Fig. 267: Repeatability at 100°C for the sample containing a blend of ZDDP and silane-functionalized TiO_2 NPs (Zn1_Tif(Si)0.5) with an applied current of 0.5A. Top graph represents the evolution of friction coefficient and bottom part the evolution of contact resistance with cycles.

The three repetitions are shown in Fig. 267 and demonstrate good repeatability. The evolution of contact resistance is also plotted, exhibiting a constant regime throughout the test, with values oscillating around 0.45 Ω. This contrasts with the behavior observed for ZDDP alone, where two distinct phases were identified, likely corresponding to periods without, then with tribofilm (Fig. 243). In the present case, only a single phase is observed, consistent with the rapid tribofilm formation promoted by the high reactivity of the nanoparticles confirmed in Chapter 3.

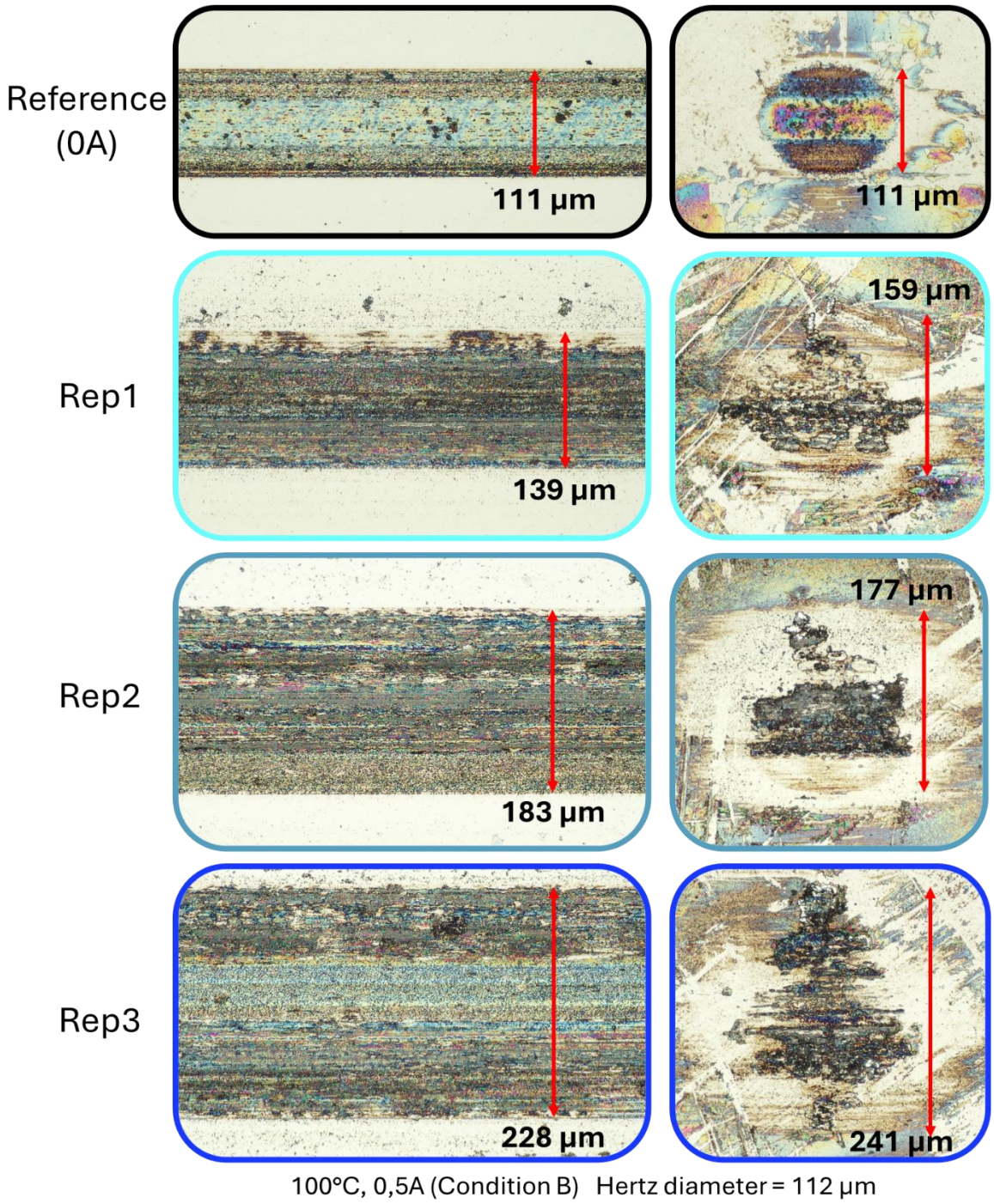

Fig. 268: Optical observations of wear tracks formed at 100°C on the discs and the balls under a 0.5A current for the sample containing a blend of ZDDP and silane-functionalized TiO_2 NPs (Zn1_Tif(Si)0.5). Three repetitions were carried out. Test at 0A is used as a reference.

Wear scar images of the discs and balls for the three repetitions are presented in Fig. 268. The observed behavior appears intermediate between that of ZDDP alone and that of nanoparticles alone. For instance, in repetition 1, the disc shows mainly current-induced wear features but retains a relatively narrow wear scar (139 µm), similar to the ZDDP-only condition (Fig. 244Fig. 159). In contrast, repetition 3 exhibits a much wider wear scar, comparable to that observed with nanoparticles alone under current, although the central zone appears covered by an intact tribofilm. Notably, the alternation of bright and dark zones characteristic of nanoparticle-only tests is absent here. On the balls, dark deposits are visible across all three repetitions.

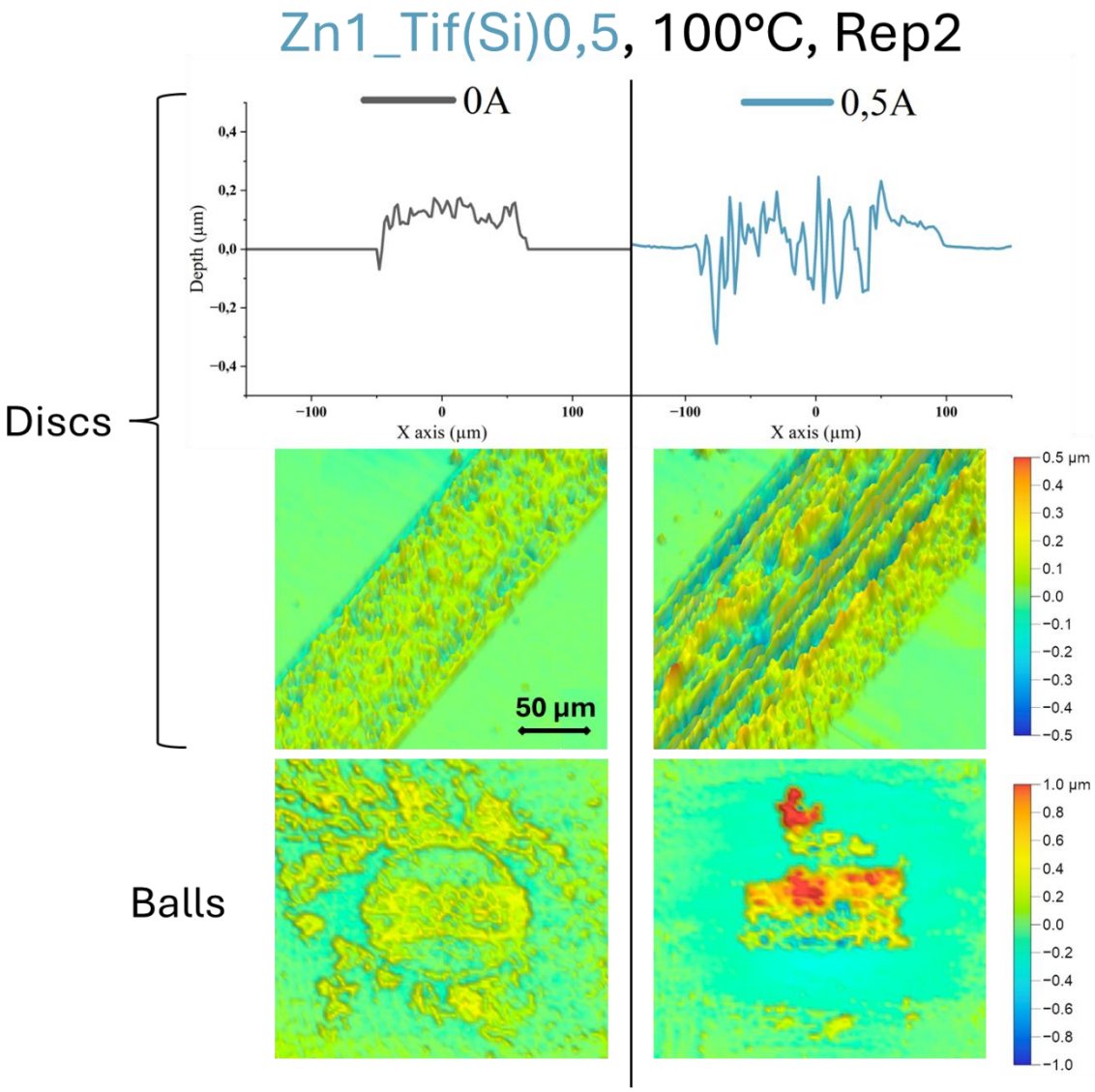

Fig. 269: Mean depth profiles and surface morphology of wear tracks formed at 100°C on the discs and the balls under a 0.5A current in the presence of solution containing a blend of ZDDP and silane-functionalized TiO_2 NPs (Zn1_Tif(Si)0.5). Test at 0A is used as a reference.

As with the individual additives, Fig. 269 confirms that disc wear is associated with the formation of a thick deposit (~1 µm) on the ball surface.

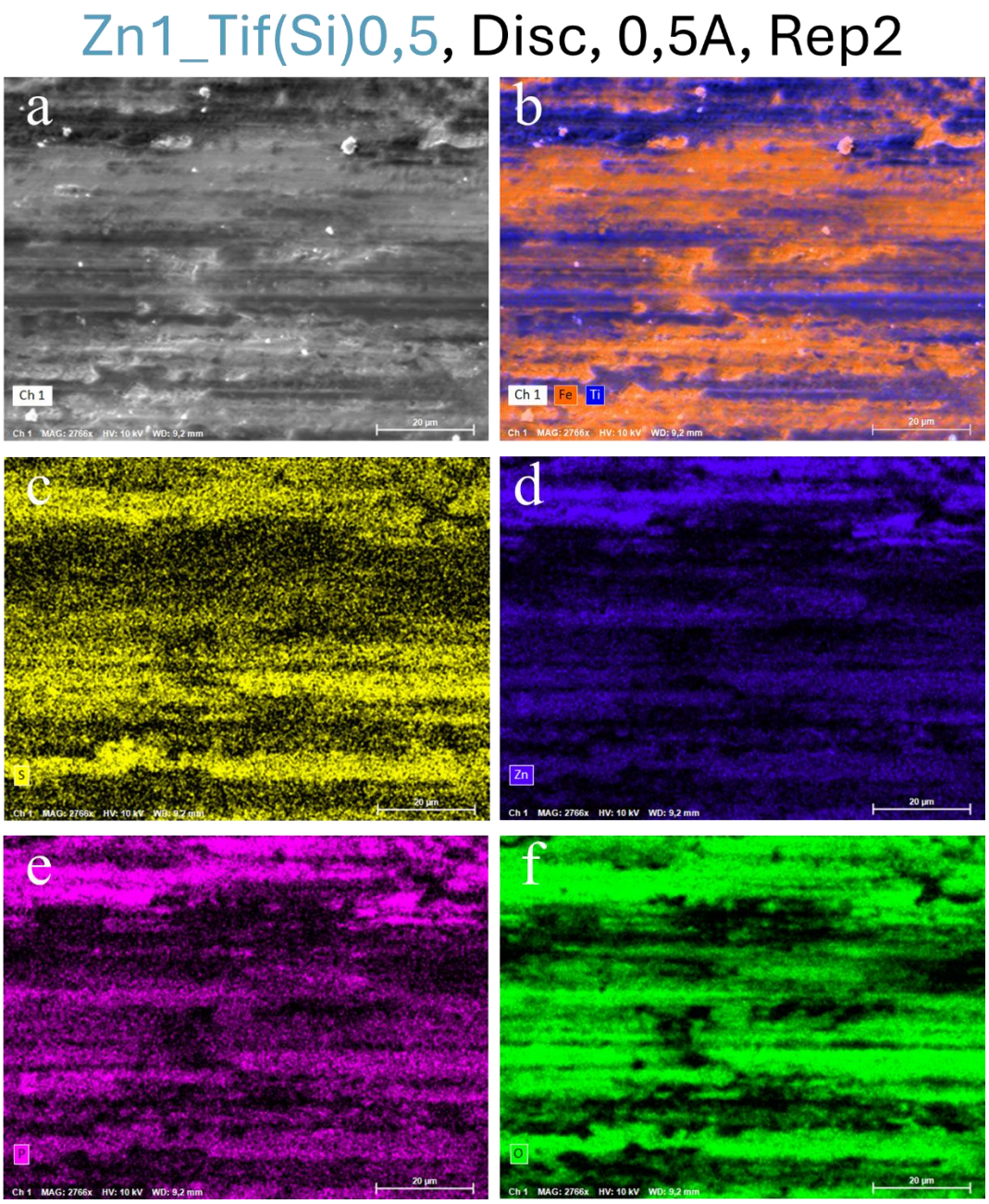

Fig. 270: SEM micrographs in SE mode (a) with EDX mapping (b, c, d, e and f) of a tribofilm formed on the disc at 100°C under a 0.5A current in the presence of a blend of ZDDP and silane-functionalized TiO_2 NPs (Zn1_Tif(Si)0.5) (orange = Fe; blue = Ti; yellow = S; purple = Zn; pink = P; green = O).

SEM observations and EDX mapping of the disc (Fig. 270) show that, similar to ZDDP alone (Fig. 248), the application of current promotes elongation of the tribofilm in the sliding direction.

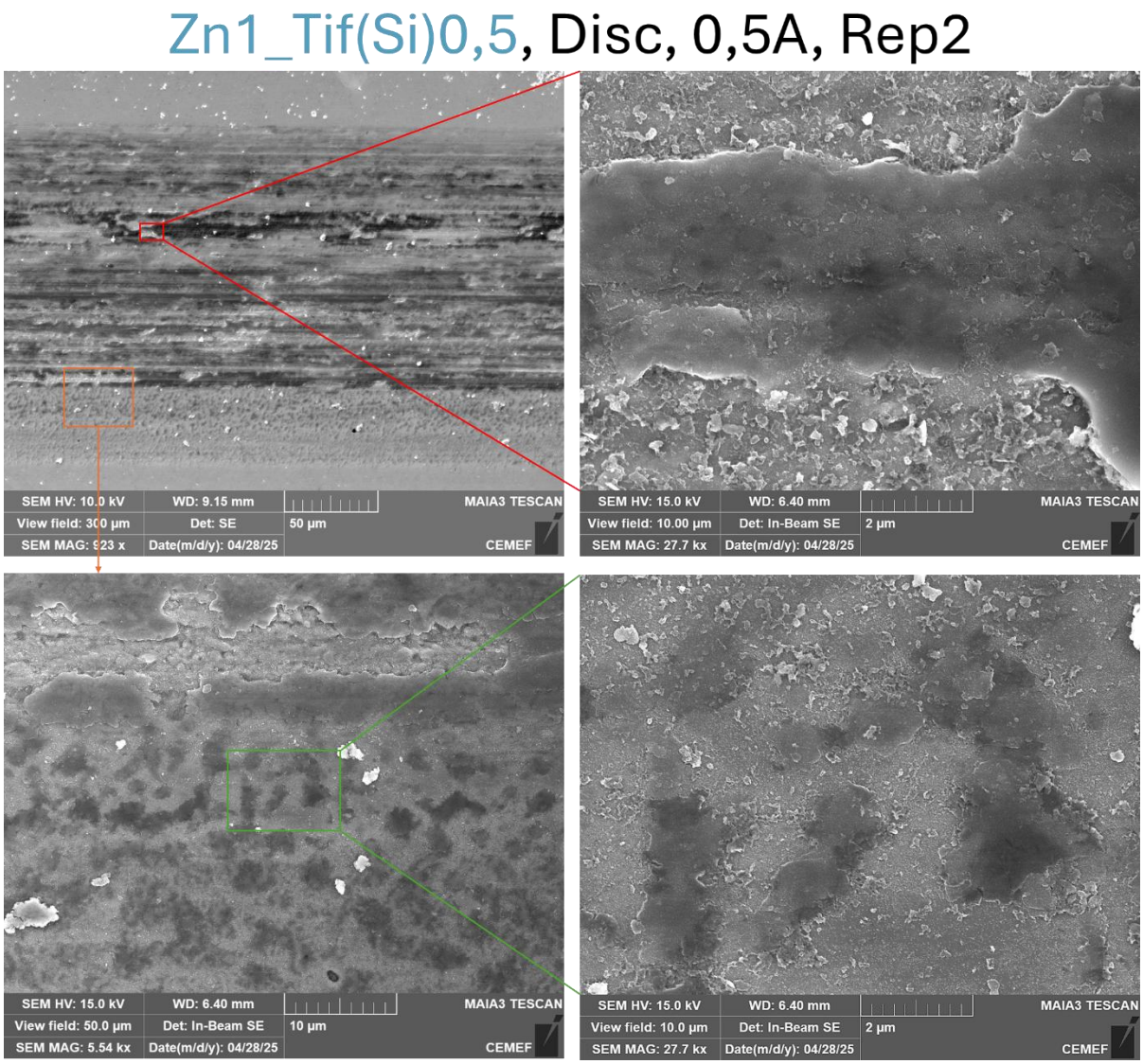

Fig. 271: High magnification SEM observations of a tribofilm formed on the disc at 100°C under a 0.5A current with a blend of ZDDP and silane-functionalized TiO_2 NPs (Zn1_Tif(Si)0.5).

High-magnification SEM images of the tribofilm formed under 0.5A (Fig. 271) highlight different microstructural features. In the intermediate region between the unaffected tribofilm and the current-affected area (orange box), a transition can be observed. A closer view of the intact tribofilm (green box) reveals a patchy-like morphology, consistent with what was observed in Chapter 3 for this mixture, particularly near the track edges where pressure is lower than at the center. However, a greater amount of wear debris is present. The current-affected region (red box) exhibits tribofilm strongly elongated in the sliding direction, appearing smooth and significantly thicker. This behavior is likely a response to the increased pressure caused by thick deposits forming on the ball, which in turn promote the growth of a thicker tribofilm.

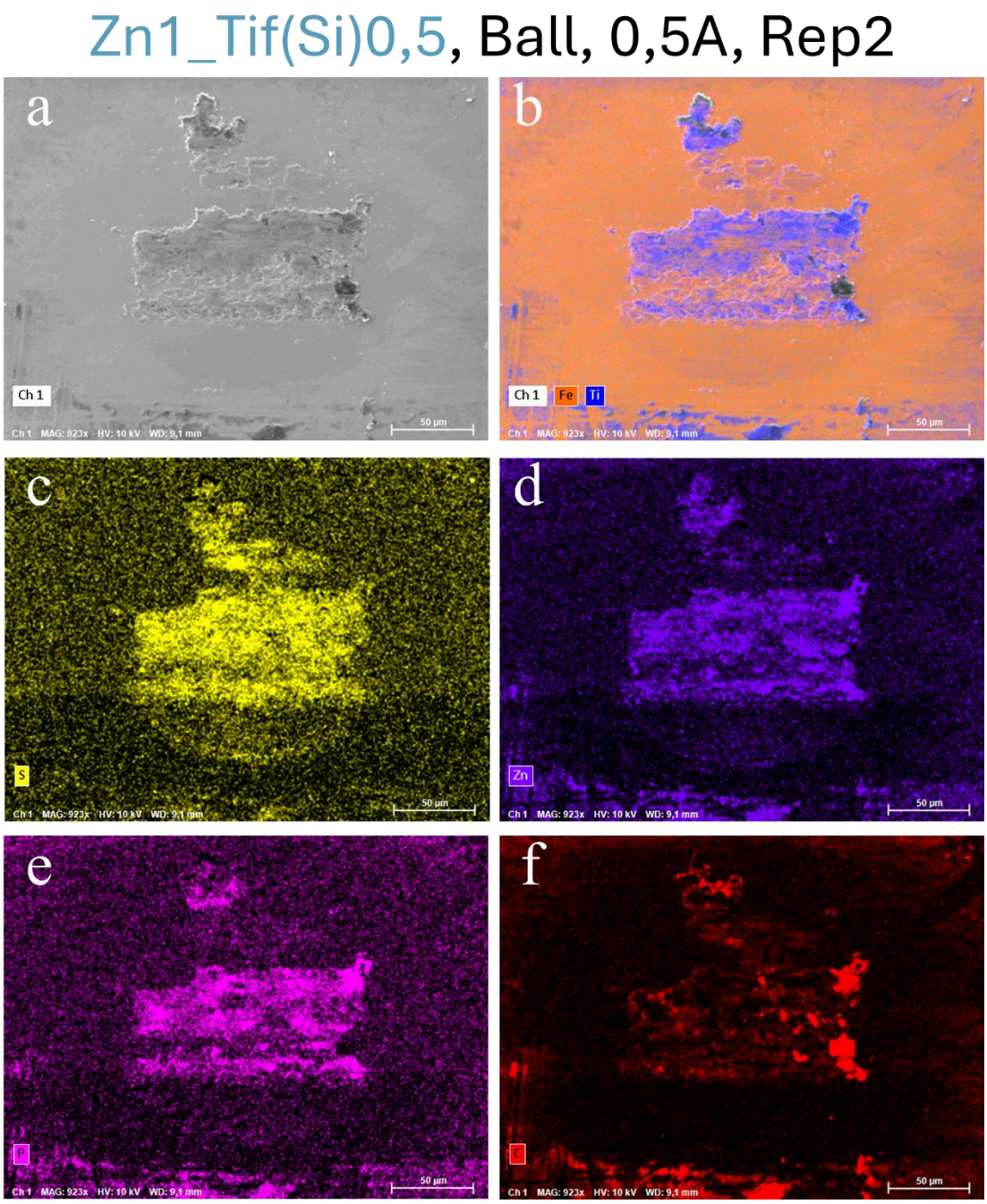

Fig. 272: SEM micrographs in SE mode (a) with EDX mapping (b, c, d, e and f) of a tribofilm formed on the ball at 100°C under a 0.5A current in the presence of a blend of ZDDP and silane-functionalized TiO_2 NPs (Zn1_Tif(Si)0.5) (orange = Fe; blue = Ti; yellow = S; purple = Zn; pink = P; red = C).

Observations and EDX mapping of the ball (Fig. 276) reveal that the entire wear scar is not covered by tribofilm. Some regions lack Ti, Zn, and P but are enriched in Fe and S, suggesting the presence of sulfur-containing species, similar to those identified for ZDDP alone (Fig. 251). Other regions are strongly enriched in carbon.

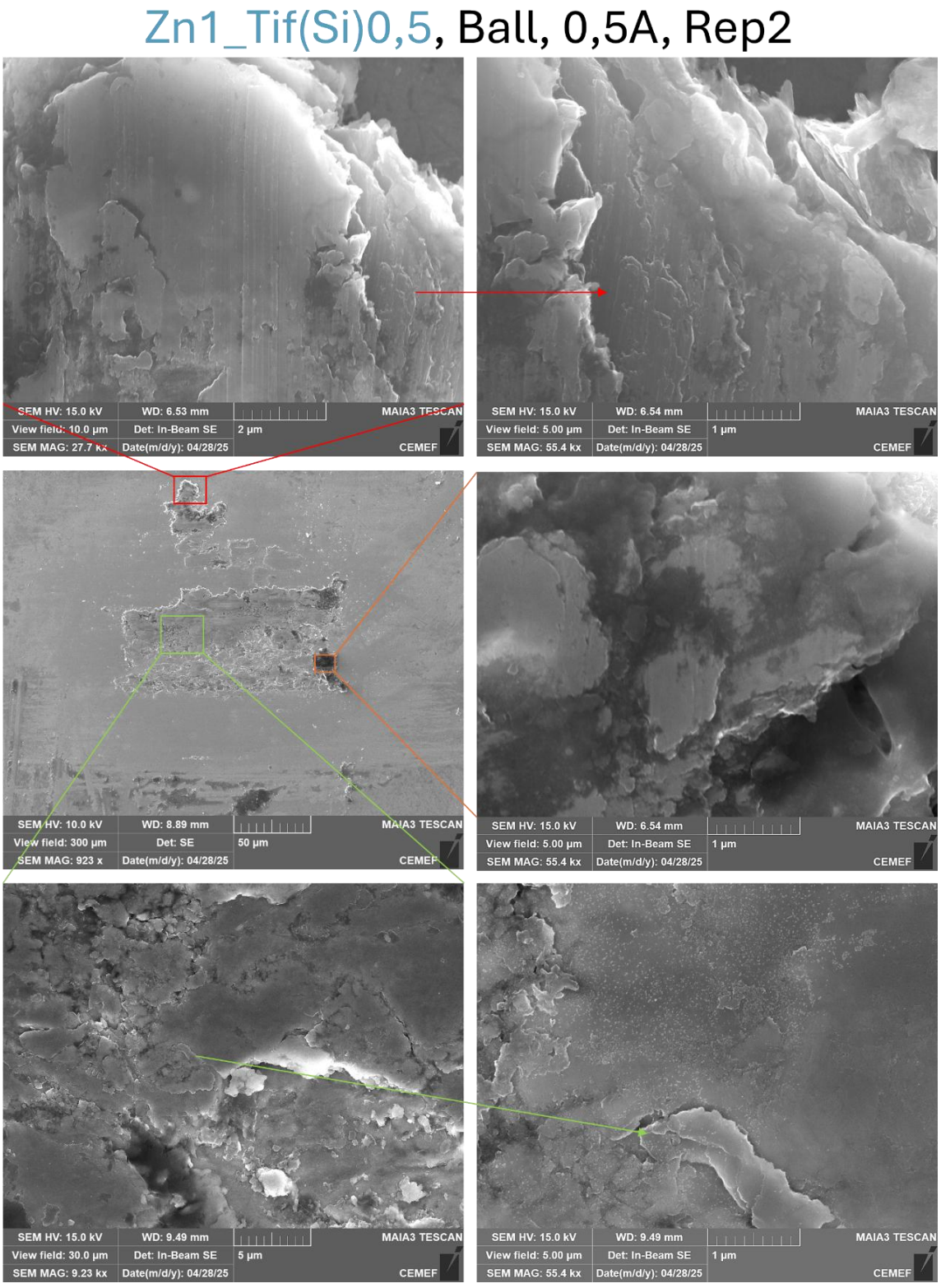

Fig. 273: High magnification SEM observations of a tribofilm formed on the ball at 100°C under a 0.5A current with a blend of ZDDP and silane-functionalized TiO_2 NPs (Zn1_Tif(Si)0.5).

These zones were further investigated at higher magnification (Fig. 273). The central region, rich in Ti, P, Zn, and S (green box), displays a locally smooth but globally rough morphology, with compacted, overlapping structures.

The carbon-rich zone (orange box) contains stacked structures with smooth surfaces partly covered by a dark deposit, likely corresponding to carbon, resembling features observed with ZDDP alone (Fig. 252). Finally, the upper region (red box), rich in both Ti and Fe, shows a striated surface that likely corresponds to exposed steel. Interestingly, the striations are perpendicular to the sliding direction. While they could have been introduced during handling of the ball prior to observation, a closer inspection of the edge reveals that the deposit is composed of successive layers, some of which also display striations in the same orientation. These features suggest that the deposit was compressed and extruded outward from the contact zone.

at.%	Zn1_Tif(Si)0,5 100°C	
	0A	**0,5A**
C 1s	**18,8**	**7,8**
Fe 2p	**1,1**	**12,8**
O 1s	**51,2**	**54,8**
P 2p	**8,6**	**3,8**
S 2p	**1,6**	**1,0**
Zn 2p	**4,6**	**2,9**
Si 2p	**0,9**	**2,5**
Ti 2p	**11,1**	**11,7**
Ca 2p	**2,1**	**2,6**

Table 40: XPS chemical composition of tribofilms formed in the presence of a solution containing a blend of ZDDP and silane-functionalized TiO_2 NPs (Zn1_Tif(Si)0.5) with an applied current of either 0A or 0.5A. Conducted using a NEXSA spectrometer.

XPS measurements (**Table 40**) show that, as with ZDDP, the application of current leads to a strong increase in the Fe content (from 1.1 at.% at 0A to 12.8 at.% at 0.5A). While all ZDDP-related elements (Zn, P, and S) decrease, the Ti content remains constant. Since nanoparticles are known to react much faster than ZDDP, the increased exposure of steel under electrified conditions would favor preferential reaction of the nanoparticles, which could explain the stable Ti content.

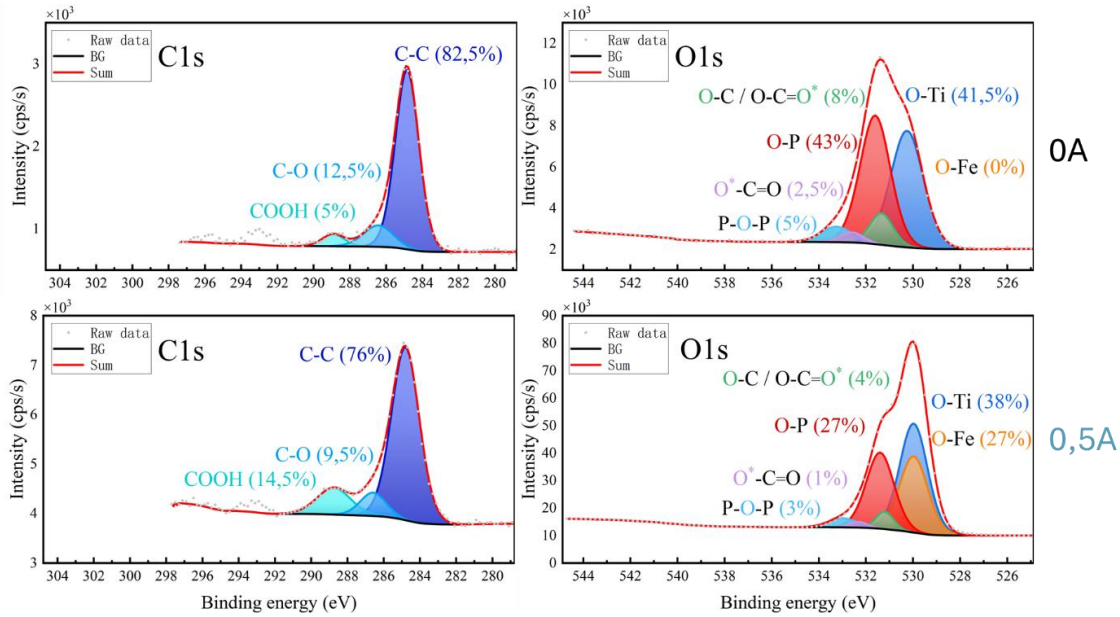

Fig. 274: C1s and O1s XPS spectra of tribofilms formed in presence of a blend of ZDDP and silane-functionalized TiO_2 NPs (Zn1_Tif(Si)0.5) with either a 0A or 0.5A applied current.

In contrast to ZDDP alone (Fig. 253), the significant increase in Fe here is directly correlated with the O1s component associated with iron (Fig. 274), indicating the formation of iron oxides.

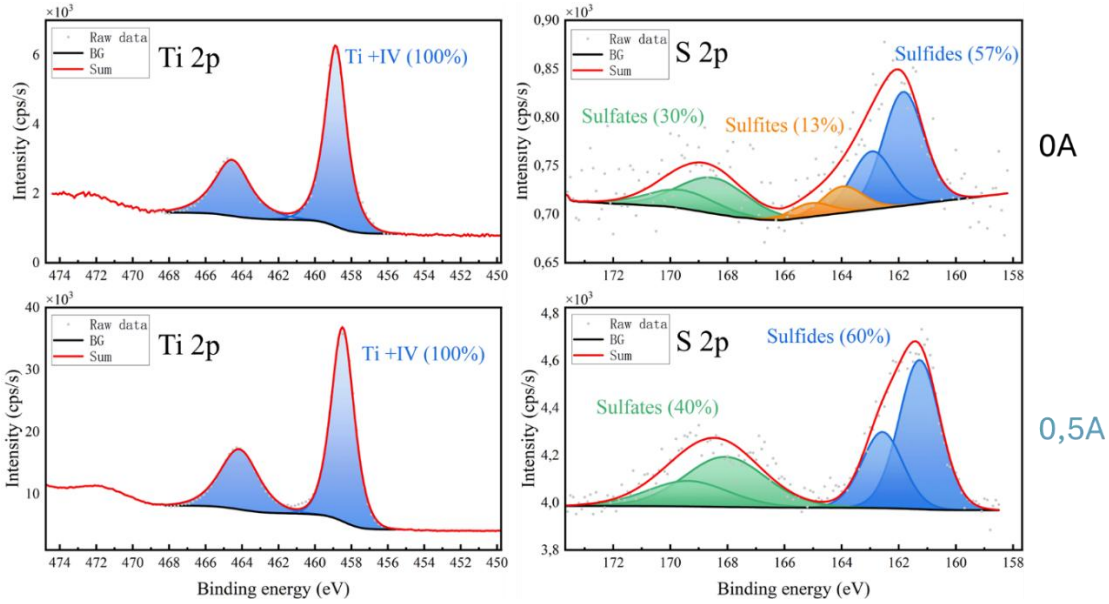

Fig. 275: Ti2p and S2p XPS spectra of tribofilms formed in presence of a blend of ZDDP and silane-functionalized TiO_2 NPs (Zn1_Tif(Si)0.5) with either a 0A or 0.5A applied current.

Oxidized sulfur species such as sulfates are also detected (Fig. 275), although these were already present in the mixture under non-electrified conditions. Titanium consistently remains in the form of TiO_2, both with and without current.

Overall, the mixture of ZDDP and silane-functionalized TiO_2 nanoparticles under electrical current exhibits a tribological response that combines features of both additives used individually. The friction behavior remains relatively stable, and tribofilms are formed rapidly due to the high reactivity of the nanoparticles. However, the application of current promotes the generation of thick deposits on the ball and iron oxide formation within the contact, leading to higher wear compared with the non-electrified condition. The nanoparticles appear to dominate the tribochemical response under current, maintaining their contribution to TiO_2 tribofilm formation while ZDDP-derived species are reduced.

The comparison of the three lubrication strategies under electrified conditions highlights distinct tribochemical mechanisms and outcomes. When ZDDP is used alone, the application of current slightly destabilizes the friction response, promotes debris accumulation, and alters the morphology of the tribofilm, leading to partial loss of surface coverage and enhanced wear. In contrast, silane-functionalized TiO_2 nanoparticles benefit from the presence of current, as the additional energy input promotes tribosintering and the formation of a dense and compact tribofilm, resulting in lower and more stable friction. However, this comes at the cost of significant wear, driven by the generation of thick deposits and the cyclic accumulation of wear particles at the contact edges. The mixture of ZDDP and nanoparticles, which showed the best performance in non-electrified conditions due to their complementary reactivity, presents an intermediate behavior under current. While the nanoparticles ensure rapid tribofilm formation and stable friction, the wear protection is reduced as ZDDP contribution becomes less effective, and iron oxide formation is promoted. Even though the nanoparticles dominate the tribological response, they also induce a pronounced increase in deposit thickness on the cathode (here, the ball). This effect, although partly compensated by the concurrent tribofilm growth on the anode (the disc), still leads to the generation of a large amount of wear debris.

These results underline that electrical current fundamentally modifies the balance between additive chemistry, tribofilm growth, and wear mechanisms.

Having examined the influence of electrical current on tribofilm growth with different lubrication additives, the next step is to assess how current affects a tribofilm that has already been established. This distinction is essential, as the response of a pre-formed tribofilm to electrification may differ significantly from its formation stage, revealing additional insights into the stability, durability, and transformation mechanisms of protective layers under current flow.

5.2 Durability of Tribofilms under Electrified Tribological Conditions

5.2.1 Effect of Current on the Durability of ZDDP Tribofilm

As shown in Fig. 276, for these new tests a tribofilm was first allowed to form over 2300 cycles. This explains why the friction curve closely resembles the reference condition, with an initially high coefficient of friction (~0.16) that gradually decreases after 500–1000 cycles as the tribofilm develops. Electrical current was then applied without interrupting the test in order to evaluate how the pre-formed tribofilm protects the surface. Upon current application, the CoF first decreases slightly before rising abruptly from 0.11 to 0.16 and then stabilizing around 0.14.

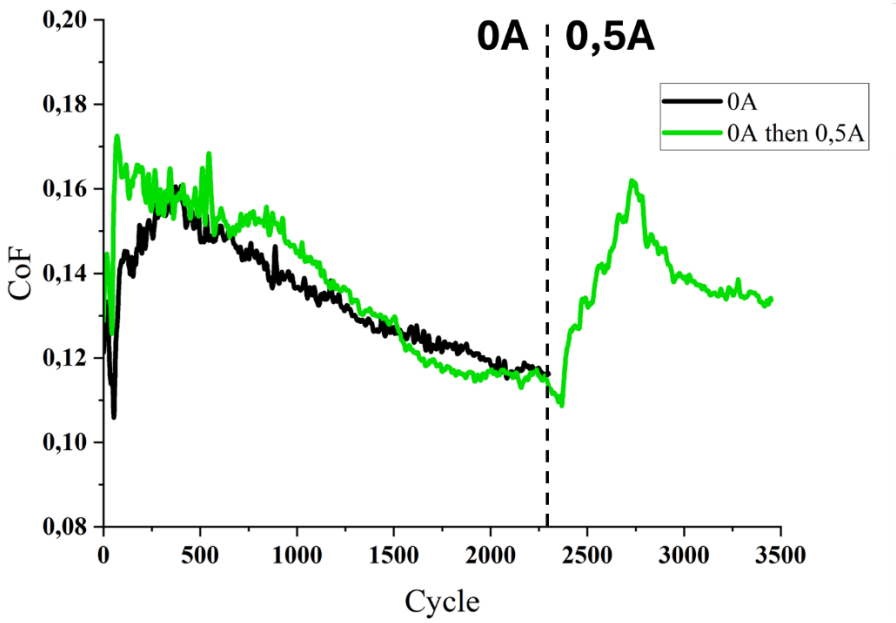

Fig. 276: Evolution of friction coefficient with cycles at 100°C for the sample containing ZDDP with an applied current of either 0A (reference) or 0A followed by 0.5A.

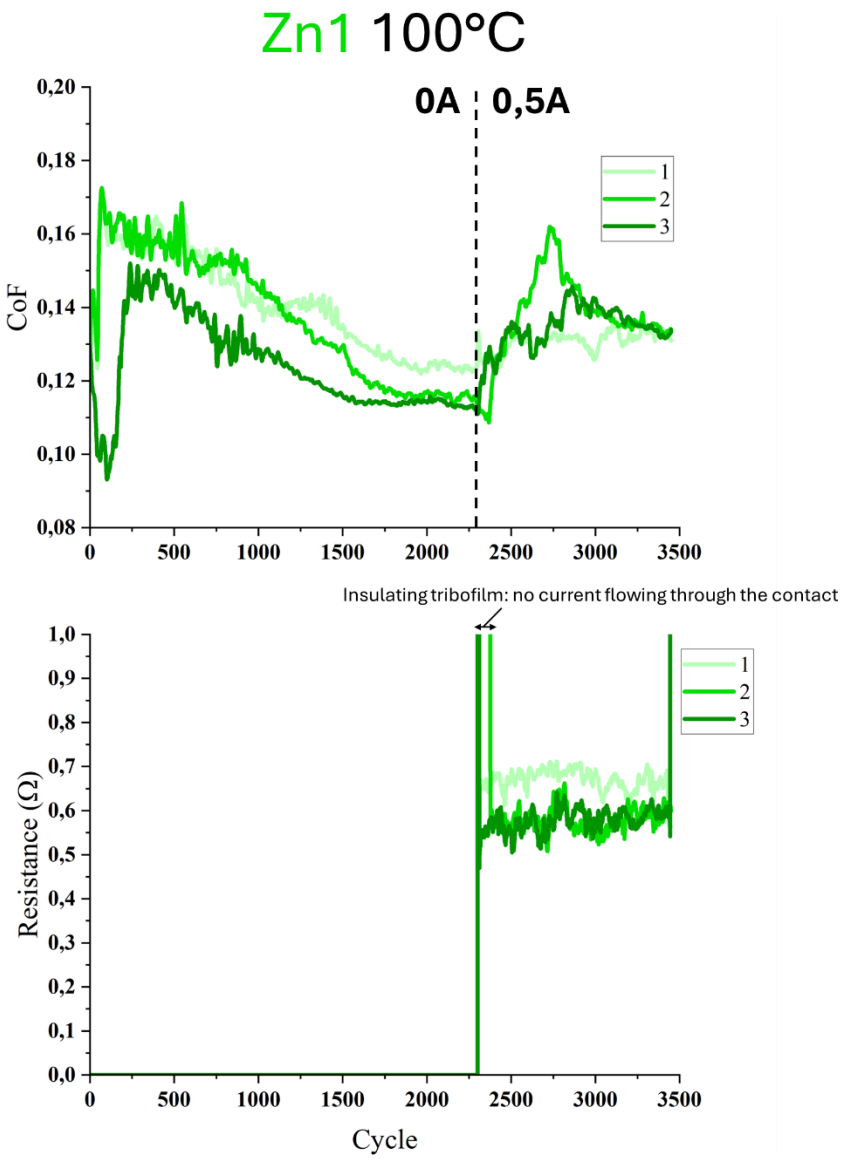

Fig. 277: Repeatability at 100°C for the sample containing ZDDP (Zn1) with an applied current of 0A followed by 0.5A. Top graph represents the evolution of friction coefficient and bottom part the evolution of contact resistance with cycles.

Fig. 277 presents the three repetitions with both CoF and contact resistance under current. In all cases, a friction increase is observed after current application, most likely because the tribofilm is rapidly damaged. The contact resistance remains relatively stable at ~0.6 Ω, and we do not observe the two distinct phases (low resistance without tribofilm, higher resistance once the tribofilm is formed) that were evident when current was applied from the beginning of the test (Fig. 243). This is consistent with the fact that in the present case, the tribofilm was already established before current was introduced. Another noteworthy point is the delay systematically observed between the moment when current was applied and when it effectively passed through the contact. In tests 1 and 3, this delay lasted only a few seconds, but in test 2 it persisted for about 2 minutes and is therefore clearly visible on the resistance curve. In this case, the resistance initially reached very high values before dropping abruptly to ~0.6 Ω. This phenomenon reflects both the insulating nature of the ZDDP tribofilm and the chosen maximum voltage of 2 V. At higher voltages, it would be more difficult for the tribofilm to withstand current passage, thus reducing the observed delay.

Voltage selection therefore appears to be a critical parameter for designing tests that realistically reproduce electrified contact conditions in electric vehicles. Interestingly, in the third repetition, an infinite resistance (2 V, ~0 A) was recorded at the end of the test, suggesting that an insulating tribofilm eventually re-formed.

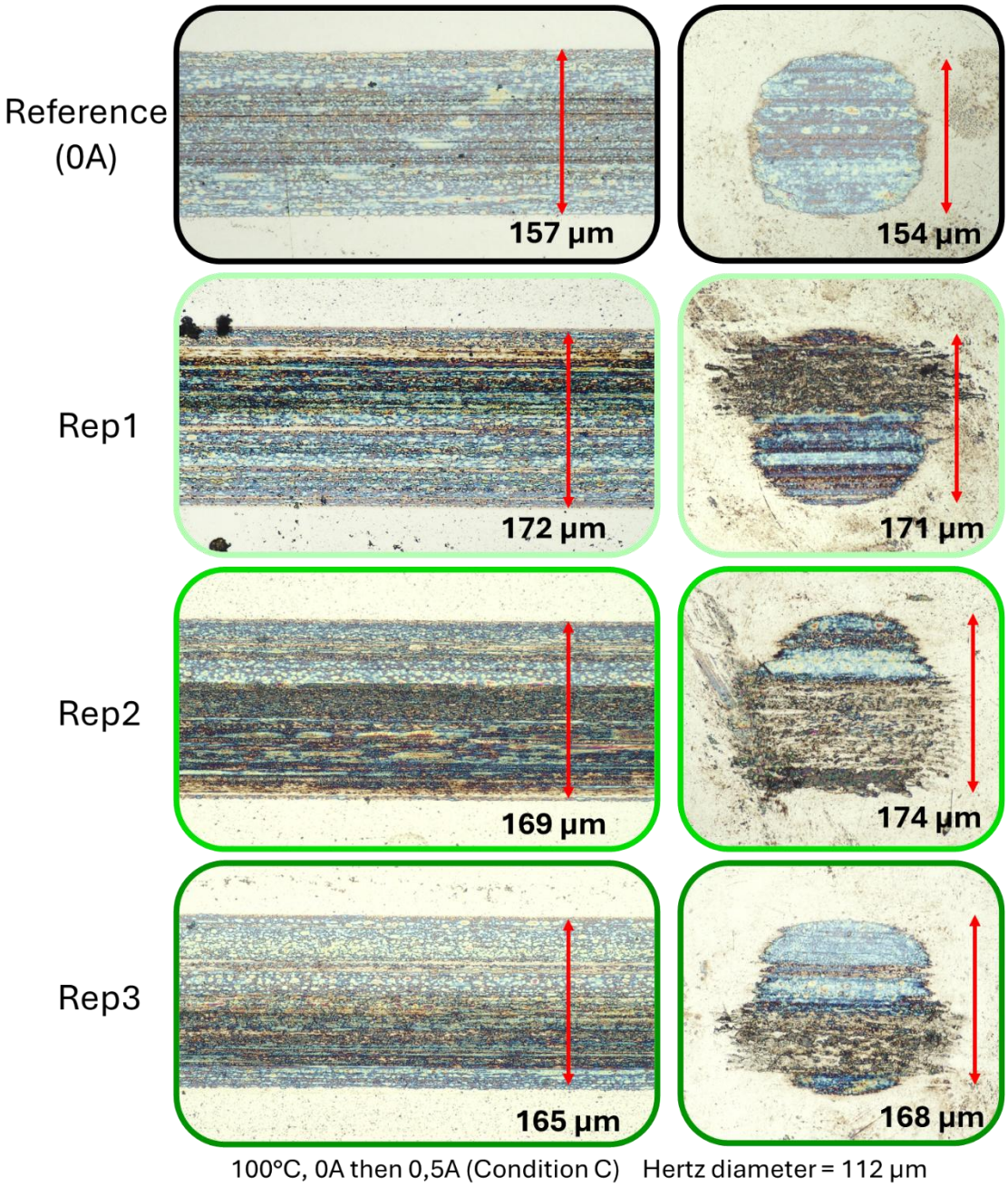

Fig. 278: Optical observations of wear tracks formed at 100°C on the discs and the balls with an applied current of 0A followed by 0.5A for the sample containing ZDDP (Zn1). Three repetitions were carried out. Test at 0A is used as a reference.

Optical observations of discs and balls (Fig. 278) confirm these interpretations: intact tribofilm areas (bluish) coexist with locally damaged darker regions, showing that current only affected some parts of the track, generating debris and compromising tribofilm integrity only locally.

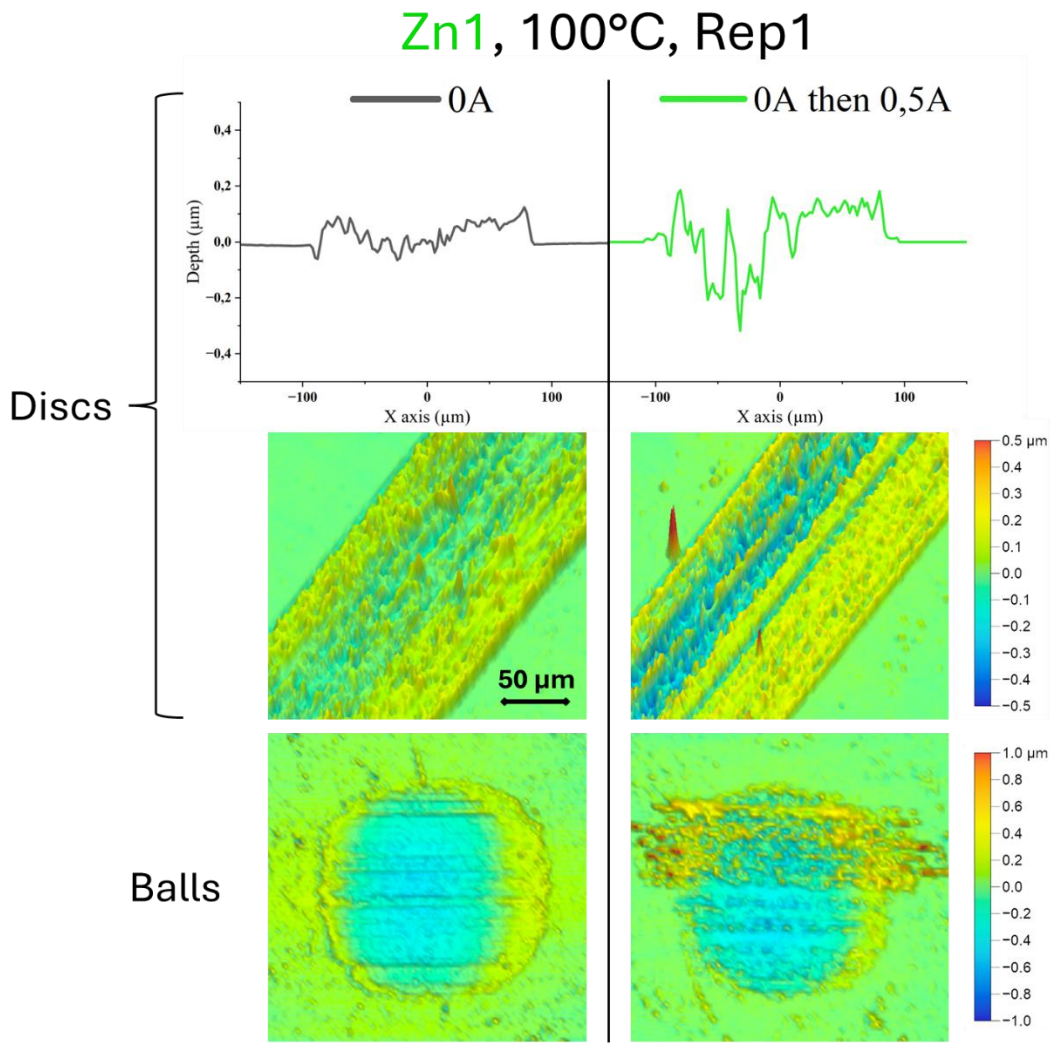

Fig. 279: Mean depth profiles and surface morphology of wear tracks formed at 100°C on the discs and the balls with an applied current of 0A followed by 0.5A in the presence of solution containing ZDDP (Zn1). Test at 0A is used as a reference.

Profilometric measurements (Fig. 279) further support those observations, with one side of the contact showing intact tribofilm while the opposite side is severely scratched. Consistently with earlier results, a thick deposit formed on the ball, on the same side as the scratched region of the disc. This confirms that current promotes the adhesion of wear debris to the cathode (the ball here), which then damages the anode (the disc). The origin of these debris particles remains uncertain: they could simply be residues generated during tribofilm formation, or they might result from current-induced processes such as local microwelding events between anode and cathode, followed by mechanical rupture, which would detach substrate fragments that subsequently adhere to the ball surface.

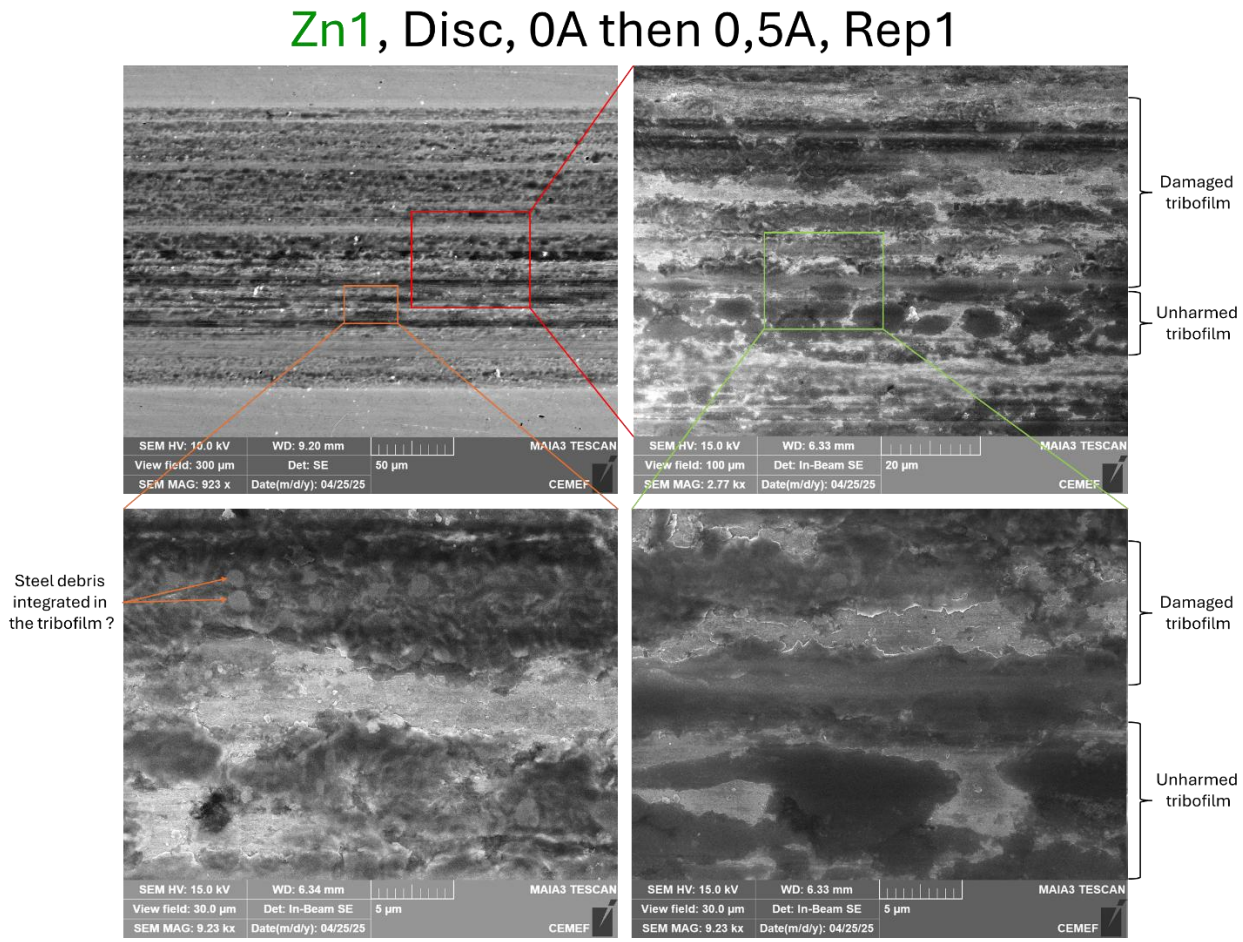

Fig. 280: High magnification SEM observations of a tribofilm formed on the disc at 100°C with an applied current of 0A followed by 0.5A in the presence of Zn1 solution.

SEM observations (Fig. 280) indicate that the damaged tribofilm exhibits a less homogeneous morphology compared with intact regions. When unaffected, the ZDDP-derived plateaus appear smooth, continuous, and relatively dark in contrast. After current passage, however, the plateaus show alternating bright and dark features: the darker zones correspond to light elements such as C, P, S, and O, whereas the brighter ones correspond to heavier elements such as Fe. This suggests that the initial tribofilm was disrupted by the deposits formed on the ball, leading to the re-formation of a tribofilm incorporating steel wear debris within its structure. This could explain why the coefficient of friction eventually decreases again after current application.

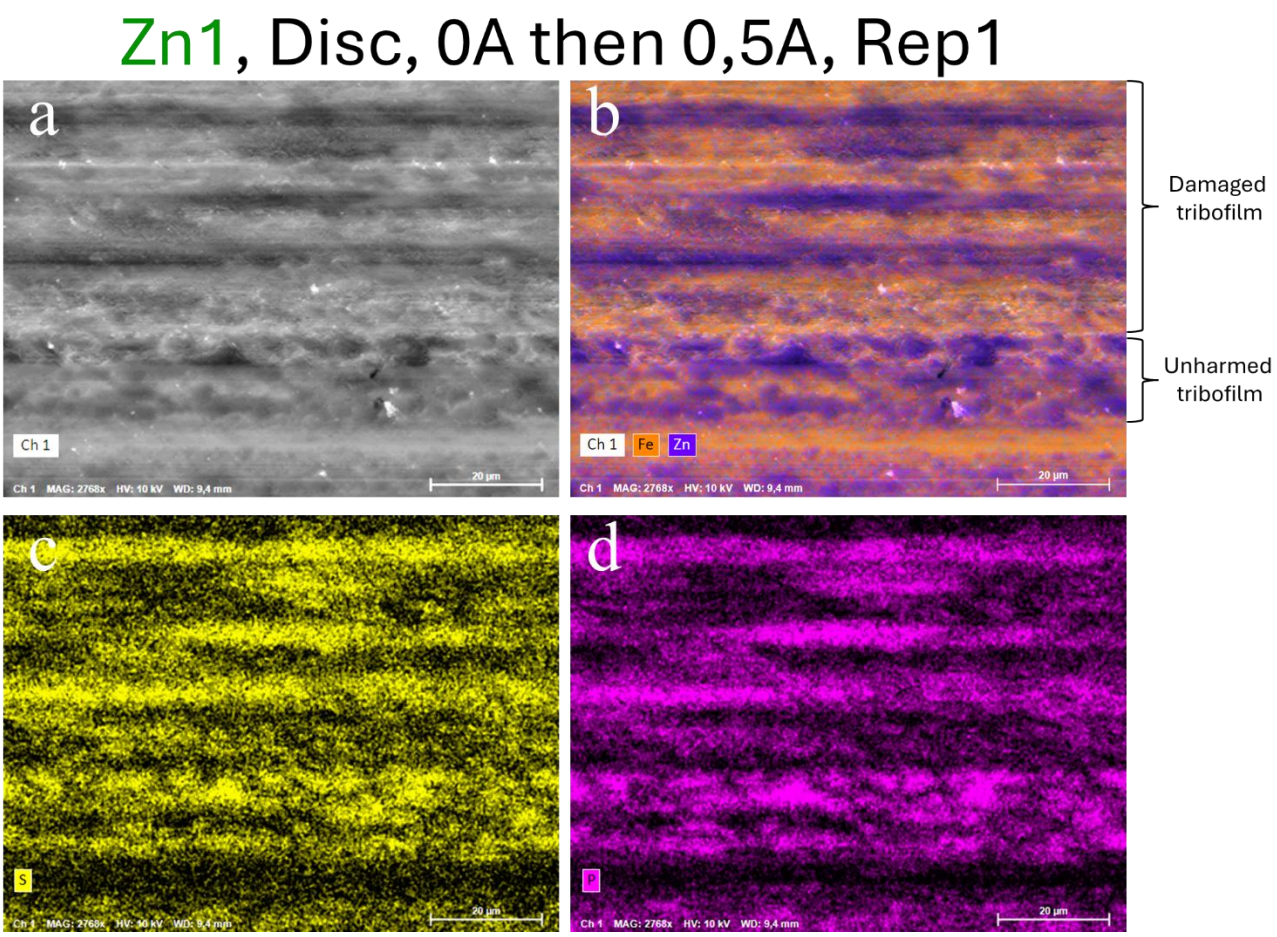

Fig. 281: SEM micrographs in SE (a) mode with EDX mapping (b, c and d) of a tribofilm formed on the disc at 100°C with an applied current of 0A followed by 0.5A in the presence of Zn1 solution (orange = Fe; purple = Zn; yellow = S; pink = P).

The EDX mapping of the disc (Fig. 281) confirms that, although a tribofilm is still present in the damaged area, it is less patchy-like and appears more elongated along the sliding direction compared with the intact region. A plausible hypothesis is that, as a deposit forms on the ball surface, it locally scratches the disc, creating elongated grooves in the sliding direction. These grooves exposes steel and therefore act as preferential sites for the reformation of the ZDDP-derived tribofilm, leading to the observed elongated appearance.

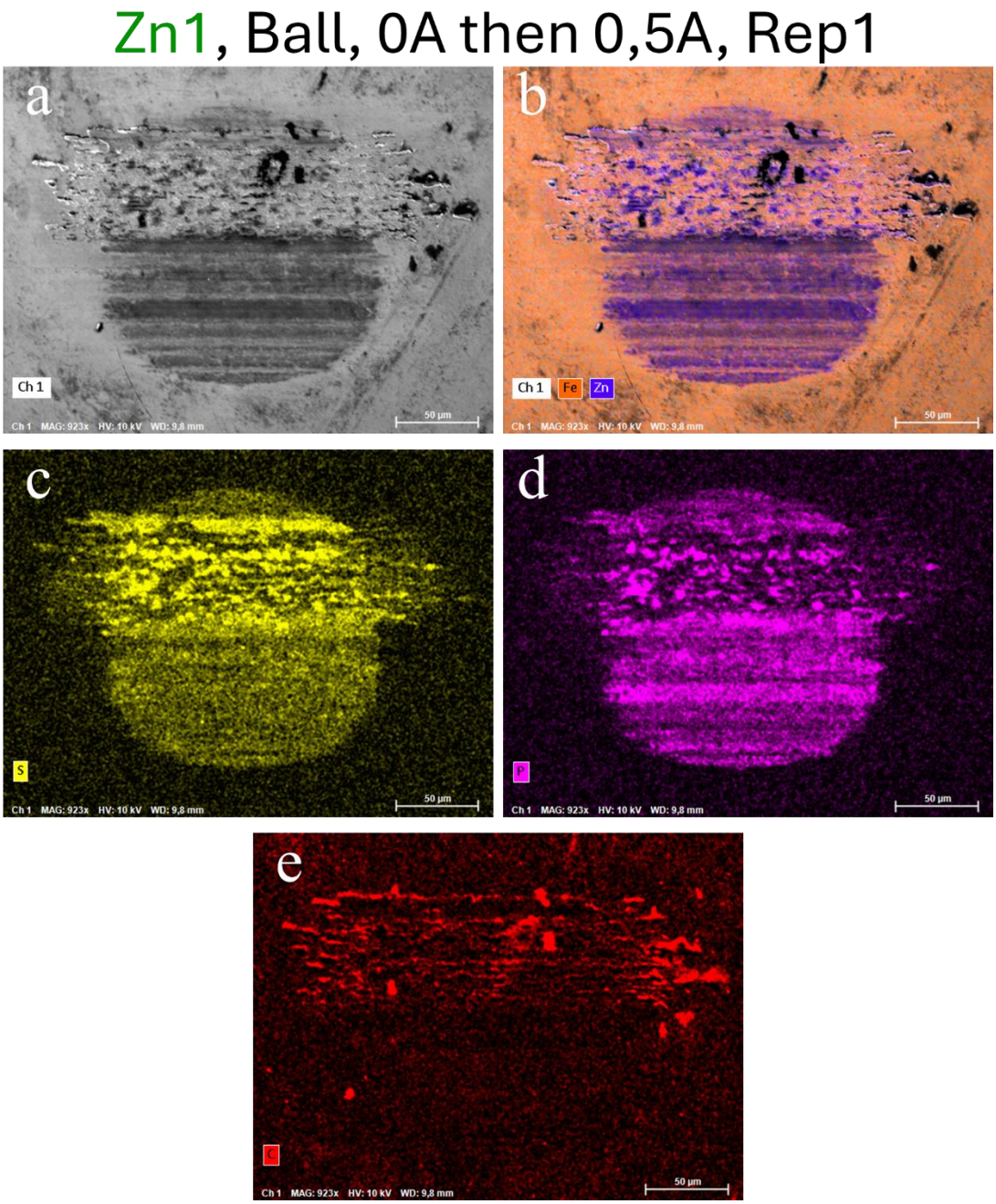

Fig. 282: SEM micrographs in SE (a) mode with EDX mapping (b, c, d and e) of a tribofilm formed on the ball at 100°C with an applied current of 0A followed by 0.5A in the presence of Zn1 solution (orange = Fe; purple = Zn; yellow = S; pink = P; red = C).

Similarly, the EDX mapping of the ball (Fig. 282) reveals that the deposit is enriched in ZDDP decomposition products, suggesting that a tribofilm may also have re-formed on the ball surface. Notably, carbon is detected in the current-affected region, which, consistent with earlier findings, points to the possible degradation of the base oil under current flow. Interestingly, P. Deshpande et al. (2024) [5] studied commercial EV lubricants under a 3A DC current ball-on-disc tribotest and showed that the decomposition of the lubricating oil led to the formation of abrasive amorphous carbon as well iron carbide, responsible for a notable increase in wear.

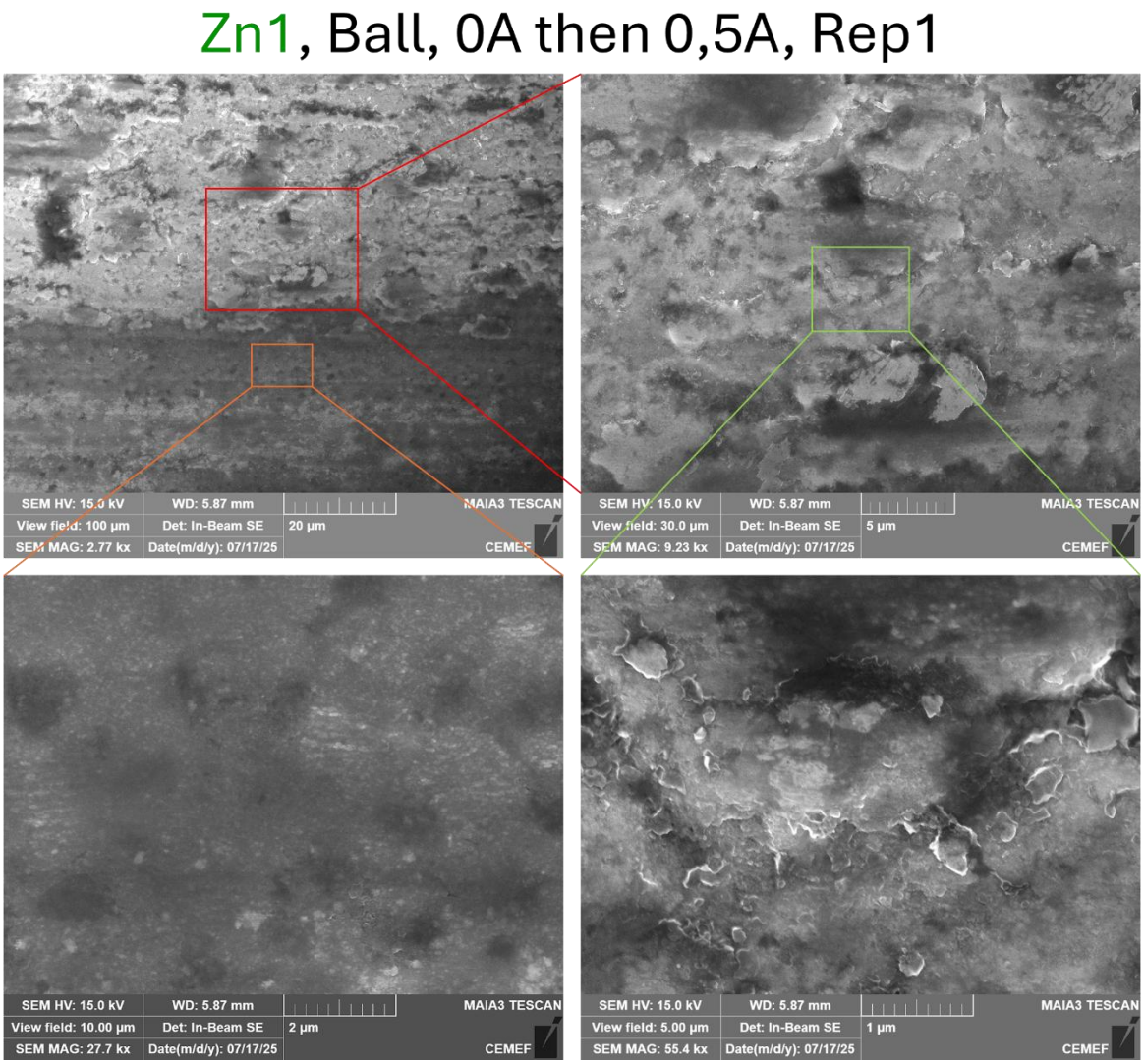

Fig. 283: High magnification SEM observations of a tribofilm formed on the ball at 100°C with an applied current of 0A followed by 0.5A in the presence of Zn1 solution.

High-magnification SEM images (Fig. 283) further illustrate these effects. On the ball, the current-affected region shows rough, uneven deposits with significant amounts of wear debris. In contrast, the unaffected region still displays a relatively continuous tribofilm, although small debris particles may be present on the surface.

at.%	Zn1 100°C		
	0A	**0,5A**	**0A then 0,5A**
C 1s	**11,7**	**12,1**	**17,4**
Fe 2p	**1,8**	**8,6**	**8,1**
O 1s	**52,2**	**52,4**	**52,1**
P 2p	**14,8**	**13,0**	**12,0**
S 2p	**2,2**	**3,4**	**3,8**
Zn 2p	**17,0**	**9,2**	**4,4**
Ca 2p	**0,4**	**1,3**	**2,3**

Table 41: XPS chemical composition of tribofilms formed in the presence of a solution containing ZDDP (Zn1) with an applied current of either 0A, 0.5A or 0A followed by 0.5A. Conducted using a NEXSA spectrometer.

XPS results (**Table 41**) show that, as in the case where current was applied from the beginning of the test, the Fe content increases, accompanied by a decrease in P and Zn. Conversely, S content rises significantly, from 2.2 at.% without current to 3.8 at.% when current is applied on an already formed tribofilm. Surprisingly, the decrease in Zn is even more pronounced than when current was applied from the onset, despite optical observations indicating that only part of the tribofilm was damaged on the wear track. One possible explanation could be that metallic debris on the surface partially masks the tribofilm. However, SEM observations did not reveal excessive amounts of debris to fully support this hypothesis. Moreover, XPS analyses were performed separately on the two zones identified optically on the disc from repetition 1 (dark in the upper region and bright in the lower region), yet no significant compositional differences were detected between them.

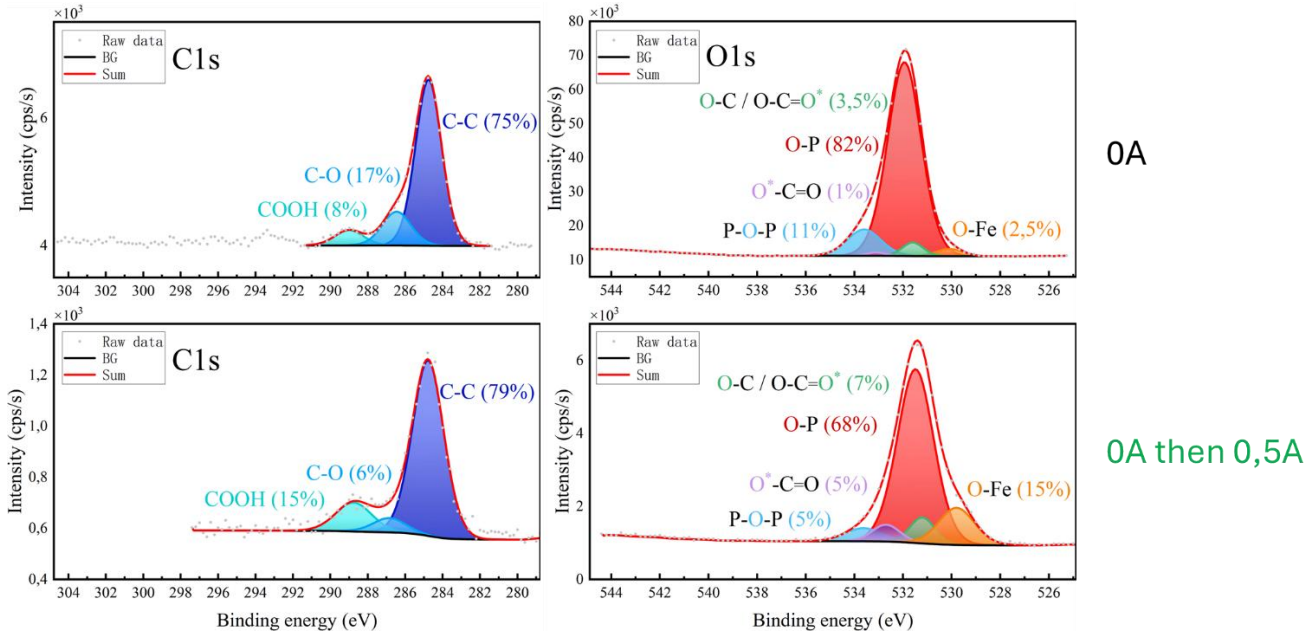

Fig. 284: C1s and O1s XPS spectra of tribofilms formed in presence of Zn1 solution with either 0A or 0A followed by 0.5A applied current.

Peak fitting of the O 1s spectrum (Fig. 284) reveals a marked increase in Fe oxides, which was less evident when current was applied from the beginning of the test (Fig. 253).

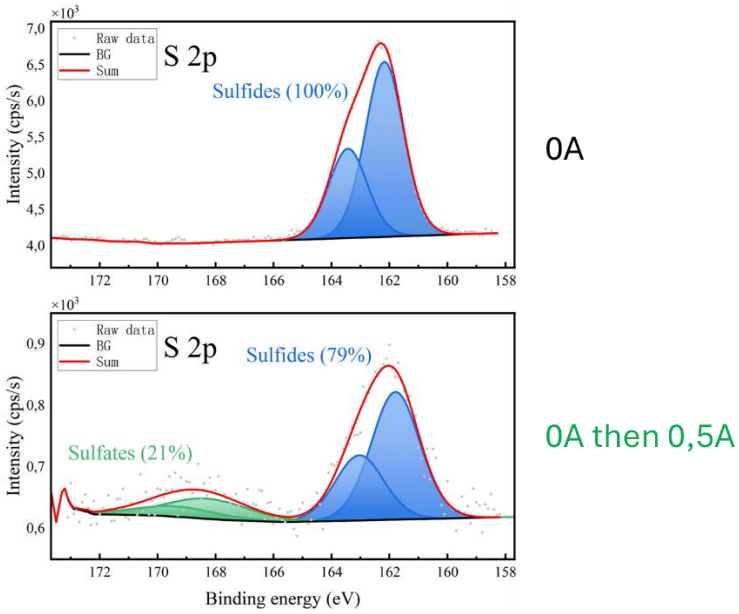

Fig. 285: S2p XPS spectrum of tribofilms formed in presence of Zn1 solution with either 0A or 0A followed by 0.5A applied current.

In addition, oxidized sulfur species such as sulfates are also detected (Fig. 285).

Overall, these results demonstrate that a pre-formed ZDDP tribofilm only partially withstands the application of electrical current. While the tribofilm initially delays current passage thanks to its insulating nature, localized breakdowns occur, leading to friction rise and instabilities, wear debris generation, and compositional changes. SEM and EDX analyses reveal that damaged areas are progressively rebuilt into tribofilms incorporating metallic debris, while XPS indicates a significant increase in Fe oxides and oxidized sulfur species, together with a pronounced depletion of Zn and P.

These findings indicate that while the ZDDP tribofilm is locally damaged by the application of current, it shows a remarkable capacity to reform, notably by incorporating metallic wear debris into its structure. This helps to restore partial surface protection and maintain friction at moderate levels. Given that the additive studied here is a primary ZDDP, which is known to form tribofilms more slowly than secondary ZDDP, the observed ability to adapt under current flow is particularly promising. One repetition even demonstrated the re-establishment of a fully insulating tribofilm by the end of the test, suggesting that long-term stabilization may be achievable. Further investigations, especially with secondary ZDDPs and prolonged tests, could therefore provide valuable insights into optimizing tribofilm resilience in electrified contacts.

After assessing the response of a ZDDP tribofilm already established before current application, the next step is to investigate the behavior of a tribofilm formed by the combination of ZDDP and silane-functionalized TiO_2 nanoparticles. This analysis will help determine whether the synergistic effects observed under non-electrified conditions are preserved under current flow. Due to time constraints, the case of tribofilms formed by nanoparticles alone could not be studied within this work.

5.2.2 Effect of Current on the Durability of a Tribofilm Formed by a blend of ZDDP and Silane-functionalized TiO_2 Nanoparticles

As in the previous section, a tribofilm was first formed without current for 2300 cycles, and then a current of 0.5A was applied (Fig. 286). The friction curves obtained over the first cycles are similar to the two cases already observed for the reference tests. When friction stabilized around 0.125 (repetitions 1 and 2), the application of current did not significantly increase the coefficient of friction, although some instability was introduced. In the case where friction stabilized around 0.11 (repetition 3), a slight increase to about 0.12 was observed, again accompanied by instability.

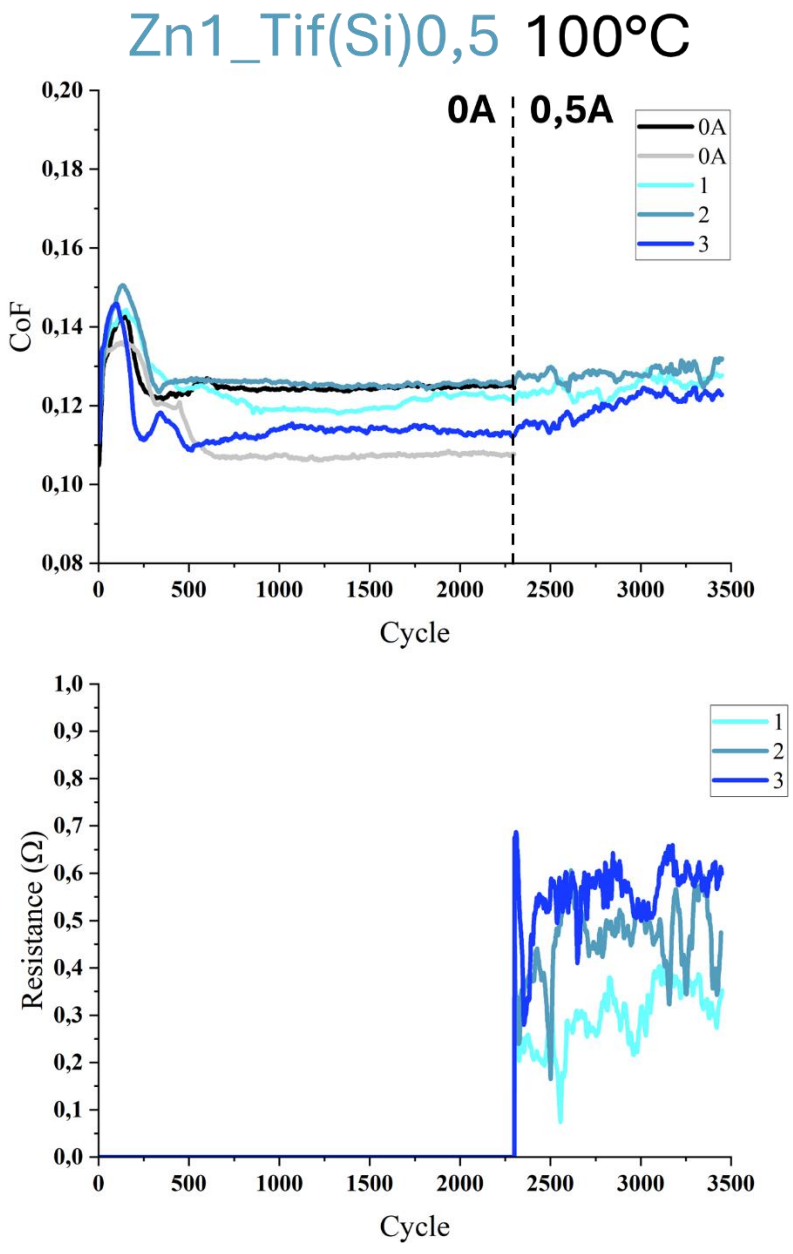

Fig. 286: Repeatability at 100°C for the sample containing a blend of ZDDP and silane-functionalized TiO_2 NPs (Zn1_Tif(Si)0.5) with an applied current of 0A followed by 0.5A. Top graph represents the evolution of friction coefficient and bottom part the evolution of contact resistance with cycles. Tests at 0A is used as references.

The measured contact resistances were relatively stable around 0.5 Ω for repetitions 2 and 3 but lower for repetition 1 (~0.3 Ω). Interestingly, unlike the tribofilm formed by ZDDP alone, the application of current occurred here almost without delay. This suggests that the tribofilm is either less insulating or that the current manages to bypass it through alternative conductive paths across the contact.

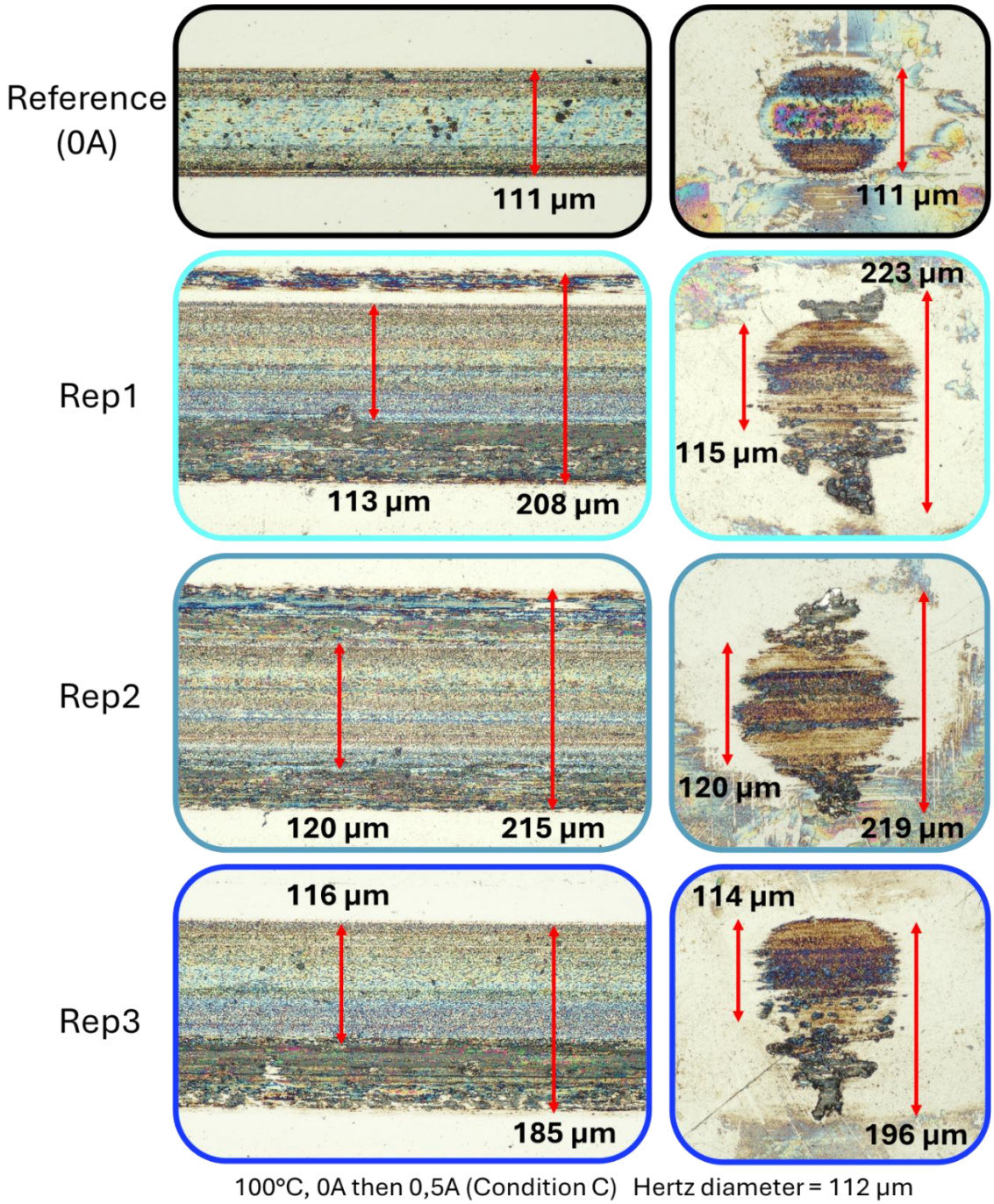

Fig. 287: Optical observations of wear tracks formed at 100°C on the discs and the balls with an applied current of 0A followed by 0.5A for the sample containing a blend of ZDDP and silane-functionalized TiO_2 NPs (Zn1_Tif(Si)0.5). Three repetitions were carried out. Test at 0A is used as a reference.

Optical observations (Fig. 287) confirm the coexistence of intact (bright) and damaged (dark) areas, as was seen with ZDDP alone. However, the location of the damaged regions differs: while they appeared in the center or at the edges of the track with ZDDP (Fig. 278), they are consistently located at the edges here, leaving the central tribofilm almost unaffected. Moreover, the track width remains very close to that of the 0A reference (111 µm), which could explain why the current flowed immediately: it bypassed the tribofilm and affected only the peripheral unprotected steel zones. On the balls, deposits were observed in locations directly facing the damaged regions of the discs. However, the central tribofilm coverage appears somewhat reduced compared with the 0A reference.

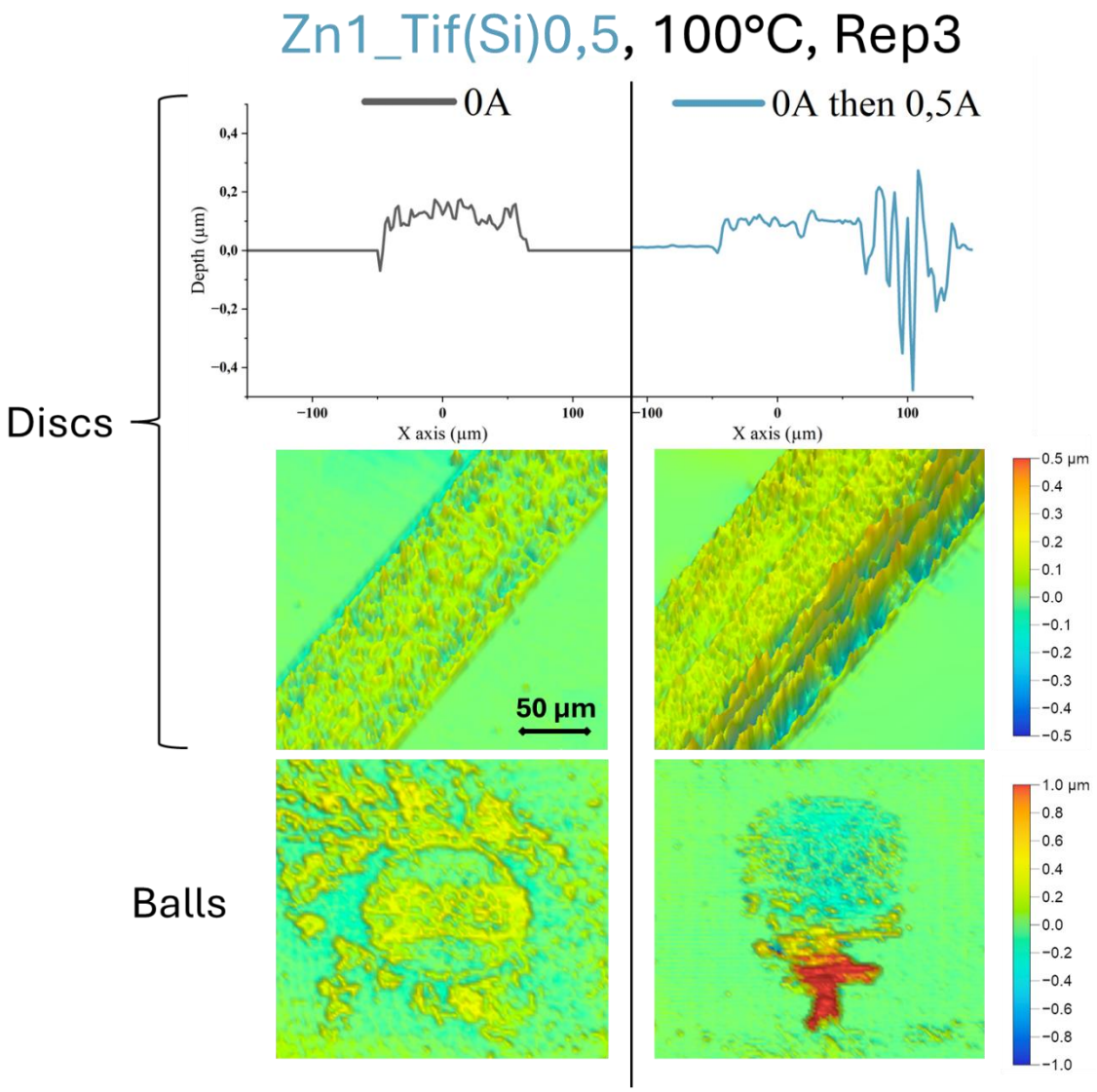

Fig. 288: Mean depth profiles and surface morphology of wear tracks formed at 100°C on the discs and the balls with an applied current of 0A followed by 0.5A in the presence of solution containing a blend of ZDDP and silane-functionalized TiO_2 NPs (Zn1_Tif(Si)0.5). Test at 0A is used as a reference.

Profilometric measurements (Fig. 288) confirm these hypotheses. The initial tribofilm does not appear to have been directly damaged by the current; instead, the adjacent steel substrate was affected. In addition, a thick deposit was observed on the ball, specifically in the area corresponding to the damaged region of the disc.

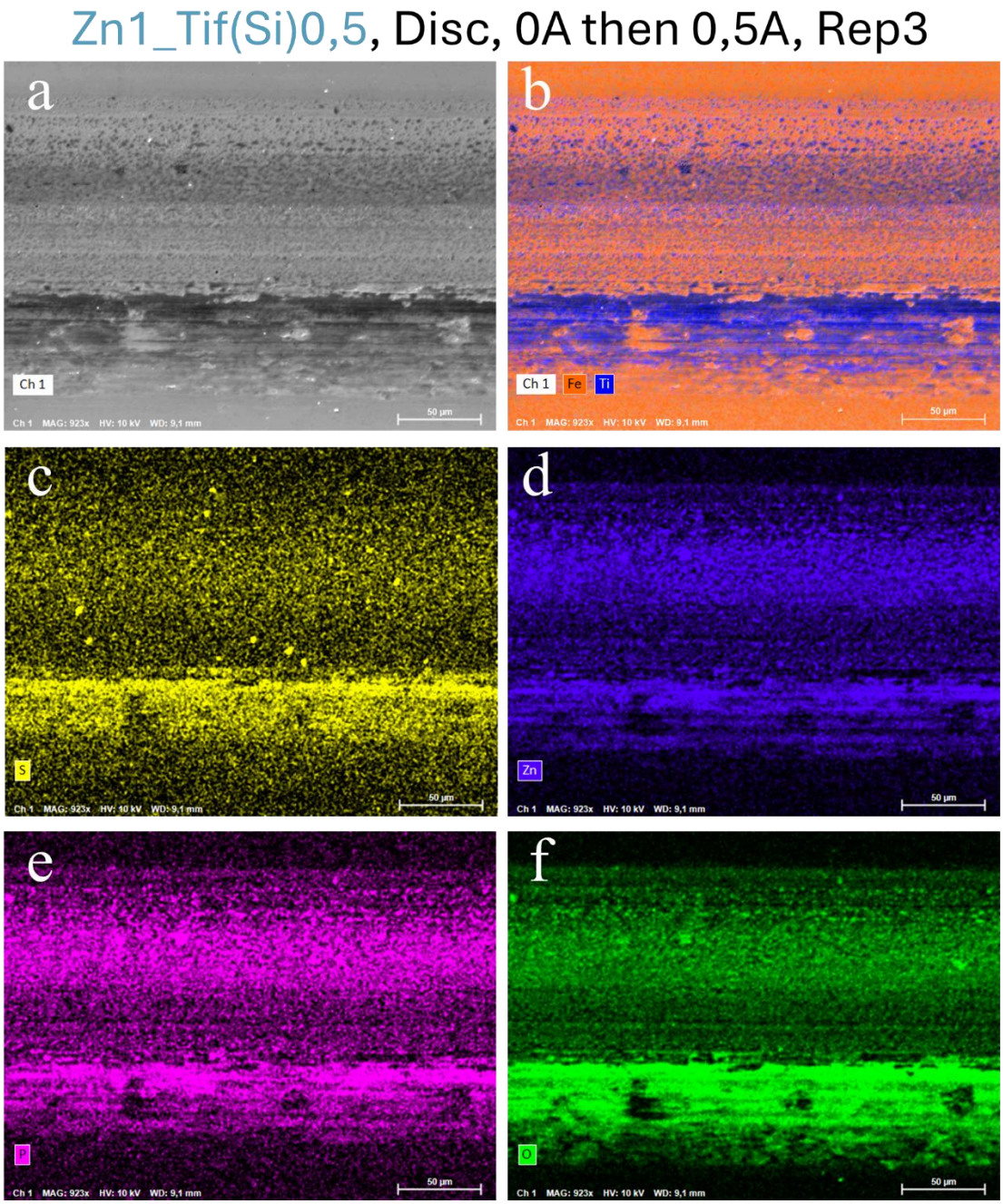

Fig. 289: SEM micrographs in SE mode (a) with EDX mapping (b, c, d, e and f) of a tribofilm formed on the disc at 100°C with an applied current of 0A followed by 0.5A in the presence of a blend of ZDDP and silane-functionalized TiO_2 NPs (Zn1_Tif(Si)0.5)
(orange = Fe; blue = Ti; yellow = S; purple = Zn; pink = P; green = O).

The EDX mapping presented in Fig. 289 shows that the region damaged after current application is rich in Ti, Zn, P, S, and O, and could therefore correspond to a tribofilm formed in response to the wear induced by the deposit on the ball, as previously observed in Section 5.1.1.

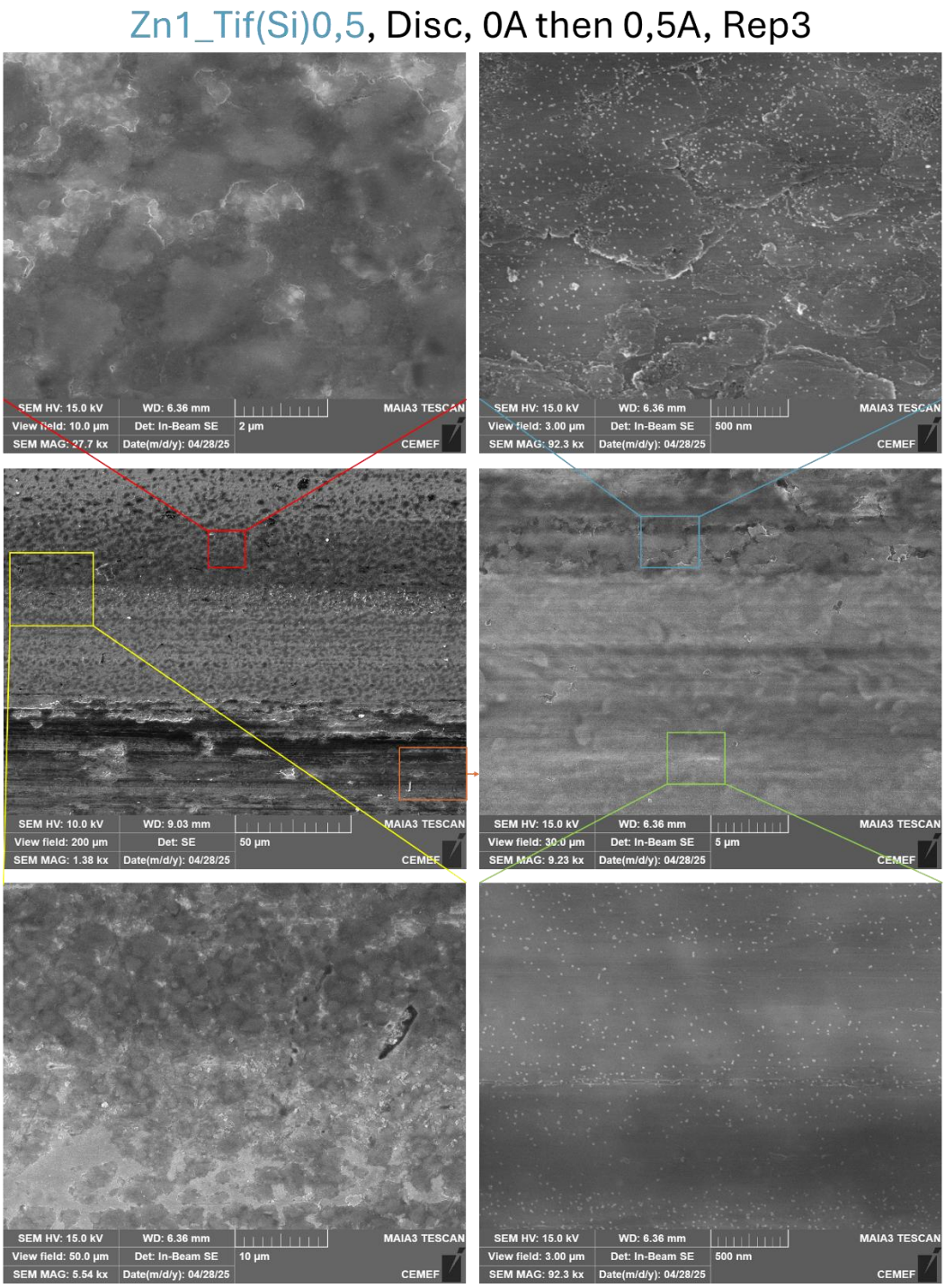

Fig. 290: High magnification SEM observations of a tribofilm formed on the disc at 100°C with an applied current of 0A followed by 0.5A in the presence of a blend of ZDDP and silane-functionalized TiO_2 NPs (Zn1_Tif(Si)0.5).

High-magnification SEM observations of the disc (Fig. 290) reveal, on one hand, a tribofilm very similar to that observed in Chapter 3, with the center of the wear track (red square) being more fully covered due to higher pressure, and the peripheral areas (yellow square) showing more widely spaced patches. In the damaged zone (orange square), both elongated patchy-like structures (blue square) and extremely smooth, elongated regions (green square) are observed. Overall, wear appears to be less severe than in the case where current was applied from the beginning of the test.

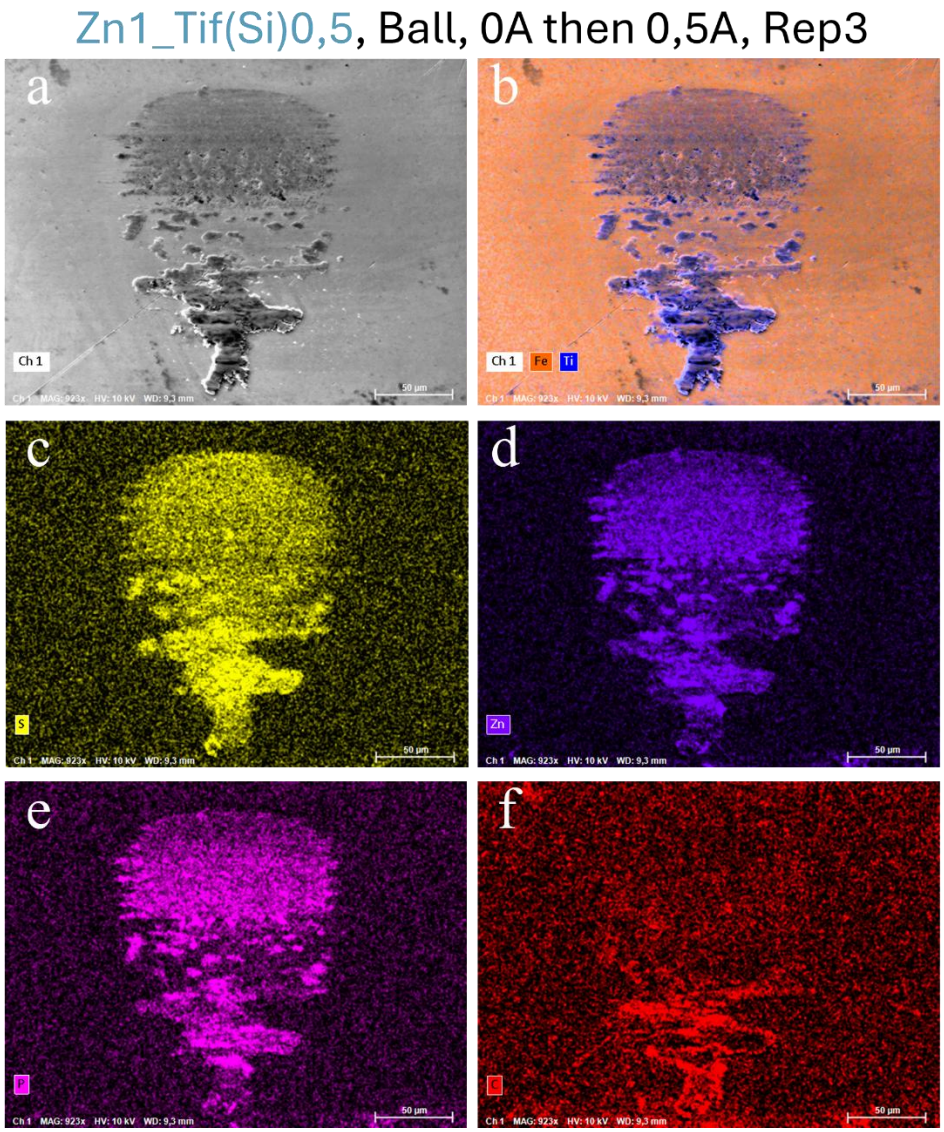

Fig. 291: SEM micrographs in SE mode (a) with EDX mapping (b, c, d, e and f) of a tribofilm formed on the ball at 100°C with an applied current of 0A followed by 0.5A in the presence of a blend of ZDDP and silane-functionalized TiO_2 NPs (Zn1_Tif(Si)0.5)
(orange = Fe; blue = Ti; yellow = S; purple = Zn; pink = P; green = O).

Similarly, the EDX mapping of the ball (Fig. 291) shows that the deposit is rich in Ti, Zn, P, and S (and O), but in this case also contains carbon, as was observed for ZDDP alone (Fig. 282).

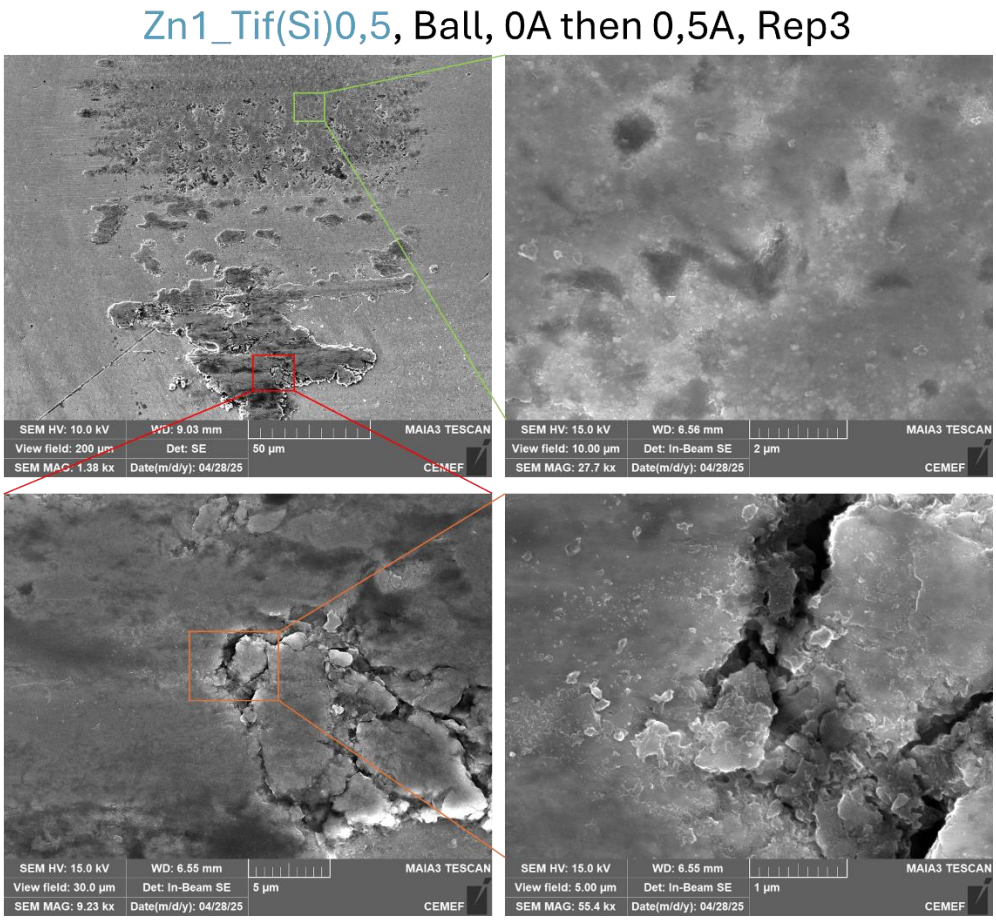

Fig. 292: High magnification SEM observations of a tribofilm formed on the ball at 100°C with an applied current of 0A followed by 0.5A in the presence of a blend of ZDDP and silane-functionalized TiO_2 NPs (Zn1_Tif(Si)0.5).

High-magnification SEM observations of the ball (Fig. 292) again show a covering tribofilm, patchy-like and relatively smooth on the plateaus in the undamaged area (green square), whereas the regions corresponding to the deposits appear highly degraded (red and orange squares).

at.%	Zn1_Tif(Si)0,5		
	0A	**0,5A**	**0A then 0,5A**
C 1s	**18,8**	**7,8**	**9,6**
Fe 2p	**1,1**	**12,8**	**9,8**
O 1s	**51,2**	**54,8**	**54,5**
P 2p	**8,6**	**3,8**	**6,3**
S 2p	**1,6**	**1,0**	**1,7**
Zn 2p	**4,6**	**2,9**	**4,5**
Si 2p	**0,9**	**2,5**	**1,3**
Ti 2p	**11,1**	**11,7**	**9,6**
Ca 2p	**2,1**	**2,6**	**2,8**

Table 42: XPS chemical composition of tribofilms formed in the presence of a solution containing a blend of ZDDP and silane-functionalized TiO_2 NPs (Zn1_Tif(Si)0.5) with an applied current of either 0A or 0A followed by 0.5A. Conducted using a NEXSA spectrometer.

The XPS measurements (**Table 42**) indicate that the tribofilm exhibits a composition intermediate between the reference condition (0A) and the case where 0.5A was applied from the start of the test. A significant amount of iron is therefore detected (9.8 at.%), most likely associated with the generation of wear debris, although its concentration remains lower than in the case of immediate 0.5A current application (12.8 at.%).

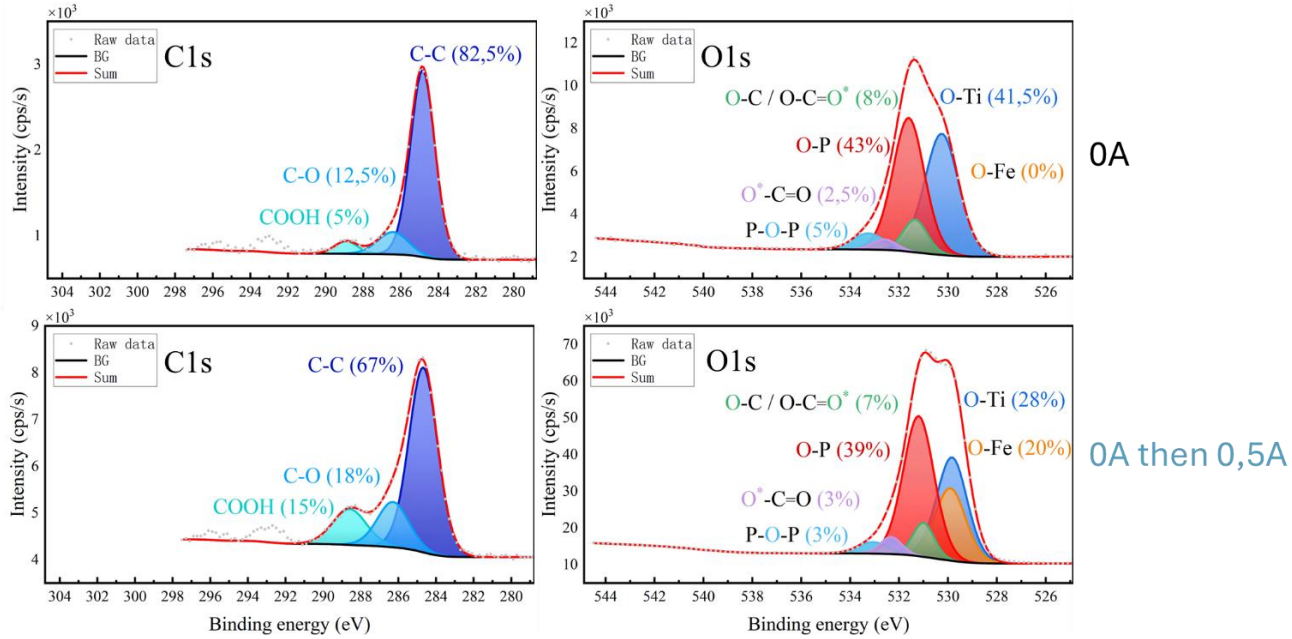

Fig. 293: C1s and O1s XPS spectra of tribofilms formed in presence of a blend of ZDDP and silane-functionalized TiO_2 NPs (Zn1_Tif(Si)0.5) with either 0A or 0A followed by 0.5A applied current.

Fig. 293 shows that this iron is mainly present in the form of iron oxides, while both phosphates resulting from ZDDP decomposition and TiO_2 nanoparticles are still present.

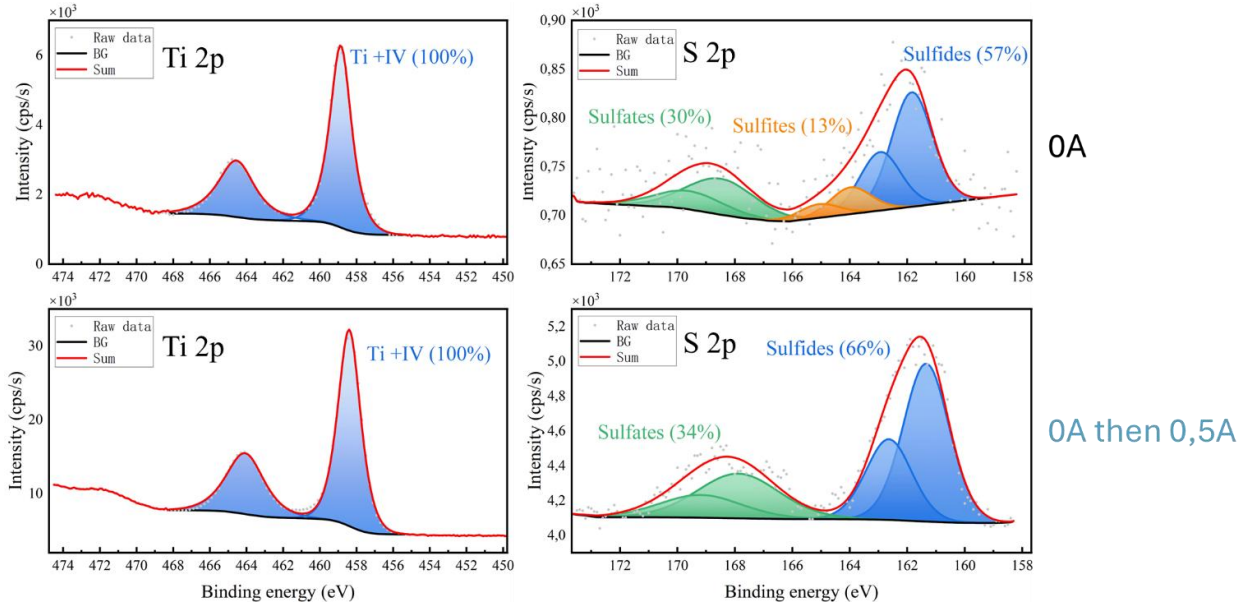

Fig. 294: Ti2p and S2p XPS spectra of tribofilms formed in presence of a blend of ZDDP and silane-functionalized TiO_2 NPs (Zn1_Tif(Si)0.5) with either 0A or 0A followed by 0.5A applied current.

Titanium is again detected as TiO_2, whereas sulfur is present as a mixture of metallic sulfides and sulfates (Fig. 294).

Overall, the results show that the tribofilm formed from the ZDDP/silane-functionalized TiO_2 nanoparticles mixture demonstrates a relatively good resistance to current flow. Unlike pure ZDDP, the current does not directly damage the tribofilm but instead bypasses it, leading to localized degradation of the adjacent steel substrate. The tribofilm is able to maintain its coverage in the most highly loaded areas and even reforms locally in response to wear. Its chemical composition does not seem to be fundamentally altered but it is likely that steel debris are integrated in the newly formed tribofilm.

During these experiments, we repeatedly observed the formation of thick deposits either on the ball alone or simultaneously on both ball and disc. In several cases, these deposits appeared to consist of successive layers of metallic wear debris and tribofilm reacting on these debris. This phenomenon seemed more pronounced in the presence of nanoparticles, owing to their ability to rapidly form tribofilms on freshly exposed steel particles.

To verify this hypothesis, we designed a final experiment. A tribofilm was first formed during 2300 cycles using the ZDDP/silane-functionalized TiO_2 nanoparticle mixture. The test was then stopped, and the disc and the ball were cleaned with hexane to remove the lubricant, which was replaced with pure PAO6. The test was then restarted for an additional 1150 cycles under an applied current of 0.5 A. This protocol allows us not only to assess the role of additives in mitigating damage caused by current flow but also to evaluate the robustness of the pre-formed tribofilm of the mixture under very severe conditions.

Fig. 295 shows the evolution of the coefficient of friction and the contact resistance for the three repetitions. In all cases, before cleaning and applying the current, the CoF stabilized around 0.125. For repetition 1, the friction did not increase after current application but became unstable, while the contact resistance remained relatively stable. For repetition 2, the CoF immediately increased to 0.14 together with the resistance (from 0.4 to 0.6 Ω). Both values then rapidly decreased, with the CoF returning to 0.125 and the resistance to ~0.2 Ω, which likely indicates a high proportion of direct metal-to-metal contact between the ball and the disc. Subsequently, a sharp rise of the CoF (up to 0.20) was observed, followed by an equally abrupt drop to 0.12, mirrored by resistance variations (0.4 Ω down to 0.15 Ω). For repetition 3, the CoF showed an even more pronounced increase (from 0.125 to 0.175), before stabilizing near 0.14. The resistance followed the same trend, first rising to 0.6 Ω, then decreasing and stabilizing at ~0.15 Ω.

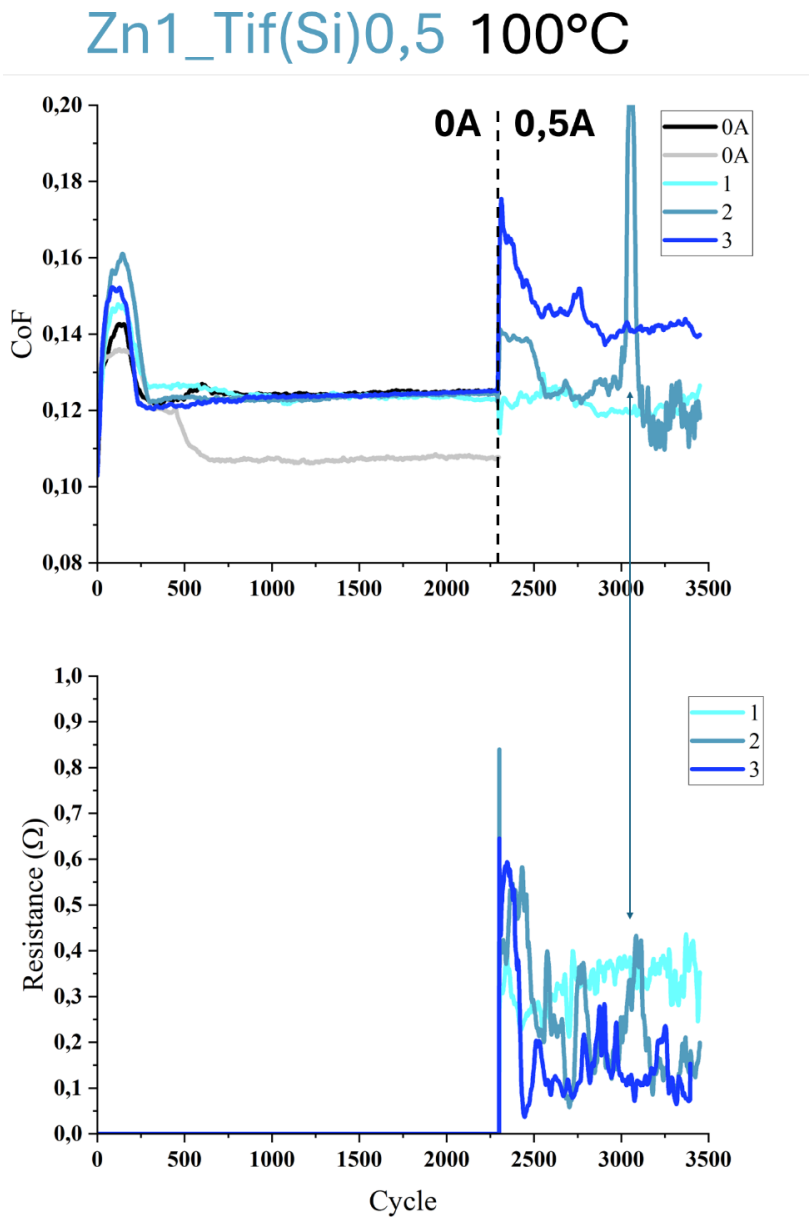

Fig. 295: Repeatability at 100°C with an applied current of 0A with a blend of ZDDP and silane-functionalized TiO_2 NPs (Zn1_Tif(Si)0.5) followed by 0.5A with PAO6. Top graph represents the evolution of friction coefficient and bottom part the evolution of contact resistance with cycles. Tests at 0A with Zn1_Tif(Si)0.5 are used as references.

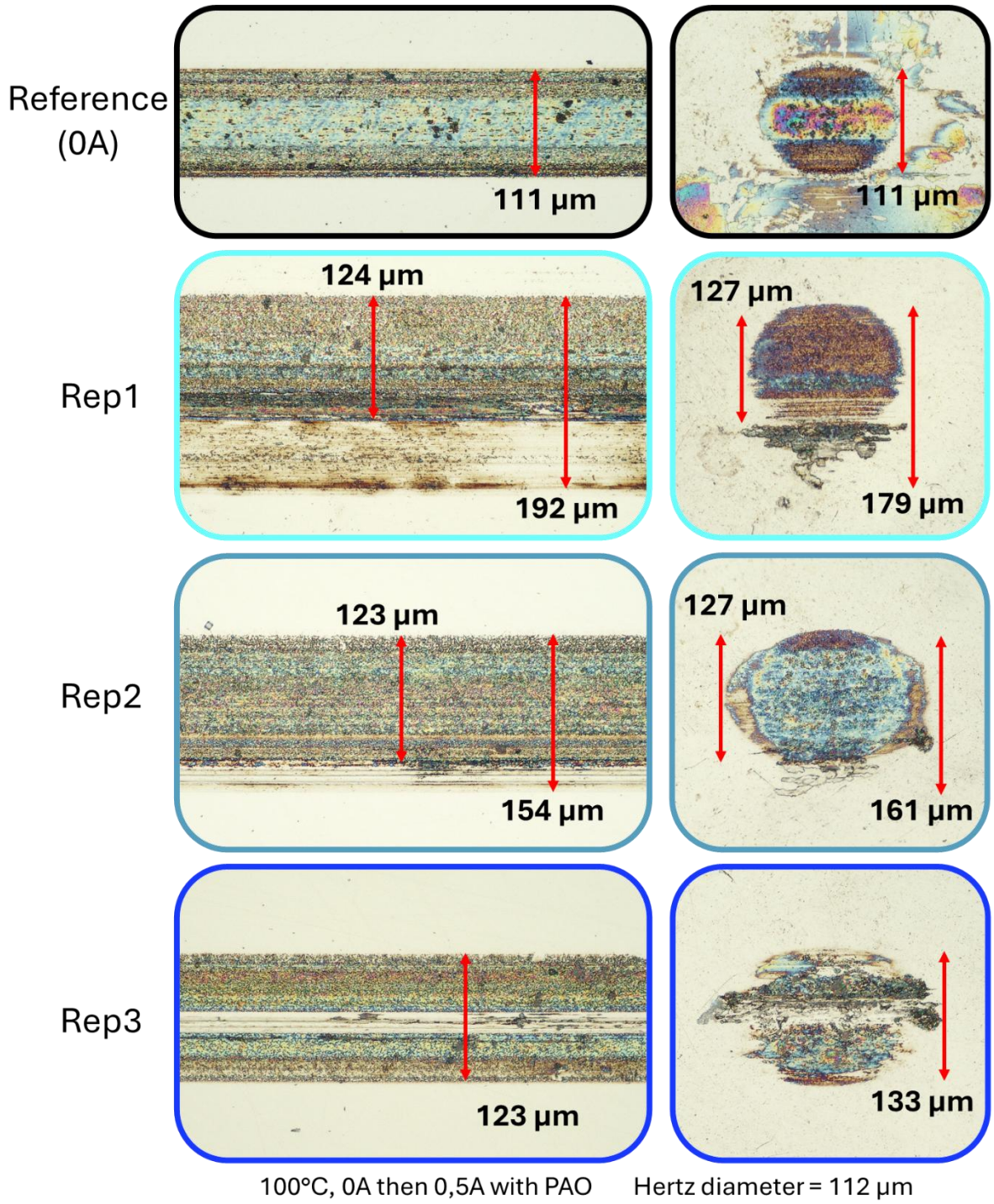

Fig. 296: Optical observations of wear tracks formed at 100°C on the discs and the balls with an applied current of 0A with a blend of ZDDP and silane-functionalized TiO_2 NPs (Zn1_Tif(Si)0.5) followed by 0.5A with PAO6. Three repetitions were carried out. Test at 0A is used as a reference.

Optical observations (Fig. 296) revealed that in the first two tests, the tribofilm remained intact on the discs, while adjacent steel areas were damaged. This indicates that the tribofilm was able to resist current flow, which bypassed it to attack unprotected steel. In contrast, in repetition 3, the tribofilm was ruptured in its central region, explaining both the sharp increase in friction and the very low, constant resistance (~0.15 Ω) characteristic of direct steel-on-steel contact. The balls did not show deposits as dark as in previous experiments, but once again, these deposits are likely responsible for damaging the disc surfaces.

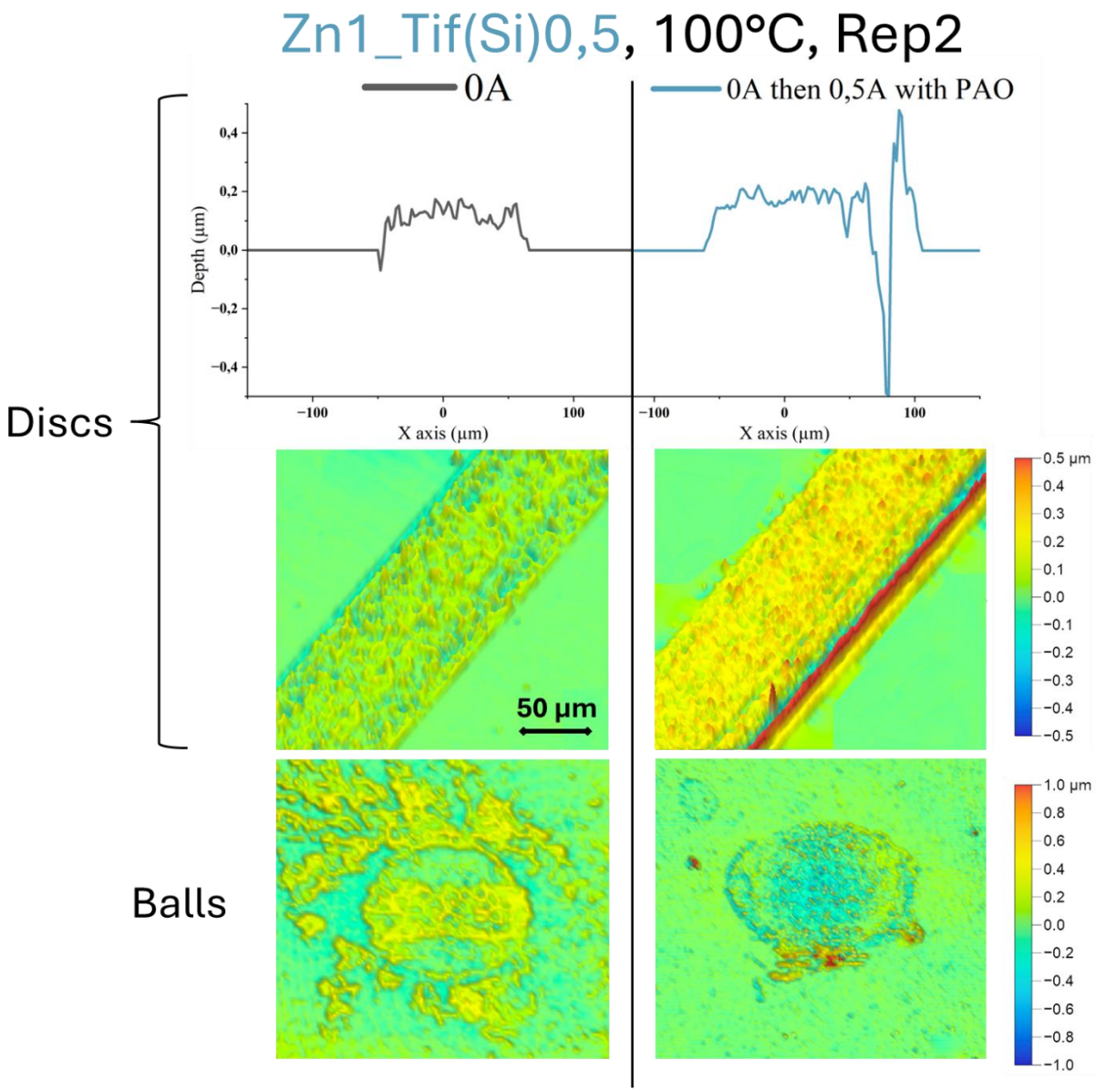

Fig. 297: Mean depth profiles and surface morphology of wear tracks formed at 100°C on the discs and the balls with an applied current of 0A with a blend of ZDDP and silane-functionalized TiO_2 NPs (Zn1_Tif(Si)0.5) followed by 0.5A with PAO6. Test at 0A is used as a reference.

Profilometric measurements (Fig. 297) confirmed these observations. In repetition 2, the tribofilm was not significantly damaged, but the adjacent steel substrate of the disc was severely scratched and ploughed, leading to noticeable material displacement. On the corresponding area on the ball, deposits were found, which are likely at the origin of the scratches observed on the disc.

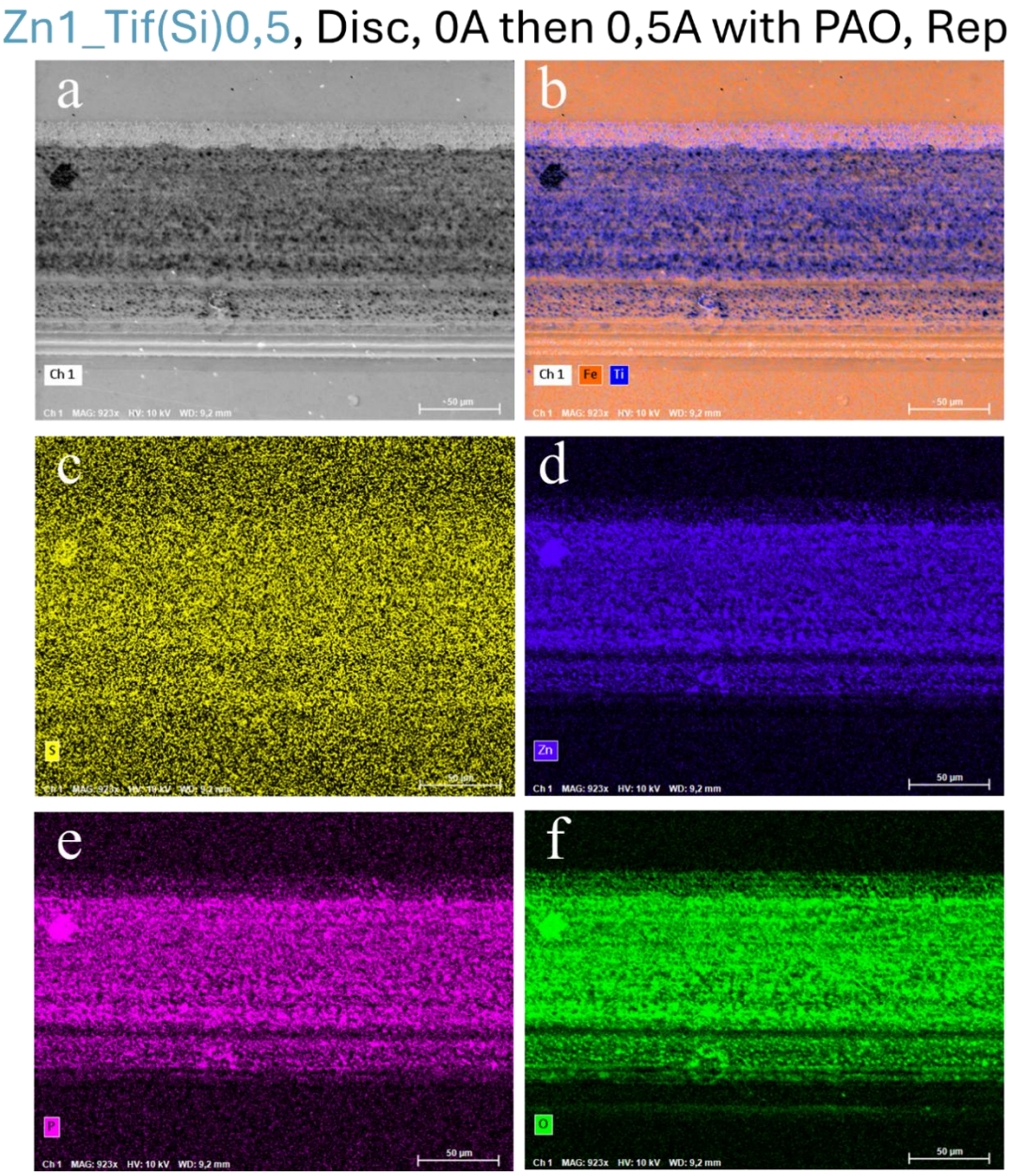

Fig. 298: SEM micrographs in SE mode (a) with EDX mapping (b, c, d, e and f) of a tribofilm formed on the disc at 100°C with an applied current of 0A with a blend of ZDDP and silane-functionalized TiO_2 NPs (Zn1_Tif(Si)0.5) followed by 0.5A with PAO6
(orange = Fe; blue = Ti; yellow = S; purple = Zn; pink = P; green = O).

The EDX mapping of the disc (Fig. 298) clearly distinguishes the tribofilm from the scratch formed at the bottom of the wear track. Unlike the previous experiments, where the lubricant still contained either ZDDP, nanoparticles, or their mixture at the time of current application, the damaged area here is composed only of steel. No traces of Ti, typically associated with nanoparticle-containing mixtures, were detected, nor were any ZDDP-derived elements, which is fully consistent with the applied test protocol.

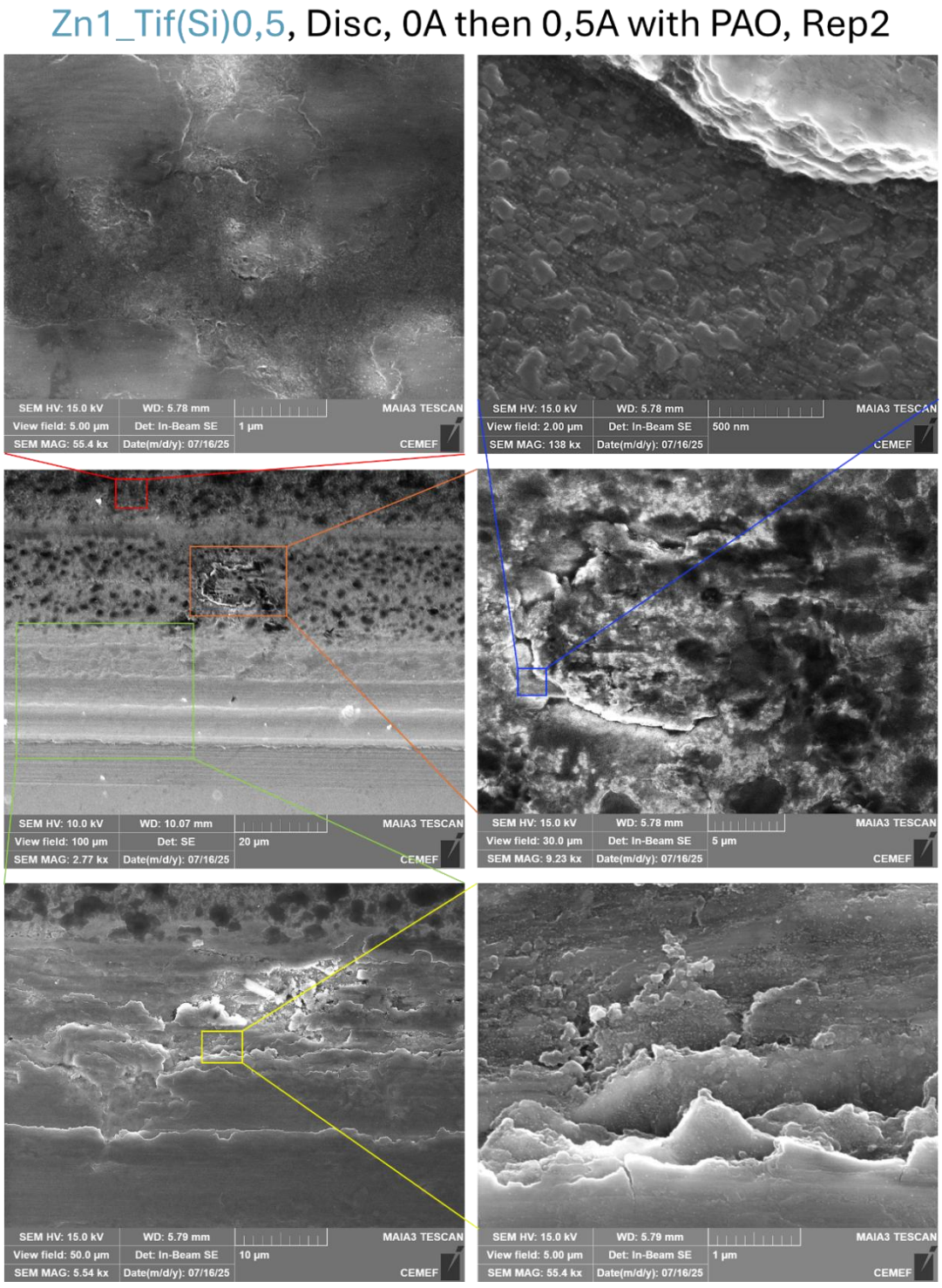

Fig. 299: High magnification SEM observations of a tribofilm formed on the disc at 100°C with an applied current of 0A with a blend of ZDDP and silane-functionalized TiO_2 NPs (Zn1_Tif(Si)0.5) followed by 0.5A with PAO6.

High magnification SEM observations of the disc (Fig. 299) highlight the different structures observed along the wear track. The undamaged tribofilm region (red square) retains its typical patchy-like morphology, with relatively smooth plateaus.

A locally damaged area (orange square) shows a fragment of tribofilm that appears on the verge of detachment. Given the size of this structure (~10 µm wide), it is even possible that it corresponds to a fragment of substrate being torn away together with the overlying tribofilm.

A zoom on the edge of this particle (blue square) reveals a layered structure, though at this scale it is difficult to determine whether the layers are tribofilm or substrate. The surrounding area exhibits a morphology that differs from the tribofilm usually formed by the ZDDP/TiO_2 (silane) mixture: small island-like features are present, but they are considerably smaller (~100 nm) than the 500–1000 nm patches typically observed.

The scratched region outside the tribofilm (green square) presents elongated grooves aligned with the sliding direction, with wear debris visible inside the troughs. A close-up view (yellow square) reveals successive layers of steel torn and plastically deformed.

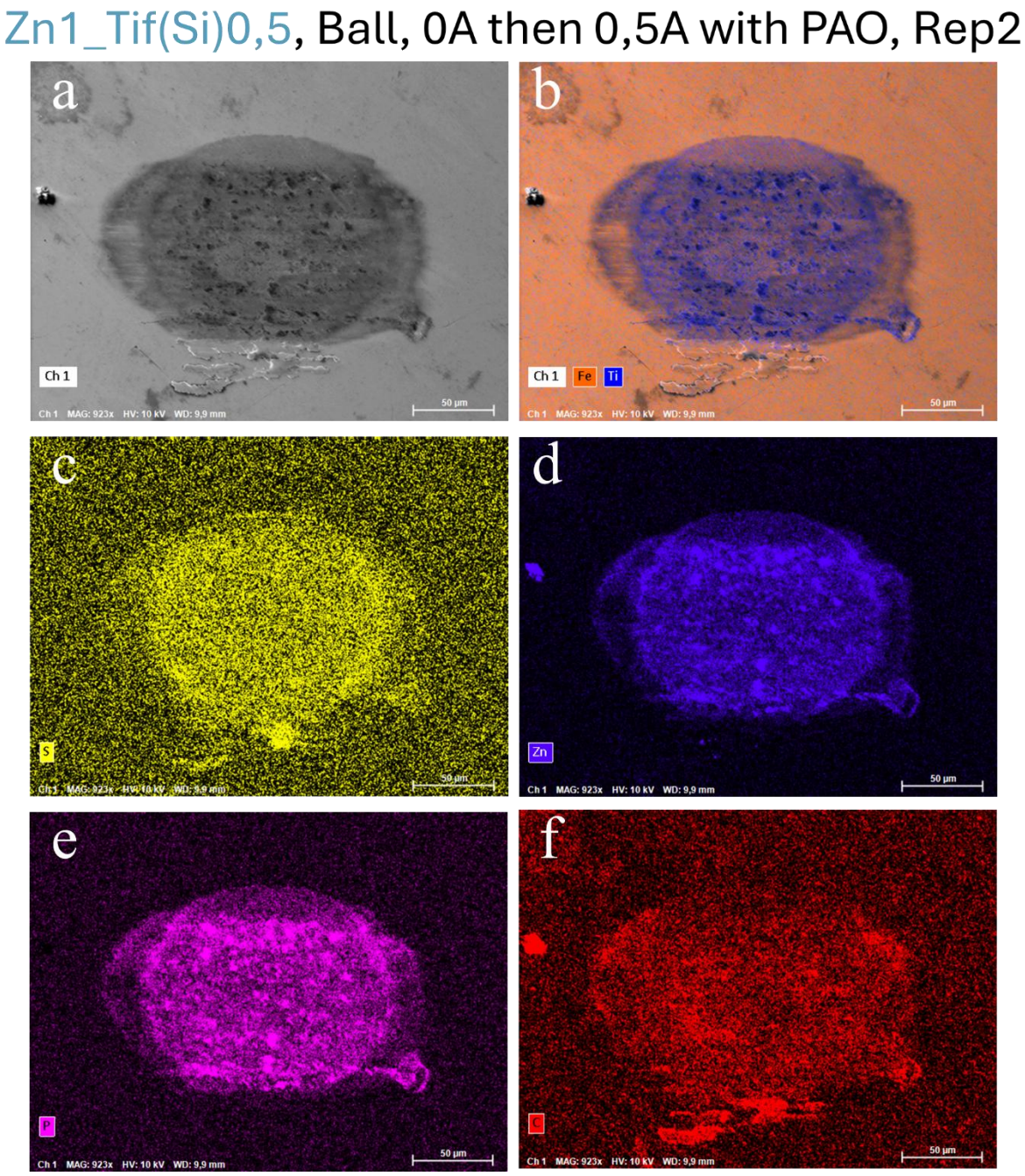

Fig. 300: SEM micrographs in SE mode (a) with EDX mapping (b, c, d, e and f) of a tribofilm formed on the ball at 100°C with an applied current of 0A with a blend of ZDDP and silane-functionalized TiO_2 NPs (Zn1_Tif(Si)0.5) followed by 0.5A with PAO6
(orange = Fe; blue = Ti; yellow = S; purple = Zn; pink = P; red = C).

EDX mapping of the ball (Fig. 300) confirms that, as on the disc, the tribofilm is still present and composed of ZDDP- and TiO_2-derived elements. However, the islands are not solely composed of Fe; a significant carbon contribution is also detected in these regions.

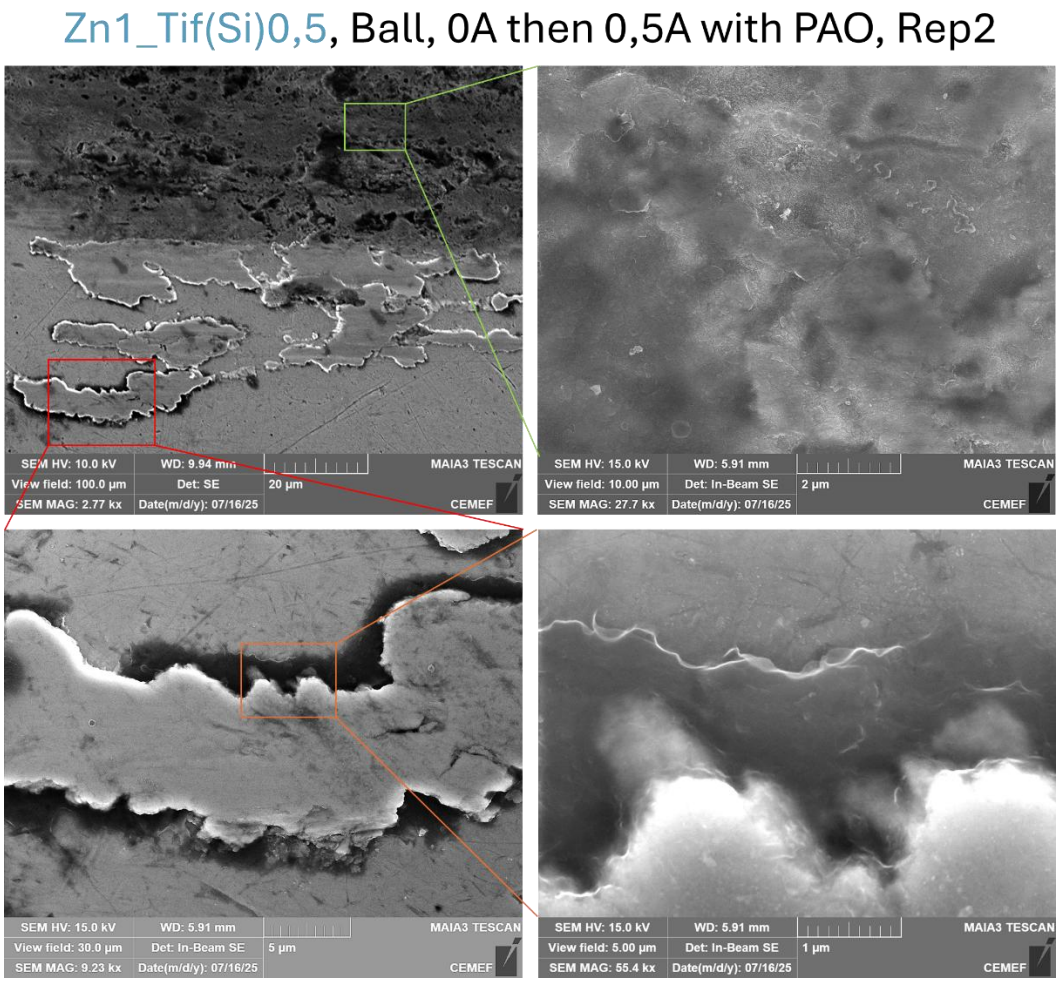

Fig. 301: High magnification SEM observations of a tribofilm formed on the ball at 100°C with an applied current of 0A with a blend of ZDDP and silane-functionalized TiO_2 NPs (Zn1_Tif(Si)0.5) followed by 0.5A with PAO6.

SEM observations of the ball (Fig. 301) show a well-developed tribofilm in the unaffected region (green square). Focusing on one of the deposits (red square), the structure appears smooth, surrounded at its base by a darker material. This darker contrast likely corresponds to a carbon-rich species, as indicated by the EDX mapping. From a distance, this feature might resemble a liquid residue such as PAO or a cleaning solvent. However, a closer inspection (orange square) reveals irregular contours at the edges, suggesting that the phase is more likely a solid.

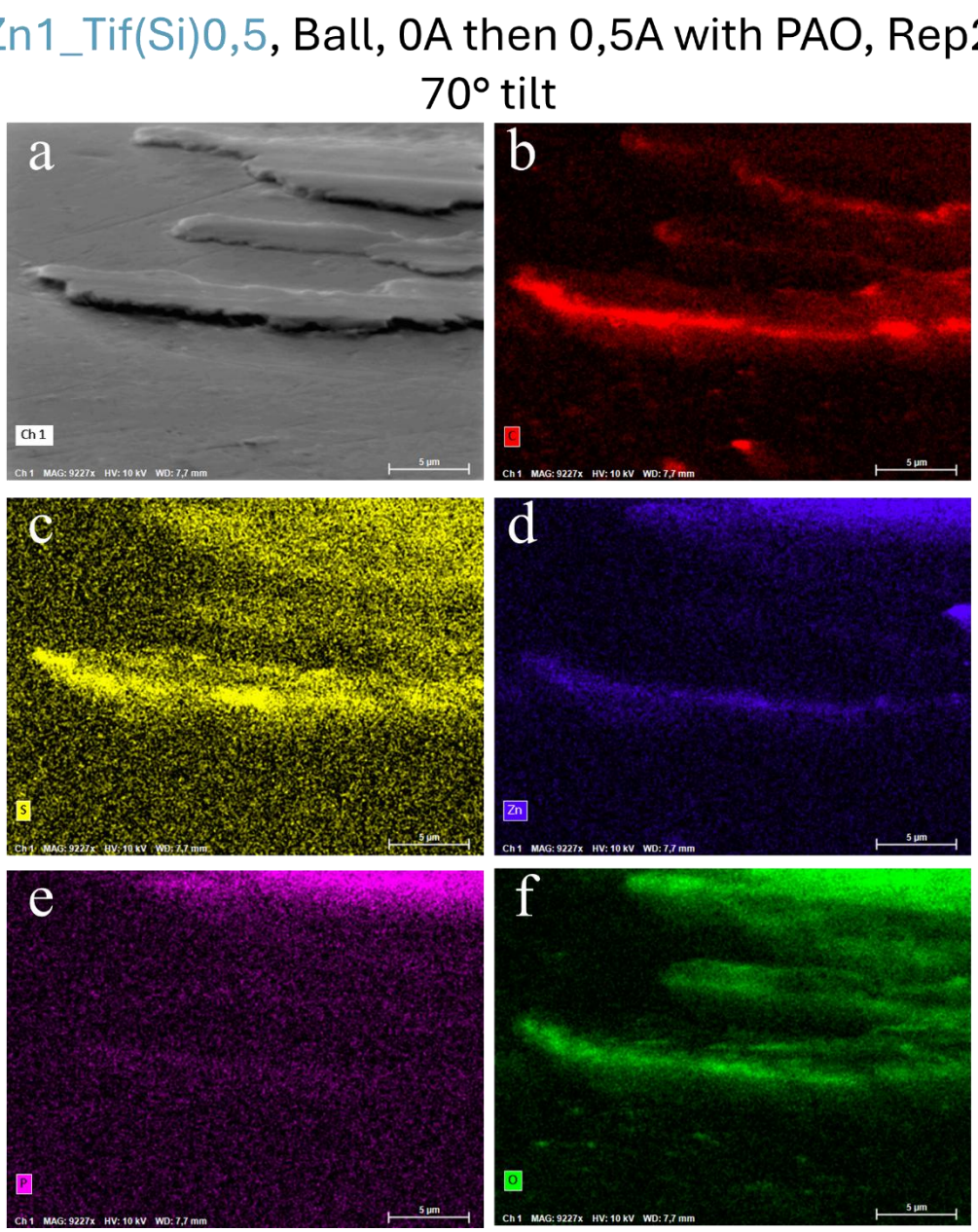

Fig. 302: SEM micrographs in SE mode (a) with EDX mapping (b, c, d, e and f) of a tribofilm formed on the ball at 100°C with an applied current of 0A with a blend of ZDDP and silane-functionalized TiO_2 NPs (Zn1_Tif(Si)0.5) followed by 0.5A with PAO6
(red = C; yellow = S; purple = Zn; pink = P; green = O).

To further investigate, the ball was tilted by 70° and re-analyzed with SEM and EDX (Fig. 302). These observations clearly reveal carbon at the base of the metallic deposit, but also sulfur, zinc, and oxygen. Although Zn, P, S, and Ti are detected, they represent only a total of 1.5 at.% - likely residual material deposited during tribofilm formation - whereas carbon accounts for 40 at.%, oxygen 15 at.%, and iron 43.5 at.% (the latter corresponding primarily to the underlying substrate). This strongly suggests that the carbon-rich material corresponds to degraded PAO resulting from the applied electric current.

at.%	Zn1_Tif(Si)0,5	
	0A	**0A then 0,5A with PAO**
C 1s	**18,8**	**19,7**
Fe 2p	**1,1**	**5,9**
O 1s	**51,2**	**51,8**
P 2p	**8,6**	**5,2**
S 2p	**1,6**	**1,2**
Zn 2p	**4,6**	**2,6**
Si 2p	**0,9**	**2,0**
Ti 2p	**11,1**	**9,4**
Ca 2p	**2,1**	**2,4**

Table 43: XPS chemical composition of tribofilms formed at 0A or with an applied current of 0A with a blend of ZDDP and silane-functionalized TiO_2 NPs (Zn1_Tif(Si)0.5) followed by 0.5A with PAO6. Conducted using a NEXSA spectrometer.

XPS analysis of the wear track on the disc (**Table 43**) once again shows an increase in Fe content, although more moderate than in the previous experiments. This increase is likely linked to the generation of metallic debris, at the expense of tribofilm-related elements (Zn, P, S, Ti).

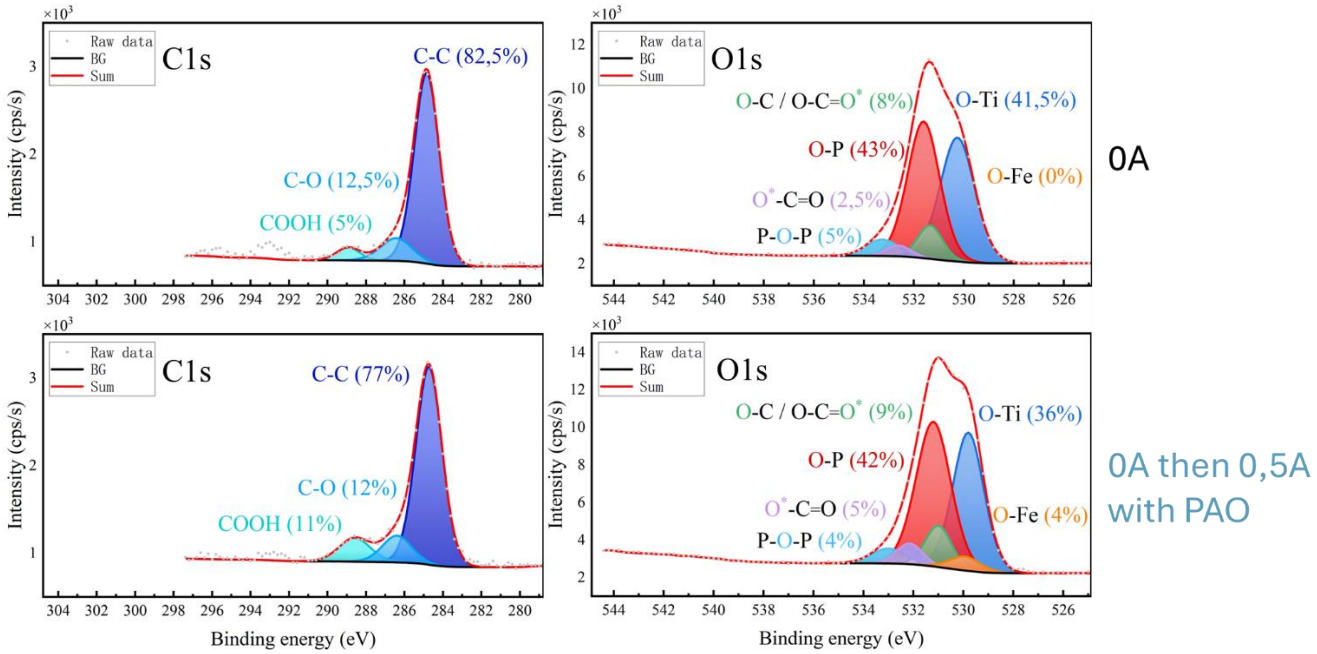

Fig. 303: C1s and O1s XPS spectra of tribofilms formed at 100°C with an applied current of 0A with a blend of ZDDP and silane-functionalized TiO_2 NPs (Zn1_Tif(Si)0.5) followed by 0.5A with PAO6.

In contrast to the conditions where the Zn1_Tif(Si)0.5 lubricant was still present during 0.5A current application, the detected Fe is only weakly oxidized (Fig. 303).

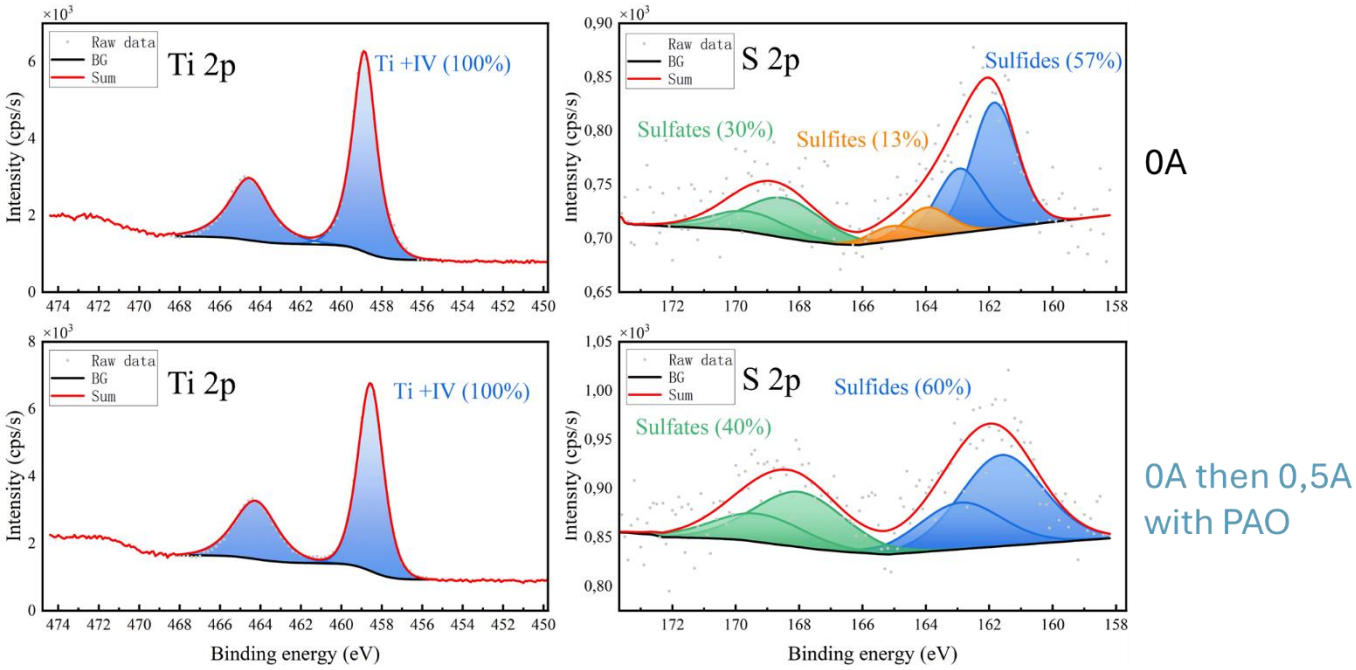

Fig. 304: Ti2p and S2p XPS spectra of tribofilms formed at 100°C with an applied current of 0A with a blend of ZDDP and silane-functionalized TiO_2 NPs (Zn1_Tif(Si)0.5) followed by 0.5A with PAO6.

Sulfur, however, is still found as a mixture of metallic sulfides and sulfates (Fig. 304), as already observed in the tribofilm formed without current. Titanium is again present in the form of TiO_2 only.

This experiment demonstrates that the tribofilm formed by the Zn1_Tif(Si)0.5 mixture is capable of effectively protecting the surface even in the absence of lubricant to regenerate the film. In most cases, the current primarily damages the unprotected substrate regions rather than the tribofilm itself. This damage is associated with the adhesion of metallic particles on the cathode (ball), which generates a local overheight that subsequently scratches the anode (disc). Evidence also suggests that the base oil may undergo degradation under current, particularly in these deposited regions.

While this tribofilm is not perfect, a single instance was observed in which a deposit formed directly in the middle of the track, causing localized damage to the tribofilm. In this sense, the tribofilm generally remains intact because the adjacent substrate is damaged first, providing a preferential path for current flow and thereby sparing the protected areas.

Conclusion and Perspectives

This chapter provides a comprehensive view of how electrical current affects tribofilm formation, structure, and performance for ZDDP, silane-functionalized TiO_2 nanoparticles, and their mixture under reciprocating sliding conditions.

Overall, the damage caused by electrification that has been observed can be summarized as the formation of thick deposits on the cathode, which then scratch the anode. The origin of these debris has not been definitively determined. They could initially originate from substrate wear occurring prior to tribofilm formation, but deposit formation has also been observed for nanoparticle suspensions, which demonstrated their ability to protect the substrate very rapidly in unelectrified conditions. Another, more mechanically severe hypothesis is that these debris result from highly localized and instantaneous heating at the contact due to the current, creating a micro-weld between the anode and the cathode. This micro-weld is then immediately broken by the relative motion of the surfaces, leading to the detachment of a portion of the substrate. These particles then adhere to the cathode, as reduction occurs there from an electrochemical standpoint.

The deposit formed on the cathode, primarily composed of freshly exposed steel, is highly reactive. It can therefore react with dissolved oxygen in the lubricant to form iron oxides or with additives to form a tribofilm. We observed that solutions containing ZDDP show areas on the ball that are very rich in sulfur, but not necessarily in other ZDDP decomposition elements (Zn and P). It is known that the tribofilm formed by ZDDP begins with the formation of a layer of iron and zinc sulfides. It is thus possible that these sulfur-rich surfaces correspond to the freshly exposed deposit on which this primary layer formed, but for which the subsequent stages of tribofilm formation (phosphate glass formation) did not have time or an opportunity to develop.

For suspensions containing nanoparticles, we observed deposits larger and thicker than those formed with ZDDP alone. Here, it appears that their high reactivity towards the freshly exposed steel of the initial deposits drives the rapid formation of a tribofilm but without preventing the generation of new wear debris. Indeed, this high reactivity leads to the formation of thick deposits that further scratch the surface, promoting the adhesion of newly generated debris to the deposit and exacerbating wear. In fact, if the tribofilm is formed first and then deprived of additives before applying current, deposit formation is still observed, but with much smaller dimensions in both width and thickness.

Since these deposits are observed on the cathode, it would also be interesting to investigate how lubricants behave under alternating current conditions, as the periodic reversal of current could influence both the formation and removal of deposits, modify tribofilm growth dynamics, and potentially alter the electrochemical interactions at the contact interface.

Bibliography

[1] Peng Z, Nassif A, Georgi F, Montmitonnet P, Lahouij I. Electric polarity: A key factor in lubricated wear of bearing steel. Tribology International 2025;209:110748. https://doi.org/10.1016/j.triboint.2025.110748.

[2] Farfan-Cabrera LI, Hernández-Peña A, Resendiz-Calderon CD, Lee P, Sanchez C, Lee S, Erdemir A. Electrified four-ball testing of ZDDP and MoDTC as additives in low-viscosity synthetic oil. Wear 2025:205835. https://doi.org/10.1016/j.wear.2025.205835.

[3] Farfan-Cabrera LI, Lee S, Skowron S, Erdemir A. Enhancing Lubrication of Electrified Interfaces by Inert Gas Atmosphere. Journal of Tribology 2025;147:051104. https://doi.org/10.1115/1.4066649.

[4] Yousuf A, Spikes H, Guo L, Kadiric A. Influence of Electric Potentials on Surface Damage in Rolling–Sliding Contacts Under Mixed Lubrication. Tribol Lett 2025;73:45. https://doi.org/10.1007/s11249-025-01977-2.

[5] Deshpande P, Yelkarasi C, Lee S, Farfan-Cabrera LI, Erdemir A. Electrotribochemical formation of abrasive nano-carbon particles under electrified conditions on lubricated sliding contacts. Carbon 2024;228:119425. https://doi.org/10.1016/j.carbon.2024.119425.

General Conclusion

The work presented in this thesis addresses the current tribological challenges associated with the transition toward more efficient and environmentally sustainable mechanical systems. The progressive electrification of the automotive industry and the pursuit of improved energy efficiency impose increasingly severe operating conditions, characterized by reduced lubricant viscosity, higher contact stresses, and the emergence of specific electro-tribological phenomena. In this context, mastering boundary lubrication regimes has become a key issue to ensure the reliability and durability of mechanical components.

This thesis therefore aimed to deepen the understanding of the mechanisms governing interactions between surfaces and tribological additives under boundary lubrication conditions, while proposing innovative technological approaches to enhance the tribological performance of next-generation mechanical systems. To achieve these objectives, two complementary strategies were developed: on one hand, the optimization of lubricant formulations through the incorporation of TiO_2 nanoparticles in combination with conventional additives such as ZDDP and MoDTC; and on the other hand, the design and elaboration of Ti/TiO_x composite coatings deposited by cold spray, intended to reinforce surfaces tribological performance under severe contact conditions.

The results obtained throughout this work provide new insights into the possible synergies between organometallic additives and nanoparticles, the physicochemical mechanisms governing tribofilm formation, and the potential of composite coatings for reducing wear and friction. Furthermore, the study of the influence of electrical currents on additive-containing systems has improved our understanding of the coupled mechanical, chemical, and electrical interactions occurring in tribological contacts.

Accordingly, this general conclusion aims to summarize the main findings of this research, highlight its scientific and technological contributions, identify the limitations encountered, and propose perspectives for future research and industrial implementation.

Following this general framework, the main findings of each chapter are summarized below to highlight the overall coherence and scientific contribution of the present research.

Chapter 1 – Literature Review

The first chapter established the scientific foundations of this work by reviewing the state of knowledge in the field of tribology, with particular attention to boundary lubrication mechanisms, lubricant formulation, and surface engineering strategies. It emphasized the growing importance of tribological optimization in the context of energy efficiency and vehicle electrification, where conventional lubrication regimes are increasingly challenged.

This review first detailed the fundamental concepts of friction, wear, and lubrication, outlining the transition between hydrodynamic, mixed, and boundary regimes. It underscored that, in boundary lubrication, surface asperities come into direct contact, making the formation of protective tribofilms by additives essential for reducing wear and friction.

Subsequently, the composition and functionality of lubricant additives were described, focusing on two key organometallic compounds: **zinc dialkyldithiophosphate (ZDDP)**, a benchmark anti-wear additive known for forming protective phosphate-based tribofilms, and **molybdenum dithiocarbamate (MoDTC)**, a friction modifier capable of generating low-shear MoS_2 nanosheets. The

complementary but sometimes competitive behavior of these additives was highlighted, underlining the complexity of their chemical and mechanochemical interactions within boundary contacts.

The chapter then introduced the emerging role of **nanoparticles - particularly TiO_2** - as potential tribological additives. Their nanoscale dimensions and reactivity offer opportunities to enhance **tribofilm robustness and durability**. However, the discussion also emphasized the challenges related to their dispersion **stability, agglomeration, and compatibility with other additives**. The review of prior studies revealed that, under certain conditions, **TiO_2 nanoparticles can act synergistically with ZDDP or MoDTC**, improving wear protection and friction reduction.

In parallel, the chapter explored the second approach of this thesis: surface engineering through advanced coatings. After presenting the main classes of tribological coatings (PVD, CVD, thermal spray, and polymeric systems), the focus was placed on the **Cold spray process** as an innovative low-temperature deposition technique. This method allows the fabrication of dense, adherent metallic or composite coatings while preserving material integrity. The review concluded by identifying research gaps regarding the application of **cold sprayed coatings in boundary lubrication conditions**.

In addition, the specific factors responsible for the **severization of the boundary lubrication regime in electric vehicles** were discussed. Electric drivetrains deliver **higher torque from standstill** compared with internal combustion engines, which increases the mechanical load on contacting surfaces during start-up. Moreover, the **broader rotational speed range** of electric powertrains often necessitates the use of **lower-viscosity transmission fluids**, further reducing the lubricating film thickness and enhancing boundary lubrication severity. The **presence of stray currents** induced by the electromagnetic fields generated by the electric motor can also markedly accelerate wear processes. These currents promote the formation of **oxidized, abrasive debris** while simultaneously hindering the development of **protective tribofilms**, ultimately leading to more severe surface degradation under electrified conditions.

Overall, Chapter 1 defined the scientific context and motivation of the study, positioning this work at the intersection of additive-nanoparticle synergy, surface engineering, and electrified tribological systems, and establishing the conceptual framework for the experimental investigations presented in the subsequent chapters.

Chapter 2 – Materials and Methods

Chapter 2 details the experimental framework supporting this research, encompassing the preparation of lubricant formulations, tribological testing setups, and the development of cold sprayed coatings.

The study employs a **polyalphaolefin (PAO) base oil** combined with conventional additives - **ZDDP** and **MoDTC** - and **TiO_2 nanoparticles**. Particular attention is given to **nanoparticle stabilization**, comparing physical dispersion and chemical functionalization methods to ensure both suspension stability and effective tribological performance.

Tribological experiments are carried out using a **ball-on-disc tribometer** under controlled loads and temperatures to simulate boundary and mixed lubrication regimes. In parallel, a custom **electrified module** was designed and integrated to the tribometer to investigate the influence of electric currents on friction, wear, and tribofilm formation, providing an experimental basis for electro-tribological analysis.

Surface and film characterization relies on a multi-scale approach, combining **profilometry**, **SEM/EDS**, **XPS**, and **TEM** to assess the morphology, thickness, and chemistry of the tribofilms.

The chapter also presents the elaboration of **Ti/TiO_x composite coatings** produced by **cold spray deposition**. A systematic optimization of **surface preparation parameters** is performed to enhance particle adhesion and interfacial bonding. Likewise, **deposition parameters** such as gas pressure, and particle morphology are adjusted to control coating density and porosity. The resulting mechanical, physical, and tribological properties - notably hardness, roughness, and tribological performances - make these coatings suitable for lubricated contact.

Overall, this chapter establishes the methodological basis for correlating additive chemistry, nanoparticle behavior, and coating properties with the tribological responses explored in the following sections.

Chapter 3 – Synergy between Traditional Additives and TiO_2 Nanoparticles

Chapter 3 focuses on the investigation of tribological interactions between conventional lubricant additives and TiO_2 nanoparticles under boundary lubrication conditions. The study aims to elucidate how these components interact, either synergistically or competitively, to influence friction, wear, and tribofilm formation mechanisms.

The chapter first examines the **intrinsic tribological behavior of TiO_2 nanoparticles** dispersed in a polyalphaolefin base oil. The results demonstrate that their performance strongly depends on the **dispersion and surface functionalization strategy**. Both stabilization routes - physical dispersion and chemical functionalization - are evaluated in terms of suspension stability and tribological efficiency. Chemically functionalized nanoparticles exhibit improved colloidal homogeneity and reduced sedimentation compared to physically dispersed ones. Among them, **silane-functionalized TiO_2 nanoparticles** show the **highest long-term stability**, whereas **oleic-acid-functionalized nanoparticles** display **better tribological performance** in boundary lubrication conditions owing to their higher reactivity and easier access to the contact zone. These results highlight the critical need to balance colloidal stability and surface reactivity to achieve optimal tribological behavior of nanoparticle-based additives.

For the silane-functionalized nanoparticles, it is shown that the nanoparticles chemically react with the steel substrate, leading to the formation of **an initial iron titanate layer**, which is then followed by the growth of the remaining TiO_2-based tribofilm.

The second part of the chapter investigates **hybrid lubricant formulations** combining TiO_2 nanoparticles with **MoDTC** and **ZDDP**.

The results reveal a **chemical synergy** between **MoDTC and unmodified TiO_2 nanoparticles**, in which the nanoparticles promote the **tribochemical conversion of MoDTC into the lubricating MoS_2 phase**. This catalytic-like effect leads to a significant reduction in friction and wear compared to formulations containing MoDTC alone. XPS analyses confirm the coexistence of MoS_2 and TiO_2 species within the tribofilm, supporting the presence of a chemically cooperative mechanism. However, this synergy is only observed when **direct interaction** between MoDTC molecules and the TiO_2 surface is possible. In the case of surface-functionalized nanoparticles, the organic capping layer acts as a barrier, hindering this interaction and thereby suppressing the synergistic effect. These findings highlight the crucial role of nanoparticle surface chemistry in governing the efficiency of additive - nanoparticle cooperative mechanisms.

The interaction between ZDDP and TiO_2 nanoparticles also exhibits a synergistic effect, but this synergy is not of chemical nature. Regardless of the nanoparticle surface state - whether oleic acid-dispersed, oleic acid-functionalized, or silane-functionalized - the combination of ZDDP and TiO_2 consistently leads to a reduction in friction and wear and to the formation of a thicker tribofilm compared to each additive used separately.

This synergy originates from a **complementarity in the kinetics and tribofilm formation conditions** of the two species rather than from direct chemical interaction. The high surface reactivity of TiO_2 nanoparticles allows them to react first with the steel substrate during the initial sliding cycles, forming a discontinuous TiO_2-rich tribofilm through a tribosintering mechanism localized at asperity contact zones. This early protective layer prevents severe wear during the initial stage of operation and prepares the surface for subsequent additive activation. As the contact temperature and shear increase, ZDDP activation occurs, promoting the growth of a phosphate-based tribofilm that extends over lower-pressure regions and complements the TiO_2-rich areas. The result is the formation of a **composite tribofilm** consisting of a phosphate glass matrix embedding TiO_2 particles.

Through these investigations, Chapter 3 provides new mechanistic insight into the **tribochemical interactions** between organometallic additives and oxide nanoparticles. It demonstrates that **TiO_2 can act as a catalytic or structural component** that modifies tribofilm composition and durability.

In addition, this study highlights the **reliability and consistency of the analytical results**, achieved by cross-correlating data from complementary characterization techniques. For instance, the **elemental compositions obtained by EDX analysis of TEM cross-sections** are found to be in very good agreement with **surface analyses performed by XPS**, confirming the robustness of the experimental observations.

Furthermore, the implementation of **intermediate-cycle tests** proves highly valuable for advancing mechanistic understanding, as it enables the monitoring of tribofilm growth kinetics. These intermediate analyses allow hypotheses regarding the **stepwise tribofilm growth mechanisms** to be formulated and subsequently confirmed by **TEM cross-sectional observations**. Such intermediate-cycle testing should therefore become **a systematic approach in future tribological studies** to refine mechanistic interpretation and improve the understanding of tribofilm dynamics.

Chapter 4 – Cold-Sprayed Ti/TiO_x Composite Coatings: From Elaboration to Tribological Properties

Chapter 4 explores another major research axis of this thesis, dedicated to the development and tribological evaluation of **cold sprayed Ti/TiO_x composite coatings**. This part investigates how processing parameters, microstructural characteristics, and tribological performance are interrelated, with the goal of designing surface systems capable of operating under severe boundary lubrication.

The chapter first details the influence of **cold spray process parameters** on coating properties. The initial part focuses on **single-component coatings** to understand and optimize both substrate surface preparation and the cold spray deposition process.

The **optimization of surface preparation** through fluid-jet methods significantly enhances particle adhesion and promotes dense interfacial bonding between the deposited particles and the substrate. Among the techniques investigated, **water jet method** provides superior adhesion compared to **liquid nitrogen jet** treatment. This improvement is attributed to the higher surface roughness generated and the lower level of contaminants introduced by the abrasive media.

As a result, this preparation method enables a reduction of the **deposition pressure** needed to achieve good coating adhesion to the substrate, thus decreasing the overall **operational cost of the cold spray process**.

Regarding deposition parameters, the results show that **increasing the gas pressure** not only improves the coating adhesion to the substrate but also enhances **interparticle cohesion** and reduces **porosity**, leading to denser and mechanically stronger coatings.

Based on these findings, a **composite Ti/TiO_x coating** is developed. Although spherical Ti particles appeared more suitable in the previous single-component study, **tribological tests reveal superior performance with irregular Ti particles**. The optimized composite coating, produced from a mixture containing **50 vol.% irregular Ti and 50 vol.% TiO_x**, corresponding to an actual reinforcement content of about **16 vol.% TiO_x** in the final deposit, exhibits excellent **wear resistance** and **compatibility with lubricant additives** such as **ZDDP** and **MoDTC**. These results demonstrate that the controlled introduction of oxide reinforcement, combined with an optimized particle morphology, enables the fabrication of **robust, tribologically efficient coatings** suitable for boundary-lubricated applications.

Chapter 5 – Effects of Electric Current on the Tribological Performance of Boundary Additives

This chapter investigated the impact of electrical current on the formation and durability of tribofilms generated by different lubricant additives in steel-steel contacts. Three systems were compared: ZDDP (the benchmark anti-wear additive), silane-functionalized TiO_2 nanoparticles, and their synergistic blend.

The application of a direct current altered the balance between friction, wear, and protective film growth:

- For **ZDDP alone**, current application disrupted tribofilm formation by promoting the generation of metallic and oxide debris, and led to a less homogeneous, less stable, and more wear-prone surface coverage. The protective tribofilm, however, remained partially active and showed some capacity for local reformation through the incorporation of metallic wear particles.
- For **silane-functionalized TiO_2 nanoparticles**, electrical current application improved the tribological behavior by lowering and stabilizing the coefficient of friction. This beneficial effect arises from **enhanced tribosintering**, as the current provides additional energy to the system - most likely in the form of localized heating - which promotes compaction and densification of the tribofilm. However, this densification was accompanied by increased wear due to the formation of thick deposits (~1 µm) at the track edges and on the **cathode (ball)**. These deposits, composed of steel debris and compacted nanoparticles, act as abrasive features that damaged the **anode (disc)** surface.
- For the **ZDDP + TiO_2 nanoparticle blend**, friction remained low and stable, and tribofilm formation was still fast due to the nanoparticles' high reactivity. Nevertheless, the application of current led to the formation of thick deposits on the **cathode**, which scratched and contributed to the wear of the anode. In parallel, the current reduced the chemical contribution of ZDDP and favored the formation of iron oxides, leading to diminished wear protection compared to the non-electrified condition.

Overall, **deposit formation on the cathode was systematically observed in all cases**. This phenomenon was particularly exacerbated in the presence of nanoparticles, whose strong reactivity caused them to interact with iron-rich deposits, increasing their thickness and hardness and thereby intensifying the scratching and wear of the anode surface.

The study of **pre-formed tribofilm durability** under electrical current revealed that:

- ZDDP-derived tribofilms were locally damaged but exhibited a notable capacity for self-repair through the incorporation of metallic debris, maintaining partial protective function.
- Hybrid ZDDP/TiO_2 tribofilms were more resistant to current flow: the current tended to bypass tribofilms rather than destroy them.

Finally, **recent studies conducted at CEMEF within the work of Zhengyuan Peng** using short-cycle electrified tribotests revealed evidence of **arcing phenomena** - partial melting, pitting, and surface cratering - within the contact area during the first cycles of friction. These localized electrical discharges are most likely responsible for the significant wear observed in our experiments, as they intensify both thermal and mechanical stresses at the sliding interface.

Perspectives

Several directions emerge from this work that could further advance the understanding and optimization of additives - nanoparticles - coating systems under both conventional and electrified lubrication conditions.

A first perspective concerns the **experimental methodology**. Among all the tests performed, the **intermediate-cycle experiments** have proven particularly valuable for elucidating tribofilm formation mechanisms. These tests enable monitoring of **wear evolution** and **tribofilm development**, while allowing detailed characterization of the film's **morphology (SEM)** and **chemical composition (XPS)** at different stages of the contact life. In future studies, these intermediate tests should be **systematically implemented**, as they provide a powerful tool for linking tribofilm kinetics to mechanical and chemical transformations within the interface.

Regarding **electrified conditions**, the present study focused on a single current intensity (0.5 A) and polarity configuration (ball as cathode). This choice ensured experimental control but future work should therefore investigate a broader range of **current intensities**, including both **lower and higher values**, to identify threshold effects. Moreover, performing tests under **alternating current (AC)** would be particularly interesting, since the current work demonstrated that under **direct current (DC)** conditions, material deposition systematically occurs on the cathode. Studying AC regimes could thus provide valuable insight into the reversibility of electrochemical processes and their influence on tribofilm formation.

A third avenue involves the **effect of contact kinematics**. Introducing a **rolling-sliding motion**, more representative of real gear contacts, could modify both the mechanical activation and the local electrical conditions, thereby influencing the formation and stability of nanoparticle-based tribofilms. In electrified configurations, such mixed kinematics might also affect the localization and morphology of the deposits formed on the cathodic surface.

Another perspective relates to the **quantitative characterization of nanoparticle stability**. In this study, colloidal stability was only evaluated **visually** over time. From an industrial standpoint, it would be valuable to conduct **quantitative measurements** using dedicated equipment (e.g., dynamic light scattering or zeta potential analysis) to determine particle size evolution, aggregation kinetics, and long-term suspension behavior in lubricant formulations.

Concerning **cold sprayed coatings**, future tribological tests could be performed using the **lubricant formulations that showed the best results in steel-steel contacts**, such as the **Zn1_Tif(Si)_0.5 mixture**, to assess whether the observed reactivity and tribochemical compatibility are **substrate-dependent**. Moreover, since a **reinforcement content of about 16 vol.% TiO_x** already provides nearly wear-free performance under boundary lubrication with additivated oils, it would be interesting to investigate whether **increasing the oxide content** could extend this benefit to **non-additivated base oils** (e.g., pure PAO).

Finally, given that **TiO_x phases exhibit electrical conductivity** - unlike stoichiometric TiO_2 - additional **electrified tribological tests** should be carried out to evaluate their influence on current flow, film formation, and electrochemical stability within the contact.

RÉSUMÉ

La réduction des émissions de CO_2 et l'amélioration de l'efficacité énergétique reposent en partie sur la maîtrise du frottement et de l'usure. En limitant les pertes d'énergie et en prolongeant la durée de vie des composants, la tribologie contribue directement à la durabilité des systèmes mécaniques. La transition vers la mobilité électrique s'inscrit dans cette démarche, mais introduit de nouveaux défis tribologiques. Les moteurs électriques délivrent un couple élevé dès les faibles régimes et génèrent des courants parasites susceptibles de modifier la réactivité des additifs et la stabilité des tribofilms. Ces conditions exigent des lubrifiants à faible viscosité, performants en lubrification limite et adaptés aux environnements électrifiés. Cette étude s'intéresse à un triplet tribologique de la lubrification limite, reliant le lubrifiant, la surface et l'environnement électrifié. Elle met en évidence la synergie entre additifs conventionnels (MoDTC et ZDDP) et nanoparticules de TiO_2, le comportement tribologique de revêtements Ti/TiO_x élaborés par projection à froid (Cold spray), et l'influence des courants électriques sur la formation et la stabilité des tribofilms. L'approche intégrée proposée apporte de nouvelles pistes pour concevoir des systèmes tribologiques durables et performants pour la mobilité de prochaine génération.

MOTS CLÉS

Lubrification limite ; Tribofilm ; Frottement, Usure ; Nanoparticules de TiO_2 ; Revêtements Cold Spray ; Contact électrifié.

ABSTRACT

The reduction of CO_2 emissions and the improvement of energy efficiency partly rely on the control of friction and wear. By minimizing energy losses and extending component lifetime, tribology directly contributes to the sustainability of mechanical systems. The transition toward electric mobility follows this objective but introduces new tribological challenges. Electric motors deliver high torque at low speeds and generate stray currents that can alter additive reactivity and tribofilm stability. These conditions require low-viscosity lubricants with strong boundary lubrication performance and compatibility with electrified environments. This study focuses on a tribological triplet of boundary lubrication regime, linking the lubricant, the surface, and the electrified environment. It highlights the synergy between conventional additives (MoDTC and ZDDP) and TiO_2 nanoparticles, the tribological behavior of Ti/TiO_x coatings produced by Cold spray deposition, and the influence of electric currents on tribofilm formation and stability. The integrated approach proposed here provides new insights for designing durable and high-performance tribological systems for next-generation mobility.

KEYWORDS

Boundary lubrication; Tribofilm; Friction, Wear; TiO_2 nanoparticles; Cold Spray coatings; Electrified contact.